

Computational characterization of novel solar light-harvesting dyes and electron-transfer systems



seit 1558

Dissertation

zur Erlangung des akademischen Grades doctor rerum naturalium

(Dr. rer. nat.)

vorgelegt dem Rat der Chemisch-Geowissenschaftlichen Fakultät der
Friedrich-Schiller-Universität Jena

von Stephan Kupfer

geboren am 18.05.1985 in Pößneck

1. Gutachter: Prof. Dr. Leticia González, Universität Wien

2. Gutachter: Prof. Dr. Benjamin Dietzek, Friedrich-Schiller-Universität Jena

Tag der öffentlichen Verteidigung: 06.02.2013

Abstract

Light-harvesting devices are of fundamental importance in solar energy conversion. By mimicking natural photosynthetic systems, artificial photosynthetic adaptations are usually based on using organic dyes and transition metal complexes as light-harvesting antennas. To this aim, donor- π -acceptor dyes are potentially used as antennas in dye sensitized solar cells. The advantages of organic dyes are their easily adjustable optical properties coupled with low production costs. However, they usually exhibit, compared to transition metal complexes, shorter excited state life times and lower photostability. Metal complexes, in particular ruthenium(II) polypyridine complexes, are widely studied because of their unique combination of chemical and physical stability, pronounced absorption, and redox and catalytic activities. Admittedly, such systems are high priced and lack intense absorption bands in the visible region of the solar radiation spectrum. The present thesis is a theoretical investigation of the photophysical and photochemical properties of several light-harvesting antennas and photosensitisers.

The first part of the thesis is devoted to study a series of donor- π -acceptor dyes, based on 4-methoxy-thiazole chromophores and ruthenium(II) polypyridine complexes with 4*H*-imidazole ligands. Such dyes are of interest in the scope of dye sensitized solar cells as well as for artificial photosynthesis. Quantum chemical and TD-DFT methods have been applied to investigate several photophysical properties of the dyes, such as e.g. their absorption and emission spectra. Special mention deserve the performed simulation of resonance Raman intensities, which is still far from routine and gives the possibility to test the accuracy of electronic excited state gradients. Based on the calculated resonance Raman spectra, protonation effects and the character of the involved excited states could be unraveled. Substitution as well as anchoring was found to be of substantial influence for the photophysical properties, such as excitation energies and excited states characters, of the ruthenium(II) complexes. Finally, to allow for applications of the dyes, as e.g. in dye sensitized solar cells, a detailed knowledge of electron transfer processes occurring at the dye-semiconductor interface is necessary. Such processes can be investigated by means of semi-classical Marcus theory. To this aim, a model system of a ruthenium(II) dye linked to a titanium dioxide cluster was constructed. Preliminary quantum mechanical/molecular mechanical simulations coupled with molecular dynamics have been performed in order to get the electron transfer rate.

Table of Contents

List of Figures	ix
List of Tables	xi
List of Abbreviations	xiii
1 Introduction	1
1.1 Artificial Adaptations of Photosynthesis	1
1.2 Dye sensitized Solar Cells	5
1.3 Electron Transfer in Nature and Artificial Systems	6
1.4 Goals and Outline of this Thesis	7
2 Theory	9
2.1 Basic Quantum Chemistry	9
2.2 Multiconfigurational Methods	10
2.3 Density Functional Theory based Methods	13
2.3.1 Density Functional Theory	13
2.3.2 Time-dependent Density Functional Theory	14
2.4 Combination of Quantum and Molecular Mechanics	15
2.5 Molecular Dynamical Simulations	15
2.6 Resonance Raman Spectroscopy	16
2.6.1 Classical Raman	16
2.6.2 Quantum mechanical resonance Raman	18
2.7 Electron Transfer Processes	21
2.7.1 Marcus Theory of Electron Transfer	21
2.7.2 Intra-molecular Electron Transfer	24
3 Results	27
3.1 Organic Dyes for Dye-Sensitized Solar Cells (DSSCs)	28
3.1.1 Excited State Properties of 4-Methoxy-1,3-Thiazole Donor-Acceptor Dyes	28

3.1.2	Influence of Charge Transfer States on Ground State Structures	31
3.1.3	Twisted Intra-Molecular Charge Transfer <i>vs.</i> Planar Intra-Molecular Charge Transfer	35
3.2	Ruthenium(II)-4 <i>H</i> -Imidazole Black Absorbers	39
3.2.1	Optical Properties of 4 <i>H</i> -Imidazole-Ruthenium(II) Complexes	39
3.2.2	Photo Induced Relaxation Pathways of Ruthenium(II)-4 <i>H</i> -Imidazole complexes	48
3.3	Electron Transfer in a Ruthenium(II)-4 <i>H</i> -Imidazole-Rutile model	50
4	Appended Publications	61
4.1	4-Methoxy-1,3-thiazole based donor-acceptor dyes: Characterization, X-ray structure, DFT calculations and test as sensitizers for DSSC	61
4.2	An Assessment of RASSCF and TDDFT Energies and Gradients on an Organic Donor-Acceptor Dye assisted by Resonance Raman Spectroscopy	75
4.3	Arylamine-Modified Thiazoles as Donor-Acceptor Dyes: Quantum Chemical Evaluation of the Charge-Transfer Process and Testing as Ligands in Ruthe- nium(II) Complexes	112
4.4	Protonation effects on the resonance Raman properties of a novel (terpyridine)Ru(4 <i>H</i> - imidazole) complex: an experimental and theoretical case study	130
4.5	Influence of Multiple Protonation on the Initial Excitation in a Black Dye	140
4.6	A Novel Ru(II) Polypyridine Black Dye Investigated by Resonance Raman Spectroscopy and TDDFT Calculations	150
4.7	Structural control of photoinduced dynamics in 4 <i>H</i> -imidazole-Ruthenium dyes	161
5	Summary and Outlook	205
6	Zusammenfassung	209
A	Appendix	215
	Acknowledgements	229
	Selbstständigkeitserklärung	231
	Curriculum vitae	233
	List of Publications	237

List of Figures

1.1	Light harvesting antennas in the PSII; a) basic porphyrin structure, b) chlorophyll a and chlorophyll b, c) β -carotin.	2
1.2	Electron donor or rather water splitting catalysts, photosensitizer with additional light-harvesting antenna, and electron acceptor or rather hydrogen forming catalysts.	3
1.3	a) blue, b) green, and c) red absorbing 4-methoxy-1,3-thiazole dyes.	4
1.4	Scheme of a hydrogen producing photonic micelle fueled by solar energy as proposed in the PhotoMic project; Förster Resonance Energy Transfer (FRET) is used to focus the absorbed energy from several dye to a transition metal photosensitizer.	4
1.5	Schematic representation of a conventional DSSC with a organic dye, a titanium dioxide photoanode, a platinum cathode and a I_3^-/I^- redox pair for charge regeneration of the oxidized dye.	5
2.1	Principles of CASSCF a) and RASSCF b) wave functions	11
2.2	Generalized scheme of RR scattering within the IMDHOM for a fundamental transition $g_0 \rightarrow g_1$ and in resonance with the excited state e . PESs of the excited state E^e and the ground state E^0 are merely displaced by $\Delta_{e,l}$	20
2.3	Marcus parabolas for the states RO and OR, the reorganization energies λ_{RO} and λ_{OR} , the reaction free energy ΔG and the activation free energy ΔG^* in terms of the gap energy ΔE ; ΔE_{RO} and ΔE_{OR} denote the mean energy gaps of the respective state.	23
2.4	Ionization energy IE_{RO} and electron affinities IE_{OR} in the ionic configuration R^N of the states RO and OR, respectively.	25

3.1	Investigated 4-methoxy-1,3-thiazole based donor-acceptor dyes: A–D have been studied applying both experimental and theoretical methods, while E was exclusively studied theoretically. A–C share the same linker and anchoring groups, while the π -system of the donor was increased from 4-methoxy-phenyl (A) to <i>N,N</i> -di-4-tolylaniline (B) and further to <i>N,N</i> -di-4-methoxy-phenyl (C). B , D , and E differ only in the size of the linker: the conjugated π -system was increased with a second thiophene (D) and in addition an 2-ethylene group (E).	28
3.2	MOs of E contributing to the main transitions of the S_1 obtained at CAM-B3LYP/6-31G(d,p) level of theory in tetrahydrofuran.	29
3.3	Molecular orbitals for RASSCF(30,2,2;14,2,11) (solid grey), RASSCF(16,2,2;7,2,7), RASSCF(16,3,3;7,2,7) and RASSCF(16,4,4;7,2,7) (left hand side) calculations.	32
3.4	RR spectra of 1 in resonance with the first absorption band. The calculated RR spectra with the B3LYP and CAM-B3LYP ground state force fields and the excited state gradients at TD-B3LYP, TD-CAM-B3LYP and SA2-RASSCF (16,3,3;7,2,7) level of theory are shown in a) and b). The RR intensity pattern with TD-M06-2X in the M06-2X optimized ground state geometry is reported in c). The calculated spectra of b) and c) are compared to the experimental RR spectrum in d) recorded at an excitation wavelength of 458 nm.	34
3.5	Investigated 4-methoxy-1,3-thiazole based donor-acceptor ligands with different donor groups, F and G were studied applying both experimental and theoretical methods, while H was exclusively studied theoretically. All three ligands share the same 4-methoxy-1,3-thiazole linker and pyridyl acceptor, while different donor groups have been used: F exhibits a bis(4-methoxy-phenyl)- <i>N</i> -phenylaniline donor, G and H <i>N</i> -phenyl-carbazole donors connected to the linker via the phenyl and carbazole, respectively.	35
3.6	Schematic representation of the electronic ground and first excited singlets state of F and G in MeOH and heptane; all values in black refer to the experimental values, while the blue values were obtained at the PCM-B3LYP(35)/6-31G(d,p) level of theory in the solvated equilibrium structures. The depicted HOMOs and LUMOs refer to the MOs involved in the absorption (optimized S_0 state) and the SOMOs to the MOs involved in the emission (optimized S_1 state).	36
3.7	PESs of the S_0 and S_1 states calculated at the B3LYP(35)/6-31G(d,p) level and with a polarizable continuum model for MeOH and heptane.	37

3.8	Investigated ruthenium(II)-4 <i>H</i> -imidazole complexes with terpyridine a) and bipyridine ligands b) for different protonation states. In case of a) a series of substituents in the 4 <i>H</i> -imidazole have been studied. In all theoretical simulations the <i>tert</i> -butyl groups of the polypyridine ligands have been approximated by methyl groups.	39
3.9	Theoretical absorption spectra of the Ru and RuH species in acetonitrile. A Lorentzian function with a half-width of 20 nm is employed to broaden the transitions in the spectrum based on the oscillator strengths represented by black sticks.	40
3.10	MOs involved in the main configurations of the states responsible for the absorption and RR properties of the deprotonated (Ru) and protonated (RuH) complexes.	41
3.11	Theoretical RR spectra of Ru (STA, state S_6 and S_{11}) and RuH (STA, state S_4 and S_9) in resonance with the first and the second absorption bands. The modes associated with vibrations located on the terpyridine ligand are given in red color. A Lorentzian function with a FWHM of 5 cm^{-1} is employed to broaden the calculated transitions.	42
3.12	Theoretical absorption spectra of the RuMe and RuMeH species in acetonitrile. A Lorentzian function with a half-width of 20 nm is employed to broaden the transitions in the spectrum based on the oscillator strengths represented by black sticks.	42
3.13	Theoretical absorption spectra of the RuNMe₂ , RuHNMe₂ , RuHNHMe₂ , and RuHNH₂Me₂ species in acetonitrile. A Lorentzian function with a half-width of 3000 cm^{-1} is employed to broaden the transitions in the spectrum based on the oscillator strengths represented by black sticks.	44
3.14	Theoretical absorption spectra of the RuCOOEt and RuHCOOEt species in acetonitrile. A Lorentzian function with a half-width of 20 nm is employed to broaden the transitions in the spectrum based on the oscillator strengths represented by black sticks.	45
3.15	Theoretical absorption spectra of the RuMeBpy and RuHMeBpy species in acetonitrile. A Lorentzian function with a half-width of 3000 cm^{-1} is employed to broaden the transitions in the spectrum based on the oscillator strengths represented by black sticks.	46
3.16	Bond lengths r_1 and r_2 as well as dihedral angles δ_1 and δ_2 for RuMe and RuMeH	48

3.17	Schematic representation of the relative energies of the singlet ground state S_0 , the excited singlet state S_6 or S_4 , the twisted triplet state T_{twist} , and the planarized triplet state T_{plan} for the equilibrium geometries (FC, $^1\text{MLCT}$, $^3\text{MLCT}$ and $^3\text{MLCT}_{\text{plan}}$) of RuMe and RuMeH . The given dihedral angles δ_1 and δ_2 refer to the torsion of the tolyl groups with respect to the <i>H</i> -imidazole (see Figure 3.16).	49
3.18	Investigated ruthenium(II)-4 <i>H</i> -imidazole complexes, in three studied protonation states (RuMeCOO⁻ , RuMeHCOO⁻ , and RuMeHCOOH), with a carboxy acid anchoring group. In all theoretical simulations the <i>tert</i> -butyl groups of the terpyridine ligand have been approximated by methyl groups.	50
3.19	Theoretical absorption spectra of RuMeCOO⁻ , RuMeHCOO⁻ , and RuMeHCOOH in acetonitrile. A Lorentzian function with a half-width of 3000 cm^{-1} is employed to broaden the transitions in the spectrum based on the oscillator strengths represented by black sticks.	51
3.20	Theoretical RR spectra of RuMeCOO⁻ (S_6 , S_{10} , S_{13} , S_{18} , and S_{24}), RuMeHCOO⁻ (S_5 , S_{11} , S_{12} , and S_{17}), and RuMeHCOOH (S_3 , S_4 , S_6 , and S_{12}) in resonance with $\omega_L = 568$ and 413 nm . The excited states were broadened with Lorentzian functions with a FWHM of 3000 cm^{-1} . The modes of the terpyridine ligand are given in red color. A Lorentzian function with a FWHM of 5 cm^{-1} is employed to broaden the calculated transitions.	51
3.21	MOs involved in the main configurations of the states responsible for the absorption and RR properties of the deprotonated (RuMeCOO⁻) and protonated (RuMeCOO⁻ and RuMeCOOH) complexes.	54
3.22	(TiO ₂) ₁₅ cluster, saturated with OH ⁻ and H ₂ O, and attached RuMeHCOO⁻ giving a total charge of ± 0 . a) illustrates the photoexcitation and subsequent IET from RuMeHCOO⁻ (π_{im}^*) to the TiO ₂ cluster. In b) and c) the QM and MM regions in the RO and the OR state are shown, while the bold sticks refer to the QM and the thin sticks to the MM region.	57
3.23	Bondind scenarios μ (a), κ^2 (b), and κ^1 (c) of a carboxylic acid anchoring group on a rutile surface.	57
3.24	SOMOs in the initial RO state (a) and in the final state OR (b) obtained at the TD-B3LYP/6-31G(d) level of theory and a polarizable continuum model (acetonitrile).	58
3.25	Starting structure of QM/MM coupled MD simulation of the RO state (QM: RuMeHCOO⁻ , MM: TiO ₂ cluster) surrounded by the acetonitrile solvent described at the MM level of theory.	59

A.1	Optimized equilibrium geometries of the electronic ground and first excited singlet states of dye A in tetrahydrofurane at the CAM-B3LYP/6-31G(d,p) level of theory.	215
A.2	Optimized equilibrium geometries of the electronic ground and first excited singlet states of dye B in tetrahydrofurane at the CAM-B3LYP/6-31G(d,p) level of theory.	215
A.3	Optimized equilibrium geometries of the electronic ground and first excited singlet states of dye C in tetrahydrofurane at the CAM-B3LYP/6-31G(d,p) level of theory.	216
A.4	Optimized equilibrium geometries of the electronic ground and first excited singlet states of dye D in tetrahydrofurane at the CAM-B3LYP/6-31G(d,p) level of theory.	216
A.5	Optimized equilibrium geometries of the electronic ground and first excited singlet states of dye E in tetrahydrofurane at the CAM-B3LYP/6-31G(d,p) level of theory.	216
A.6	Optimized equilibrium geometries of the electronic ground and first excited singlet states of dye F in MeOH (up) and heptane (down) at the CAM-B3LYP/6-31G(d,p) level of theory.	217
A.7	Optimized equilibrium geometries of the electronic ground and first excited singlet states of dye G in MeOH (up) and heptane (down) at the CAM-B3LYP/6-31G(d,p) level of theory.	217
A.8	Optimized equilibrium geometries of the electronic ground states of dye H in MeOH (left) and heptane (right) at the CAM-B3LYP/6-31G(d,p) level of theory.	218

List of Tables

3.1	S_1 main transitions with weight, excitation energies (ΔE^e), oscillator strengths (f) and the deviations from the experimental values ($\Delta\Delta E_{\text{exp}}$) for the absorption and emission properties of the dyes A–E obtained with CAM-B3LYP/6-31G(d,p) taking into account solvent effects (tetrahydrofuran).	29
3.2	Calculated vertical excitation energies (E^e), wavelengths (λ), oscillator strengths (f) and singly-excited configurations of the main excited states of the deprotonated (Ru) and protonated form (RuH) in the visible range. The principal orbitals are depicted in Figure 3.10.	40
3.3	Bond lengths r_1 and r_2 and dihedral angles δ_1 and δ_2 in the equilibria: FC, $^1\text{MLCT}$, $^3\text{MLCT}$, and $^3\text{MLCTplan}$ for RuMe and RuMeH , respectively.	48
3.4	Calculated vertical excitation energies (E^e), wavelengths (λ), oscillator strengths (f) and singly-excited configurations of the main excited states of the deprotonated form (RuMeCOOH⁻) and protonated forms (RuMeHCOOH⁻ and RuMeHCOOH) in the visible range. The relevant orbitals are depicted in Figure 3.21.	53

List of Abbreviations

AS	Active Space
(MS-)CASPT2	(multi-state) Complete Active Space Second-Order Perturbation Method
(SA-)CASSCF	(state average) Complete Active Space Self-Consistent-Field Method
CT	Charge Transfer
DFT	Density Functional Theory
DSSC	Dye sensitized Solar Cell
FC	Franck-Condon
FCI	Full Configuration Interaction
GGA	Generalized Gradient Approximation
HOMO	Highest Occupied Molecular Orbital
IET	Intra-molecular Electron Transfer
ILCT	Intra-Ligand Charge Transfer
IMDHOM	Independent Mode Displaced Harmonic Oscillator Model
ISC	Inter System Crossing
LLCT	Ligand to Ligand Charge Transfer
LDA	Local Density Approximation
LSDA	Local Spin-Density Approximation
LUMO	Lowest Unoccupied Molecular Orbital
MLCT	Metal to Ligand Charge Transfer
MCSCF	Multi-Configurational Self-Consistent Field
PICT	Planar Intra-molecular Charge Transfer
(MS-)RASPT2	(multi-state) Restricted Active Space Second-Order Perturbation Method
(SA-)RASSCF	(state average) Restricted Active Space Self-Consistent-Field Method
RR	Resonance Raman
PES	Potential Energy (Hyper)Surface
STA	Short-Time Approximation
SCF	Self-Consistent Field
SOS	Sum over State
TDDFT	Time Dependent Density Functional Theory

TDSE	Time-dependent Schrödinger Equation
TISE	Time-independent Schrödinger Equation
TICT	Twisted Intra-molecular Charge Transfer

Chapter 1

Introduction

This thesis concentrates on the investigation of different systems able to harvest sunlight, which is an attractive regenerative energy source. In the field of solar energy conversion, different attempts have been pursued, e.g. artificial photosynthesis and the generation of electricity. On the one hand, artificial photosynthesis is aimed to mimic nature in order to transform light into chemical energy and, hence, the formation of high-energy compounds such as molecular hydrogen via water splitting. On the other hand, the conversion of solar radiation into electricity is inextricably linked to the development of solar cells. In this field, dye sensitized solar cells (DSSCs) are of great interest due to their, compared to silicon based solar cells, low costs coupled with an ecological production. Such light-harvesting devices, either in biological or artificial systems, are fundamentally correlated to electron transfer (ET) processes and ET cascades. In the following, an overview of the biological photosynthesis and its artificial counterpart as well as DSSCs and ET processes is provided.

1.1 Artificial Adaptations of Photosynthesis

In modern society, mankind reached a number of more than seven billion individuals. To satisfy their thirst for electricity, providing new sources of regenerative energy is of vital importance. As stated above, a promising technology might be artificial photosynthesis. However, a preliminary step is to understand the mechanisms of the “natural” photosynthesis. A crucial aspect is the water splitting reaction:



where the generated electrons are used to provide high-energy compounds e.g. adenosine triphosphate (ATP) and glucose. This first step in the photosynthesis takes place in the photosystem two (PSII). Along the lines of Francis Crick, “*If you want to understand function, study structure.*”, a great number of experimental¹⁻¹⁰ as well as theoretical^{9,11-18} studies concentrated

on the structural determination of PSII on a molecular level. In general, PSII contains a large number of light-harvesting antennas connected to a redox center where the light-triggered water splitting reaction (see equation 1.1) occurs. Preliminary is the absorption of light; autotrophic organisms (plants and bacteria) created a manifold of antennas absorbing in different regions of the solar radiation spectrum. The best-known families of natural antenna systems are chlorophylls and carotins. Chlorophylls are in general porphyrin (see Figure 1.1a) complexes of the

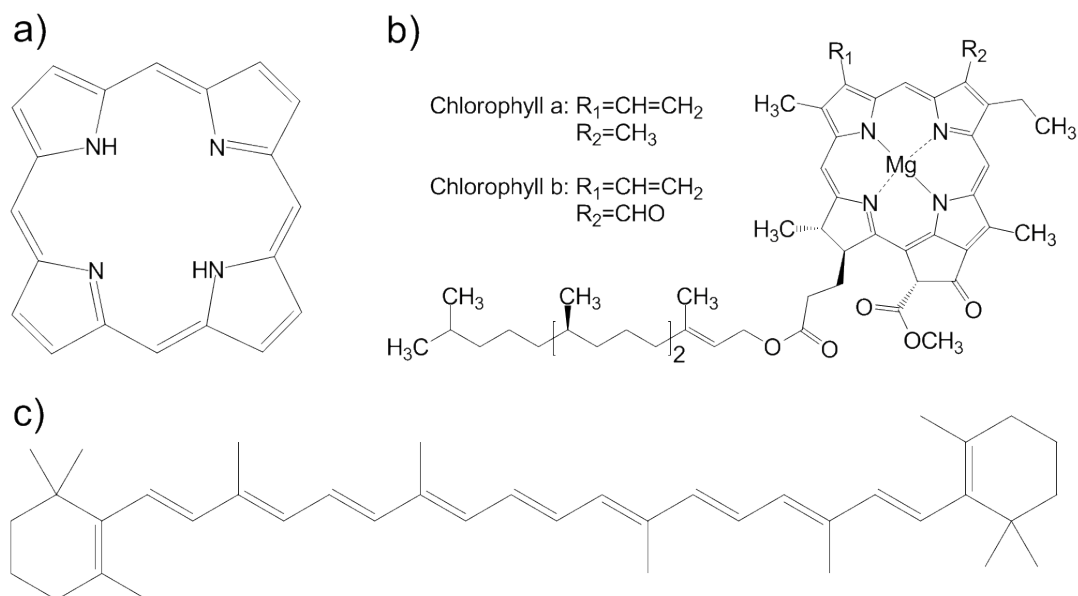


Figure 1.1: Light harvesting antennas in the PSII; a) basic porphyrin structure, b) chlorophyll a and chlorophyll b, c) β -carotin.

magnesium ion. Two examples of those complexes are chlorophyll a and chlorophyll b (see Figure 1.1b), which are important representatives of this family of compounds. However, a great number of derivatives exist in nature changing not only the substitution of the ligand sphere but also the central metal ion, allowing considerable shifts of the respective absorption bands. Besides chlorophyll, carotenoids, e.g. carotins and xanthophylls, serve as absorbers in biological systems; β -carotin (see Figure 1.1c) is an example for these tetra-terpenes. The harvested energy is transferred to the catalytic Mn_4Ca cluster, where the water oxidation occurs.^{10,13,19–24} The complex arrangement of the different antenna systems and the catalytic center, allowing this reaction, is only defined by inter-molecular interactions between these subunits.

Due to the intricacy of the molecular structure of PSII, a synthetic effigy is nowadays impossible. In the field of artificial photosynthesis different attempts are made to harness sunlight in order to split water into hydrogen and oxygen. One of the big challenges is the development of efficient light-driven catalysts for oxygen (electron donor) as well as for hydrogen formation. The interface connecting the catalytic centers is the photosensitizer. Upon photoexcitation of this sensitizer, the electron is transferred to the electron acceptor, while the electron hole in the ground state is replenished via the electron donor. Such a scheme is illustrated in Fig-

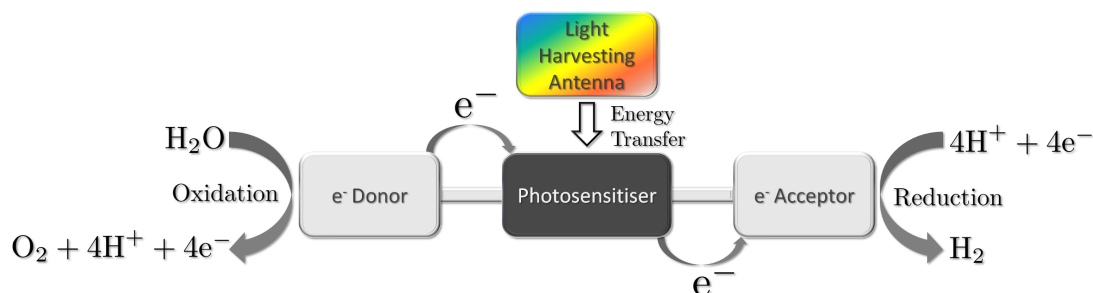


Figure 1.2: Electron donor or rather water splitting catalysts, photosensitizer with additional light-harvesting antenna, and electron acceptor or rather hydrogen forming catalysts.

ure 1.2. In order to achieve such an ET from the donor via the photosensitizer to the acceptor, several conditions need to be fulfilled: the donor state is higher (or at least equal) in energy than the acceptor state, the charge separated state (excited photosensitizer) exhibits long lifetimes, and fast ET from the charge separated state to the acceptor state is needed to prevent charge recombination via radiation or radiationless deactivation pathways. Natural porphyrin complexes, recall Figure 1.1a) and b), fulfill this condition and may serve as models for photosensitizers in artificial photosynthesis. An immense variety of arrangements, for instance as cyclic assemblings,^{25,26} stacks,²⁷ grids,²⁸ and dendrimers,^{29–31} can be found in the literature. In order to prevent charge recombination, porphyrin-fullerenes^{32–34} are often proposed. Also ruthenium(II) polypyridine complexes are widely studied due to their broad absorption in the visible region coupled with long living low-lying excited states (³MLCT). In these complexes, pronounced spin orbit couplings lead consequentially to a population transfer to the triplet manifold via inter system crossing (ISC).

Since the solar radiation spectrum covers the spectral region from the UV to the near IR (NIR), harvesting this entire range is desired. However, this is very challenging using merely the photosensitizer. Hence, the light-harvesting capability can be increased using antenna systems. These antennas may contain several chromophores to cover the entire solar radiation spectrum. The absorbed energy is subsequently transferred from the antennas to the sensitizer; other deactivation mechanisms should feature smaller time constants. Of vital importance are the optical properties, namely the absorption of the applied chromophores in the antenna. Besides porphyrins also other chromophores such as the 4-methoxy-1,3-thiazole, which is similar to the naturally occurring luciferine (light-emitting dye of fireflies), are of potential interest due to their outstanding optical properties. This chromophore is easy functionalizable and features tunable absorption and emission spectra, high quantum yields, and high extinction coefficients. Exemplarily, three dyes of this family of compounds are shown in Figure 1.3 featuring absorption maxima that cover the entire visible spectrum.^{35,36}

Several design strategies have been pursued in order to construct artificial photosynthesis devices. One idea is to use one compound system for hydrogen evolution.³⁷ Other strategies

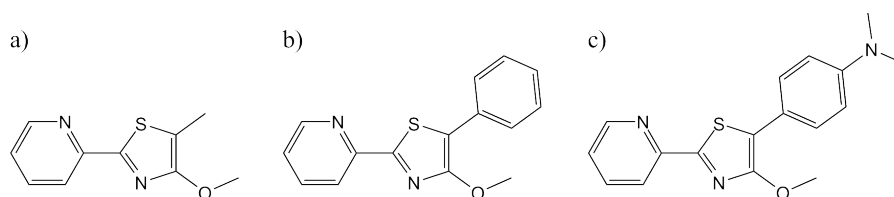


Figure 1.3: a) blue, b) green, and c) red absorbing 4-methoxy-1,3-thiazole dyes.

employ macromolecular antenna systems coupled with several photosensitizers - this ansatz was chosen in the PhotoMic (Photonic Micelle) consortium located at the Friedrich-Schiller Universität Jena. The general scheme is illustrated in Figure 1.4. The concept included an

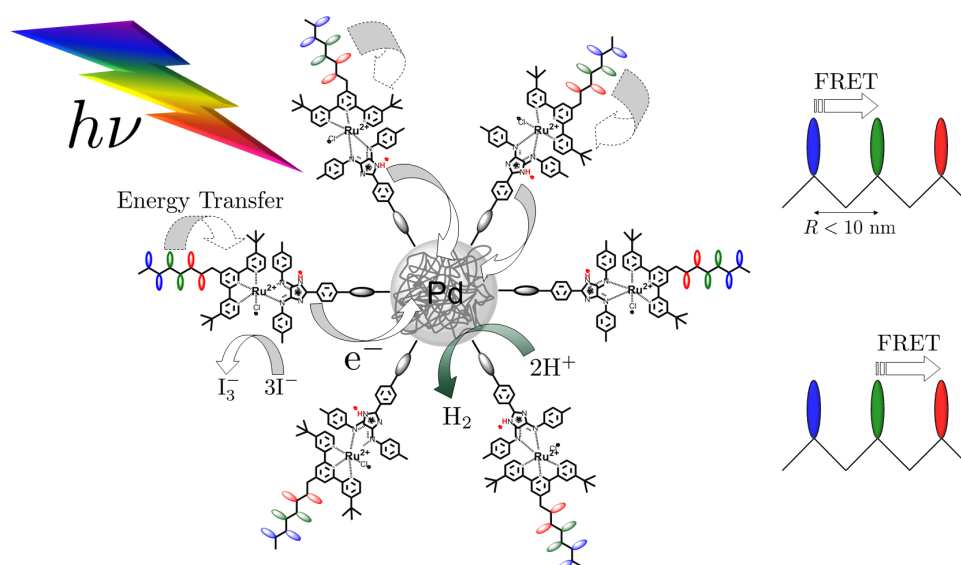


Figure 1.4: Scheme of a hydrogen producing photonic micelle fueled by solar energy as proposed in the PhotoMic project; Förster Resonance Energy Transfer (FRET) is used to focus the absorbed energy from several dye to a transition metal photosensitizer.

antenna system with several different chromophores implemented in a polymer backbone. The absorbed energy of the incidental light is then transferred via Förster Resonance Energy Transfer³⁸ (FRET) from dye to dye. In order to accomplish such FRET between several pairs of dyes, hierarchically overlapping emission and absorption bands of the dyads are essential. Also, the arrangement of the dyes is crucial to allow an effective energy transfer from one to another and eventually further to the photosensitizers, based on polypyridine transition metal complexes.³⁹ The subsequent ET occurs from the photoexcited state of the sensitizer (over a bridging ligand) to the hydrogen producing catalyst. Since this scheme is incapable to split water, hence, a secondary electron donor, for instance iodine or triethylamine, needs to be provided.

1.2 Dye sensitized Solar Cells

In DSSCs, sunlight is converted directly into electricity. Contrary to conventional silicon based semiconductor devices, such DSSCs separate the absorption process from the charge transport. The publication of such a cell, showing a sunlight conversion rate of up to 12% using only low-cost compounds by Grätzel and coworkers in 1991,⁴⁰ captured the interest of the scientific community. This technology spares expensive materials such as highly pure silicon (Czochralski process⁴¹). In general, DSSCs employ titanium dioxide nanoparticles at the anode covered with a mono-layer of light-absorbing dyes connected, via a carboxylic acid anchoring group, to the surface. Upon photoexcitation, an electron of the dye is injected into the conduction band of the TiO₂ semiconductor (photoanode), while the charge of the dye is regenerated by a redox pair such as I₃⁻/I⁻ in the electrolyte solution. The I₃⁻/I⁻ redox pair is regenerated at the cathode. This general scheme is illustrated in Figure 1.5.

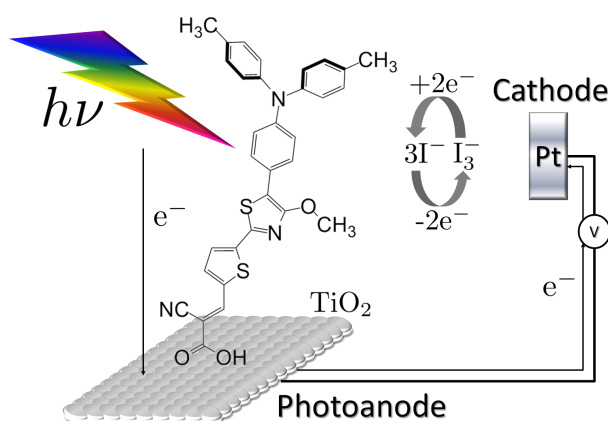


Figure 1.5: Schematic representation of a conventional DSSC with a organic dye, a titanium dioxide photoanode, a platinum cathode and a I₃⁻/I⁻ redox pair for charge regeneration of the oxidized dye.

The performance of such a solar cell highly depends on the properties of the components as well as on their interaction. As stated in Section 1.1, the solar radiation spectrum reaches from the UV to the NIR region, while the maximum of the intensity is located around 550 nm. Since DSSCs typically feature only one dye species, an intense absorption of the dye in this spectral range is desired. The huge surface of the TiO₂ nanoparticles offers binding positions for a great number of dyes, which ensures the absorption of photons in high quantity. However, unintended dye-dye interactions, leading for instance to the formation of aggregates, may arise with increasing density of the dye mono-layer. The electronic excited state correlated to the absorption process is typically of charge transfer (CT) character. This state injects an electron into the conduction band of the TiO₂ semiconductor. To ensure an efficient electron injection or rather ET, long-lived excited states of the excited dye may be necessary in order to compete with internal deactivation channels. Admittedly, low-lying excited states (absorbing in the maximum of the solar radiation spectrum) increase the rate of this unwanted internal deactiva-

tion via the energy gap law.⁴² Upon electron injection, charge recombination with the oxidized dye and direct reduction of the iodate ion ($I_3^- \xrightarrow{2e^-} 3I^-$) may occur, lowering the performance of the cell. From the photoanode, the electrons are transferred along the gradient of the electronic potential to the cathode, where the aforementioned reduction of the iodate ion takes place. The form iodine ion then reduces the oxidized dye. To allow this oxidation/reduction cycle, the energetic positions of all involved states of the dye, the TiO_2 semiconductor, and of the iodate/iodine redox pair need to be aligned.

In order to improve the performance of DSSCs the obvious way is to design new photostable dyes with bright low-lying excited states and long excited state lifetimes. In this manner numerous transition metal complexes as well as pure organic chromophores have been investigated. Black absorbers based on transition metal complexes, e.g. the ruthenium(II) polypyridine, lack typically intense absorption bands in the visible region (located below 550 nm), especially toward the NIR. Several attempts have been made to increase the absorption of such dyes in the NIR range, for instance attaching additional dyes in the periphery of the polypyridine ligands.⁴³ However, in such dye assemblies only weak coupling between both chromophores exist which limits the application potential in DSSCs. Alternatively, partial substitution of the polypyridine ligand sphere with ligands featuring chromophores absorbing in the desired spectral region may be beneficial.⁴⁴ The major disadvantage of these dyes is, besides their toxicity, the high price of metals, such as ruthenium, osmium, platinum, rhenium, and iridium.

An alternative to transition metal complexes are organic dyes. These systems exhibit most often high molar extinction coefficients and tunable optical properties, which is highly encouraging for their application in DSSCs. Appropriate dyes (coumarin, indoline, and triphenylamines) are mostly desired in a donor-acceptor fashion.^{44,45} Here, an electron donating group is linked by a conjugated π -system to an electron acceptor, e.g. 2-cyanoacrylic acid, which also anchors the dye to the semiconductor surface. However, organic dyes show in general smaller excited state lifetimes and are more sensitive to photo bleaching than transition metal complexes.

1.3 Electron Transfer in Nature and Artificial Systems

ET reactions are of outstanding importance in biology, for instance in energy conversion in a living cell,^{46,47} but also in molecular devices^{48,49} or in the generation of electricity in photo voltaic devices.^{44,50} Also ET phenomena in DNA are a widely studied field.^{51,52} In biological systems, proteins can catalyze ET process by several orders of magnitude, which enables fundamental process as photosynthesis and cell respiration. ET between Fe^{2+} and Fe^{3+} occurs in aqueous solution within seconds,^{53,54} while it takes place in the microsecond time scale in a protein environment.^{55,56}

In 1956, R. A. Marcus derived the first quantitative expression for the rate of ET reaction,

which is nowadays known as Marcus Theory.⁵⁷ In the Marcus picture, the two reaction states (electron donor and electron acceptor) are in contact with a bath, e.g. the surrounding protein environment or the solvent, while rare thermal fluctuations of the solvent lead to a crossing of these two states. Marcus Theory assumes that the rate of an ET process is fully described by the reorganization energy and the reaction free energy at a certain temperature. Later on, the coupling matrix of the reaction states, taking tunneling processes into account, was additionally considered.^{58–60}

In the same way as in PSII, ET processes are of fundamental importance for artificial light-harvesting devices.^{46,50,61} As stated in Section 1.1 and 1.2, ET rates are crucial for the performance of artificial light-harvesting systems. Upon photoexcitation, there is always the concurrence of ET and internal deactivation pathways. An important goal is to understand all these processes occurring at the interface of the dye and electron acceptor unit, which is either a catalytic center, as in artificial photosynthesis, or the titanium dioxide semiconductor in DSSCs. Such knowledge is vital to design novel antenna systems, photosensitizers, and catalysts in a systematic manner.

1.4 Goals and Outline of this Thesis

The cornerstone of solar energy conversion is the design of dyes based on rational understanding of optical properties, regardless whether they are used in artificial photosynthesis or in solar cells (or DSSCs), and whether they consist of transition metal complexes or organic dyes. In order to obtain detailed insight into the photophysics of such dyes, spectroscopical methods alone are insufficient. Quantum chemical methods are capable to unravel optical properties, e.g. absorption and emission, but they may also provide a more fundamental and general picture of the dye. Nowadays, it is possible to directly study excited states and their characteristics, which is of conceptual importance, as it represents the basis for any approach aiming at a spectroscopy/theory-guided design of molecular functional materials.

The goal of this thesis is to determine correlations between structural and electronic properties, for instance effects of protonation, substitution, and solvation, within the scope of light-harvesting dyes. Special emphasis is put on CT states. An effective and directional CT is mandatory to achieve charge separation for applications in artificial photosynthesis or DSSCs, see Section 1.1 and 1.2.³⁷ To this aim, the focus is set on the one hand on organic donor- π -acceptor dyes, and on the other hand on black absorbers based on ruthenium(II) complexes. To address solvatochromism and pH dependency, high-level quantum chemical methods, that are able to accurately describe electronic ground and excited states, and especially CT states, are stringently required. Simulating excited states is still considered complicated nowadays.

Herein, state-of-art multiconfigurational methods and time-dependent density functional theory are employed to characterize the investigated dyes via absorption and emission spectroscopy. In addition, it will be determined whether the simulation of resonance Raman spectra is appropriate to study excited states properties depending on protonation, substitution, and solvation effects.

The next modeling step is to go beyond the simulation of isolated dyes, but rather model real light-harvesting devices, e.g. a DSSCs. This requires to gain an insight into ET processes that are crucial for the performance of such devices. This way, fundamental knowledge concerning undesired internal relaxation pathways versus ET can be predicted. To this aim, quantum mechanical/molecular mechanics in conjunction with molecular dynamical simulations can be performed to determine ET rates within semi-classical Marcus theory.

In order to address the previously defined goals, various quantum chemical methods, molecular dynamics and a detailed understanding of the principles behind resonance Raman and the Marcus theory are essential. This theoretical background is provided in Chapter 2. In Chapter 3, an overview of the results achieved in this thesis is given, while Chapter 4 collects the appended publications. Finally, a summary and outlook is given in Chapter 5.

Chapter 2

Theory

This chapter provides an overview of the employed quantum chemical methods and their application to study spectroscopical features as well as ET processes. A variety of sized organic dyes and transition metal complexes have been investigated. As can be seen in Chapter 2.2 state-of-the-art multiconfigurational methods provide the tools to study complex chemical situations that require chemical intuition coupled with a pronounced knowledge of the system of interest. As a consequence of the size, density functional theory (DFT) and time-dependent DFT (TDDFT) methods are widely applied for large molecular systems, see Chapter 2.3. However, such methods exhibit a series of problems that will be addressed in the following chapter. Both DFT and TDDFT as well as multiconfigurational methods are applied in this thesis to calculate spectroscopic properties e.g. absorption, emission and resonance Raman (RR). Especially, the calculation of RR intensities is still a non-standard procedure; therefore, the theoretical background of RR scattering as well as two methods suitable to compute such intensities are provided in Chapter 2.6. Naturally, the interest is not limited to photophysical processes at the Franck-Condon (FC) region but also to processes taking place after photoexcitation, such as photoinduced ET processes. Such ET processes can be studied by virtue of Marcus theory, however, there are few theoretical implementations. Chapter 2.7 presents a methodology based on gaussian statistics focused on intra-molecular charge transfer (ICT).

2.1 Basic Quantum Chemistry

Derived from the time-dependent Schrödinger equation (TDSE):

$$i\frac{\partial}{\partial t}|\Psi(\vec{r}, \vec{R}, t)\rangle = \hat{\mathcal{H}}|\Psi(\vec{r}, \vec{R}, t)\rangle, \quad (2.1)$$

where $|\Psi(\vec{r}, \vec{R}, t)\rangle$ is the global wave function depending on the electron and nuclear positions, \vec{r} and \vec{R} , at time t and $\hat{\mathcal{H}}$ the global Hamiltonian, the electronic time-independent Schrödinger

equation (TISE):

$$\hat{H}|\psi(\vec{r}, \bar{R})\rangle = E|\psi(\vec{r}, \bar{R})\rangle, \quad (2.2)$$

is defined for a stationary state. The electronic wave function $|\psi(\vec{r}, \bar{R})\rangle$ is, within the Born-Oppenheimer approximation⁶², given by the separation of the electronic and the nuclear wave function $|\chi(\bar{R})\rangle$, only parametrically depending on the nuclear coordinates. Hence, the electronic energy E and the electronic Hamiltonian \hat{H} are defined in equation 2.2. Summing up the electronic energy and the nuclear repulsion at the geometry \bar{R} yields the potential energy; if \bar{R} involves one degree of freedom it is denoted as potential energy curve (PEC) and in case of higher dimensionality, potential energy surface (PES).

Since the explicit form of the electronic Hamilton operator is well known, we need to define an appropriate wave function $|\psi\rangle$, e.g. a Slater determinant⁶³. Hereafter, the electron-electron interaction, the most crucial aspect in quantum chemistry, needs to be addressed; the basic approach to tackle this interaction is given within the Hartree-Fock (HF) method⁶⁴⁻⁶⁶. The fundamental ideas of HF are given by two assumptions:

- i) The effective HF potential describes the interaction of one electron with an average field of all other electrons.
- ii) The electronic wave function can be described in every nuclei configuration with one single Slater determinant.

However, these approximations lead two major calamities. First of all, the movement of the electrons depend on the immediate positions of all other electrons, hence the use of an average field is inappropriate. This type of correlation is the so-called dynamical correlation. The lack of dynamical correlation leads e.g. to shorter bond distances caused by the too small electron-electron distances. Therefore, the dynamical correlation is a short-range effect correlation.

The second drawback of the HF method can be summarized by the lack of non-dynamical correlation. This type of correlation appears when one determinant is not enough to describe the system. That is especially the case upon bond breaking, electronically excited states, and transition metals, whose electronic wave functions require more than one electronic configuration. The non-dynamical correlation is also known as long-range effect correlation.

2.2 Multiconfigurational Methods

The ambition to study chemical situations where one single Slater determinant is insufficient led to the development of multiconfigurational methods. Multi-Configurational Self-Consistent Field (MCSCF) methods are based on the idea to construct a wave function $|\psi_{\text{MCSCF}}\rangle$ by a linear combination of the HF ground state wave function $|\psi_0\rangle$ and the sum of possible excitations:

$$|\psi_{\text{MCSCF}}\rangle = c_0|\psi_0\rangle + \sum_{a,r} c_a^r |\psi_a^r\rangle + \sum_{\substack{a<b \\ r<s}} c_{ab}^{rs} |\psi_{ab}^{rs}\rangle + \sum_{\substack{a<b<c \\ r<s<t}} c_{abc}^{rst} |\psi_{abc}^{rst}\rangle + \sum_{\substack{a<b<c<d \\ r<s<t<d}} c_{abcd}^{rstu} |\psi_{abcd}^{rstu}\rangle \dots, \quad (2.3)$$

where $|\psi_0\rangle$ represents the HF wave function, $|\psi_a^r\rangle$ the single excitations, $|\psi_{ab}^{rs}\rangle$ the double excitations $|\psi_{ab}^{rs}\rangle$ and so on, while each excitation is weighted by the corresponding coefficients c_0 , c_a^r , c_{ab}^{rs} etc. If every possible excitation is taken into account, the wave function is denoted as a Full Configuration Interaction (FCI) wave function. In multiconfigurational methods, not only the coefficients for each wave function are optimized in a variational fashion, but also the orbitals of each Slater determinant; this gives the wave function the flexibility to describe resonance structures, dissociation processes and, of course, points of degeneration in the PES. However, even for very small molecules the computational limit of FCI calculations is rapidly reached. Hence, the major difficulty in the multiconfigurational methods is to select the essential configuration state functions (CSFs) needed to describe the current problem. Profound knowledge of the system of interest coupled with chemical intuition is inevitably. One common approach to select CSFs is the Complete Active Space Self-Consistent Field (CASSCF) method⁶⁷, where all configurations are considered for a given active space (AS) constructed by a certain number of electrons and orbitals. Figure 2.1a) illustrates the principles of the CASSCF methodology, whereas the entirety of the orbitals is divided into frozen, inactive and active orbitals. Inactive orbitals are either always double occupied or empty, frozen orbitals are

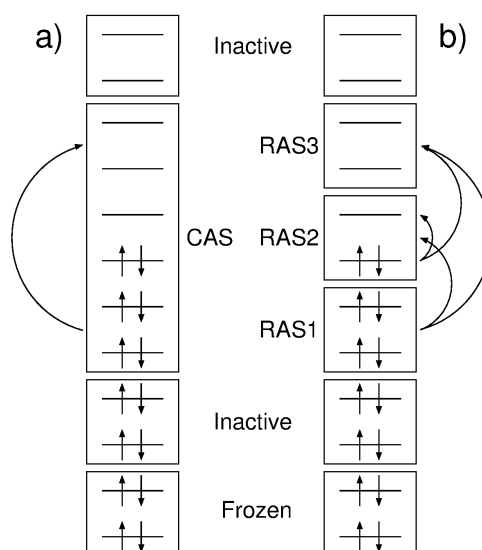


Figure 2.1: Principles of CASSCF a) and RASSCF b) wave functions

also always double occupied, but in contrast to the inactive orbitals not optimized. Within the active orbitals a FCI is performed, hence the coefficients of each CSF, as well as the respective set of orbitals, are optimized. These orbitals should be those with a substantial importance

for the investigated chemical situation. However, the size of the AS is limited by the corresponding number of CSFs. One approach to enlarge the AS, while restraining the number of CSFs to a reasonable value, is given within the Restricted Active Space Self-Consistent Field (RASSCF)^{68,69} methodology, where the excitation level is restricted by distributing the active electrons and orbitals further into three subspaces, RAS1, RAS2 and RAS3, see Figure 2.1b). The RAS1 includes typically orbitals with large occupation numbers. In these orbitals only a maximal number of electron holes is allowed. Accordingly, the RAS3 subspace comprises virtual orbitals with small occupation numbers and here only a maximal number of electrons is allowed. The RAS2 subspace is equivalent to the AS of CASSCF, where all possible configurations are taken into account. RASSCF opened the door to study extended molecular systems with high level multiconfigurational methods.

In order to describe electronic excited states applying the state average (SA) algorithm is highly recommended to consider the mixing of close-lying excited states. This algorithm spans a SA wave function over all electronic states of the same symmetry with a certain weight.

CASSCF and RASSCF calculations deliver only static correlation; in order to describe accurately photophysical and photochemical processes, dynamical correlation needs to be included. One common approach uses a CASSCF/RASSCF wave function with second-order perturbation theory^{70,71}. This method is called CASPT2 (Complete Active Space Second-Order Perturbation Method)⁷²⁻⁷⁴ or RASPT2 (Restricted Active Space Second-Order Perturbation Method)⁷⁵, respectively. The ansatz for perturbative methods is then to define the Hamiltonian as a sum of a zero-order Hamiltonian $\hat{H}^{(0)}$ and a perturbation \hat{V} , whereas the multiconfigurational wave function is used as reference. The respective energy at CASPT2 or RASPT2 level is obtained by summing the zeroth-order $E^{(0)}$ and second-order $E^{(2)}$ energies:

$$E^{\text{PT2}} = E^{(0)} + E^{(2)} = \langle \psi_{\text{MCSCF}} | \hat{H}^{(0)} | \psi_{\text{MCSCF}} \rangle - \sum_{k=1}^M \frac{|\langle \psi_{k,\text{MCSCF}}^{(1)} | \hat{V} | \psi_{\text{MCSCF}} \rangle|^2}{\epsilon_k - E^{(0)}}, \quad (2.4)$$

where $|\psi_{\text{MCSCF}}\rangle$ and $|\psi_{k,\text{MCSCF}}^{(1)}\rangle$ represent the reference and the first-order perturbative wave functions of the k th interacting configuration space and ϵ_k the corresponding energy. The computational demand of such calculations arises by virtue of the first-order perturbative wave function, since the interacting configuration space is constructed by two-electron excitations of the reference wave function. Furthermore, several techniques have been developed to treat the interaction of the excited states at the CASPT2/RASPT2 level of theory. The interaction of highly mixed SA-CASSCF/RASSCF states is addressed in the multi state (MS)-CASPT2⁷⁶/RASPT2⁷⁵ algorithm, where the diagonal elements of the effective Hamiltonian matrix contains the single state CASPT2/RASPT2 energies of the excited states, while the off-diagonal elements describe the coupling between the electronic states. The diagonalization of this matrix gives a new set of eigenvalues and eigenfunctions, the MS excitation energies and the respective electronic wave functions. Problematic is the interaction with so-called intruder states, when ϵ_k is

close to $E^{(0)}$, see equation 2.4. In order to prevent the denominator from going to zero a level shift⁷⁷ can be introduced to displace the two interacting states.

The CASPT2/CASSCF and the RASPT2/RASSCF methods are among the most accurate methods used nowadays. With the introduction of the RASPT2/RASSCF, multiconfigurational methods are applicable not any more only to small molecular systems, but also to medium sized systems, e.g. organic chromophores with extensive π -systems, such as those treated in this thesis.

2.3 Density Functional Theory based Methods

2.3.1 Density Functional Theory

In contrast to the methods described in the previous section Density Functional Theory (DFT) is based on the electron density $\rho(\vec{r})$. The cornerstone of modern DFT was laid by the theorems of Hohenberg and Kohn⁷⁸, stating a unique relationship of the electronic ground state energy and the electron density as well as the introduction of the variational principle. With the Kohn-Sham equations⁷⁹, related to the HF methodology, a pathway to determine electron-electron interaction was given. Therefore, DFT is exact; however, the explicit form of an universally valid functional, in particular the exchange correlation functional $E_{XC}[\rho]$, is unknown.

The approximations adopted for the exchange correlation functional resulted in a variety of different categories of functionals, e.g. local density approximation (LDA), local spin-density approximation (LSDA) and generalized gradient approximation (GGA)⁸⁰. However, the most widely used functionals in chemistry are hybrid functionals^{80,81} with the general form of:

$$E_{xc} = \int_0^1 \langle \psi_{0,\lambda} | V_{XC}^{\text{hole}}(\lambda) | \psi_{0,\lambda} \rangle d\lambda = E_x + E_c . \quad (2.5)$$

The simplest approximation for the exchange correlation hole potential V_{XC}^{hole} utilizes a linear function of the parameter λ that "turns on" electron-electron interaction. With "turned off" electron-electron interaction ($\lambda = 0$) there is in consequence no correlation energy (E_c), only exchange energy (E_x). This exchange energy is due to the single reference wave function composed of the Kohn-Sham orbitals exactly given by the HF approach and hence often labeled as exact-exchange. One of the most widely applied hybrid functionals is B3LYP^{82,83} created by Becke in 1993:

$$E_{xc}^{\text{B3LYP}} = (1 - a_0)E_x^{\text{LSDA}} + a_0E_x^{\text{HF}} + a_xE_x^{\text{B88}} + a_cE_c^{\text{LYP}} + (1 - a_c)E_c^{\text{VWN}} . \quad (2.6)$$

B3LYP uses HF exchange with B88⁸⁴ and the LSDA to account for the exchange energy and the LYP⁸³ and VWN⁸⁵ functionals for electron-electron correlation. The mixing of the individual functionals, given by the parameters $a_0 = 0.20$, $a_x = 0.72$ and $a_c = 0.81$, was obtained

by fitting to experimental atomization energies.⁸⁰

Opposite to other correlation methods, where each electron depends on three spatial and one spin coordinate, the electronic density $\rho(\vec{r})$ depends only on the three spatial coordinates x , y , and z . Hence, DFT methods are of substantial interest, especially in case of big molecular ensembles, where other correlated methods are not feasible from a computational point of view. However, hybrid functionals as B3LYP are known to show problems in molecular systems featuring long chains, Rydberg states^{86,87} and CT states⁸⁸⁻⁹² even when describing electronic ground state properties⁹³. The reason is that the behavior of the exchange potential at long-range is of $-0.2r^{-1}$ instead of the exact $-r^{-1}$ form. To address this limitation several new hybrid functionals have been created with a more pronounced amount of exact-exchange e.g. PBE0⁹⁴ (25 %), M06⁹⁵ (27 %) and M06-2X⁹⁵ (54 %). Also the parameters a_0 and a_x , controlling the mixing of HF and B88 exchange in B3LYP (equation 2.6) can be modified to increase the ratio of HF exchange, creating e.g. the B3LYP based functionals labeled as B3LYP32⁹⁶ ($a_0 = 0.32$ and $a_x = 0.72$) and B3LYP35⁹⁷ ($a_0 = 0.35$ and $a_x = 0.585$) with 32 and 35 % of exact-exchange, respectively. Another approach to incorporate long-range effects is to introduce a distance dependency of the HF and B88 exchange ratio into the B3LYP functional:

$$\frac{1}{r_{12}} = \frac{1 - [a_0 + a_b \cdot \text{erf}(\mu r_{12})]}{r_{12}} + \frac{a_0 + a_b \cdot \text{erf}(\mu r_{12})}{r_{12}}. \quad (2.7)$$

This ansatz known as Coulomb Attenuating Method is eponym of the long-range corrected CAM-B3LYP⁹⁸ functional where the mixing of E_x^{HF} and E_x^{B88} (see B3LYP functional in equation 2.6) is controlled by the three parameters $a_0 = 0.19$, $a_b = 0.46$ and $\mu = 0.33$. The amount of HF exchange is given by $a_0 + a_b$, hence CAM-B3LYP uses at zero electron-electron distance 19 and at infinite distance 65 % of exact-exchange.

2.3.2 Time-dependent Density Functional Theory

The introduction of a time-dependent external potential into the DFT formalism by Runge and Gross⁹⁹ paved the path to calculate excited states with DFT. The Runge-Gross theorem states a unique dependency of the time-dependent density and the time-dependent external potential with the restrictions that the ground state density is the initial density and that the time-dependent external potential is expandable in a Taylor series.

Typically, the excited states properties are extracted from the TDSE applying linear response theory and transforming the eigenvalue problem from the time to the frequency domain. Linear response theory assumes the perturbation via the time-dependent external potential to be marginal compared to the unperturbed system. The response function, for instance, the isotropic polarizability α depending of the frequency of the external electric field (ω_L) is then

given by:

$$\alpha(\omega_L) = \sum_e \frac{f_{g,e}}{\omega_{g,e}^2 - \omega_L^2}, \quad (2.8)$$

where f_{ge} is the oscillator strength, depending on the excitation energy $\omega_{g,e}$ and the corresponding transition dipole moment $\vec{\mu}_{g,e}$ for an excitation from the electronic ground state g to the e th excited state.

Another ansatz is real-time TDDFT (RT-TDDFT)¹⁰⁰, which describes the explicit evolution of the system in time and hence the TDSE is explicitly solved for each time step. RT-TDDFT is capable to describe non-linear polarizabilities in the presence of large electric fields. Nevertheless, the computational demands of RT-TDDFT exceed those of TDDFT substantially.

In analogy to DFT, TDDFT holds weaknesses in describing long-range effects, problematic is especially the estimation of spectroscopical properties of CT states. Increasing the amount of exact-exchange either in an uniform or a parameterized fashion allows typically a reasonable description of CT states in e.g. organic dyes. More challenging are transition metal complexes with a variety of excited states with different character such as local excitations, Metal to Ligand CT (MLCT), Ligand to Ligand CT and Intra-Ligand CT.¹⁰¹

2.4 Combination of Quantum and Molecular Mechanics

The quantum mechanical/molecular mechanics¹⁰² (QM/MM) approach allows the combination of high level quantum mechanics (QM), typically DFT or TDDFT, with molecular-mechanics (MM). In QM/MM, the total energy of a electronic state is given by:

$$E = E_{\text{QM}} + E_{\text{MM}} + E_{\text{QM/MM}}, \quad (2.9)$$

where E_{QM} is the energy obtained using QM, E_{MM} the energy at MM level, and $E_{\text{QM/MM}}$ the interaction energy between QM and MM picture. MM enables the simulation of large molecular systems, for instance proteins, via classical mechanics. The QM/MM scheme is often used to calculate biochemical interesting species, where the reaction center, e.g. a metal complex, is investigated with accurate QMs and the surrounding protein environment via less demanding MMs. Also, QM/MM can be applied to study effects of solvation in the ground as well as in excited states, this is an alternative to polarizable continuum models.¹⁰³

2.5 Molecular Dynamical Simulations

Molecular dynamics (MD) provide the opportunity to study the dynamics of large molecular or atomic systems. The foundation of MD is given by the classical laws of motion discovered by Sir Isaac Newton.¹⁰⁴ These laws are:

- i) Law of inertia: The velocity \vec{v} of any particle is constant as long as no force induces a change of the particle.
- ii) Law of motion: The acceleration \vec{a} of a particle is parallel and directly proportional to the acting force \vec{F} on the particle.
- iii) Law of Action-Reaction: If a first particle exerts a force on a second particle, this second particle exerts a force equal in magnitude but opposite in direction on the first particle.

The combination of MD with a QM is known as semi-classical MD, here the nuclei evolve in time using classical dynamics, while the underlying PES is obtained using accurate QM. The connection between QM and classical mechanics is given by Newton's ii) law of motion. The force \vec{F} acting on the nuclei is defined by:

$$\vec{F} = -\nabla E(\vec{R}) , \quad (2.10)$$

where $\nabla E(R)$ is the gradient of the PES. With the initial conditions of mass and velocity, integration of equation 2.10 yields the time evolution of the nuclei. Since, velocity and positions underlie Heisenbergs indeterminacy principle¹⁰⁵, a set different initial conditions also known as Wigner distribution has to be provided.¹⁰⁶

2.6 Resonance Raman Spectroscopy

2.6.1 Classical Raman

The interaction of a molecule with incident light is described by the frequency dependency of the dipole moment $\vec{\mu}$:

$$\vec{\mu} = \alpha \vec{E} , \quad (2.11)$$

where α is the polarizability tensor of the molecule depending on the nuclei configuration and hence the vibrational modes, and \vec{E} the linearly polarized, monochromatic electric field with the frequency ω_L . The variation of α in terms of the vibrational normal modes for a spatial fixed and non-rotating molecular system is expanded in a Taylor series:

$$\alpha_{\alpha,\beta} = (\alpha_{\alpha,\beta})_0 + \sum_l \left(\frac{\partial \alpha_{\alpha,\beta}}{\partial Q_l} \right)_0 Q_l + \sum_{l,m} \left(\frac{\partial^2 \alpha_{\alpha,\beta}}{\partial Q_l \partial Q_m} \right)_0 Q_l Q_m \dots , \quad (2.12)$$

here $(\alpha_{\alpha,\beta})_0$ is the polarizability in the equilibrium geometry and Q_l and Q_m the corresponding normal coordinates along the l th and m th mode. Within the harmonic approximation the Taylor series is truncated after the second term. We now apply the time-dependent electronic field

$\vec{E} = E_0 \vec{e}_{x/y/z} \cos(\omega_L t)$ on the polarizability tensor:

$$\alpha_{\alpha,\beta} \vec{E} = (\alpha_{\alpha,\beta})_0 E_0 \vec{e}_{x/y/z} \cos(\omega_L t) + \sum_l \left(\frac{\partial \alpha_{\alpha,\beta}}{\partial Q_l} \right)_0 Q_{l_0} \cos(\omega_l t + \delta_l) E_0 \vec{e}_{x/y/z} \cos(\omega_L t), \quad (2.13)$$

where Q_{l_0} and E_0 are the amplitudes of the normal coordinate and of the incidental electric field, $\vec{e}_{x/y/z}$ the polarization of the electric field and δ_l the phase factor. The rearrangement of equation 2.13 yields:

$$\vec{\mu} = \vec{\mu}(\omega_L) + \vec{\mu}(\omega_L - \omega_l) + \vec{\mu}(\omega_L + \omega_l), \quad (2.14)$$

where the three summands describe different scattering processes.

1. The first term:

$$\vec{\mu}(\omega_L) = (\alpha_{\alpha,\beta})_0 E_0 \vec{e}_{x/y/z} \cos(\omega_L t), \quad (2.15)$$

describes the predominant elastic scattering named after the English physicist Lord Rayleigh. The electric dipole moment of the molecule oscillates at ω_L , whereas the molecule itself also oscillates at ω_L . Therefore, the necessary condition for Rayleigh scattering is $(\alpha_{\alpha,\beta})_0 \neq 0$. Since all molecules are polarizable to a certain extent all molecules show Rayleigh scattering.

2. The second and the third term:

$$\vec{\mu}(\omega_L \pm \omega_l) = \frac{1}{2} \sum_l \left(\frac{\partial \alpha_{\alpha,\beta}}{\partial Q_l} \right)_0 E_0 \vec{e}_{x/y/z} Q_l \cos((\omega_L \pm \omega_l \pm \delta_l) t), \quad (2.16)$$

describe inelastic or rather Raman scattering,¹⁰⁷⁻¹⁰⁹ named after the Indian physicist Sir Raman. The two terms, depending linearly on the derived polarizability tensor, describe the Stokes ($\vec{\mu}(\omega_L - \omega_l)$) and Anti-Stokes scattering ($\vec{\mu}(\omega_L + \omega_l)$), respectively. Raman scattering arises from the electric dipole moment oscillating at $\omega_L \pm \omega_l$, which is generated when ω_L is modified by the frequency ω_l of the l th normal mode. Raman scattering occurs only, if at least one component of the derived polarizability tensor $(\partial \alpha_{\alpha,\beta} / \partial Q_l)_0$ of the l th normal mode evaluated at the equilibrium geometry exhibits a non-zero gradient along the coordinate of the normal mode Q_l .

This way the classical treatment provides a useful qualitative picture of Rayleigh and Raman scattering. Within the harmonic approximation exclusive fundamental transitions are considered. In order to take into account overtones and combination bands also anharmonicity effects need to be included; nevertheless, such bands feature steadily much lower intensities than the fundamental transitions.

The classical theory on Raman spectroscopy is sufficient for a qualitative analysis of the vibrational frequencies of a molecular system. However, the classical theory fails to determine

information from $(\partial\alpha_{\alpha,\beta}/\partial Q_l)_0$ concerning the transition frequencies and the frequency of the incident light. Hence, quantum mechanical theory will be applied to study Raman scattering, and in particular, the special case where the frequency of the incident light is in resonance with at least one electronic excited state of the molecular system. This resonance is denoted as resonance Raman (RR).

2.6.2 Quantum mechanical resonance Raman

In the quantum mechanical picture the polarizability tensor with its components $(\alpha_{\alpha,\beta})_{i\rightarrow f}$ for a transition from the initial state $|i\rangle$ to the final state $|f\rangle$ via the intermediate state $|n\rangle$, neglecting two-photon emission, is given by:

$$(\alpha_{\alpha,\beta})_{i\rightarrow f} = \frac{1}{2\hbar} \sum_{n \neq i,f} \left(\frac{\langle f|\hat{\mu}_\alpha|n\rangle\langle n|\hat{\mu}_\beta|i\rangle}{\omega_{n,i} - \omega_L - i\Gamma} + \frac{\langle f|\hat{\mu}_\alpha|n\rangle\langle n|\hat{\mu}_\beta|i\rangle}{\omega_{n,i} + \omega_L + i\Gamma} \right) \quad (2.17)$$

$$+ \frac{1}{2\hbar} \sum_{n \neq i,f} \left(\frac{\langle f|\hat{\mu}_\alpha|n\rangle\langle n|\hat{\mu}_\beta|i\rangle}{\omega_{n,f} - \omega_L - i\Gamma} + \frac{\langle f|\hat{\mu}_\alpha|n\rangle\langle n|\hat{\mu}_\beta|i\rangle}{\omega_{n,f} + \omega_L + i\Gamma} \right). \quad (2.18)$$

In the following, two approaches to calculate RR intensities based on equation 2.17 will be described.

2.6.2.1 Sum-over-State Formulation

After averaging over all orientations and integrating over all orientations and polarizations of the scattered light, the quantum mechanical theory of Raman scattering provides the Raman cross-section by^{110,111}:

$$\sigma_{i\rightarrow f} = \frac{\omega_L \omega_S^3}{18\pi \epsilon_0^2 c^4} \sum_{\alpha,\beta} \left| (\alpha_{\alpha,\beta})_{i\rightarrow f} \right|^2, \quad (2.19)$$

where ω_L and ω_S are the frequencies of the incident and the scattered light, ϵ_0 the electric field constant, c the speed of light and $(\alpha_{\alpha,\beta})_{i\rightarrow f}$ the Raman polarizability tensor for a transition from the initial $|i\rangle$ to the final $|f\rangle$ vibrational state. Kramers, Heisenberg and Dirac^{112,113} derived the Sum-over-State (SOS) expression for the Raman polarizability tensor:

$$(\alpha_{\alpha,\beta})_{i\rightarrow f} = \frac{1}{\hbar} \sum_n \left(\frac{\langle f|\hat{\mu}_\alpha|n\rangle\langle n|\hat{\mu}_\beta|i\rangle}{\omega_{n,i} - \omega_L - i\Gamma} + \frac{\langle f|\hat{\mu}_\beta|n\rangle\langle n|\hat{\mu}_\alpha|i\rangle}{\omega_{n,f} + \omega_L + i\Gamma} \right), \quad (2.20)$$

where $\hat{\mu}_\alpha$ is a component of the dipole moment operator, $\omega_{n,i}$ the Bohr frequency for a transition between two vibrational states defined as $\omega_{n,i} \equiv (E_n - E_i)/\hbar$ and Γ the dumping factor describing homogeneous broadening.

A direct evaluation of equation 2.20 is, due to the enormous computational cost, not feasible. Hence, several assumptions have to be made in order to compute RR intensities:

1. The polarizability tensor of equation 2.20 holds a “resonant” and a “non-resonant” term; the latter is neglected. This approximation is appropriate if ω_L is in close resonance with the intermediate vibrational states $|n\rangle$ ($\omega_L \approx \omega_{n,i}$). This way, the sum of equation 2.20 is dominated by these states.
2. The electronic and vibrational eigenstates are separated by virtue of the BO approximation.⁶²
3. The Condon Principle^{114–116} is applied, where the transition dipole moments are assumed to be invariant of the nuclear coordinates:

$$\langle \chi_f \psi_f | \hat{\mu} | \chi_i \psi_i \rangle \approx \langle \chi_f | \chi_i \rangle \langle \psi_f | \hat{\mu} | \psi_i \rangle$$
 This approximation is qualified for strong dipole-allowed electronic transitions.
4. The ground and excited states PESs are assumed to be harmonic, allowing to calculate vibrational states and frequencies of the PESs and thus the Franck-Condon (FC) factors in a straightforward manner.
5. The excited state PESs are assumed to be merely displaced with respect to the ground state equilibrium structure, so that the PESs share the same set of vibrational states and frequencies. This approximation is known as the independent mode displaced harmonic oscillator model (IMDHOM).
6. Only RR intensities for transitions from the vibrational ground state of the electronic ground state $|g0\rangle$ to the first excited vibrational state of the electronic ground $|g1_l\rangle$ state are calculated, these transitions are called fundamental transitions.

With these approximations at hand the Raman polarizability tensor of equation 2.20 is given here within the transform theory originally derived by Hizhnyakov and Tehver^{117–121}:

$$(\alpha_{\alpha,\beta})_{g0 \rightarrow g1_l} = \frac{1}{\hbar} \sum_e (\mu_{g,e})_\alpha (\mu_{g,e})_\beta \frac{\Delta_{e,l}}{\sqrt{2}} \{ \Phi_e(\omega_L) - \Phi_e(\omega_L - \omega_l) \}, \quad (2.21)$$

where the summation over e takes all contributing electronic excited states to the RR scattering into account, $(\mu_{g,e})_\alpha$ represent a component of the transition dipole moment at the ground state equilibrium geometry, $\Delta_{e,l}$ represents the dimensionless displacement of the minimum of the excited state e PES in the l th normal coordinate and ω_l denotes the frequency of the l th normal coordinate. Figure 2.2 illustrates a schematic representation of RR theory within the IMDHOM and the key parameters of equation 2.21 within a two state picture.

By summing over the excited states e , interference effects between the contributing electronic states are taken into account leading to constructive or destructive effects on the RR intensity

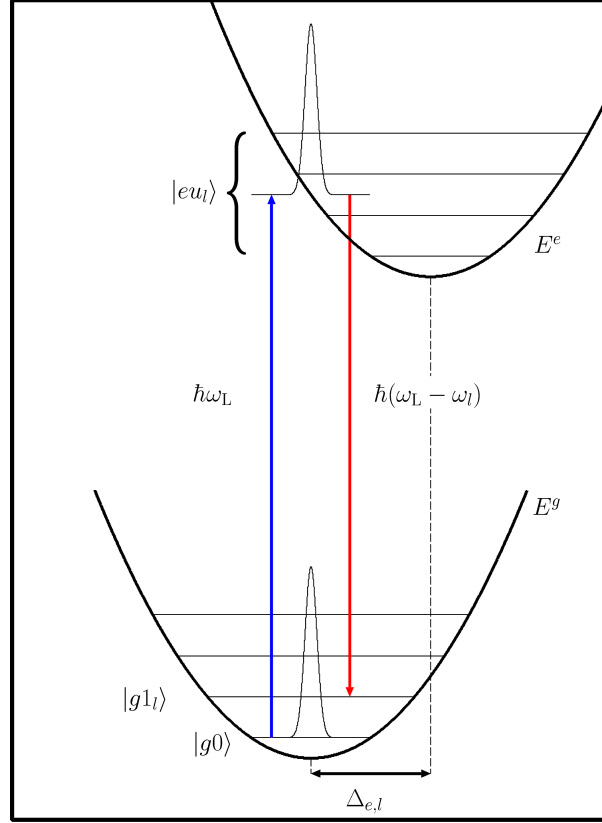


Figure 2.2: Generalized scheme of RR scattering within the IMDHOM for a fundamental transition $g0 \rightarrow g1_l$ and in resonance with the excited state e . PESs of the excited state E^e and the ground state E^0 are merely displaced by $\Delta_{e,l}$.

pattern. On the basis of $\Phi_e(\omega_L)$ the dependency of the RR signal on the frequency of the incidental light ω_L is described:

$$\Phi_e(\omega_L) = \sum_u \frac{\prod_i^{3N-6} |\langle \chi_{g0_i} | \chi_{eu_i} \rangle|^2}{\omega_{g0,e0} + \sum_j^{3N-6} u_j \omega_j - \omega_L - i\Gamma}. \quad (2.22)$$

The summation of the u runs over all vibrational quantum numbers u_i of the respective electronic excited state e , this way the one-dimensional FC factors along the l th vibrational coordinate are defined. The frequency $\omega_{g0,e0}$ refers to the energy gap between $|g0\rangle$ and $|e0\rangle$.

Φ_e of equation 2.22 can be further simplified if the absorption band features a large broadening and no resolved vibronic structure. Then, the one dimensional FC factors can be neglected and Φ_e becomes:

$$\Phi_e(\omega_L) = \frac{1}{\omega_{g,e} - \omega_L - i\Gamma}, \quad (2.23)$$

here $\omega_{g,e}$ is the vertical excitation energy within the FC region of the electronic ground state. The dimensionless displacement $\Delta_{e,l}$ of the excited state e with respect to the ground state g is defined in the IMDHOM by the partial derivative of the excited PES E^e along the mass-

weighted normal mode Q_l :

$$\Delta_{e,l} = -\frac{1}{\sqrt{\hbar\omega_l^3}} \left(\frac{\partial E^e}{\partial Q_l} \right)_0 \quad (2.24)$$

$$= -\frac{1}{\sqrt{\hbar\omega_l^3}} L^T M^{-\frac{1}{2}} \left(\frac{\partial E^e}{\partial x_l} \right)_0 . \quad (2.25)$$

The partial derivatives along Q_l are obtained from the non-mass-weighted Cartesian coordinates x_l applying the matrix M , containing the atomic masses, and the orthogonal matrix L , obtained from solving the ground state normal mode eigenvalue problem.

Consequently, the RR intensities for a fundamental transition $g0 \rightarrow g1_l$ with respect to the excitation energy ω_L are given by:

$$I_{g0 \rightarrow g1_l}(\omega_L) \propto \omega_L (\omega_L - \omega_l)^3 \sum_{\alpha,\beta} \left| (\alpha_{\alpha,\beta})_{g0 \rightarrow g1_l} \right|^2 . \quad (2.26)$$

2.6.2.2 Short-Time Approximation

A further simplification of equation 2.26 can be employed if merely one excited state e is in resonance with ω_L . Thus, the so called short-time approximation¹²² (STA) neglects the dependency of the relative RR intensities on ω_L :

$$I_{e,g0 \rightarrow g1_l} \propto \frac{1}{\hbar\omega_l} \left(\frac{\partial E^e}{\partial Q_l} \right)_0^2 = \omega_l^2 \Delta_{e,l}^2 . \quad (2.27)$$

Within the STA the obtained RR intensity is only depending on the frequency of the l th vibrational normal mode and the gradient of the excited state $\partial E^e / \partial Q_l$ within the electronic ground state minimum.

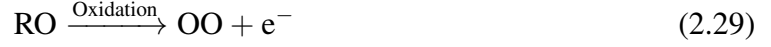
2.7 Electron Transfer Processes

2.7.1 Marcus Theory of Electron Transfer

An appropriate method to describe ET processes, both thermodynamically and kinetically, is given within the semi-classical Marcus theory.^{57,123} Here, the transfer between two redox states is divided into processes occurring via chemical bonds (known as inner-sphere effect) and via interactions with solvent molecules (known as outer-sphere effect). Every ET is characterized via two processes, oxidation and reduction:



where R and O refer to the reduced and oxidized states of a single ionizable group. In order to describe ET processes between two ionizable groups, we assume the donor state to be given by RO and the acceptor state by OR, hence one group is oxidized while the other one is reduced:



and



With this at hand, we can apply the approach derived by Warshel, Sprik and Blumberger based on classical statistical mechanics,¹²⁴⁻¹²⁶ in order to define the driving force, the classical reaction free energy, ΔG in terms of the vertical ionization energy or rather the energy gap (also known as ET energy) ΔE :¹²⁷

$$\Delta E(R^N) = E_{\text{OR}}(R^N) - E_{\text{RO}}(R^N) \quad (2.31)$$

$$\Delta G = G_{\text{OR}} - G_{\text{RO}} = -k_{\text{B}}T \ln \langle e^{-\frac{\Delta E}{k_{\text{B}}T}} \rangle_{\text{RO}} = k_{\text{B}}T \ln \langle e^{\frac{\Delta E}{k_{\text{B}}T}} \rangle_{\text{OR}} , \quad (2.32)$$

where $E_{\text{OR}}(R^N)$ and $E_{\text{RO}}(R^N)$ are the electronic ground state energies of the reactant and product states in the ionic configuration R^N , the brackets $\langle \dots \rangle$ indicate the canonical average of the potential energy of the respective state, k_{B} the Boltzmann constant and T the temperature. In case of well separated redox centers, the diabatic curves G_{OR} and G_{RO} describe the kinetics of the ET process along the reaction coordinate given by the energy gap of the states. The activation free energy ΔG^* for the non-adiabatic ET is then extracted from the crossing of the two diabatic curves of the reactant and product states. A key feature to describe ET processes is the reorganization energy λ , this energy refers to the free energy needed to move the donor from its equilibrium structure into the acceptor equilibrium structure and vice versa, while the electronic configuration remains unaffected. Figure 2.3 illustrates the reorganization energies λ_{RO} and λ_{OR} in the respective diabatic potential curves (G_{RO} and G_{OR}), as well as the activation free energy ΔG^* and the reaction free energy ΔG .

Within the linear response approximation^{124,126,128,129}, we now assume the populations of RO and OR to be distributed in Gaussians centered in the equilibria, whereas the equilibria ΔE_{RO} and ΔE_{OR} (see Figure 2.3) refer to the mean energy gaps $\langle \Delta E_{\text{RO}} \rangle$ and $\langle \Delta E_{\text{OR}} \rangle$. As a consequence of Gaussian statistics, both free energy curves, $G_{\text{RO}}(\Delta E)$ and $G_{\text{OR}}(\Delta E)$, are harmonic and share the same curvature, while the driving force and the reorganization energies are defined as:

$$\Delta G = \frac{1}{2} (\Delta E_{\text{RO}} + \Delta E_{\text{OR}}) , \quad (2.33)$$

and

$$\lambda = \lambda_{\text{RO}} = \lambda_{\text{OR}} = \frac{1}{2} (\Delta E_{\text{RO}} - \Delta E_{\text{OR}}) = \frac{\sigma^2}{2k_{\text{B}}T} . \quad (2.34)$$

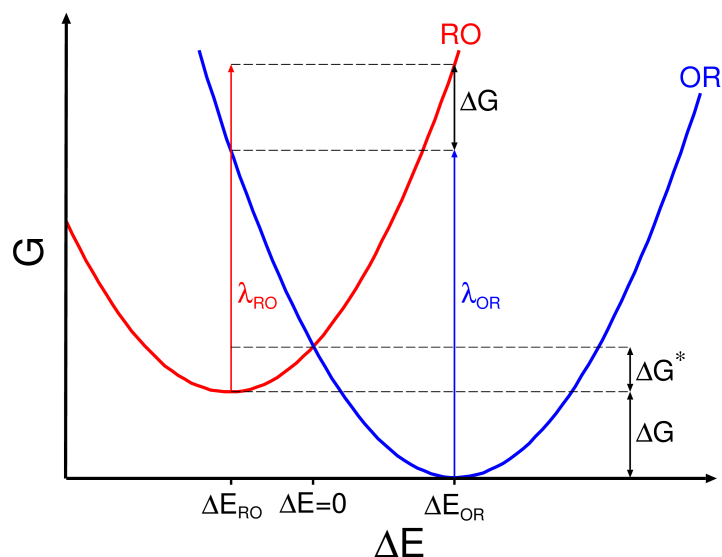


Figure 2.3: Marcus parabolas for the states RO and OR, the reorganization energies λ_{RO} and λ_{OR} , the reaction free energy ΔG and the activation free energy ΔG^* in terms of the gap energy ΔE ; ΔE_{RO} and ΔE_{OR} denote the mean energy gaps of the respective state.

The variance σ^2 is identical for both equilibrium distributions. With equations 2.33 and 2.34, ΔG is given by the average mean energy gaps and λ by half of the difference of these gaps.

The kinetics of ET processes are determined by rare thermal fluctuations of the environment that degenerate the two diabatic potentials. Marcus theory describes such kinetics via the ET rate constant k_{ET} .^{57,123,130}

$$k_{ET} = \frac{2\pi}{\hbar} |H_{RO/OR}|^2 (4\pi\lambda k_B T)^{-1/2} \exp\left(-\frac{(\Delta G + \lambda)^2}{4\lambda k_B T}\right), \quad (2.35)$$

where $H_{RO/OR}$ is the electronic coupling matrix between the donor and acceptor states. The product of the last two factors in equation 2.35, where $(\Delta G + \lambda)^2/4\lambda$ is the activation free energy, refers to the FC factor and hence the overlap of the vibronic states at a given temperature. The overlap is defined completely in terms of λ and ΔG . In case of intra-molecular ET (IET) equation 2.35 can be approximated using the semi-empirical expression:^{131,132}

$$\log(k_{IET}) = 15 - 0.6R - 3.1 \frac{(\Delta G + \lambda)^2}{\lambda}, \quad (2.36)$$

where the exponential decay of k_{IET} is given by the distance R (in Å) between the donor and the acceptor and a quadratic dependency on ΔG and λ (both in eV).

In the microscopic Marcus theory the key quantity to characterize ET, both thermodynamically and kinetically, is given by the energy gap. The following section illustrates the application of Marcus theory in order to predict rates of IET.

2.7.2 Intra-molecular Electron Transfer

IET processes take place between donor and acceptor groups of one compound. Hence, the primarily ET processes is described based on the inner-sphere effect, while solvating effects, described by the outer-sphere effect, affect the ET less. The crudest approximation is to completely neglect the outer-sphere effect. This way, the equilibria of the donor and acceptor states are given by the respective optimized geometries. ΔG and λ are then obtained from the energy gaps ΔE_{RO} and ΔE_{OR} in these structures. With this at hand k_{IET} can be calculated via equation 2.36.

Admittedly, the total neglect of solvent interactions leads typically to an overestimation of the reorganization energy.^{126,133,134} A more sophisticated picture is given QM/MM calculations, where the total potential energy is given by the sum over the QM, the MM and the QM/MM interaction energy (recall Section 2.4). In order to account for the outer-sphere effect MD simulations need to be carried out, describing solvation with several layers of solvent molecules via MM. The MD simulations are performed in the relaxed solvated equilibrium structures of the donor and the acceptor state. The obtained structural distributions are then used to construct the Marcus's parabolas around the well relaxed equilibrium structures.^{124–126}

In case of large donor-acceptor distances, e.g. $R > 10 \text{ \AA}$, where both groups are not interacting, one redox-active center can be treated in the QM and the other one in the MM frame. Then the common approach estimates ΔE at each R^N with two ground state energies for the reduction and oxidation (see equation 2.29 and 2.30), respectively:

1. $E_{\text{RQMOMM}}(R^N)$ labels the energy, where the donor side is calculated using QM and the acceptor (and the solvent) is described via MM.
2. $E_{\text{OQMOMM}}(R^N)$ is obtained in analogy to 1 for the oxidized donor.
3. $E_{\text{OMMOQM}}(R^N)$ and
4. $E_{\text{OMMRQM}}(R^N)$ refer to the respective energies of the reduction, while the donor (and the solvent) is treated via QM and the acceptor via MM.

The ionization energies $IE_{\text{RO}}(R^N)$ of RO and the electron affinities $IE_{\text{OR}}(R^N)$ of OR, obtained by these four ground state energies (illustrated in Figure 2.4), are then used to estimate $\Delta E(R^N)$:

$$IE_{\text{RO}}(R^N) = E_{\text{RQMOMM}}(R^N) - E_{\text{OQMOMM}}(R^N) \quad (2.37)$$

$$IE_{\text{OR}}(R^N) = E_{\text{OMMRQM}}(R^N) - E_{\text{OMMOQM}}(R^N) \quad (2.38)$$

$$\Delta E(R^N) = IE_{\text{RO}}(R^N) - IE_{\text{OR}}(R^N) . \quad (2.39)$$

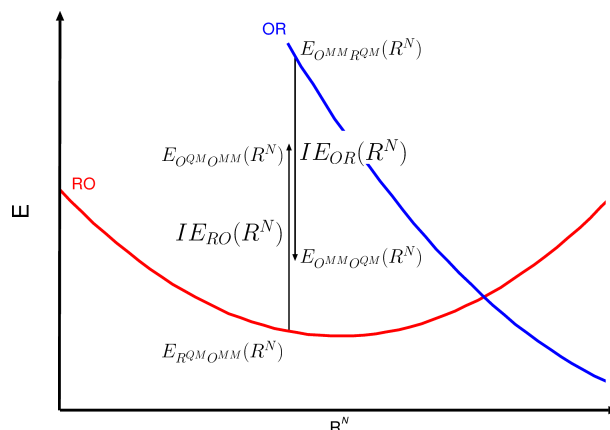


Figure 2.4: Ionization energy IE_{RO} and electron affinities IE_{OR} in the ionic configuration R^N of the states RO and OR, respectively.

This way, the mean gap energies ΔE_{RO} and ΔE_{OR} can be obtained and hence ΔG and λ comprise inner-sphere and outer-sphere effects.

The QM/MM ansatz is known to give a good estimation of the inner-sphere as well as the outer-sphere contributions to the reorganization energy and the driving force. Typically, the QM region is described at the DFT level of theory applying GGA and hybrid functionals, unfortunately these functionals show the electron self-interaction error.^{126,135} However, since the donor and the acceptor are not treated simultaneously via QM methods, the electron self-interaction is avoided.

The computational costs of such calculations should not be underestimated, despite the fact that the QM part can be described at the DFT level of theory and the MM region is of low-cost. Firstly, the solvated equilibrium geometries of RO and OR are typically obtained from molecular structures equilibrated using MD simulations up to the ns-time scale.^{126,132} Secondly, each ionic configuration R^N is correlated to four single point calculations, while a large number of points is needed to estimate the mean energy gaps. In case of short-range ET, the QM/MM model is inappropriate, due to the spatial overlap of the donor and acceptor orbitals. In this case, both redox sides need to be described via QM simultaneously and the problematic of the electron self-interaction as well as the of the computational costs rise.

Chapter 3

Results

The following Chapter is organized as follows. Chapter 3.1 concerns with the evaluation of spectroscopical properties such as absorption and emission spectra based on quantum chemical methods for several organic compounds. DFT, TDDFT, and accurate multiconfigurational methods are applied to unravel excited state properties of donor-acceptor dyes and to obtain insight into the underlying principles. Furthermore, the influence of solvent stabilization on charge separation is discussed. With this at hand, mechanistically information of CT states, e.g. twisted and planar intra-molecular CT states can be obtained. Chapter 3.2 deals with the detailed characterization of a series of novel ruthenium(II)-4*H*-imidazole-polypyridine based black absorbers showing a pronounced pH dependency of their photophysical properties. The application of TDDFT methods enabled us to study a variety of derivatives with electron donating as well as withdrawing groups and their electronic properties. Fundamental for the analysis of these transition metal complexes was the simulation of RR intensities. Such simulations have been carried out for cases, where only one but also several electronic states are in resonance with the incidental light. It is demonstrated that RR spectroscopy is a powerful tool to study the nature of excited states in the FC region. In addition, the relaxation pathways upon photoexcitation have been studied for two of these ruthenium(II) complexes. Finally, Chapter 3.3 addresses the first steps in order to study IET processes based on Marcus theory in a theoretical manner in ruthenium(II)-4*H*-imidazole-polypyridine complexes and, hence, their real life application in DSSCs.

3.1 Organic Dyes for Dye-Sensitized Solar Cells (DSSCs)

3.1.1 Excited State Properties of 4-Methoxy-1,3-Thiazole Donor-Acceptor Dyes

A series of novel donor- π -acceptor dyes has been synthesized in the group of Prof. Dr. Beckert in the IOMC at the Friedrich-Schiller Universität Jena (see chromophores **A–D** depicted in Figure 3.1) using 4-methoxy-1,3-thiazole based linkers that remarkably shift the UV-vis absorption to longer wavelengths. These dyes have been characterized in a joint experimental and theoretical study, see appended publication 4.1, in order to address their applicability in the field of DSSCs. In the following, we will focus on the quantum chemical analysis.

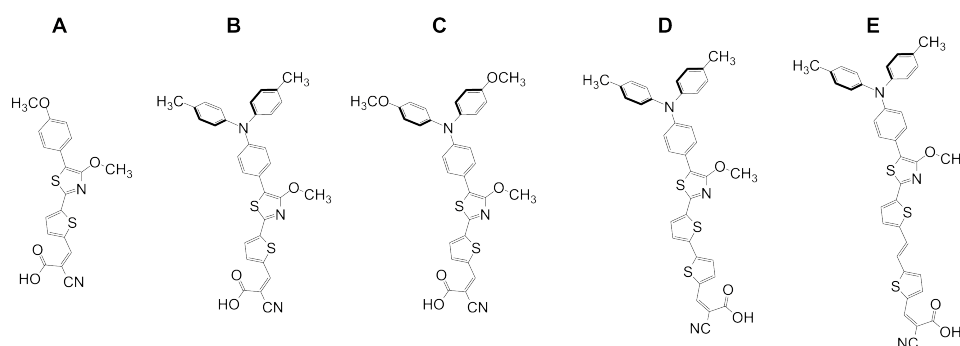


Figure 3.1: Investigated 4-methoxy-1,3-thiazole based donor-acceptor dyes: **A–D** have been studied applying both experimental and theoretical methods, while **E** was exclusively studied theoretically. **A–C** share the same linker and anchoring groups, while the π -system of the donor was increased from 4-methoxy-phenyl (**A**) to *N,N*-di-4-tolylaniline (**B**) and further to *N,N*-di-4-methoxy-phenyl (**C**). **B**, **D**, and **E** differ only in the size of the linker: the conjugated π -system was increased with a second thiophene (**D**) and in addition a 2-ethylene group (**E**).

Common triarylamine based dyes feature one major drawback, the red-sided absorption band is typically below 500 nm. Hence, the ansatz to include linkers that are chromophores themselves, e.g. the 4-methoxy-1,3-thiazole, enables an enhanced overlap of the absorption and the solar radiation spectrum. For the present dyes the influence of the size of the donor has been investigated using the dyes **A–C**. These dyes feature the same linker and anchoring groups, while the π -system of the donor was increased from 4-methoxy-phenyl (**A**) to *N,N*-di-4-tolylaniline (**B**) and further to *N,N*-di-4-methoxy-phenyl (**C**). In addition, the size of the π -system of the linker has been increased from **B** with a second thiophene (**D**) and a further 2-ethylene-thiophene group (**E**). The applied quantum chemical methods gave insight into spectroscopical properties such as absorption and emission as well as the equilibrium structures of both the electronic ground state and the lowest excited singlet state, which is involved in the fluorescence of the dyes **A–D**. In addition, the dye **E**, with an even more extended conjugated π -system, has been studied only in a theoretical manner.

	Transition	Absorption					Emission			
		weight / %	ΔE^e / eV	f	$\Delta\Delta E_{\text{exp}}$ / eV		Transition	weight / %	ΔE^e / eV	f
A	HOMO \rightarrow LUMO	88	2.75	1.364	0.12	HOMO \rightarrow LUMO	95	2.12	1.558	0.01
B	HOMO \rightarrow LUMO	72	2.58	1.511	0.09	HOMO \rightarrow LUMO	91	1.91	1.838	-0.02
	HOMO-1 \rightarrow LUMO	20								
C	HOMO \rightarrow LUMO	71	2.54	1.502	0.11	HOMO \rightarrow LUMO	89	1.88	1.85	-0.06
	HOMO-1 \rightarrow LUMO	20								
D	HOMO \rightarrow LUMO	54	2.64	1.958	0.16	HOMO \rightarrow LUMO	85	1.85	2.198	-0.15
	HOMO-1 \rightarrow LUMO	26								
	HOMO \rightarrow LUMO+1	12								
E	HOMO \rightarrow LUMO	48	2.57	2.500	-	HOMO \rightarrow LUMO	83	1.79	2.699	-
	HOMO-1 \rightarrow LUMO	32								
	HOMO \rightarrow LUMO+1	11								

Table 3.1: S_1 main transitions with weight, excitation energies (ΔE^e), oscillator strengths (f) and the deviations from the experimental values ($\Delta\Delta E_{\text{exp}}$) for the absorption and emission properties of the dyes **A–E** obtained with CAM-B3LYP/6-31G(d,p) taking into account solvent effects (tetrahydrofuran).

All five species show similar FC geometries (see Appendix A), optimized at the DFT level of theory with the long-range corrected CAM-B3LYP functional and a polarizable continuum model (tetrahydrofuran). The conjugated π -system is planar from the bridge to the 2-cyanoacrylic acid anchoring group, while the 4-thiophyl (**B**, **D**, and **E**) and the 4-methoxy-phenyl (**C**) moieties of the donor fragment are twisted out of planarity due to sterical hindrance. A pronounced torsion was also observed for the C–C bond joining the donor and the 4-methoxy-1,3-thiazole fragments. The solvated geometries of the respective S_1 , shown in Appendix A, optimized at TDDFT level of theory with the same exchange correlation functional as above, showed only minor deviations from the S_0 equilibrium structures, the only exception is the torsion of the linker and the donor. In the S_1 a planarization of the thiazole-phenyl fragment is observed by virtue of the bonding character of the LUMO in this position, see exemplarily the LUMO of **B** in the attached publication 4.1.

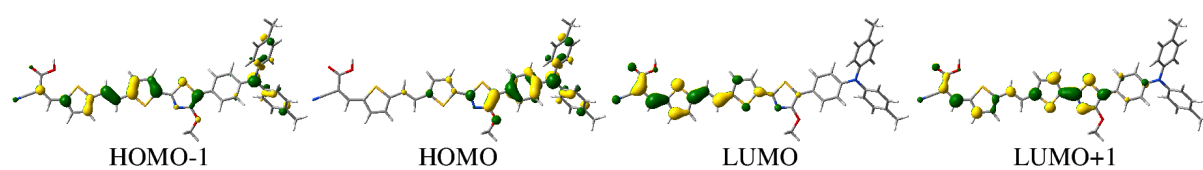


Figure 3.2: MOs of **E** contributing to the main transitions of the S_1 obtained at CAM-B3LYP/6-31G(d,p) level of theory in tetrahydrofuran.

The visible region of the absorption spectra of the five dyes are characterized by very bright S_1 states. Table 3.1 summarizes the absorption properties of the S_1 states for all five dyes, while the involved MOs are illustrated in Figure 3.2 using the example of **E**; the orbitals of **A–D** are depicted in the attached publication 4.1. As expected, the S_1 excitation energy decreased from **A** to **B** as a consequence of the extended π -system of the donor. Further increase of the π -system utilizing methoxy groups (see **C**) is of minor influence. The S_1 states of **A**

to **C** were found to be mainly of CT character, based on the HOMO \rightarrow LUMO transitions, however also the HOMO-1 \rightarrow LUMO transitions of more local character showed substantial weights in **B** and **C**. Surprisingly, the S_1 excitation energy in **D** and **E**, where the conjugated π -system of the linker was further increased, were not bathochromic but hypochromic shifted with respect to **B**. The reason was found upon analysis of the S_1 wave functions: The CT character (HOMO \rightarrow LUMO) decreases and the weight of local (HOMO-1 \rightarrow LUMO and HOMO \rightarrow LUMO+1) transitions increases as the π -system was extended from **A** to **E**.

Due to the planarization of the linker-donor fragment in the S_1 equilibrium geometries with respect to the S_0 structures, the emission spectra are substantially bathochromic shifted by approximately 0.5 to 0.8 eV compared to the absorption, see Table 3.1. This planarization is accompanied by an increase of the weights of the HOMO \rightarrow LUMO transitions.

Unfortunately, the dyes **A–D** show very low electron injection efficiencies on a TiO_2 surface due to their tendency to form aggregates. However, the determined properties of the S_1 states are in very good agreement with the experimental data and rationalized two competitive effects influencing the position of the S_1 . On the one hand, the extension of the π -system, in particular that of the donor, lowers the S_1 excitation energy. This was confirmed by means of the chromophores **A**, **B** and **C**. On the other hand, increasing the π -system of the linker led to a contamination of the CT state with local transitions and, hence, to a raise of the S_1 excitation energy. This was observed for the dyes **B**, **D** and **E** exhibiting equal donor groups but different linkers. The gained knowledge should be taken into account when designing new efficient dyes.

3.1.2 Influence of Charge Transfer States on Ground State Structures

In this study we investigate the excited states properties of the 4-methoxy-1,3-thiazole donor-acceptor dye **B** (see Section 3.1.1) in a more detailed manner. TDDFT and RASPT2/RASSCF methods are employed to access excitation energies and gradients of the first excited state. To this aim, equilibrium geometries, UV/vis absorption and RR spectra were calculated in order to characterize the bright CT state (S_1) that is located at a remarkably low excitation energy of for this family of push-pull chromophores.

Therefore, the solvated equilibrium geometries (chloroform) and vibrational frequencies were calculated using the global hybrid functionals B3LYP and M06-2X as well as the range-separated CAM-B3LYP functional. These geometries and the same functionals were employed within TDDFT to calculate the vertical energies of the low-lying excited states in the presence of a polarized continuum to model solution. It was found that the amount of exact-exchange in the functional not only has a strong influence on the accuracy of the excitation energies but the latter also markedly depend on the equilibrium structure employed. Deviations up to 0.2 eV were found when going from the B3LYP (TD-CAM-B3LYP//B3LYP: 2.36 eV) to the CAM-B3LYP (TD-CAM-B3LYP//CAM-B3LYP: 2.58 eV) equilibrium geometry, while the experimental absorption maximum is located in chloroform at 2.39 eV. These energy differences can be rationalized analysing the variations of the torsion angle of the carbon-carbon bond joining the bridge and the donor group (dihedral angle δ) as well as the extent of localization of the single and double bonds. The latter aspect was analyzed based on the bond length alternation (BLA) index,^{136,137} which is calculated from the difference of the average carbon-carbon single and double bond lengths. PESs of S_0 and S_1 along δ showed that torsion is of minor importance to the S_1 excitation energy. However, a more pronounced amount of exact-exchange leads to larger BLA indexes, i.e. a more localized nature of the single and double bonds, increasing thus the excitation energies. In this way, changes of the BLA index and, hence, in the ground state structures, are correlated to differences in excitation energy. From the three functionals investigated, B3LYP fails to predict the excitation energies of **B**, due to its intrinsic problems in describing CT states such as the S_1 in the present molecular system. The CAM-B3LYP and M06-2X functionals (TD-M06-2X//M06-2X: 2.55 eV) deliver good agreements with the experiment provided solvation effects are considered. TDDFT estimated a solvent stabilization of the CT states by approximately 0.1 eV independent of the applied functional. The best estimation of the S_1 energy was found using TD-CAM-B3LYP//B3LYP (2.36 eV) with respect to the experimental value of 2.39 eV.

The position of the S_1 state was also investigated by means of MS-RASPT2/RASSCF calculations at the B3LYP and CAM-B3LYP geometries. Four different partitions, changing the active space and the level of excitation were employed: (30,2,2;14,2,11), (16,2,2;7,2,7), (16,3,3;7,2,7), and (16,4,4;7,2,7). All of them contain merely the HOMO and LUMO orbitals

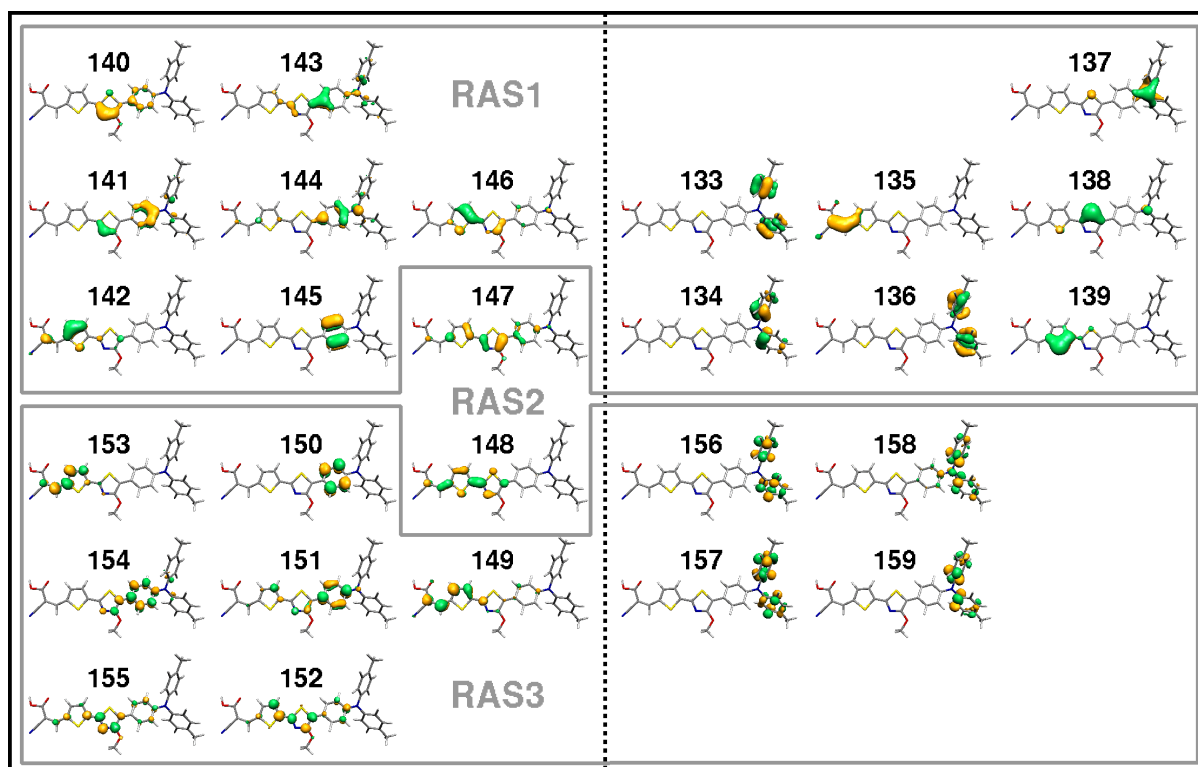


Figure 3.3: Molecular orbitals for RASSCF(30,2,2;14,2,11) (solid grey), RASSCF(16,2,2;7,2,7), RASSCF(16,3,3;7,2,7) and RASSCF(16,4,4;7,2,7) (left hand side) calculations.

in the RAS2, while a different number of active orbitals, holes, and particles are allowed within the RAS1 and RAS3 subspaces. An overview of these four partitions is provided in Figure 3.3; for more detailed information the reader is referred to the appended publication 4.2. The MS-RASPT2 calculations showed similarly to the TDDFT simulations, i.e. a pronounced dependency of the S_1 excitation energy on the equilibrium structure and the partition employed. Although in some cases errors can be considered acceptable (0.1-0.2 eV), it seems that in this particular case, where the RAS2 is reduced to HOMO-LUMO, the inclusion of at least triple excitations is necessary to achieve good excitation energies. The best agreement to the first absorption band was obtained with the CAM-B3LYP geometry and the (16,4,4;7,2,7) partition yielding an excitation energy of 2.37 eV taking into account a bathochromic shift of 0.1 eV due to solvent effects. The excitation energy obtained with the B3LYP structure and the same level of excitation is underestimated (2.25 eV). The large (30,2,2;14,2,11) partition also provides with 2.35 eV a good estimation of the excitation energy for the present dye in combination with the B3LYP geometry. However, from the computational point of view the (30,2,2;14,2,11) partition is associated with an enormous cost in the MS-RASPT2 procedure, arising from the first-order perturbative wavefunction, see equation 2.4 in Section 2.2.

Since MS-RASPT2/RASSCF calculations cannot provide a clear-cut answer on which ground state geometry is more adequate, RR intensity patterns were calculated, paying special attention

to the B3LYP and CAM-B3LYP structures. TDDFT and RASSCF gradients using the compromised (16,3,3;7,2,7) partition were employed. Up to our knowledge, this is the first time that RASSCF gradients are used to compute RR intensities. The results, illustrated in Figure 3.4, clearly evidence that only the RR spectra using the CAM-B3LYP (and M06-2X) equilibrium structure show an excellent agreement with experiment, which allows an unambiguous assignment of the normal modes. CAM-B3LYP, M06-2X and RASSCF excited state gradients and energies in combination with CAM-B3LYP or M06-2X, respectively, ground state gradients are appropriate to describe the low-lying CT state of this push-pull chromophore. Particularly encouraging is the agreement on RR intensities based on RASSCF, since despite the computational cost, it paves the way to employ multiconfigurational gradients in situations where conventional TDDFT calculations might fail completely to provide accurate results.

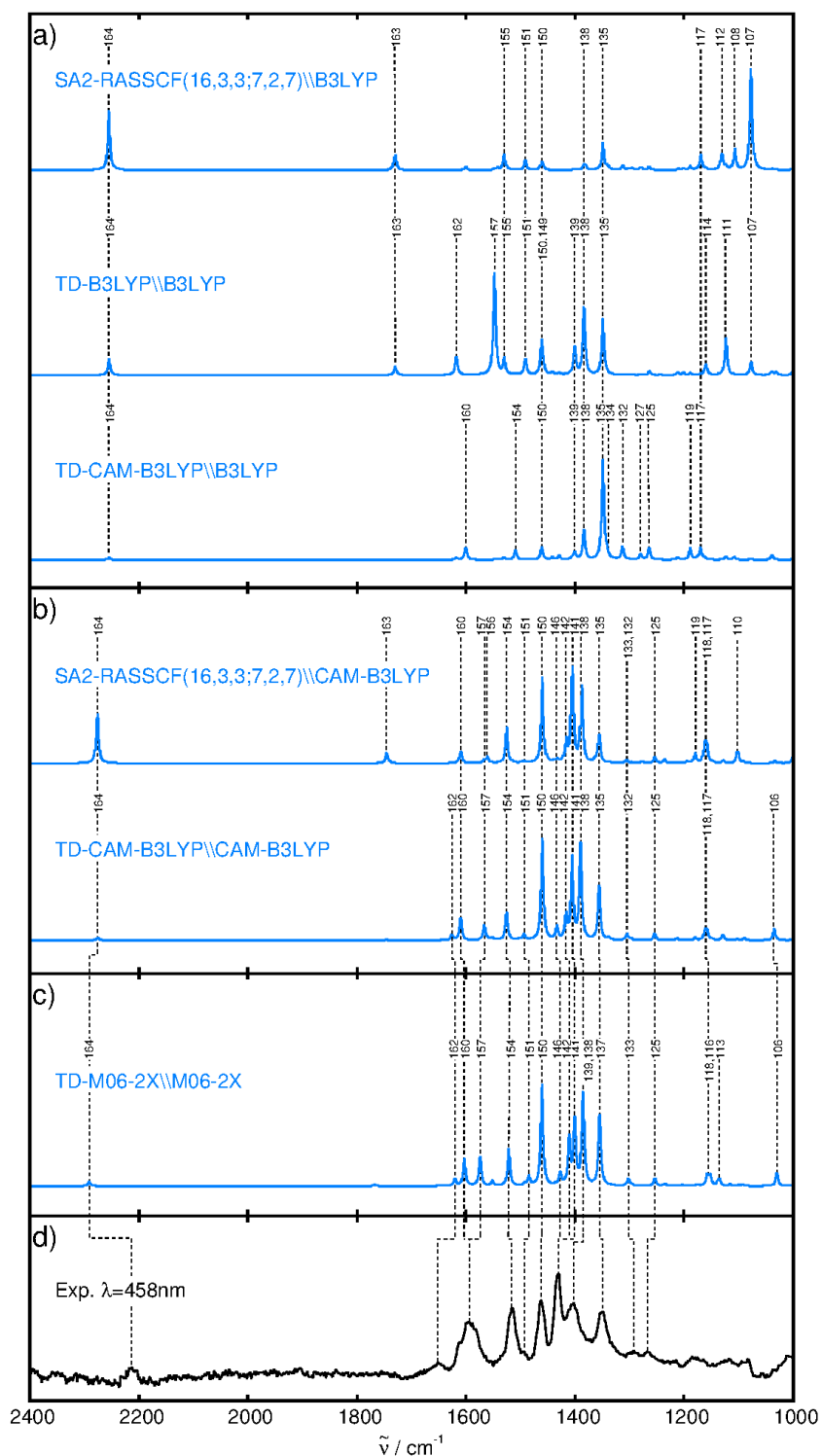


Figure 3.4: RR spectra of **1** in resonance with the first absorption band. The calculated RR spectra with the B3LYP and CAM-B3LYP ground state force fields and the excited state gradients at TD-B3LYP, TD-CAM-B3LYP and SA2-RASSCF (16,3,3;7,2,7) level of theory are shown in a) and b). The RR intensity pattern with TD-M06-2X in the M06-2X optimized ground state geometry is reported in c). The calculated spectra of b) and c) are compared to the experimental RR spectrum in d) recorded at an excitation wavelength of 458 nm.

3.1.3 Twisted Intra-Molecular Charge Transfer vs. Planar Intra-Molecular Charge Transfer

The 4-methoxy-thiazole chromophore is not only limited to applications in Grätzel-type DSSCs, furthermore it can be applied as ligands for ruthenium(II) based black absorbers. A series of such compounds was synthesized in the group of Prof. Dr. Beckert in the IOMC at the Friedrich-Schiller Universität Jena. Two of these ligands, together with an additional one studied exclusive theoretically, are illustrated in Figure 3.5. They are constructed in a donor- π -linker-acceptor fashion and have been theoretically investigated applying DFT and TDDFT methods, for more details the reader is referred to the appended publication 4.3.

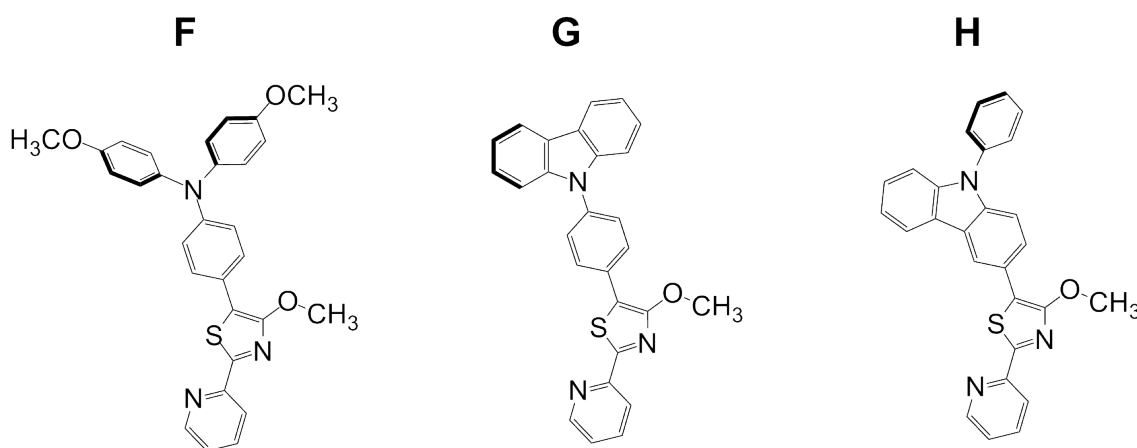


Figure 3.5: Investigated 4-methoxy-1,3-thiazole based donor-acceptor ligands with different donor groups, **F** and **G** were studied applying both experimental and theoretical methods, while **H** was exclusively studied theoretically. All three ligands share the same 4-methoxy-1,3-thiazole linker and pyridyl acceptor, while different donor groups have been used: **F** exhibits a bis(4-methoxy-phenyl)-*N*-phenylaniline donor, **G** and **H** *N*-phenyl-carbazole donors connected to the linker via the phenyl and carbazole, respectively.

The dyes **F**, **G** and **H** contain bis(4-methoxy-phenyl)-*N*-phenylaniline and carbazole donors, with a 4-methoxy-1,3-thiazole linker and a pyridyl acceptor. The thermodynamic stable isomer of the free ligands is the *trans*-isomer, while the bounded ligands coordinate the ruthenium(II) center in the *cis*-conformation (via the two nitrogen atoms of the thiazole and the pyridyl moieties).

These ligands are interesting in two aspects:

- i) The absorption spectra measured in a series from unpolar to polar solvents point to a unique phenomenon: the intra-molecular CT (ICT) state is stabilized by unpolar solvents and not as expected by polar solvents.
- ii) A controversial discussion concerning the nature of the ICT in donor-acceptor dyes is found in the literature, where both planar intra-molecular charge transfer (PICT) and

twisted intra-molecular charge transfer (TICT) mechanisms are put forward. Hence, unraveling the ICT mechanisms, e.g. in the present dyes **F** and **G**, can be achieved applying theoretical methods.

The first step in order to address the effects of solvation as well as to study the ICT mechanism was to find a suitable functional that is capable to describe absorption and emission with the same accuracy. The absorption and emission spectra are both determined by the S_1 state, however, the ICT character of this state increases substantially from the FC region to the equilibrium geometry of the S_1 . This trend was already observed for the dyes **A-E** (see Section 3.1.1) and is connected to the planarization of the 4-methoxy-thiazole-phenyl fragment. In contrast to the results obtained for **A-E**, range-separated functionals as CAM-B3LYP overestimate the excitation energy of the S_1 in the ground state geometry by the same value as global hybrid functionals (B3LYP and PBE0) underestimate it. The emission was found in excellent agreement with CAM-B3LYP. A balanced description of absorption as well as emission is given by B3LYP(35) with medium amount of exact-exchange. Hence, the relative energetic positions of the S_0 and S_1 states of **F** and **G** were evaluated in a polar (methanol; abbreviated as MeOH) and an unpolar solvent (heptane), while solvation was considered for the ground and excited states. The calculated vertical excitation energies for the absorption as well as for the emission along with the experimental values are collected in Figure 3.6. The calculated S_1

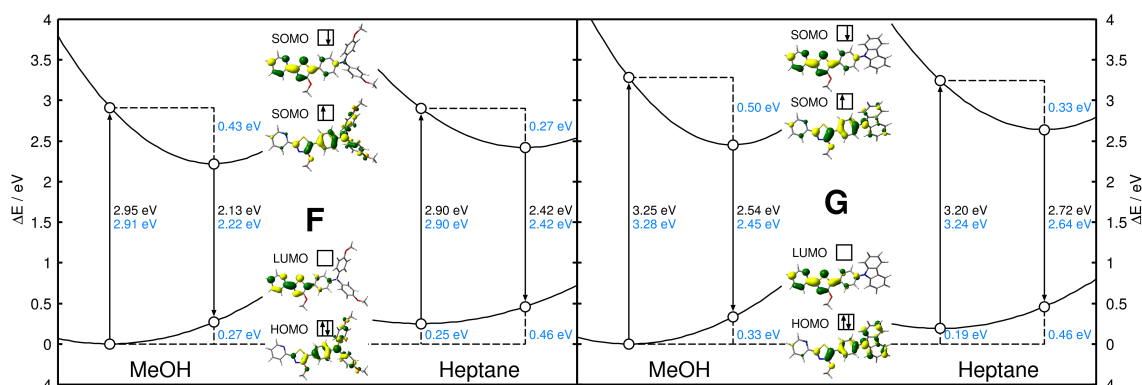


Figure 3.6: Schematic representation of the electronic ground and first excited singlets state of **F** and **G** in MeOH and heptane; all values in black refer to the experimental values, while the blue values were obtained at the PCM-B3LYP(35)/6-31G(d,p) level of theory in the solvated equilibrium structures. The depicted HOMOs and LUMOs refer to the MOs involved in the absorption (optimized S_0 state) and the SOMOs to the MOs involved in the emission (optimized S_1 state).

excitation energies in the FC region were found in very good agreement with the experimental data, and the excitation energy is almost unaffected by the solvent. However, the S_0 in the FC region is by 0.25 (**F**) and 0.19 eV (**G**) more stable in MeOH. The ground and the excited states are equally stabilized, whereas the excitation energies in heptane are slightly bathochromically shifted compared to MeOH. Relaxing the S_1 state from the FC regions to the excited state min-

ima led to a planarization of the thiazole-phenyl fragment accompanied by an increase of the ICT character given by the HOMO \rightarrow LUMO transition (see MOs of Figure 3.6) and, hence, to an enhanced charge separation. As a consequence, the S_1 states relax by 0.43 and 0.50 eV (**F** and **G**) in the polar solvent and merely by 0.27 and 0.33 eV in the unpolar solvent (**F** and **G**). Simultaneously, the energy of the ground state is lifted equally in both dyes and for both solvents by approximately 0.2 to 0.3 eV. This way, the unusual bathochromic effect of polar solvents, e.g. heptane, observed in the absorption spectra of **F** and **G** was rationalized.

The second interesting aspect concerning these dyes is the ICT and hence, the evaluation of PICT and TICT states. In the ground state as well as in the excited state equilibrium structures, depicted in A.6 and A.7 of the Appendix, the donor groups (bis(4-methoxy-phenyl)-*N*-phenylaniline and carbazole) are oriented approximately in the plane of the thiazole and the pyridyl acceptor, while the terminal 4-methoxy-phenyl groups and the carbazole are twisted by approximately 30° due to sterical hindrances. Consequently, no TICT state is observed in these dyes and the TICT is not connected to a barrier-free evolution in the excited state PES, as described in the literature. In order to study the possibility of twisting in the excited state, the PESs of S_0 and S_1 were calculated for the torsion of the C–NR₂ bond in the chromophore **F**. The ground state PESs (in both solvents) showed minima at 30° and 210° separated by barriers

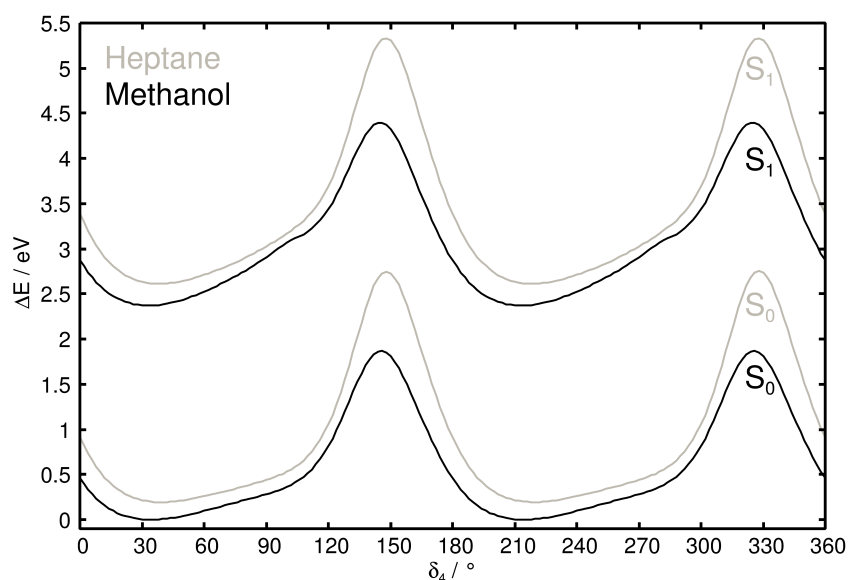


Figure 3.7: PESs of the S_0 and S_1 states calculated at the B3LYP(35)/6-31G(d,p) level and with a polarizable continuum model for MeOH and heptane.

of 1.87 eV (MeOH) and even 2.55 eV (heptane). The excited states exhibit a similar behavior. Here, the minima here were found at ca. 34° (MeOH) and 38° (heptane). These values are consistent with the angles observed in the optimized S_1 geometries of **F**, recall A.6 of the Appendix. The PESs of the ground and the excited states are almost parallel and no evidence for a minimum at 90° was found. A further optimization of the S_1 starting in the twisted geometry

(90°) evolved to the same structure as the S_1 optimization from the FC region. Therefore, the quantum chemical simulations yielded no evidence for a TICT state in the investigated ligands. The ligand **H** (depicted in Figure 3.5) is unable to show a TICT by virtue of the rigid *N*-phenyl-carbazole donor connected to the linker in position 3 and was only theoretically investigated. The donor group of this ligand exhibits an enhanced planar π -system that is able to interact with the π -systems of the linker and the acceptor. This way, the S_1 excitation energies were slightly reduced by 0.05 and 0.02 eV in MeOH and heptane with respect to **G**. The binding of the carbazole donor in position 3 led to an increase of the weight of the HOMO \rightarrow LUMO transitions to 96% and hence to an increase of the ICT character. This shows that the S_1 excitation energy is not only connected to the size of the π -system of the donor but also to the structural arrangement of the donor and the capability to interact with the linker and the acceptor. Based on the quantum chemical analysis of absorption and emission spectra and the correlated structural properties, theory could explain the observed unusual solvent effects. Furthermore, the ICT mechanism of the studied dyes was determined to be of PICT nature.

3.2 Ruthenium(II)-4H-Imidazole Black Absorbers

3.2.1 Optical Properties of 4H-Imidazole-Ruthenium(II) Complexes

Ruthenium(II) polypyridine complexes have been studied intensively due to their outstanding photophysical properties combined with redox and catalytic activities and a strong stability on light, heat and electricity. In cooperation with the groups of Prof. Dr. Beckert (IOMC Friedrich-Schiller Universität Jena), Prof. Dr. Rau (Universität Ulm), Prof. Dr. Dietzek (IPC Friedrich-Schiller Universität Jena) and Prof. Dr. Popp (IPC Friedrich-Schiller Universität Jena) a wide range of novel ruthenium(II) polypyridine complexes with 4H-imidazole ligands have been investigated. In this context, photophysical properties in the FC region, such as absorption and RR spectra, of the complexes depicted in Figure 3.8 were extensively examined applying theoretical methods, see the appended publication 4.4, 4.5, 4.6, and 4.7. Effects of substitution were

$R = \text{H, Me, NMe}_2, \text{NHMe}_2^+, \text{COOEt}$

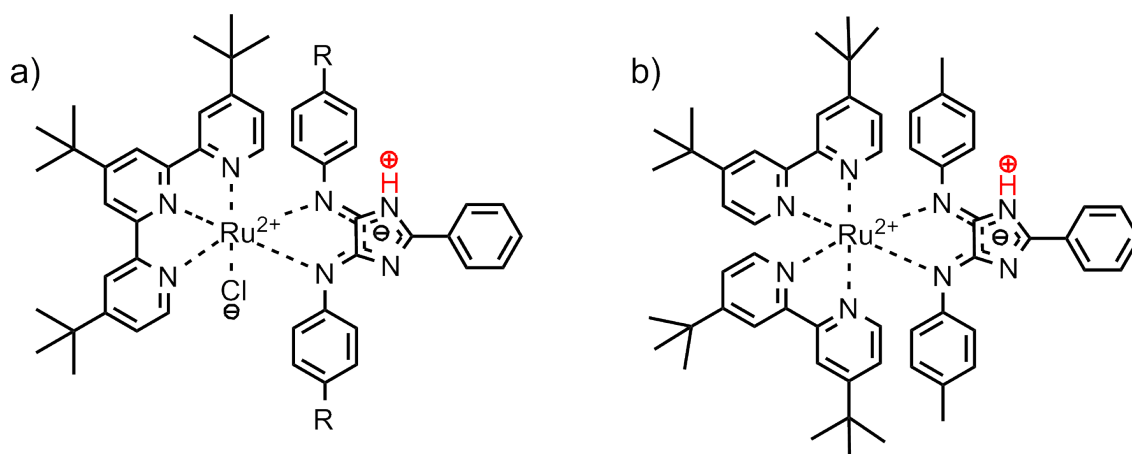


Figure 3.8: Investigated ruthenium(II)-4H-imidazole complexes with terpyridine a) and bipyridine ligands b) for different protonation states. In case of a) a series of substituents in the 4H-imidazole have been studied. In all theoretical simulations the *tert*-butyl groups of the polypyridine ligands have been approximated by methyl groups.

studied by changing the character of **R** from electron donating to electron withdrawing groups ($\text{NMe}_2 > \text{Me} > \text{H} > \text{NHMe}_2^+ > \text{COOEt}$), see Figure 3.8a). In addition, the influences of the polypyridine coordination sphere (terpyridine and bipyridine Figure 3.8b)) and protonation of the 4H-imidazole ligands on the spectroscopical properties were investigated.

The spectroscopical features of the 4H-imidazole-ruthenium(II) complexes were unraveled using DFT and TDDFT methods for the ground and the singlet excited states, respectively. Solvation effects (acetonitrile) on the ground and excited states (equilibrium geometries, vibrational frequencies, excitation energies, oscillator strengths, and excited state gradients) have been taken into account applying a polarizable continuum model. The standard B3LYP func-

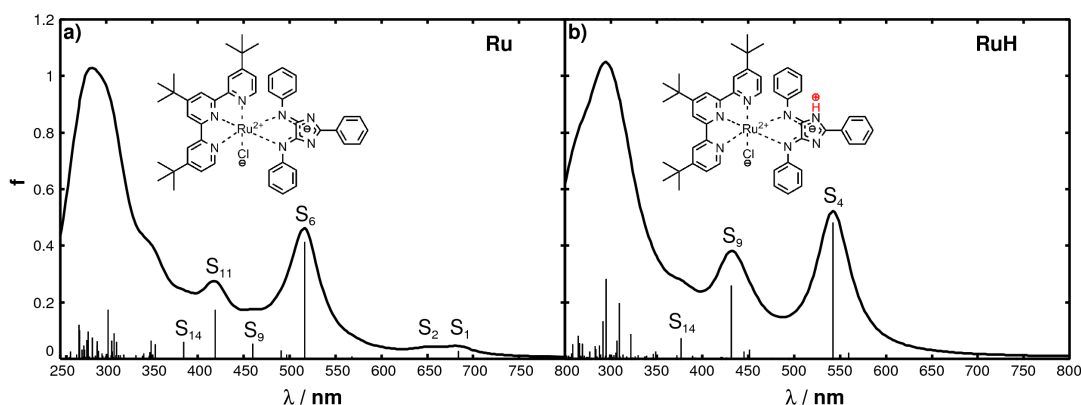


Figure 3.9: Theoretical absorption spectra of the **Ru** and **RuH** species in acetonitrile. A Lorentzian function with a half-width of 20 nm is employed to broaden the transitions in the spectrum based on the oscillator strengths represented by black sticks.

State	Transition		weight / %	ΔE^e / eV	λ / nm	f
Ru						
S_1	$d_{xz}(174) \rightarrow \pi_{im}^*(175)$ (MLCT)		96	1.81	684	0.0285
S_2	$d_{xz}(174) \rightarrow \pi_{terpy}^*(176)$ (MLCT)		96	1.91	650	0.0175
S_6	$d_{xy}(173) \rightarrow \pi_{im}^*(175)$ (MLCT)		52	2.40	517	0.4125
	$d_{yz}(172) \rightarrow \pi_{terpy}^*(176)$ (MLCT)		28			
	$d_{yz}(172) \rightarrow \pi_{im}^*(175)$ (MLCT)		11			
S_9	$d_{yz}(172) \rightarrow \pi_{terpy}^*(176)$ (MLCT)		29	2.70	460	0.0526
	$d_{xy}(173) \rightarrow \pi_{terpy}^*(177)$ (MLCT)		20			
	$d_{xy}(173) \rightarrow \pi_{im}^*(175)$ (MLCT)		17			
	$d_{xz}(174) \rightarrow \pi_{terpy}^*(177)$ (MLCT)		10			
S_{11}	$\pi_{im}(171) \rightarrow \pi_{im}^*(175)$ (ILCT)		94	2.96	419	0.1746
S_{14}	$d_{xz}(174) \rightarrow \pi_{terpy}^*(178)$ (MLCT)		91	3.22	385	0.0603
RuH						
S_1	$d_{xz}(174) \rightarrow \pi_{im}^*(175)$ (MLCT)		0.96	1.47	844	0.0075
S_4	$d_{xy}(172) \rightarrow \pi_{im}^*(175)$ (MLCT)		0.83	2.29	542	0.4820
S_9	$\pi_{im}(171) \rightarrow \pi_{im}^*(175)$ (ILCT)		0.94	2.87	431	0.2594
S_{14}	$\pi_{im}(168) \rightarrow \pi_{im}^*(175)$ (ILCT)		0.90	3.29	377	0.0730

Table 3.2: Calculated vertical excitation energies (E^e), wavelengths (λ), oscillator strengths (f) and singly-excited configurations of the main excited states of the deprotonated (**Ru**) and protonated form (**RuH**) in the visible range. The principal orbitals are depicted in Figure 3.10.

tional with 20% of exact-exchange gives the most balanced description of the excited states for this class of complexes, whereas the global hybrid functional PBE0 as well as the long-range corrected CAM-B3LYP functional increase the global deviations from experiment.^{138–140}

The starting point for the evaluation of substitution effects of the 4*H*-imidazole were the unsubstituted complexes (R=H), in the deprotonated and protonated forms denoted as **Ru** and **RuH**, respectively. These complexes served as reference systems and have been exclusively studied in a theoretical manner. In this study the three *tert*-butyl groups of the terpyridine ligand were approximated by methyl groups in order to decrease the computational effort. Figure 3.9a) and b) show the calculated absorption spectra for both species, while Table 3.2 collects the properties of the main excited singlet states contributing to the visible region. The MOs involved in the transitions of Table 3.2 are depicted in Figure 3.10. The absorption spectra and the under-

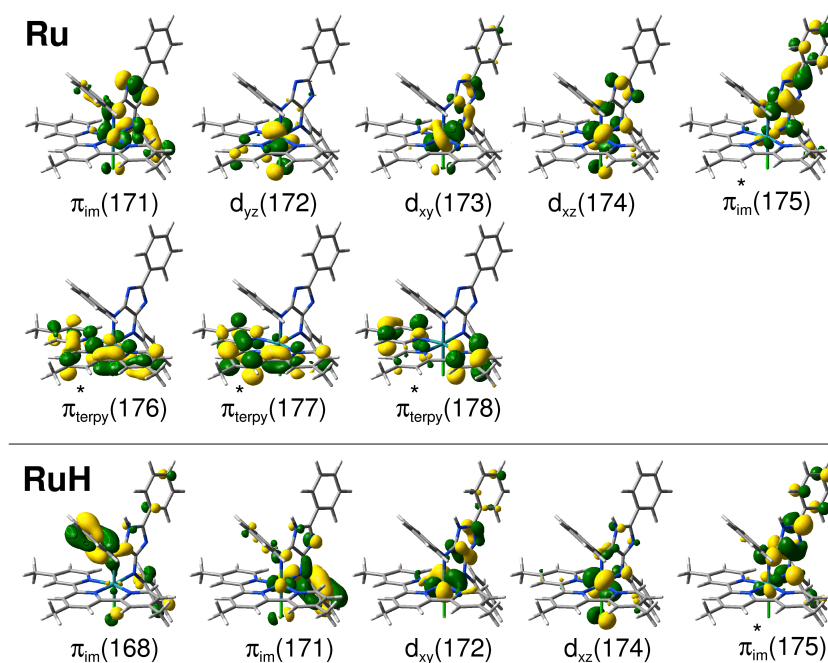


Figure 3.10: MOs involved in the main configurations of the states responsible for the absorption and RR properties of the deprotonated (**Ru**) and protonated (**RuH**) complexes.

lying excited states show a distinct dependency on the pH. The deprotonated complex exhibits two weakly absorbing MLCT states (S_1 and S_2) of CT character to either the 4*H*-imidazole or the terpyridine ligand. The very bright S_6 of MLCT character displays a mixing of transitions to the 4*H*-imidazole as well as to the terpyridine ligand sphere. The second absorption band, by virtue of the S_{11} , is of ILCT character in the 4*H*-imidazole moiety and is surrounded by two weakly absorbing MLCT states involving the terpyridine ligand. Protonation of the 4*H*-imidazole lowered the energies of the S_1 as well as of the bright S_4 and S_9 states, while the terpyridine character of the MLCT state was drastically decreased. This decrease of the terpyridine character was also confirmed based on RR spectroscopy. The RR intensities were calculated within the STA (see Chapter 2.6.2.2) for the S_6 and S_{11} of deprotonated and for the S_4 and S_9 of the protonated species, see Figure 3.11. The frequencies of the vibrational modes were scaled by the factor 0.97 in order to correct for the lack of anharmonicity as well as the approximated treatment of electron correlation. The RR intensity pattern of the first absorption band (S_6) of the deprotonated complex exhibits several vibrational modes centered at the terpyridine moiety (68, 79, 107, 128, 164, and 190). This is in accordance with the composition of the S_6 wavefunction given in Table 3.2. In contrast, the RR spectrum of the second absorption band, which is of ILCT character, shows exclusively modes of the 4*H*-imidazole ligand. Upon protonation, the influence of the terpyridine ligand is substantially reduced. Hence, the S_4 RR spectrum holds merely two minor intense modes of the terpyridine ligand (165, 185) and the S_9 (ILCT state) shows only modes centered at the 4*H*-imidazole.

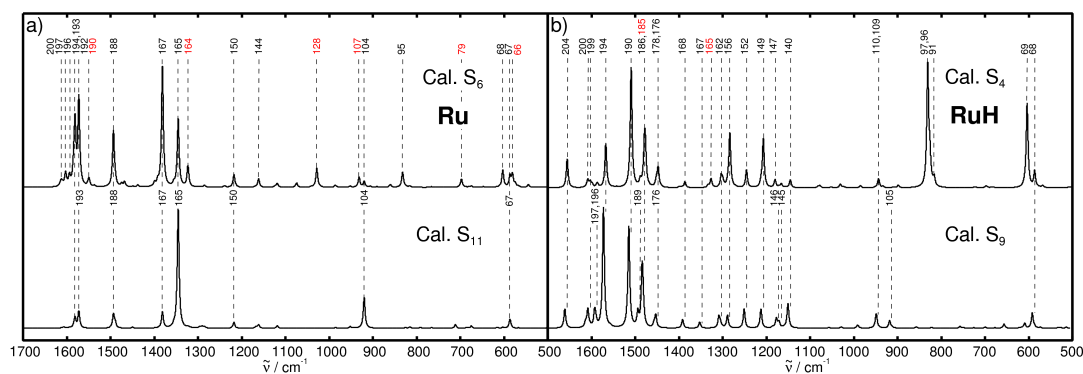


Figure 3.11: Theoretical RR spectra of **Ru** (STA, state S_6 and S_{11}) and **RuH** (STA, state S_4 and S_9) in resonance with the first and the second absorption bands. The modes associated with vibrations located on the terpyridine ligand are given in red color. A Lorentzian function with a FWHM of 5 cm^{-1} is employed to broaden the calculated transitions.

Substituting the two phenyl with tolyl groups (recall Figure 3.8) increases the electron donating character. The deprotonated (**RuMe**) and protonated (**RuMeH**) complexes have been characterized applying experimental and theoretical methods, while the theoretical analysis was performed analogous to the unsubstituted complexes (**Ru** and **RuH**). Detailed information concerning the theoretical method and the obtained properties of the excited states of **RuMe** and **RuMeH** can be found in the attached publication 4.4. The absorption spectra of the methyl substituted complexes, depicted in Figure 3.12a) and b), differ only slightly from the results obtained for the unsubstituted complexes. The excitation energies of the bright MLCT states in

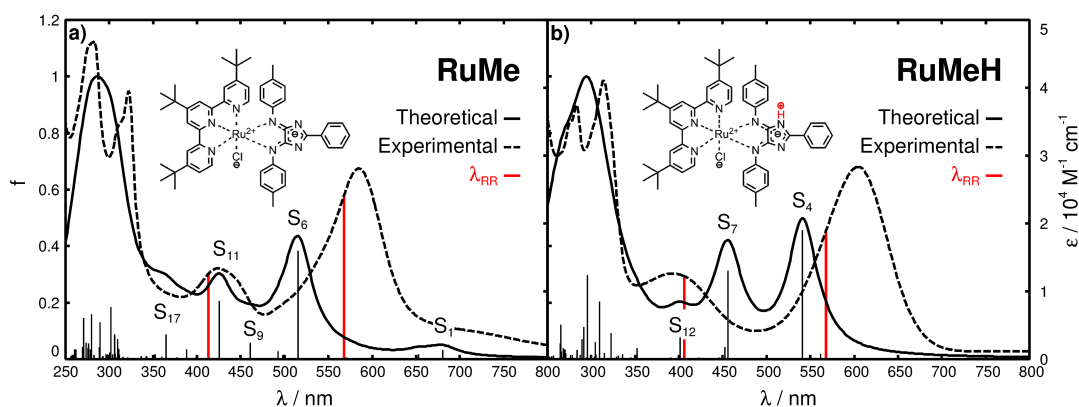


Figure 3.12: Theoretical absorption spectra of the **RuMe** and **RuMeH** species in acetonitrile. A Lorentzian function with a half-width of 20 nm is employed to broaden the transitions in the spectrum based on the oscillator strengths represented by black sticks.

the visible region (S_1 , S_6 , and S_9) show merely variations of $\pm 0.01 \text{ eV}$ from the data obtained for **Ru**. Also the obtained oscillator strengths and the main transitions are almost identical. The ILCT state in the $4H$ -imidazole moiety (S_{11} for both **Ru** and **RuMe**) is stabilized by 0.05 eV upon substitution. The comparison of the protonated species (**RuH** and **RuMeH**) gives very

similar results: On the one hand, the S_1 and S_4 MLCT states are almost unaffected when increasing the donor character from R=H to Me. On the other hand, the ILCT state, S_9 and S_7 in **RuH** and **RuMeH**, respectively, is bathochromically shifted from 2.87 to 2.72 eV upon substitution. Protonation of the 4*H*-imidazole ligand leads to a decrease of the influence of the terpyridine on the first absorption band. This effect was observed in the composition of the bright MLCT states, S_6 and S_4 in **RuH** and **RuMeH**, as well as in the RR spectra. Since only one bright singlet state was contributing to the each absorption band and no resolved vibronic structure was observed in the experimental data, the RR intensities were simulated within the STA. An excellent agreement between the measured and computed RR spectra was observed for both absorption bands in the visible region for both protonation states.

Despite the simplifications made in the description of RR intensities (see Section 2.6.2) the calculation of such intensities based on TDDFT gradients gave a very encouraging agreements with the experimental data. Since TDDFT calculations are widely employed in the investigation of photophysical properties of transition metal complexes, this study has shown that the simulation of RR spectra can give detailed information about the excited states.

Increasing the electron donor character from tolyl to *N,N*-dimethylaniline considerably affects the absorption spectra. Two further protonation states were found in addition to the deprotonated and the protonated 4*H*-imidazole ligand, where besides to the 4*H*-imidazole also one or both amino groups of the substituent are protonated. These four experimentally and theoretically observed acid / base equilibria will be denoted as **RuNMe₂** (deprotonated), **RuHNMe₂** (single protonated; 4*H*-imidazole), **RuHNHMe₂** (double protonated; 4*H*-imidazole and one amino group), and **RuHNH₂Me₂** (triple protonated; 4*H*-imidazole and both amino groups), see Figure 3.13a), b), c), and d) for the structure of respective species. The excited states in the FC regions have been investigated in an analogous manner as reported above, detailed information is given in the attached publication 4.5. The absorption spectrum of **RuNMe₂**, depicted in Figure 3.13a), is characterized by an intense double band structure located between 650 and 450 nm, TDDFT calculations predict the underlying excited states (S_6 , S_7 , S_8 , S_9 , and S_{12}) to be of MLCT character, while both transitions to the imidazole as well as to the terpyridine ligand sphere were found. The red-sided band is mainly given by the S_6 an MLCT excitation to the 4*H*-imidazole at 2.35 eV, while the blue-sided band is created by virtue of S_7 , S_8 , S_9 , and S_{12} . Protonation of the 4*H*-imidazole (**RuHNHMe₂**) led to a bathochromic shift of the MLCT states of the imidazole, see Figure 3.13b). The S_3 , S_5 , and S_7 contribute to the double band structure; the lowest of these states is found at 1.97 eV. Hence, the electron donating dimethylamino groups stabilize the low-lying excited states in **RuNMe₂** and **RuHNMe₂** by 0.06 and 0.32 eV. Similar to the unsubstituted and methyl substituted complexes protonation of the 4*H*-imidazole ligand reduces the proportion of terpyridine transitions. Since in case

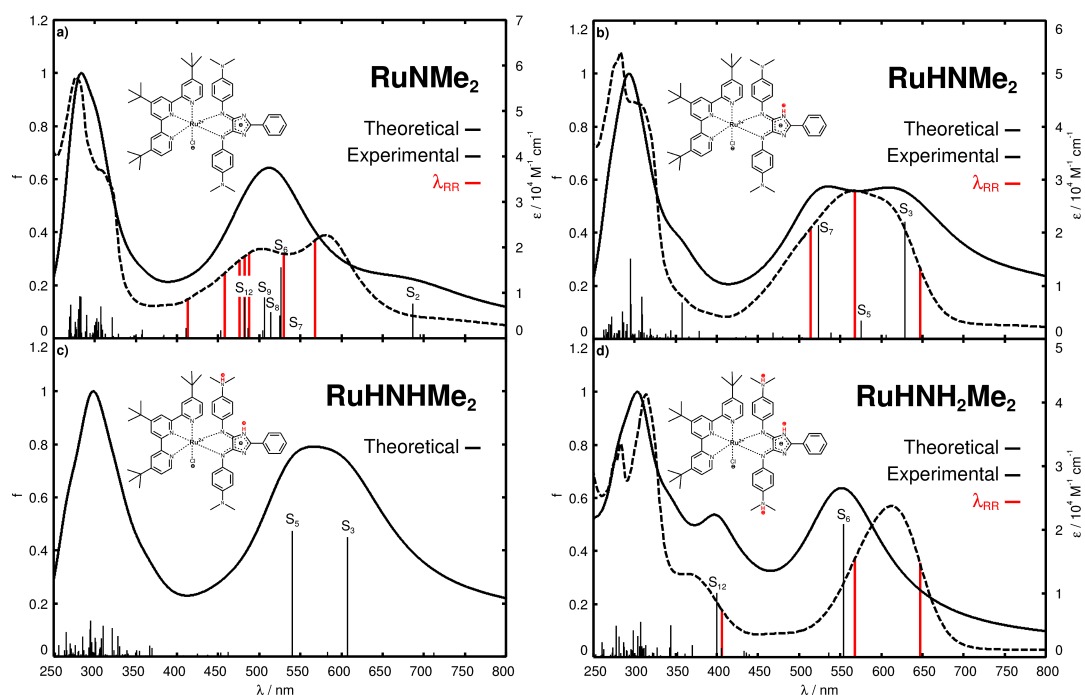


Figure 3.13: Theoretical absorption spectra of the **RuNMe₂**, **RuHNMe₂**, **RuHNHMe₂**, and **RuHNH₂Me₂** species in acetonitrile. A Lorentzian function with a half-width of 3000 cm^{-1} is employed to broaden the transitions in the spectrum based on the oscillator strengths represented by black sticks.

of the deprotonated and the single protonated forms five (S_6 , S_7 , S_8 , S_9 , and S_{12}) and three (S_3 , S_5 , and S_7) excited states contribute to the respective absorption bands, the RR spectra were calculated within the SOS approach for an excitation wavelength of 568 nm. The excited states have been broadened with a full width at half maximum (FWHM) of 3000 cm^{-1} . The resulting RR intensity patterns show a good agreement with the experimental data. However, the excitation energies obtained at TDDFT level of theory are red-shifted up to 0.2 eV with respect to experiment. This is particularly problematic for **RuNMe₂**, since the influence of the S_6 is now overestimated at the applied excitation wavelength of 568 nm. Thus, the RR spectra of **RuNMe₂** shows only few less intense vibrational modes centered at the terpyridine ligand, whereas the S_7 , S_8 , S_9 , and S_{12} show a pronounced terpyridine character. In case of **RuHNMe₂** no terpyridine modes were observed in the calculated RR spectrum, what is in accordance with the results obtained for the protonated forms **RuH** and **RuMeH**.

Further double and triple protonations at the amino groups change its character from electron donating to electron withdrawing. **RuHNHMe₂** shows two bright MLCT states (S_3 and S_5) to the 4*H*-imidazole (see Figure 3.13c), while the excitation energy of the red-sided state (S_3) is lifted again from 1.97 in the single protonated complex to 2.04 eV in the double protonated one. Protonating the complex to the triple protonated form shifts the excitation energy of the respective MLCT state (S_3) further to 2.24 eV. Both, the composition of the respective excited state wavefunctions as well as the calculated RR spectra showed no terpyridine contributions.

Since **RuHNHMe**₂ could not be isolated from the other forms, there is no experimental RR data at hand of this protonation state. In case of **RuHNH**₂**Me**₂ an excellent agreement between the measured and the calculated RR intensity pattern was found (see Figure 3.13c)), however, here one state, the *S*₃, predominately contributed to the RR intensity pattern.

In summary, multiple protonation and its influence on excited states properties have been investigated in a joint experimental theoretical study. It was shown that protonation effects can be of vital importance for the excitation energies as well as for the character of excited states and thus tune electronic donating to electron withdrawing groups. The calculation of RR intensities, even in case for a resonance with several excited states, has been shown to be feasible. However, a balanced description of the contributing states is essential.

In order to enhance the electron withdrawing character of the substituent with respect to the protonated dimethylamino species, ethylcarboxy groups were used, see Figure 3.8a). The respective deprotonated and protonated complexes are denoted as **RuCOOEt** and **RuHCOOEt**. The excited states were studied analog as described for the unsubstituted and the methyl substituted complexes; further details are given in the publication 4.7. The determined absorption properties of **RuCOOEt** (see Figure 3.14a)) and its protonated form **RuHCOOEt** (see Figure 3.14b)) are very similar to those of **Ru** and **RuH** or to **RuMe** and **RuHMe**. In the

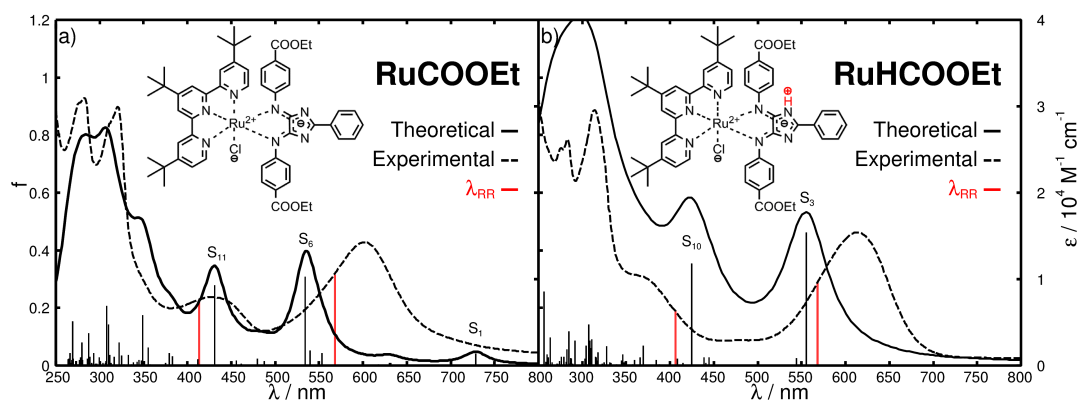


Figure 3.14: Theoretical absorption spectra of the **RuCOOEt** and **RuHCOOEt** species in acetonitrile. A Lorentzian function with a half-width of 20 nm is employed to broaden the transitions in the spectrum based on the oscillator strengths represented by black sticks.

deprotonated form the first absorption band is correlated to the bright *S*₆ with an excitation energy of 2.32 eV. Similar to the other deprotonated complexes the excited state wavefunction shows a distinct mixing of MLCT transitions involving both transitions to the 4*H*-imidazole as well as to the terpyridine ligand. The second absorption band results from the *S*₁₁, a bright ILCT state in the 4*H*-imidazole moiety with an excitation energy of 2.88 eV. Protonation of the 4*H*-imidazole ligand lowers the excitation energy of the MLCT state (*S*₃ for **RuHCOOEt**) to 2.23 eV, while the terpyridine character is decreased. In contrast, the ILCT state is slightly

lifted to 2.92 eV. The simulated RR spectra, obtained by applying the STA, are in very good agreement with the experimental data in resonance with both absorption bands and for both protonation states. The RR intensities of **RuCOOEt** in resonance with the S_6 showed several weak and medium intense vibrational modes of the terpyridine ligand, while the respective RR spectrum of the S_3 for **RuHCOOEt** holds no significant terpyridine contributions.

Besides the influence of substitution in the $4H$ -imidazole ligand sphere also different polypyridine ligands were investigated. Thus, the terpyridine as well as the chloro ligands were exchanged by two bipyridine ligands. These bipyridine complexes, illustrated in Figure 3.8b), are denoted as **RuMeBpy** and **RuMeHBpy** in the deprotonated and the protonated form. The modification of the polypyridine sphere led to substantial changes in the photophysical properties of these black absorbers in particular for **RuMeBpy**, see Figure 3.15a). On the one hand,

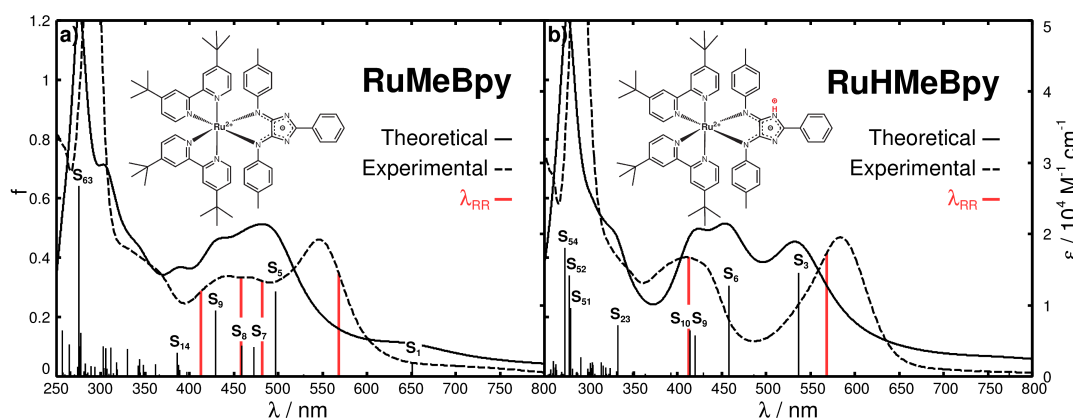


Figure 3.15: Theoretical absorption spectra of the **RuMeBpy** and **RuHMeBpy** species in acetonitrile. A Lorentzian function with a half-width of 3000 cm^{-1} is employed to broaden the transitions in the spectrum based on the oscillator strengths represented by black sticks.

the absorption spectrum of **RuMeBpy** shows an intense band at 546 nm accompanied by a red-sided shoulder. This is in accordance with the absorption spectra obtained for all deprotonated terpyridine complexes. On the other hand, the high energy region of the visible region is dominated by an intense double band structure at 467 and 443 nm, respectively. Hence, a large part of the visible range is covered by intense absorption bands and an enhanced overlap with the solar radiation spectrum is obtained. The protonated bipyridine complex shows similar absorption features (see Figure 3.15b)) as the above discussed terpyridine species e.g. **RuH**, **RuMeH**, **RuHNH₂Me₂**, and **RuHCOOEt**, whereas a double band structure is observed at higher energy. The theoretical analysis of the absorption spectra of **RuMeBpy** and **RuMeHBpy** was performed in the same manner as reported above for the terpyridine complexes. It was found that the visible region is determined by several excited states of different character. The MLCT states S_1 and S_5 of $4H$ -imidazole character correspond to the first absorption band and its red-sided shoulder. The higher excited states of either MLCT character to the bipyri-

dine ligand (S_7 and S_8) or ILCT character to the 4*H*-imidazole ligand (S_9) are correlated to the double band structure. Upon protonation the two 4*H*-imidazole MLCT states (S_1 and S_5 in **RuMeBpy**) are stabilized by 0.2 to 0.3 eV. The high energy region of the visible range is given by two bright ILCT states (S_6 and S_9) of the 4*H*-imidazole ligand as well as a bright MLCT state (S_{10}) involving the bipyridine moiety.

After the main excited states that contribute to the absorption spectra have been identified, the RR have been thoroughly studied experimental and theoretically. The theoretical analysis of the RR spectra, using the SOS approach, was performed with contributions of the four main excited singlet states of the deprotonated (S_5 , S_7 , S_8 , and S_9) and the protonated (S_3 , S_6 , S_9 , and S_{10}) complexes. The RR intensity pattern of **RuMeBpy** was obtained in terms of several excitation wavelengths covering the visible range. In the case of **RuMeHBpy** only two excitation wavelengths have been studied: One in resonance with the first and the other one with the second absorption band. The comparison of the simulated and calculated RR spectra revealed inaccuracies based on the deviation of the TDDFT predictions of the excitation energies of the contributing states with respect to the experiment. Hence, the RR spectra have been recalculated employing shifted excitation energies that allowed for better reproduction of the experimental intensity pattern of the absorption spectra. The new obtained RR intensities were then found to be in excellent agreement with the experimental data. Therefore, the wavelength dependency was correctly reproduced for both protonation states. These results showed that the main source of errors in the simulation of RR intensities is correlated to inaccuracies in the estimation of excitation energies. This is especially the case if electronic states of different character, e.g. as in the present case MLCT and ILCT, contribute to the absorption and thus also to the RR spectra. In addition, interference effects between the electronic states have been determined based on calculated RR intensities and found to be almost negligible for **RuMeBpy** and **RuHMeBpy**.

This study showed that accurate RR spectra can be obtained for transition metal complexes even in cases where several excited states of different character contribute to the absorption band.

3.2.2 Photo Induced Relaxation Pathways of Ruthenium(II)-4*H*-Imidazole complexes

The photoinduced relaxation pathways of a terpyridine 4*H*-imidazole based ruthenium complex, namely **RuMe** in the respective protonation state, have been investigated in a joint experimental theoretical study. The synthesis of the complex was achieved in the groups of Prof. Dr. Beckert (IOMC Friedrich-Schiller Universität Jena) and Prof. Dr. Rau (Universität Ulm), while the spectroscopy and dynamical studies were performed in the group of Prof. Dr. Dietzek (IPC Friedrich-Schiller Universität Jena). The theoretical analysis was carried out in order to obtain detailed insight into the deactivation mechanisms after photoexcitation, the obtained results are collected in publication 4.7.

The starting point to understand the photoinduced dynamics of **RuMe** and **RuMeH** (recall Figure 3.8a)) were the already determined absorption properties in the FC, see appended publication 4.4.¹³⁸ To complete the understanding of the conformational relaxation behavior four electronic states, namely the singlet ground state (S_0), the bright low-lying excited singlet state (**RuMe**: S_6 and **RuMe**: S_4) populated upon excitation, the triplet ground state in the FC structure (T_{twist}) and a planarizing triplet state (T_{plan}), have been studied for both complexes. For details concerning the nature of these states the reader is referred to the appended publication 4.7. The respective equilibrium structures of these states are denoted as: FC for S_0 , $^1\text{MLCT}$ for S_6 or S_4 , $^3\text{MLCT}$ for T_{twist} , and $^3\text{MLCT}_{\text{plan}}$ for T_{plan} . These equilibrium structures differ mainly in the ruthenium-4*H*-imidazole bond lengths (r_1 and r_2) as well as in the torsion of the tolyl groups with respect to the 4*H*-imidazole ligand. These coordinates are labeled in Figure 3.16 and their values are collected in Table 3.3. On the one hand, the equilibrium geometries of the

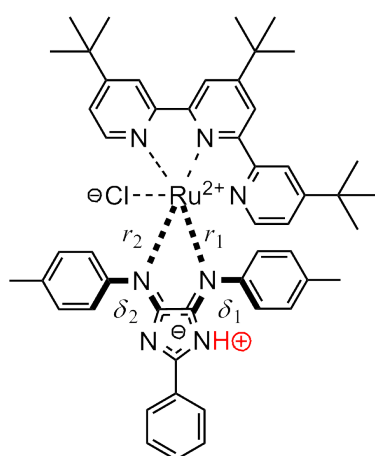


Figure 3.16: Bond lengths r_1 and r_2 as well as dihedral angles δ_1 and δ_2 for **RuMe** and **RuMeH**.

Geometry	$r_1 / \text{\AA}$	$r_2 / \text{\AA}$	$\delta_1 / ^\circ$	$\delta_2 / ^\circ$
RuMe				
FC	2.11	2.19	66.1	48.2
$^1\text{MLCT}$	2.14	2.17	50.2	38.7
$^3\text{MLCT}$	2.07	2.12	44.5	40.4
$^3\text{MLCT}_{\text{plan}}$	2.74	2.16	16.3	69.5
RuMeH				
FC	2.11	2.17	60.7	46.1
$^1\text{MLCT}$	2.18	2.28	49.5	30.2
$^3\text{MLCT}$	2.10	2.12	50.0	44.8
$^3\text{MLCT}_{\text{plan}}$	2.82	2.18	38.9	59.3

Table 3.3: Bond lengths r_1 and r_2 and dihedral angles δ_1 and δ_2 in the equilibria: FC, $^1\text{MLCT}$, $^3\text{MLCT}$, and $^3\text{MLCT}_{\text{plan}}$ for **RuMe** and **RuMeH**, respectively.

deprotonated and protonated complex FC, $^1\text{MLCT}$, and $^3\text{MLCT}$ show similar structural features. Here, both tolyl moieties are twisted out of planarity and both ruthenium–4*H*-imidazole bonds are within 2.1 to 2.3 Å. On the other hand, $^3\text{MLCT}_{\text{plan}}$ features a planarization in δ_1 in case of **RuMe**, while for **RuMeH** merely a partial planarization in δ_2 was observed. For both protonation states the planarization or rather the partial planarization is accompanied by an opening of the bond r_1 , while the other ruthenium–4*H*-imidazole bond is unaffected.

The excitation energies of the four states in their equilibria with respect to S_0 in the FC structure are illustrated in Figure 3.17a) and b) for the deprotonated and protonated form. Two

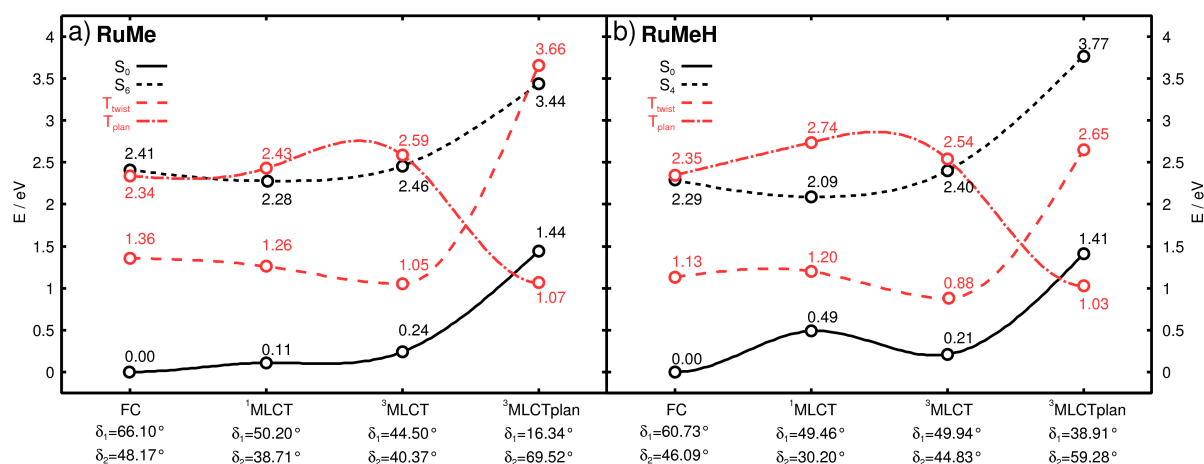


Figure 3.17: Schematic representation of the relative energies of the singlet ground state S_0 , the excited singlet state S_6 or S_4 , the twisted triplet state T_{twist} , and the planarized triplet state T_{plan} for the equilibrium geometries (FC, $^1\text{MLCT}$, $^3\text{MLCT}$ and $^3\text{MLCT}_{\text{plan}}$) of **RuMe** and **RuMeH**. The given dihedral angles δ_1 and δ_2 refer to the torsion of the tolyl groups with respect to the *H*-imidazole (see Figure 3.16).

competitive relaxation pathways upon photoexcitation to the S_6 or S_4 were determined. After ISC to the triplet manifold T_{twist} and T_{plan} are accessible. Experimentally, it was found that for **RuMe** the planarized triplet state is populated, while for **RuMeH** the twisted triplet state is populated, since this state is stabilized upon protonation of the 4*H*-imidazole ligand. The theoretical analysis of the deprotonated complex has predicted equal energies of the two competitive triplet states in their respective equilibria (T_{twist} : 1.05 eV and T_{plan} : 1.07 eV). Thus, a population of both states is likely to take place. The results for the protonated form indicated a preferred population of the twisted triplet state, since it is stabilized by 0.15 eV with respect to the equilibrium of the planar triplet state.

Our calculations provided evidence for the experimentally observed relaxation pathways. In addition, it was proven that one deactivation channel is correlated to pronounced structural changes in the ligand sphere of the *H*-imidazole. More insight into the dynamics upon photoexcitation, can only be obtained with quantum dynamical simulations performed on accurate multiconfigurational PESs. Unfortunately, such calculations are currently a formidable task and have not been attempted here.

3.3 Electron Transfer in a Ruthenium(II)-4*H*-Imidazole-Rutile model

After extensively studying the photophysical properties of a new family of black absorbers based on ruthenium(II)-4*H*-imidazole complexes with respect to substitution effects as well as the dynamics upon photoexcitation (recall Chapter 3.2.1 and 3.2.2) it seems natural to concentrate now on their application in real life DSSCs. All investigated dyes of Chapter 3.2.1 are lacking an anchoring group in order to attach the complex on a surface. Thus, a complex based on **RuMe** containing a carboxylic acid group on the phenyl ring was utilized. This complex, depicted in Figure 3.18, exhibits several protonation states involving the 4*H*-imidazole as well as the carboxylic acid group. The focus was set on three protonation states: **RuMeCOO⁻** (4*H*-imidazole and anchoring group deprotonated), **RuMeHCOO⁻** (4*H*-imidazole protonated and anchoring group deprotonated), and **RuMeHCOOH** (4*H*-imidazole and anchoring group protonated).

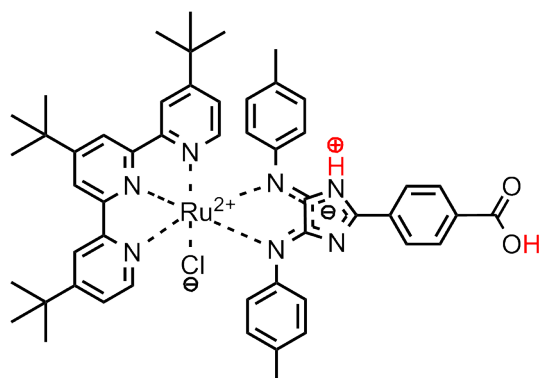


Figure 3.18: Investigated ruthenium(II)-4*H*-imidazole complexes, in three studied protonation states (**RuMeCOO⁻**, **RuMeHCOO⁻**, and **RuMeHCOOH**), with a carboxy acid anchoring group. In all theoretical simulations the *tert*-butyl groups of the terpyridine ligand have been approximated by methyl groups.

In order to estimate the influence of the anchoring group on the excited state properties the three respective protonation states were analyzed by means of absorption and RR spectroscopy. The equilibrium structures have been optimized at the DFT level of theory using the B3LYP functional and the 6-31G(d) double- ζ basis set as well as the MBW-28¹⁴¹ effective core potential for the inner shells of the ruthenium. The corresponding absorption spectra were simulated by means of TDDFT using the 120 lowest singlet excited states with the same exchange correlation functional and basis set as for the electronic ground state. Interactions with the solvent (acetonitrile) have been taken into account using the integral equation formalism of the polarizable continuum model for both the ground and excited states.

The simulated UV-vis spectra (with a FWHM of 3000 cm⁻¹) are depicted in Figure 3.19 for **RuMeCOO⁻**, **RuMeHCOO⁻**, and **RuMeHCOOH** along with the experimental spectra.

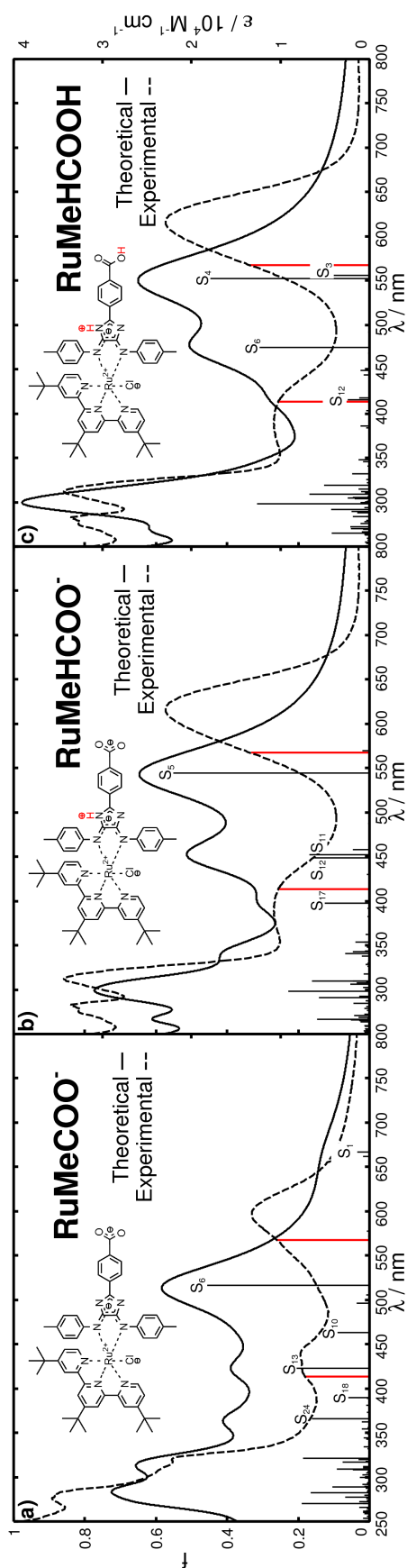


Figure 3.19: Theoretical absorption spectra of **RuMeCOO⁻**, **RuMeHCOO⁻**, and **RuMeHCOOH** in acetonitrile. A Lorentzian function with a half-width of 3000 cm^{-1} is employed to broaden the transitions in the spectrum based on the oscillator strengths represented by black sticks.

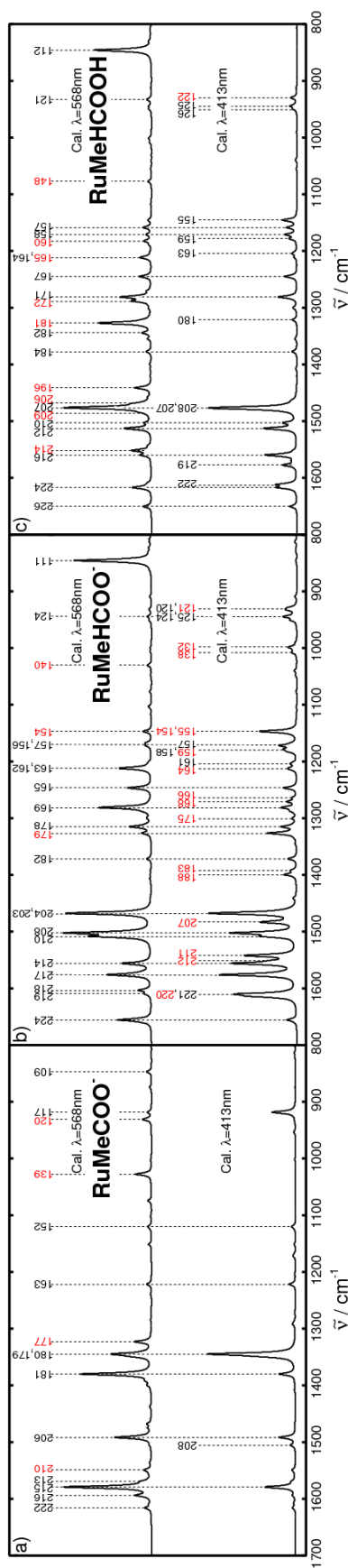


Figure 3.20: Theoretical RR spectra of **RuMeCOO⁻** (S_6 , S_{10} , S_{13} , S_{18} , and S_{24}), **RuMeHCOO⁻** (S_5 , S_{11} , S_{12} , and S_{17}), and **RuMeHCOOH** (S_3 , S_4 , S_6 , and S_{12}) in resonance with $\omega_L = 568$ and 413 nm . The excited states were broadened with Lorentzian functions with a FWHM of 3000 cm^{-1} . The modes of the terpyridine ligand are given in red color. A Lorentzian function with a FWHM of 5 cm^{-1} is employed to broaden the calculated transitions.

Experimentally, only the absorption spectrum of the deprotonated and for one unidentified protonated species were available. Table 3.4 collects the data of the main excited singlet states contributing to the absorption in the visible region, while the MOs involved in the main transitions are illustrated in Figure 3.21. The obtained results state very similar absorption properties of the deprotonated form (RuMeCOO^-) with respect to RuMe . The visible range is mainly characterized by two excited states: S_6 and S_{13} . The S_6 state (2.40 eV) is of MLCT nature, while transitions to the 4*H*-imidazole ligand as well as to the terpyridine ligand are involved. The less intense S_1 was assigned to the red-sided shoulder at approximately 700 nm in the experimental spectrum. In addition, the medium absorbing S_{10} and S_{18} are found at 2.68 and 3.18 eV. Both states comprise mainly MLCT transitions to the terpyridine ligand sphere. Furthermore, an additional bright ILCT state (S_{24}) is located at 3.39 eV. The simulated absorption spectra of both protonated complexes (RuMeHCOO^- and RuMeHCOOH) feature a similar shape. However, the composition of the underlying excited states showed distinct differences for the two protonation states. The main absorption bands of RuMeHCOOH^- are given by the S_5 (2.28 eV) MLCT state (transitions to the 4*H*-imidazole), of the states S_{11} and S_{12} (2.74 and 2.76 eV) of mixed ILCT (4*H*-imidazole) and MLCT (terpyridine) character, and of a ILCT state (S_{17}) at 3.12 eV of the 4*H*-imidazole ligand. Upon further protonation of the anchoring group, the energetic position of the first absorption band is conserved. TDDFT revealed the two underlying excited states, S_3 and S_4 , to be composed of MLCT transitions to both aromatic ligand spheres. The second absorption band is correlated to a ILCT state, the S_6 , with a main transition involved in the 4*H*-imidazole. At 2.98 eV a mixed state (S_{12}) with ILCT (4*H*-imidazole) as well as MLCT (terpyridine) character was found. Based on the simulated absorption spectra, no significant influence of the anchoring group on the excited state properties was found for the deprotonated complex, RuMeCOO^- . However, the absorption bands in the visible range of protonated complexes, RuMeHCOO^- and RuMeCOOH , were found to feature, in contrast to the findings for RuMeH , an enhanced terpyridine character. The only exception is the first absorption band (S_5) in RuMeHCOO^- , which shows analogous to the S_4 of RuMeH a decreased influence of the terpyridine ligand.

In order to unravel the changes in the nature of the corresponding excited states in more detail and further to allow an unambiguous assignment of the protonated complexes to spectroscopical features, RR spectroscopy was applied. Based on the calculated absorption spectra, recall Figure 3.18, several excited states contribute to the respective absorption bands. This is especially the case for the protonated complexes. Thus, the RR spectra have been simulated using the SOS method; all three protonation states have been broadened with a FWHM of 3000 cm^{-1} . For RuMeHCOO^- contributions from the five excited states S_6 , S_{10} , S_{13} , S_{18} , and S_{24} have been taken into account. In case of the protonated forms four state have been considered, namely S_5 , S_{11} , S_{12} , and S_{17} for RuMeHCOO^- and S_3 , S_4 , S_6 , and S_{12} for RuMeHCOOH .

3.3. ELECTRON TRANSFER IN A RUTHENIUM(II)-4H-IMIDAZOLE-RUTILE MODEL53

State	Transition		weight / %	ΔE^e / eV	λ / nm	f
RuMeCOO⁻						
S_1	$d_{xz}(193) \rightarrow \pi_{im}^*(194)$	(MLCT)	82	1.86	667	0.0347
	$d_{xz}(193) \rightarrow \pi_{terpy}^*(195)$	(MLCT)	13			
S_6	$d_{xy}(192) \rightarrow \pi_{im}^*(194)$	(MLCT)	58	2.40	516	0.4562
	$d_{yz}(191) \rightarrow \pi_{terpy}^*(195)$	(MLCT)	37			
S_{10}	$d_{yz}(191) \rightarrow \pi_{terpy}^*(195)$	(MLCT)	34	2.68	463	0.0890
	$d_{xy}(192) \rightarrow \pi_{im}^*(194)$	(MLCT)	24			
	$d_{xy}(192) \rightarrow \pi_{terpy}^*(196)$	(MLCT)	19			
	$d_{xz}(193) \rightarrow \pi_{terpy}^*(196)$	(MLCT)	9			
S_{13}	$\pi_{im}(187) \rightarrow \pi_{im}^*(194)$	(ILCT)	0.94	2.94	422	0.2038
S_{18}	$d_{xz}(193) \rightarrow \pi_{terpy}^*(197)$	(MLCT)	0.94	3.18	390	0.0592
S_{24}	$\pi_{im}(186) \rightarrow \pi_{im}^*(194)$	(ILCT)	0.91	3.39	366	0.1617
RuMeHCOO⁻						
S_1	$d_{xz}(193) \rightarrow \pi_{im}^*(194)$	(MLCT)	96	1.53	812	0.0104
S_5	$d_{xy}(190) \rightarrow \pi_{im}^*(194)$	(MLCT)	82	2.28	544	0.5521
S_{11}	$\pi_{im}(187) \rightarrow \pi_{im}^*(194)$	(ILCT)	30	2.74	452	0.1696
	$d_{yz}(191) \rightarrow \pi_{terpy}^*(196)$	(MLCT)	22			
	$d_{yz}(191) \rightarrow \pi_{terpy}^*(195)$	(MLCT)	19			
	$d_{xy}(190) \rightarrow \pi_{terpy}^*(196)$	(MLCT)	14			
S_{12}	$\pi_{im}(187) \rightarrow \pi_{im}^*(194)$	(ILCT)	63	2.76	449	0.1543
	$d_{yz}(191) \rightarrow \pi_{terpy}^*(195)$	(MLCT)	13			
	$d_{xy}(190) \rightarrow \pi_{terpy}^*(196)$	(MLCT)	12			
S_{17}	$\pi_{im}(186) \rightarrow \pi_{im}^*(194)$	(ILCT)	97	3.12	398	0.1251
RuMeHCOOH						
S_1	$d_{xz}(193) \rightarrow \pi_{im}^*(194)$	(MLCT)	95	1.39	892	0.0094
S_3	$d_{xz}(193) \rightarrow \pi_{terpy}^*(195)$	(MLCT)	83	2.23	556	0.1055
	$d_{xy}(191) \rightarrow \pi_{im}^*(194)$	(MLCT)	13			
S_4	$d_{xy}(191) \rightarrow \pi_{im}^*(194)$	(MLCT)	71	2.25	552	0.4475
	$d_{xz}(193) \rightarrow \pi_{terpy}^*(195)$	(MLCT)	14			
S_6	$\pi_{im}(190) \rightarrow \pi_{im}^*(194)$	(ILCT)	93	2.61	475	0.3090
S_{12}	$\pi_{im}(189) \rightarrow \pi_{im}^*(194)$	(ILCT)	57	2.98	415	0.0616
	$d_{xy}(191) \rightarrow \pi_{terpy}^*(196)$	(MLCT)	32			

Table 3.4: Calculated vertical excitation energies (E^e), wavelengths (λ), oscillator strengths (f) and singly-excited configurations of the main excited states of the deprotonated form (**RuMeCOOH⁻**) and protonated forms (**RuMeHCOOH⁻** and **RuMeHCOOH**) in the visible range. The relevant orbitals are depicted in Figure 3.21.

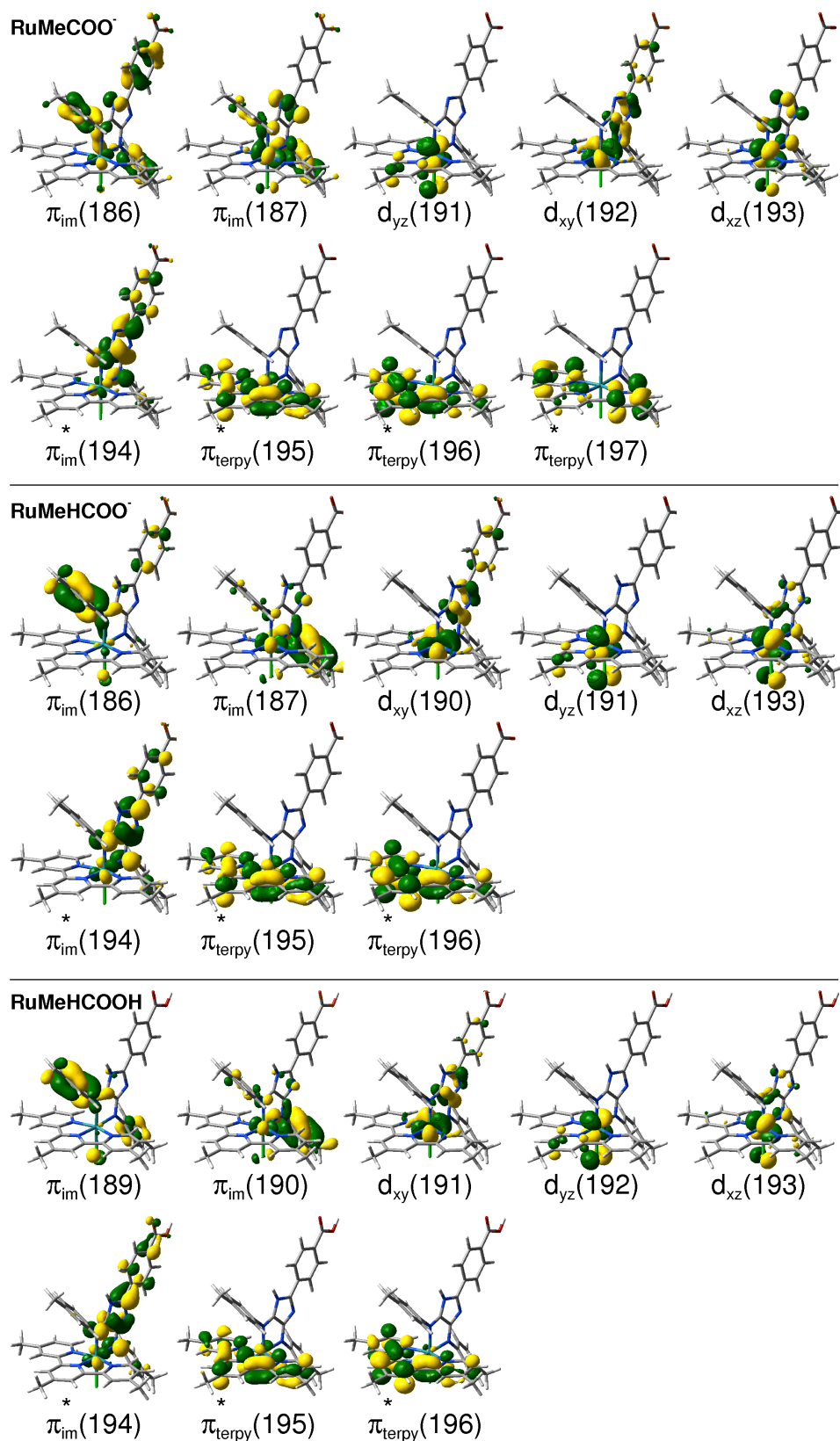


Figure 3.21: MOs involved in the main configurations of the states responsible for the absorption and RR properties of the deprotonated (RuMeCOO^-) and protonated (RuMeCOO^- and RuMeCOOH) complexes.

3.3. ELECTRON TRANSFER IN A RUTHENIUM(II)-4H-IMIDAZOLE-RUTILE MODEL55

For all three complexes excitation wavelengths of 568 and 413 nm have been used for the RR intensities. Due to the lack of information concerning the experimental position of the absorption bands no shifts on the calculated excitation energies were applied. The resulting simulated RR spectra are depicted in Figure 3.20a), b), and c) for the **RuMeCOO⁻**, **RuMeHCOO⁻**, and **RuMeHCOOH**, respectively. Similar to the absorption, the simulated RR spectra of **RuMeCOO⁻** were found to be almost identical to the RR spectra of **RuMe**. The RR intensity pattern shows few weak vibrational modes located at the terpyridine ligand (120, 139, 177, and 210) for the first absorption band (excitation wavelength: 568 nm). The resonance with the second absorption band (excitation wavelength: 413 nm) revealed exclusively 4*H*-imidazole centered normal modes. Upon single protonation to **RuMeHCOO⁻** the influence of the terpyridine ligand is slightly decreased, here merely three very weak terpyridine modes are observed (140, 154, and 179). However, the intensities of the terpyridine modes, correlated to the S_{11} and S_{12} , are most likely overestimated for the excitation wavelength of 568 nm. This is caused by the excitation energies of the states corresponding to the second absorption bands. Especially in the protonated complexes, the excitation energies of the states correlated to the second band are underestimated. For this family of ruthenium(II) complexes deviations of approximately 0.3 eV have been determined.^{138-140,142} The RR spectrum of the second absorption band, simulated for an excitation wavelength of 413 nm, showed mainly vibrational modes of the terpyridine ligand, due to the predominance of S_{11} and S_{12} . In contrast, the RR intensity pattern of the second absorption in **RuMeH** featured exclusively 4*H*-imidazole contributions. The double protonated complex, **RuMeHCOOH**, shows a very different composition of the RR intensively patterns. In resonance with 568 nm, the simulated RR spectrum implied a pronounced mixing of vibrational modes of the 4*H*-imidazole as well as of the terpyridine ligand sphere. The reason for this is that the main contributing excited states, S_3 and S_4 , are both of ambivalent character, see Table 3.4. The RR spectra of the second absorption band (413 nm) features (except for the mode 122) only modes of the 4*H*-imidazole ligand, due to the very bright S_6 involving an ILCT in the 4*H*-imidazole.

It was shown that a carboxy acid anchoring group influences the composition of the bright excited states in the FC region substantially. This is especially the case, for **RuMeHCOO⁻** and **RuMeHCOOH**. On the one hand, the first absorption band in **RuMeHCOO⁻** showed only marginal terpyridine contributions, while the terpyridine character of the second absorption band in **RuMeHCOO⁻** was enhanced based on the results obtained for **RuMeH**. On the other hand, the first absorption band in **RuMeHCOOH** exhibits a pronounced mixing of 4*H*-imidazole and terpyridine contributions, while the second absorption band is predominantly given by the 4*H*-imidazole ligand. Based on the theoretical analysis of the absorption spectra of the single and double protonated complexes, no unambiguous assignment of the experimental UV-vis spectrum and hence, an identification of the present protonation state is possible, recall

Figure 3.19a) and b). However, the simulated RR spectra indicated to very different intensity patterns of **RuMeHCOO⁻** and **RuMeHCOOH** for both applied excitation wavelengths. Hence, an unambiguous assignment of the protonation state, based on RR spectroscopy, will be possible once the experimental measurements are performed.

In the investigation of the spectroscopical features of **RuMeCOO⁻**, **RuMeHCOO⁻**, and **RuMeHCOOH** it was shown that **RuMeHCOO⁻** is suitable to allow an almost quantitative CT to the 4*H*-imidazole ligand by virtue of S_5 . In addition, the results obtained for **RuMeH**, see attached publication 4.7, indicated to a population of the twisted triplet state, where one electron is located in the d_{xz} and the other one in a π_{im}^* orbital, see Chapter 3.2.2. In case of **RuMeHCOO⁻** the minimum of the twisted triple state is located 1.19 eV above the S_0 in the FC region and is stabilized by 0.26 eV (with respect to S_0 in the FC structure) in its equilibrium geometry. This equilibrium structure ($r_1 = 2.10$ Å, $r_2 = 2.13$ Å, $\delta_1 = 50.1^\circ$, and $\delta_2 = 44.8^\circ$) showed merely small deviation from the respective ³MLCT structure, see **RuMeH** Table 3.3. Thus, **RuMeHCOO⁻** was selected to study an IET, after photoexcitation to the S_5 state and a subsequent relaxation via the triple manifold to the twisted triple state, to a titanium dioxide surface.

Three main modifications of TiO₂, namely rutile, anatase, and brookite, are well-known. The TiO₂ surface has been approximated by means of a (TiO₂)₁₅ cluster in the thermodynamical stable rutile modification. The rutile cluster was constructed based on symmetry using the space group $P4_2/mnm$. The atom positions (x, y, z) of the respective titanium and oxygen atoms are obtained multiplying the Wyckoff positions (2a) or (4f) with the lattice parameters.¹⁴³ The Wyckoff positions (2a) and (4f) are given by:

$$(2a) : (0, 0, 0); \left(\frac{1}{2}, \frac{1}{2}, \frac{1}{2}\right), \quad (3.1)$$

for two adjacent titanium atoms and by:

$$(4f) : \pm(u, u, 0); \left(u + \frac{1}{2}, \frac{1}{2} - u, \frac{1}{2}\right), \quad (3.2)$$

for the respective four oxygen atoms. Applying the lattice parameters:

$$a = 4.59373 \text{ \AA}, b = 4.59373 \text{ \AA}, c = 2.95812 \text{ \AA}, \quad (3.3)$$

and $u = 0.3053$ to the Wyckoff positions yielded the atom positions.¹⁴³ This resulted in the TiO₂ cluster depicted in Figure 3.22. Further, the cluster was saturated using hydroxid ions and water to give with the attached **RuMeHCOO⁻** a neutral charge. For the coordination of the deprotonated carboxylic acid anchoring group, there are several possibilities, while the three most relevant scenarios are given by:

- μ , see Figure 3.23a), where each oxygen of the deprotonated carboxylic acid coordinates each one titanium,

3.3. ELECTRON TRANSFER IN A RUTHENIUM(II)-4H-IMIDAZOLE-RUTILE MODEL57

- κ^2 , see Figure 3.23b), where both oxygens coordinate the same titanium,
- κ^1 , see Figure 3.23c), where only one oxygen is coordinated to one titanium atom.

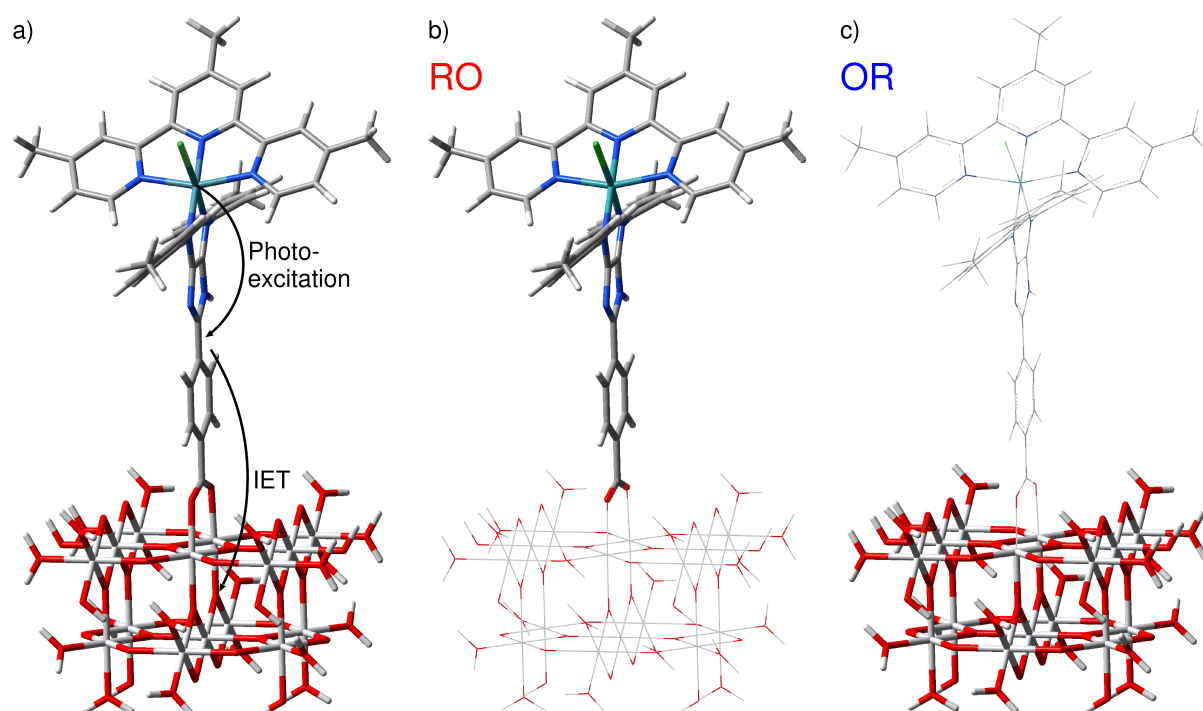


Figure 3.22: (TiO₂)₁₅ cluster, saturated with OH⁻ and H₂O, and attached **RuMeHCOO⁻** giving a total charge of ± 0 . a) illustrates the photoexcitation and subsequent IET from **RuMeHCOO⁻** (π_{im}^*) to the TiO₂ cluster. In b) and c) the QM and MM regions in the RO and the OR state are shown, while the bold sticks refer to the QM and the thin sticks to the MM region.

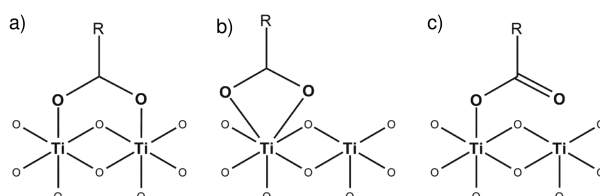


Figure 3.23: Bonding scenarios μ (a), κ^2 (b), and κ^1 (c) of a carboxylic acid anchoring group on a rutile surface.

The dissociative bridging-bidentate configuration (μ) was found to be the most stable one for rutile type TiO₂ surfaces using DFT methods.^{50,144–146} Hence, this configuration was used as a starting condition for the investigation of the IET following photoexcitation, see Figure 3.22.

In a global picture, the IET is described by an oxidation of ruthenium(II) to ruthenium(III), while the TiO₂ cluster is reduced. However, the actual IET occurs after photoexcitation and relaxation in the triplet manifold (see above) from the twisted triplet state, where one electron resides in the d_{xz} and the excited electron is located in a π_{im}^* orbital. From here, the electron in the π_{im}^* orbital may be transferred to the TiO₂ cluster, as illustrated in Figure 3.22a). Thus, the

initial state (RO) is a triplet, since RuMeHCOO^- is in the twisted triplet state and the TiO_2 cluster is a singlet. Likewise, the final state (OR) is also a triplet because RuMeHCOO^- and the TiO_2 cluster are both doublets. A representation of the electronic configuration of RO and OR is provided in Figure 3.24a) and b). The simulation was performed, using the Gaussian 09

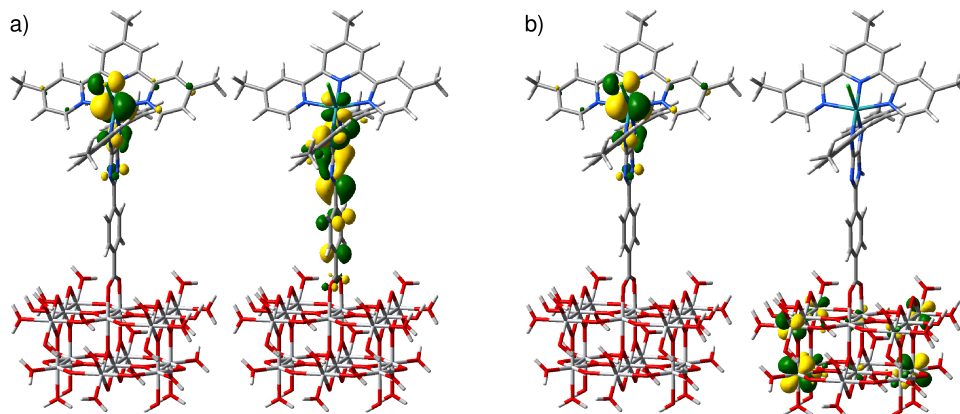


Figure 3.24: SOMOs in the initial RO state (a) and in the final state OR (b) obtained at the TD-B3LYP/6-31G(d) level of theory and a polarizable continuum model (acetonitrile).

program, at the TDDFT level of theory with the B3LYP functional and the 6-31G(d) basis set within acetonitrile (polarizable continuum model). The effective core potentials MBW-28 and MDF-10¹⁴⁷ were applied for the inner shells of the ruthenium and titanium, respectively.

In order to predict an IET rate between the two states, RO and OR, well relaxed equilibria for these states are inevitable. Hence, QM/MM coupled MD simulations using the CP2K package^{148–151} with the pure function PBE^{152,153} have been initiated. In order to account for inner as well as outer-sphere contributions to the IET, the initial structures have been surrounded by three layers of acetonitrile molecules described at MM level of theory. As illustrated in Figure 3.22b), in RO the RuMeHCOO^- fragment is described at QM and the titanium dioxide cluster at MM level of theory (recall Section 2.7.2). Exemplarily, Figure 3.25 shows the molecular system in the RO state surrounded by the solvating acetonitrile molecules. Accordingly, OR is described with the rutile cluster via QM and the RuMeHCOO^- fragment at MM level of theory, see Figure 3.22c). The evolution (relaxation) of RO and OR is studied within 3 ns and a time step of 1 fs. Hence, 3.000.000 steps are calculated within each state, respectively. Unfortunately, these relaxations, in the acetonitrile solvent bath, are still running. Subsequently, a distribution of the geometries, starting from the well relaxed RO and OR equilibria, will be obtained employing further QM/MM coupled MD simulations. In each obtained configuration, the ionization energy and electron affinities are calculated, giving access to the respective energy gaps and, hence, to the reorganization energy as well as to the free reaction energy and thus to the IET rate; see Section 2.7.2.

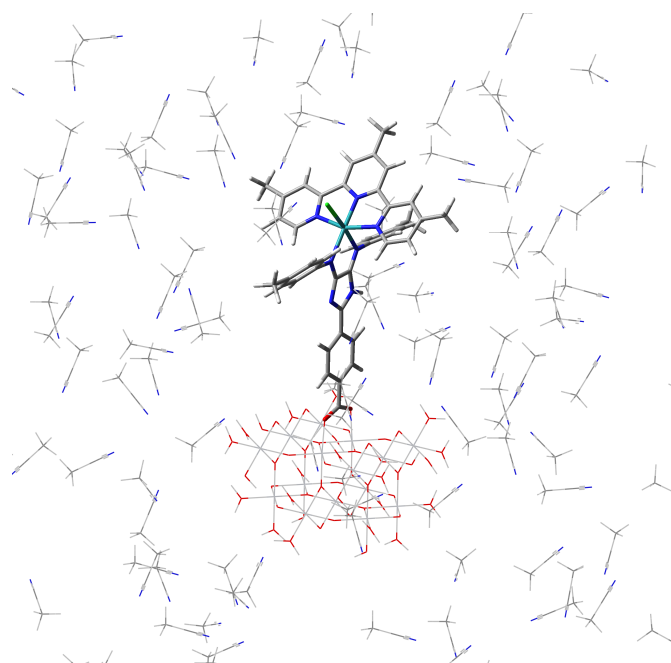


Figure 3.25: Starting structure of QM/MM coupled MD simulation of the RO state (QM: RuMeHCOO^- , MM: TiO_2 cluster) surrounded by the acetonitrile solvent described at the MM level of theory.

Chapter 4

Appended Publications

4.1 4-Methoxy-1,3-thiazole based donor-acceptor dyes: Characterization, X-ray structure, DFT calculations and test as sensitizers for DSSC

Reprinted from Menzel et al. Dyes Pigm. **94**, 512-524 (2012), with permission from Elsevier.



4-Methoxy-1,3-thiazole based donor-acceptor dyes: Characterization, X-ray structure, DFT calculations and test as sensitizers for DSSC

Roberto Menzel^a, Daniel Ogermann^b, Stephan Kupfer^c, Dieter Weiß^a, Helmar Görls^d, Karl Kleinermanns^{b,**}, Leticia González^{c,e,***}, Rainer Beckert^{a,*}

^a Institute of Organic and Macromolecular Chemistry, Friedrich Schiller University Jena, Humboldtstraße 10, 07743 Jena, Germany

^b Institute of Physical Chemistry I, Heinrich Heine University, Universitätsstraße 1, 40225 Düsseldorf, Germany

^c Institute of Physical Chemistry, Friedrich Schiller University Jena, Helmholtzweg 4, 07743 Jena, Germany

^d Institute of Inorganic and Analytical Chemistry, Friedrich Schiller University Jena, Lessingstr. 8, 07743 Jena, Germany

^e Institute of Theoretical Chemistry, University of Vienna, Waehring Str. 17, 1090 Vienna, Austria

ARTICLE INFO

Article history:

Received 27 January 2012

Received in revised form

20 February 2012

Accepted 21 February 2012

Available online 25 February 2012

Keywords:

4-Hydroxy-1,3-thiazoles

Double N-arylation

DSSC

DFT calculations

Donor- π -acceptor dyes

X-ray structure

ABSTRACT

Four donor-(π -conjugated-bridge)-acceptor type dyes **A–D** were designed and synthesized. These new compounds use an unconventional 4-hydroxy-1,3-thiazole building block as an additional chromophore for light harvesting and to extend the π -conjugated system of the molecules. The synthetic route involved a double *N*-arylation Hartwig–Buchwald reaction using Pd(dba)₂ as precatalyst and P(^tBu)₃ as ligand. Two different triaryl amines and a 4-methoxyphenyl group were used as electron donor moieties. The electron acceptor (anchoring) group was 2-cyanoacrylic acid for all dyes, whereas the π -spacer was varied and the influence was investigated. The dyes were thoroughly characterized using photophysical and electrochemical methods and by density functional theory calculations. Additionally, they were evaluated in nanocrystalline TiO₂-based dye-sensitized solar cells (DSSCs). The DSSCs were prepared with and without deoxycholic acid (DCA) as a co-adsorbent to inhibit dye aggregation. The efficiencies obtained were low for DSSCs fabricated without DCA, but were significantly improved for DSSCs with co-adsorbed DCA. Additionally, the X-ray structure of dye **D** was obtained, demonstrating the stereochemistry and planar geometry of the molecule. The DSSC based on dye **A** showed an efficiency of $\eta = 1.70\%$ ($J_{sc} = 4.49 \text{ mA cm}^{-2}$, $V_{oc} = 0.61 \text{ V}$, $FF = 0.62$) under 100 mW cm^{-2} simulated AM 1.5 G solar irradiation compared to $\eta = 4.1\%$ of the standard N₃ obtained under same conditions.

© 2012 Elsevier Ltd. All rights reserved.

1. Introduction

The 4-hydroxy-1,3-thiazoles are a well known type of heterocyclic compounds [1]. This building block was revived from our group due to the similarity to the naturally occurring luciferine, the light-emitting dye of fireflies, and their interesting optical properties. Since then, they have received interest due to their use as light harvesting ligands in Ru(II) polypyridyl complexes [2], as blue-emitting dyes in polymers [3], and because of their tuneable absorption and emission spectra [4], high quantum yields and extinction coefficients, and easy functionalization [5].

* Corresponding author. Fax: +49 3641 948212.

** Corresponding author. Fax: +49 211 81 12179.

*** Corresponding author. Fax: +49 3641 9 48302.

E-mail addresses: kleinermanns@uni-duesseldorf.de (K. Kleinermanns), leticia.gonzalez@univie.ac.at (L. González), c6bera@uni-jena.de (R. Beckert).

In this paper, new thiazole dyes were designed, that consist of a donor-(π -conjugated-bridge)-acceptor structure (D- π -A), e.g. a main prerequisite of sensitizers in dye-sensitized solar cells (DSSCs). Molecules with this special structural architecture have attracted attention since they can be used as emissive materials in molecular electronics [6,7], as fluorescent probes in biochemical applications [8], as nonlinear optical (NLO) materials [9,10], in organic light-emitting diodes (OLEDs) [11] and of course, in DSSCs.

DSSCs have received considerable attention as one possibility to convert solar energy into electricity. Numerous compounds have been tested [12–15] since their description by Grätzel et al. in 1991 [16], and the efficiency was driven up to 11.1% for small DSSCs sensitized with N₃ and up to 10.3% for DSSCs sensitized by an organic-dye [17,18]. Recently, a new record was obtained from Yella et al. using a porphyrine dye as sensitizer and a cobalt (II/III) redox electrolyte instead of the commonly used iodide/triiodide (I⁻/I₃⁻) redox couple, exceeding an efficiency of 12% [19]. The advantages of organic sensitizers toward Ru(II) polypyridyl complexes, such as N₃, N719, and the black dye, are higher molar absorption coefficients,

often simpler synthesis procedures and structure varieties and, naturally, lower costs for the production of a DSSC [20]. The record mentioned for a DSSC with an organic sensitizer was set by a dye containing a triarylamine-based donor. This moiety is extraordinarily promising in various fields of organic dyes [21–26] and was, therefore, predominantly used in this study.

One important possibility to tune the optical properties of organic sensitizers is by alternating the π -conjugated bridge which typically consists of thiophenes and corresponding derivatives (e.g. bithiophene, ethyldioxythiophene). They proved to be more advantageous than an oligoene bridge, which undergoes *cis-trans* isomerisation or oxidation reactions [27]. In this contribution, we substituted the commonly used thiophene unit with a novel etherified 4-hydroxy-1,3-thiazole chromophore to build up D- π -A dyes with high molar extinction coefficient and to expand the absorption spectra further into the solar spectral region. Dyes with a similar structure already proved to be effective as sensitizers in DSSCs [28,29]. Consequently, two different triarylamines and one 4-methoxyphenyl unit were used as electron donors and the influence of the length of the conjugated bridge was verified. 2-cyanoacrylic acid was used as the electron acceptor/anchoring group for the nanocrystalline TiO₂ surface. The dyes obtained were characterized by UV/Vis and emission spectroscopy, electrochemical measurements, and quantum chemical methods. Furthermore, they were tested regarding their application as sensitizers in DSSCs.

2. Experimental section

2.1. General procedures and spectroscopic measurements

¹H, ¹³C NMR and the corresponding correlation spectra were recorded on a Bruker AC-250 (250 MHz) and AC-400 (400 MHz) spectrometer. Chemical shifts (δ) are given relative to solvents and all coupling constants are given in Hz. UV/Vis data of the compounds were collected on a Lambda 19 from PERKIN-ELMER and fluorescence spectra were measured on a Jasco FP 6500. Optical absorption spectra of the adsorbed dyes were recorded by using a Cary 300 UV/Vis spectrophotometer operated at a resolution of 1 nm. The absorption spectra of the electrodes were measured in a reflection arrangement and the absorption of pure TiO₂ nanoparticles was subtracted. Measurements of the fluorescence intensity were carried out on a Perkin Elmer lambda16 UV/VIS spectrometer in the perpendicular excitation-emission geometry, at excitation conditions where the absorbance in the most red-shifted absorption was <0.05. The emission quantum yields were determined by comparing the corrected emission spectra with the reference spectrum of quinine sulfate ($\Phi = 0.55$). All compounds were excited in their absorption maximum. The fluorescence lifetimes of the thiazoles were obtained by time-correlated single photon counting (TCSPC) after excitation with a frequency-doubled Ti-sapphire laser (Tsunami, Newport Spectra-Physics GmbH), i.e. $\lambda_{\text{ex}} = 650$ nm. The repetition rate of the laser was adjusted to 0.8 MHz by a pulse selector (Model 3980, Newport Spectra-Physics GmbH). The emission of the thiazoles was detected using a streak-camera in TCSPC mode. Elemental analysis was carried out on a Leco CHNS-932. Mass spectra were measured either on a Finnigan MAT S50 710 (EI) or MAZ 95 XL (FAB) system. MALDI-TOF MS was performed on a Bruker Ultraflex TOF/TOF mass spectrometer equipped with a 337 nm nitrogen laser operated in the reflectron mode using an acceleration voltage of 25 kV, and dithranol (Bruker, #209783) was used as matrix. Electrochemical measurements were performed on a Metrohm Autolab PGSTAT30 potentiostat with a standard three-electrode configuration. The experiments were carried out in degassed solvents containing 0.1 M Bu₄NPF₆ salt. At the end of each

measurement ferrocene (Fc/Fc⁺) was added as an internal standard. Starting materials were commercially obtained from Sigma–Aldrich and used as received. TLC was from Merck (Polygram SIL G/UV254, aluminum oxide 60 F254). The material for Column chromatography was also obtained from Merck (Silica gel 60).

2.2. Synthesis of the compounds

2.2.1. 5-(4-Nitrophenyl)-2-(thiophen-2-yl)thiazol-4-ol (1)

A mixture of thiophene-2-carbothioamide (2.50 g, 17.5 mmol) and ethyl 2-bromo-2-(4-nitrophenyl)acetate (5.46 g, 19.0 mmol, 1.1 equiv) in 100 mL toluene was heated under reflux for 24 h, and an orange precipitate occurred. After the reaction was cooled down to 50 °C, pyridine (5 mL) was added and stirring was continued for additional 30 min. The mixture was cooled to 0 °C, filtered through a glass frit, washed with cold EtOH and pentane, and dried *in vacuo*. The orange product was pure in terms of elemental analysis and used without further purification (3.57 g, 11.7 mmol, 67%). mp 279 °C (decomp.). ¹H NMR (250 MHz, DMSO-*d*₆): δ 7.19 (dd, $J = 4.0$ Hz, $J = 4.8$ Hz, 1H), 7.69 (d, $J = 3.2$ Hz, 1H), 7.78 (d, $J = 5.0$ Hz, 1H), 7.87 (m, 2H), 8.20 (m, 2H), 12.53 (s, 1H). ¹³C NMR (63 MHz, DMSO-*d*₆): δ 160.42, 156.86, 144.09, 138.77, 136.05, 129.949, 128.76, 127.60, 125.63, 124.19, 104.65. MS-EI: m/z 304 (M⁺, 100%), 110 (M⁺ - C₈H₄N₂O₃S, 60%). Anal. Calc. for C₁₃H₈N₂O₃S₂: C, 51.30; H, 2.65; N, 9.20; S, 21.07. Found: C, 51.43; H, 2.84; N, 9.16; S, 20.92. UV/Vis (DMSO): λ_{max} (log ϵ): 325 (3.78), 429 (4.10), 611 (4.39).

2.2.2. 4-Methoxy-5-(4-nitrophenyl)-2-(thiophen-2-yl)thiazole (2)

A mixture of **1** (1.86 g, 6.11 mmol) and KOH (0.41 g, 7.33 mmol, 1.2 equiv) in DMSO (50 mL) was stirred for 30 min followed by the addition of CH₃I (1.04 g, 7.33 mmol, 1.2 equiv). The deep blue mixture was stirred for 24 h at room temperature. The solution was poured into H₂O (150 mL) and was extracted with CHCl₃ (3 × 50 mL). The combined organic phases were additionally washed with H₂O (3 × 50 mL) to remove the DMSO, dried over MgSO₄ and concentrated *in vacuo* to give a brown oil which was further purified by a short gel filtration (silica, CHCl₃) to yield the ether as an orange solid (1.3 g, 4.09 mmol, 67%). mp 144–145 °C. ¹H NMR (250 MHz, CDCl₃): δ 4.22 (s, 3H), 7.10 (dd, $J = 3.8$ Hz, $J = 5.0$ Hz, 1H), 7.44 (dd, $J = 1.1$ Hz, $J = 5.1$ Hz, 1H), 7.54 (dd, $J = 1.1$ Hz, $J = 3.7$ Hz, 1H), 7.81 (m, 2H), 8.20 (m, 2H). ¹³C NMR (63 MHz, CDCl₃): δ 161.00, 157.02, 145.14, 138.48, 137.18, 128.63, 128.17, 126.71, 126.24, 124.12, 107.81, 58.12. MS-EI: m/z 318 (M⁺, 100%), 288 (M⁺ - CH₂O, 10%). Anal. Calc. for C₁₄H₁₀N₂O₃S₂: C, 52.82; H, 3.17; N, 8.80; S, 20.14. Found: C, 52.67; H, 2.90; N, 9.11; S 20.02. UV/Vis (CH₂Cl₂): λ_{max} (log ϵ): 254 (3.80), 413 (4.30).

2.2.3. 4-(4-Methoxy-2-(thiophen-2-yl)thiazol-5-yl)aniline (3)

N₂H₅OH (1.7 mL, 18.7 mmol, 5 equiv, solution 80% in H₂O) was added to a suspension of **2** (1.18 g, 3.73 mmol) and freshly prepared Raney nickel (catalytic amounts) in MeOH (100 mL) at 50 °C. The suspension turned green and became clear as the reaction proceeded. After the reaction had finished, as indicated by TLC (if the conversion was not complete, more hydrazine was added), the mixture was diluted with CH₂Cl₂ (100 mL) and filtered through a frit on which a 2 cm-thick silica bed was applied to efficiently remove the Raney nickel. The mixture was concentrated till dryness and the crude product was either purified using flash chromatography (silica, CHCl₃/EtOAc 5:1) or by recrystallization from heptane/CH₂Cl₂ by slow evaporation of the CH₂Cl₂, yielding the pure amine as a yellow solid (1.02 g, 3.54 mmol, 95%). mp 114–115 °C. ¹H NMR (250 MHz, CDCl₃): δ 7.56–7.47 (m, 2H), 7.44 (dd, $J = 3.7$ Hz, $J = 1.1$ Hz, 1H), 7.34 (dd, $J = 5.1$ Hz, $J = 1.1$ Hz, 1H), 7.06 (dd, $J = 5.1$, $J = 3.7$ Hz, 1H), 6.77–6.64 (m, 2H), 4.12 (s, 3H), 3.73 (s, 2H). ¹³C NMR (63 MHz, CDCl₃): δ 157.86, 152.60, 145.36, 138.27, 128.22, 127.99,

126.98, 125.20, 121.92, 115.35, 111.55, 57.93. MS-EI: m/z 288 (M^+ , 70%), 136 (M^+ - C_7H_6NOS , 100%). Anal. Calc. for $C_{14}H_{12}N_2S_2O$: C, 58.31; H, 4.19; N, 9.71; S 22.24. Found: C, 57.98; H, 4.12; N, 9.51; S, 22.01. UV/Vis (CH_3CN): λ_{max} (log ϵ): 233 (4.05), 248 (4.03), 283 (3.92), 397 (4.35).

2.2.4. 4-(4-Methoxy-2-(thiophen-2-yl)thiazol-5-yl)-*N,N*-dip-tolyl-aniline (**3a**)

To a solution of **3** (740 mg, 2.57 mmol) in dry and degassed toluene (30 mL) were added $Pd(dba)_2$ (74 mg, 0.128 mmol, 5 mol%), $P(tBu)_3$ (130 μ L of a 1 M solution in toluene, 0.130 mmol, 5 mol%), *p*-bromotoluene (970 mg, 5.70 mmol, 2.2 equiv) and KO^tBu (633 mg, 5.70 mmol, 2.2 equiv). The mixture was degassed for 30 min and heated to 90 °C for 2 days till no educt and monosubstituted product was left as indicated by TLC (silica, $CHCl_3$ /heptane 3:1 R_f educt = 0.2, R_f monosubstituted product = 0.6, R_f disubstituted product = 0.7). After the reaction was finished, the mixture was allowed to cool down to RT, was washed with H_2O (3×50 mL), dried over $MgSO_4$ and concentrated *in vacuo* till dryness. Purification using column chromatography yielded the product as a yellow solid (1.10 g, 2.34 mmol, 91%). mp 174–175 °C. 1H NMR (250 MHz, $CDCl_3$): δ 2.32 (s, 6H), 4.12 (s, 3H), 7.13–6.96 (m, 11H), 7.35 (dd, $J = 5.1$ Hz, $J = 1.0$ Hz, 1H), 7.45 (dd, $J = 3.7$ Hz, $J = 1.1$ Hz, 1H), 7.57–7.49 (m, 2H). ^{13}C NMR (63 MHz, $CDCl_3$): δ 158.21, 153.04, 146.70, 145.05, 138.01, 132.64, 129.87, 127.87, 127.41, 127.03, 125.24, 124.65, 124.51, 122.47, 110.83, 57.77, 20.79. MS-EI: m/z 468 (M^+ , 100%), 316 (M^+ - C_7H_6NOS , 90%). Anal. Calc. for $C_{28}H_{24}N_2O_2S_2$: C, 71.76; H, 5.16; N, 5.98; S, 13.68. Found: C, 71.98; H, 5.18; N, 5.82; S, 13.44. UV/Vis ($CHCl_3$): λ_{max} (log ϵ): 311 (4.23), 417 (4.35).

If the reaction was aborted earlier (after 2 h), the mono-substituted product, 4-(4-methoxy-2-(thiophen-2-yl)thiazol-5-yl)-*N-p*-tolylaniline, was obtained in 70% yield after purification. 1H NMR (250 MHz, $CDCl_3$): δ 7.58 (d, $J = 8.7$ Hz, 1H), 7.45 (d, $J = 3.4$ Hz, 1H), 7.35 (d, $J = 4.9$ Hz, 1H), 7.21–6.89 (m, 2H), 5.69 (s, 1H), 4.14 (s, 1H), 2.32 (s, 1H). MS-EI: m/z 378 (M^+ , 70%), 226 (M^+ - C_7H_6NOS , 100%).

2.2.5. 4-Methoxy-*N*-(4-(4-methoxy-2-(thiophen-2-yl)thiazol-5-yl)phenyl)-*N*-(4-methoxyphenyl)aniline (**3b**)

The procedure was similar to that for **3a**. **3** (170 mg, 0.59 mmol), $Pd(dba)_2$ (10.2 mg, 0.018 mmol, 3 mol%), $P(tBu)_3$ (30 μ L of a 1 M solution in toluene, 0.030 mmol, 5 mol%), *p*-bromoanisole (243 mg, 1.29 mmol, 2.2 equiv), KO^tBu (146 mg, 0.29 mmol, 2.2 equiv), toluene (10 mL). After purification (silica, $CHCl_3$ /heptane 3:1 R_f educt = 0.2, R_f monosubstituted product = 0.7, R_f disubstituted product = 0.8), the product was obtained as an orange oil which solidified after a few hours (266 mg, 0.53 mmol, 90%). mp 131–132 °C. 1H NMR (250 MHz, $CDCl_3$): δ 7.56–7.47 (m, 2H), 7.45 (dd, $J = 3.7$ Hz, $J = 1.0$ Hz, 1H), 7.34 (dd, $J = 5.1$ Hz, $J = 1.0$ Hz, 1H), 7.13–7.02 (m, 5H), 6.93 (d, $J = 8.8$ Hz, 2H), 6.89–6.79 (m, 4H), 4.12 (s, 3H), 3.81 (s, 6H). ^{13}C NMR (63 MHz, $CDCl_3$): δ 158.19, 156.04, 152.88, 147.40, 140.86, 138.18, 128.00, 127.55, 127.10, 126.67, 125.31, 123.59, 120.73, 114.84, 111.15, 57.90, 55.62; HRMS Micro-ESI: m/z 500.123743 (calc. for $C_{28}H_{24}N_2O_4S_2$: 500.12283). UV/Vis (CH_3CN): λ_{max} (log ϵ): 238 (4.20), 302 (4.30), 414 (4.42).

2.2.6. 4-(2-(2,2'-Bithiophen-5-yl)-4-methoxythiazol-5-yl)-*N,N*-dip-tolylaniline (**3c**)

To a solution of **3a** (600 mg, 1.28 mmol) in dry THF (15 mL) at –78 °C under a nitrogen atmosphere was added *n*-BuLi (0.615 mL, 1.54 mmol, 1.2 equiv, 2.5 M solution in hexanes) and the mixture was stirred for 30 min. After warming up to room temperature and additional stirring for 30 min, the mixture was cooled again to –78 °C and tributyltin chloride (625 mg, 1.92 mmol, 1.5 equiv) was added, and stirring was continued for 30 min more,

followed by warming up to room temperature and stirring for 24 h. The mixture was concentrated and dried *in vacuo* and used without further purification. The tin organyl thereby obtained was dissolved in dry DMF (15 mL) and the mixture was degassed for 15 min. To this solution, 2-bromothiophene (313 mL, 1.92 mmol, 1.5 equiv) and freshly prepared $Pd(PPh_3)_4$ (60 mg, 0.052 mmol, 4 mol%) were added, and the mixture was heated to 95 °C for 16 h till no educt was left, as indicated by TLC (silica, $CHCl_3$ /heptane 5:2, R_f educt = 0.6, R_f product = 0.8). The mixture was concentrated and directly applied to column chromatography yielding the product as a red solid (578 mg, 1.05 mmol, 82%). mp 161–162 °C. 1H NMR (300 MHz, $CDCl_3$): δ 7.58 (d, $J = 8.7$ Hz, 2H), 7.34 (d, $J = 3.9$ Hz, 1H), 7.27 (d, $J = 4.4$ Hz, 2H), 7.20–7.01 (m, 12H), 4.17 (s, 3H), 2.37 (s, 6H). ^{13}C NMR (75 MHz, $CDCl_3$): δ 158.37, 152.55, 146.76, 145.13, 138.96, 137.02, 136.46, 132.72, 130.00, 128.10, 127.49, 125.91, 125.12, 124.78, 124.60, 124.35, 124.29, 122.52, 111.02, 57.84, 20.94. HRMS Micro-ESI: m/z 551.12687 (calc. for $C_{32}H_{26}N_2O_3 + H^+$: 551.12855). UV/Vis (CH_3CN): λ_{max} (log ϵ): 240 (3.93), 304 (4.15), 442 (4.36).

2.2.7. 5-(5-(4-(Dip-tolylamino)phenyl)-4-methoxythiazol-2-yl)thiophene-2-carbaldehyde (**4a**, general procedure)

To a solution of **3a** (626 mg, 1.34 mmol) in dry THF (10 mL) at –78 °C under a nitrogen atmosphere, was added *n*-BuLi (0.59 mL, 1.47 mmol, 1.1 equiv, 2.5 M solution in hexanes) and the mixture was stirred for 30 min. After warming up to room temperature and additional stirring for 30 min, the mixture was cooled again to –78 °C and approx. Dry DMF (1 mL) was added and stirring was continued for 30 min followed by warming up to room temperature and further stirring for 1 h. The mixture was neutralized with saturated NH_4Cl solution, diluted with $CHCl_3$ (50 mL) and washed with H_2O (3×50 mL). The organic phase was dried over $MgSO_4$ and concentrated *in vacuo*. Column chromatography (silica, $CHCl_3$ to $CHCl_3$ /EtOAc 3:1) yielded the product as a red solid (600 mg, 1.21 mmol, 90%). mp 151–152 °C. 1H NMR (400 MHz, $CDCl_3$): δ 9.90 (s, 1H), 7.69 (d, $J = 4.0$ Hz, 1H), 7.54 (d, $J = 8.8$ Hz, 2H), 7.47 (d, $J = 4.0$ Hz, 1H), 7.08 (d, $J = 8.3$ Hz, 4H), 7.05–6.97 (m, 6H), 4.13 (s, 3H), 2.33 (s, 6H). ^{13}C NMR (100 MHz, $CDCl_3$): δ 182.59, 159.00, 150.45, 147.41, 146.60, 144.84, 143.33, 136.55, 133.01, 129.95, 127.66, 125.00, 124.93, 123.55, 121.96, 114.30, 57.88, 20.81. MS-EI: m/z 496 (M^+ , 100%), 468 (M^+ - CO, 20%), 316 (M^+ - $C_8H_6NO_2S$, 70%). Anal. Calc. for $C_{29}H_{24}N_2O_4S_2$: C, 70.13; H, 4.87; N, 5.64; S, 12.91; Found: C, 70.08; H, 4.68; N, 5.92; S, 13.04. UV/Vis ($CHCl_3$): λ_{max} (log ϵ): 311 (4.29), 332 (4.18), 485 (4.39).

2.2.8. 5-(5-(4-(Bis(4-methoxyphenyl)amino)phenyl)-4-methoxythiazol-2-yl)thiophene-2-carbaldehyde (**4b**)

The procedure was similar to that for **4a**. **3b** (249 mg, 0.50 mmol), THF (10 mL), *n*-BuLi (0.22 mL, 0.55 mmol, 1.1 equiv), DMF (1 mL). After purification (silica, $CHCl_3$), the product was obtained as a deep red solid (230 mg, 0.44 mmol, 87%). mp 90–91 °C. 1H NMR (250 MHz, $CDCl_3$): δ 9.89 (s, 1H), 7.68 (d, $J = 4.0$ Hz, 1H), 7.55–7.47 (m, 2H), 7.45 (d, $J = 4.0$ Hz, 1H), 7.13–7.00 (m, 4H), 6.96–6.88 (m, 2H), 6.88–6.78 (m, 4H), 4.12 (s, 3H), 3.80 (s, 6H). ^{13}C NMR (63 MHz, $CDCl_3$): δ 182.79, 158.98, 156.27, 150.29, 148.05, 146.79, 143.35, 140.56, 136.81, 127.79, 126.93, 125.06, 122.64, 120.21, 114.90, 114.62, 58.01, 55.63. MALDI-TOF: 528.1 (M^+). Anal. Calc. for $C_{29}H_{24}N_2O_4S_2$: C, 65.89; H, 4.58; N, 5.30; O, 12.11; S, 12.13. Found: C, 65.87; H, 4.54; N, 5.30; S, 12.13. UV/Vis (CH_3CN): λ_{max} (log ϵ): 298 (4.29), 331 (4.18), 476 (4.41).

2.2.9. 5'-(5-(4-(Dip-tolylamino)phenyl)-4-methoxythiazol-2-yl)-2,2'-bithiophene-5-carbaldehyde (**4c**)

The procedure was similar to that for **4a**. **3c** (390 mg, 0.715 mmol), THF (5 mL), *n*-BuLi (0.37 mL, 0.93 mmol, 1.1 equiv), DMF (1 mL). After purification (silica, $CHCl_3$), the product was

obtained as a black solid (380 mg, 0.66 mmol, 93%). mp 193–194 °C. ¹H NMR (250 MHz, CDCl₃): δ 2.33 (s, 6H), 4.13 (s, 3H), 7.03 (m, 10H), 7.27 (d, *J* = 4.3 Hz, 2H), 7.33 (d, *J* = 4.0 Hz, 1H), 7.52 (d, *J* = 8.7 Hz, 2H), 7.66 (d, *J* = 4.0 Hz, 1H). ¹³C NMR (63 MHz, CDCl₃): δ 182.29, 158.44, 151.38, 146.93, 146.35, 144.88, 141.99, 139.16, 137.21, 136.83, 132.78, 129.89, 127.42, 126.72, 125.76, 124.76, 124.48, 123.99, 122.14, 112.10, 57.77, 20.80. MS-EI: *m/z* 578 (M⁺, 100%), 316 (M⁺ - C₁₂H₈NO₂S₂, 80%). Anal. Calc. for C₃₃H₂₆N₂O₂S₃: C, 68.48; H, 4.53; N, 4.84; S, 16.62. Found: C, 68.46; H, 4.65; N, 4.77; S, 16.40. UV/Vis (CHCl₃): λ_{max} (log ε): 263 (4.13), 313 (4.32), 376 (4.24), 486 (4.50).

2.2.10. 2-Cyano-3-(5-(5-(4-(dip-tolylamino)phenyl)-4-methoxythiazol-2-yl)thiophen-2-yl)acrylic acid (**Dye A**, general procedure)

To a solution of **4a** (143 mg, 0.29 mmol) and cyanoacetic acid (27 mg, 0.32 mmol, 1.1 equiv) in CH₃CN (5 mL) was added piperidine (cat. amounts, one drop). The deep red mixture was heated to reflux under a nitrogen atmosphere for 4 h till no starting material was left as indicated by TLC. After cooling down to room temperature, the suspension was diluted with CHCl₃ (20 mL) and washed with H₂O (3 × 20 mL). The organic phase was dried over MgSO₄, concentrated *in vacuo* and the residue was purified by flash chromatography (silica, CHCl₃ to CHCl₃/MeOH 5:1) to yield the product as a glasslike black solid (123 mg, 0.22 mmol, 76%). mp 190 °C (decomp.). ¹H NMR (400 MHz, DMSO-*d*₆): δ 8.25 (s, 1H), 7.77 (d, *J* = 4.0 Hz, 1H), 7.65 (d, *J* = 4.0 Hz, 1H), 7.50 (d, *J* = 8.7 Hz, 2H), 7.10 (d, *J* = 8.2 Hz, 4H), 6.91 (d, *J* = 8.3 Hz, 4H), 6.86 (d, *J* = 8.7 Hz, 2H), 4.04 (s, 3H), 2.26 (s, 6H). ¹³C NMR (100 MHz, DMSO-*d*₆): δ 163.43, 158.35, 150.87, 146.75, 144.24, 142.38, 141.84, 137.67, 137.47, 132.74, 130.07, 127.51, 126.39, 124.63, 122.98, 121.32, 117.93, 112.72, 106.36, 57.88, 20.37. MS-EI: *m/z* 563 (M⁺, 10%), 519 (M⁺ - CO₂, 30%). Anal. Calc. for C₃₂H₂₅N₃O₃S₂: C, 68.18; H, 4.47; N, 7.45; S, 11.38. Found: C, 68.27; H, 4.31; N, 7.49; S, 11.31. IR (ATR, cm⁻¹): 2970 (br), 2360 (m), 2330 (m), 1730 (s), 1560 (s), 1550 (s), 1495 (s), 1365 (s), 1320 (m), 1270 (m), 1230 (m), 1090 (w). UV/Vis (CHCl₃): λ_{max} (log ε): 308 (4.32), 360 (4.16), 517 (4.38). UV/Vis (THF): λ_{max} (log ε): 302 (4.36), 354 (4.15), 520 (4.43).

2.2.11. 3-(5-(5-(4-(Bis(4-methoxyphenyl)amino)phenyl)-4-methoxythiazol-2-yl)thiophen-2-yl)-2-cyanoacrylic acid (**Dye B**)

The procedure was similar to that for **Dye A. 4b** (163 mg, 0.31 mmol), cyanoacetic acid (29 mg, 0.34 mmol, 1.1 equiv), CH₃CN (5 mL), piperidine. After purification, the product was obtained as a black solid (164 mg, 0.28 mmol, 89%). mp 220 °C (decomp.). ¹H NMR (400 MHz, DMSO-*d*₆): δ 8.16 (s, 1H), 7.67 (t, *J* = 7.9 Hz, 1H), 7.61 (d, *J* = 4.0 Hz, 1H), 7.45 (d, *J* = 8.8 Hz, 2H), 7.03–6.98 (m, 4H), 6.93–6.87 (m, 4H), 6.75 (d, *J* = 8.8 Hz, 2H), 4.03 (s, 3H), 3.73 (s, 6H). ¹³C NMR (100 MHz, DMSO-*d*₆): δ = 158.05, 155.96, 150.77, 147.45, 140.90, 140.84, 139.64, 137.94, 136.46, 127.48, 126.83, 126.23, 121.69, 119.07, 118.72, 115.00, 112.59, 109.27, 57.87, 55.25. MALDI-TOF: 595.1 (M⁺). Anal. Calc. for C₃₂H₂₅N₃O₅S₂: C, 64.52; H, 4.23; N, 7.05; O, 13.43; S, 10.77. Found: C, 64.36; H, 4.20; N, 7.12; O, 13.32; S, 10.82. IR (ATR, cm⁻¹): 3030 (w), 2940 (br), 2840 (w), 2350 (m), 2325 (m), 1741 (s), 1600 (m), 1500 (s), 1370 (s), 1240 (s), 1090 (m), 1030 (m). UV/Vis (THF): λ_{max} (log ε): 300 (4.37), 364 (4.16), 505 (4.46).

2.2.12. 2-Cyano-3-(5'-(5-(4-(dip-tolylamino)phenyl)-4-methoxythiazol-2-yl)-2,2'-bithiophen-5-yl)acrylic acid (**Dye C**)

The procedure was similar to that for **Dye A. 4c** (230 mg, 0.40 mmol), cyanoacetic acid (37 mg, 0.44 mmol, 1.1 equiv), CH₃CN (10 mL), piperidine. After purification, the product was obtained as a black solid (230 mg, 0.36 mmol, 90%). mp 243 °C (decomp.). ¹H NMR (250 MHz, DMSO-*d*₆): δ 8.05 (s, 1H), 7.66 (d, *J* = 4.0 Hz, 1H), 7.60 (d, *J* = 4.0 Hz, 1H), 7.58–7.43 (m, 4H), 7.12 (d, *J* = 8.2 Hz, 4H), 6.99–6.81 (m, *J* = 8.6 Hz, 6H), 4.04 (s, 3H), 2.26 (s, 6H). ¹³C NMR

(63 MHz, DMSO-*d*₆): δ 163.50, 157.98, 151.22, 146.55, 146.11, 144.61, 144.33, 141.28, 137.79, 136.44, 134.67, 132.71, 130.14, 128.01, 127.43, 125.84, 125.82, 124.62, 123.26, 121.48, 116.53, 111.41, 98.71, 57.84, 20.45. MS-Micro-ESI (neg.): *m/z* 644 (M⁺). Anal. Calc. for C₃₆H₂₇N₃O₃S₃: C, 66.95; H, 4.21; N, 6.51; O, 7.43; S, 14.90. Found: C, 66.87; H, 4.31; N, 6.40; S, 15.01. IR (ATR, cm⁻¹): 3030 (w), 2930 (br), 2350 (m), 2315 (m), 1600 (s), 1500 (s), 1380 (s), 1320 (s), 1270 (s), 1080 (m). UV/Vis (THF): λ_{max} (log ε): 278 (4.13), 307 (4.24), 400 (4.23), 490 (4.50).

2.2.13. 5-(4-Methoxyphenyl)-2-(thiophen-2-yl)thiazol-4-ol (**5**)

To a solution of thiophene-2-carbothioamide (3.25 g, 22.7 mmol) in DMF (50 mL) was added ethyl 2-bromo-2-(4-methoxyphenyl)acetate (9.30 g, 34.1 mmol, 1.5 equiv). The solution was heated to 50 °C and maintained there for 24 h under continuous stirring. After cooling down to RT, H₂O (100 mL) was added and the product precipitated as a yellow solid. The mixture was stirred for additional 30 min. The product was filtered off, washed thoroughly with EtOH and Et₂O, and dried *in vacuo*. The light yellow solid was used without further purification (4.6 g, 15.9 mmol, 70%). mp 227–228 °C. ¹H NMR (250 MHz, DMSO-*d*₆): δ 3.75 (s, 3H), 6.96 (d, *J* = 8.77 Hz, 2H), 7.15 (dd, *J* = 4.73 Hz, *J* = 3.98 Hz, 1H), 7.65–7.54 (m, 3H), 7.68 (d, *J* = 4.93 Hz, 1H), 11.41 (s, 1H). ¹³C NMR (63 MHz, DMSO-*d*₆): δ 157.56, 156.64, 152.51, 136.71, 128.46, 128.33, 127.12, 125.98, 123.96, 114.23, 106.58, 55.05. MS-EI: *m/z* 289 (M⁺, 100%), 274 (M⁺ - CH₃, 15%). Anal. Calc. for C₁₄H₁₁NO₂S₂: C, 58.11; H, 3.83; N, 4.84; S, 22.16. Found: C, 58.27; H, 4.08; N, 4.47; S, 21.80. UV/Vis (DMSO): λ_{max} (log ε): 394 (4.12).

2.2.14. 4-Methoxy-5-(4-methoxyphenyl)-2-(thiophen-2-yl)thiazole (**6**)

The procedure was similar to that for **2. 5** (1.67 g, 5.78 mmol), DMSO (40 mL), K₂CO₃ (96 g, 6.93 mmol, 1.2 equiv, red solution), CH₃I (0.98 g 6.93 mmol, 1.2 equiv). After purification, the product was obtained as a yellow solid (1.01 g, 3.33 mmol, 58%). mp 75–76 °C. ¹H NMR (250 MHz, CDCl₃): δ 7.63 (d, *J* = 8.7 Hz, 2H), 7.45 (d, *J* = 3.2 Hz, 1H), 7.35 (d, *J* = 4.9 Hz, 1H), 7.11–7.01 (m, 1H), 6.92 (d, *J* = 8.7 Hz, 2H), 4.13 (s, 3H), 3.83 (s, 3H). ¹³C NMR (63 MHz, CDCl₃): δ = 158.48, 158.19, 153.35, 138.10, 128.21, 128.00, 127.19, 125.41, 124.19, 114.30, 110.62, 57.92, 55.45. HRMS Micro-ESI: *m/z* 304.04572 (calc. for C₁₅H₁₃NO₂S₂ + H⁺: 304.0466). UV/Vis (CHCl₃): λ_{max} (log ε): 252 (3.98), 385 (4.26).

2.2.15. 5-(4-Methoxy-5-(4-methoxyphenyl)thiazol-2-yl)thiophene-2-carbaldehyde (**7**)

The procedure was similar to that for **4a. 6** (477 mg, 1.57 mmol), THF (20 mL), *n*-BuLi (0.69 mL, 1.73 mmol, 1.1 equiv), DMF (2 mL). After purification (silica, CHCl₃), the product was obtained as an orange solid (389 mg, 1.17 mmol, 75%). mp 128–129 °C. ¹H NMR (250 MHz, CDCl₃): δ = 9.91 (s, 1H), 7.69 (d, *J* = 4.0 Hz, 1H), 7.68–7.61 (m, 2H), 7.48 (d, *J* = 4.0 Hz, 1H), 7.01–6.87 (m, 2H), 4.15 (s, 3H), 3.82 (s, 3H). ¹³C NMR (100 MHz, CDCl₃): 182.69, 158.90, 150.80, 146.53, 143.41, 136.60, 130.64, 128.35, 125.09, 123.44, 114.30, 113.80, 57.91, 55.35. MS-EI: *m/z*: 331 (M⁺, 50%), 316 (M⁺ - CH₄, 10%), 151 (M⁺ - C₈H₆NO₂S, 70%). Anal. Calc. for C₁₆H₁₃NO₃S: C, 57.99; H, 3.95; N, 4.23; S, 19.35. Found: C, 58.16; H, 3.99; N, 4.23; S, 19.36.

2.2.16. 2-Cyano-3-(5-(4-methoxy-5-(4-methoxyphenyl)thiazol-2-yl)thiophen-2-yl)acrylic acid (**Dye D**)

The procedure was similar to that for **Dye A. 7** (324 mg, 0.98 mmol), cyanoacetic acid (92 mg, 1.08 mmol, 1.1 equiv), CH₃CN (15 mL), piperidine. The product precipitated as a red solid during the reaction. The mixture was diluted with CHCl₃ (50 mL) and washed with H₂O (3 × 50 mL). The organic phase was dried over MgSO₄ and concentrated *in vacuo*. The crude product was

recrystallized from a mixture THF/EtOH by slow evaporation of the THF, yielding a deep red-black fine crystalline compound (351 mg, 0.88 mmol, 90%). mp 260 °C (decomp.). ¹H NMR (400 MHz, DMSO-*d*₆): δ 8.47 (s, 1H), 7.96 (d, *J* = 4.1 Hz, 1H), 7.75 (d, *J* = 3.9 Hz, 1H), 7.62 (d, *J* = 8.7 Hz, 2H), 6.99 (d, *J* = 8.7 Hz, 2H), 4.08 (s, 3H), 3.78 (s, 3H). ¹³C NMR (100 MHz, DMSO-*d*₆): δ 163.25, 158.63, 158.38, 150.54, 145.94, 143.98, 140.50, 136.33, 128.03, 126.58, 122.53, 116.35, 114.49, 113.32, 99.99, 57.96, 55.19. MS-El: *m/z* 398.5 (M⁺, 50%), 354.4 (M⁺ - CO₂, 60%), 151.5 (M⁺ - C₁₁H₇N₂O₃S 100%). Anal. Calc. for C₁₉H₁₄N₂O₄S₂: C, 57.27; H, 3.54; N, 7.03; S, 16.09. Found: C, 57.31; H, 3.49; N, 6.82; S, 16.06. IR (ATR, cm⁻¹): 3000 (w), 2970 (m), 2930 (w), 2360 (m), 2320 (m), 1730 (s), 1580 (w), 1500 (m), 1420 (m), 1370 (s), 1230 (s), 1215 (s), 1200 (s). UV/Vis (THF): λ_{max} (log ε): 278 (4.11), 338 (4.00), 478 (4.60).

2.3. Preparation of the DSSC

TiO₂ nanopowder (5 g, AEROXIDE® TiO₂ P25, Evonik) was suspended in HNO₃ (1 N, Fluka) to prepare a suitable TiO₂ paste. This suspension was heated at 80 °C for 24 h. The HNO₃ was evaporated and the TiO₂ solid was dried for three days at 100 °C. Finally, the TiO₂ solid was treated with 25 mL H₂O, acetylacetone (2.5 g, 25.0 mmol, Merck), Triton X-100 (1.25 g, 1.92 mmol, Avocado), and polyethylene oxide (M.W. 100 000, Alfa Aesar). Aluminoborosilicate glass, coated with fluorine doped tin oxide (FTO, SnO₂:F), was used as a conducting, transparent substrate (resistance ~ 10 Ω/cm², Solaronix SA, Switzerland). The active area was masked with scotch tape and was coated with TiO₂ suspension by using a glass scraper and dried at 80 °C for 10 min. After removal of the scotch tape, approx. 11 μm were measured as deposit thickness. This primed photo electrode was sintered in a muffle furnace for ~ 45 min at 450 °C. The TiO₂ electrode was then immersed in the dye solution (0.2 mM in THF) for 24 h at room temperature. A thin platinum layer was spread on the FTO coating of the counter electrode (Platisol, Solaronix SA, Switzerland). A few drops of the active redox couple iodine/iodide (0.1 M LiI (Fluka), 0.05 M I₂ (Aldrich), 0.6 M Bu₄NI (Aldrich) and 0.5 M 4-*tert*-butylpyridine (Aldrich) in CH₃CN) were added to the photoelectrode. Finally, the counter electrode was clamped to the photoelectrode/electrolyte system.

2.4. Measurements

Measurements of the wavelength dependence of the short circuit current density (*J*_{SC}) were carried out in a light-proof box with a 70 W Xenon lamp (Oriel, Germany) and a grating monochromator (Zeiss, Germany) in the spectral range of 300–800 nm with a resolution of 1 nm. The light intensity incident (*I*_{inc}) on the electrode was measured with a power meter (Coherent, USA). The IPCE was calculated using the following expression:

$$\text{IPCE}(\%) = \frac{J_{\text{SC}} [\text{A cm}^{-2}] 1240}{\lambda [\text{nm}] I_{\text{inc}} [\text{W cm}^{-2}]} 100$$

The photocurrent-voltage (*I*–*V*) curves were measured using a focused 120 W Xenon lamp (Oriel, Germany) and a special filter to simulate solar irradiation (100 mW cm⁻², 1 sun, 1.5 air mass (AM) global). The fill factors (FF) and overall efficiencies (η) were calculated according to following equations.

$$\text{FF} = \frac{\text{MPP} [\text{W cm}^{-2}]}{J_{\text{SC}} [\text{A cm}^{-2}] V_{\text{OC}} [\text{V}]}$$

$$\eta(\%) = \frac{J_{\text{SC}} [\text{A cm}^{-2}] V_{\text{OC}} [\text{V}] \text{FF}}{I_{\text{inc}} [\text{W cm}^{-2}]} 100$$

Here MPP is the “maximum power point” and *V*_{OC} the open-circuit voltage [30].

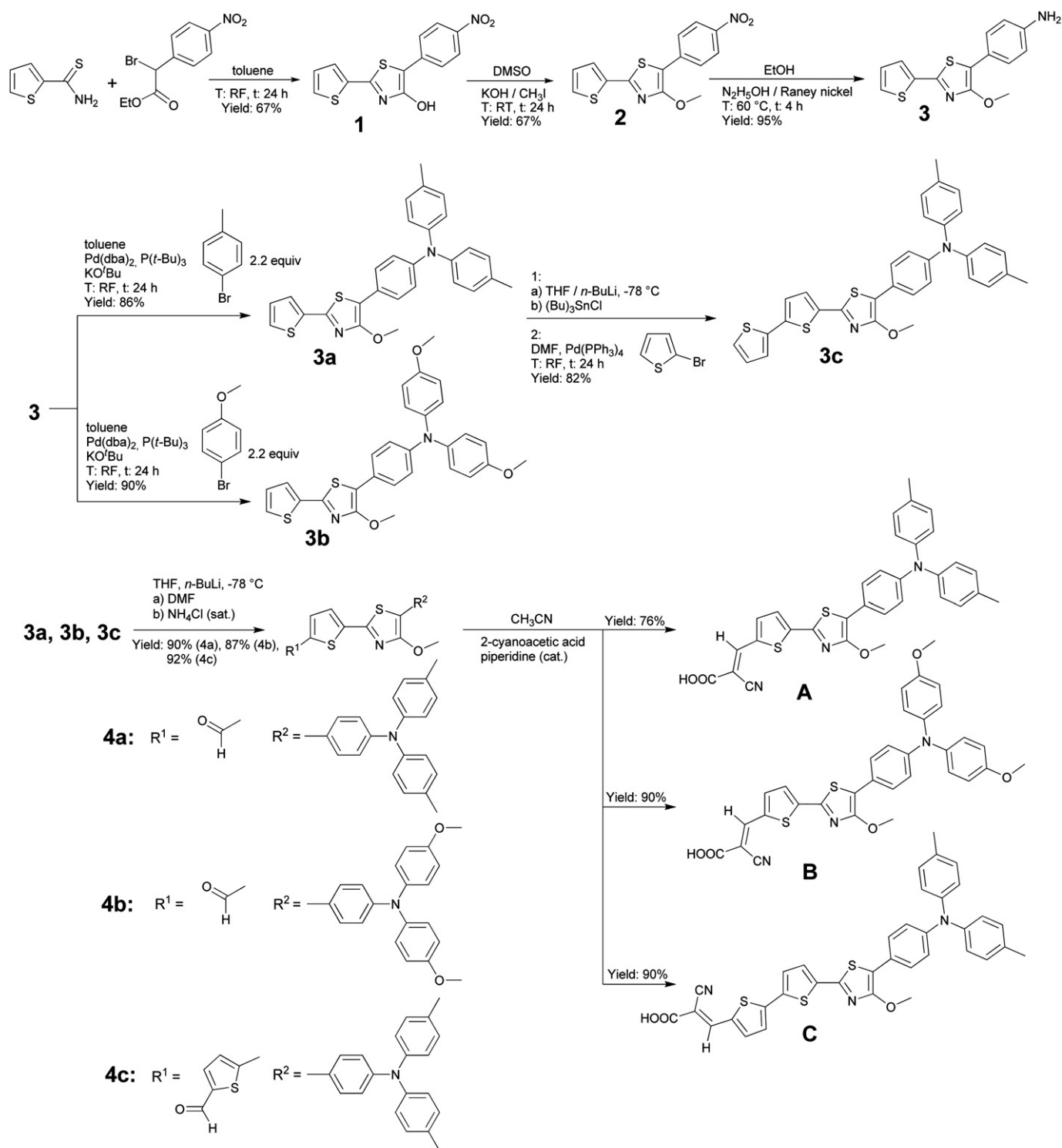
2.5. Computational methods

All calculations were performed with the GAUSSIAN 09 program [31] in the presence of solvent (tetrahydrofuran, ε = 7.4257, *n* = 1.4070) via the integral equation formalism of the polarizable continuum model [32]. The ground state equilibrium structures were optimized with the long-range corrected CAM-B3LYP XC functional [33] and the 6–31G(d,p) double-ξ basis set. [34]. Harmonic vibrational frequencies at the same level of theory proved that the stationary points obtained corresponded to the minima of the potential energy surfaces. Excited state properties, such as excitation energies, oscillator strengths and excited states geometries, were computed via TDDFT and the same XC functional and basis set as was employed for the ground state. The absorption spectra in the FC region were simulated by the first ten singlet excited states. According to Kasha's rule fluorescence occurs from the lowest excited singlet state [35], the S₁ state was optimized to obtain the emission energies from the S₁.

3. Results and discussion

3.1. Synthesis and structure of the dyes

The synthetic route and molecular structures of the triarylamine-based dyes are depicted in Scheme 1. The starting material, 5-(4-nitrophenyl)-2-(thiophen-2-yl)thiazol-4-ol (**1**), was synthesized using a Hantzsch cyclization of thiophene-2-carbothioamide with ethyl 2-bromo-2-(4-nitrophenyl)acetate. The 4-hydroxy-1,3-thiazole obtained was alkylated following a Williamson-type etherification with K₂CO₃ as the base and methyl iodide as the nucleophile to yield the 4-methoxy-5-(4-nitrophenyl)-2-(thiophen-2-yl)thiazole (**2**). The reduction of the nitro group was realized following a standard protocol using freshly prepared Raney nickel and hydrazine hydrate solution as the hydrogen source in ethanol to almost quantitatively yield the amine 4-(4-methoxy-2-(thiophen-2-yl)thiazol-5-yl)aniline (**3**). The crucial step in the synthetic route was the Hartwig–Buchwald coupling of the aryl amine **3** with an appropriate aryl halide using a Pd-catalyst. Although thoroughly described in literature, this type of coupling is difficult and strongly depends on the nature of the catalysts, ligands and reaction conditions [36,37]. In addition, the coupling has to take place twice to obtain the desired product. This double *N*-arylation of primary amines is not often described in literature. Examples exist for simple triarylamines basically consisting of tolyl or anisole groups [38], or for a catalytic process with a second, intramolecular coupling to generate different types of carbazoles [39, 40]. Tri-*tert*-butylphosphine (P(^tBu)₃) was chosen as a promising ligand, which has already been successfully applied in the synthesis of different indole derivatives [41]. For the coupling reaction, *bis*(dibenzylideneacetone)palladium(0) (Pd(dba)₂) was used as the precatalyst, KO^tBu as the base to deprotonate the amine in the catalytic cycle and toluene as solvent. The aryl halides chosen were *p*-bromotoluene and *p*-bromoanisole because of a better stability of the corresponding triarylamines toward oxidative coupling reactions in *para*-position after excitation and radical formation (charge separation), which is well known for these radicals [42,43]. Surprisingly, the coupling reaction with P(^tBu)₃ as ligand (several attempts using, for example, triphenylphosphine or 1,1'-*bis*(diphenylphosphino)ferrocene as ligands failed completely) produced the coupling products in very good yields (>86%). Furthermore, the two-step process of the reaction was confirmed and the monosubstituted product formed was isolated and identified for **3a** (see experimental section). A noteworthy observation was that



Scheme 1. Synthesis and structure of the triarylamine-based dyes A-C.

when a high excess of coupling agent together with longer reaction times were applied, an additional spot (TLC) eluting in front of the coupling products, occurred. This by-product was identified (MS) as the coupling product of the thiophene moiety at the electron rich 5-position with the aryl halide.

In order to vary the conjugation lengths of the dyes, a further thiophene ring was introduced in **3a** via a Stille coupling with 2-bromothiophene to yield 4-(2-(2,2'-bithiophen-5-yl)-4-methoxy-

thiazol-5-yl)-*N,N*-di-4-tolylaniline (**3c**) in very good yields (86%). The introduction of the aldehyde group via a Vilsmeier–Haack reaction with DMF and POCl₃ was not successful. Therefore, the thiophene was deprotonated with *n*-BuLi followed by the addition of DMF and quenching with saturated NH₄Cl solution to give the corresponding aldehydes in excellent yields (>87%). No side product due to a possible directed *ortho*-metalation at the 4-methoxyphenyl ring for **3b** was observed if *n*-BuLi was added very slowly at –78 °C and the excess was

kept small. The last step, the introduction of the 2-cyanoacrylic acid acceptor group, was achieved by a Knoevenagel condensation of the aldehyde group with cyanoacetic acid and catalytical amounts of piperidine in acetonitrile to give the dyes **A–C** in moderate to good yields (>75%). Similar to the synthesis of **1**, the starting material for **D**, 5-(4-methoxyphenyl)-2-(thiophen-2-yl)thiazol-4-ol (**5**), was obtained by a cyclization reaction of the thiophene-2-carbothioamide and ethyl 2-bromo-2-(4-methoxyphenyl)acetate. The reaction in toluene only resulted in a sluggish conversion to **5**, therefore a second method, with DMF as the solvent and slightly elevated temperature was used, which gave the product in a satisfactory yield (70%). All the following reactions (alkylation, introduction of the aldehyde and Knoevenagel condensation) were similar to that for dyes **A–C** and the synthetic route is depicted in Scheme 2.

3.2. X-ray structure of dye **D**

Single Crystals suitable for X-ray structure analysis were obtained from a mixture ethylene glycol/THF in an NMR tube by slow evaporation of the THF. The presented structure is a rare example in this field, because of the weak crystallization tendency of this D- π -A type compounds. Usually, crystallization leads to amorphous precipitates or very thin plates because of the planarity of the molecules (aggregation).

The crystal structure of **D** is depicted in Fig. 1 and a more detailed look, selected bond lengths and angles in comparison with the calculated values and additional crystallographic data are given in the ESI (S1 and S2). The structure reveals the almost planar arrangement of the dye. Two hydrogen bonds between the carboxylic acid groups of two adjacent molecules lead to the formation of a dimer. The distance between the two oxygens forming the hydrogen bonds is 2.593(3) Å. The cyano group of the 2-cyanoacrylic acid acceptor unit is in *cis*-position to the sulfur of the thiophene moiety. The NMR spectrum of **D** shows only one signal for the ethylene hydrogen bound to C16. (ESI, S3). Therefore, it can be considered that the presented isomer is exclusively formed in the Knoevenagel condensation reaction. This is similar to one infrequent literature example where the cyano group is also in *cis*-position to the sulfur of the thiophene moiety [44]. As expected, the conjugation pathway of the molecule shows an almost planar geometry. The distance between two layers formed from the dimers is only 3.5 Å, which is typical for strong π -stacking interactions between the molecules [45]. The torsion angles between the three aromatic rings and the anchoring group are 4.47(2) (C20–C8–C7–S2), 7.21(2) (N1–C5–C4–S1) and 8.99(2) ° (S1–C1–C16–C17). This planarity allows an electron flow from the donor to the acceptor group.

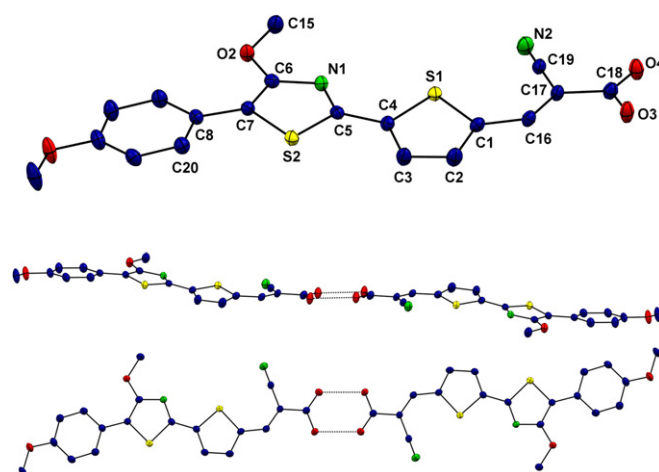


Fig. 1. Ortep plot of dye **D**. Ellipsoids are at 50% probability level. Shown are the numbering scheme (above) and the two hydrogen bonds to form the dimer (below).

3.3. Photophysical properties

The UV/Vis spectra of the protonated and deprotonated dyes are depicted in Fig. 2 and the spectroscopic data are summarized in Table 1. The small unmodified etherified 4-hydroxy-1,3-thiazoles usually show an intense band in the region of 380 nm (see experimental section for **2**, **3** and **6**) due to π - π^* transition of the thiazole moiety. These λ_{max} of absorption were successfully shifted bathochromically after the formation of the electron-donating triarylamine moieties for **3a** and **3b**, furthermore, after the introduction of the electron accepting aldehyde and up to 505 nm for **B** after the generation of the electron-accepting cyanoacrylic acid group due to an intense intramolecular charge transfer (ICT) transition. The absorption maximum of **A–C** is at moderate longer wavelengths compared to very similar triarylamines using thiophenes and oligothiophenes [46], thiophenes and 3,4-ethylenedioxythiophene [47], and thiophenes and 3,4-thienothiophene [23] instead of 4-methoxy-1,3-thiazoles units as a π -spacer. This is promising in terms of the light harvesting properties of the dyes presented. The influence of the 4-methoxy group at the triarylamine moiety for **B** compared to the tolyl group (**A**) resulted in a bathochromic shift of

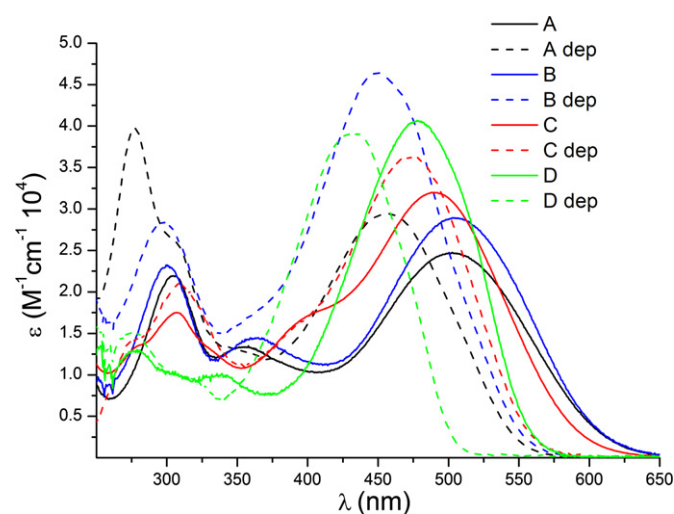
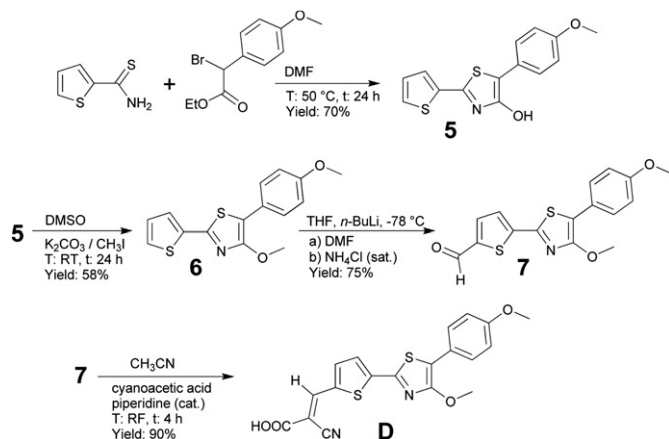


Fig. 2. UV/Vis spectra of the protonated and deprotonated dyes **A–D** in THF solution at room temperature.



Scheme 2. Synthesis and structure of the 4-methoxyphenyl-based dye **D**.

Table 1
Spectroscopic properties, and redox potentials of the protonated and deprotonated (dep) dyes **A–D**.

Dye	λ_{Abs} (nm) [ϵ ($10^2 \text{ M}^{-1} \text{ cm}^{-1}$)]	λ_{Fl} (nm) ^a	Stokes S. (cm^{-1}) ^b	τ (ns) ^c	Φ (%)	$E_{1/2 \text{ Ox}}$ (V) ^d	$E_{1/2 \text{ red}}$ (V) ^d	E_{0-0} (eV) ^e	$E(S^+/S^*)$ vs NHE (V) ^f
A	305 [220], 355 [133], 503 [247]	611	3500	2.5	4	0.35, 0.59 ^g	–1.95	2.30	–1.32
A (dep)	277 [400], 457 [295]	592	5000	–	–	–	–	–	–
B	300 [230], 363 [145], 505 [289]	640	4200	1.1	< 1	0.20, 0.56 ^g	–1.93	2.35	–1.52
B (dep)	297 [280], 450 [460]	558	4300	–	–	–	–	–	–
C	307 [175], 400 [170], 490 [320]	622	4300	1.4	1	0.28, 0.68 ^g	–1.99	2.23	–1.32
C (dep)	309 [210], 474 [360]	598	4400	–	–	–	–	–	–
D	277 [130], 339 [100], 477 [400]	599	4300	2.9	54	0.69	–1.53	2.34	–1.02
D (dep)	276 [150], 433 [390]	507	3400	–	–	–	–	–	–

^a Excitation at the longest wavelength absorption.

^b Relative to maximum of the absorption.

^c Excitation at $\lambda = 650$ nm.

^d $E_{1/2} = (E_{\text{pa}} - E_{\text{pc}})/2$ vs Fc/Fc⁺.

^e Calc from the onset (10%) of the photoluminescence spectra.

^f The excited-state oxidation potential $E(S^+/S^*) = E_{1/2}$ (first oxidation) - E_{0-0} with Fc/Fc⁺ vs NHE = 0.63 V.

^g Peaks are irreversible, E derived from differential pulse polarographic (DPP) measurements.

only 2 nm (0.01 eV), which is in accordance with the quantum chemical calculations. In the energetic representations of the HOMO, it can be seen that participation of the 4-methoxy groups is very small and, therefore, the influence to the ICT is negligible (see Fig. 5 dye **B**). Surprisingly, the extension of the conjugation length for **C** did not lead to a bathochromic shift of the absorption maximum. This is contrary to the literature examples mentioned and can be attributed to an insufficient ICT transition, which is also in accordance with the quantum chemical calculations (see Fig. 5 dye **C**). The bands in the UV-A region at 300–310 nm with extinction coefficients (ϵ) from 17 500 to 23 000 $\text{M}^{-1} \text{ cm}^{-1}$ correspond to a mixture of $\pi-\pi^*$ transitions in triarylamine and ICT states (see ESI, S11). Accordingly, this band is missing in the spectra of **C**, which only shows a weak UV absorption at 277 nm due to the 4-methoxyphenyl ring. The extinction coefficients of the absorption bands in the visible region are up to 40 000 $\text{M}^{-1} \text{ cm}^{-1}$, which is characteristic for an ICT and 2½ times higher than those of Ru(polypyridyl) complexes [48]. Deprotonation of the dyes was carried out by adding the appropriate amount (1.1 equiv) of a tetrabutylammonium hydroxide (TBAOH) solution directly to the cuvette, followed instantaneously by the measurement.

The longest wavelength absorptions for all dyes are hypsochromically shifted (46 nm or 0.25 eV for **A**, to 16 nm or 0.09 eV for **C**). The energy acceptor strength (electronegativity) of the cyanoacrylic acid after deprotonation is lowered, which leads to

a diminished ICT character of the transition and, consequently, to a hypsochromic shift of the absorption [49]. This is also in accordance with the small change of the absorption maximum for **C** and the lower ICT character of the transition in the visible part of the spectra. Furthermore, after deprotonation the extinction coefficients for all triarylamine dyes increased (up to 46 000 $\text{M}^{-1} \text{ cm}^{-1}$ for **B**), whereas for **D**, it slightly decreased. The triarylamine-based dyes show moderate room temperature fluorescence in THF and DMSO, but not in CHCl_3 and MeOH. Their emission spectra in THF solution are shown in Fig. 3.

The large Stokes Shift is typical for these D- π -A dyes. In accordance with the UV/Vis spectra, the emission is also hypsochromically shifted after deprotonation. The fluorescence lifetimes vary from 1.1 to 2.9 ns for **B** and **D**, respectively. The dye emissions showed the expected monoexponential decay curves, which are presented in the ESI (S4). The values obtained are consistent with the measured fluorescence quantum yields (Φ) of the dyes. They are very low for the triarylamine **A–C** (below 4%) and higher for the 4-methoxyphenyl-based dye **D** (54%).

3.4. Electrochemical properties

In order to gain deeper insights into the electrochemical properties of the dyes, cyclic voltammetry (CV) and differential pulse polarography (DPP) measurements were applied. They were

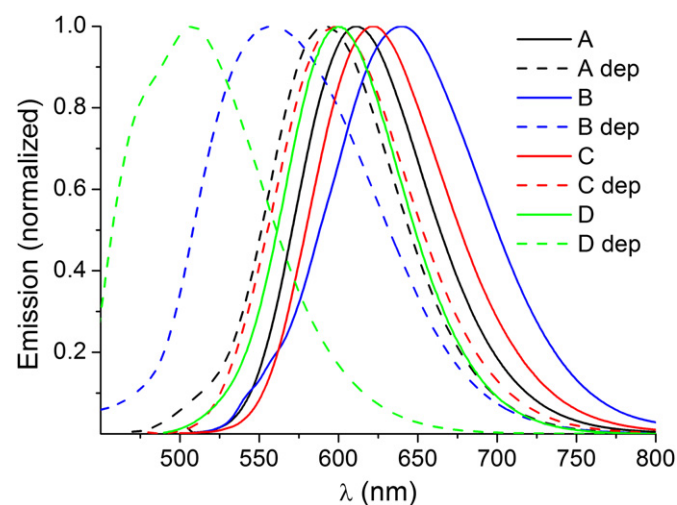


Fig. 3. Emission spectra of the protonated and deprotonated dyes **A–D** in THF solution at room temperature after excitation in the longest wavelength absorption band.

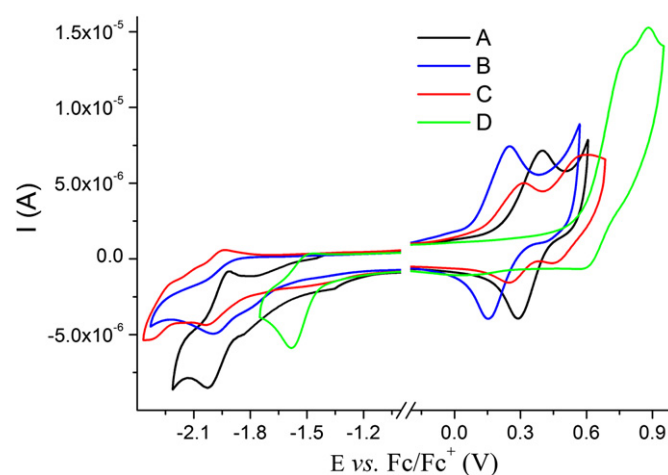


Fig. 4. Cyclic voltammetry spectra of dyes **A–D** in THF; experimental conditions: 0.1 M TBAPF₆, $c \approx 10^{-4}$ M, 25 °C, scan rate 200 mV s^{-1} , RE: Ag/AgCl, WE: carbon, AE: platinum.

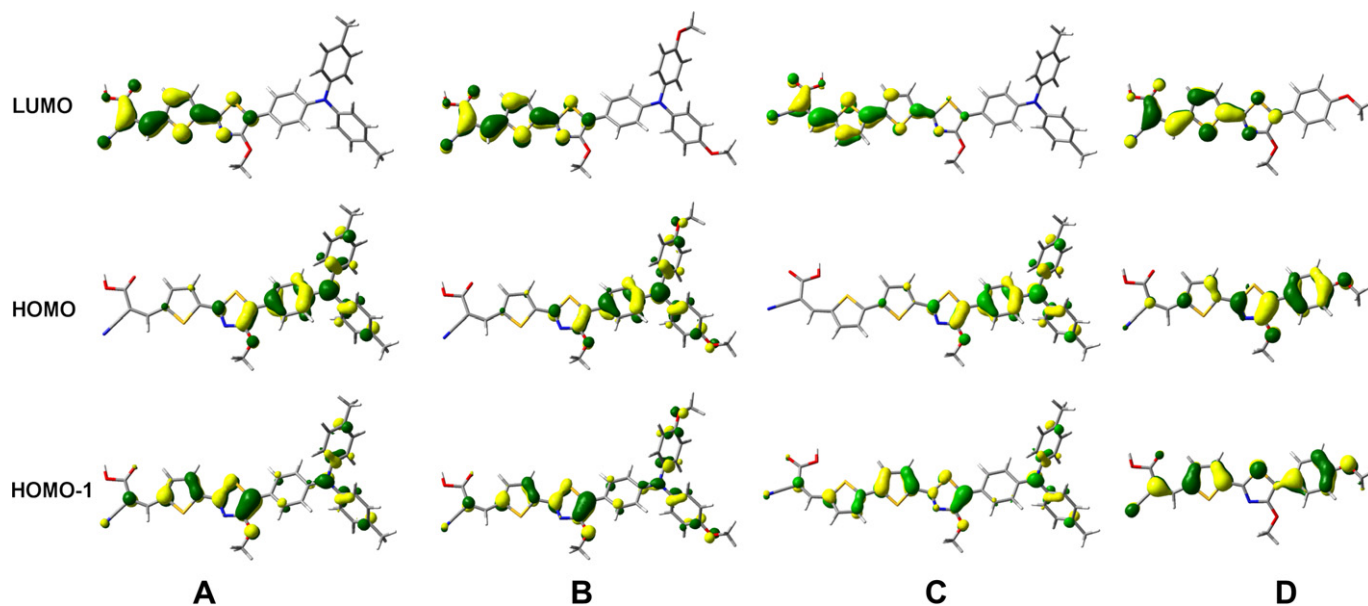


Fig. 5. Frontier orbitals of the four dyes optimized at the CAM-B3LYP/6–31G(d,p) level of theory.

carried out in THF with 0.1 M TBAPF₆ at 25 °C with a scan rate of 200 mV s⁻¹, with Ag/AgCl as the reference, carbon as the working and platinum as the auxiliary electrode. Ferrocene was added as the internal standard after every measurement. All potentials discussed here are given relative to the normal hydrogen electrode (NHE) with Fc/Fc⁺ vs NHE = 0.63 V [50]. The cyclic voltammetry spectra of the compounds are depicted in Fig. 4 and data are summarized in Table 1.

The dyes **A–C** show a reversible first oxidation wave, caused by the oxidation of the triarylamine donor in the region from 0.98 to 0.83 V for **A** and **B**, respectively. This suggests that the first oxidized state of these dyes is stable, which is one prerequisite for a good long term stability of DSSCs [13]. The oxidation potential for **B** is lowered by 0.15 V compared to **A** due to the introduction of the electron-donating 4-methoxy group at the triarylamine core, which facilitates the oxidation of the amine. Additionally, compound **C** is oxidized more easily than **A** after the incorporation of the thiophene unit in the conjugation pathway, leading to an increase of the electron density of the aromatic linker which, consequently, lowers the oxidation potential of the end-capped amine unit [51]. The oxidation wave for compound **D** is superimposed by the oxidation of the solvent and, therefore, it is not possible to assign if the oxidation process is reversible or not.

Nonetheless, due to the missing triarylamine moiety, the oxidation occurs at a significant higher potential (1.32 V) compared to the dyes **A–C**, but it could not be clarified where the oxidation and radical formation takes place.

The first reduction peaks appear to be irreversible for all dyes. They are very similar for the triarylamines (–1.30 for **B** to –1.33 V for **C**) and shifted to a higher potential for compound **D** (–0.90 V). In a water-free environment, it could be attributed to the reduction of the double bond forming a radical which then undergoes dimerization or hydrodimerization reactions (if traces of water are present) [52,53]. This would explain the overall irreversible nature of the process. The higher potential for **D** is in agreement with the lower ICT character and a reduced dipole moment, which leads to a less pronounced electron density at the cyanoacrylic acid group, which makes it easier to reduce [54].

In order to judge the possibility for efficient charge injection in the conducting band of TiO₂, the excited-state oxidation potential

$E(S^+/S^*)$ was calculated from the first oxidation potential and the zero–zero transition energy E_{0-0} , which was determined from the onset (10%) of the emission spectra ($E(S^+/S^*) = E_{1/2} \text{ Ox} - E_{0-0}$). A schematic representation of the energy levels is given in the ESI (S5). The calculated potentials vary from –1.52 to –1.02 V for **B** and **D**, respectively. They are sufficiently more negative ($\Delta E > 0.2$ V) [55] than the conducting band (CB) edge of the TiO₂ (standard potential $E_{\text{CB}} = -0.5$ V vs NHE) [56] and electron injection should be possible. The regeneration of the oxidized dyes is also energetically favored. The oxidation potential, the energy of the HOMO, lies in the range of 1.32 V (**D**) to 0.98 V (**A**), which is high enough for an efficient reduction by the I⁻/I₃⁻ redox couple ($E = 0.35$ V vs NHE) [57]. Thus, electron injection of the excited molecules and, subsequently, regeneration of the oxidized species is energetically permitted. This allows the application of the dyes in DSSC.

3.5. Computational results

In order to gain more detailed insight into the structural and the spectroscopic properties of the chromophores, density functional theory (DFT) and its time-dependent version (TDDFT) was applied. The four dyes were investigated in the protonated form and in the *trans*-arrangement of the nitrile group to the thiophene. TDDFT calculations on both the *trans* and the *cis*-isomer were performed and details are summarized in the ESI. It was shown that both isomers exhibit very similar photophysical properties. Therefore an influence of the different isomers on the spectroscopic properties can be neglected. The ground state equilibrium geometries of the protonated species show similar structural features. The conjugated π -system from the bridge to the anchoring group is planar in all dyes. The phenyl groups of the triphenylamine fragment (**A–C**) are twisted out of planarity due to steric hindrance. All dyes exhibit a torsionated phenyl ring connected to the 4-methoxy-1,3-thiazole fragment, with a dihedral angle independent of the length of the bridge, as well as of the size of the donor system. It varies only marginally from 18.3° (**C**) up to 20.4° (**D**). The analysis of the harmonic vibrational modes corresponding to the torsion indicates a shallow minimum in this normal coordinate. Wavenumbers of ca. 30 cm⁻¹ have been determined for this vibrational mode for all compounds. For this reason, a thermal distribution in this

coordinate is to be expected. According to the low frequencies, the HOMOs show a non-constructive overlap of the π -systems from the 4-methoxy-1,3-thiazole and the adjacent phenyl moiety leading to a single bond in these positions.

The optimized geometries of the S_1 states hold similarities to the ground state equilibrium structures. The reason is the π - π^* nature of the S_1 and the partial occupation of the LUMOs. Therefore, the excited state structures show only minor shifts in the bond lengths and angles. However, the 4-methoxy-1,3-thiazole-phenyl fragments are planarized as a result of the bonding character of the LUMOs in these positions. The most important molecular orbitals involved in the electronic excitations are shown in Fig. 5. The absorption spectra of the four dyes were calculated using the Franck-Condon (FC) geometry and the first ten singlet excited states. Table 2 collects vertical and adiabatic excitations from the S_1 state. The absorption energies to higher excited states, together with an overlay of the experimental and calculated absorption spectra and the molecular orbitals contributing to those states, are summarized in the ESI (S6–S11). In all dyes the S_1 is assigned to a π - π^* excitation, with the main transition occurring from the HOMO to the LUMO. The main contribution to the HOMO of **A**, **B** and **C** is due to the π -systems of the donor and thiazole fragments, while in the case of **D**, the donor and the entire bridge contribute to the HOMO. The LUMO for all dyes is spread over the anchoring group and the bridge. Hence, an ICT from the donor to the acceptor occurs.

The expansion of the aromatic π -system tends to increase the weight of further configurations. The HOMO/LUMO transition for **D** has a weight of 88%, while the implementation of the *N,N*-di-4-tolyl (**A**) and *N,N*-bis(4-methoxyphenyl) (**B**) donor groups decreases the weight to 72 and 71%, respectively. The weight is decreased further to 54% by the introduction of an additional thiophene moiety (**C**). As a consequence, the S_1 of **C** features a less pronounced ICT leading to an increase of the excitation energy and, consequently, to a hypsochromic shift of the λ_{\max} of the absorption compared to **A** and **B**. Additionally, **D** shows a blueshift of the S_1 . The reason is the more local π - π^* transition between the frontier orbitals. The wavelength dependency of the first absorption band is in good agreement to the experiment. In general, the excitation energies of the S_1 are marginally overestimated (**A**: 0.12, **B**: 0.09, **C**: 0.11, and **D**: 0.16 eV), showing that the CAM-B3LYP functional is very well suited to describe ICT in these dyes. By comparing the oscillator strengths (f) with the experimentally obtained molecular extinction coefficients, a general trend of increasing absorption is obvious for **A**, **B** and **C**.

Table 2

Calculated absorption/emission (fluorescence) properties to/from the first excited state S_1 . Main contributions to the wavefunction (weight), vertical (absorption) or adiabatic (emission) excitation energies (ΔE^e in eV and nm), oscillator strengths (f) and deviations from experimental values (ΔE_{Exp}). H = HOMO, L = LUMO.

Transition	Weight (%)	ΔE^e		f	ΔE_{Exp} (eV)
		(eV)	(nm)		
Absorption					
A H \rightarrow L	72	2.58	479	1.511	0.12
H-1 \rightarrow L	20				
B H \rightarrow L	71	2.54	487	1.502	0.09
H-1 \rightarrow L	20				
C H \rightarrow L	54	2.64	470	1.958	0.11
H-1 \rightarrow L	26				
H \rightarrow L + 1	12				
D H \rightarrow L	88	2.75	451	1.364	0.16
Emission					
A H \leftarrow L	91	1.91	650	–	–0.02
B H \leftarrow L	89	1.88	658	–	–0.06
C H \leftarrow L	85	1.85	669	–	–0.15
D H \leftarrow L	95	2.12	586	–	0.01

The first absorption band of **D** exhibits the largest measured molecular extinction coefficient, while the calculated oscillator strength is considerably too small. This is caused by the more local HOMO/LUMO transition for **D**, and the fact that CAM-B3LYP tends to underestimate the oscillator strength of such systems.

The adiabatic emission spectra were obtained using the optimized geometry of the first excited singlet state. The measured and simulated fluorescence wavelengths are also collected in Table 2. A comparison of the theoretical and experimental fluorescence spectra, as well as the molecular orbitals contributing to the relevant transitions, can be found in the ESI (S12 and S13). In agreement with the configurations of the S_1 in the ground state equilibrium structure, the weight of the LUMO/HOMO transitions decreases with the enhancement of the π -system. Nevertheless, the weight is significantly increased (**A**: 91, **B**: 89, **C**: 85, and **D**: 95%) compared to the vertical excitations in the FC region. The emission wavelengths obtained are in excellent agreement with the experimental data. Only minor deviations of –0.02, –0.06 and 0.01 eV for **A**, **B** and **D**, respectively, were generated, while **C** shows a slight underestimation of –0.15 eV.

3.6. Photovoltaic devices and solar cell performance

In order to test the dyes for a possible application as sensitizers, DSSCs with nanocrystalline TiO_2 (70% anatase, 30% rutile) were prepared. The exact protocol is given in the experimental part and the results, together with the standard N3 (*cis*-bis(isothiocyanato) bis(2,2'-bipyridyl-4,4'-dicarboxylato)-ruthenium(II)), are summarized in Table 3. The incident photon-to-current conversion efficiencies (IPCE) spectra obtained are shown in Fig. 6. Only moderate IPCEs were achieved, with values varying from 25 (**D**) to 13% (**C**) for the absorption maximum of the dyes, though several different preparation conditions (different solvents, dye concentrations) were utilized. IPCEs of up to 80% are usually expected for these types of compounds [12,23]. Therefore, it can be assumed that the electron injection efficiency in the electron acceptor states of the TiO_2 is low. The amount of dyes adsorbed on the TiO_2 was determined by measuring the absorption spectra of a solution of the corresponding dye before and after soaking of the TiO_2 plate. After correlation with the measured extinction coefficient, the adsorbed amount was calculated to be 5.0×10^{-8} (**A** and **B**), 6.6×10^{-8} (**D**) and 4.0×10^{-8} mol cm^{-2} for the largest sensitizer **C**. The values correspond very well with the size of the molecules and are in good agreement with literature examples and cannot account for the low IPCEs [58,59]. The absorption spectra of the adsorbed dyes are depicted in the ESI (S18). They were similar to the absorption spectra of the dyes in solution. The main difference is the broadening of the longest wavelength ICT band (absorption from approx. 370–700 nm compared to 425–600 nm for the dyes in solution)

Table 3

Photovoltaic performance of DSSCs based on dyes **A–D** without and with the addition of DCA (10 mM) as a co-adsorbent.

Dye	J_{sc} (mA cm^{-2})	V_{oc} (mV)	FF	η (%)
Without DCA				
A	1.81	519	0.46	0.44
B	1.42	558	0.51	0.41
C	1.37	524	0.47	0.36
D	1.03	468	0.52	0.25
N3	11.73	690	0.51	4.1
With DCA				
A	4.49	612	0.62	1.70
B	3.55	611	0.50	1.08
C	3.27	616	0.51	1.02
D	2.23	511	0.52	0.61

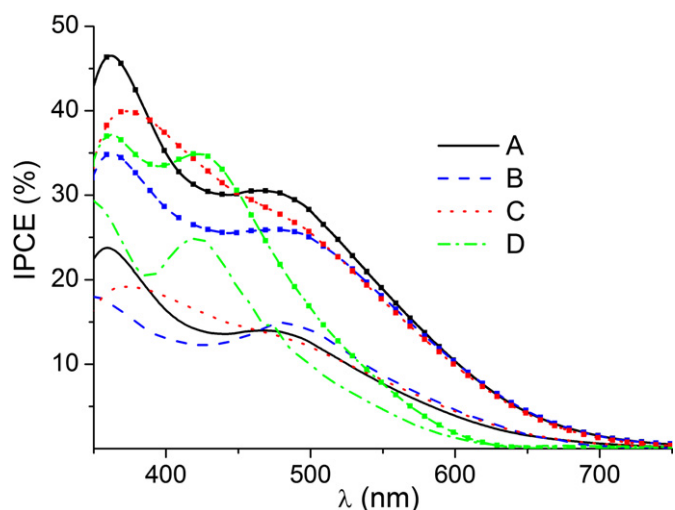


Fig. 6. Spectra of the incident photon-to-current conversion efficiencies obtained for nanocrystalline TiO₂ solar cells sensitized by the dyes **A–D** without (—) and with (---) co-adsorption of DCA (10 mM).

due to the absorption on the TiO₂ surface. This ensures a sufficient light harvesting over a broad wavelength range. Two reasons can be assumed for this broadening: Firstly, the energy of the π^* level is lowered due to interaction of the carboxylic acid with the Ti⁴⁺ ions on the TiO₂ surface, which consequently leads to a bathochromic shift of the absorption spectra [60], and (more important) secondly, unfavorable dye aggregation and excimer formation (J-aggregates) would lead to this behavior [61,62]. The DSSCs prepared only showed a low short circuit photocurrent density J_{SC} (Fig. 7) from 1.81 to 1.03 mA cm⁻² for **A** and **D**, respectively. Because of the low J_{SC} , the maximum power outputs ($MPP = j_{mp} \cdot V_{mp}$) and, consequently, the fill factors (FF) were small. The resulting solar energy-to-electricity conversion yield (η) is low and follows the trend **A** > **B** > **C** > **D** with values from 0.44 to 0.25%.

Two possible reasons for the weak solar cell performance can be: (i) an electron accepting property of the 4-methoxy-1,3-thiazole, which can effect an efficient electron injection in the CB of TiO₂ as observed for anthraquinone-based dyes [63] or (ii) the formation of aggregates leading to a loss of excitation energy through intermolecular processes [64,65]. The first fact is supported from the TDDFT calculations. The LUMO is not only spread over the anchoring group, but also includes contribution from the thiophene and also the thiazole moieties, leading to an insufficient electron injection. In order to verify the second reason as crucial for the low performance, DSSCs were prepared using deoxycholic acid (DCA) as a co-adsorbent. It has been proven several times that co-adsorption of either DCA or chenodeoxycholic acid (CDCA) can efficiently suppress dye aggregation [61,66,67]. Therefore, DCA (10 mM in THF) was chosen for the preparation of more elaborated DSSCs (Table 3). The IPCE values (Fig. 6) were improved by about the factor two (from 14 to 30% for **A** and up to 35% for **D**) at the longest wavelength absorption band. Consequently, the short circuit photocurrent densities and the open-circuit voltages were also significantly improved (Fig. 7). The FF was increased by 35% for **A** (FF = 0.62), whereas they remained almost unchanged for the other dyes. A reason for the poor FFs of all dyes can be a poor performance of the counter electrode, which was made of TiO₂ P25. This will affect the I–V characteristics of the DSSC and, consequently, lowering the FF. For further experiments mesoporous anatase TiO₂ beads will be used to improve the cell performance as described in literature [68]. The overall efficiencies of the optimized DSSCs obtained varied from 0.61 to 1.7% for **D** and **A**, respectively.

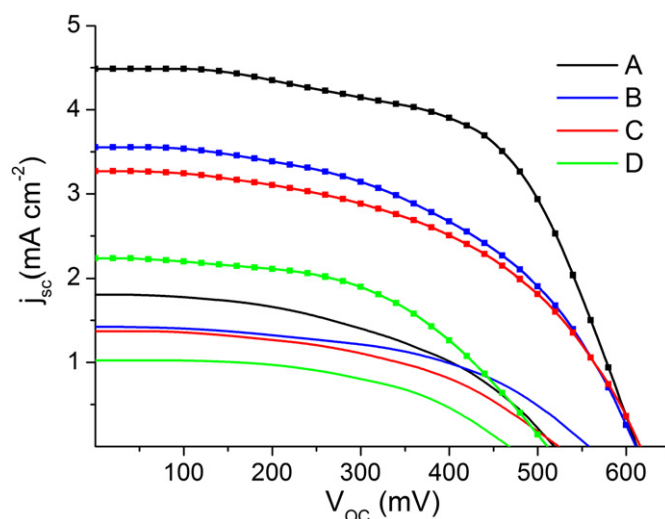


Fig. 7. Photocurrent-voltage characteristics for **A–D** sensitized DSSCs under illumination of simulated solar light (100 mW cm⁻², 1.5 AM global) without (—) and with (---) co-adsorption of DCA (10 mM).

This equals a remarkable increase of a factor 4 of the efficiency in the case of dye **A**. Keeping in mind that the efficiency of a DSSC prepared from the standard N3 with the preparation technique described was 4.1%, the best performance DSSC using **A** as sensitizer achieved reasonable 42% of this value. The trend of the efficiencies of the cells equals the trend without co-adsorbed DCA. For **A** and **B** the efficiency is very similar, whereas for **C** it is decreased. Most likely electron recombination is enhanced for compound **C** due to the extended bridge and, therefore, electron injection in the CB of TiO₂ is less favored leading to lower IPCE values [69]. Most likely due to the missing strong electron donor and the low ICT character of the first excited state, DSSCs sensitized with **D** showed the lowest performance.

In summary, the dyes tend to aggregate on the surface of TiO₂. This effect was more pronounced for the triarylamine-based dyes than for **D**. Further improvements to overcome this aggregation could be the introduction of long alkyl chains [70,71], for example, via the alkylation reaction or by bridging two dye molecules [72]. Also the introduction of the strong electron-withdrawing benzo-thiadiazole unit in the conjugation pathway to further shift the absorption maximum will be considered in the construction of novel dyes [73]. Also photophysical experiments, like electrochemical impedance spectroscopy (EIS) and electron lifetime measurement of the adsorbed dyes, have to be carried out to account the photovoltaic properties further [74,75].

4. Conclusion

A series of donor- π -acceptor dyes were successfully synthesized. Instead of the commonly used thiophene derivatives, an unconventional chromophore based on a 4-hydroxy-1,3-thiazole was used in the conjugation pathway of the dyes, to efficiently shift the absorption maximum toward longer wavelengths compared to similar triarylamines. A double *N*-arylation Hartwig–Buchwald reaction, rarely described in literature, was successful applied in the synthetic route for the triarylamine-based dyes. All dyes have been fully characterized including a series of spectroscopic and theoretical methods. The quantum chemical TDDFT calculations used proved to be well suited to reproduce the experimental values as supported by the X-ray structure of the **D** and the absorption and emission characteristics.

Electrochemical measurements and DFT calculations approved a possible application of the synthesized dyes as sensitizers in DSSCs. The efficiencies obtained of DCCSs without co-adsorption of DCA proved to be very low. Nevertheless, the performance was significantly increased after the addition of DCA. This demonstrated the distinct tendency of the dyes to form aggregates on the surface of nanocrystalline TiO₂. The best performance solar cell sensitized with dye **A** achieved 42% of the performance of a DSSC prepared with the standard N3 dye. In further investigations, the NLO properties of this class of molecules will be reviewed. For molecules of type **D** this property has already been proven in experiment. Furthermore, the use as fluorescent probes, bearing a reactive –OH group instead of the methoxy ether to interact with biological systems, will be the subject of further research.

Acknowledgment

The authors thank the Thuringian Ministry for Education, Science and Culture (grant #B514-09049, Photonische Mizellen (PhotoMIC)) for financial support. Johann Schäfer is also gratefully acknowledged for measuring the fluorescence lifetimes and the quantum yields of the dyes.

Appendix. Supporting information

Supplementary data related to this article can be found online at [10.1016/j.dyepig.2012.02.014](http://dx.doi.org/10.1016/j.dyepig.2012.02.014).

References

- Liescher J. *Methoden Org Chem* (Houben-Weyl). 4 ed. Stuttgart-New York: Georg Thieme; 1993.
- Menzel R, Täuscher E, Weiß D, Beckert R, Görls H. The combination of 4-hydroxythiazoles with azaheterocycles: efficient bidentate ligands for novel ruthenium complexes. *Z Anorg Allg Chem* 2010;636(7):1380–5.
- Menzel R, Breul A, Pietsch C, Schäfer J, Friebe C, Täuscher E, et al. Blue-emitting polymers based on 4-hydroxythiazoles incorporated in a methacrylate backbone. *Macromol Chem Phys* 2011;212(8):840–8.
- Täuscher E, Weiß D, Beckert R, Fabian J, Assumpção A, Görls H. Classical heterocycles with surprising properties: the 4-hydroxy-1,3-thiazoles. *Tetrahedron Lett* 2011;52(18):2292–4.
- Täuscher E, Weiß D, Beckert R, Görls H. Synthesis and characterization of new 4-hydroxy-1,3-thiazoles. *Synthesis-Stuttgart* 2010;10:1603–8.
- Kim E, Park SB. Chemistry as a prism: a review of light-emitting materials having tunable emission wavelengths. *Chem Asian J* 2009;4(11):1646–58.
- Otsubo T, Aso Y, Takimiya K. Functional oligothiophenes as advanced molecular electronic materials. *J Mater Chem* 2002;12(9):2565–75.
- Jose J, Burgess K. Benzophenoxazine-based fluorescent dyes for labeling biomolecules. *Tetrahedron* 2006;62(48):11021–37.
- Reinhardt BA, Brott LL, Clarson SJ, Dillard AG, Bhatt JC, Kannan R, et al. Highly active two-photon dyes: design, synthesis, and characterization toward application. *Chem Mater* 1998;10(7):1863–74.
- Oliva MM, Casado J, Raposo MMM, Fonseca AMC, Hartmann H, Hernández V, et al. Structure-property relationships in push-pull amino/cyanovinyl end-capped oligothiophenes: quantum chemical and experimental studies. *J Org Chem* 2006;71(20):7509–20.
- Duan L, Qiao J, Sun YD, Qiu Y. Strategies to design bipolar small molecules for OLEDs: donor-acceptor structure and non-donor-acceptor structure. *Adv Mater* 2011;23(9):1137–44.
- Mishra A, Fischer MKR, Bäuerle P. Metal-free organic dyes for dye-sensitized solar cells: from structure: property relationships to design rules. *Angew Chem Int Ed* 2009;48(14):2474–99.
- Hagfeldt A, Boschloo G, Sun L, Kloo L, Pettersson H. Dye-sensitized solar cells. *Chem Rev* 2010;110(11):6595–663.
- Li L, Yang X, Gao J, Tian H, Zhao J, Hagfeldt A, et al. Highly efficient CdS quantum dot-sensitized solar cells based on a modified polysulfide electrolyte. *J Am Chem Soc* 2011;133(22):8458–60.
- Wu TY, Tsao MH, Chen FL, Su SG, Chang CW, Wang HP, et al. Synthesis and characterization of organic dyes containing various donors and acceptors. *Int J Mol Sci* 2010;11(1):329–53.
- O'Regan B, Grätzel M. A low-cost, high-efficiency solar cell based on dye-sensitized colloidal TiO₂ films. *Nature* 1991;353(6346):737–40.
- Chiba Y, Islam A, Watanabe Y, Komiyama R, Koide N, Han L. Dye-sensitized solar cells with conversion efficiency of 11.1%. *Jpn J Appl Phys Part 2* 2006;45(24–28):L638–40.
- Zeng W, Cao Y, Bai Y, Wang Y, Shi Y, Zhang M, et al. Efficient dye-sensitized solar cells with an organic photosensitizer featuring orderly conjugated ethylenedioxythiophene and dithienosilole blocks. *Chem Mater* 2010;22(5):1915–25.
- Yella A, Lee H-W, Tsao HN, Yi C, Chandiran AK, Nazeeruddin MK, et al. Porphyrin-sensitized solar cells with cobalt (II/III)-based redox electrolyte exceed 12 Percent efficiency. *Science* 2011;334(6056):629–34.
- Tian Z, Huang M, Zhao B, Huang H, Feng X, Nie Y, et al. Low-cost dyes based on methylthiophene for high-performance dye-sensitized solar cells. *Dyes Pigm* 2010;87(3):181–7.
- Ning Z, Tian H. Triarylamine: a promising core unit for efficient photovoltaic materials. *Chem Commun* 2009;37:5483–95.
- Tian H, Yang X, Chen R, Zhang R, Hagfeldt A, Sun L. Effect of different dye baths and dye-structures on the performance of dye-sensitized solar cells based on triphenylamine dyes. *J Phys Chem C* 2008;112(29):11023–33.
- Li G, Jiang K-J, Li Y-F, Li S-L, Yang L-M. Efficient structural modification of triphenylamine-based organic dyes for dye-sensitized solar cells. *J Phys Chem C* 2008;112(30):11591–9.
- Liang M, Xu W, Cai F, Chen P, Peng B, Chen J, et al. New triphenylamine-based organic dyes for efficient dye-sensitized solar cells. *J Phys Chem C* 2007;111(11):4465–72.
- Hagberg DP, Marinado T, Karlsson KM, Nonomura K, Qin P, Boschloo G, et al. Tuning the HOMO and LUMO energy levels of organic chromophores for dye sensitized solar cells. *J Org Chem* 2007;72(25):9550–6.
- Hwang S, Lee JH, Park C, Lee H, Kim C, Park C, et al. A highly efficient organic sensitizer for dye-sensitized solar cells. *Chem Commun* 2007;46:4887–9.
- Hara K, Kurashige M, Dan-Oh Y, Kasada C, Shinpo A, Suga S, et al. Design of new coumarin dyes having thiophene moieties for highly efficient organic-dye-sensitized solar cells. *New J Chem* 2003;27(5):783–5.
- Chen C-H, Hsu Y-C, Chou H-H, Thomas KRJ, Lin JT, Hsu C-P. Dipolar compounds containing fluorene and a heteroaromatic ring as the conjugating bridge for high-performance dye-sensitized solar cells. *Chem Eur J* 2010;16(10):3184–93.
- He J, Wu W, Hua J, Jiang Y, Qu S, Li J, et al. Bithiazole-bridged dyes for dye-sensitized solar cells with high open circuit voltage performance. *J Mater Chem* 2011;21(16):6054–62.
- Ooyama Y, Harima Y. Molecular designs and Syntheses of organic dyes for dye-sensitized solar cells. *Eur J Org Chem* 2009;18:2903–34.
- Frisch MJ, Trucks GW, Schlegel HB, Scuseria GE, Robb MA, Cheeseman JR, et al. Gaussian 09, Revision A.02. Wallingford CT2009.
- Tomasi J, Mennucci B, Cammi R. Quantum mechanical continuum solvation models. *Chem Rev* 2005;105(8):2999–3093.
- Yanai T, Tew DP, Handy NC. A new hybrid exchange-correlation functional using the Coulomb-attenuating method (CAM-B3LYP). *Chem Phys Lett* 2004;393(1–3):51–7.
- Hariharan PC, Pople JA. The influence of polarization functions on molecular orbital hydrogenation energies. *Theor Chem Acc* 1973;28(3):213–22.
- Kasha M. Characterization of electronic transitions in complex molecules. *Discuss Faraday Soc* 1950;9:14–9.
- Fors BP, Krattiger P, Strieter E, Buchwald SL. Water-mediated catalyst pre-activation: an efficient protocol for C–N cross-coupling reactions. *Org Lett* 2008;10(16):3505–8.
- Surry DS, Buchwald SL. Dialkylbiaryl phosphines in Pd-catalyzed amination: a user's guide. *Chem Sci* 2011;2(1):27–50.
- Harris MC, Buchwald SL. One-pot synthesis of unsymmetrical triarylaminines from aniline precursors. *J Org Chem* 2000;65(17):5327–33.
- Nozaki K, Takahashi K, Nakano K, Hiyama T, Tang H-Z, Fujiki M, et al. The double N-arylation of primary amines: toward multisubstituted carbazoles with unique optical properties. *Angew Chem* 2003;115(18):2097–9.
- Zhou Y, Verkade JG. Highly efficient ligands for the palladium-assisted double N-arylation of primary amines for one-sep construction of carbazoles. *Adv Synth Catal* 2010;352(4):616–20.
- Newman SG, Lautens M. The role of reversible oxidative addition in selective palladium(0)-catalyzed intramolecular cross-couplings of polyhalogenated substrates: synthesis of brominated Indoles. *J Am Chem Soc* 2010;132(33):11416–7.
- Seo ET, Nelson RF, Fritsch JM, Marcoux LS, Leedy DW, Adams RN. Anodic oxidation pathways of aromatic amines. electrochemical and electron paramagnetic resonance studies. *J Am Chem Soc* 1966;88(15):3498–503.
- Zhao H, Tanjutco C, Thayumanavan S. Design and synthesis of stable triarylaminines for hole-transport applications. *Tetrahedron Lett* 2001;42(27):4421–4.
- Olivier C, Sauvage F, Ducasse L, Castet F, Grätzel M, Toupance T. Fine-tuning of triarylamine-based photosensitizers for dye-sensitized solar cells. *ChemSusChem*. 2011;4(6):731–6.
- Coates GW, Dunn AR, Henling LM, Dougherty DA, Grubbs RH. Spezifische phenyl-perfluorphenyl-stapelwechselwirkungen: eine neue Strategie zum Aufbau supramolekularer Strukturen. *Angew Chem* 1997;109(3):290–3.
- Thomas KRJ, Hsu Y-C, Lin JT, Lee K-M, Ho K-C, Lai C-H, et al. 2,3-Disubstituted thiophene-based organic dyes for solar cells. *Chem Mater* 2008;20(5):1830–40.
- Li G, Jiang K-J, Bao P, Li Y-F, Li S-L, Yang L-M. Molecular design of triarylamine-based organic dyes for efficient dye-sensitized solar cells. *New J Chem* 2009;33(4):868–76.
- Nazeeruddin MK, Kay A, Rodicio I, Humphry-Baker R, Mueller E, Liska P, et al. Conversion of light to electricity by cis-X2bis(2,2'-bipyridyl)-4,4'

- dicarboxylate)ruthenium(II) charge-transfer sensitizers (X = Cl-, Br-, I-, CN-, and SCN-) on nanocrystalline titanium dioxide electrodes. *J Am Chem Soc* 1993;115(14):6382–90.
- [49] Lee JY, Kim KS, Mhin BJ. Intramolecular charge transfer of pi-conjugated push-pull systems in terms of polarizability and electronegativity. *J Chem Phys* 2001;115(20):9484–9.
- [50] Pavlishchuk VV, Addison AW. Conversion constants for redox potentials measured versus different reference electrodes in acetonitrile solutions at 25 °C. *Inorg Chim Acta* 2000;298(1):97–102.
- [51] Thomas KRJ, Singh P, Baheti A, Hsu YC, Ho K-C, Lin JT. Electro-optical properties of new anthracene based organic dyes for dye-sensitized solar cells. *Dyes Pigm* 2011;91(1):33–43.
- [52] Zhdanov SI, Feoktistov LG. The reductive dimerization of acrylonitrile on the mercury cathode. *Russ Chem Bull* 1963;12(1):45–8.
- [53] Baizer MM. Electrolytic reductive coupling. IV.1 mixed couplings among derivatives of α,β -unsaturated acids. *J Org Chem* 1964;29(7):1670–3.
- [54] Dietz F, Olbrich G, Karabunarliev S, Tyutyulkov N. Photoswitching of dipole moments, charge-transfer and spectroscopic properties. *Chem Phys Lett* 2003; 379(1–2):11–9.
- [55] Hagfeldt A, Grätzel M. Light-induced redox reactions in nanocrystalline systems. *Chem Rev* 1995;95(1):49–68.
- [56] Angelis F, Fantacci S, Selloni A. Alignment of the dye's molecular levels with the TiO₂ band edges in dye-sensitized solar cells: a DFT–TDDFT study. *Nanotechnology* 2008;19(42):424002.
- [57] Boschloo G, Hagfeldt A. Characteristics of the iodide/triiodide redox mediator in dye-sensitized solar cells. *Acc Chem Res* 2009;42(11):1819–26.
- [58] Liang M, Zong X-P, Han H-Y, Chen C, Sun Z, Xue S. An efficient dye-sensitized solar cell based on a functionalized-triarylamine dye. *Mater Lett* 2011;65(9): 1331–3.
- [59] Stergiopoulos T, Ghicov A, Likodimos V, Tsoukleris DS, Kunze J, Schmuki P, et al. Dye-sensitized solar cells based on thick highly ordered TiO₂ nanotubes produced by controlled anodic oxidation in non-aqueous electrolytic media. *Nanotechnology* 2008;19(23):235602.
- [60] Wang Z-S, Hara K, Dan-Oh Y, Kasada C, Shinpo A, Suga S, et al. Photophysical and (photo)electrochemical properties of a coumarin dye. *J Phys Chem B* 2005;109(9):3907–14.
- [61] Wang Z-S, Cui Y, Dan-Oh Y, Kasada C, Shinpo A, Hara K. Thiophene-functionalized coumarin dye for efficient dye-sensitized solar cells: electron lifetime improved by coadsorption of deoxycholic acid. *J Phys Chem C* 2007; 111(19):7224–30.
- [62] Pastore M, Angelis F. Aggregation of organic dyes on TiO₂ in dye-sensitized solar cells models: an ab initio investigation. *ACS Nano* 2009;4(1):556–62.
- [63] Li C, Yang X, Chen R, Pan J, Tian H, Zhu H, et al. Anthraquinone dyes as photosensitizers for dye-sensitized solar cells. *Sol Energy Mater Sol Cells* 2007;91(19):1863–71.
- [64] Lee J-K, Yang M. Progress in light harvesting and charge injection of dye-sensitized solar cells. *Mater Sci Eng B* 2011;176(15):1142–60.
- [65] Hara K, Dan-Oh Y, Kasada C, Ohga Y, Shinpo A, Suga S, et al. Effect of additives on the photovoltaic performance of coumarin-dye-sensitized nanocrystalline TiO₂ solar cells. *Langmuir* 2004;20(10):4205–10.
- [66] Chen R, Yang X, Tian H, Wang X, Hagfeldt A, Sun L. Effect of tetrahydroquinoline dyes structure on the performance of organic dye-sensitized solar cells. *Chem Mater* 2007;19(16):4007–15.
- [67] Xu W, Pei J, Shi J, Peng S, Chen J. Influence of acceptor moiety in triphenylamine-based dyes on the properties of dye-sensitized solar cells. *J Power Sources* 2008;183(2):792–8.
- [68] Sauvage Fdr, Chen D, Comte P, Huang F, Heiniger L-P, Cheng Y-B, et al. Dye-sensitized solar cells employing a single film of mesoporous TiO₂ beads achieve power conversion efficiencies over 10%. *ACS Nano* 2010;4(8):4420–5.
- [69] Marinado T, Nonomura K, Nissfolk J, Karlsson MK, Hagberg DP, Sun L, et al. How the nature of triphenylamine-polyene dyes in dye-sensitized solar cells affects the open-circuit voltage and electron lifetimes. *Langmuir* 2009;26(4): 2592–8.
- [70] Shen P, Liu Y, Huang X, Zhao B, Xiang N, Fei J, et al. Efficient triphenylamine dyes for solar cells: effects of alkyl-substituents and π -conjugated thiophene unit. *Dyes Pigm* 2009;83(2):187–97.
- [71] Ning Z, Fu Y, Tian H. Improvement of dye-sensitized solar cells: what we know and what we need to know. *Energy Environ Sci* 2010;3(9).
- [72] Sirohi R, Kim DH, Yu S-C, Lee SH. Novel di-anchoring dye for DSSC by bridging of two mono anchoring dye molecules: a conformational approach to reduce aggregation. *Dyes Pigm* 2012;92(3):1132–7.
- [73] Zhu W, Wu Y, Wang S, Li W, Li X, Chen J, et al. Organic D-A- π -A solar cell sensitizers with improved stability and spectral response. *Adv Funct Mater* 2011;21(4):756–63.
- [74] Wang C, Li J, Cai S, Ning Z, Zhao D, Zhang Q, et al. Performance improvement of dye-sensitizing solar cell by semi-rigid triarylamine-based donors. *Dyes Pigm* 2012;94(1):40–8.
- [75] Ko S-B, Cho A-N, Kim M-J, Lee C-R, Park N-G. Alkyloxy substituted organic dyes for high voltage dye-sensitized solar cell: effect of alkyloxy chain length on open-circuit voltage. *Dyes Pigm* 2012;94(1):88–98.

4.2 An Assessment of RASSCF and TDDFT Energies and Gradients on an Organic Donor-Acceptor Dye assisted by Resonance Raman Spectroscopy

Reproduced with permission from J. Chem. Theo. Comput. accepted for publication. Unpublished work copyright 2012 American Chemical Society.

<http://pubs.acs.org/doi/abs/10.1021/ct3009057>

An Assessment of RASSCF and TDDFT Energies and Gradients on an Organic Donor-Acceptor Dye assisted by Resonance Raman Spectroscopy.

Stephan Kupfer, Julien Guthmuller, and Leticia González

J. Chem. Theory Comput., **Just Accepted Manuscript** • DOI: 10.1021/ct3009057 • Publication Date (Web): 26 Nov 2012

Downloaded from <http://pubs.acs.org> on November 28, 2012

Just Accepted

“Just Accepted” manuscripts have been peer-reviewed and accepted for publication. They are posted online prior to technical editing, formatting for publication and author proofing. The American Chemical Society provides “Just Accepted” as a free service to the research community to expedite the dissemination of scientific material as soon as possible after acceptance. “Just Accepted” manuscripts appear in full in PDF format accompanied by an HTML abstract. “Just Accepted” manuscripts have been fully peer reviewed, but should not be considered the official version of record. They are accessible to all readers and citable by the Digital Object Identifier (DOI®). “Just Accepted” is an optional service offered to authors. Therefore, the “Just Accepted” Web site may not include all articles that will be published in the journal. After a manuscript is technically edited and formatted, it will be removed from the “Just Accepted” Web site and published as an ASAP article. Note that technical editing may introduce minor changes to the manuscript text and/or graphics which could affect content, and all legal disclaimers and ethical guidelines that apply to the journal pertain. ACS cannot be held responsible for errors or consequences arising from the use of information contained in these “Just Accepted” manuscripts.

1
2
3
4
5
6
7
8
9
10
11
12
13
14
15
16
17
18
19
20
21
22

An Assessment of RASSCF and TDDFT Energies and Gradients on an Organic Donor-Acceptor Dye assisted by Resonance Raman Spectroscopy

23
24
25
26
27

Stephan Kupfer¹, Julien Guthmuller², Leticia González^{3*}

28
29
30

¹ *Institute for Physical Chemistry, Friedrich Schiller University Jena, Helmholtzweg 4, 07743 Jena, Germany*

31
32
33

² *Faculty of Applied Physics and Mathematics, Gdansk University of Technology, Narutowicza 11/12, 80233 Gdansk, Poland*

34
35
36

³ *Institute of Theoretical Chemistry, University of Vienna, Währinger Str. 17, 1090 Vienna, Austria*

37
38
39
40
41

* Corresponding author: leticia.gonzalez@univie.ac.at

42
43
44
45
46
47
48
49
50
51
52
53
54
55
56
57
58
59
60

Keywords: ab initio calculations, DFT, multiconfigurational methods, Resonance Raman

Abstract

The excitation energies and gradients in the ground and the first excited state of a novel donor- $(\pi$ -bridge)-acceptor 4-methoxy-1,3-thiazole based chromophore were investigated by means of MS-RASPT2/RASSCF and TDDFT in solution. Within both methods, the excitation energies strongly depend on the employed equilibrium structures, whose differences can be rationalized in terms of bond length alternation indexes. It is shown that functionals with an increased amount of exact exchange provide the best estimation of the ground and excited state properties. While B3LYP fails to predict the excitation energies due to its intrinsic problems in describing charge transfer (CT) states, the long-range corrected CAM-B3LYP and M06-2X functionals deliver good agreement with the experimental UV/vis absorption spectrum. The calculation of resonance Raman intensity patterns is used to discern which ground and excited state gradients are best. The results clearly evidence that both CAM-B3LYP and RASSCF excited state gradients and energies in combination with CAM-B3LYP ground state gradients are appropriate to describe the CT state of this push-pull chromophore.

1 Introduction

The evaluation of molecular properties in the electronic ground state, e.g. energies, equilibrium structures and dipole moments, can be considered nowadays almost routine, at least in the case of small and medium sized organic systems. In these situations, the electronic ground state is often described by density functional theory (DFT) methods. Specially hybrid functionals, have proven very useful as they can give an accurate description of equilibrium geometries, potential energy surfaces and dipole moments in various chemical situations, see e.g.¹⁻⁴.

More challenging however is the simulation of electronic excited states properties, such as excitation energies and transition dipole moments.⁵⁻⁷ In particular, the investigation of excited states involving charge transfer (CT) character is a difficult task.⁷⁻¹⁰ Multiconfigurational methods, such as the recently developed RASPT2^{11,12}/RASSCF^{13,14} (Restricted Active Space Perturbation Theory of second order/Restricted Active Space Self-Consistent Field) or the well-established CASPT2¹⁵/CASSCF¹⁶ (Complete Active Space Perturbation Theory of second order/Complete Active Space SCF) approaches are able to deliver a reliable description of excited states, irrespective of the character of the wavefunctions. While in the CASSCF method the orbitals are classified into inactive, active, and secondary orbitals, in the RASSCF the active orbitals are further divided into three subspaces: RAS1, RAS2, and RAS3, bringing additional flexibility to the wavefunction. The orbitals in the RAS2 subspace keep the same meaning as in the active space of CASSCF (i.e. a full configuration interaction (CI) calculation is performed) and the RAS CI is built by restricting the number of holes in RAS1 and particles in RAS3, typically by two or three. In this way, a wise choice of the RAS subspaces can drastically reduce the number of configuration state functions (CSFs) and therefore the computational demand, in comparison to CASSCF. Alternatively, for the same computational effort as in a CASSCF calculation, RASSCF allows extending the number of active orbitals by restricting the excitation level and therefore can be used in larger systems or those demanding larger active spaces. Recently, the performance of RASPT2/RASSCF has been benchmarked in a number of organic molecules^{11,17,18} and was shown to provide accurate results.

Despite the promising advantages of multiconfigurational procedures, the golden standard to calculate excited states of medium or large molecular systems is the by far more econom-

1
2
3
4 ical time dependent DFT (TDDFT)¹⁹ method. An acute problem of TDDFT is that in the
5 case of CT states it gives poor predictions of excitation energies.²⁰ To palliate this deficiency
6 range-separated functionals, such as CAM-B3LYP²¹, and global hybrid functionals²² with an
7 enhanced ratio of exact-exchange, such as M06-2X²³, have been recently developed. A good
8 number of papers can be found in the literature devoted to investigate the performance of dif-
9 ferent functionals in such complicated cases.^{7,8,24–28}

10
11
12
13
14
15
16 While a lot of studies deal with excited state energies, much less is known on the perfor-
17 mance of quantum chemical methods concerning excited state gradients²⁹ and excited states
18 equilibrium geometries.^{30–33} Excited states gradients are fundamental to explore potential en-
19 ergy surfaces, e.g. in light-induced processes, but also are the main ingredients for optical
20 quantity in emission and resonance Raman (RR) spectroscopy, which is extremely useful to
21 provide relationships between the geometrical structures and the electronic character of the
22 states.^{18,29,34} In particular, the RR intensities of the vibrational modes are directly correlated
23 to the excited states gradients in the Franck-Condon (FC) region. Thus, the comparison of
24 simulated and experimental RR spectra provides a unique scenario to evaluate the accuracy of
25 calculated excited states gradients. Several studies have reported calculations of RR spectra for
26 organic compounds (see e.g. Refs. 29,35–40) or for transition metal complexes (see e.g. Refs.
27 18,34,41–43 and references herein). These studies made mostly use of TDDFT but very rarely
28 of wavefunction based methods.

29
30
31
32
33
34
35
36
37
38
39
40
41 In the present study, the 2-Cyano-3-(5-(5-(4-(dip-tolylamino)phenyl)-4-methoxythiazol-2-
42 yl)thiophen-2-yl)acrylic acid³² dye (see **1** in Figure 1) is chosen as a large organic chro-
43 mophore to benchmark excited state gradients in the context of RR spectroscopy. The donor-(π -
44 conjugated bridge)-acceptor 4-methoxy-1,3-thiazole chromophore is based on the naturally oc-
45 ccurring luciferin and has found multiple applications as light-harvesting ligand in ruthenium(II)
46 polypyridyl complexes,^{33,44} as emissive materials in molecular electronics,^{45,46} as fluorescent
47 probes in biochemical applications,⁴⁷ in organic light-emitting diodes,⁴⁸ as blue-emitters in
48 a polymer backbones,⁴⁹ as nonlinear optical materials,^{50,51} as dyes for Förster resonance en-
49 ergy transfer,⁵² and as chromophores in dye-sensitized solar cells.³² Because the thiazole dye
50 **1** shows an intense absorption band in the visible region resulting from a CT excitation³²,
51 it constitutes an excellent reference compound to challenge multiconfigurational and TDDFT
52
53
54
55
56
57
58
59
60

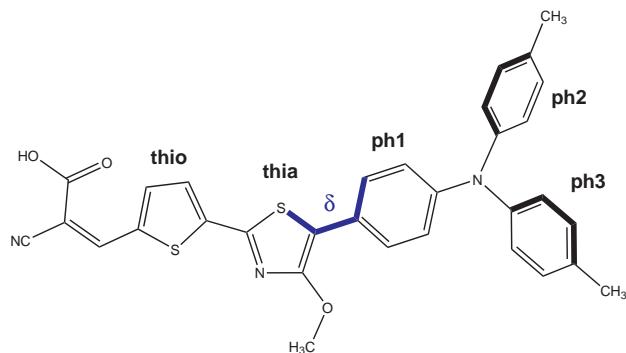


Figure 1: Structure of **1** comprising the labels of the thiophene (thio), thiazole (thia) and the phenyl moieties (ph1, ph2 and ph3) of the donor group. The dihedral angle δ describes the torsion between the bridge and the donor subunits.

methods. In the present work, the first application of the multiconfigurational RASSCF method to the calculation of RR intensities is reported. The RR spectrum of compound **1** in resonance with the first absorption band is calculated with both RASSCF and TDDFT methods. The results are compared to experimental data, allowing the identification of the functional which is best suited to describe the ground state properties of dye **1**, as well as whether RASSCF alone is suitable to calculate RR intensities.

2 Computational Details

2.1 Quantum Chemistry

In order to simulate optical properties an adequate molecular structure is essential since small changes in the ground state geometry can lead to significant differences in the optical properties. This is especially true in the case of conjugated push-pull chromophores like **1**. The ground state equilibrium geometry was optimized by means of DFT using three different functionals with a different amount of exact exchange: the global hybrid functionals B3LYP^{53,54} and M06-2X²³, and the long-range corrected CAM-B3LYP²¹ functional. The 6-31G(d,p)⁵⁵ double- ζ basis set was employed in combination with all the functionals. A harmonic vibrational analysis was carried out at the same level of theory to confirm that the obtained structures are minima of the potential energy surface. Because experimental data to sustain the calculated RR spectra is available in solution (chloroform, $\epsilon = 4.711$, $n = 1.445$), both the geometries

1
2
3
4 and the vibrational frequencies are calculated using the equilibrium procedure of the integral
5 equation formalism of the polarizable continuum model (IEFPCM).⁶
6
7

8 Vertical excitation energies and oscillator strengths were calculated using TDDFT as well
9 as the multi-state (MS) version of RASPT2/RASSCF. The TDDFT calculations are performed
10 over the lowest ten singlet excited states using the three functionals B3LYP, M06-2X and CAM-
11 B3LYP with the same basis set as for the ground state properties and are carried out on their
12 respective ground state geometries. These calculations are referred as TD-B3LYP//B3LYP, TD-
13 M06-2X//M06-2X, and TD-CAM-B3LYP//CAM-B3LYP. Additionally, a TDDFT calculation
14 employing CAM-B3LYP was performed on the B3LYP equilibrium geometry –this is denoted
15 as TD-CAM-B3LYP//B3LYP. Gaseous as well as solvated (chloroform with IEFPCM) excited
16 state properties have been considered to assess the influence of the solvent. In the case of the
17 solvated compound, the excitation energies and excited state gradients have been calculated
18 with the nonequilibrium procedure of IEFPCM. This treatment is well adapted for the processes
19 of absorption and RR, for which only the fast reorganization of the electronic distribution of
20 the solvent is important.
21
22
23
24
25
26
27
28
29
30
31

32 The MS-RASPT2/RASSCF calculations employed the atomic natural orbitals small basis
33 set (ANO-S)⁵⁶ with the contractions S[7s7p4d] / C,N,O[3s2p1d] / H[2s1p]. The Cholesky
34 decomposition⁵⁷ was applied to generate the two-electron integrals. The calculations were
35 performed on two solvated DFT equilibrium geometries (B3LYP and CAM-B3LYP) since,
36 as it will be shown, the results show a pronounced dependency of the excitation energy on
37 the geometry (about 0.2 eV). Four different partitions were considered within the RASSCF
38 calculations using different sizes and excitation levels, comprising up to 700.000 CSFs.
39
40
41
42
43
44
45

46 In order to label the RAS calculations, the notation RAS($n,l,m;i,j,k$) of Gagliardi and coworkers¹⁷
47 is used. The index n labels the number of active electrons, l is the maximum number of
48 holes in the RAS1, and m is the maximum number of electrons in the RAS3. The labels i , j ,
49 and k refer to the number of active orbitals in the RAS1, RAS2 and RAS3, respectively. The
50 RAS1 includes typically orbitals with large occupation numbers, where only a maximal number
51 of electron holes is allowed. Accordingly, the RAS3 subspace comprises virtual orbitals
52 with small occupation numbers where only a maximal number of electrons is allowed. In the
53 RAS2 subspace all possible configurations are taken into account.
54
55
56
57
58
59
60

1
2
3
4 In order to describe the UV/vis absorption spectrum of **1** the orbitals of the π -systems of the
5 donor group (triphenylamine), the bridge (thiazole and thiophene) and the acceptor (ethylene,
6 2-cyanoacrylic acid) need to be considered. Furthermore, contributions of the two nitrogen
7 lone-pairs (triphenylamine and thiazole) and of the p-orbitals in the molecular plane of the
8 two sulfur atoms (thiazole and thiophene) should also be taken into account (cf. Figure 1).
9 This makes a total amount of 42 electrons in 38 orbitals, which even for RASSCF would be a
10 formidable task. Therefore, several restrictions were made in designing the active space:
11
12
13
14
15
16
17

- 18 i) The contributions of the donor group were estimated only by the three pairs of π_{ph1} -
19 orbitals, two pairs of π_{ph2} and the π_{ph3} -orbitals and the nitrogen lone-pair.
20
21
22
- 23 ii) In the case of ph2 and ph3 moieties, the lowest occupied $\pi_{\text{ph2}}/\pi_{\text{ph3}}$ and highest unoccu-
24 pied $\pi_{\text{ph2}}^*/\pi_{\text{ph3}}^*$ molecular orbitals (MO) were excluded because these molecular groups
25 contribute only marginally to the S_1 state.
26
27
28
- 29 iii) In the π -conjugated bridge the entire π/π^* -systems of the thiazole and thiophene were
30 included (two pairs of π/π^* -orbitals respectively), in addition the lone-pairs of the nitrogen
31 and the two sulfur atoms were considered.
32
33
34
35
- 36 iv) The contribution of the 2-cyanoacrylic acid-acceptor group was reduced to the π/π^* -
37 orbitals of the ethylene.
38
39

40 Under these constraints, the active space is reduced to 27 with 30 electrons that can be re-
41 distributed to the three subspaces as follows: The HOMO and LUMO (within the canonical
42 formulation of SCF or DFT calculations) are assigned to the RAS2 and the remaining occupied
43 and unoccupied orbitals were distributed in the RAS1 and RAS3, respectively. We note that
44 the approach of considering only HOMO and LUMO in the RAS2, while distributing the rest
45 of orbitals within RAS1 and RAS3 has been shown to be successful by Gagliardi and cowork-
46 ers in the case of organic molecules.¹⁷ The orbitals of the resulting RASSCF(30,2,2;14,2,11)
47 calculation are depicted in Figure 2.
48
49
50
51
52
53

54 An additional RASSCF partition was considered taking the entire π/π^* -systems of the bridge
55 and the ph1-moiety. Due to the orbital mixing with one π -orbital of ph2/ph3 and the π^* of the
56 ethylene an active space collecting 16 electrons in 16 orbitals was created. Those orbitals were
57
58
59
60

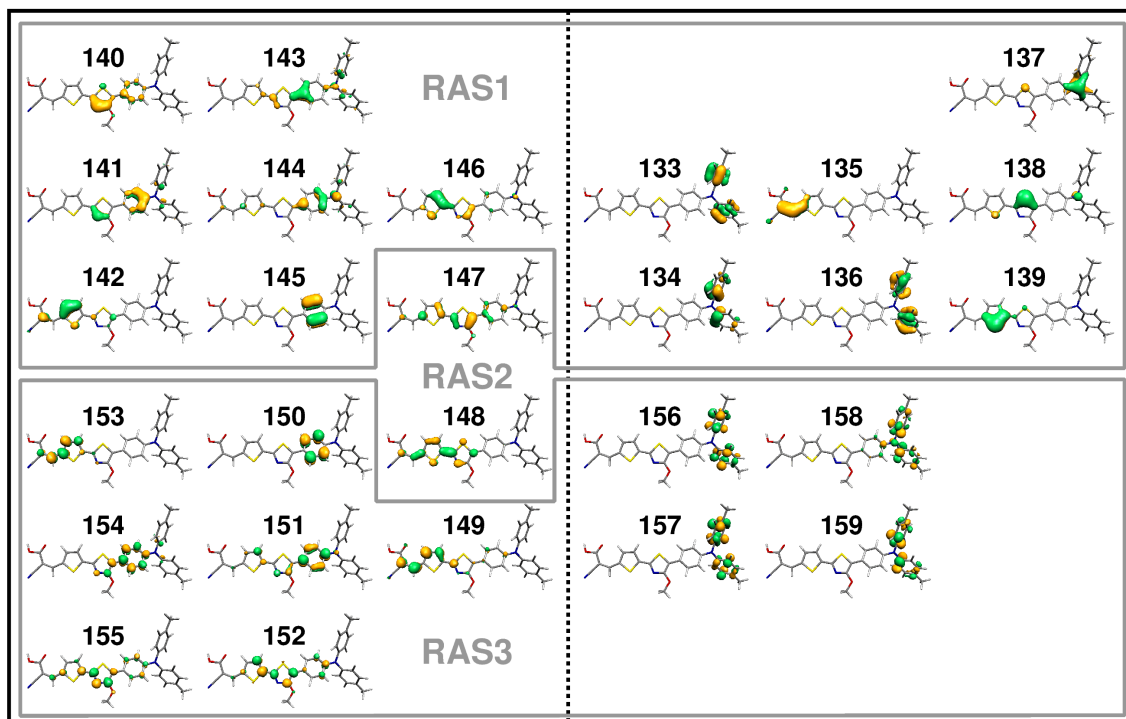


Figure 2: Molecular orbitals for RASSCF(30,2,2;14,2,11) (solid grey), RASSCF(16,2,2;7,2,7), RASSCF(16,3,3;7,2,7) and RASSCF(16,4,4;7,2,7) (left hand side) calculations.

distributed over the three RAS subspaces applying different excitation levels (see Figure 2): In the RAS(16,2,2;7,2,7) the HOMO and the LUMO were assigned to the RAS2, the remaining orbitals were assigned to the RAS1 and RAS3, and only single and double excitations are considered. The RAS(16,3,3;7,2,7) and RAS(16,4,4;7,2,7) prescriptions share the same orbital partition but allow up to triple and quadruple excitations, respectively. All RASSCF wavefunctions are obtained through state-average (SA) calculations over two roots with equal weight. Dynamical correlation was included by performing multi-state (MS) RASPT2 to improve the energies. In all the MS-RASPT2 calculations the core electrons were kept frozen. The oscillator strengths have been obtained at the RASSCF and MS-RASPT2 levels of theory with the CAS State Interaction method.⁵⁸

The analytical gradients required to calculate RR intensities are calculated at both TDDFT and RASSCF levels of theory with the same specifications as the excitation energies. The structural and TDDFT electronic data was obtained using the GAUSSIAN 09 program.⁵⁹ The MS-RASPT2/RASSCF calculations were performed with the Molcas 7.8⁶⁰⁻⁶² software.

2.2 Resonance Raman

The relative RR intensities for an excitation in resonance with the first absorption band were obtained within the short-time approximation (STA).⁶³ In particular, this approach was recently applied to the molecule of *o*-nitrophenol²⁹ to assess the accuracy of calculated excited state gradients. In the STA, the RR intensity for a fundamental transition $0 \rightarrow 1_l$ is calculated from the partial derivative of the excited state electronic energy (E^e) along the l th normal coordinate (Q_l) evaluated at the ground state equilibrium geometry,

$$I_{0 \rightarrow 1_l} \propto \frac{1}{\omega_l} \left(\frac{\partial E^e}{\partial Q_l} \right)_0^2 \quad (1)$$

where ω_l is the frequency of the l th normal mode. The excited state gradients were obtained from the analytical (TDDFT) and numerical (RASSCF) derivatives of the excited state electronic energy (E^e) along the non-mass-weighted Cartesian coordinates.^{29,35} The use of the STA for dye **1** is motivated by several reasons:

- i) A single excited state is in resonance with the laser frequency. Therefore, contributions of other states can be neglected.
- ii) The excited state in resonance (S_1) is strongly dipole-allowed. This indicates that only FC scattering is important.
- iii) The first absorption band displays a large broadening and no resolved vibronic structure. This indicates that vibronic coupling effects should be small and that the relative RR intensities should show a weak dependence with respect to the excitation wavelength. Therefore, more sophisticated methods to simulate RR intensities (see e.g. Refs. 34,35,38–40) were not employed for the present application.

The relative RR intensities have been calculated with the functionals B3LYP, CAM-B3LYP and M06-2X, as specified in Section 2.1 and by means of SA2-RASSCF(16,3,3;7,2,7) on the B3LYP and the CAM-B3LYP equilibrium geometries. The vibrational frequencies were scaled by the factor 0.97 for B3LYP and by 0.95 for CAM-B3LYP and M06-2X in order to correct for the lack of anharmonicity and the approximate treatment of electron correlation.^{64,65}

3 Results

3.1 Electronic excited states calculated at the TDDFT level of theory

The excitation energies, oscillator strengths and main character of the wavefunction of the ten lowest excited states calculated with the B3LYP, CAM-B3LYP and M06-2X functionals are collected in Table 1. The MOs involved in the main configurations are depicted exemplarily for TD-CAM-B3LYP//CAM-B3LYP in Figure 4. The absorption spectra obtained for all the functionals are depicted in solid lines in Figure 3.

The TD-B3LYP//B3LYP calculation predicts the S_1 bright state in chloroform at 1.69 eV (734 nm) with an oscillator strength of 1.02, see Table 1. This state involves a CT transition from the HOMO (147) orbital, mainly localized on the thiazole and the phenyl units, to the LUMO (148) orbital, localized on the anchoring group and the bridge (thia and thio). As it is expected from a CT state, the excitation energy in gas phase is blue-shifted (1.83 eV). The S_2 is another bright ($f = 0.58$) state at 2.57 eV, resulting from the CT of the π -systems of the bridge and the donor to the bridge and the anchoring group. This state also blue-shifts in gas phase by ca 0.1 eV. The third excited singlet state at 3.01 eV features a less pronounced CT character, and therefore this state is only stabilized by 0.05 eV upon solvation. The following nearly degenerated states S_4 and S_5 at 3.49 and 3.51 eV refer to moderately intense CT states, while the higher excited states (S_6 - S_{10}) are within 3.62 and 3.84 eV and show small oscillator strengths between 0.00 and 0.04. The CT S_6 , S_7 , S_9 and S_{10} are stabilized by approximately 0.1 eV by going from gas phase to chloroform. The experimental spectrum measured in chloroform is also depicted in Figure 3a and a direct comparison with the solvated TD-B3LYP//B3LYP values shows that the obtained bands are significantly red shifted by about 1 eV compared to the experimental spectrum. This disagreement can be associated to the tendency of hybrid functionals with a small amount of exact exchange, such as B3LYP, to underestimate CT states^{20,66-68}.

The amount of Hartree-Fock exchange is increased in the long-range corrected CAM-B3LYP functional, depending on the electron-electron distance: for short range it is 19% (B3LYP is 20%) and rises with an inverse error function to 65% for long-range interactions.²¹ Since

1
2
3
4 B3LYP is known to reproduce experimental equilibrium structures reasonably well, the B3LYP
5 structure was first used to calculate the vertical spectrum of **1** with TD-CAM-B3LYP. As shown
6 in Table 1, the solvated S_1 state (2.36 eV) is now in very good agreement with the first absorp-
7 tion band of the experimental spectrum at 2.39 eV. This very bright CT state is, similarly to
8 TD-B3LYP//B3LYP, mainly due to HOMO/LUMO transition. However, with CAM-B3LYP
9 also the HOMO-1/LUMO transition exhibits a significant weight. The S_2 state is also shifted
10 to higher energies with TD-CAM-B3LYP (3.44 eV), and can be assigned to the second ab-
11 sorption band of the experimental spectrum at 3.49 eV, see Figure 3a. The oscillator strength
12 is drastically decreased in comparison to that predicted by TD-B3LYP. The third experimen-
13 tal band at 4.09 eV is mainly a superposition of two bright CT states from the bridge to the
14 anchoring group (S_3 and S_4) and of one bright CT state from the bridge to donor group (S_7).
15 The remaining states (S_5 , S_6 and $S_8 - S_{10}$) are weakly absorbing and do not contribute to the
16 absorption spectrum significantly. As in the TD-B3LYP//B3LYP calculation, solvation effects
17 on the CT states leads to a red-shift of about 0.1 eV, with respect to the gas phase values.
18
19
20
21
22
23
24
25
26
27
28
29

30
31 Interestingly, the use of the CAM-B3LYP equilibrium structure (see TD-CAM-B3LYP//CAM-
32 B3LYP results in Table 1) retains the order of states and leads to comparable intensities, but
33 the excitation energies of the first four excited states are blue-shifted. Most significantly, the
34 energy of S_1 increases by 0.22 eV, which makes the agreement with experiment less good, see
35 also Figure 3c. Applying the M06-2X functional, which possess the highest amount of exact
36 exchange (54%) gives very similar results to the long-range corrected CAM-B3LYP functional
37 (compare Figures 3c and d). Indeed, the S_1 , S_2 and S_3 keep the same order as the TD-CAM-
38 B3LYP//CAM-B3LYP calculation, but the order of the higher excited states is only slightly
39 altered.
40
41
42
43
44
45
46
47

48 In summary, the B3LYP functional fails to predict the excitation energies of **1**, while the long-
49 range corrected CAM-B3LYP and M06-2X functionals show a good performance on calculat-
50 ing the energetic positions of the UV absorption bands, provided solvation effects are included
51 both in the geometry optimization and the calculation of excitation energies. In the particular
52 case of the dye **1**, the first absorption band can be assigned to the S_1 state, the second band to
53 the S_2 , and the third band results from a superposition of three states: S_3 , S_4 and S_7 in case
54 of CAM-B3LYP and S_3 , S_5 and S_6 in case of M06-2X. The relative intensities of the second
55
56
57
58
59
60

1
2
3
4 and third calculated bands are underestimated in comparison to the experiment, but the overall
5 pattern of the spectrum is reasonably reproduced by the calculations. Interestingly, the com-
6 bination of the B3LYP structure with the CAM-B3LYP functional (TD-CAM-B3LYP//B3LYP
7 calculations) give the best agreement with the experimental values, whereas the TD-CAM-
8 B3LYP//CAM-B3LYP energies are blue shifted with respect to the experimental spectrum. It
9 should be mentioned that this comparison relies on the assumption that vertical excitation en-
10 ergies can be compared to the maximum of absorption. However, for related compounds it
11 was shown (see e.g. Refs. 69,70) that differences between the vertical excitation energies and
12 the maximum of absorption can be as large as 0.3eV. Such shift is comparable to the obtained
13 accuracy of the TDDFT calculations. Therefore, the comparison of TDDFT excitation energies
14 with experimental absorption spectra cannot provide an unambiguous identification of which
15 ground state geometry is best.
16

17
18 From the comparison of gas phase and solvated values, we see that the solvent influences
19 the excitation energies of the low-lying singlet excited states in a different way. Note that
20 the geometries employed in all the calculations (gas phase and IEFPCM) are always the sol-
21 vated ones, in order to separate the solvation effect on the energies from the solvation ef-
22 fect on the geometries (not considered here due to its small effect). In general, the exci-
23 tation energies of CT states red-shift by about 0.1 eV from gas to chloroform. The exact
24 amount obtained with each functional is though not identical: The solvent stabilization for
25 S_1 is 0.14 eV with TD-B3LYP//B3LYP and TD-CAM-B3LYP//B3LYP) and of 0.10 eV with
26 TD-CAM-B3LYP//CAM-B3LYP and TD-M06-2X//M06-2X. Comparable shifts have been de-
27 termined for the CT states contributing to the second (0.08 to 0.12 eV) and third absorption
28 band (0.05 to 0.08 eV), while the states S_7 with TD-CAM-B3LYP//B3LYP and TD-CAM-
29 B3LYP//CAM-B3LYP and S_6 with TD-M06-2X//M06-2X, respectively, are almost unaffected
30 (0.01 to 0.03 eV) by solvent interactions.
31
32
33
34
35
36
37
38
39
40
41
42
43
44
45
46
47
48
49
50
51

52 **3.2 Electronic excited states calculated at the MS-RASPT2 level of theory**

53
54
55 The MS-RASPT2/RASSCF study focuses exclusively in the first CT state (S_1), which is the one
56 responsible of many of the applications of **1** as a dye. Due to the computational cost in using
57 a PCM model with multiconfigurational methods, the calculations were performed only in gas
58
59
60

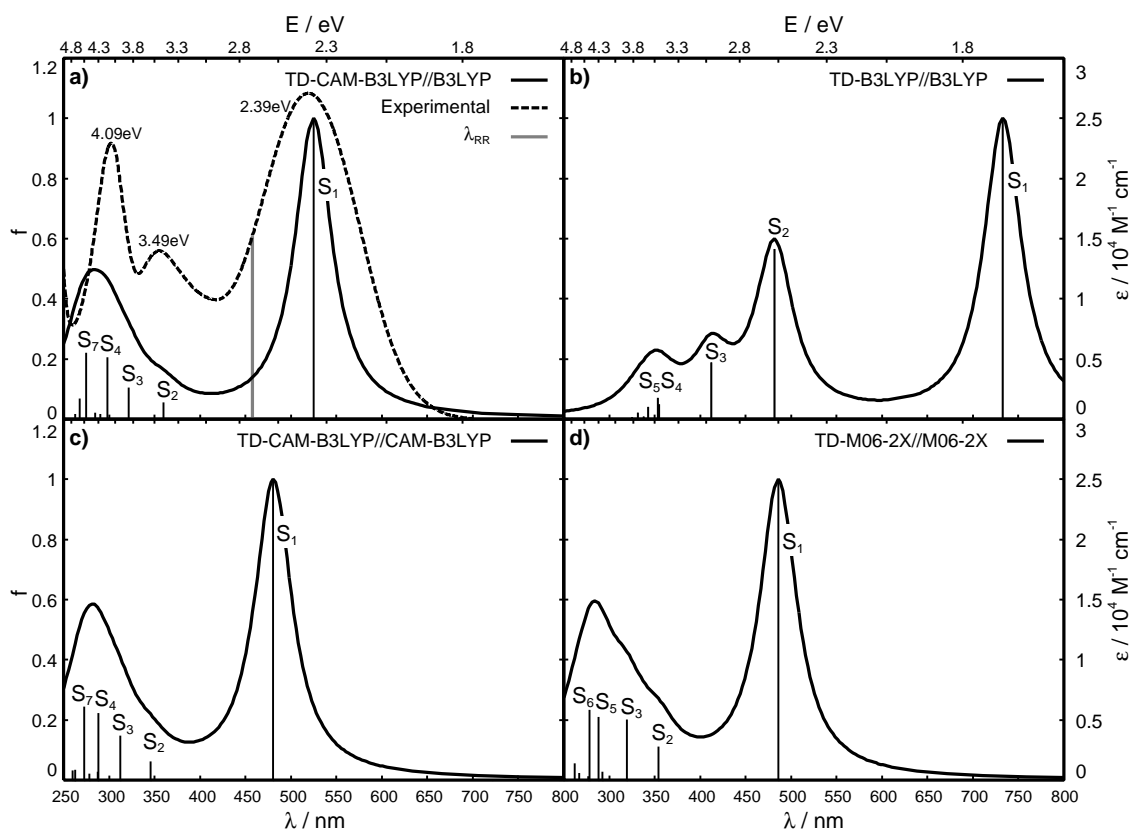


Figure 3: UV/vis absorption spectra of **1** (solid lines) in chloroform calculated as indicated. The experimental absorption spectra recorded in chloroform (dashed lines) is also plotted in a). The absorption maxima correspond to 2.39 eV ($\epsilon = 27050 \text{ M}^{-1}\text{cm}^{-1}$), 3.49 eV ($\epsilon = 14050 \text{ M}^{-1}\text{cm}^{-1}$) and 4.09 eV ($\epsilon = 22950 \text{ M}^{-1}\text{cm}^{-1}$). The excitation wavelength of 2.70 eV (458 nm) used in the RR measurement is plotted in grey.

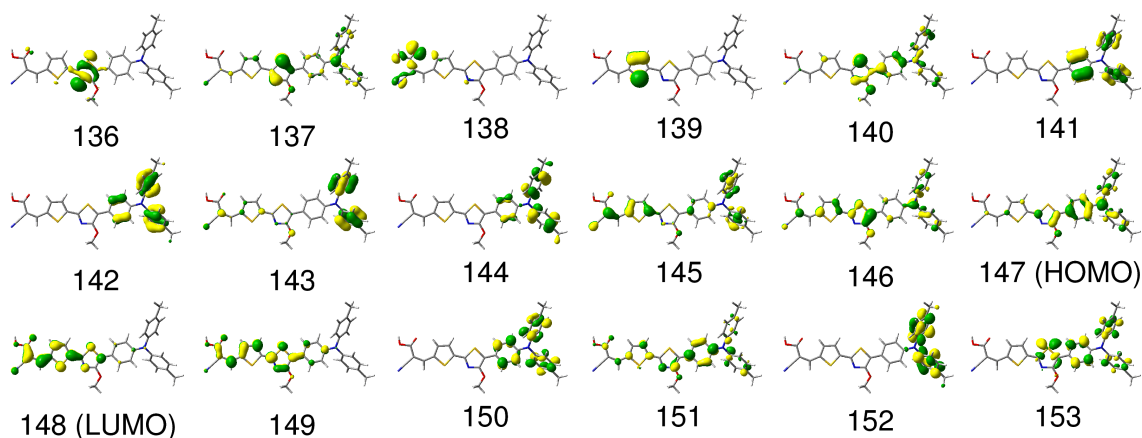


Figure 4: Molecular orbitals involved in the singlet excited states of **1** at the TD-CAM-B3LYP//CAM-B3LYP level of theory.

1
2
3
4 phase –although using both the B3LYP and the CAM-B3LYP solvated equilibrium geometries.
5
6 The corresponding vertical excitation energies, oscillator strengths and associated wavefunc-
7
8 tions of the CT transitions are collected in Table 2. The orbital numbering corresponds to
9
10 that of Figure 2. First, the properties of the S_1 state obtained with the B3LYP equilibrium
11
12 structure shall be reported, followed by the results obtained on the CAM-B3LYP structure.
13
14 All four RASSCF partitions, (30,2,2;14,2,11), (16,2,2;7,2,7), (16,3,3;7,2,7) and (16,4,4;7,2,7),
15
16 were employed.

17
18 All levels of theory predict the S_1 state as a very bright CT state, mainly described by the
19
20 HOMO(147)/LUMO(148) transition. The large MS-RASPT2 (30,2,2;14,2,11) calculation pre-
21
22 dicts an excitation energy of 2.45 eV, with an oscillator strength of 1.34. The HOMO-LUMO
23
24 transition dominates with a weight of 73% while examination of the remaining wavefunction
25
26 coefficients shows only marginal influence of the π -system of ph2 and ph3. Using the smaller
27
28 (16,2,2;7,2,7) partition, where these orbitals with negligible contributions to the wavefunction
29
30 are removed and including only SD excitations, an increase of the excitation energy of 0.12 eV,
31
32 an increase of the weight of the HOMO/LUMO transition (78%), and a decrease of the oscilla-
33
34 tor strength (1.06), is obtained. The increase of the excitation level up to triples or quadruples,
35
36 lowers the energy to 2.42 and 2.35 eV, respectively, whereas the oscillator strength increases
37
38 to 1.26 and 1.41. Interesting to note is the associated computational cost of these calcula-
39
40 tions: while the smaller (16,2,2;7,2,7) partition involves ten times less CSFs (and substantial
41
42 less amount of memory) than (30,2,2;14,2,11) at the same level of excitation, the inclusion
43
44 of triple and quadruples excitations in (16,2,2;7,2,7) again rises the number of CSFs by one
45
46 and two orders of magnitude, at the expense of decreasing the energy by ca 0.1 and 0.2 eV,
47
48 respectively. Noticeable is also the decrease of the HOMO/LUMO transition weight in the
49
50 MS-RASPT2 (16,4,4;7,2,7) calculation, while the weight of the 147 \rightarrow 149 transition is in-
51
52 creased. In passing we note that this transition was also observed in the S_1 state predicted by
53
54 TD-CAM-B3LYP//B3LYP, see Table 1.

55
56 Using the optimized CAM-B3LYP geometry, MS-RASPT2 (30,2,2;14,2,11) yields an exci-
57
58 tation energy of 2.62 eV and the composition of the S_1 and oscillator strength (1.27) resembles
59
60 that obtained with the B3LYP geometry. Again, reducing the active space to (16,2,2;7,2,7)
increases the excitation energy (2.74 eV) and decreases the oscillator strength (1.02). The in-

1
2
3
4 clusion of triples and quadruples stabilizes the S_1 to 2.61 eV and 2.47 eV, respectively. As
5
6 with using the B3LYP geometry, a more pronounced multiconfigurational character of the S_1
7
8 state is obtained including Q excitations. Note that a similar wavefunction composition was
9
10 also observed in the TD-CAM-B3LYP//CAM-B3LYP and TD-M06-2X//M06-2X calculations,
11
12 see Table 1.

13
14 While the trends obtained with the different RASSCF partitions are similar with both ge-
15
16 ometries, the specific excitation energies are strongly dependent on the ground state geometry.
17
18 The RASPT2 energy based on the CAM-B3LYP geometry fluctuates up to 0.27 eV, depend-
19
20 ing on the partition, while the variation within the B3LYP geometry is, with 0.22 eV, slightly
21
22 smaller. In order to discuss which of both geometries performs better and which partition is
23
24 more adequate, and in the light of the experimental values available, it is necessary to take
25
26 solvent effects into account. From the previous TD-DFT calculations (see Section 3.1), the
27
28 effect of chloroform on the absorption energy of the CT state S_1 can be estimated as a red-
29
30 shift of ca. 0.1 eV. The result of subtracting this correction to the gas phase values is shown
31
32 in parenthesis in Table 2. From these values, it can be seen that the best agreement with the
33
34 experimental value of 2.39 eV is obtained with the (30,2,2;14,2,11) calculation in combination
35
36 with the B3LYP geometry (2.35 eV) and the (16,4,4;7,2,7) calculation in combination with the
37
38 CAM-B3LYP geometry (2.37 eV). Acceptable errors (within 0.1 – 0.2 eV) are nevertheless
39
40 obtained with all the partitions regardless of the geometry, except the (16,2,2;7,2,7) and the
41
42 CAM-B3LYP geometry (2.64 eV). It seems that the inclusion of SD is in general not sufficient
43
44 to account for enough dynamical correlation to provide good energies, as found by Gagliardi
45
46 and coworkers.¹⁷ The fact that the inclusion of T and Q systematically decreases the energy
47
48 with respect to SD indicates that such level of excitation might be necessary. In combination
49
50 with the CAM-B3LYP geometry, the obtained energy with SDTQ is the best; in combination
51
52 with the B3LYP structure the good value obtained with SDT is again undershoot by including
53
54 Q.

55
56 In conclusion, similarly to the TDDFT results the RASPT2 calculations cannot give a definite
57
58 answer about which equilibrium energy is best to be used in combination with RASPT2/RASSCF.
59
60 In that respect, RR provides a unique framework to assess further the quality of the electronic
structures and corresponding gradients. Before discussing RR spectra, we shall analyse the

1
2
3
4 geometrical features obtained with both, B3LYP and CAM-B3LYP functionals.
5
6
7

8 **3.3 Electronic ground state geometries** 9

10 As predicted in sections 3.1 and 3.2, the ground state geometry can have a substantial impact
11 on the excitations energies. This is especially true in the case of the S_1 of **1**, but changes are
12 also obtained in the vertical energies of the S_2 , S_3 and S_4 states. In order to interpret the origin
13 of these changes, two geometrical parameters were investigated in more detail, namely the
14 dihedral angle δ (Figure 1) and the bond length alternation (BLA) index.^{36,71} The BLA index is
15 defined as the difference between the average length of carbon-carbon single bonds and double
16 bonds and it can be applied to polyenes, conjugated π -systems, or push-pull chromophores such
17 as **1**. A positive BLA index is correlated to a neutral form, a negative value to a zwitterionic
18 form and a zero value to a delocalized system. For **1**, the BLA index was calculated along the
19 conjugated path joining the triphenylamine moiety (donor group) to the cyano group (anchoring
20 group) (see Figure S1 and Table S1 of the ESI).
21
22
23
24
25
26
27
28
29
30

31 The comparison of the B3LYP and CAM-B3LYP equilibrium structures reveals a difference
32 in the dihedral angle δ , which takes values of -14 and -19° at the B3LYP and CAM-B3LYP
33 geometries, respectively. These changes affect the conjugation between the donor group and
34 the bridge and therefore could modify the excitation energies. In order to explicitly study the
35 influence of δ on the S_1 excitation energies, potential energy curves (PEC) of S_0 and S_1 states
36 along δ were calculated starting from the B3LYP and CAM-B3LYP equilibrium structures, and
37 leaving the other coordinates frozen. The PECs were investigated in the interval $[-30^\circ; 30^\circ]$
38 with a step size of 0.5° using TD-CAM-B3LYP in the presence of chloroform. As can be seen
39 from Figure 5, the B3LYP and CAM-B3LYP minima for the S_0 state are associated with a
40 twisted structure, whereas the minima of the S_1 are nearly planar, which can be understood
41 from the double bonding character of the LUMO (see Figure 4) between the ph1 and thia units.
42 Moreover, Figure 5 shows that the PECs obtained with both geometries display a very similar
43 shape. In particular, the 0.22 eV energy difference between the S_0 and the S_1 is almost inde-
44 pendent from the dihedral angle δ with both geometries, i.e. both curves run mostly parallel.
45 This indicates that the difference in the S_1 excitation energy obtained with B3LYP and CAM-
46 B3LYP geometries is not a consequence of the different torsion angle but must be associated
47
48
49
50
51
52
53
54
55
56
57
58
59
60

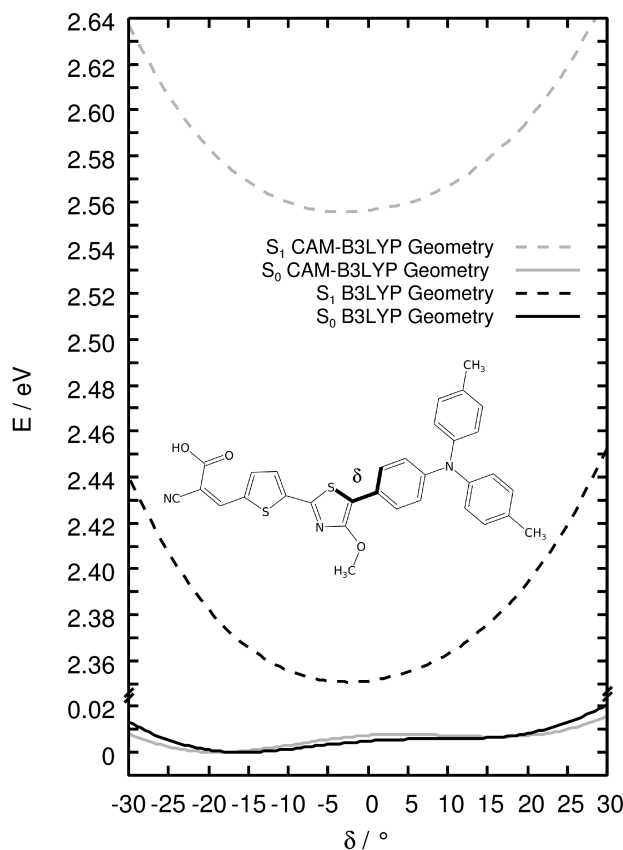


Figure 5: Potential energy curves of the S_0 and S_1 states calculated with CAM-B3LYP along the dihedral angle δ starting from the optimized B3LYP (black) and CAM-B3LYP (grey) geometries.

to other geometrical changes along the conjugated path.

The calculated BLA index for **1** are all positive, corresponding to a neutral form. The BLA index obtained with CAM-B3LYP (0.0335 Å) is larger than that calculated with B3LYP (0.0203 Å). Hence, the geometry obtained with CAM-B3LYP is more localized than the B3LYP geometry. This fact allows for an interpretation of the difference in excitation energy for the S_1 state. The virtual MO 148 involved in the S_1 excitation (Figure 4, see also Figure 2), shows a bonding character on the single bonds and an anti-bonding character on the double bonds, i.e. photoexcitation leads to a more zwitterionic form (see Table S1 of the ESI and e.g. Refs. 35,36). Therefore, since the single and double bonds of the CAM-B3LYP equilibrium structure are more localized than those of the B3LYP geometry, the MO 148 is stabilized (0.16 eV) when going from the CAM-B3LYP to the B3LYP geometry and, as a consequence, the excitation energy for a transition to the MO 148 is higher in TD-CAM-B3LYP//CAM-B3LYP than in TD-CAM-B3LYP//B3LYP. In passing we note that the BLA

1
2
3
4 index for the M06-2X geometry (0.0332 Å) is similar to that of CAM-B3LYP, and hence, a
5 similar excitation energy for S_1 is obtained. Analogous reasonings can explain the decrease
6 observed in the excitation energies of S_2 , S_3 and S_4 states, when going from the CAM-B3LYP
7 to the B3LYP structures.
8
9

10
11 In conclusion, the differences in the excitation energies obtained with the different optimized
12 structures can be attributed to the changes in the bond length alternation of single and double
13 bonds.
14
15
16

17 18 19 **3.4 Resonance Raman spectra**

20
21 A non-negligible effect of the ground state structure has been observed on the excitation ener-
22 gies. However, it is not clear which method is more suited to describe the ground state geometry
23 of compound **1** and consequently of structurally related dyes. Therefore, the calculation of RR
24 spectra in resonance with the first absorption band is used to obtain additional information on
25 the quality of ground and excited state structures.
26
27

28
29 Figure 6 shows the RR spectra calculated with the different methods, compared to the exper-
30 imental one recorded for an excitation wavelength of 2.7 eV (458 nm). For completeness,
31 the RR spectra is not only calculated with the B3LYP and CAM-B3LYP geometries using
32 TD-CAM-B3LYP and RASSCF procedures, but also employing the TD-B3LYP//B3LYP and
33 TD-M06-2X//M06-2X protocols. The calculated vibrational modes and corresponding assign-
34 ments are in Tables 3, 4 and 5.
35
36
37
38
39
40
41

42 The spectrum simulated with TD-B3LYP//B3LYP (Figure 6a) allows for a rough assignment
43 of the vibrational bands (Table 3) but the relative intensities of the peaks are very inaccu-
44 rate, in comparison to the experimental spectrum (Figure 6g). This could indicate a wrong
45 estimation of the excited state gradients by B3LYP and it might be also related to the strong
46 underestimation of the S_1 excitation energy by this functional (recall Table 1). Since energies
47 of CT states can be corrected with CAM-B3LYP, the RR spectrum was also calculated using
48 the TD-CAM-B3LYP//B3LYP method. Recently, this approach has provided improved RR
49 spectra in comparison to the TD-B3LYP//B3LYP one in the case of *o*-nitrophenol.²⁹ However,
50 as shown in Figure 6b, the obtained results for **1** are very poor. Also the RR intensity pattern
51 at SA2-RASSCF(16,3,3;7,2,7)//B3LYP level of theory is extremely bad (Figure 6c). Here, the
52
53
54
55
56
57
58
59
60

1
2
3
4 (16,3,3;7,2,7) partition including up to T excitations has been chosen as a reasonable compromise between accuracy and computational cost (cf. Table 2). The results obtained with the latter
5
6
7
8
9
10
11
12
13
14
15
16
17
18
19
20
21
22
23
24
25
26
27
28
29
30
31
32
33
34
35
36
37
38
39
40
41
42
43
44
45
46
47
48
49
50
51
52
53
54
55
56
57
58
59
60

(16,3,3;7,2,7) partition including up to T excitations has been chosen as a reasonable compromise between accuracy and computational cost (cf. Table 2). The results obtained with the latter two methods indicate that the inaccuracies in the RR spectra are more likely to be associated to inaccuracies of the ground state geometry and associated vibrational normal coordinates rather than to excited states energies and gradients.

Indeed, the RR spectrum calculated with the TD-CAM-B3LYP//CAM-B3LYP method (Figure 6d) presents a much better agreement with experiment (Figure 6g). Almost all calculated vibrational modes (see Table 4) were assigned to the experiment, merely the assignment of the modes between 1000 and 1300 cm^{-1} was not feasible due to the pronounced experimental noise. The frequencies of the modes in the range between 1300 and 1700 cm^{-1} are in good agreement with the experiment with a typical mean absolute deviation of 15 cm^{-1} . The RR spectrum obtained with the TD-M06-2X//M06-2X method is very similar to the TD-CAM-B3LYP//CAM-B3LYP spectrum (Figure 6f and Table 5), even if some differences are found for the relative intensities of the modes 135, 142, 154 and 157. The remaining disagreements with the experimental spectrum can be attributed to limitations of the XC functionals, of the description of the solvent as well as of the STA, which makes only use of excited state gradients at the FC point. However, these inaccuracies are small enough to allow an assessment of the calculated geometries and gradients.

Almost all intense RR normal modes in the CAM-B3LYP and the M06-2X equilibrium structures are centered either at the bridge or the anchoring group, see Tables 4 and 5. Only the less intense modes 118, 119, and 132 (CAM-B3LYP structure) or rather 116 and 133 (M06-2X structure) as well as 151, 160, and 162 are located at the donor group. This is consistent with the observed CT nature of the S_1 state discussed in the Sections 3.1 and 3.2. The obtained intensity patterns at TD-CAM-B3LYP//CAM-B3LYP (Figure 6d) and TD-M06-2X//M06-2X (Figure 6f) are very similar. However, SA2-RASSCF(16,3,3;7,2,7)//CAM-B3LYP (Figure 6e) features besides some minor variations in the intensities in the region between 1500 and 1600 cm^{-1} , such as a substantially increased intensity of mode 164, which is related to the stretching of the cyano group.

These results confirm that both ground and excited state properties of **1** are better described with the long-range corrected CAM-B3LYP (or the M06-2X) functional and should be preferred to

1
2
3
4 calculate ground and excited state geometries for push-pull chromophores similar or related to
5 the dye **1**. The adequacy of the CAM-B3LYP ground state structure is also corroborated by the
6 SA2-RASSCF(16,3,3;7,2,7)//CAM-B3LYP RR spectrum (Figure 6e), which presents a similar
7 pattern than the spectrum obtained with the CAM-B3LYP//CAM-B3LYP calculation. These
8 results are very encouraging and constitute a first application of the RASSCF methodology to
9 the simulation of RR intensities.
10
11
12
13
14
15
16
17

18 **4 Conclusions**

19
20
21 In this paper the excitation energies and gradients in the ground and the first excited state of an
22 organic push-pull chromophore have been assessed with TDDFT and RASPT2/RASSCF meth-
23 ods. To this aim, equilibrium geometries, UV/vis absorption- and RR spectra are calculated for
24 the 4-methoxy-1,3-thiazole donor-acceptor dye (**1**). Substantial effort was put on characteriz-
25 ing the bright CT state (S_1) that is located at a remarkably low excitation energy for this family
26 of push-pull chromophores.
27
28
29
30
31
32

33 In order to compare with available absorption and RR spectra obtained in chloroform, first
34 the solvated equilibrium geometries were calculated using the global hybrid functionals B3LYP
35 and M06-2X and the long-range corrected CAM-B3LYP functional. These geometries and the
36 same functionals were employed within TDDFT to calculate the vertical energies of the low-
37 lying excited states in the presence of a polarized continuum to model solution. It was found
38 that the amount of exact exchange in the functional not only has a strong influence on the accu-
39 racy of the excitation energies but the latter also markedly depend on the equilibrium structure
40 employed. Up to 0.2 eV differences can be found when going from the B3LYP to the CAM-
41 B3LYP geometry. These energy differences can be rationalized analysing the variations of the
42 torsion angle of the carbon-carbon bond joining the bridge and the donor group (dihedral an-
43 gle δ) as well as the extent of localization of the single and double bonds, measured by the
44 BLA index. While energy profiles along δ showed that torsion is of minor importance to the
45 S_1 excitation energy, it was found that a more pronounced amount of exact exchange leads to
46 larger BLA indexes, i.e. a more localized nature of the single and double bonds, increasing thus
47 the excitation energies. In this way, changes of the BLA index in the ground state structures
48
49
50
51
52
53
54
55
56
57
58
59
60

1
2
3
4
5
6
7
8
9
10
11
12
13
14
15
16
17
18
19
20
21
22
23
24
25
26
27
28
29
30
31
32
33
34
35
36
37
38
39
40
41
42
43
44
45
46
47
48
49
50
51
52
53
54
55
56
57
58
59
60

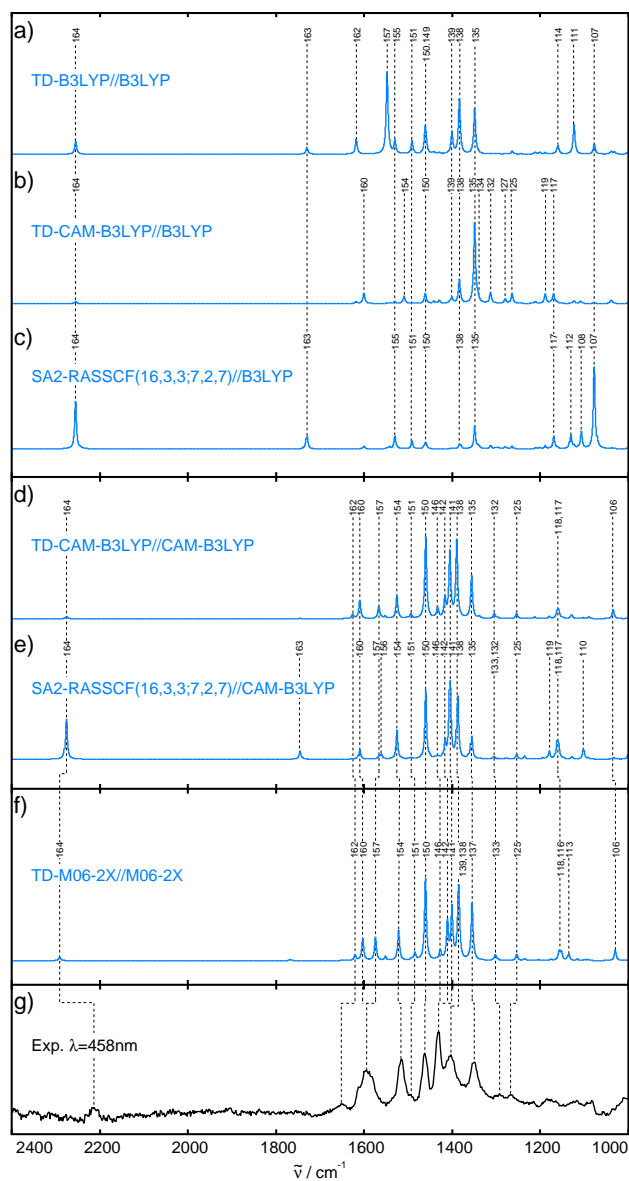


Figure 6: RR spectra of **1** in resonance with the first absorption band. The notation F2//F1 is used, in which F1 represents the XC functional employed for the ground state properties and F2 is the method used for the excited state gradients calculation.

1
2
3
4 could be correlated to differences in excitation energy. From the three functionals investigated,
5 B3LYP fails to predict the excitation energies of **1**, due to its intrinsic problems in describ-
6 ing CT states, while CAM-B3LYP and M06-2X functionals deliver good agreement with the
7 experiment, provided solvation effects are included. As estimated from TDDFT, the solvent
8 red-shifts the excitation energies by about 0.1 eV. The best estimation of the S_1 energy, with
9 respect to the experimental data, was found using TD-CAM-B3LYP//B3LYP.
10
11
12
13
14

15
16 Using the B3LYP and CAM-B3LYP geometries, the position of the S_1 state was also inves-
17 tigated by means of MS-RASPT2/RASSCF calculations. Four different partitions, changing
18 the active space and the level of excitation were employed: (30,2,2;14,2,11), (16,2,2;7,2,7),
19 (16,3,3;7,2,7), and (16,4,4;7,2,7). All of them contain only the HOMO and LUMO orbitals in
20 the RAS2, while a different number of ligand orbitals, holes, and particles are allowed within
21 the RAS1 and RAS3 subspaces. As with TDDFT, the MS-RASPT2 calculations also showed
22 a dependency of the S_1 excitation energy on the equilibrium structure and the partition em-
23 ployed. Although in some cases errors can be considered acceptable (0.1 – 0.2 eV), it seems
24 that in this particular case, where the RAS2 is reduced to HOMO-LUMO, the inclusion of at
25 least T excitations is necessary to achieve good excitation energies – similar to the results of
26 Gagliardi et al in Ref. 17. The best agreement in the first absorption band was obtained with the
27 CAM-B3LYP geometry and the (16,4,4;7,2,7) partition, while the excitation energy obtained
28 with the B3LYP structure and the same level of excitation (SDTQ) is underestimated. The
29 large (30,2,2;14,2,11) partition also provides a good estimation of the excitation energy for the
30 present dye in combination with the B3LYP geometry. However, from the computational point
31 of view the (30,2,2;14,2,11) partition is associated with an enormous cost in the MS-RASPT2
32 procedure, arising from the first-order perturbative wavefunction.
33
34
35
36
37
38
39
40
41
42
43
44
45
46
47

48 Since MS-RASPT2/RASSCF calculations cannot provide a clear-cut answer on which ground
49 state geometry is more adequate, RR intensity patterns were calculated, paying special atten-
50 tion to the B3LYP and CAM-B3LYP structures. TDDFT and RASSCF gradients using the
51 compromised (16,3,3;7,2,7) partition were employed. Up to our knowledge, this is the first
52 time that RASSCF gradients are used to compute RR intensities. The results clearly evidence
53 that only the RR spectra using the CAM-B3LYP (and M06-2X) equilibrium structure show an
54 excellent agreement with experiment, which allows an unambiguous assignment of the normal
55
56
57
58
59
60

1
2
3
4 modes. Both CAM-B3LYP and RASSCF excited state gradients and energies in combina-
5 tion with CAM-B3LYP ground state gradients are appropriate to describe the CT state of this
6 push-pull chromophore. Particularly encouraging is the agreement on RR intensities based on
7 RASSCF, since despite the computational cost, it paves the way to employ multiconfigura-
8 tional gradients in situations where conventional TDDFT calculations might fail completely to
9 provide accurate results.
10
11
12
13
14
15
16
17
18
19
20

21 **Acknowledgments**

22
23
24
25
26 This research was supported financially by the Thüringer Ministerium für Bildung, Wissenschaft
27 und Kultur (PhotoMIC, Grant No. B 514-09049) and the Carl-Zeiss Stiftung (J.G.). J. G. is
28 also thankful to the 7th Framework Programme of the European Union for his Marie Curie Ca-
29 reer Integration Grant (VibRaman). Roberto Menzel and Johann Schäfer are deeply thanked for
30 providing the experimental UV/vis absorption- and RR- spectrum of **1**, respectively. All the
31 calculations have been performed at the Universitätsrechenzentrum of the Friedrich-Schiller
32 University of Jena and at the HP computers of the Theoretical Chemistry group in Jena and
33 Vienna.
34
35
36
37
38
39
40
41
42
43
44
45
46

47 **Supporting Information**

48
49
50
51 Bond lengths of the ground state equilibrium structures (B3LYP, CAM-B3LYP, and M06-2X),
52 excited state geometries calculated from the excited state gradients assuming displaced har-
53 monic oscillators (B3LYP//B3LYP, CAM-B3LYP//CAM-B3LYP, and M06-2X//M06-2X) and
54 BLA indexes are provided in Figure S1 and Table S1. This material is available free of charge
55 via the Internet at <http://pubs.acs.org>.
56
57
58
59
60

References

- [1] Lynch, B. J.; Truhlar, D. G. *J. Phys. Chem. A* **2001**, *105*, 2936–2941.
- [2] Budyka, M. F.; Zyubina, T. S.; Zarkadis, A. K. *J. Mol. Struct.-Theochem.* **2002**, *594*, 113–125.
- [3] Chai, J.-D.; Head-Gordon, M. *J. Chem. Phys.* **2008**, *128*, 084106–1–084106–15.
- [4] Georgieva, I.; Aquino, A. J. A.; Trendafilova, N.; Santos, P. S.; Lischka, H. *Inorg. Chem.* **2010**, *49*, 1634–1646.
- [5] Cramer, C. J.; Truhlar, D. G. *Chem. Rev.* **1999**, *99*, 2161–2200.
- [6] Tomasi, J.; Mennucci, B.; Cammi, R. *Chem. Rev.* **2005**, *105*, 2999–3093.
- [7] González, L.; Escudero, D.; Serrano-Andrés, L. *Chem. Phys. Chem.* **2012**, *13*, 28–51.
- [8] Magyar, R. J.; Tretiak, S. *J. Chem. Theory Comput.* **2007**, *3*, 976–987.
- [9] Pastore, M.; Mosconi, E.; De Angelis, F.; Grätzel, M. *J. Phys. Chem. C* **2010**, *114*, 7205–7212.
- [10] Faber, C.; Duchemin, I.; Deutsch, T.; Attaccalite, C.; Olevano, V.; Blase, X. *J. Mater. Sci.* **2012**, *47*, 7472–7481.
- [11] Malmqvist, P.-Å.; Pierloot, K.; Shahi, A. R. M.; Cramer, C. J.; Gagliardi, L. *J. Chem. Phys.* **2008**, *128*, 204109–10–204109–1.
- [12] Manni, G. L.; Aquilante, F.; Gagliardi, L. *J. Chem. Phys.* **2011**, *134*, 034114–1–034114–5.
- [13] Malmqvist, P.-Å.; Rendell, A.; Roos, B. O. *J. Phys. Chem.* **1990**, *94*, 5477–5482.
- [14] Olsen, J.; Roos, B. O.; Jørgensen, P.; Jensen, H. J. A. *J. Chem. Phys.* **1988**, *89*, 2185–2192.

- 1
2
3
4 [15] Finley, J.; Malmqvist, P.-A.; Roos, B. O.; Serrano-Andrés, L. *Chem. Phys. Lett.* **1998**,
5 288, 299–306.
6
7
8
9 [16] Roos, B. O. *In Ab initio Methods in Quantum Chemistry II*; Wiley-VCH: Chichester, 1987.
10
11
12 [17] Sauri, V.; Serrano-Andrés, L.; Shahi, A. R. M.; Gagliardi, L.; Vancoillie, S.; Pierloot, K.
13 *J. Chem. Theory and Comput.* **2011**, 7, 153–168.
14
15
16 [18] Kupfer, S.; Pérez-Hernández, G.; González, L. *Theo. Chem. Acc.* **2012**.
17
18
19 [19] Runge, E.; Gross, E. K. U. *Phys. Rev. Lett.* **1984**, 52, 997–1000.
20
21
22 [20] Dreuw, A.; Head-Gordon, M. *J. Am. Chem. Soc.* **2004**, 126, 4007–4016.
23
24
25 [21] Yanai, T.; Tew, D. P.; Handy, N. C. *Chem. Phys. Lett.* **2004**, 393, 51–57.
26
27
28 [22] Becke, A. D. *J. Chem. Phys.* **1993**, 98, 1372–1377.
29
30
31 [23] Zhao, Y.; Truhlar, D. G. *Theor. Chem. Acc.* **2008**, 120, 215–241.
32
33
34 [24] Lange, A. W.; Rohrdanz, M. A.; Herbert, J. M. *J. Phys. Chem. B* **2008**, 112, 6304–6308.
35
36
37 [25] Jacquemin, D.; Wathelet, V.; Perpète, E. A.; Adamo, C. *J. Chem. Theory Comput.* **2009**,
38 5, 2420–2435.
39
40
41 [26] Jacquemin, D.; Mennucci, B.; Adamo, C. *Phys. Chem. Chem. Phys.* **2011**, 13, 16987–
42 16998.
43
44
45 [27] Aquino, A. J.; Nachtigallova, D.; Hobza, P.; Truhlar, D. G.; Hättig, C.; Lischka, H. *J.*
46 *Comput. Chem.* **2011**, 32, 1217–1227.
47
48
49 [28] Steinmann, S. N.; Piemontesi, C.; Delachat, A.; Corminboeuf, C. *J. Chem. Theory Com-*
50 *put.* **2012**, 8, 1629–1640.
51
52
53 [29] Guthmuller, J. *J. Chem. Theo. Comput.* **2011**, 7, 1082–1089.
54
55
56 [30] Jang, S.; Jin, S. I.; Park, C. R. *Bull. Korean Chem. Soc.* **2007**, 28, 2343–2353.
57
58
59
60

- 1
2
3
4 [31] Bahers, T. L.; Pauporté, T.; Scalmani, G.; Adamo, C.; Ciofini, I. *Phys. Chem. Chem. Phys.*
5 **2009**, *11*, 11276–11284.
6
7
8
9 [32] Menzel, R.; Ogermann, D.; Kupfer, S.; Weiß, D.; Görls, H.; Kleinermanns, K.; González,
10 L.; Beckert, R. *Dyes Pigm.* **2012**, *94*, 512–524.
11
12
13 [33] Menzel, R.; Kupfer, S.; Mede, R.; Weiß, D.; Görls, H.; González, L.; Beckert, R. *Euro. J.*
14 *Organ. Chem.* **2012**, *27*, 5231–5247.
15
16
17 [34] Wächtler, M.; Guthmuller, J.; González, L.; Dietzek, B. *Coord. Chem. Rev.* **2012**, *256*,
18 1479–1508.
19
20
21
22 [35] Guthmuller, J.; Champagne, B. *J. Chem. Phys.* **2007**, *127*, 164507–1–164507–11.
23
24
25 [36] Mennucci, B.; Cappelli, C.; Guido, C. A.; Cammi, R.; Tomasi, J. *J. Phys. Chem. A* **2009**,
26 *113*, 3009–3020.
27
28
29 [37] Boereboom, J. M.; van Hemert, M. C.; Neugebauer, J. *Chem. Phys. Chem.* **2011**, *12*,
30 3157–3169.
31
32
33
34 [38] Silverstein, D. W.; Jensen, L. *J. Chem. Theory Comput.* **2010**, *6*, 2845–2855.
35
36
37 [39] Santoro, F.; Cappelli, C.; Barone, V. *J. Chem. Theory Comput.* **2011**, *7*, 1824–1839.
38
39
40 [40] Ma, H.; Liu, J.; Liang, W. *J. Chem. Theory Comput.* **2012**, *8*, 4474–4482.
41
42
43 [41] Guthmuller, J.; González, L. *Phys. Chem. Chem. Phys.* **2010**, *12*, 14812–14821.
44
45 [42] Tschierlei, S.; Karnahl, M.; Presselt, M.; Dietzek, B.; Guthmuller, J.; González, L.;
46 Schmitt, M.; Rau, S.; Popp, J. *Angew. Chem. Int. Ed.* **2010**, *49*, 3981–3984.
47
48
49 [43] Kupfer, S.; Guthmuller, J.; Wächter, M.; Losse, S.; Rau, S.; Dietzek, B.; Popp, J.;
50 González, L. *Phys. Chem. Chem. Phys.* **2011**, *13*, 15580–15588.
51
52
53 [44] Menzel, R.; Täucher, E.; Weiß, D.; Beckert, R.; Görls, H. *Z. Anorg. Allg. Chem.* **2010**,
54 *636*, 1380–1385.
55
56
57 [45] Otsubo, T.; Aso, Y.; Takimiya, K. *J. Mater. Chem.* **2002**, *12*, 2565–2575.
58
59
60

- 1
2
3
4 [46] Kim, E.; Park, S. B. *Chem. Asian J.* **2009**, *4*, 1646–1658.
5
6
7 [47] Jose, J.; Burgess, K. *Tetrahedron* **2006**, *62*, 11021–11037.
8
9
10 [48] Duan, L.; Qiao, J.; Sun, Y. D.; Qiu, Y. *Adv. Mater.* **2011**, *23*, 1137–1144.
11
12 [49] Menzel, R.; Breul, A.; Pietsch, C.; Schäfer, J.; Friebe, C.; Täuscher, E.; Weiß, D.; Dietzek,
13 B.; Popp, J.; Beckert, R.; Schubert, U. S. *Macromol. Chem. Phys.* **2011**, *212*, 840–848.
14
15
16 [50] Reinhardt, B. A.; Brott, L. L.; Clarson, S. J.; Dillard, A. G.; Bhatt, J. C.; Kannan, R.;
17 Yuan, L.; He, G. S.; Prasad, P. N. *Chem. Mater.* **1998**, *10*, 1863–1874.
18
19
20 [51] Oliva, M. M.; Casado, J.; Raposo, M. M.; Fonseca, A. M.; Hartmann, H.; Hernández, V.;
21 Navarrete, J. T. L. *J. Org. Chem.* **2006**, *71*, 7509–7520.
22
23
24 [52] Happ, B.; Schäfer, J.; Menzel, R.; Hager, M. D.; Winter, A.; Popp, J.; Beckert, R.;
25 Dietzek, B.; Schubert, U. S. *Macromol.* **2011**, *44*, 6277–6287.
26
27
28
29 [53] Becke, A. D. *J. Chem. Phys.* **1993**, *98*, 5648–5652.
30
31
32
33 [54] Lee, C.; Yang, W.; Parr, R. G. *Phys. Rev. B* **1988**, *37*, 785–789.
34
35
36 [55] Hariharan, P. C.; Pople, J. A. *Theor. Chim. Acta* **1973**, *28*, 213–222.
37
38
39 [56] Pierloot, K.; Dumez, B.; Widmark, P.-O.; Roos, B. O. *Theor. Chim. Acta* **1995**, *90*, 87–
40 114.
41
42
43 [57] Aquilante, F.; Malmqvist, P.-Å.; Pedersen, T. B.; Ghosh, A.; Roos, B. O. *J. Chem. Theory*
44 *and Comput.* **2008**, *4*, 694–702.
45
46
47 [58] Malmqvist, P.-Å.; Roos, B. O. *Chem. Phys. Lett.* **1989**, *155*, 189–194.
48
49
50 [59] Frisch, M. J.; Trucks, G. W.; Schlegel, H. B.; Scuseria, G. E.; Robb, M. A.; Cheeseman,
51 J. R.; Scalmani, G.; Barone, V.; Mennucci, B.; Petersson, G. A.; Nakatsuji, H.; Caricato,
52 M.; Li, X.; Hratchian, H. P.; Izmaylov, A. F.; J. Bloino, G. Z.; Sonnenberg, J. L.; Hada,
53 M.; Ehara, M.; Toyota, K.; Fukuda, R.; Hasegawa, J.; Ishida, M.; Nakajima, T.; Honda,
54 Y.; Kitao, O.; Nakai, H.; Vreven, T.; Montgomery, J. J. A.; Peralta, J. E.; Ogliaro, F.;
55
56
57
58
59
60

- 1
2
3
4 Bearpark, M.; Heyd, J. J.; Brothers, E.; Kudin, K. N.; Staroverov, V. N.; Kobayashi, R.;
5 Normand, J.; Raghavachari, K.; Rendell, A.; Burant, J. C.; Iyengar, S. S.; Tomasi, J.;
6 Cossi, M.; Rega, N.; Millam, J. M.; Klene, M.; Knox, J. E.; Cross, J. B.; Bakken, V.;
7 Adamo, C.; Jaramillo, J.; Gomperts, R.; Stratmann, R. E.; O. Yazyev, A. J. A.; R. Cammi,
8 C. P.; Ochterski, J. W.; Martin, R. L.; Morokuma, K.; Zakrzewski, V. G.; Voth, G. A.;
9 Salvador, P.; Dannenberg, J. J.; Dapprich, S.; Daniels, A. D.; Farkas, O.; Foresman,
10 J. B.; Ortiz, J. V.; Cioslowski, J.; Fox, D. J.; *Gaussian 09*, Revision A.02, Gaussian, Inc.,
11 Wallingford, CT, 2009.
- 12
13
14
15
16
17
18
19
20 [60] Aquilante, F.; Vico, L. D.; Ferré, N.; Ghigo, G.; Malmqvist, P.-Å.; Neogrády, P.; Pedersen,
21 T. B.; Pitonak, M.; Reiher, M.; Roos, B. O.; Serrano-Andrés, L.; Urban, M.; Veryazov,
22 V.; Lindh, R. *J. Comput. Chem.* **2010**, *31*, 224–247.
- 23
24
25
26 [61] Veryazov, V.; Widmark, P. O.; Serrano-Andrés, L.; Lindh, R.; Roos, B. O. *Int. J. Quantum*
27 *Chem.* **2004**, *100*, 626–635.
- 28
29
30 [62] Karlström, G.; Lindh, R.; Malmqvist, P.-Å.; Roos, B. O.; Ryde, U.; Veryazov, V.; Wid-
31 mark, P. O.; Cossi, M.; Schimmelpfennig, B.; Neogrády, P.; Seijo, L. *Comp. Mater. Sci.*
32 **2003**, *28*, 222–239.
- 33
34
35
36 [63] Heller, E. J.; Sundberg, R.; Tannor, D. *J. Phys. Chem.* **1982**, *86*, 1822–1833.
- 37
38
39 [64] Merrick, J. P.; Moran, D.; Radom, L. *J. Phys. Chem.* **2007**, *111*, 11683–11700.
- 40
41
42 [65] Comparison, N. C. C.; Database, B.; NIST Standard Reference Database Number 101,
43 Release 15b, August 2011, R. D. Johnson III.
- 44
45
46 [66] Tozer, D. J. *J. Chem. Phys.* **2003**, *119*, 12697–12699.
- 47
48
49 [67] Autschbach, J. *Chem. Phys. Chem.* **2009**, *10*, 1757–1760.
- 50
51
52 [68] Kuritz, N.; Stein, T.; Baer, R.; Kronik, L. *J. Chem. Theory Comput.* **2011**, *7*, 2408–2415.
- 53
54
55 [69] Guillaume, M.; Champagne, B.; Zutterman, F. *J. Phys. Chem. A* **2006**, *110*, 13007–13013.
- 56
57 [70] Guthmuller, J.; Zutterman, F.; Champagne, B. *J. Chem. Theory Comput.* **2008**, *4*, 2094–
58 2100.
59
60

1
2
3
4 [71] Marder, S. R.; Perry, J. W.; Bourhill, G.; Gorman, C. B.; Tiemann, B. G.; Mansour, K.
5
6 *Science* **1993**, *261*, 186–189.
7
8
9
10
11
12
13
14
15
16
17
18
19
20
21
22
23
24
25
26
27
28
29
30
31
32
33
34
35
36
37
38
39
40
41
42
43
44
45
46
47
48
49
50
51
52
53
54
55
56
57
58
59
60

State	TD-B3LYP/B3LYP		TD-CAM-B3LYP/B3LYP		TD-CAM-B3LYP/CAM-B3LYP		TD-M06-2X/M06-2X		
	$\Delta E/eV$	f	$\Delta E/eV$	f	$\Delta E/eV$	f	$\Delta E/eV$	f	
S_1	1.69 (1.83)	1.02 (0.83)	2.36 (2.50)	1.60 (1.45)	2.58 (2.68)	1.52 (1.14)	2.55 (2.65)	1.44 (1.29)	1.47 → 1.48 1.46 → 1.48 1.46 → 1.48
		100 (100)	77 (79)	77 (79)	71 (74)	20 (17)	71 (74)	71 (74)	
		147 → 148	147 → 148	147 → 148	147 → 148	147 → 148	147 → 148	147 → 148	
S_2	2.57 (2.69)	0.58 (0.64)	3.44 (3.54)	0.09 (0.13)	3.59 (3.67)	0.09 (0.14)	3.50 (3.58)	0.16 (0.22)	1.46 → 1.48 1.47 → 1.48 1.47 → 1.48
		97 (94)	66 (71)	66 (71)	61 (67)	11 (10)	61 (67)	61 (67)	
		147 → 149	147 → 149	147 → 149	147 → 149	147 → 149	147 → 149	147 → 149	
S_3	3.01 (3.06)	0.19 (0.17)	3.86 (3.92)	0.17 (0.16)	3.97 (4.02)	0.22 (0.20)	3.88 (3.93)	0.29 (0.24)	1.47 → 1.49 1.45 → 1.48 1.47 → 1.49
		91 (87)	68 (72)	68 (72)	62 (67)	10 (9)	62 (67)	62 (67)	
		147 → 148	147 → 148	147 → 148	147 → 148	147 → 148	147 → 148	147 → 148	
S_4	3.49 (3.58)	0.05 (0.05)	4.16 (4.24)	0.33 (0.26)	4.30 (4.37)	0.34 (0.27)	4.23 (4.24)	0.04 (0.03)	1.47 → 1.48 1.44 → 1.48 1.47 → 1.48
		44 (50)	45 (56)	45 (56)	30 (45)	8 (8)	30 (45)	30 (45)	
		145 → 148	145 → 148	145 → 148	145 → 148	145 → 148	145 → 148	145 → 148	
S_5	3.51 (3.59)	0.07 (0.10)	4.27 (4.29)	0.03 (0.02)	4.31 (4.32)	0.04 (0.03)	4.31 (4.39)	0.30 (0.25)	1.45 → 1.48 1.44 → 1.48 1.46 → 1.49
		44 (48)	74 (72)	74 (72)	71 (80)	9 (9)	71 (80)	71 (80)	
		144 → 148	147 → 150	147 → 150	147 → 150	147 → 150	147 → 150	147 → 150	
S_6	3.62 (3.71)	0.04 (0.01)	4.35 (4.43)	0.04 (0.04)	4.45 (4.52)	0.03 (0.03)	4.45 (4.47)	0.33 (0.26)	1.47 → 1.52 1.46 → 1.52 1.46 → 1.52
		90 (90)	83 (79)	83 (79)	12 (10)	9 (9)	12 (10)	9 (9)	
		143 → 148	139 → 148	140 → 148	139 → 148	140 → 148	139 → 148	140 → 148	
S_7	3.67 (3.80)	0.01 (0.00)	4.52 (4.53)	0.35 (0.29)	4.54 (4.57)	0.37 (0.29)	4.47 (4.53)	0.02 (0.01)	1.47 → 1.48 1.47 → 1.48 1.47 → 1.48
		53 (68)	78 (79)	78 (79)	83 (83)	19 (29)	83 (83)	19 (29)	
		142 → 148	147 → 152	146 → 152	147 → 152	146 → 152	147 → 152	146 → 152	
S_8	3.74 (3.72)	0.02 (0.02)	4.63 (4.66)	0.11 (0.08)	4.72 (4.75)	0.05 (0.03)	4.64 (4.67)	0.03 (0.03)	1.47 → 1.51 1.42 → 1.48 1.44 → 1.48
		70 (70)	42 (41)	42 (41)	37 (32)	39 (37)	37 (32)	39 (37)	
		147 → 150	147 → 151	146 → 149	147 → 151	146 → 149	147 → 151	146 → 149	
S_9	3.82 (3.90)	0.01 (0.02)	4.65 (4.62)	0.00 (0.00)	4.73 (4.71)	0.00 (0.00)	4.73 (4.73)	0.08 (0.07)	1.40 → 1.48 1.41 → 1.48 1.39 → 1.48
		43 (49)	72 (74)	72 (74)	55 (66)	63 (60)	55 (66)	63 (60)	
		140 → 148	138 → 148	138 → 149	138 → 148	136 → 148	138 → 149	146 → 150	
S_{10}	3.84 (3.93)	0.00 (0.02)	4.71 (4.71)	0.03 (0.03)	4.78 (4.77)	0.05 (0.05)	4.78 (4.75)	0.00 (0.00)	1.41 → 1.48 1.40 → 1.48 1.42 → 1.48
		58 (62)	42 (43)	42 (43)	54 (44)	12 (15)	54 (44)	12 (15)	
		141 → 148	147 → 153	141 → 148	146 → 150	146 → 150	147 → 153	138 → 148	

Table 1: TDDFT excitation energies (ΔE), oscillator strengths (f) and main configurations of the solvated (chloroform) first ten singlet excited states at TD-B3LYP/B3LYP, TD-CAM-B3LYP/B3LYP, TD-CAM-B3LYP/CAM-B3LYP and TD-M06-2X/M06-2X levels of theory obtained with the 6-31G(d,p) basis set; all values in parentheses refer to the respective gas phase calculations.

B3LYP Geometry					CAM-B3LYP Geometry				
ΔE / eV	f	Character	c^2 / %		ΔE / eV	f	Character	c^2 / %	
RASPT2 (30,2,2;14,2,11) (CSFs: 61131)									
2.45	(2.35)	1.34	147 \rightarrow 148	73	2.62	(2.52)	1.27	147 \rightarrow 148	75
RASPT2 (16,2,2;7,2,7) (CSFs: 6947)									
2.57	(2.47)	1.06	147 \rightarrow 148	78	2.74	(2.64)	1.02	147 \rightarrow 148	79
RASPT2 (16,3,3;7,2,7) (CSFs: 96323)									
2.42	(2.32)	1.26	147 \rightarrow 148	72	2.61	(2.51)	1.15	147 \rightarrow 148	75
RASPT2 (16,4,4;7,2,7) (CSFs: 725875)									
2.35	(2.25)	1.41	147 \rightarrow 148	62	2.47	(2.37)	1.31	147 \rightarrow 148	65
			147 \rightarrow 149	7				147 \rightarrow 149	4
								144 \rightarrow 148	4

Table 2: MS-RASPT2 excitation energies (ΔE), oscillator strengths (f), and wavefunctions for the partitions (30,2,2;14,2,11), (16,2,2;7,2,7), (16,3,3;7,2,7) and (16,4,4;7,2,7) for the S_1 state in the B3LYP and CAM-B3LYP equilibrium structures; all values in parentheses refer to the approximated excitation energies in chloroform taking solvent stabilization of 0.1 eV into account (see TDDFT results of Table 1).

mode	$\bar{\nu} / \text{cm}^{-1}$	$I_{\text{rel. B3LYP}}$	$I_{\text{rel. CAM-B3LYP}}$	$I_{\text{rel. RASSCF}}$	Assignment
107	1077.5	0.12	0.01	0.36	Bridge, Donor
108	1108.4	0	0.03	0.07	Bridge, Acceptor
111	1123.5	0.36	0.03	0.01	Acceptor, Bridge
112	1130.8	0	0	0.06	Donor
114	1159.8	0.1	0	0	Donor
117	1170	0	0.12	0.05	Bridge
119	1188.8	0.02	0.12	0.01	Donor
125	1264.1	0.04	0.12	0.01	Bridge, Donor
127	1279.7	0	0.05	0.01	Donor
132	1313.1	0.01	0.13	0.02	Donor
134	1341.5	0.01	0.06	0.01	Acceptor, Bridge
135	1349.1	0.54	1	0.1	Acceptor, Bridge
138	1383.8	0.65	0.29	0.02	Bridge, Donor
139	1400.7	0.26	0.07	0	Acceptor, Bridge
149	1458.8	0.06	0.01	0	Bridge
150	1461.3	0.31	0.12	0.03	Bridge
151	1491.2	0.16	0	0.03	Bridge, Donor
154	1509.4	0.01	0.09	0	Donor, Bridge, Acceptor
155	1530.1	0.15	0.02	0.06	Bridge, Donor
157	1547.9	1	0	0	Acceptor, Bridge
160	1600.5	0	0.13	0.01	Donor
162	1617.8	0.18	0.02	0	Donor
163	1729.9	0.08	0	0.05	Acceptor, Bridge
164	2254.8	0.16	0.02	0.21	Acceptor, Bridge

Table 3: Assignment of the vibrational frequencies (cm^{-1}) and calculated relative RR intensities ($I_{\text{rel.}}$) using the B3LYP optimized structure. The theoretical frequencies were scaled by a factor of 0.97.

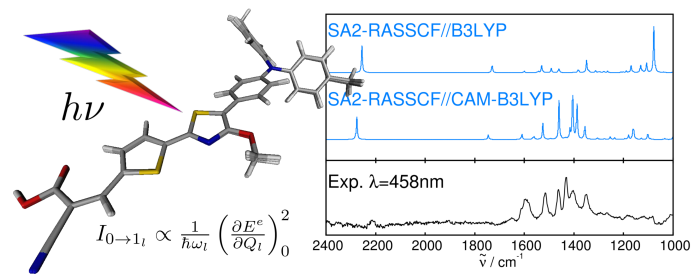
mode	$\tilde{\nu}(\text{Cal.})/\text{cm}^{-1}$	$\tilde{\nu}(\text{Exp.})/\text{cm}^{-1}$	$I_{\text{rel.}}$, CAM-B3LYP	$I_{\text{rel.}}$, RASSCF	Assignment
106	1034.6	0	0.11	0.02	Bridge, Acceptor
110	1102.9	0	0.01	0.12	Bridge, Acceptor
117	1158.5	0	0.07	0.16	Bridge
118	1162	0	0.08	0.2	Donor
119	1179.8	0	0.03	0.1	Donor
125	1253.7	0	0.07	0.07	Bridge
132	1304.5	0	0.05	0.02	Donor
135	1356	1351	0.53	0.3	Acceptor, Bridge
138	1389.8	1403	0.93	0.81	Bridge
141	1405.4	1431	0.8	1	Bridge, Acceptor
142	1416.5	1431	0.23	0.22	Bridge, Donor
146	1433.2	1431	0.12	0.03	Bridge, Acceptor
150	1460.2	1462	1	0.91	Bridge
151	1493.7	1494	0.05	0.02	Donor
154	1525.7	1516	0.28	0.38	Bridge
156	1560.8	0	0.01	0.06	Donor, Bridge, Acceptor
157	1566.7	1595	0.14	0.03	Acceptor
160	1609.9	1595	0.22	0.12	Donor
162	1626	1652	0.05	<0.01	Donor
163	1745.4	0	0	0.11	Acceptor
164	2275.8	2213	0.03	0.53	Acceptor

Table 4: Assignment of the vibrational frequencies (cm^{-1}) and calculated relative RR intensities ($I_{\text{rel.}}$) using the CAM-B3LYP optimized structure. The theoretical frequencies were scaled by a factor of 0.95.

mode	$\tilde{\nu}(\text{Cal.})/\text{cm}^{-1}$	$\tilde{\nu}(\text{Exp.})/\text{cm}^{-1}$	$I_{\text{rel. M06-2X}}$	Assignment
106	1029.9	-	0.13	Bridge, Acceptor
113	1135.2	-	0.07	Acceptor, Bridge
116	1151.9	-	0.09	Donor
118	1157.8	-	0.09	Bridge
125	1253.4	-	0.08	Bridge, Donor
133	1302.3	-	0.07	Donor
137	1355.1	1351	0.68	Bridge
138	1384.8	1403	0.58	Acceptor
139	1386.5	1403	0.42	Acceptor
141	1400.8	1431	0.62	Bridge, Acceptor
142	1410.8	1431	0.46	Bridge, Donor
146	1427.1	1431	0.11	Bridge, Acceptor
150	1460.7	1462	1.00	Bridge
151	1484.6	1494	0.08	Donor
154	1521.7	1516	0.36	Bridge, Donor
157	1574.2	1595	0.27	Acceptor
160	1603.2	1595	0.27	Donor
162	1620.4	1652	0.07	Donor
164	2290.8	2213	0.04	Acceptor

Table 5: Assignment of the vibrational frequencies (cm^{-1}) and calculated relative RR intensities ($I_{\text{rel.}}$) using the M06-2X optimized structure. The theoretical frequencies were scaled by a factor of 0.95.

Table of Content



4.3 Arylamine-Modified Thiazoles as Donor-Acceptor Dyes: Quantum Chemical Evaluation of the Charge-Transfer Process and Testing as Ligands in Ruthenium(II) Complexes

Reprinted with permission from Menzel et al. *Eur. J. Org. Chem.* **27**, 5231-5247 (2012).
Copyright 2012 John Wiley and Sons.

Arylamine-Modified Thiazoles as Donor–Acceptor Dyes: Quantum Chemical Evaluation of the Charge-Transfer Process and Testing as Ligands in Ruthenium(II) Complexes

Roberto Menzel,^{[a],‡} Stephan Kupfer,^{[b],c||‡} Ralf Mede,^[a] Dieter Weiß,^[a] Helmar Görls,^[d] Leticia González,^{*[c]} and Rainer Beckert^{*[a]}

Keywords: N,S-Heterocycles / Heterocycles / Chromophores / Dyes / Charge transfer / Density functional calculations / Ruthenium complexes

A series of new 4-hydroxy-1,3-thiazole-based chromophores bearing different arylamine components (triarylamines, carbazole, and phenothiazine) as electron donors and azaheterocycle components (pyridine, pyrazine and pyrimidine) as electron-acceptor moieties have been synthesized. Elaborate quantum chemical calculations were carried out with two selected compounds to identify the natures of the HOMO/LUMO transition and of the intramolecular charge-transfer state. The electrochemical properties were investigated: the dyes show reversible first oxidation and reduction peaks, with the former strongly dominated by the type of arylamine.

The donor moieties were synthesized under Buchwald–Hartwig conditions. Several of the presented X-ray structures provide deeper insight into the geometries of the ligands. The bidentate nature of the chromophores makes them suitable as ligands in transition metal complexes. The corresponding ruthenium(II) polypyridine complexes—Ru(dmbpy)₂-(L)(PF₆)₂ (dmbpy = 4,4'-dimethyl-2,2'-bipyridine) — were successfully synthesized for seven of the ligands. The MLCT bands in these complexes are significantly broadened, resulting in improved light-harvesting efficiencies.

Introduction

The classical heterocyclic 4-hydroxy-1,3-thiazole core was described by R. Dodson and H. Turner in 1951.^[1] Since then, several compounds have been synthesized^[2] but only a few data relating to applications of these compounds exist. Some of the derivatives have been tested as drugs (e.g., as cyclooxygenase, 5-lipoxygenase, and cyclin-dependent kinase 5 inhibitors).^[3]

Our group revived the 4-hydroxy-1,3-thiazole unit as a chromophore and fluorophore, due to its similarities to the naturally occurring luciferin and its remarkable spectroscopic characteristics. Several applications of its derivatives

have been developed since then. Thanks to their easy functionalization and tunable optical properties they have been successfully incorporated as blue-emitting species in a polymer backbone,^[4] as a FRET energy donor in a terpolymer together with a Ru^{II} complex as the acceptor unit,^[5] and as chromophores in donor- π -acceptor (D- π -A) dyes in dye-sensitized solar cells (DSSCs).^[6] In addition, they were very recently reported to be fast and specific systems for fluoride ion detection^[7] and have been employed as light-harvesting ligands in Ru^{II} polypyridyl complexes.^[8]

The last of these in particular is of significant interest, due to the potential application of Ru^{II} dyes as sensitizers in DSSCs, which usually lack chromophores to harvest sunlight efficiently. Furthermore, ruthenium(II) complexes, especially Ru^{II} polypyridine complexes, have attracted considerable interest due to their outstanding properties, such as good chemical stability, reversible redox behavior, and long-lived excited states with distinct reactivities and unique, tunable emission characteristics.^[9] This has opened the doorway to numerous applications.^[10] Nonetheless, the investigation of new complexes is still an evolving field and is one part of this contribution.

Additionally, arylamines have also been the focus of intense research, due to potential applications in various functional materials. They have been used as materials that show photoconductive and nonlinear optical (NLO) properties,^[11] and were employed for that purpose as chromo-

[a] Friedrich Schiller University Jena, Institute of Organic and Macromolecular Chemistry, Humboldtstraße 10, 07743 Jena, Germany
Fax: +49-3641-948212
E-mail: c6bera@uni-jena.de
Homepage: <http://www.agbeckert.uni-jena.de/>

[b] Friedrich Schiller University Jena, Institute of Physical Chemistry, Helmholtzweg 4, 07743 Jena, Germany

[c] University of Vienna, Institute of Theoretical Chemistry, Währinger Str. 17, 1090 Vienna, Austria
Homepage: <http://theochem.univie.ac.at/>

[d] Friedrich Schiller University Jena, Institute of Inorganic and Analytical Chemistry, Humboldtstraße 8, 07743 Jena, Germany

‡ Both authors contributed equally to this article

Supporting information for this article is available on the WWW under <http://dx.doi.org/10.1002/ejoc.201200688>.

phores in ultrafast electro-optic (EO) applications.^[12] Furthermore, they can act as photoconductors and hole-transporting materials in organic light-emitting diodes (OLEDs),^[13] and are promising cores both in bulk heterojunction (BHJ) solar cells^[14] and in Grätzel-type DSSCs.^[15]

The synthesis and characterization of different dyes based on the 4-methoxy-1,3-thiazole core as a chromophore with an arylamine donor in the 5-position (i.e., with a phenyl-, *p*-anisole-, *p*-tolyl-, or phenothiazine-based arylamine) and a pyridine, pyrimidine, or pyrazine moiety in the 2-position as acceptor is presented. Two of the dyes were further investigated by quantum chemical methods in order to assign their longest-wavelength absorptions either to a twisted (TICT) or to a planar (PICT) intramolecular charge-transfer process. The successful synthesis of seven heteroleptic Ru^{II} complexes was achieved by use of the activated precursor *cis*-Ru(dmbpy)₂(acetone)₂(PF₆)₂.^[16] The complexes were synthesized in order to test the abilities and characteristics of these dyes as ligands, which is considered a first step to establishing this class of chromophores as electron-donating and light-harvesting ligands in Ru^{II} complexes utilized as sensitizers in DCCSs.^[17] All compounds were investigated with regard to their electronic and electrochemical properties. Furthermore, the emission behavior of the dyes was characterized in terms of lifetime and quantum efficiency measurements.

Results and Discussion

Synthesis

The synthesis of the dyes/ligands is depicted in Scheme 1. The new 4-hydroxy-1,3-thiazoles **1a–1c** were prepared by Hantzsch thiazole cyclizations between the thioamides of the corresponding azaheterocycles and ethyl 2-bromo-2-(4-nitrophenyl)acetate, which can in turn easily be prepared from the commercially available 2-(4-nitrophenyl)acetic acid by a standard protocol.^[18] Compound **1d** was prepared similarly, from ethyl 2-bromo-2-(4-bromophenyl)acetate and pyridine-2-carbothioamide, as described in the literature.^[19] Alkylation of the “phenolic” 4-hydroxy group was achieved in a manner similar to the Williamson ether synthesis, by treatment of the deprotonated thiazole with methyl iodide in DMSO. The reduction of the nitro group in **2a–2c** was accomplished with freshly prepared Raney nickel and hydrazine as the hydrogen source in EtOH in excellent yields (>95%).

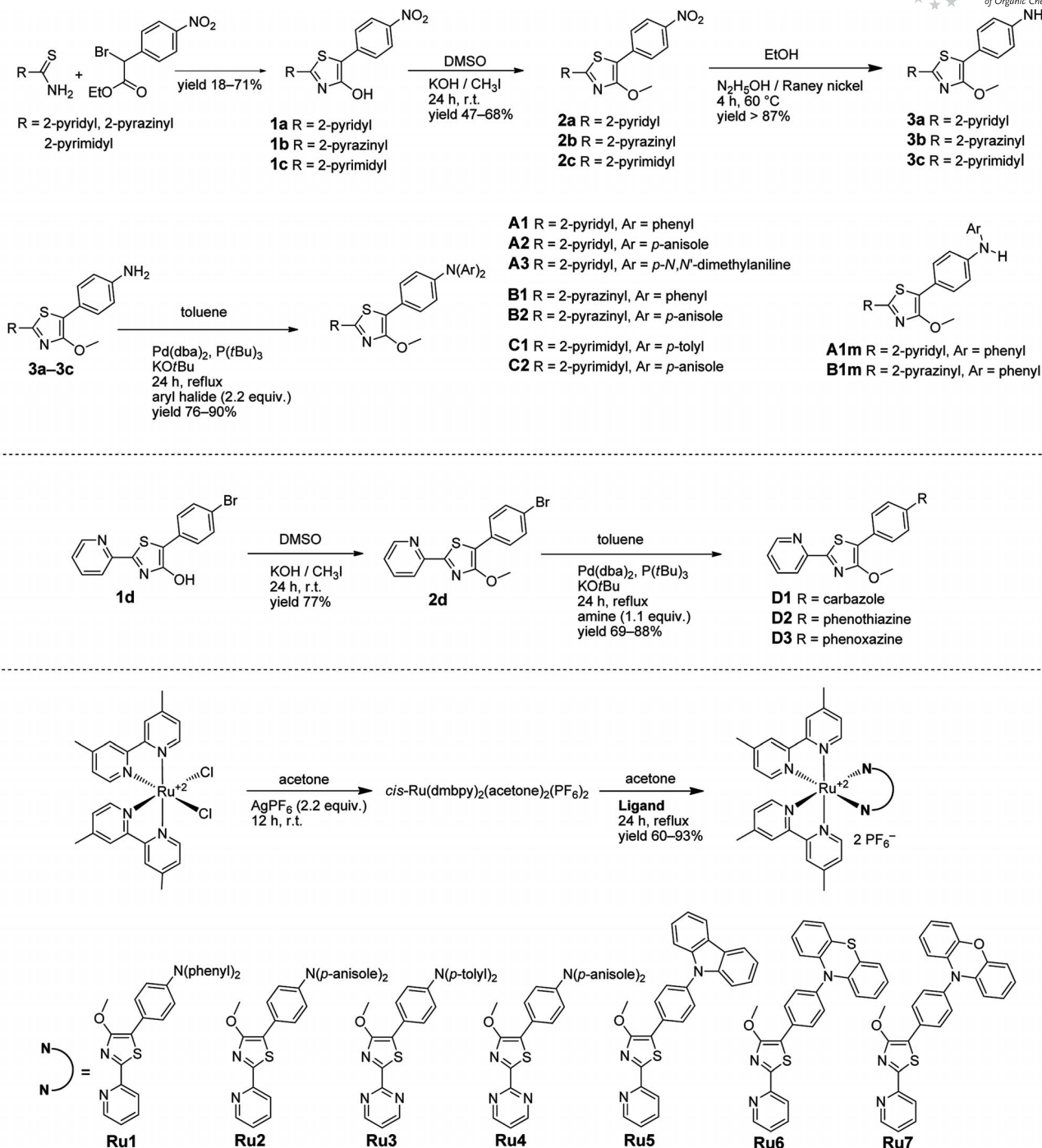
The bottleneck for the synthesis of the arylamines was the Buchwald–Hartwig cross-coupling reaction, involving a double *N*-arylation. Although thoroughly described in the literature, the reaction depends strongly on the natures of the catalysts and ligands and on the conditions used.^[20] Several attempts with, for example, triphenylphosphane or 1,1'-bis(diphenylphosphanyl)ferrocene as ligand together with NaH or KO^{*t*}Bu as base have failed completely. Therefore, the electron-rich ligand tri-*tert*-butylphosphane [P(*t*Bu)₃], which had already been successfully applied in the synthesis of different carbazole derivatives,^[21] was cho-

sen as a promising candidate. For the coupling reaction, bis(dibenzylideneacetone)palladium(0) [Pd(dba)₂] was used as the precatalyst, KO^{*t*}Bu as the base to deprotonate the amine in the catalytic cycle, and toluene as solvent. Fortunately, the desired products were obtained with use of P(*t*Bu)₃ in good yields (76–90%). In addition, the two-step nature of the reaction was demonstrated. As representative examples, for **A1** and **B1** the monosubstituted products **A1m** (69%) and **B1m** (88%) were obtained. This opens the door for the construction of unsymmetrically substituted triarylamines useful for photonic applications.^[22] Unlike the double *N*-arylation of the amines **3a–3c**, the Buchwald–Hartwig reaction starting with **2d**, in which the aryl halide is connected to the thiazole, was not successful by the described method: with the commonly used diphenylamine as the amine component no conversion to the substituted product was observed under various conditions. The biarylphosphane ligand 2-(dicyclohexylphosphanyl)-2',6'-dimethoxy-1,1'-biphenyl (SPHOS) was therefore chosen as a promising ligand.^[20b,23] SPHOS has already been successfully applied in the amination of chloro-terpyridine and is widely used in the Suzuki–Miyaura reaction.^[24] Finally, the coupling reaction with employment of SPHOS yielded the arylamines **D1–D3** (69 to 88%).

The synthesis of the heteroleptic Ru^{II} complexes is also depicted in Scheme 1. The standard procedure – heating of precursor *cis*-(dmbpy)₂RuCl₂ (1 equiv.) in EtOH with the appropriate ligand (1 equiv.) for 24 h under reflux conditions and precipitating the product with NH₄PF₆ – yielded an inseparable mixture of products, so the precursor was activated with AgPF₆ prior to the complexation reaction with the ligand. The synthesized complexes can easily be purified by size exclusion chromatography either with Bio-Beads[®] S-X1 with DCM or with Sephadex[®] LH-20 with acetone as solvent if they are only sparingly soluble in DCM. After precipitation of the products with diethyl ether, they were obtained as deep red solids in moderate to good yields (75–93%). Although several attempts were made, it was not possible to obtain pure samples of all possible complexes. No homogeneous products were obtained in the cases of compounds **B1** and **B2**. Most likely unfavorable complexation at the second pyrazine nitrogen atom led to a mixture of differently substituted complexes. The complexation was also unsuccessful in the case of ligand **A3**.

X-ray Structures

X-ray structures of the molecules **A1**, **B1**, **C1**, and **D2** were obtained from crystals grown directly in NMR tubes by slow evaporation of CHCl₃/EtOH solvent mixtures. The structures are depicted in Figure 1 and data are listed in Table 1 (additional refinement data are reported in Scheme S1 in the Supporting Information). Each dye shows a more or less planar geometry along the acceptor 1,3-thiazole unit, with the nitrogen atoms arranged in a *transoid* conformation due to N–H hydrogen-bonding interactions between N1 of the 1,3-thiazole and the hydrogen of the ap-



Scheme 1. Synthesis and structure of the ligands and the complexes.

appropriate *N*-heterocycle (except for **C1**). The torsion angles are 9.10(7)° for **C1** with the pyrimidine moiety (no hydrogen bond possible) and are decreased to 2.86(6), 7.79(8), and 2.48(9)° for **A1**, **B1**, and **D2**, respectively. Each dye is also twisted to some extent along the 1,3-thiazole-phenyl single bond. Because there is no appreciable steric hindrance it can be assumed that free rotation occurs at room temperature, leading to an unsteady torsion angle in the crystalline state, from almost planar with 9.10(7)° in the case of **C1** to highly twisted with 37.89(10)° in that of **A1**.

The triarylamines display propeller-type geometries of the aromatic rings. They are twisted in a well-known fashion out of the plane into conformations with fewest steric interactions with the adjacent rings, as reported for several arylamines.^[25] The nitrogen N3 of the triarylamine in each case adopts an almost planar geometry, in agreement with the *sp*² hybridization and the resulting intramolecular *p*– π interactions. The interatomic distances and angles both in the arylamine donor and in the 4-methoxy-1,3-thiazole core are all in the expected range.^[26] Additionally, the X-ray

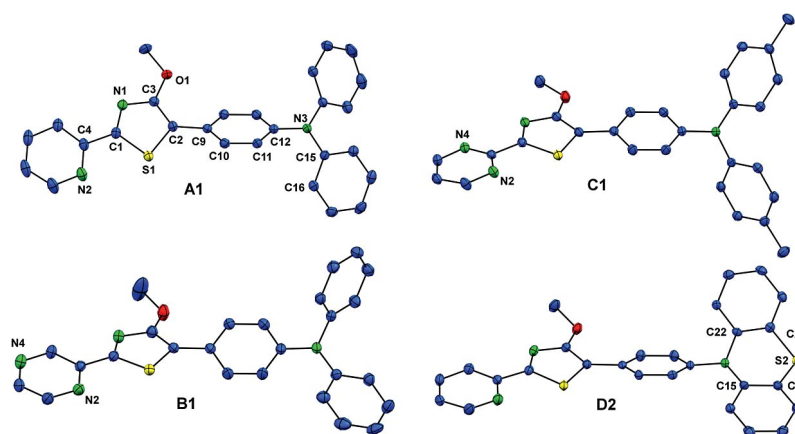


Figure 1. ORTEP plots of the arylamines **A1**, **B1**, **C1**, and **D2**. The numbering of **A1** also applies for the other compounds. Hydrogen atoms are omitted; ellipsoid probability 50%.

Table 1. Selected interatomic distances [Å] and angles [°] in **A1**, **B1**, **C1**, and **D2**.

	A1	B1	C1	D2
Bonds				
N2–C4	1.345(2)	1.342(2)	1.342(2)	1.342(3)
C4–C1	1.467(2)	1.462(2)	1.471(2)	1.463(3)
C1–S1	1.725(1)	1.723(2)	1.725(1)	1.722(2)
S1–C2	1.727(1)	1.733(2)	1.730(1)	1.727(2)
C2–C3	1.376(2)	1.377(2)	1.388(2)	1.383(3)
C3–N1	1.358(2)	1.358(2)	1.359(2)	1.360(3)
C3–O1	1.353(2)	1.355(2)	1.350(2)	1.354(3)
C2–C9	1.467(2)	1.466(2)	1.465(2)	1.468(3)
C12–N3	1.414(2)	1.427(2)	1.417(2)	1.446(3)
Angles				
C1–S1–C2	89.76(6)	89.83(8)	90.17(7)	90.10(10)
S1–C2–C3	107.95(10)	107.70(12)	107.41(10)	107.76(15)
C2–C3–N1	117.56(12)	117.45(15)	117.51(12)	117.40(19)
C3–N1–C1	109.60(11)	109.93(14)	109.89(12)	109.71(18)
N1–C1–S1	115.13(10)	115.08(12)	115.03(10)	115.02(16)
Torsion angles				
N2–C4–C1–S1	2.86(6)	7.79(8)	9.10(7)	2.48(9)
S1–C2–C9–C10	37.89(10)	18.04(12)	1.65(10)	18.47(15)
C11–C12–N3–C15	40.21(11)	62.88(14)	48.35(12)	112.21(18)
C12–N3–C15–C16	34.97(11)	20.10(14)	48.14(12)	6.50(18)

structure of the monosubstituted product **A1m** is given in Scheme S2 in the Supporting Information. It features a geometry very similar to those of the doubly substituted derivatives.

In order to describe the butterfly conformation of the phenothiazine dye **D1**, it is necessary to introduce the folding angle θ and the tilt angle α .

The former refers to the extent of the butterfly conformation, whereas the latter represents the deviation of these planes from coplanarity ($\alpha = 0^\circ$). For **D1**, θ is 153° , corresponding to $\alpha = 27^\circ$, which conforms very well with unsubstituted ($\theta = 159^\circ$) or *N*-phenyl-substituted ($\theta = 155^\circ$) phenothiazine.^[27] Additionally, the phenothiazine is almost completely twisted out of the plane of the attached phenyl ring [$112.21(18)^\circ$]. This corroborates the assumption that the annulated arylamines (the same applies for **D1** and **D3**)

contribute only marginally to the π -conjugated system, as is also supported by the absorption spectra and quantum chemical calculations.

Electronic Absorption Spectra of the Dyes

The UV/Vis spectra of the ligands are shown in Figure 2 (see also Table 2). Every triarylamine dye shows several high energy transitions below 250 nm where the assignments are tentative (not shown) and two main transitions at 305 and 420 nm. The bands located at 305 nm are due to mixtures of π - π^* transitions in the triarylamines. They are not affected either by the donor or by the acceptor. The bands located in the visible part are of charge-transfer (CT) character, as recently shown for similar 4-methoxy-1,3-thiazole dyes.^[6] The lowest-energy absorption maxima are influenced both by the donors and by the acceptors. The absorption λ_{max} values are slightly bathochromically shifted by approx. 10 nm for the dyes with the pyrazine instead of the pyridine acceptors. Further shifts of these bands can be observed for the derivatives with more strongly electron-donating arylamines. For **A1–A3**, the absorption λ_{max} values are bathochromically shifted from 405 nm for the phenyl- to 417 nm (0.09 eV) for the *p*-anisole-, and further to 433 nm (0.20 eV) for the *p*-*N,N'*-dimethylaniline-based triarylamine. This coincides with the behavior of the thiazoles with the pyrazine and pyrimidine acceptor. For compounds **D1–D3**, the λ_{max} values of this transition are significantly shifted towards higher energies. This can be explained by the very weak participation of the annulated arylamines in the conjugation pathway, as can be seen from the X-ray structure of **D2**. The extinction coefficients (ϵ) of the longest-wavelength absorptions are high, varying from 18000 (**D1**) to 30000 $\text{M}^{-1}\text{cm}^{-1}$ (**B1**). Additionally, the absorption spectra of **D2** and **D3** display a very strong, typical n - π^* transition for **D2** ($\lambda = 257$ nm, $\epsilon = 53000$ $\text{M}^{-1}\text{cm}^{-1}$) and a strong π - π^* transition for **D3** ($\lambda = 240$, $\epsilon = 58000$ $\text{M}^{-1}\text{cm}^{-1}$) for the phenothiazine or phenoxazine moieties, as described for various *N*-aryl-substituted derivatives.^[28] The emission spectra of the dyes are depicted in Scheme S3 in the Sup-

porting Information. The emission quantum yields (Φ_F) are also strongly dependent on the arylamine donors. In contrast with the phenyl-based triarylamines, with $\Phi_F = 40$ –47%, the *p*-anisole-based triarylamines show Φ_F values below 1%, and consequently no fluorescence was detected for the *p*-*N,N'*-dimethylaniline derivative in CH_3CN solution at room temp. The obtained Φ_F values corresponded well with the measured emission lifetimes (τ_F). They were significantly decreased for the compounds with the lower Φ_F values. This prompts the assumption that several radiationless deactivation processes must efficiently depopulate the S_1 state if additional donors (*p*-methoxy **A2**, **B2**, **C2**, *p*-dimethylamino **A3**, or even *p*-methyl **C1**) are present in the triarylamine. More complicated behavior was observed for the derivatives **D1**–**D3**. As a result of the weak overlap of the two chromophores (thiazole and carbazole, phenothiazine, or phenoxazine) the emission spectra are hypsochromically shifted relative to those of the triarylamines **A1**–**A3**. The emission bands for **D2** and **D3** each show several peaks, most likely from transitions into different vibronic states of the electronic ground state. Only one main emission band can be observed for compound **D1** in the polar solvent CH_3CN , with a very high Φ_F of 90%, coincidentally with an emission due to the carbazole moiety,^[29] whereas for **D2** and **D3** the emissions are very weak.

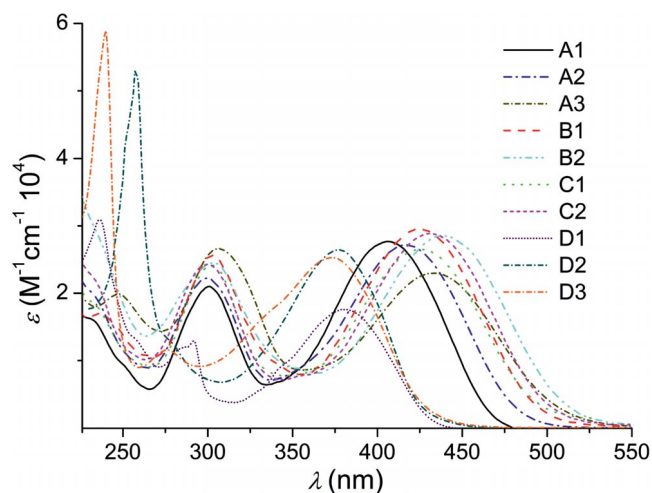


Figure 2. Absorption spectra of the ligands at room temp.

In order to investigate the longest-wavelength absorptions (and emissions) of the dyes in more detail, measurements in different solvents were carried out for compounds **A2** and **D1**. If a simple π – π^* transition takes place, both the absorption and the emission maximum should be bathochromically shifted with higher solvent polarities. Surprisingly, it was shown for both compounds (for spectra see Scheme S4 in the Supporting Information) that the absorption λ_{max} values are slightly shifted toward shorter wavelengths with increasing solvent polarity, but the emission maxima are shifted toward longer wavelengths. Consequently, the Stokes shifts increased significantly from 2700 (heptane) to 7400 cm^{-1} (CH_3CN) for **A2** and (less pronounced) from 4300 (heptane) to 5700 cm^{-1} (MeOH) for

Table 2. Spectroscopic properties of the dyes measured in CH_3CN at room temp.

	λ_{abs} [nm] [log ϵ]	λ_{em} [nm] ^[a]	Φ_F [%]	τ_F [ns]
A1	301 [4.33], 405 [4.44]	547	47	3.83
A2	299 [4.35], 417 [4.43]	605	<1	0.26
A3	307 [4.43], 433 [4.36]	n.d.	n.d.	n.d.
B1	303 [4.40], 425 [4.47]	593	40	2.99
B2	302 [4.40], 439 [4.46]	611	<1	0.13
C1	302 [4.32], 426 [4.36]	601	8	1.26
C2	301 [4.38], 433 [4.46]	630	<1	< 0.1 ^[c]
D1	292 [4.11], 380 [4.24]	478	90	3.12
D2	257 [4.72], 377 [4.42] ^[b]	484 sh, 507	2	0.11
D3	240 [4.77], 373 [4.40]	455 sh, 470	<1	0.13

[a] λ_{max} of emission after excitation in the maximum of the longest wavelength absorption. [b] Measured in THF. [c] Below demand interval, n.d.: not detected, sh: shoulder.

D1. This behavior has been explained in the literature in terms of a conformational transformation from a planar locally excited (LE) state to an intramolecular charge-transfer (ICT) or, consequently, to a twisted intramolecular charge-transfer (TICT) state.^[30]

In our case, the ground-state conformations of the dyes are not planar, as is supported by the X-ray structures. The energies of the S_0 states are basically independent of the solvents used and are only marginally decreased in polar solvents, such as MeOH, leading to small hypsochromic shifts in the absorption spectra for **A2** (Table 3) and **D1** (Table 4). According to the Franck–Condon principle, the geometries of the LE states of S_1 do not change during excitation, leading to very similar energies for these transitions for all solvents. LE states in nonpolar solvents are not stabilized through interactions with solvent molecules, and their conformations are predominately affected by the ground state geometries [sometimes considered partial charge-transfer (PCT) transitions].^[12,31] In contrast, the charge-separated ICT states (excitation leads to a formal

Table 3. Spectroscopic behavior of **A2** in different solvents.

Solvent	λ_{abs} [nm] [log ϵ]	λ_{em} [nm]	Φ_F [%]	Stokes shift [cm^{-1}]	τ_F [ns]
Heptane	427 [4.585]	483, 512	63	3900	2.6
Dioxane	425 [4.441]	530	59	4700	3.8
CHCl_3	428 [4.422]	561	40	5500	4.0
THF	425 [4.485]	552	43	5400	3.8
MeOH	421 [4.456]	581	< 1	6500	0.1
CH_3CN	417 [4.434]	603	1	7400	0.1

Table 4. Spectroscopic behavior of **D1** in different solvents.

Solvent	λ_{abs} [nm] [log ϵ]	λ_{em} [nm] ^[a]	Φ_F [%]	Stokes shift [cm^{-1}]	τ_F [ns]
Heptane	387 [4.466]	456, 464	97	4300	2.4
Dioxane	385 [4.399]	472	100	4800	2.7
CHCl_3	387 [4.235]	475	95	4800	2.9
THF	384 [4.474]	473	100	4900	2.8
CH_3CN	380 [4.244]	475	90	5300	3.1
MeOH	382 ^[a]	489	81	5700	3.3

[a] Extinction coefficient could not be measured, due to poor solubility.

cation radical at the arylamine and an anion radical at the acceptor) in polar solvents are extraordinarily stabilized by solvent molecules. It is assumed that the ICT transitions are facilitated by planarization along the phenyl-1,3-thiazole bond during the vibrational cooling process (see quantum chemical section). This accounts for the energy gain due to electronic conjugation (mesomeric interactions) and, consequently, the bathochromic shifts of the emission maxima and increased Stokes shifts in solvents with higher polarities. In order to clarify whether a TICT is likely to occur, we used the Lippert–Mataga equation to estimate the change in the dipole moment between S_0 and S_1 .^[32]

$$\Delta\tilde{\nu} = (\tilde{\nu}_A - \tilde{\nu}_F) = \frac{2}{hc} \left(\frac{\epsilon - 1}{2\epsilon + 1} - \frac{n^2 - 1}{2n^2 + 1} \right) \frac{(\Delta\mu)^2}{a^3} + C$$

The Lippert–Mataga plots obtained are shown in Figure 3 and further details are summarized in Scheme S5 in the Supporting Information. It is known that protic solvents (hydrogen bonding) and 1,4-dioxane do not yield reproducible values,^[33] so they were excluded from the analysis. The main uncertainty in this equation is the Onsager cavity radius (a). As described in the pioneering work by Lippert, a was calculated from the major axis of the molecule (simplified as an ellipsoid) and the correction value 0.8 (according to a equal energetic sphere).^[34] The lengths of the two molecules can both be derived from the X-ray structures as 17 Å, and the cavity radii are then 13.6 Å. The changes in dipole moment ($\Delta\mu = \mu_E - \mu_G$) were calculated to be 4.6 D for **A2** and 2.8 D for **D1**. This is a strong hint that a planar ICT (PICT) process is taking place rather than a TICT. TICT states usually show significantly higher changes in dipole moments ($\Delta\mu \geq 20$ D) than those observed here.^[35]

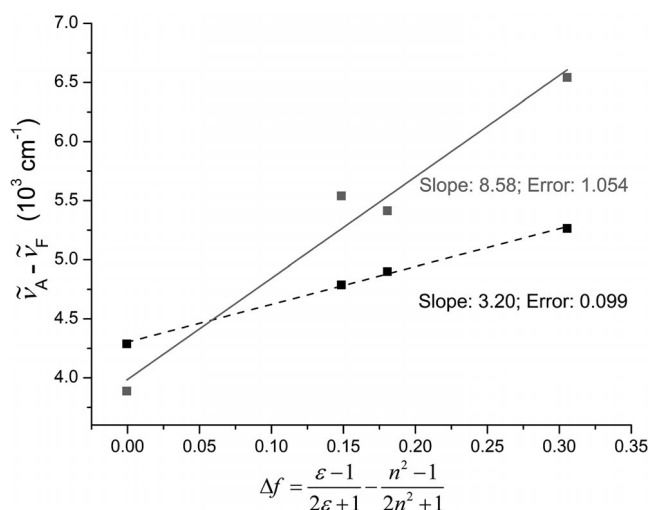


Figure 3. Lippert–Mataga plots for **A1** (solid) and **D2** (dashed). Solvents: heptane, CHCl_3 , THF, and MeOH, at room temp.

Quantum chemical calculations were carried out in order to evaluate the spatial distributions and energies of the HOMO and LUMO orbitals and whether or not rotations (TICTs) about either the phenyl-1,3-thiazole bonds or the phenyl-amine bonds in the excited states, leading to charge

separation, occur. It was found here that the S_1 states are sufficiently stabilized by a polar solvent after planarization along the phenyl-1,3-thiazole bonds, which leads to slightly broadened and red-shifted emission bands, as observed in the UV/Vis measurements. It is noteworthy that no concentration dependencies of either the absorption or the emission spectra were observed, ruling out excimer formation. The bathochromic shifts of the emission are also accompanied by decreased quantum yields and increased emission lifetimes (no clear trend of τ_F was observed for **A1**, unlike for **D2**). Two possible apparently conflictive assumptions can be made to explain this behavior: i) stabilization of the excited state from polar solvent molecules might raise the energy barrier (increased “activation” energy) for the deactivation process (in polar solvents the CT state directly decays radiationlessly to the ground state by the back CT reaction), leading to an increase in τ_F .^[31] or ii) various nonradiative quenching processes might be accessible due to additional conformational twists.^[30a] The first is consistent with the τ_F measured for **D2**. The second fact was described and discussed in detail by Hu et al. for dyes bearing additional dimethylamino groups on their arylamine donor components (similar to **A3**).^[30b] It is assumed that the *p*-dimethylamino (or for **A2** the *p*-methoxy) groups give rise to additional rotatable junctions and radiationless deactivation pathways if the charge-separated states are sufficiently stabilized by polar solvent molecules. The latter explanation would also be consistent with the significantly decreased Φ_F and τ_F values and the lack of emission of the triarylamines in which the donor component is a *p*-dimethylamino, *p*-anisole, or even *p*-tolyl system rather than a phenyl group, as described above. Additionally, it is noteworthy that no wavelength dependency of τ_F was observed in the transient emission spectroscopy for **A2** and **D1** in heptane, ruling out second emissive states (dual fluorescence).

Electronic Absorption Spectra of the Ru^{II} Complexes

The studied complexes each show several intense absorption bands due to the different possible electronic transitions of Ru^{II} polypyridyl complexes. The spectra are shown in Figure 4 and the data are summarized in Table 5. The high-energy bands at 258 nm can be assigned to spin-allowed metal-to-ligand charge-transfer (MLCT) transitions. The intense ligand-centered (LC) π – π^* transitions ($\epsilon > 65000 \text{ M}^{-1} \text{ cm}^{-1}$) of the two dmbpy ligands are located at 285 nm. The high-energy LC transitions of the triarylamines **A1–C2** can be observed at approximately 325 nm, and they are presumably superimposed with weak metal-centered (MC) transitions.^[9a]

The broad absorption bands of the complexes in the visible region at 400–600 nm are due to MLCT transitions and LC transitions of the thiazole-based ligands. It is not possible to assign any distinct transition to these broad featureless bands ($\epsilon > 28000 \text{ M}^{-1} \text{ cm}^{-1}$) for the complexes **Ru1–Ru4**. For **Ru5–Ru7** the different transitions are better resolved. The bands of the LC transitions for **Ru5**, **Ru6**, and **Ru7** are

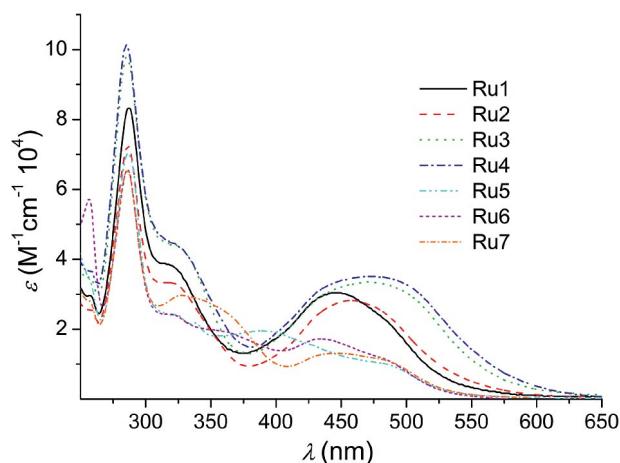


Figure 4. Absorption spectra of the complexes measured in CH_3CN at room temp.

Table 5. Spectroscopic properties of the complexes measured in CH_3CN at room temp.

	λ_{abs} [nm] [log ϵ]	λ_{em} [nm] ^[a]
Ru1	258 [4.47], 287 [4.92], 319 [4.59], 447 [4.48]	606, 689
Ru2	258 [4.41], 286 [4.86], 324 [4.52], 457 [4.45]	619, 710
Ru3	258 [4.54], 285 [4.99], 326 [4.64], 471 [4.53]	629, 727
Ru4	258 [4.57], 285 [5.00], 328 [4.63], 473 [4.55]	627, 736
Ru5	258 [4.52], 286 [4.85], 389 [4.29], 486 [4.00]	676
Ru6	286 [4.82], 362 [4.29], 434 [4.24], 485 [4.05]	679
Ru7	286 [4.82], 327 [4.47], 446 [4.12], 483 [4.05]	667

[a] Measured in ethanol/methanol (4:1, v/v) glass at 77 K after excitation at 450 nm.

located at 390, 370, and 360 nm (broad), respectively. This is in accordance with the absorption maxima of the free ligands and leads to the conclusion that the longest-wavelength ligand-based CT transitions are marginally affected by complexation. The bands of the MLCT transitions to the dmbpy ligand are located at approx. 435 nm. Unlike those for **Ru1–Ru4**, the MLCT bands for the three complexes **Ru5–Ru7** are acceptably resolved and each display an additional shoulder located at 490 nm. This can be explained by absorption into two different ¹MLCT states caused by the presence of two different ligands (the thiazole-based and the dmbpy ligands).^[36]

In conclusion, as a result of the complexation of the additional light-absorbing ligands, leading to several intense bands in the absorption spectra of the complexes superimposed with the “classic” transitions, the complexes show enhanced light-harvesting efficiencies in the UV/Vis and visible regions of the solar spectrum.

Unlike the very similar thiazole-based complexes described in the literature,^[8] the compounds do not show any room temperature emission, so emission spectroscopy was carried out in EtOH/MeOH (4:1, v/v) glass at 77 K. The measured complexes each exhibit emission between 606 and 736 nm. For complexes **Ru1–Ru4**, with the triarylamine-based ligands, two different main emission bands can be observed in each case, whereas for **Ru5–Ru7** only one main emission band is present. The emission spectra of **Ru1**, **Ru2**,

Ru5, and **Ru6** are shown as representative examples in Figure 5. The unexpected behavior of **Ru1–Ru4**, although it violates Kasha’s rule, is not new (especially at a temperature of 77 K) and has been described in the literature. Two possible mechanisms have been discussed as an explanation. Firstly, two emitting ³MLCT states might be present, as documented for, for example, heteroleptic Ru^{II} complexes containing two bpy and one 2,3-bis(2-pyridyl)pyrazine ligand^[37] or two bpy and different phenanthroline-based ligands^[38] or for acetylene-linked dinuclear Ru^{II} complexes.^[39] This behavior can usually be assigned only by time-resolved emission dynamics measurements, due to the superimposition of the two emission bands. Secondly, one emitting ³MLCT and one emitting ligand localized triplet excited state (³IL) might be present, as extensively discussed in a review by Wang et al.^[40]

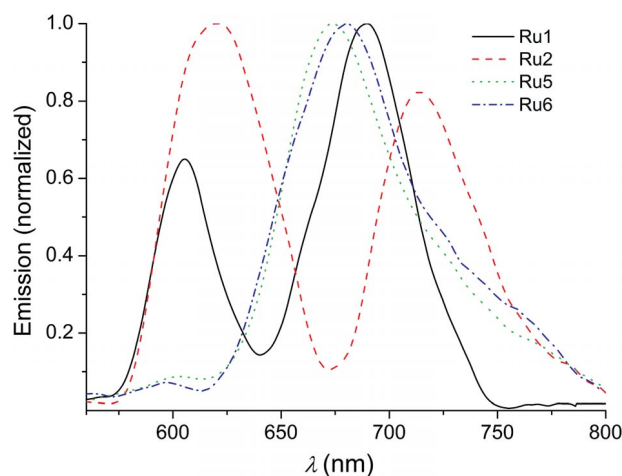


Figure 5. Emission spectra of the heteroleptic Ru^{II} complexes **Ru1**, **Ru2**, **Ru5**, and **Ru6** in ethanol/methanol (4:1, v/v) glass at 77 K.

In the cases of the complexes **Ru1–Ru4** the two bands are well resolved. Excitation at 400 nm leads in each case to an increase in the intensity of the higher-energy emission at approx. 620 nm whereas excitation at the longest-wavelength absorption >500 nm leads to an increase in the lower-energy emission band at approx. 710 nm. Two different emitting states separated by a distinct energy barrier are populated in a manner dependent on the excitation wavelength, as was also supported by measurement of excitation spectra. We assume that one of these emissive states is of ³MLCT character and is localized on a dmbpy–Ru pair and that the other is the lower-energy ³MLCT state localized on the thiazole–Ru pair and not a ³IL state. The latter assumption is also supported by measurement of the emission spectra of the ligands. The locations and differences of the maxima of/and between the ligands do not fit with either the short- or the long-wave emissions of the complexes. Nonetheless, unambiguous assignment will be the subject of further time-dependent measurements carried out at 77 K. For the complexes **Ru5–Ru7** only one broad emission band is apparent in each case. Presumably the energies of the two possible ³MLCT states are too close, which

would lead to superimposed emission bands, in contrast with the absorption spectra, in which the two different ¹MLCT transitions are well resolved.

Quantum Chemical Calculations on A1 and D1

In order to gain more detailed insight into the structural and the spectroscopic properties of **D1** and **A2**, density functional theory (DFT) and its time-dependent variant (TDDFT)^[41] were applied. The influence of solvation was studied for an apolar (heptane, $\epsilon = 1.9113$, $n = 1.3878$) and a polar (MeOH, $\epsilon = 32.613$, $n = 1.3288$) solvent with use of a polarized continuum model.^[42] All calculations were performed with the GAUSSIAN 09 program.^[43] The ground-state equilibrium structures of **A2** and **D1** were optimized with a functional based on B3LYP^[44] and denoted as B3LYP(35),^[45] combining 35% of exact exchange, 58.5% of non-local B88^[46] exchange, and the LYP correlation along with the 6–31G(d,p) double- ξ basis set.^[47] Harmonic vibrational frequencies at the same level of theory confirmed that the obtained stationary points corresponded to the minima of the potential energy surfaces (PESs). Excited state properties, such as excitation energies, oscillator strengths, and excited states geometries, were computed by use of TDDFT and the same exchange-correlation functional and basis set as for the ground states. The absorption spectra in the Franck–Condon (FC) region were simulated from the first ten singlet excited states. The S_1 states were optimized to obtain the emission energies. Furthermore, PESs of the S_0 and the S_1 states of **A2** were generated along the dihedral angle δ_4 (starting from the optimized S_1 geometries for heptane and MeOH), describing the internal torsion of the donor group (for a graphic representation of the angles see Scheme S6 in the Supporting Information) in order to study the presence of a TICT state in the S_1 state. The PESs were calculated with rotation of the phenyl group with respect to the bis(4-methoxyphenyl)-*N*-phenylaniline moiety with a step size of 2° and at the same level of theory as the previous calculations.

The ground-state equilibrium geometries of both molecules exhibit similar structural features, as shown in Table 6 and Figure 6. The *trans* isomer of the thiazole-pyridine moiety is in each case energetically favored over the *cis* isomer by approximately 0.3 eV in heptane and by 0.2 eV in MeOH. As can be seen from the dihedral angles, the 4-methoxy-1,3-thiazole fragment adopts a configuration almost planar to the pyridine. The angle δ_2 describes the torsion around the C–C bond between the thiazole fragment and the donor moiety. It was found that δ_2 is almost independent both of the donor group [carbazole and bis(4-methoxyphenyl)-*N*-phenylaniline] and of the solvent (for **A2** $\delta_2 = 18^\circ$ in heptane and 19° in MeOH, whereas for **D1** $\delta_2 = 17^\circ$ in both solvents). The phenyl groups of the donor in both dyes are twisted out of planarity due to steric hindrance. This twisting is in the range of ca. 30°, as illustrated by the angles δ_3 and δ_4 in **A2**. The torsion of the carbazole in the case of **D1** is significantly more pronounced ($\delta_3 =$

56°), whereas the carbazole is completely planar. In general, and consistently with the results of the solvent-dependent UV/Vis measurements, the ground-state structures of **A2** and **D1** are basically invariant to solvation. The optimized geometries of the S_1 states show similarities to the ground-state equilibrium structures. The reason is the π – π^* nature of the S_1 states and the partial occupation of the LUMOs; the excited-state structures therefore show only minor shifts in bond lengths and angles. The thiazole-phenyl fragments, however, are planarized ($\delta_2 \approx -1^\circ$ for **A2** and 2° for **D1**) as

Table 6. Calculated torsion angles and dipole moments of the ground (S_0) and first excited (S_1) states of **A2** and **D1**.

Geom.	Solvent	δ_1 [°]	δ_2 [°]	δ_3 [°]	δ_4 [°]	μ [D]
A2						
S_0	heptane	0.32	–17.99	30.61	31.56	1.37
	MeOH	0.34	–19.01	28.09	29.67	1.55
S_1	heptane	–0.43	–1.19	39.11	38.30	1.58
	MeOH	–0.32	–1.58	32.68	32.10	2.62
D1						
S_0	heptane	0.03	–16.65	56.42	–0.09	5.38
	MeOH	0.00	–17.32	56.54	–0.12	6.12
S_1	heptane	–0.22	–2.22	44.39	–0.09	4.64
	MeOH	–0.27	–2.02	45.46	0.00	5.22

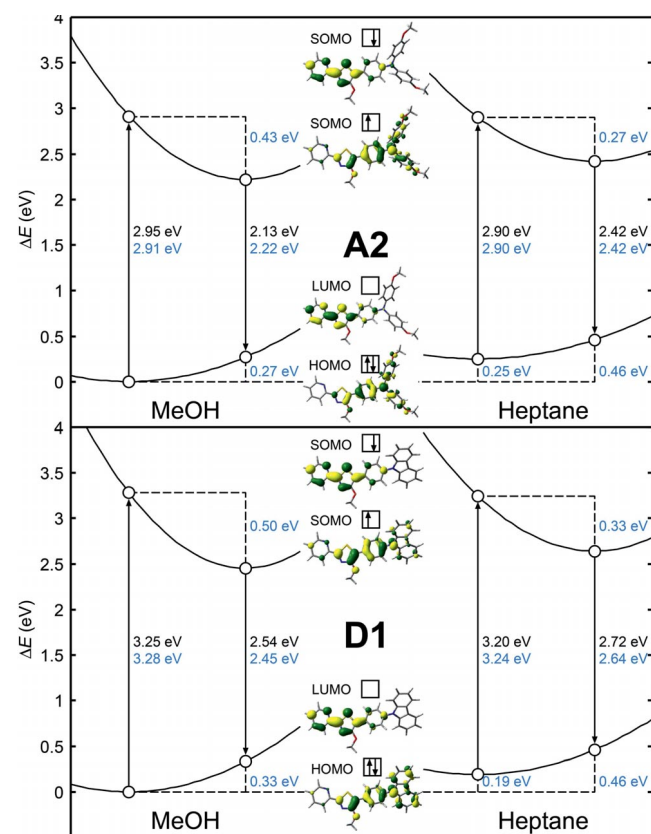


Figure 6. Potential curves, representations of the HOMO, LUMO, and SOMO orbitals, and energies of the S_0 and S_1 states before and after stabilization through either heptane or MeOH solvent molecules and experimentally determined (upper values of the absorption and emission energies) and calculated energies.

a result of the bonding characters of the LUMOs in these positions. Additionally, the torsions in the donor groups are slightly changed. In the case of **D1**, the angle δ_3 decreases by approximately 12 to 44° in heptane and to 45° in MeOH. This supports the assumption that excitation leads to a PICT and not a TICT state.

The absorption spectra of the two dyes were calculated by using FC geometries and the first ten singlet excited states. Table 7 lists the vertical and adiabatic S_1 excitations for the compounds in both solvents. A summary of the photophysical properties and a representation of the orbitals of the higher excited singlet states are given in Schemes S7–S10 in the Supporting Information. The S_1 state of **D1** is mainly characterized by a π – π^* excitation with significant CT participation predominantly from the carbazole donor (HOMO) to the thiazole/pyridine acceptor (LUMO). The ratio of this transition in heptane is 87% and it is slightly enhanced to 89% in MeOH. An additional π – π^* transition of **D1** from the HOMO–1 to the LUMO shows a significant weight of 11% (heptane) and 9% (MeOH).

Table 7. Calculated absorption/emission properties to/from the first singlet excited states S_1 . Main contributions to the wave function (weight), vertical (absorption) or adiabatic (emission) excitation energies (ΔE^v in eV and nm), oscillator strengths (f), and deviations from experimental results ($\Delta\Delta E_{\text{exp}}$). H: HOMO, L: LUMO.

Solvent	Transition	Weight [%]	ΔE^v [eV]	λ [nm]	f	$\Delta\Delta E_{\text{exp}}$ [eV]	
A2							
Abs.	heptane	H→L	94	2.90	428	1.021	0.00
		H–1→L	4				
	MeOH	H→L	94	2.91	426	1.006	–0.04
		H–1→L	4				
Em.	heptane	H←L	96	2.42	512	1.088	0.00
	MeOH	H←L	96	2.22	559	1.341	0.09
D1							
Abs.	heptane	H→L	87	3.24	382	0.986	0.04
		H–1→L	11				
	MeOH	H→L	89	3.28	378	0.995	0.03
		H–1→L	9				
Em.	heptane	H←L	97	2.64	469	1.137	–0.08
	MeOH	H←L	97	2.45	506	1.306	–0.09

The HOMO–1/LUMO transition has a less pronounced CT character than the HOMO/LUMO transition, because the HOMO–1 is delocalized over the entire molecule. On the other hand, the S_1 state of **A2** has a weighting of 94% in favor of the HOMO/LUMO transition (heptane and MeOH), whereas the HOMO–1/LUMO transition only has a weighting of 4%.

In conclusion, the S_1 state of **A2** has a more pronounced CT character than that of **D1**. The wavelength dependency of the first absorption band on solvent polarities is in very good agreement with the experimental findings (Table 7, Figure 6). The excitation energies of the S_1 states are marginally overestimated by 0.04 eV or underestimated by –0.04 eV, respectively, showing that the B3LYP(35) func-

tional is very well suited to describe the CT in these dyes in both polar and apolar solvents. Comparison of the oscillator strengths (f) with the experimentally observed ϵ values shows that they are constant for **A2** and **D1** in both solvents. The trend of decreasing ϵ values with increasing solvent polarity was also reproduced in the electronic structure calculations.

The adiabatic emission spectra were obtained by use of the optimized geometries of the first excited singlet states. The vertical emissions to the S_0 were calculated by use of these structures. The fluorescence energies, measured and simulated, are listed in Table 7. The energies obtained are in excellent agreement with the experimental findings. In the case of **A2**, the divergences from the simulations to the experimentally determined values are 0.00 (heptane) and 0.09 eV (MeOH), whereas for **D1** they are –0.09 (MeOH) and –0.08 eV (heptane). Relaxation in the S_1 state leads to a wave function with a significantly increased weight of the HOMO/LUMO transition. A similar trend was observed for the two chromophores. In the case of **A2**, the weight, the CT nature of the S_1 state, of the HOMO/LUMO transition increases from 94 to 96%, whereas for **D1** it rises from 87 (heptane) and 89% (MeOH) to 97% in both solvents. This can be explained in terms of the planarization in the dihedral angle δ_2 , which leads to a greater amount of CT character for this transition. The energy of the S_1 state is substantially dependent on the solvent; the polar solvent stabilizes the excited state considerably, by 0.43 and 0.50 eV for **A2** and **D1**, respectively, whereas the apolar solvent stabilizes the S_1 by only 0.27 and 0.33 eV, respectively. The significant difference in the emission energies in heptane and in MeOH can be explained in terms of the enhanced weight of the HOMO/LUMO transition in the S_1 wave function of the planarized geometry.

Further investigations were carried out in order to study the likelihood of PICT or TICT states. The optimization in the S_1 states did not affect the arrangements of the donor groups drastically (see δ_3 and δ_4), leading to the conclusion that no TICT state is observed in these dyes. However, the TICT is not connected to a barrier-free evolution in the excited state PES, as described in the literature, so a scan of the S_0 and the S_1 states around the dihedral angle δ_4 was performed for the chromophore **A2**. The PESs obtained for both solvents are depicted in Figure 7. The minima of the ground states in both solvents are found at approx. 30 and 210°. These minima are separated by barriers of 1.87 (MeOH) and even 2.55 eV (heptane). The excited state PESs show similar behavior: the minima here are located at ca. 34 (MeOH) and 38° (heptane), values consistent with the angles in the optimized S_1 geometries of **A2**. The PESs of the S_1 state are almost parallel to those of the electronic ground state and no evidence for a minimum at 90° was found. In order to support this statement an additional optimization procedure was performed with a starting torsion of δ_4 of 90°. However, the obtained structure evolved to that of the optimized geometry at the FC region. In summary, the appearance of a TICT state in this chromophore can be excluded from the quantum chemical calculations.

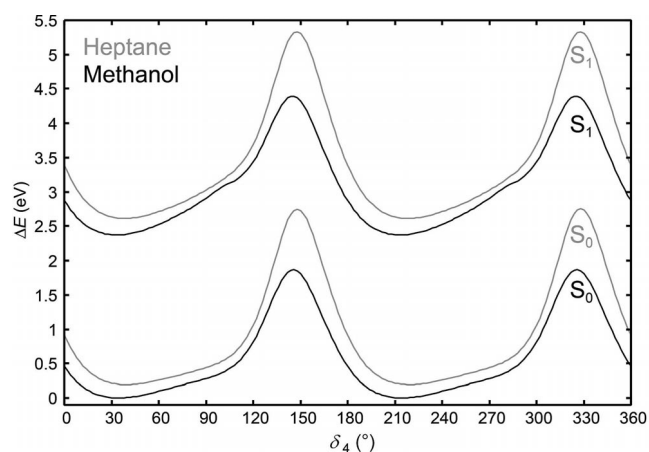


Figure 7. Scan around the dihedral angle δ_4 for **A2**.

Electrochemical Properties of the Dyes

Electrochemical measurements were carried out with CH_3CN as solvent, with platinum as counter, Ag/AgCl as reference, and carbon as working electrodes, and with tetrabutylammonium hexafluorophosphate (TBAPF_6) as the conducting salt (scan rate 0.2 V s^{-1}). Ferrocene was added as the internal standard after every measurement. All values discussed here are relative to the Fc/Fc^+ redox couple and the data are listed in Table 8. The cyclic voltammetry (CV) spectra of **A1–A3** are depicted as representative examples in Figure 8 (spectra of the other compounds can be found in Scheme S11 in the Supporting Information). For these types of compounds it is known that the first oxidations occur at the triarylamine components, leading to the formation of positively charged cation species.^[48] Each dye therefore shows a first reversible oxidation wave that is strongly

influenced by the electronic properties of the arylamine. No reactions of the radical cations or dication of the triarylamines to form σ -dimers with additional discharging waves at more negative potentials (at ca. -1.0 V) or carbazole derivatives with additional discharging waves at 0.7 V were detected under the conditions used.^[49] The half-wave potentials ($E_{1/2}$) of the first oxidation are 0.23 – 0.26 V for the arylamines **A2**, **B2**, and **C2**, with the strongly electron-donating 4-methoxyphenyl groups, 0.36 V for arylamine **C1**, with the 4-tolyl substituents, and 0.41 and 0.43 V for the triphenylamines **A1** and **B1**, respectively. For **A3**, with the very strongly electron-donating dimethylamine groups on the arylamine, the oxidation potential is significantly lowered to -0.17 V . This is consistent with the observation that this compound is already oxidized by atmospheric O_2 in solution (CDCl_3 , reduction of the cation radical with Zn in an NMR tube; see Scheme S12 in the Supporting Information). Additionally, **A3** shows a reversible second oxidation wave due to the formation of a doubly-charged quinoid bication at 0.13 V ,^[50] whereas all other triarylamines exhibit second irreversible oxidation waves. The $E_{1/2}$ values for these second oxidations are located in a very small range of 0.66 – 0.77 V and are independent of the triarylamine components. The oxidation wave for the carbazole-derived dye **D1** is completely irreversible, due to the coupling of the cation radical in *para*-position.^[51] The half-wave potential ($E_{1/2}$) is 0.84 V , which is in accordance with examples in the literature.^[52] For the phenothiazine-based dye **D2** the oxidation wave is reversible. The $E_{1/2}$ is 0.31 V vs. Fc/Fc^+ or 0.68 V vs. the reference electrode used (Ag/AgCl , KCl , 0.1 M). This is consistent with the electronically similar arylamine 10-phenylphenothiazine (0.88 V vs. Ag/AgCl , sat. KCl) and with other phenothiazines reported in the literature.^[53]

Table 8. Electrochemical data for the donor–acceptor dyes and the Ru^{II} complexes.

Dye	$E_{1/2,\text{ox}}$ [V] ^[a]	$E_{1/2,\text{red}}$ [V] ^[a]	E^{HOMO} [eV] ^[b]	E^{LUMO} [eV] ^[b]	ΔE^{cv} [eV] ^[b]	$E_{\text{g}}^{\text{opt}}$ [eV] ^[c]
A1	0.41, 0.73 ^[d]	−2.19	−5.19	−2.74	2.45	2.67
A2	0.23, 0.66 ^[d]	−2.23	−5.02	−2.74	2.28	2.57
A3	−0.17, 0.13	−2.25	−4.56	−2.62	1.94	2.42
B1	0.43, 0.77 ^[d]	−1.97	−5.22	−2.96	2.26	2.54
B2	0.26, 0.77 ^[d]	−1.98	−5.06	−2.95	2.11	2.44
C1	0.36, 0.76 ^[d]	−2.03	−5.16	−2.90	2.26	2.51
C2	0.25, 0.77 ^[d]	−2.05	−5.05	−2.88	2.17	2.49
D1	0.84 ^[d]	−2.15	−5.65	−2.78	2.87	2.85
D2	0.31, 1.05 ^[d]	−2.11	−5.09	−2.87	2.22	2.93
D3	0.34, 1.00 ^[d]	−2.14	−5.07	−2.74	2.33	2.92
Complex						
Ru1	0.61, 0.83	−1.58, −1.98, −2.21	−5.37	−3.34	2.03	2.32
Ru2	0.36, 0.83	−1.61, −1.97, −2.20	−5.16	−3.32	1.84	2.25
Ru3	0.52, 0.90	−1.42, −1.95, −2.14	−5.33	−3.52	1.81	2.13
Ru4	0.37, 0.89	−1.44, −1.96, −2.16	−5.14	−3.51	1.63	2.09
Ru5	0.80 ^[d] , 0.85	−1.53, −1.94, −2.18	−5.61	−3.41	2.20	2.39
Ru6	0.33, 0.81	−1.53, −1.97, −2.19	−5.13	−3.41	1.77	2.32
Ru7	0.34, 0.82	−1.52, −1.98, −2.19	−5.07	−3.35	1.72	2.26

[a] Measurements were performed in CH_3CN containing TBAPF_6 (0.1 M). The potentials are given vs. ferrocene/ferrocenium (Fc/Fc^+). [b] Determined by use of $E^{\text{HOMO}} = -(E_{\text{onset, ox}} - E_{\text{onset, Fc/Fc}^+}) - 4.8$ eV and $E^{\text{LUMO}} = -(E_{\text{onset, red}} - E_{\text{onset, Fc/Fc}^+}) - 4.8$ eV.^[59] [c] Estimated from the UV/Vis spectra at 10% of the maximum of the longest-wavelength absorption band on the low-energy side. [d] Derived from differential pulse polarographic measurements; peaks are irreversible.

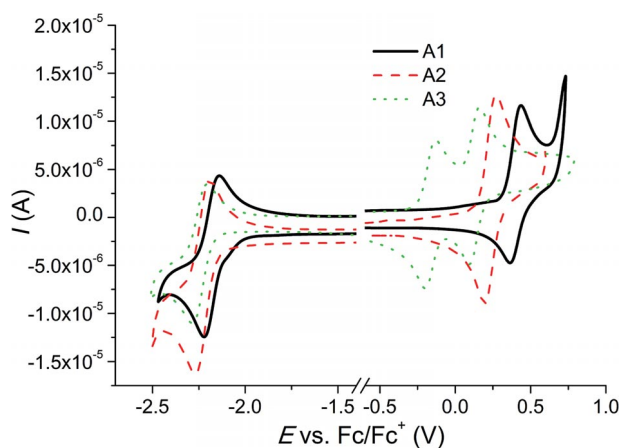


Figure 8. Cyclic voltammetry of dyes **A1**–**A3**. Experimental conditions: 0.1 M TBAPF₆/CH₃CN solution, $c \approx 1 \times 10^{-4}$ M, room temp., scan rate 0.2 V s⁻¹. RE: Ag/AgCl. WE: carbon. AE: platinum.

The first oxidation wave for **D3** is also reversible and is located at 0.34 V, consistently with an oxidation of the phenoxazine.^[54] The similar $E_{1/2}$ values for **D2** and **D3** are in accordance with the very similar electronic behavior of phenothiazine and phenoxazine.^[55] Additionally, **D2** and **D3** each show a second irreversible oxidation wave located at approx. 1.0 V.

All dyes show reversible first reductions. The $E_{1/2}$ values of the first reduction are slightly dependent on the acceptors and not on the arylamines. The redox potentials vary from –2.19 to –2.25 V for the dyes with the pyridine acceptor (**A1**–**A3**). They are shifted to more positive potentials (the reduction is facilitated) when the electron deficiency of the acceptor is increased. The reductions occur at ca. –1.97 V for the dyes **B1** and **B2** and at –2.03 and –2.05 V for **C1** and **C2**, respectively. It can therefore be assumed that the reductions each take place at the acceptor, leading to a negatively charged azabenzene, as described in the literature.^[56] Irreversible reduction due to proton abstraction of the radical anion from residual water, to form a free radical that would be immediately reduced at the potential of its formation,^[57] was not observed (the measurements were carried out under water-free conditions).

Electrochemical Properties of the Ru^{II} Complexes

The complexes **Ru1**–**Ru7** were characterized by CV under the same conditions as discussed above. The electrochemical results are presented in Table 8 and the spectra of **Ru1**, **Ru2**, **Ru5**, and **Ru6** are given as representative examples in Figure 9 (spectra of the other compounds can be found in Scheme S13 in the Supporting Information). They each show two reversible oxidation waves (except **Ru5**) and three reversible reduction waves. The former can be attributed to oxidation of the arylamines and of the Ru^{II} ruthenium center to Ru^{III}.^[58] The oxidations of the arylamines of the coordinated ligands are marginally shifted towards higher potentials relative to the free dyes, confirming the assumption that the corresponding ligand-centered π -orbitals are low-

ered in energy after complexation. The Ru^{II}/Ru^{III} oxidations are shifted slightly towards higher potentials for the thiazoles with pyrimidine rather than pyridine acceptor moieties, due to the more strongly electron-accepting properties of the pyrimidine, lowering the energies of the t_{2g} orbitals. The three reversible reduction waves are well resolved in each case and are located at approx. –1.42 to –1.61, –2.0, and –2.2 V. No clear trend is obvious, and assignment to reduction of the ligand-located antibonding π^* -orbitals of either a thiazole or dmbpy ligand would be tentative. Additionally, behavior similar to that of **A3** was found for the complex **Ru4**. The signals of the arylamine protons are extremely broadened in the ¹H NMR spectra due to partial formation of the radical cation in aerated CD₃CN solution (see Scheme S14 in the Supporting Information). The signals became well resolved after the addition of Zn and reduction of the cation radical.

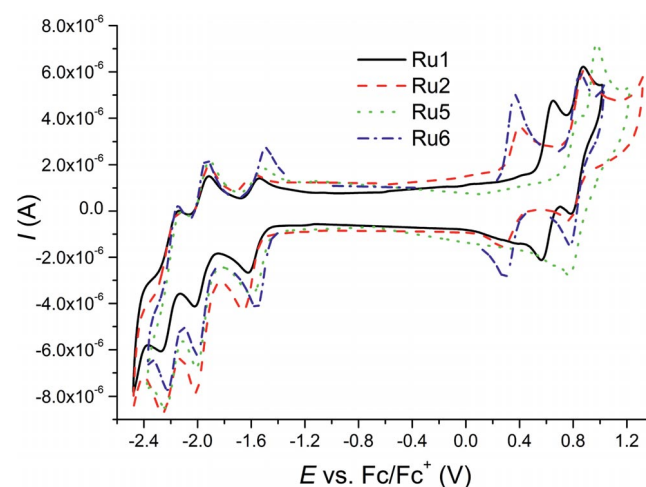


Figure 9. Cyclic voltammetry of **Ru1**, **Ru2**, **Ru5**, and **Ru6**. Experimental conditions: 0.1 M TBAPF₆/CH₃CN solution, $c \approx 5 \times 10^{-5}$ M, room temp., scan rate 0.2 V s⁻¹. RE: Ag/AgCl. WE: carbon. AE: platinum.

Conclusions

A series of donor–acceptor dyes featuring different arylamines moieties as electron donating units have been successfully prepared by a Buchwald–Hartwig cross-coupling approach. Different azaheterocycles were employed as acceptor moieties. The spectroscopic and electrochemical properties, as well as the HOMO/LUMO gaps, of these dipolar compounds are significantly affected by the different donors used. The natures of the intramolecular charge-transfer states were identified as PICT processes for one of the triarylamine-based (**A2**) and one of the tricyclic arylamine dyes (**D1**) with the aid of spectroscopic methods and quantum chemical calculations. Furthermore, the absorption and emission spectra and energies of the transitions, oscillator strengths, and weights were calculated for the optimized ground- and excited-state structures of these two dyes. The synthesis and characterization of the corresponding Ru^{II} polypyridyl complexes of seven of the dyes/ligands

are reported. Each complex shows an enhanced absorption in the visible part of the UV/Vis spectrum, due to additional LC and MLCT transitions originating from 4-methoxy-1,3-thiazole ligands. All compounds were unambiguously identified by NMR spectroscopy, elemental analysis, mass spectrometry, and MALDI-TOF measurements. Further research into the presented dyes will focus on the synthesis of the analogous Ru(dcbpy)(L)(SCN)₂ (dcbpy = 2,2'-bipyridine-4,4'-dicarboxylic acid) for DSSC applications. The dyes will also be tested with regard to their two-photon excitation behavior, which could open doorways to several new applications such as two-photon excitation microscopy. First tests established this ability for a dye with a methoxy donor group similar to **A1**.

Experimental Section

Ethyl 2-bromo-2-(4-nitrophenyl)acetate and 5-(4-bromophenyl)-2-(pyridin-2-yl)thiazol-4-ol (**1d**) were synthesized by literature procedures.^[18–19] Pyridine-2-carbothioamide, pyrazine-2-carbothioamide, and pyrimidine-2-carbothioamide are commercially available or can be prepared from the corresponding nitriles and H₂S. Pd(dba)₂ and P(*t*Bu)₃ (1 M solution in toluene) were purchased from Sigma–Aldrich. Ru(dmbpy)₂Cl₂ was prepared with use of microwave irradiation by a literature procedure and was readily purified by column chromatography (Al₂O₃ activity 10, CH₂Cl₂ to CH₂Cl₂/MeOH 50:1 as eluent).^[60] All other chemicals used were reagent grade and purchased from Sigma–Aldrich or Acros. Solvents were purified by standard procedures. Solvents for UV/Vis, emission spectroscopy, and CV were of analytical grade and bought from Sigma–Aldrich. ¹H and ¹³C NMR and the corresponding correlation spectra were recorded with Bruker AC-250 (250 MHz) and AC-400 (400 MHz) spectrometers. Chemical shifts (δ) are given relative to solvents. UV/Vis data for the compounds were collected with a Lambda 19 instrument from Perkin–Elmer and emission spectra were measured with a Jasco FP 6500 instrument. Quantum yields were determined relative to fluorescein (NaOH, 0.1 M, $\Phi_F = 0.82$) with refractive indices $n(\text{NaOH}) = 1.334$ and $n(\text{CH}_3\text{CN}) = 1.344$.^[35d] Elemental analysis was carried out with a Leco CHNS-932 instrument. Mass spectra were measured either with a Finnigan MAT SSQ 710 (EI) or a MAZ 95 XL (FAB) system. MALDI-TOF MS was performed with a Bruker Ultraflex TOF/TOF mass spectrometer fitted with a 337 nm nitrogen laser operated in the reflectron mode with an acceleration voltage of 25 kV. Dithranol was used as matrix. Electrochemical measurements were performed with a Metrohm Autolab PGSTAT30 potentiostat with a standard three-electrode configuration. The experiments were carried out in degassed solvents containing Bu₄NPF₆ salt (0.1 M). At the end of each measurement ferrocene (Fc/Fc⁺) was added as an internal standard. TLC materials were from Merck (Polygram SIL G/UV254, aluminum oxide 60 F254). The material for column chromatography was also obtained from Merck (silica gel 60).

Structure Determinations: The intensity data for the compounds were collected with a Nonius KappaCCD diffractometer and use of graphite-monochromated Mo-K α radiation. Data were corrected for Lorentz and polarization effects but not for absorption effects.^[61] The structures were solved by direct methods (SHELXS)^[62] and refined by full-matrix, least-squares techniques against F_o^2 (SHELXL-97).^[62] The hydrogen atoms of **B1** (without the methyl group hydrogen atoms at C4), **C1**, and **D2** and the amine hydrogen atom at N3 of **A1m** were located by difference

Fourier synthesis and refined isotropically. The hydrogen atoms of **A1** and **A1m** were included at calculated positions with fixed thermal parameters. All non-hydrogen atoms were refined anisotropically.^[62] Crystallographic data and structure solution and refinement details are summarized in Table 1. XP (SIEMENS Analytical X-ray Instruments, Inc.) was used for structure representations. CCDC-876513 (for **A1**), -879865 (for **A1m**), -876514 (for **B1**), -876515 (for **C1**), and -876516 (for **D2**) contain the supplementary crystallographic data for this paper. These data can be obtained free of charge from The Cambridge Crystallographic Data Centre via www.ccdc.cam.ac.uk/data_request/cif.

5-(4-Nitrophenyl)-2-(pyridin-2-yl)thiazol-4-ol (1a): A suspension of pyridine-2-carbothioamide (1.00 g, 7.24 mmol), ethyl 2-bromo-2-(4-nitrophenyl)acetate (2.50 g, 8.68 mmol, 1.2 equiv.), and pyridine (8.58 g, 10.8 mmol, 2 equiv.) in toluene (100 mL) was stirred under reflux for six hours and a yellow fluffy precipitate was produced. After the system had cooled to room temperature, the precipitate was filtered off, washed with EtOH and Et₂O, and dried in vacuo; yield 3.05 g (10.2 mmol, 71%). ¹H NMR (400 MHz, [D₆]DMSO): $\delta = 12.44$ (s, 1 H), 8.65 (d, $J = 4.4$ Hz, 1 H), 8.24 (d, $J = 8.9$ Hz, 2 H), 8.07–7.94 (m, 4 H), 7.52 (t, $J = 5.5$ Hz, 1 H) ppm. ¹³C NMR (100 MHz, [D₆]DMSO): 164.0, 161.6, 150.4, 150.0, 145.0, 139.5, 138.4, 126.7, 126.0, 124.7, 119.3, 108.8 ppm. UV/Vis (DMSO): λ_{max} [log($\epsilon/\text{M}^{-1}\text{cm}^{-1}$)] = 414 [4.40], 609 [3.64] nm. MS (EI): m/z (%) = 299 (100) [M]⁺, 105 (30). C₁₄H₉N₃O₃S (299.30): calcd. C 56.18, H 3.03, N 14.04, S 10.71; found C 56.17, H 3.13, N 13.99, S 10.60.

5-(4-Nitrophenyl)-2-(pyrazin-2-yl)thiazol-4-ol (1b): A solution of pyrazine-2-carbothioamide (3.75 g, 26.9 mmol), ethyl 2-bromo-2-(4-nitrophenyl)acetate (9.30 g, 32.3 mmol, 1.2 equiv.), and pyridine (4.25 g, 53.8 mmol, 2 equiv.) in DMF (100 mL) was stirred at 50 °C for 24 h and a yellow precipitate was produced. After the system had cooled to room temperature, the mixture was diluted with EtOH (100 mL). The precipitate was filtered off, washed with EtOH and Et₂O, and dried in vacuo; yield 2.95 g (9.83 mmol, 37%). ¹H NMR (250 MHz, [D₆]DMSO): $\delta = 12.30$ (s, $J = 5.9$ Hz, 1 H), 9.22 (s, 1 H), 8.73 (d, $J = 13.4$ Hz, 2 H), 8.25 (d, $J = 7.9$ Hz, 2 H), 8.04 (d, $J = 8.9$ Hz, 2 H) ppm. ¹³C NMR (63 MHz, [D₆]DMSO): $\delta = 160.91$, 160.34, 145.64, 144.99, 144.85, 144.23, 139.75, 138.20, 126.29, 123.75, 109.40 ppm. UV/Vis (DMSO): λ_{max} [log($\epsilon/\text{M}^{-1}\text{cm}^{-1}$)] = 419 [4.20] nm. MS (EI): m/z (%) = 300 (60) [M]⁺, 106 (100). C₁₃H₈N₄O₃S (300.29): calcd. C 52.00, H 2.69, N 18.66, S 10.68; found C 52.24, H 2.71, N 18.34, S 10.52.

5-(4-Nitrophenyl)-2-(pyrimidin-2-yl)thiazol-4-ol (1c): A mixture of pyrimidine-2-carbothioamide (2.60 g, 18.7 mmol), ethyl 2-bromo-2-(4-nitrophenyl)acetate (6.46 g, 22.4 mmol, 1.2 equiv.), and triethylamine (10 mL) was stirred at room temperature. The suspension solidified after a few minutes and was allowed to react for 24 h. The mixture was suspended in EtOH (100 mL). The precipitate was filtered off, washed with EtOH and Et₂O, and dried in vacuo; yield 1.12 g (3.73 mmol, 18%). ¹H NMR (400 MHz, [D₆]DMSO): $\delta = 12.34$ (s, 1 H), 8.92 (d, $J = 4.8$ Hz, 2 H), 8.25 (d, $J = 8.9$ Hz, 2 H), 8.05 (d, $J = 8.9$ Hz, 2 H), 7.55 (t, $J = 4.8$ Hz, 1 H) ppm. ¹³C NMR (100 MHz, [D₆]DMSO): $\delta = 161.28$, 160.61, 157.97, 157.67, 144.85, 138.35, 126.32, 123.76, 121.20, 109.89 ppm. UV/Vis (DMSO): λ_{max} [log($\epsilon/\text{M}^{-1}\text{cm}^{-1}$)] = 412 [4.10] nm. MS (EI): m/z (%) = 300 (60) [M]⁺, 106 (100). C₁₃H₈N₄O₃S (300.29): calcd. C 52.00, H 2.69, N 18.66, S 10.68; found C 51.64, H 2.81, N 18.54, S 10.72.

General procedure, illustrated for **2a**, for the etherification of the 4-hydroxy-1,3-thiazoles:

4-Methoxy-5-(4-nitrophenyl)-2-(pyridin-2-yl)thiazole (2a): A mixture of 5-(4-nitrophenyl)-2-(pyridin-2-yl)thiazol-4-ol (4.00 g, 13.4 mmol) and K₂CO₃ (2.22 g, 16.1 mmol, 1.2 equiv.) in DMSO

(100 mL) was stirred for 30 min, followed by the addition of CH₃I (2.09 g, 14.7 mmol, 1.1 equiv.). The deep blue mixture was stirred for 24 h at room temperature. The solution was poured into H₂O (300 mL) and extracted with CHCl₃ (3 × 100 mL). The combined organic phases were additionally washed with H₂O (3 × 100 mL) to remove the DMSO, dried with MgSO₄, and concentrated in vacuo to give a brown oil, which was further purified by a short gel filtration (silica, CHCl₃ to CHCl₃/EtOAc 1:1) to yield the product as an orange solid; yield 2.86 g (9.11 mmol, 68%). ¹H NMR (250 MHz, CDCl₃): δ = 8.61 (d, *J* = 4.2 Hz, 1 H), 8.26–8.18 (m, 2 H), 8.15 (d, *J* = 7.9 Hz, 1 H), 7.96–7.87 (m, 2 H), 7.81 (td, *J* = 7.7, 1.7 Hz, 1 H), 7.35 (ddd, *J* = 7.5, 4.8, 1.1 Hz, 1 H), 4.25 (s, 3 H) ppm. ¹³C NMR (63 MHz, CDCl₃): δ = 163.44, 161.57, 150.65, 149.60, 145.46, 138.63, 137.03, 126.67, 124.85, 124.12, 119.31, 111.62, 57.89 ppm. UV/Vis (CH₂Cl₂): λ_{max} [log(ε/M⁻¹cm⁻¹)] = 226 [4.05], 399 [4.49] nm. MS (EI): *m/z* (%) = 313 (100) [M]⁺, 166 (45). C₁₅H₁₁N₃O₃S (313.33): calcd. C 57.70, H 3.54, N 13.32, S 10.23; found C 57.70, H 3.86, N 13.32, S 10.19.

4-Methoxy-5-(4-nitrophenyl)-2-(pyrazin-2-yl)thiazole (2b): The procedure was similar to that used for **2a**, with purification by recrystallization from EtOH/CHCl₃ with slow evaporation of the CHCl₃ to give the product as yellow needles; yield 45%. ¹H NMR (250 MHz, CDCl₃): δ = 9.38 (d, *J* = 1.4 Hz, 1 H), 8.62 (d, *J* = 2.5 Hz, 1 H), 8.58–8.53 (m, 1 H), 8.28–8.19 (m, 2 H), 7.98–7.88 (m, 2 H), 4.28 (s, 3 H) ppm. ¹³C NMR (63 MHz, CDCl₃): δ = 162.00, 160.55, 146.31, 145.97, 145.53, 144.14, 141.26, 138.22, 127.08, 124.32, 112.98, 58.27 ppm. UV/Vis (CH₃CN): λ_{max} [log(ε/M⁻¹cm⁻¹)] = 245 [3.97], 403 [4.46] nm. MS (EI): *m/z* (%) = 314 (100) [M]⁺, 166 (30). C₁₄H₁₀N₄O₃S (314.32): calcd. C 53.50, H 3.21, N 17.82, S 10.20; found C 53.18, H 3.12, N 18.08, S 10.13.

4-Methoxy-5-(4-nitrophenyl)-2-(pyrimidin-2-yl)thiazole (2c): Yield 44%. ¹H NMR (300 MHz, CDCl₃): δ = 8.84 (d, *J* = 4.5 Hz, 2 H), 8.19 (d, *J* = 8.3 Hz, 2 H), 7.91 (d, *J* = 8.3 Hz, 2 H), 7.30 (t, *J* = 4.5 Hz, 1 H), 4.30 (s, 3 H) ppm. ¹³C NMR (100 MHz, CDCl₃): δ = 162.16, 160.63, 158.91, 157.76, 145.79, 137.95, 127.00, 124.06, 120.78, 113.95, 58.29 ppm. UV/Vis (CH₃CN): λ_{max} [log(ε/M⁻¹cm⁻¹)] = 232 [4.03], 396 [4.41] nm. MS (EI): *m/z* (%) = 314 (100) [M]⁺, 166 (20). C₁₄H₁₀N₄O₃S (314.32): calcd. C 53.50, H 3.21, N 17.82, S 10.20; found C 53.58, H 3.17, N 17.99, S 10.18.

5-(4-Bromophenyl)-4-methoxy-2-(pyridin-2-yl)thiazole (2d): Yield 77%. ¹H NMR (250 MHz, CDCl₃): δ = 9.15–9.10 (m, 1 H), 8.64 (d, *J* = 4.8 Hz, 1 H), 8.20–8.15 (m, 1 H), 7.61 (dd, *J* = 6.8 Hz, 2 H), 7.51 (dd, *J* = 6.8 Hz, 2 H), 7.39–7.34 (m, 1 H), 4.19 (s, 3 H) ppm. ¹³C NMR (63 MHz, CDCl₃): δ = 160.01, 156.92, 150.67, 146.95, 132.63, 131.72, 130.21, 129.42, 128.26, 123.68, 120.43, 110.9, 57.96 ppm. MS (EI): *m/z* (%) = 346 (45) [M]⁺, 200 (100), 120 (67). C₁₅H₁₁BrN₂O₃S (347.23): calcd. C 51.89, H 3.19, N 8.07, S 9.23; found C 51.64, H 3.23, N 8.24, S 9.42.

General procedure, illustrated for **3a**, for the reduction of the nitro groups to afford the corresponding aniline derivatives:

4-[4-Methoxy-2-(pyridin-2-yl)thiazol-5-yl]aniline (3a): A suspension of 4-methoxy-5-(4-nitrophenyl)-2-(pyridin-2-yl)thiazole (2.66 g, 8.50 mmol) in EtOH (100 mL) was heated to 50 °C. Freshly prepared Raney nickel (catalytic amounts) and N₂H₅OH (several portions approx. 2 equiv. until no starting material was left as indicated by TLC) were added to the solution. The reaction mixture was filtered through a frit on which a silica bed (2 cm thick) had been applied to remove the Raney nickel. The silica bed was washed with EtOH/CHCl₃ 1:1. The product was purified by gradient gel filtration (silica, CHCl₃ to CHCl₃/EtOAc 1:2) to yield the amine as a yellow solid; yield 2.16 g (7.62 mmol, 90%). ¹H NMR (250 MHz, CDCl₃): δ = 3.76 (s, 2 H), 4.15 (s, 3 H), 6.68–6.72 (m, 2 H), 7.24

(dd, *J* = 4.8, 7.5 Hz, 1 H), 7.58–7.60 (m, 2 H), 7.74 (dd, *J* = 7.7, 7.8 Hz, 1 H), 8.10 (d, *J* = 8.0 Hz, 1 H), 8.57 (d, *J* = 4.9 Hz, 1 H) ppm. ¹³C NMR (63 MHz, CDCl₃): δ = 158.63, 158.38, 151.51, 149.37, 145.53, 136.81, 128.28, 123.72, 121.91, 118.77, 115.42, 115.19, 57.58 ppm. UV/Vis (CH₂Cl₂): λ_{max} [log(ε/M⁻¹cm⁻¹)] = 224 [4.01], 277 [3.83], 399 [4.19] nm. MS (EI): *m/z* (%) = 283 (100) [M]⁺, 136 (60). C₁₅H₁₃N₃OS (283.35): calcd. C 63.58, H 4.62, N 14.83, S 11.32; found C 63.20, H 4.57, N 14.60, S 11.19.

4-[4-Methoxy-2-(pyrazin-2-yl)thiazol-5-yl]aniline (3b): Yield 89%. ¹H NMR (300 MHz, CDCl₃): δ = 9.32 (d, *J* = 1.1 Hz, 1 H), 8.51–8.46 (m, 2 H), 7.58 (d, *J* = 8.6 Hz, 2 H), 6.70 (d, *J* = 8.6 Hz, 2 H), 4.17 (s, 3 H), 3.74 (s, 2 H) ppm. ¹³C NMR (75 MHz, CDCl₃): δ = 159.20, 155.24, 147.11, 146.00, 144.16, 143.85, 140.96, 128.52, 121.51, 117.00, 115.25, 57.80 ppm. UV/Vis (CH₃CN): λ_{max} [log(ε/M⁻¹cm⁻¹)] = 259 [4.02], 278 [3.98], 317 [3.68], 420 [4.31] nm. MS (EI): *m/z* (%) = 284 (100) [M]⁺, 136 (80). C₁₄H₁₂N₄O₃S (284.34): calcd. C 59.14, H 4.25, N 19.70, S 11.03; found C 58.84, H 4.18, N 19.52, S 11.08.

4-[4-Methoxy-2-(pyrimidin-2-yl)thiazol-5-yl]aniline (3c): Yield 87%. ¹H NMR (250 MHz, CDCl₃): δ = 8.79 (d, *J* = 4.9 Hz, 2 H), 7.60 (d, *J* = 8.6 Hz, 2 H), 7.20 (t, *J* = 4.8 Hz, 1 H), 6.69 (d, *J* = 8.6 Hz, 2 H), 4.22 (s, 3 H), 3.78 (s, 2 H) ppm. ¹³C NMR (63 MHz, CDCl₃): δ = 159.84, 159.80, 157.84, 155.73, 146.13, 128.73, 128.67, 121.60, 119.97, 115.30, 58.10 ppm. UV/Vis (CH₃CN): λ_{max} [log(ε/M⁻¹cm⁻¹)] = 223 [4.16], 243 [3.99], 275 [3.98], 411 [4.33] nm. MS (EI): *m/z* (%) = 284 (100) [M]⁺, 136 (80). C₁₄H₁₂N₄O₃S (284.34): calcd. C 59.14, H 4.25, N 19.70, S 11.03; found C 59.30, H 4.33, N 19.47, S 11.03.

General procedure, illustrated for **A1**, for the Buchwald–Hartwig couplings of the arylamines with the corresponding aryl halides:

4-[4-Methoxy-2-(pyridin-2-yl)thiazol-5-yl]-*N,N*-diphenylaniline (A1): Bromobenzene (345 mg, 2.2 mmol, 2.2 equiv.) and KO^{*t*}Bu (246 mg, 2.2 mmol, 2.2 equiv.) were added under nitrogen to a solution of 4-[4-methoxy-2-(pyridin-2-yl)thiazol-5-yl]aniline (238 mg, 1 mmol) in dry toluene (20 mL). The mixture was additionally purged thoroughly with nitrogen for 30 min, followed by the addition of Pd(dba)₂ (23 mg, 0.04 mmol, 4 mol-%) and P(*t*Bu)₃ (80 μL of a 1.0 M solution in toluene, 0.08 mmol, 8 mol-%). The mixture was heated to reflux (6 to 24 h) until no starting material was left as indicated by TLC (silica, CHCl₃, *R*_f starting material = 0.1, *R*_f monosubstituted product = 0.6, *R*_f disubstituted product = 0.8). After the reaction was complete, the mixture was allowed to cool down to room temp. and the solvent was evaporated in vacuo. Purification by column or flash chromatography yielded the product as a yellow solid. To obtain crystals suitable for X-ray crystallography, the product was recrystallized from EtOH/CHCl₃ to afford the compound as yellow block crystals; yield 331 mg (0.76 mmol, 76%). ¹H NMR (250 MHz, CDCl₃): δ = 8.59 (d, *J* = 4.3 Hz, 1 H), 8.12 (d, *J* = 7.9 Hz, 1 H), 7.77 (td, *J* = 7.7, 1.7 Hz, 1 H), 7.66 (d, *J* = 8.7 Hz, 2 H), 7.34–7.22 (m, 5 H), 7.19–6.95 (m, 8 H), 4.18 (s, 3 H) ppm. ¹³C NMR (63 MHz, CDCl₃): δ = 159.23, 159.24, 151.36, 149.40, 147.47, 146.51, 136.82, 129.26, 127.74, 125.61, 124.51, 123.89, 123.51, 123.03, 118.86, 114.55, 57.58 ppm. UV/Vis (CHCl₃): λ_{max} [log(ε/M⁻¹cm⁻¹)] = 306 [4.33], 417 [4.44] nm. MS (EI): *m/z* (%) = 435 (100) [M]⁺, 288 (55). C₂₇H₂₁N₃O₃S (435.54): calcd. C 74.46, H 4.86, N 9.65, S 7.36; found C 74.25, H 4.71, N 9.40, S 7.16.

Monosubstituted Product of A1. 4-[4-Methoxy-2-(pyridin-2-yl)thiazol-5-yl]-*N*-phenylaniline (A1m): If the reaction to **A1** was aborted earlier (*t* > 2 h), the monosubstituted product was obtained in 70% yield after purification (column chromatography, silica, CHCl₃). Recrystallization from EtOH/CHCl₃ yielded the compound as orange needles suitable for X-ray structure analysis. ¹H NMR

(250 MHz, CDCl₃): δ = 8.58 (d, J = 4.8 Hz, 1 H), 8.12 (d, J = 8.0 Hz, 1 H), 7.77 (td, J = 7.8, 1.7 Hz, 1 H), 7.69 (d, J = 8.7 Hz, 2 H), 7.36–7.22 (m, 3 H), 7.16–7.03 (m, 4 H), 6.96 (t, J = 7.3 Hz, 1 H), 5.79 (s, 1 H), 4.18 (s, 3 H) ppm. ¹³C NMR (63 MHz, CDCl₃): δ = 158.99, 158.93, 151.45, 149.40, 142.58, 142.07, 136.82, 129.38, 128.11, 124.14, 123.82, 121.37, 118.84, 118.25, 117.45, 114.91, 57.60 ppm. UV/Vis (CH₃CN): λ_{\max} [log($\epsilon/M^{-1} \text{cm}^{-1}$)] = 229 [4.17], 295 [4.21], 405 [4.44] nm. MS (EI): m/z (%) = 359 (100) [M]⁺, 212 (80). C₂₁H₁₇N₃OS (359.44): calcd. C 70.17, H 4.77, N 11.69, S 8.92; found C 70.29, H 4.72, N 11.67, S 8.95.

4-Methoxy-*N*-{4-[4-methoxy-2-(pyridin-2-yl)thiazol-5-yl]phenyl}-*N*-(4-methoxyphenyl)aniline (A2): Yield 90%. ¹H NMR (400 MHz, CDCl₃): δ = 8.57 (d, J = 4.7 Hz, 1 H), 8.10 (d, J = 8.0 Hz, 1 H), 7.75 (td, J = 7.8, 1.7 Hz, 1 H), 7.63–7.56 (m, 2 H), 7.29–7.22 (m, 1 H), 7.11–7.03 (m, 4 H), 6.93 (d, J = 8.8 Hz, 2 H), 6.88–6.81 (m, 4 H), 4.15 (s, 3 H), 3.80 (s, 6 H) ppm. ¹³C NMR (100 MHz, CDCl₃): δ = 159.17, 158.96, 156.21, 151.70, 149.56, 147.77, 140.89, 136.93, 127.85, 126.84, 123.90, 123.80, 120.61, 118.99, 115.31, 114.94, 57.70, 55.67 ppm. UV/Vis (CH₃CN): λ_{\max} [log($\epsilon/M^{-1} \text{cm}^{-1}$)] = 299 [4.35], 417 [4.43] nm. HRMS (ESI): calcd. 518.1514 [C₂₉H₂₅N₃O₃S + Na]⁺; found 518.1517.

***N*¹-[4-(Dimethylamino)phenyl]-*N*¹-[4-[4-methoxy-2-(pyridin-2-yl)thiazol-5-yl]phenyl]-*N*⁴,⁴-dimethylbenzene-1,4-diamine (A3):** Yield 86%. ¹H NMR (400 MHz, CDCl₃): δ = 8.56 (d, J = 4.5 Hz, 1 H), 8.10 (d, J = 7.9 Hz, 1 H), 7.74 (td, J = 7.8, 1.6 Hz, 1 H), 7.56 (d, J = 8.8 Hz, 2 H), 7.24 (dd, J = 7.0, 5.4 Hz, 1 H), 7.07 (d, J = 8.9 Hz, 4 H), 6.90 (d, J = 8.8 Hz, 2 H), 6.69 (d, J = 8.9 Hz, 4 H), 4.16 (s, 3 H), 2.93 (s, 12 H) ppm. ¹³C NMR (100 MHz, CDCl₃): δ = 158.94, 158.39, 151.78, 149.52, 148.42, 147.63, 137.48, 136.88, 127.74, 127.03, 123.74, 122.34, 119.16, 118.91, 115.87, 113.81, 57.67, 41.10 ppm. UV/Vis (CH₃CN): λ_{\max} [log($\epsilon/M^{-1} \text{cm}^{-1}$)] = 247 [4.30], 206 [4.80], 307 [4.43], 433 [4.36] nm. MS (EI): m/z (%) = 521 (100) [M]⁺, 374 (80). C₃₁H₃₁N₅OS: C 71.37, H 5.99, N 13.42, S 6.15; found C 71.23, H 4.66, N 13.17, S 5.77.

4-[4-Methoxy-2-(pyrazin-2-yl)thiazol-5-yl]-*N,N*-diphenylaniline (B1): Yield 90%. ¹H NMR (400 MHz, CDCl₃): δ = 9.34 (d, J = 1.3 Hz, 1 H), 8.53 (d, J = 2.5 Hz, 1 H), 8.52–8.49 (m, 1 H), 7.65 (d, J = 8.8 Hz, 2 H), 7.33–7.18 (m, 4 H), 7.17–7.00 (m, 8 H), 4.19 (s, 3 H) ppm. ¹³C NMR (100 MHz, CDCl₃): δ = 159.72, 156.18, 147.42, 147.01, 146.92, 144.30, 143.77, 140.96, 129.33, 127.94, 125.01, 124.71, 123.26, 116.11, 109.95, 57.75 ppm. MS (EI): m/z (%) = 436 (100) [M]⁺, 288 (90). UV/Vis (CH₃CN): λ_{\max} [log($\epsilon/M^{-1} \text{cm}^{-1}$)] = 237 [4.01], 303 [4.20], 426 [4.27] nm. C₂₆H₂₀N₄OS (436.53): calcd. C 71.54, H 4.62, N 12.83, S 7.35; found C 71.27, H 4.66, N 12.61, S 7.67.

Monosubstituted Product of B1 – 4-[4-Methoxy-2-(pyrazin-2-yl)thiazol-5-yl]-*N*-phenylaniline (B1m): If the reaction to afford B1 was aborted earlier ($t > 3$ h), the monosubstituted product was obtained in 79% yield after purification (column chromatography, silica, CHCl₃/EtOAc 4:1). Recrystallization from EtOH/CHCl₃ yielded the compound as orange block crystals. ¹H NMR (250 MHz, CDCl₃): δ = 8.82 (d, J = 4.9 Hz, 2 H), 7.76–7.68 (m, 2 H), 7.33–7.20 (m, 3 H), 7.17–7.04 (m, 4 H), 7.02–6.91 (m, 1 H), 5.88 (s, 1 H), 4.26 (s, 3 H) ppm. ¹³C NMR (63 MHz, CDCl₃): δ = 160.10, 159.70, 157.83, 156.20, 142.81, 142.44, 129.54, 128.54, 123.57, 121.75, 120.06, 118.65, 117.89, 117.29, 58.11 ppm. MS (EI): m/z (%) = 360 (50) [M]⁺, 212 (100). C₂₀H₁₆N₄OS (360.43): calcd. C 66.65, H 4.47, N 15.54, S 8.90; found C 66.60, H 4.45, N 15.60, S 8.79.

4-Methoxy-*N*-{4-[4-methoxy-2-(pyrazin-2-yl)thiazol-5-yl]phenyl}-*N*-(4-methoxyphenyl)aniline (B2): Yield 84%. ¹H NMR (400 MHz, CDCl₃): δ = 9.33 (d, J = 1.4 Hz, 1 H), 8.51 (d, J = 2.5 Hz, 1 H),

8.50–8.48 (m, 1 H), 7.61–7.55 (m, 2 H), 7.10–7.04 (m, 4 H), 6.95–6.90 (m, 2 H), 6.87–6.81 (m, 4 H), 4.17 (s, 3 H), 3.80 (s, 6 H) ppm. ¹³C NMR (100 MHz, CDCl₃): δ = 159.56, 156.25, 155.61, 148.09, 147.11, 144.26, 143.91, 141.04, 140.63, 127.95, 126.94, 123.04, 120.26, 116.70, 114.90, 57.86, 55.64 ppm. UV/Vis (CH₃CN): λ_{\max} [log($\epsilon/M^{-1} \text{cm}^{-1}$)] = 240 [4.42], 302 [4.40], 439 [4.46] nm. MS (micro-ESI): m/z = 519.1 [M + Na]⁺. C₂₈H₂₄N₄O₃S (496.58): calcd. C 67.72, H 4.87, N 11.28, S 6.46; found C 67.39, H 4.88, N 11.16, S 6.15.

4-[4-Methoxy-2-(pyrimidin-2-yl)thiazol-5-yl]-*N,N*-di-*p*-tolylaniline (C1): Yield 85%. ¹H NMR (400 MHz, CDCl₃): δ = 8.83 (d, J = 4.9 Hz, 1 H), 7.65 (d, J = 8.8 Hz, 1 H), 7.24 (t, J = 4.9 Hz, 1 H), 7.13–7.07 (m, 2 H), 7.07–7.00 (m, 3 H), 4.26 (s, 2 H), 2.34 (s, 3 H) ppm. ¹³C NMR (100 MHz, CDCl₃): δ = 160.23, 159.71, 157.85, 156.29, 147.69, 145.01, 133.13, 130.10, 128.08, 125.10, 124.04, 122.10, 120.06, 117.89, 58.11, 20.98 ppm. UV/Vis (CH₃CN): λ_{\max} [log($\epsilon/M^{-1} \text{cm}^{-1}$)] = 233 [4.21], 302 [4.32], 426 [4.36] nm. MS (EI): m/z (%) = 464 (30) [M]⁺, 316 (100). HRMS (micro-ESI): C₂₈H₂₄N₄O₃S: 464.1671; found 464.1665. C₂₈H₂₄N₄O₃S (464.58): calcd. C 72.39, H 5.21, N 12.06, S 6.90; found C 72.30, H 5.33, N 12.47, S 6.03.

4-Methoxy-*N*-{4-[4-methoxy-2-(pyrimidin-2-yl)thiazol-5-yl]phenyl}-*N*-(4-methoxyphenyl)aniline (C2): Yield 90%. ¹H NMR (250 MHz, CDCl₃): δ = 8.80 (d, J = 4.9 Hz, 2 H), 7.61 (d, J = 8.8 Hz, 2 H), 7.25–7.17 (m, 1 H), 7.13–7.03 (m, 4 H), 6.93 (d, J = 8.8 Hz, 2 H), 6.88–6.79 (m, 4 H), 4.23 (s, 3 H), 3.80 (s, 6 H) ppm. ¹³C NMR (63 MHz, CDCl₃): δ = 160.09, 159.71, 157.82, 156.25, 155.99, 148.20, 140.60, 128.07, 126.95, 122.99, 120.21, 119.99, 118.08, 114.89, 58.08, 55.62 ppm. UV/Vis (CH₃CN): λ_{\max} [log($\epsilon/M^{-1} \text{cm}^{-1}$)] = 231 [4.36], 301 [4.38], 433 [4.46] nm. MS (EI): m/z (%) = 496 (100) [M]⁺, 348 (90). HRMS (micro-ESI): C₂₈H₂₄N₄O₃S: 496.1569; found 496.1568. C₂₈H₂₄N₄O₃S: C 67.72, H 4.87, N 11.28, S 6.46; found C 67.69, H 4.83, N 11.46, S 6.03.

5-[4-(9*H*-Carbazol-9-yl)phenyl]-4-methoxy-2-(pyridin-2-yl)thiazole (D1): The procedure was similar to that used for A1. Instead of P(*t*Bu)₃, SPHOS was used as the phosphane ligand. Compound 2d (393 mg, 1.13 mmol), Pd(*dba*)₂ (13 mg, 0.023 mmol, 2 mol-%), SPOS (18 mg, 0.046 mmol, 4 mol-%), carbazole (208 mg, 1.25 mmol, 1.1 equiv.), KO*t*Bu (140 mg, 1.25 mmol, 1.1 equiv.), and toluene (dry and degassed, 30 mL) were used. Purification was by column chromatography (silica, CHCl₃/EtOAc 10:1, R_f starting material = 0.7, R_f product = 0.75!) and additionally by recrystallization from EtOH/CHCl₃ by slow evaporation of the CHCl₃, to yield the arylamine as a yellow amorphous solid; yield 336 mg (0.78 mmol), 69%. ¹H NMR (400 MHz, CDCl₃): δ = 8.63 (d, J = 4.7 Hz, 1 H), 8.22–8.12 (m, 3 H), 8.03 (d, J = 8.5 Hz, 2 H), 7.81 (td, J = 7.7, 1.4 Hz, 1 H), 7.60 (d, J = 8.5 Hz, 2 H), 7.53–7.38 (m, 4 H), 7.37–7.23 (m, 3 H), 4.27 (s, 3 H) ppm. ¹³C NMR (100 MHz, CDCl₃): δ = 161.13, 160.25, 151.39, 149.67, 141.00, 137.06, 136.19, 131.12, 128.36, 127.38, 126.12, 124.41, 123.63, 120.44, 120.15, 119.22, 113.59, 110.03, 57.87 ppm. UV/Vis (CHCl₃): λ_{\max} [log($\epsilon/M^{-1} \text{cm}^{-1}$)] = 293 [4.04], 387 [4.13] nm. UV/Vis (CH₃CN): λ_{\max} [log($\epsilon/M^{-1} \text{cm}^{-1}$)] = 236 [4.49], 292 [4.11], 380 [4.24] nm. MS (EI): m/z (%) = 433 (100) [M]⁺, 286 (90). C₂₇H₁₉N₃OS (433.53): calcd. C 74.80, H 4.42, N 9.69, S 7.40; found C 74.79, H 4.30, N 9.39, S 7.26.

10-[4-[4-Methoxy-2-(pyridin-2-yl)thiazol-5-yl]phenyl]-10*H*-pheno-thiazine (D2): The procedure was similar to that used for D1; yield 88%. Purification was achieved by recrystallization from CHCl₃. ¹H NMR (400 MHz, CDCl₃): δ = 8.62 (ddd, J = 4.8, 1.5, 0.8 Hz, 1 H), 8.16 (d, J = 7.9 Hz, 1 H), 8.03–7.97 (m, 2 H), 7.80 (td, J = 7.8, 1.7 Hz, 1 H), 7.42–7.36 (m, 2 H), 7.32 (ddd, J = 7.5, 4.8, 1.1 Hz, 1

H), 7.04 (dd, $J = 7.4, 1.7$ Hz, 2 H), 6.92–6.78 (m, 4 H), 6.34 (dd, $J = 8.1, 1.2$ Hz, 2 H), 4.24 (s, 3 H) ppm. ^{13}C NMR (100 MHz, CDCl_3): $\delta = 161.20, 160.27, 151.30, 149.68, 144.28, 139.55, 137.10, 131.66, 130.74, 129.08, 127.03, 126.94, 124.48, 122.77, 120.85, 119.24, 116.66, 113.38, 57.88$ ppm. UV/Vis (THF): λ_{max} [$\log(\epsilon/\text{M}^{-1}\text{cm}^{-1})$] = 257 [4.72], 377 [4.42] nm. MS (EI): m/z (%) = 465 (100) $[\text{M}]^+$, 318 (90). $\text{C}_{27}\text{H}_{19}\text{N}_3\text{OS}_2$ (465.59): calcd. C 69.65, H 4.11, N 9.03, S 13.77; found C 69.55, H 4.02, N 9.21, S 13.89.

10-{4-[4-Methoxy-2-(pyridin-2-yl)thiazol-5-yl]phenyl}-10H-phenoxazine (D3): Yield 80%. ^1H NMR (400 MHz, CDCl_3): $\delta = 8.62$ (ddd, $J = 4.8, 1.5, 0.9$ Hz, 1 H), 8.16 (d, $J = 7.9$ Hz, 1 H), 8.03–7.97 (m, 2 H), 7.80 (td, $J = 7.8, 1.7$ Hz, 1 H), 7.39–7.29 (m, 3 H), 6.72–6.57 (m, 6 H), 6.02 (dd, $J = 7.7, 1.6$ Hz, 2 H), 4.24 (s, 3 H) ppm. ^{13}C NMR (100 MHz, CDCl_3): $\delta = 161.32, 160.32, 151.26, 149.67, 144.11, 137.24, 137.11, 134.47, 132.20, 131.21, 129.40, 124.51, 123.40, 121.46, 119.25, 115.56, 113.49, 113.24$ 57.88 ppm. UV/Vis (CH_3CN): λ_{max} [$\log(\epsilon/\text{M}^{-1}\text{cm}^{-1})$] = 240 [4.77], 276 [4.06], 373 [4.40] nm. MS (EI): m/z (%) = 449 (50) $[\text{M}]^+$, 302 (100). $\text{C}_{27}\text{H}_{19}\text{N}_3\text{O}_2\text{S}$ (449.53): calcd. C 72.14, H 4.26, N 9.35, S 7.13; found C 72.09, H 4.12, N 9.44, S 7.55.

General Procedure, illustrated for **Ru1**, for the synthesis of the $\text{Ru}(\text{dmbpy})_2(\text{L})(\text{PF}_6)_2$ complexes:

$\text{Ru}(\text{dmbpy})_2(\text{A1})(\text{PF}_6)_2$ (Ru1): The activated precursor *cis*- $\text{Ru}(\text{dmbpy})_2(\text{acetone})_2(\text{PF}_6)_2$ was synthesized by stirring *cis*- $(\text{dmbpy})_2\text{-RuCl}_2$ (68 mg, 0.126 mmol) and AgPF_6 (64 mg, 0.252 mmol, 2 equiv.) in dried and nitrogen-purged acetone (5 mL) for 6 h at room temp. under inert conditions with use of Schlenk techniques. The precipitated AgCl was filtered off and the corresponding ligand **A1** (55 mg, 0.126 mmol) was added to the solution. The mixture was heated under reflux for 24 h. Subsequently, the reaction mixture was allowed to cool to room temp. and filtered through a cellulose filter. The solvent was removed in vacuo and the crude product was purified by size exclusion chromatography (Bio-Beads S-X1, CH_2Cl_2 as eluent) to remove traces of the ligand (if the complex was not sufficiently soluble in CH_2Cl_2 , it was applied with a 1:1 mixture of $\text{CH}_2\text{Cl}_2/\text{acetone}$ and eluted with CH_2Cl_2). After evaporation of the solvent, the solid was dissolved in a small amount of CH_2Cl_2 and precipitated with Et_2O (200 mL) to give the complex as a red solid; yield 99 mg (0.083 mmol, 67%). ^1H NMR (250 MHz, CD_3CN): $\delta = 8.39\text{--}8.26$ (m, 4 H), 8.20 (d, $J = 7.9$ Hz, 1 H), 7.97 (td, $J = 7.9, 1.2$ Hz, 1 H), 7.91 (d, $J = 5.8$ Hz, 1 H), 7.63 (d, $J = 5.5$ Hz, 1 H), 7.59 (d, $J = 5.8$ Hz, 2 H), 7.50–6.88 (m, 20 H), 2.99 (s, 3 H), 2.61–2.46 (m, 12 H) ppm. ^{13}C NMR (63 MHz, CD_3CN): $\delta = 161.39, 158.02, 157.99, 157.94, 157.51, 157.50, 154.59, 152.79, 152.23, 152.01, 151.61, 151.31, 151.23, 151.21, 150.64, 150.22, 147.70, 138.52, 130.66, 129.67, 129.41, 129.29, 129.19, 128.30, 127.85, 126.46, 125.88, 125.83, 125.49, 125.46, 125.42, 124.99, 124.18, 122.23, 121.17, 62.11, 21.24, 21.18, 21.11$ ppm. UV/Vis (CH_3CN): λ_{max} [$\log(\epsilon/\text{M}^{-1}\text{cm}^{-1})$] = 258 [4.47], 287 [4.92], 319 [4.59], 447 [4.48] nm. MS (MALDI-TOF, dithranol): calcd. for $\text{C}_{51}\text{H}_{45}\text{F}_6\text{N}_7\text{OPRuS}$ 1050.209 $[\text{M} - \text{PF}_6]^+$; found 1050.345. HRMS (micro-ESI): calcd. for $\text{C}_{51}\text{H}_{45}\text{F}_6\text{N}_7\text{OPRuS}$ 1044.2124; found 1044.2122.

$\text{Ru}(\text{dmbpy})_2(\text{A2})(\text{PF}_6)_2$ (Ru2): Yield 67%. ^1H NMR (400 MHz, CD_3CN): $\delta = 8.36\text{--}8.31$ (m, 3 H), 8.28 (s, 1 H), 8.17 (d, $J = 8.0$ Hz, 1 H), 7.96 (td, $J = 7.9, 1.3$ Hz, 1 H), 7.90 (d, $J = 5.8$ Hz, 1 H), 7.62 (d, $J = 5.6$ Hz, 1 H), 7.58 (d, $J = 5.8$ Hz, 2 H), 7.45 (d, $J = 5.8$ Hz, 1 H), 7.36–7.25 (m, 5 H), 7.21 (d, $J = 5.8$ Hz, 1 H), 7.16 (d, $J = 5.8$ Hz, 1 H), 7.13–7.07 (m, 4 H), 6.96–6.90 (m, 4 H), 6.80 (d, $J = 8.9$ Hz, 2 H), 3.78 (s, 6 H), 2.98 (s, 3 H), 2.56 (s, 3 H), 2.55 (s, 3 H), 2.53 (s, 3 H), 2.50 (s, 3 H) ppm. ^{13}C NMR (100 MHz, CD_3CN): $\delta = 161.20, 158.30, 158.16, 158.13, 158.10, 157.66, 157.01, 154.80,$

152.88, 152.85, 152.32, 152.12, 151.72, 151.43, 151.42, 151.35, 151.33, 150.75, 140.43, 138.61, 129.63, 129.51, 129.40, 129.29, 128.93, 128.40, 127.81, 126.13, 125.98, 125.94, 125.59, 125.10, 124.15, 119.03, 118.90, 116.11, 62.10, 56.25, 21.35, 21.34, 21.28, 21.21 ppm. UV/Vis (CH_3CN): λ_{max} [$\log(\epsilon/\text{M}^{-1}\text{cm}^{-1})$] = 248 [4.45], 258 [4.41], 286 [4.86], 324 [4.52], 457 [4.45] nm. MS (MALDI-TOF, dithranol): calcd. for $\text{C}_{53}\text{H}_{49}\text{F}_6\text{N}_7\text{O}_3\text{PRuS}$ 1110.26 $[\text{M} - \text{PF}_6]^+$; found 1110.23. HRMS (micro-ESI): calcd. for $\text{C}_{53}\text{H}_{49}\text{F}_6\text{N}_7\text{O}_3\text{PRuS}$ 1104.2335; found 1104.2336.

$\text{Ru}(\text{dmbpy})_2(\text{C1})(\text{PF}_6)_2$ (Ru3): Yield 60%. ^1H NMR (400 MHz, CD_3CN): $\delta = 8.84$ (dd, $J = 4.8, 1.9$ Hz, 1 H), 8.37–8.29 (m, 4 H), 7.93 (d, $J = 5.8$ Hz, 1 H), 7.86 (dd, $J = 5.8, 1.9$ Hz, 1 H), 7.75 (d, $J = 5.8$ Hz, 1 H), 7.57 (d, $J = 5.8$ Hz, 1 H), 7.44 (d, $J = 5.8$ Hz, 1 H), 7.41 (d, $J = 8.9$ Hz, 2 H), 7.37–7.33 (m, 1 H), 7.33–7.28 (m, 2 H), 7.22 (d, $J = 4.9$ Hz, 1 H), 7.19–7.13 (m, 5 H), 7.01 (d, $J = 8.3$ Hz, 4 H), 6.89 (d, $J = 8.9$ Hz, 2 H), 3.00 (s, 3 H), 2.56 (d, $J = 2.6$ Hz, 6 H), 2.51 (d, $J = 6.2$ Hz, 6 H), 2.31 (s, 6 H) ppm. ^{13}C NMR (100 MHz, CD_3CN): $\delta = 164.05, 161.96, 160.34, 158.28, 158.09, 158.04, 157.86, 157.48, 155.41, 153.13, 152.72, 152.08, 151.89, 151.63, 151.59, 151.54, 150.96, 150.93, 145.00, 135.65, 131.29, 129.71, 129.66, 129.39, 129.36, 129.28, 128.45, 126.89, 126.01, 125.94, 125.61, 125.14, 122.84, 120.65, 120.04, 62.20, 21.31, 21.24, 21.18, 20.93$ ppm. UV/Vis (CH_3CN): λ_{max} [$\log(\epsilon/\text{M}^{-1}\text{cm}^{-1})$] = 247 [4.58], 258 [4.54], 285 [4.99], 326 [4.64], 471 [4.53] nm. MS (MALDI-TOF, dithranol): calcd. for $\text{C}_{52}\text{H}_{48}\text{F}_6\text{N}_8\text{OPRuS}$ 1079.2718 $[\text{M} - \text{PF}_6]^+$; found 1079.2713. HRMS (micro-ESI): calcd. for $\text{C}_{52}\text{H}_{48}\text{F}_6\text{N}_8\text{OPRuS}$ 1073.2389; found 1073.2400.

$\text{Ru}(\text{dmbpy})_2(\text{C2})(\text{PF}_6)_2$ (Ru4): Yield 75%. ^1H NMR (400 MHz, CD_3CN): $\delta = 8.83$ (dd, $J = 4.8, 1.9$ Hz, 1 H), 8.34 (s, 2 H), 8.31 (d, $J = 8.6$ Hz, 2 H), 7.92 (d, $J = 5.8$ Hz, 1 H), 7.85 (dd, $J = 5.8, 1.9$ Hz, 1 H), 7.75 (d, $J = 5.8$ Hz, 1 H), 7.57 (d, $J = 5.8$ Hz, 1 H), 7.43 (d, $J = 5.8$ Hz, 1 H), 7.40–7.35 (m, 2 H), 7.35–7.26 (m, 3 H), 7.21 (d, $J = 5.8$ Hz, 1 H), 7.17 (d, $J = 5.8$ Hz, 1 H), 7.14–7.07 (m, 4 H), 6.95–6.89 (m, 4 H), 6.82–6.75 (m, 2 H), 3.78 (s, 6 H), 2.98 (s, $J = 6.0$ Hz, 3 H), 2.56 (s, 3 H), 2.55 (s, 3 H), 2.52 (s, 3 H), 2.50 (s, 3 H) ppm. ^{13}C NMR (100 MHz, CD_3CN): $\delta = 164.07, 161.79, 160.32, 158.30, 158.27, 158.09, 158.04, 157.87, 157.48, 155.02, 153.12, 152.72, 152.08, 151.89, 151.61, 151.58, 151.53, 150.96, 140.21, 129.72, 129.65, 129.38, 129.27, 128.97, 128.44, 126.01, 125.94, 125.61, 125.14, 122.75, 118.86, 118.61, 116.05, 62.13, 56.19, 21.31, 21.24, 21.18$ ppm. UV/Vis (CH_3CN): λ_{max} [$\log(\epsilon/\text{M}^{-1}\text{cm}^{-1})$] = 247 [4.62], 258 [4.57], 285 [5.00], 328 [4.63], 473 [4.55] nm. MS (MALDI-TOF, dithranol): calcd. for $\text{C}_{52}\text{H}_{48}\text{F}_6\text{N}_8\text{O}_3\text{PRuS}$ 1111.23 $[\text{M} - \text{PF}_6]^+$; found 1111.30. HRMS (micro-ESI): calcd. for $\text{C}_{52}\text{H}_{48}\text{F}_6\text{N}_8\text{O}_3\text{PRuS}$ 1105.2288; found 1105.2274.

$\text{Ru}(\text{dmbpy})_2(\text{D1})(\text{PF}_6)_2$ (Ru5): Yield 93%. ^1H NMR (400 MHz, CH_3CN): $\delta = 8.41\text{--}8.25$ (m, 5 H), 8.20 (d, $J = 7.8$ Hz, 2 H), 8.02 (dd, $J = 11.3, 4.4$ Hz, 1 H), 7.98 (d, $J = 5.8$ Hz, 1 H), 7.83 (d, $J = 8.6$ Hz, 2 H), 7.74 (d, $J = 8.5$ Hz, 2 H), 7.69 (d, $J = 5.5$ Hz, 1 H), 7.63 (d, $J = 5.8$ Hz, 2 H), 7.51–7.41 (m, 5 H), 7.40–7.28 (m, 5 H), 7.24 (d, $J = 5.1$ Hz, 1 H), 7.19 (d, $J = 5.0$ Hz, 1 H), 3.09 (s, 3 H), 2.58 (s, 3 H), 2.57 (s, 3 H), 2.54 (s, 3 H), 2.52 (s, 3 H) ppm. ^{13}C NMR (100 MHz, CH_3CN): $\delta = 162.46, 159.40, 158.15, 158.10, 158.08, 157.62, 154.58, 152.98, 152.94, 152.33, 152.11, 151.70, 151.45, 151.39, 151.37, 150.80, 141.41, 139.72, 138.67, 130.67, 129.50, 129.37, 129.30, 128.53, 128.40, 128.30, 127.91, 127.31, 125.97, 125.94, 125.61, 125.11, 124.64, 124.54, 123.88, 121.55, 121.45, 110.72, 62.63, 21.31, 21.30, 21.24, 21.17$ ppm. UV/Vis (CH_3CN): λ_{max} [$\log(\epsilon/\text{M}^{-1}\text{cm}^{-1})$] = 238 [4.73], 257 [4.53], 286 [4.85], 322 [4.38], 338 [4.34], 389 [4.29], 486 [4.00] nm. MS (MALDI-TOF, dithranol): calcd. for $\text{C}_{51}\text{H}_{43}\text{F}_6\text{N}_7\text{OPRuS}$ 1110.26 $[\text{M} - \text{PF}_6]^+$; found 1110.23. HRMS (micro-ESI): calcd. for $\text{C}_{51}\text{H}_{43}\text{F}_6\text{N}_7\text{OPRuS}$ 1042.1968; found 1042.1959.

Ru(dmbpy)₂(D2)(PF₆)₂ (Ru6): Yield 57%. ¹H NMR (400 MHz, CD₃CN): δ = 8.36 (s, 2 H), 8.35 (s, 1 H), 8.31 (s, 1 H), 8.26 (d, J = 7.9 Hz, 1 H), 8.01 (td, J = 7.9, 1.3 Hz, 1 H), 7.95 (d, J = 5.8 Hz, 1 H), 7.69–7.64 (m, 3 H), 7.63–7.59 (m, 2 H), 7.47 (d, J = 5.8 Hz, 1 H), 7.38–7.32 (m, 4 H), 7.30 (d, J = 4.9 Hz, 1 H), 7.27 (dd, J = 7.6, 1.5 Hz, 2 H), 7.24 (d, J = 5.8 Hz, 1 H), 7.18 (d, J = 4.8 Hz, 1 H), 7.13 (td, J = 7.8, 1.6 Hz, 2 H), 7.05 (td, J = 7.5, 1.3 Hz, 2 H), 6.73 (dd, J = 8.0, 1.0 Hz, 2 H), 3.03 (s, 3 H), 2.58 (s, 3 H), 2.57 (s, 3 H), 2.54 (s, 3 H), 2.52 (s, 3 H) ppm. ¹³C NMR (100 MHz, CD₃CN): δ = 162.05, 158.80, 158.09, 158.06, 158.03, 157.58, 154.58, 152.93, 152.91, 152.32, 152.09, 151.70, 151.41, 151.34, 151.31, 150.75, 145.18, 143.78, 138.63, 130.92, 129.47, 129.36, 129.26, 128.62, 128.42, 128.37, 128.17, 126.71, 126.34, 125.95, 125.91, 125.59, 125.44, 125.08, 124.52, 124.36, 121.66, 21.33, 21.31, 21.26, 21.18, 15.64 ppm. UV/Vis (CH₃CN): λ_{max} [log(ε/M⁻¹cm⁻¹)] = 257 [4.76], 286 [4.82], 320 [4.38], 367 [4.27], 434 [4.24] nm. MS (MALDI-TOF, dithranol): calcd. for C₅₁H₄₃F₆N₇OPRuS₂ 1080.17 [M – PF₆]⁺; found 1080.17. HRMS (micro-ESI): calcd. for C₅₁H₄₃F₆N₇OPRuS₂ 1074.1692; found 1074.1711. C₅₁H₄₃F₁₂N₇OP₂RuS₂ (1225.06): calcd. C 50.00, H 3.54, N 8.00, S 5.23; found C 49.98, H 3.76, N 7.87, S 4.87.

Ru(dmbpy)₂(D3)(PF₆)₂ (Ru7): Yield 68%. ¹H NMR (400 MHz, CD₃CN): δ = 8.42–8.28 (m, 5 H), 8.04 (td, J = 7.9, 1.3 Hz, 1 H), 7.98 (d, J = 5.8 Hz, 1 H), 7.88–7.79 (m, 2 H), 7.70 (d, J = 5.3 Hz, 1 H), 7.63 (d, J = 5.8 Hz, 2 H), 7.54–7.47 (m, 3 H), 7.44–7.35 (m, 2 H), 7.32 (dd, J = 5.7, 0.9 Hz, 1 H), 7.25 (dd, J = 5.8, 0.9 Hz, 1 H), 7.20 (dd, J = 5.8, 0.9 Hz, 1 H), 6.73–6.60 (m, 6 H), 5.98 (d, J = 8.4 Hz, 2 H), 3.07 (d, J = 6.1 Hz, 3 H), 2.59 (s, 3 H), 2.59 (s, 3 H), 2.56 (s, 3 H), 2.54 (s, 3 H) ppm. ¹³C NMR (100 MHz, CD₃CN): δ = 162.51, 159.65, 158.11, 158.06, 158.03, 157.58, 154.51, 153.00, 152.95, 152.33, 152.11, 151.71, 151.44, 151.37, 151.35, 150.78, 144.78, 141.24, 138.66, 134.93, 132.76, 131.88, 129.49, 129.37, 129.36, 129.29, 128.40, 128.36, 125.97, 125.93, 125.60, 125.09, 124.70, 124.56, 123.57, 122.82, 116.44, 114.40, 62.64, 21.32, 21.26, 21.18 ppm. UV/Vis (CH₃CN): λ_{max} [log(ε/M⁻¹cm⁻¹)] = 286 [4.82], 327 [4.47], 446 [4.12], 483 [4.05] nm. MS (MALDI-TOF, dithranol): calcd. for C₅₁H₄₃F₆N₇O₂PRuS 1064.19 [M – PF₆]⁺; found 1064.20. HRMS (micro-ESI): calcd. for C₅₁H₄₃F₆N₇O₂PRuS: 1058.1916; found 1058.1923.

Supporting Information (see footnote on the first page of this article): Lippert–Mataga calculation, emission spectra of the dyes and of **A2** and **D1** in different solvents, ¹H NMR spectra of the radical cations of **A3** and **Ru4**, X-ray structure of **A1m**, refinement data and X-ray structure files for **A1**, **B1**, **C1**, **D2** and **A1m**, MALDI-TOF spectra of the complexes, graphical representation of the torsion angles for **A2** and **D1**, summary of the photophysical properties and representations of the orbitals of the higher excited singlet states, CV spectra of the complexes **Ru3**, **Ru4** and **Ru7**. ¹H and ¹³C NMR spectra of the final products.

Acknowledgments

The authors thank the Thuringian Ministry for Education, Science and Culture (grant number #B514–09049, project “Photonische Mizellen [PhotoMIC]”) for financial support. We gratefully acknowledge the help of Dr. Eckhard Birckner and Erika Kielman with the emission spectroscopy of the complexes at 77 K.

[1] R. M. Dodson, H. W. Turner, *J. Am. Chem. Soc.* **1951**, *73*, 4517–4519.

[2] J. Liebscher, *Houben–Weyl Methoden der Organischen Chemie*, vol. E8b, 4th ed., Thieme, Stuttgart, Germany, **1994**.

- [3] a) F. A. J. Kerdesky, C. D. W. Brooks, K. I. Hulkower, J. B. Bouska, R. L. Bell, *Bioorg. Med. Chem.* **1997**, *5*, 393–396; b) R. M. Rzasla, M. R. Kaller, G. Liu, E. Magal, T. T. Nguyen, T. D. Osslund, D. Powers, V. J. Santora, V. N. Viswanadhan, H.-L. Wang, X. Xiong, W. Zhong, M. H. Norman, *Bioorg. Med. Chem.* **2007**, *15*, 6574–6595; c) F. A. J. Kerdesky, J. H. Holms, J. L. Moore, R. L. Bell, R. D. Dyer, G. W. Carter, D. W. Brooks, *J. Med. Chem.* **1991**, *34*, 2158–2165.
- [4] R. Menzel, A. Breul, C. Pietsch, J. Schäfer, C. Friebe, E. Täuschler, D. Weiß, B. Dietzek, J. Popp, R. Beckert, U. S. Schubert, *Macromol. Chem. Phys.* **2011**, *212*, 840–848.
- [5] B. Happ, J. Schäfer, R. Menzel, M. D. Hager, A. Winter, J. Popp, R. Beckert, B. Dietzek, U. S. Schubert, *Macromolecules (Washington, DC, USA)* **2011**, *44*, 6277–6287.
- [6] R. Menzel, D. Ogermann, S. Kupfer, D. Weiß, H. Görls, K. Kleinermanns, L. González, R. Beckert, *Dyes Pigm.* **2012**, *94*, 512–524.
- [7] L. K. Calderón-Ortiz, E. Täuschler, E. Leite Bastos, H. Görls, D. Weiß, R. Beckert, *Eur. J. Org. Chem.* **2012**, 2535–2541.
- [8] R. Menzel, E. Täuschler, D. Weiß, R. Beckert, H. Görls, *Z. Anorg. Allg. Chem.* **2010**, *636*, 1380–1385.
- [9] a) S. Campagna, F. Puntoriero, F. Nastasi, G. Bergamini, V. Balzani, in: *Photochemistry and Photophysics of Coordination Compounds I*, vol. 280 (Eds.: V. Balzani, S. Campagna), Springer, Berlin, **2007**, pp. 117–214; b) V. Balzani, G. Bergamini, S. Campagna, F. Puntoriero, vol. 280 (Eds.: V. Balzani, S. Campagna), Springer Berlin/Heidelberg, **2007**, pp. 1–36; c) V. Balzani, A. Juris, *Coord. Chem. Rev.* **2001**, *211*, 97–115; d) J. P. Collin, S. Guillerrez, J. P. Sauvage, F. Barigelletti, L. De Cola, L. Flamigni, V. Balzani, *Inorg. Chem.* **1991**, *30*, 4230–4238; e) V. Balzani, A. Juris, M. Venturi, S. Campagna, S. Serroni, *Chem. Rev.* **1996**, *96*, 759–834.
- [10] a) G. J. Meyer, *Inorg. Chem.* **2005**, *44*, 6852–6864; b) N. L. Fry, P. K. Mascharak, *Acc. Chem. Res.* **2011**, *44*, 289–298; c) M. Su, W. Wei, S. Liu, *Anal. Chim. Acta* **2011**, *704*, 16–32; d) D. B. Watson, *Ruthenium: Properties, Production and Applications*, 1st ed., Nova Science Publishers Inc, New York, **2011**, pp. 157–188; e) G. C. Vougioukalakis, R. H. Grubbs, *Chem. Rev.* **2009**, *110*, 1746–1787; f) G. C. Vougioukalakis, A. I. Philippopoulos, T. Stergiopoulos, P. Falaras, *Coord. Chem. Rev.* **2011**, *255*, 2602–2621.
- [11] M. Thelakkat, C. Schmitz, C. Hohle, P. Strohhriegl, H.-W. Schmidt, U. Hofmann, S. Schloter, D. Haarer, *Phys. Chem. Chem. Phys.* **1999**, *1*, 1693–1698.
- [12] X. Ma, F. Ma, Z. Zhao, N. Song, J. Zhang, *J. Mater. Chem.* **2010**, *20*, 2369–2380.
- [13] a) M. Thelakkat, *Macromol. Mater. Eng.* **2002**, *287*, 442–461; b) C.-H. Yang, F.-J. Liu, L.-R. Huang, T.-L. Wang, W.-C. Lin, M. Sato, C.-H. Chen, C.-C. Chang, *J. Electroanal. Chem.* **2008**, *617*, 101–110; c) Z. Jiang, T. Ye, C. Yang, D. Yang, M. Zhu, C. Zhong, J. Qin, D. Ma, *Chem. Mater.* **2011**, *23*, 771–777.
- [14] a) G. Wei, X. Xiao, S. Wang, J. D. Zimmerman, K. Sun, V. V. Diev, M. E. Thompson, S. R. Forrester, *Nano Lett.* **2011**, *11*, 4261–4264; b) W. Zhang, S. C. Tse, J. Lu, Y. Tao, M. S. Wong, *J. Mater. Chem.* **2010**, *20*, 2182–2189; c) L. Zhang, C. He, J. Chen, P. Yuan, L. Huang, C. Zhang, W. Cai, Z. Liu, Y. Cao, *Macromolecules (Washington, DC, USA)* **2010**, *43*, 9771–9778.
- [15] a) Z. Ning, H. Tian, *Chem. Commun.* **2009**, 5483–5495; b) A. Mishra, M. K. R. Fischer, P. Bäuerle, *Angew. Chem.* **2009**, *121*, 2510; *Angew. Chem. Int. Ed.* **2009**, *48*, 2474–2499; c) A. Hagfeldt, G. Boschloo, L. Sun, L. Klöö, H. Pettersson, *Chem. Rev.* **2010**, *110*, 6595–6663.
- [16] D. N. Lee, J. K. Kim, H. S. Park, Y. M. Jun, R. Y. Hwang, W.-Y. Lee, B. H. Kim, *Synth. Met.* **2005**, *150*, 93–100.
- [17] a) Y. Nishikitani, T. Kubo, H. Masuda, *Mol. Cryst. Liq. Cryst.* **2011**, *538*, 1–9; b) Z. Jin, H. Masuda, N. Yamanaka, M. Minami, T. Nakamura, Y. Nishikitani, *ChemSusChem* **2008**, *1*, 901–904.
- [18] D. Ciez, J. Svetlik, *Synlett* **2011**, 315–318.

- [19] E. Täuscher, D. Weiß, R. Beckert, H. Görls, *Synthesis* **2010**, 1603–1608.
- [20] a) B. P. Fors, P. Krattiger, E. Strieter, S. L. Buchwald, *Org. Lett.* **2008**, *10*, 3505–3508; b) D. S. Surry, S. L. Buchwald, *Angew. Chem.* **2008**, *120*, 6438; *Angew. Chem. Int. Ed.* **2008**, *47*, 6338–6361.
- [21] A. Sakalyte, J. Simokaitiene, A. Tomkeviciene, J. Keruckas, G. Buika, J. V. Grazulevicius, V. Jankauskas, C.-P. Hsu, C.-H. Yang, *J. Phys. Chem. C* **2011**, *115*, 4856–4862.
- [22] a) S. Thayumanavan, S. Barlow, S. R. Marder, *Chem. Mater.* **1997**, *9*, 3231–3235; b) P. Zacharias, M. C. Gather, M. Rojahn, O. Nuyken, K. Meerholz, *Angew. Chem.* **2007**, *119*, 4467; *Angew. Chem. Int. Ed.* **2007**, *46*, 4388–4392.
- [23] M. R. Biscoe, T. E. Barder, S. L. Buchwald, *Angew. Chem.* **2007**, *119*, 7370; *Angew. Chem. Int. Ed.* **2007**, *46*, 7232–7235.
- [24] a) O. Johansson, *Synthesis* **2006**, 2585–2589; b) R. A. Altman, S. L. Buchwald, *Nat. Protocols* **2007**, *2*, 3115–3121.
- [25] X. Wu, A. P. Davis, P. C. Lambert, L. Kraig Steffen, O. Toy, A. J. Fry, *Tetrahedron* **2009**, *65*, 2408–2414.
- [26] a) A. N. Sobolev, V. K. Belsky, I. P. Romm, N. Y. Chernikova, E. N. Guryanova, *Acta Crystallogr., Sect. C* **1985**, *41*, 967–971; b) E. Täuscher, L. Calderón-Ortiz, D. Weiß, R. Beckert, H. Görls, *Synthesis* **2011**, 2334–2339.
- [27] a) J. McDowell, *Acta Crystallogr., Sect. B* **1976**, *32*, 5–10; b) C. L. Klein, J. M. Conrad III, S. A. Morris, *Acta Crystallogr., Sect. C* **1985**, *41*, 1202–1204.
- [28] a) M. V. Jovanovic, E. R. Biehl, R. D. Rosenstein, S. S. C. Chu, *J. Heterocycl. Chem.* **1984**, *21*, 661–667; b) J. R. Huber, W. W. Mantulin, *J. Am. Chem. Soc.* **1972**, *94*, 3755–3760.
- [29] X. Zhang, Z. Chi, Z. Yang, M. Chen, B. Xu, L. Zhou, C. Wang, Y. Zhang, S. Liu, J. Xu, *Opt. Mater.* **2009**, *32*, 94–98.
- [30] a) J. M. Chudomel, B. Yang, M. D. Barnes, M. Achermann, J. T. Mague, P. M. Lahti, *J. Phys. Chem. A* **2011**, *115*, 8361–8368; b) R. Hu, E. Lager, A. I. Aguilar-Aguilar, J. Liu, J. W. Y. Lam, H. H. Y. Sung, I. D. Williams, Y. Zhong, K. S. Wong, E. Peña-Cabrera, B. Z. Tang, *J. Phys. Chem. C* **2009**, *113*, 15845–15853; c) H. Cao, V. Chang, R. Hernandez, M. D. Heagy, *J. Org. Chem.* **2005**, *70*, 4929–4934; d) K. Rotkiewicz, K. H. Grellmann, Z. R. Grabowski, *Chem. Phys. Lett.* **1973**, *19*, 315–318.
- [31] N. Asami, T. Takaya, S. Yabumoto, S. Shigeto, H.-o. Hamaguchi, K. Iwata, *J. Phys. Chem. A* **2010**, *114*, 6351–6355.
- [32] a) J. R. Lakowicz, *Principles of fluorescence spectroscopy*, 3rd ed., Springer, New York, **2006**; b) N. Mataga, Y. Kaifu, M. Koizumi, *Bull. Chem. Soc. Jpn.* **1955**, *28*, 690–691.
- [33] E. Lippert, *Z. Naturforsch., A* **1955**, *10*, 541–545.
- [34] E. Lippert, *Z. Elektrochem. Ber. Bunsenges. Physik. Chem.* **1957**, *61*, 962–975.
- [35] a) S. Techert, K. A. Zachariasse, *J. Am. Chem. Soc.* **2004**, *126*, 5593–5600; b) E. Castanheira, A. Abreu, M. Carvalho, M.-J. Queiroz, P. Ferreira, *J. Fluoresc.* **2009**, *19*, 501–509; c) Z. R. Grabowski, K. Rotkiewicz, W. Rettig, *Chem. Rev.* **2003**, *103*, 3899–4032; d) K. Rurack, in *Standardization and Quality Assurance in Fluorescence Measurements I*, vol. 5 (Ed.: U. Resch-Genger), Springer, Berlin, Heidelberg, **2008**, pp. 101–145.
- [36] B. Happ, D. Escudero, M. D. Hager, C. Friebe, A. Winter, H. Görls, E. Altuntas, L. González, U. S. Schubert, *J. Org. Chem.* **2010**, *75*, 4025–4038.
- [37] J. L. Zambrana, E. X. Ferloni, J. C. Colis, H. D. Gafney, *Inorg. Chem.* **2007**, *46*, 2–4.
- [38] E. C. Glazer, D. Magde, Y. Tor, *J. Am. Chem. Soc.* **2007**, *129*, 8544–8551.
- [39] E. C. Glazer, D. Magde, Y. Tor, *J. Am. Chem. Soc.* **2005**, *127*, 4190–4192.
- [40] X.-y. Wang, A. Del Guerso, R. H. Schmehl, *J. Photochem. Photobiol. C: Photochem. Rev.* **2004**, *5*, 55–77.
- [41] E. Runge, E. K. U. Gross, *Phys. Rev. Lett.* **1984**, *52*, 997–1000.
- [42] J. Tomasi, B. Mennucci, R. Cammi, *Chem. Rev.* **2005**, *105*, 2999–3094.
- [43] M. J. Frisch, G. W. Trucks, H. B. Schlegel, G. E. Scuseria, M. A. Robb, J. R. Cheeseman, G. Scalmani, V. Barone, B. Mennucci, G. A. Petersson, H. Nakatsuji, M. Caricato, X. Li, H. P. Hratchian, A. F. Izmaylov, J. Bloino, G. Zheng, J. L. Sonnenberg, M. Hada, M. Ehara, K. Toyota, R. Fukuda, J. Hasegawa, M. Ishida, T. Nakajima, Y. Honda, O. Kitao, H. Nakai, T. Vreven, J. A. Montgomery, J. E. Peralta, F. Ogliaro, M. Bearpark, J. J. Heyd, E. Brothers, K. N. Kudin, V. N. Staroverov, R. Kobayashi, J. Normand, K. Raghavachari, A. Rendell, J. C. Burant, S. S. Iyengar, J. Tomasi, M. Cossi, N. Rega, J. M. Millam, M. Klene, J. E. Knox, J. B. Cross, V. Bakken, C. Adamo, J. Jaramillo, R. Gomperts, R. E. Stratmann, O. Yazyev, A. J. Austin, R. Cammi, C. Pomelli, J. W. Ochterski, R. L. Martin, K. Morokuma, V. G. Zakrzewski, G. A. Voth, P. Salvador, J. J. Dannenberg, S. Dapprich, A. D. Daniels, O. Farkas, J. B. Foresman, J. V. Ortiz, J. Cioslowski, D. J. Fox, *Gaussian 09*, rev. B.01, Gaussian, Inc., Wallingford CT, **2009**.
- [44] a) A. D. Becke, *J. Chem. Phys.* **1993**, *98*, 5648–5652; b) C. Lee, W. Yang, R. G. Parr, *Phys. Rev. B* **1988**, *37*, 785–789.
- [45] J. Guthmuller, B. Champagne, *J. Chem. Phys.* **2007**, *127*.
- [46] A. D. Becke, *Phys. Rev. A* **1988**, *38*, 3098–3100.
- [47] P. C. Hariharan, J. A. Pople, *Theor. Chim. Acta* **1973**, *28*, 213–222.
- [48] a) W. Schmidt, E. Steckhan, *Chem. Ber.* **1980**, *113*, 577–585; b) M. Matis, P. Rapta, V. R. Lukes, H. Hartmann, L. Dunsch, *J. Phys. Chem. B* **2010**, *114*, 4451–4460; c) L. Hagopian, G. Koehler, R. I. Walter, *J. Phys. Chem.* **1967**, *71*, 2290–2296.
- [49] O. Yurchenko, D. Freytag, L. zur Borg, R. Zentel, J. Heinze, S. Ludwigs, *J. Phys. Chem. B* **2011**, *116*, 30–39.
- [50] V. Dvořák, I. Němec, J. Zýka, *Microchem. J.* **1967**, *12*, 350–370.
- [51] J. F. Ambrose, L. L. Carpenter, R. F. Nelson, *J. Electrochem. Soc.* **1975**, *122*, 876–894.
- [52] S. M. Bonesi, R. Erra-Balsells, *J. Lumin.* **2001**, *93*, 51–74.
- [53] a) A. W. Franz, F. Rominger, T. J. J. Muller, *J. Org. Chem.* **2008**, *73*, 1795–1802; b) B. Paduszek, M. K. Kalinowski, *Electrochim. Acta* **1983**, *28*, 639–642; c) D. J. Freed, L. R. Faulkner, *J. Am. Chem. Soc.* **1972**, *94*, 4790–4792.
- [54] Y. Zhu, A. P. Kulkarni, S. A. Jenekhe, *Chem. Mater.* **2005**, *17*, 5225–5227.
- [55] X.-Q. Zhu, Z. Dai, A. Yu, S. Wu, J.-P. Cheng, *J. Phys. Chem. B* **2008**, *112*, 11694–11707.
- [56] P. J. Elving, J. E. O'Reilly, *J. Am. Chem. Soc.* **1971**, *93*, 1871–1879.
- [57] J. E. O'Reilly, P. J. Elving, *J. Am. Chem. Soc.* **1972**, *94*, 7941–7949.
- [58] a) M. R. McDevitt, A. W. Addison, *Inorg. Chim. Acta* **1993**, *204*, 141–146; b) C. M. Elliott, E. J. Hershenhart, *J. Am. Chem. Soc.* **1982**, *104*, 7519–7526.
- [59] J. Pommerehne, H. Vestweber, W. Guss, R. F. Mahrt, H. Bässler, M. Porsch, J. Daub, *Adv. Mater.* **1995**, *7*, 551–554.
- [60] S. Rau, M. Ruben, T. Buttner, C. Temme, S. Dautz, H. Görls, M. Rudolph, D. Walther, A. Brodkorb, M. Duati, C. O'Connor, J. G. Vos, *J. Chem. Soc., Dalton Trans.* **2000**, 3649–3657.
- [61] a) R. Hooft, Nonius BV, Delft, The Netherlands, **1998**; b) Z. Otwinowski, W. Minor, in: *Methods Enzymol.*, vol. 276 (Ed.: Charles W. Carter Jr.), Academic Press, **1997**, pp. 307–326.
- [62] G. Sheldrick, *Acta Crystallogr., Sect. A* **2008**, *64*, 112–122.

Received: May 22, 2012

Published Online: August 9, 2012

4.4 Protonation effects on the resonance Raman properties of a novel (terpyridine)Ru(4*H*-imidazole) complex: an experimental and theoretical case study

Kupfer et al. Phys. Chem. Chem. Phys. **13**, 15580-15588 (2011). Reproduced by permission of the PCCP Owner Societies.

<http://pubs.rsc.org/en/Content/ArticleLanding/2011/CP/c1cp21521c>

Cite this: *Phys. Chem. Chem. Phys.*, 2011, **13**, 15580–15588

www.rsc.org/pccp

PAPER

Protonation effects on the resonance Raman properties of a novel (terpyridine)Ru(4*H*-imidazole) complex: an experimental and theoretical case study†

Stephan Kupfer,^a Julien Guthmuller,^a Maria Wächtler,^{abc} Sebastian Losse,^d Sven Rau,^{ef} Benjamin Dietzek,^{abc} Jürgen Popp^{abc} and Leticia González^{*ab}

Received 11th May 2011, Accepted 23rd June 2011

DOI: 10.1039/c1cp21521c

The optically active states in a novel (terpyridine)Ru(4*H*-imidazole) complex displaying an unusually broad and red-shifted absorption in the visible range are investigated experimentally and theoretically. Since this property renders the complex promising for an application as sensitizer in dye-sensitized solar cells, a detailed knowledge on the correlation between features in the absorption spectrum and structural elements is indispensable in order to develop strategies for spectroscopy/theory-guided design of such molecular components. To this aim, time-dependent density functional theory calculations, including solvent effects, are employed to analyze the experimental UV-vis absorption and resonance Raman (RR) spectra of the unprotonated and protonated forms of the complex. This provides a detailed photophysical picture for a complex belonging to a novel class of Ru–polypyridine black absorbers, which can be tuned by external pH stimuli. The complex presents two absorption maxima in the visible region, which are assigned by the calculations to metal-to-ligand charge transfer (MLCT) and intra-ligand states, respectively. RR simulations are performed in resonance with both bands and are found to correctly reproduce the observed effects of protonation. Finally, the examination of the molecular orbitals and of the RR spectra for the MLCT state shows that protonation favors a charge transfer excitation to the 4*H*-imidazole ligand.

1. Introduction

Transition metal polypyridine complexes have recently gained wide interest in a variety of research fields and applications. Amongst the most prominent research areas is the design of white emitters for light-emitting diodes,^{1–3} molecular DNA-sensors,^{4–9} supramolecular photocatalysts^{10–14} and sensitizers for dye-sensitized solar cells.^{15–20} In each of these applications the central question arises to what extent individual structural elements, *i.e.*, substituents,^{21–25} anchoring

groups^{25–29} *etc.*, or external stimuli, *e.g.*, specific or non-specific solvent–solute interactions,^{30–33} impact the envisioned photophysical function of the supramolecular unit. In this respect, this work presents a detailed theoretical and experimental investigation of a novel ruthenium complex having potential applications as sensitizer in dye-sensitized solar cells (DSSC).

As a matter of fact, in the (terpyridine)Ru(4*H*-imidazole) system under investigation, (chloro-*n*3-4,4',4''-tri-*tert*-butyl-2,2':6',2''-terpyridin-*n*2-2-phenyl-4,5-*p*-tolyliminoimidazol-*ruthenium*(II), abbreviated as [*tbterpyRuIm*], see Fig. 1), the combination of a terpyridine coordinating the central metal in concert with a chloride and a novel 4*H*-imidazole ligand, yields a coordination compound having an absorption spectrum that covers almost the entire visible range of the electromagnetic spectrum. Such black absorbers are promising candidates to replace conventional Ru(II)–bipyridine dyes used in DSSCs,³⁴ which present a typical absorption maximum centered below 550 nm. Several attempts have been made to increase the absorbance of the complexes in the NIR range. For example, one approach has been to attach additional dyes in the periphery of the polypyridine ligands.³⁵ However, in such assemblies only weak coupling between both chromophores

^a Institute for Physical Chemistry, Friedrich Schiller University Jena, Helmholtzweg 4, 07743, Jena, Germany.

E-mail: leticia.gonzalez@uni-jena.de

^b Abbe Center of Photonics, Friedrich Schiller University Jena, Helmholtzweg 4, 07743, Jena, Germany

^c Institute for Photonic Technology (IPHT) Jena, Albert-Einstein-Str. 9, 07745, Jena, Germany

^d Leibniz-Institut für Katalyse e. V. (LIKAT), Albert-Einstein-Str. 29 a, 18059 Rostock, Germany

^e Friedrich-Alexander-University Erlangen-Nuremberg, Department of Chemistry and Pharmacy, Egerlandstrasse 1, 91058 Erlangen, Germany

^f University of Ulm, Institute of Inorganic Chemistry I, Albert-Einstein-Allee 11, 89081 Ulm, Germany

† Electronic supplementary information (ESI) available. See DOI: 10.1039/c1cp21521c

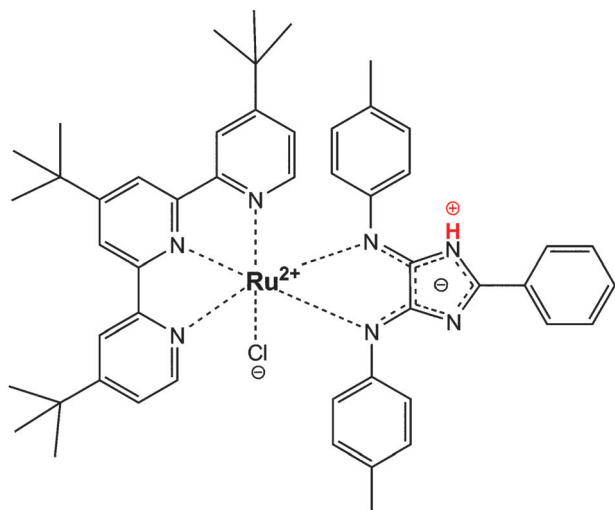


Fig. 1 Structure of the investigated complex [tbterpyRuIm] in the unprotonated (RITP) and protonated (RITPH) forms. The three *tert*-butyl groups were substituted by methyl groups in the theoretical calculations.

are generated, which limits their applicability in dye-sensitized solar cells. The (terpyridine)Ru(4*H*-imidazole) system investigated, follows a different design concept. The organic chromophore, a 4*H*-imidazole,³⁶ is directly bound to the Ru–terpyridine chromophore. This allows a direct and strong interaction between both chromophoric systems. Furthermore, the photophysical properties of the system under investigation strongly depend on the protonation state of the imidazole ligand. This was already observed for Ru–imidazole based complexes,³⁷ in which it was shown that protonation induces shifts of the metal-to-ligand charge transfer (MLCT) absorption band of up to 100 nm.

In order to unravel the contributions of the individual structural elements to the unusually broad and pH-responsive absorption spectrum, this study combines experimental absorption and resonance Raman (RR) spectroscopy. Particular emphasis is put on the detailed correlation between the experimental spectra and theoretical calculations, because this presents the primary way of assigning absorption features to structural elements. This assignment is of conceptual importance, as it represents the basis for any approach aiming at a spectroscopy/theory-guided design of molecular functional materials.

Several theoretical studies have dealt with the simulation of absorption spectra for transition metal complexes (see for example ref. 38–42) and for specific ruthenium dyes in DSSCs.^{43,44} Due to the large size of the considered systems, most of these studies made use of time-dependent density functional theory (TDDFT), which is known to provide a good compromise between accuracy and computational cost. In most cases, it is usually recognized that TDDFT calculations can give a satisfactory reproduction of the absorption band-shapes and positions, provided that hybrid exchange–correlation (XC) functionals are employed and provided that the effects of the solvent are taken into account. However, fewer studies have investigated the simulation of RR spectra for transition metal complexes^{45–47} and none of them have considered the effects of protonation on the electronic structure, which can strongly affect the photophysical properties. Nevertheless, previous work has shown that

TDDFT calculations can provide a reliable assignment of the vibrational bands and can establish a connection between the charge transfer (CT) processes occurring upon photoexcitation to the excited state and the localization of the RR active vibrational modes. Such information is of great interest for the interpretation of ongoing experimental work with the aim of designing new compounds with desired functionalities.

The rest of the paper is organized as follows. Sections 2 and 3 describe the theoretical and experimental approaches, respectively. Section 4.1 presents the absorption spectra and associated excited states of the unprotonated and protonated complex, whereas Section 4.2 discusses the RR spectra. Finally, conclusions are drawn in Section 5.

2. Theory and computational details

In order to allow for a reduction of the computational cost of the simulations without affecting the spectroscopic properties of the complexes, the three *tert*-butyl groups of the synthesized compounds [tbterpyRuIm] (Fig. 1) were approximated in the calculations by methyl groups. The structural and electronic data of the unprotonated (RITP) and protonated (RITPH) complexes were obtained from quantum chemistry calculations performed with the GAUSSIAN 09 program.⁴⁸ The geometry, vibrational frequencies, and normal coordinates of the ground state were calculated by means of DFT with the XC functional B3LYP.^{49,50} The 28-electron relativistic effective core potential MWB⁵¹ was used with its basis set for the ruthenium atom, that is, 4s, 4p, 4d and 5s electrons are treated explicitly, whereas the three first inner shells are described by the core pseudopotential. The 6-31G(d) double- ζ basis set⁵² was employed for the ligands. To correct for the lack of anharmonicity and the approximate treatment of electron correlation,⁵³ the harmonic frequencies were scaled by the factor 0.97. The vertical excitation energies, oscillator strengths and analytical Cartesian energy derivatives of the excited states were obtained from TDDFT calculations within the adiabatic approximation with the same XC functional, pseudopotential and basis set. The absorption spectra were simulated by determining the excitation energies and oscillator strengths of the 80 lowest singlet excited states. The effects of the interaction with a solvent (acetonitrile, $\epsilon = 35.688$, $n = 1.344$) on the geometry, frequencies, excitation energies and excited state gradients were taken into account by the integral equation formalism of the polarizable continuum model.⁵⁴ The nonequilibrium procedure of solvation was used for the calculation of the excitation energies and of the excited state gradients, which is well adapted for processes where only the fast reorganization of the electronic distribution of the solvent is important.

The relative RR intensities were obtained within the short-time approximation⁵⁵ (STA). In the STA, the RR intensity for a fundamental transition $0 \rightarrow 1_l$ is calculated from the partial derivative of the excited state electronic energy (E^e) along the l th normal coordinate (Q_l) evaluated at the ground state equilibrium geometry,

$$I_{0 \rightarrow 1_l} \propto \frac{1}{\omega_l} \left(\frac{\partial E^e}{\partial Q_l} \right)_0^2 \quad (1)$$

where ω_l is the frequency of the l th normal mode. These gradients were obtained from the analytical derivatives of the excited state electronic energy (E^e) along the non-mass-weighted Cartesian coordinates according to the relation

$$\left(\frac{\partial E^e}{\partial Q}\right)_0 = L^T M^{-\frac{1}{2}} \left(\frac{\partial E^e}{\partial x}\right)_0 \quad (2)$$

where M is the matrix containing the atomic masses, L is the orthogonal matrix obtained from the solution of the ground state normal mode eigenvalue problem, and $(\partial E^e/\partial Q)_0$ and $(\partial E^e/\partial x)_0$ are column vectors containing the derivatives along the normal coordinates and Cartesian coordinates, respectively.

The use of the STA is appropriate for the complexes investigated here. Indeed, the RR measurements are performed for excitation wavelengths in resonance with absorption bands displaying a large broadening and no resolved vibronic structure, each of them being associated with a single electronic excited state. These facts indicate that no significant interference effects should occur between different excited states and that the relative RR intensities should show a weak dependence with respect to the excitation wavelength. The adequacy of the STA was validated for excitations in resonance with the first absorption band according to a method described elsewhere.^{47,56} These results show negligible differences with respect to the STA at the considered experimental excitation wavelengths. Therefore, only the STA RR spectra are reported and discussed in this work.

3. Experimental methods

3.1. Synthesis and characterization

¹H NMR and ¹³C NMR spectra were recorded at ambient temperature on a Bruker AC 400 MHz spectrometer. All spectra were referenced to TMS or deuterated solvent as an internal standard. Mass spectra were recorded using a MAT 95 XL or a SSQ 170, Finnigan Mat. The positive ES mass spectra were obtained with voltages of 3–4 kV applied to the electrospray needle. Elemental analyses were carried out in-house with an automatic analyzer LECO CHNS 932.

[*t*terpy₂Ru](PF₆)₂. Starting from RuCl₃·3H₂O, in modification of ref. 57, 500 mg (0.82 mmol) *t*terpyRuCl₃ and 363 mg (1.1 equiv.) *t*terpy were dissolved in a mixture of 100 mL ethanol, 2 mL *N*-ethylmorpholine and 10 mL water and heated to reflux for 18 h. After evaporation of the solvent, the residue was dissolved in a minimal volume of ethanol. To the stirred solution 10 equiv. of NH₄PF₆ was added and the product was precipitated by adding water. The orange to red solid was filtered through a glass sintered frit, washed with water, ethanol and diethyl ether and dried *in vacuo*, yield: 930 mg (95%). Analytical data were identical to previously reported procedures.⁵⁷

[*t*terpyRuIm]. 500 mg (0.75 mmol) *t*terpyRuCl₃ and 266 mg (0.75 mmol) 2-phenyl-5-*p*-tolylamino-4-*p*-tolylimino-4*H*-imidazole⁵⁸ were dissolved in a mixture of 70 mL DMF, 5 mL H₂O and 10 mL Et₃N. The suspension was heated to reflux under microwave irradiation for 1.5 h at 160 W.

After this time water was added until the product starts to precipitate. The formed solid was filtrated and washed with water and diethyl ether. The blue powder was recrystallised from acetone/water to give the pure compound.

Yield: 703 mg (98%) MS (ESI in acetonitrile and methanol): $m/z = 890.3$ [M + H]⁺. RITP ¹H NMR (δ , 400 MHz, CD₃CN): 8.36 (d, 5.7 Hz, 2H), 8.21 (s, 2H), 8.11 (d, 6.9 Hz, 2H), 8.10 (s, 2H), 8.03 (d, 8.4 Hz, 2H), 7.52 (d, 6.0 Hz, 2H), 7.50 (d, 6.0 Hz, 2H), 7.46 (d, 7.5 Hz, 1H), 7.39 (d, 7.5 Hz, 1H), 7.36 (d, 7.1 Hz, 1H), 7.30 (d, 8.1 Hz, 2H), 6.55 (d, 8.1 Hz, 2H), 5.46 (d, 8.1 Hz, 2H), 2.42 (s, 3H), 2.08 (s, 3H), 1.49 (s, 9H), 1.42 (s, 18H) ppm. ¹³C NMR (δ , 100 MHz, CD₃CN): 176.64, 161.89, 160.39, 159.38, 158.13, 154.38, 147.66, 145.40, 136.41, 136.13, 135.79, 132.52, 129.58, 129.43, 129.27, 128.48, 125.41, 122.98, 121.17, 120.01, 36.63, 36.25, 31.28, 30.98, 21.45, 21.12 ppm. RITPH ¹H NMR (δ , 400 MHz, CD₃CN + TFA-*d*): 8.26 (s, 2H), 8.17 (s, 2H), 8.16 (d, 5.6 Hz, 2H), 7.98 (d, 8.4 Hz, 2H), 7.91 (d, 8.0 Hz, 2H), 7.68 (t, 7.6 Hz, 1H), 7.51 (m, 4H), 7.42 (d, 8.4 Hz, 2H), 6.69 (d, 8.0 Hz, 2H), 5.66 (d, 8.0 Hz, 2H), 2.46 (s, 3H), 2.13 (s, 3H), 1.48 (s, 9H), 1.41 (s, 18H) ppm. ¹³C NMR (δ , 100 MHz, CD₃CN + TFA-*d*): 170.98, 164.16, 161.76, 159.49, 159.20, 158.39, 157.56, 155.53, 145.34, 144.36, 139.30, 138.33, 134.94, 130.77, 130.53, 130.44, 129.27, 128.89, 128.45, 127.34, 125.74, 124.69, 122.37, 122.04, 121.06, 36.97, 36.49, 31.21, 30.85, 21.58, 21.24 ppm. C₅₀H₅₄ClN₇Ru·H₂O calcd C 66.17, H 6.22, N 10.8%; found C 65.40, H 6.30, N 10.94%.

3.2. Spectroscopy

The electronic absorption spectra in air-equilibrated acetonitrile were measured with a Jasco V-670 spectrophotometer. The protonated form RITPH was generated by adding an excess of trifluoroacetic acid (TFA). The resonance Raman spectra were recorded in a conventional 90° scattering arrangement using a setup described elsewhere.⁵⁹ Excitation light was delivered by a krypton ion laser (Model Coherent Innova 302C) and an argon ion laser (Model Spectra-Physics 2010). The sample concentration was optimized to obtain the maximum signal-to-noise ratio and was in the range of 10⁻⁴ M. No changes in the absorption spectra could be detected after the exposure to the laser light.

4. Results and discussion

4.1. Excited states and absorption spectra

The experimental absorption spectra of the unprotonated and protonated forms of the complex are presented in Fig. 2(a) and (b), respectively. The unprotonated form shows two absorption maxima in the visible range at 425 nm ($\epsilon = 15\,300\text{ M}^{-1}\text{ cm}^{-1}$) and at 585 nm ($\epsilon = 28\,100\text{ M}^{-1}\text{ cm}^{-1}$) as well as a weak shoulder on the red side at about 720 nm. This shoulder disappears upon protonation. Furthermore, the absorption maximum at 585 nm is bathochromically shifted to 605 nm ($\epsilon = 28\,100\text{ M}^{-1}\text{ cm}^{-1}$), whereas the absorption maximum at 425 nm is hypsochromically shifted to 386 nm ($\epsilon = 12\,900\text{ M}^{-1}\text{ cm}^{-1}$) in RITPH. In the UV region, both species are characterized by two intense absorption bands. In the unprotonated form, the first band is located at 322 nm ($\epsilon = 39\,600\text{ M}^{-1}\text{ cm}^{-1}$) and is shifted to 314 nm

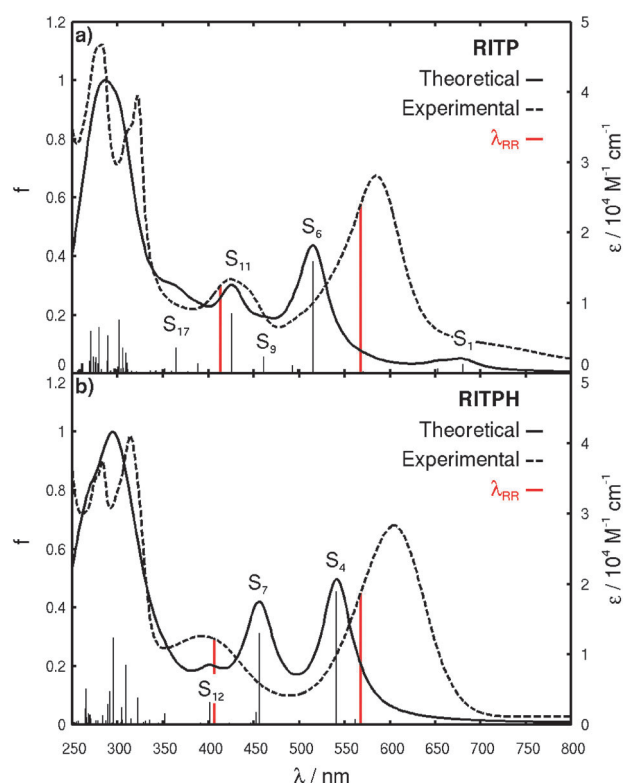


Fig. 2 Experimental (dashed line) and theoretical (black line) absorption spectra of the RITP and RITPH species in acetonitrile. The calculated oscillator strengths are represented by black sticks. A Lorentzian function with a half-width of 20 nm is employed to broaden the transitions in the simulated spectrum. The two vertical lines indicate the wavelengths at which the RR measurements are performed for the unprotonated (568 and 413 nm) and the protonated species (568 and 406 nm).

($\epsilon = 41\,100\text{ M}^{-1}\text{ cm}^{-1}$) upon protonation. The second UV maximum is located at 283 nm for both species with values of the extinction coefficient of $46\,900$ and $37\,500\text{ M}^{-1}\text{ cm}^{-1}$ for the unprotonated and protonated form, respectively.

In order to unravel the nature of the underlying excited states involved in the experimental absorption spectra,

theoretical calculations are essential. Fig. 2 presents the simulated absorption spectra and Table 1 reports the properties of the main excited states present in the visible range. The molecular orbitals involved in these excitations are depicted in Fig. 3.

In the unprotonated form, the first absorption band of the complex is associated to a MLCT state (S_6) and mainly involves a CT from the ruthenium atom to both the imidazole and terpyridine ligands (Table 1 and Fig. 3). It is seen that the calculations overestimate the energy of this state by about 0.28 eV in comparison to the experimental absorption maximum. Such difference is within the typical accuracy of TDDFT calculations for MLCT excitations in transition metal complexes.^{38,47} Additionally, the weak MLCT state S_1 calculated at 681 nm (1.82 eV) can be associated with the shoulder at 720 nm (1.72 eV) in the experimental spectrum. The higher energy excitations involve a MLCT state (S_9), which is mostly composed of transitions to the terpyridine ligand, as well as two intra-ligand (IL) states (S_{11} and S_{17}), which are dominated by transitions between π orbitals localized on the 4*H*-imidazole ligand. According to its energy position and its significant oscillator strength, the state S_{11} can be assigned to the experimental band at 425 nm. Moreover, the state S_9 might be assigned to the weak shoulder at about 500 nm in the experimental spectrum, whereas state S_{17} is more likely associated with the experimental bands located in the UV range. Finally, the calculations reveal a superposition of different types of excitations (IL, ligand–ligand charge transfer, MLCT) in the UV range (350–250 nm). The properties of these excitations will not be discussed further because the present study mainly aims at investigating the visible spectrum of the complexes, which is of relevance in using such complexes as molecular sensors or sensitizers in DSSCs.

The effects of protonation lead to important differences in the electronic properties of the excited states (Fig. 2b). First, the S_1 state is shifted to lower energy (from 681 to 837 nm) and has decreased its oscillator strength from 0.034 to 0.010. This fact is in agreement with the experimental observation that the shoulder at about 720 nm (Fig. 2a) disappears. Another important difference concerns the energetically lowest MLCT

Table 1 Calculated vertical excitation energies (E^e), oscillator strengths (f) and singly-excited configurations of the main excited states and experimental absorption maxima in the visible range. The principal orbitals are depicted in Fig. 3

State	Transition	Weight (%)	E^e/eV	λ/nm	f	$\lambda_{\text{Exp}}/\text{nm}$
RITP						
S_1	$d_{xz}(182) \rightarrow \pi_{\text{im}}^*(183)$ (MLCT)	95	1.82	681	0.034	720
S_6	$d_{xy}(181) \rightarrow \pi_{\text{im}}^*(183)$ (MLCT)	54	2.41	516	0.402	585
	$d_{yz}(180) \rightarrow \pi_{\text{terpy}}^*(184)$ (MLCT)	32				
S_9	$d_{yz}(180) \rightarrow \pi_{\text{terpy}}^*(184)$ (MLCT)	31	2.69	461	0.060	—
	$d_{xy}(181) \rightarrow \pi_{\text{terpy}}^*(185)$ (MLCT)	22				
	$d_{xy}(181) \rightarrow \pi_{\text{im}}^*(183)$ (MLCT)	20				
	$d_{xz}(182) \rightarrow \pi_{\text{terpy}}^*(185)$ (MLCT)	9				
S_{11}	$\pi_{\text{im}}(179) \rightarrow \pi_{\text{im}}^*(183)$ (IL)	93	2.91	425	0.215	425
S_{17}	$\pi_{\text{im}}(178) \rightarrow \pi_{\text{im}}^*(183)$ (IL)	89	3.40	365	0.093	—
RITPH						
S_1	$d_{xz}(182) \rightarrow \pi_{\text{im}}^*(183)$ (MLCT)	96	1.48	837	0.010	—
S_4	$d_{xy}(180) \rightarrow \pi_{\text{im}}^*(183)$ (MLCT)	82	2.29	541	0.468	605
S_7	$\pi_{\text{im}}(179) \rightarrow \pi_{\text{im}}^*(183)$ (IL)	83	2.72	456	0.320	386
S_{12}	$\pi_{\text{im}}(178) \rightarrow \pi_{\text{im}}^*(183)$ (IL)	98	3.09	401	0.078	—

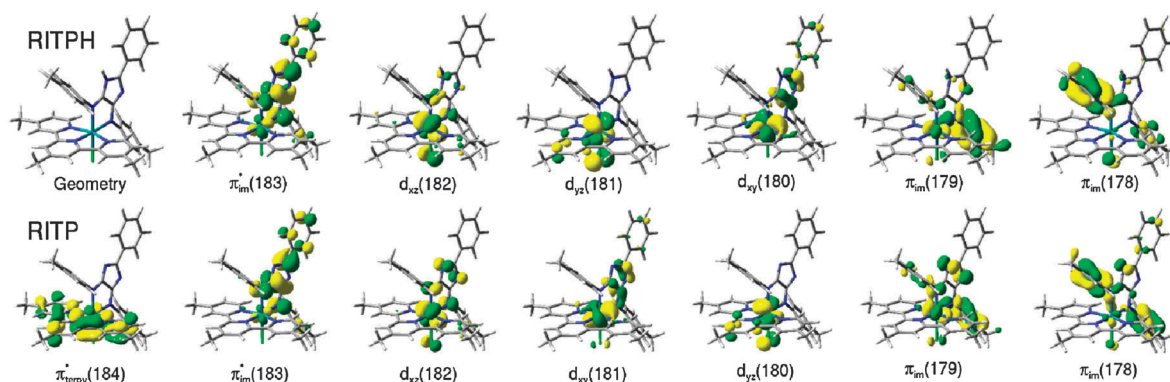


Fig. 3 Molecular orbitals involved in the main configurations of the states responsible for the absorption and RR properties of the protonated (up) and unprotonated (down) complexes.

absorption band, which is associated with the state S_4 . In contrast to the state S_6 (unprotonated form), S_4 presents no significant transition to the terpyridine ligand but is dominated by a transition from the d_{xy} ruthenium orbital to a π^* orbital localized on the 4*H*-imidazole ligand. Additionally, the experimental bathochromic shift (-0.07 eV) of the first absorption band is reasonably reproduced by theory (-0.12 eV). However, the assignment of the experimental band at 386 nm is less straightforward. Indeed, the two excited states S_7 and S_{12} display bathochromic shifts of -0.19 and -0.31 eV with respect to the S_{11} and S_{17} states of the unprotonated form, respectively. Such energy shifts are in disagreement with the experimental hypsochromic shift (0.29 eV) of the second absorption band, when going from RITP (425 nm) to RITPH (386 nm). Furthermore, it can be seen that the orbitals $\pi_{im}(178)$ and $\pi_{im}(179)$ (Fig. 3) involved in the states S_7 and S_{12} are mainly localized on the two tolyl groups attached to the imidazole center, whereas the corresponding orbitals of the unprotonated form show also a non-negligible contribution on the imidazole center (specially $\pi_{im}(179)$). This shows that these states have a more pronounced CT character in the protonated form, which could be related to their lower energies, knowing that TDDFT/B3LYP calculations have the tendency of underestimating the excitation energies of CT states.^{60,61} In order to investigate such effects in more detail, the absorption spectra of RITP(H) were also calculated with the PBE0⁶² and CAM-B3LYP⁶³ functionals (see the ESI†). Both functionals provide excited states with similar orbital characters and comparable oscillator strengths as those obtained with B3LYP. It is found that PBE0 shifts the excited states to higher energies by about 0.1 eV. This improves the agreement with experimental results only for the second absorption band of RITPH but enlarges the deviations for the other absorption bands. CAM-B3LYP provides even higher excitation energies, with deviations from the experimental values as large as 0.69 eV for the first band of RITP. Similarly to PBE0, the only improvement given by CAM-B3LYP concerns the position of the second absorption band of RITPH, which presents a deviation of 0.05 eV with respect to experimental results. The better reproduction of this band position results in an improved shift of the second absorption band upon protonation (-0.09 eV) in comparison to B3LYP and PBE0 (-0.19 eV), but which still remains in disagreement with the experimental hypsochromic

shift (0.29 eV). Overall, a comparison between the calculated and the experimental spectra shows that B3LYP provides the most balanced description of the absorption features for this complex. Therefore, this functional will be employed in the following to simulate RR spectra and to obtain additional information about the nature of the excited states.

4.2. Resonance Raman spectra

4.2.a. RR spectra in resonance with the energetically lowest MLCT band. The RR measurements were performed at an excitation wavelength of 568 nm, *i.e.*, in resonance with the first MLCT band. The corresponding simulated RR spectra were obtained within the STA by evaluating the excited state gradients of states S_6 and S_4 for the unprotonated and protonated forms, respectively. As it can be seen from Fig. 4a and b, the theoretical RR spectra show a good agreement with the experimental results. Thus, the simulated spectra allowed an assignment of most of the experimental bands to vibrations either localized on the imidazole or the terpyridine ligands (Tables 2 and 3). This assignment was also confirmed by the experimental RR spectrum of the homoleptic $[tbterpy_2Ru]^{2+}$ (bis(tris(*tert*-butyl))terpyridine-ruthenium(II)) complex recorded at 476 nm, which was used as reference to assign the characteristic vibrational modes coupled to a MLCT transition from the ruthenium center to the terpyridine ligand.

The RR spectrum of the unprotonated form (Fig. 4a and Table 2) is dominated by vibrations localized on the 4*H*-imidazole ligand. Indeed, several vibrations (modes 173, 175, 200, 208 and 209) have a strong RR intensity with calculated wavenumbers of 1344, 1380, 1494, 1576 and 1582 cm^{-1} , which are in agreement with the experimental intensities and wavenumbers of 1357, 1386, 1493, 1562, 1576 cm^{-1} , respectively. Moreover, some bands having weaker RR intensities were also assigned to vibrations localized on the terpyridine ligand (modes 141, 171, 204 and 215) or to normal coordinates delocalized on both ligands (modes 114, 134 and 146). The assignment of terpyridine vibrations is confirmed from a comparison with the spectrum of the reference compound $[tbterpy_2Ru]^{2+}$. In particular, it is seen that the modes 171 and 204 display the largest RR intensities. Obviously, the presence of noticeable terpyridine vibrations in the spectrum is related to the fact that state S_6 shows a contribution involving a

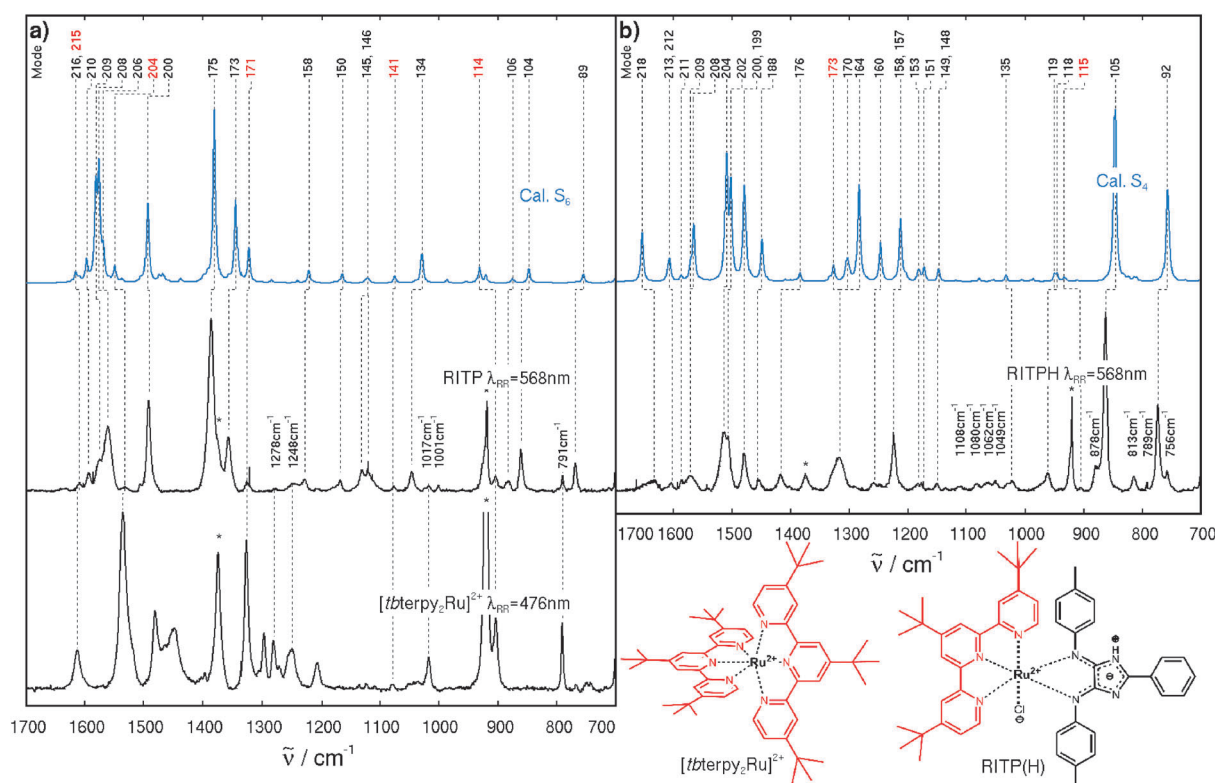


Fig. 4 Experimental and theoretical RR spectra of RITP (STA, state S_6) and RITPH (STA, state S_4) in resonance with the first absorption band. The experimental RR spectra of the reference complex $[tberpy_2Ru]^{2+}$ is given for the assignment of the terpyridine vibrations. The solvent bands are indicated by asterisks. The modes associated with vibrations located on the terpyridine ligand are given in red color. A Lorentzian function with a FWHM of 5 cm^{-1} is employed to broaden the calculated transitions.

Table 2 Assignment of the vibrational frequencies (cm^{-1}) and calculated relative RR intensities ($I_{\text{rel.}}$) in the STA for the main excited states of the unprotonated complex. The theoretical frequencies were scaled by a factor of 0.97

Mode type	Freq. (Cal.)/ cm^{-1}	Freq. (Exp.)/ cm^{-1}	$I_{\text{rel.}}(S_6)$	$I_{\text{rel.}}(S_{11})$	$I_{\text{rel.}}(S_{17})$
im (89)	753.8	769	0.05	<0.01	0.02
im (104)	846.6	861	0.09	<0.01	<0.01
im (106)	874.1	884	0.03	<0.01	0.01
im (110)	920.0	—	0.04	0.25	0.11
terpy (114)	930.9	904	0.09	<0.01	<0.01
terpy,im (134)	1028.3	1047	0.17	<0.01	<0.01
terpy (141)	1074.3	1076	0.04	<0.01	<0.01
im (145)	1118.8	1121	0.01	0.02	<0.01
terpy,im (146)	1121.0	1131	0.02	0.02	0.01
im (150)	1163.2	1168	0.06	0.03	0.04
im (151)	1169.5	—	0.01	0.01	0.10
im (152)	1173.1	—	<0.01	0.02	0.08
im (158)	1221.1	1228	0.08	0.07	0.25
terpy (171)	1323.1	1327	0.20	<0.01	<0.01
im (173)	1344.1	1357	0.47	1.00	0.83
im (174)	1356.0	—	0.02	0.01	0.11
im (175)	1380.4	1386	1.00	0.26	0.62
im (200)	1493.8	1493	0.46	0.19	0.46
im (202)	1505.6	1506	0.01	0.05	0.10
terpy (204)	1549.6	1534	0.09	<0.01	0.01
im (206)	1568.7	1562	0.16	0.07	0.17
im (208)	1576.3	1562	0.62	0.22	1.00
im (209)	1581.9	1576	0.51	0.15	0.73
im (210)	1597.0	1594	0.12	0.02	0.13
im (211)	1608.8	—	<0.01	0.01	0.14
terpy (215)	1615.9	1609	0.02	<0.01	0.01
im (216)	1616.5	1609	0.04	0.03	0.18

MLCT transition to the π_{terpy}^* (184) orbital (Table 1). Even if an overall good agreement is found between theory and experiment, it is also seen that some parts of the spectrum are more difficult to assign. In particular, the wavenumber region between 1550 and 1620 cm^{-1} involves an overlap of several vibrational modes and many peaks with small RR intensities are present in the experimental spectrum below 1300 cm^{-1} . A tentative assignment is provided for most of the experimental bands, whereas the non-assigned frequencies are listed in Fig. 4. Finally, the mean absolute deviation of the vibrational wavenumbers with respect to experiment is 9 cm^{-1} , which is in agreement with the values obtained in previous theoretical investigations on RR intensities.^{46,47,64}

The RR spectrum of the protonated form (Fig. 4b and Table 3) of the complex shows important differences in comparison to the spectrum of the unprotonated form. In particular the vibrations associated with the 4*H*-imidazole ligand present large variations, which emphasize the strong effects of protonation within the imidazole ligand sphere. As can be seen from both the experimental and theoretical spectra, these variations concern mainly: (i) a significant enhancement of the RR intensities for the modes 92 and 105 (corresponding to the modes 89 and 104 of RITP) with calculated wavenumbers of 756 and 846 cm^{-1} , respectively, (ii) the presence of several intense bands in the 1100–1350 cm^{-1} wavenumber range, and (iii) a different intensity pattern in the 1350–1650 cm^{-1} region. Furthermore, the RR spectrum of RITPH displays only two bands corresponding to terpyridine

Table 3 Assignment of the vibrational frequencies (cm^{-1}) and calculated relative RR intensities ($I_{\text{rel.}}$) in the STA for the main excited states of the protonated complex. The theoretical frequencies were scaled by a factor of 0.97

Mode type	Freq. (Cal.)/ cm^{-1}	Freq. (Exp.)/ cm^{-1}	$I_{\text{rel.}} (S_4)$	$I_{\text{rel.}} (S_7)$	$I_{\text{rel.}} (S_{12})$
im (92)	756.2	772	0.44	0.04	0.01
im (105)	845.5	862	1.00	<0.01	<0.01
im (111)	910.8	—	0.01	0.05	0.02
im (114)	929.4	—	0.01	0.07	0.02
terpy(115)	932.2	904	0.02	<0.01	<0.01
im (118)	944.6	959	0.04	0.06	0.02
im (119)	949.2	959	0.04	0.04	0.02
terpy, im (135)	1030.9	1019	0.04	<0.01	<0.01
terpy, im (148)	1145.8	1148	0.04	0.13	0.02
terpy, im (149)	1146.2	1148	0.03	0.14	0.02
im (151)	1171.4	1175	0.08	0.16	0.19
im (152)	1178.5	1178	0.01	0.12	<0.01
im (153)	1180.5	1181	0.06	0.01	0.01
im (155)	1201.9	—	0.02	0.02	0.10
im (156)	1204.5	—	0.01	0.06	<0.01
terpy, im (157)	1210.9	1222	0.08	0.03	0.03
terpy, im (158)	1212.0	1222	0.29	0.05	0.04
im (160)	1245.9	1257	0.22	0.18	0.03
im (164)	1282.5	1316	0.56	0.19	0.27
terpy, im (169)	1300.1	1316	0.02	0.02	0.02
im (170)	1303.3	1316	0.11	0.13	0.02
terpy (173)	1326.4	1316	0.09	0.01	<0.01
im (176)	1384.2	1416	0.05	0.10	<0.01
im (188)	1448.9	1455	0.24	0.20	0.08
terpy, im (199)	1476.3	1479	0.17	0.15	0.03
im (200)	1479.1	1479	0.47	0.68	0.11
im (202)	1502.5	1506	0.53	0.68	0.27
im (204)	1509.9	1513	0.69	0.66	0.23
im (208)	1565.5	1569	0.32	1.00	0.38
im (209)	1571.0	1569	0.08	0.37	0.28
im (211)	1587.5	1587	0.03	0.14	0.15
im (212)	1606.8	1604	0.10	0.03	<0.01
im (213)	1609.2	1604	0.05	0.01	1.00
im (215)	1613.7	1605	<0.01	0.48	0.06
im (218)	1654.1	1635	0.28	0.19	0.35

vibrations (modes 115 and 173). The mode 115 has a weak RR intensity, whereas mode 173 is found with a decreased relative intensity in comparison to the unprotonated form (mode 171). This behavior can be understood from the fact that, contrary to RITP, the state in resonance (S_4) involves mainly a MLCT transition to the π_{im}^* (183) orbital (Table 1). Moreover, several modes are both located on the imidazole and terpyridine ligands, *i.e.* modes 135, 148, 149, 157, 158, 169 and 199. The noticeable RR intensities of these modes (in particular modes 158 and 199) are likely to arise from their vibrational contributions localized on the imidazole ligand. Finally, the mean absolute deviation of the vibrational wavenumbers for the protonated form (10 cm^{-1}) is found with a comparable value as the one (9 cm^{-1}) obtained for the unprotonated complex.

4.2.b. RR spectra in resonance with the IL band. The RR spectra (Fig. 5a and b) were also recorded in resonance with the second absorption band employing excitation wavelengths of 413 and 406 nm for RITP and RITPH, respectively. It is seen that the RR spectra in resonance with the second absorption band clearly differ from those obtained in resonance with the first absorption band; this is related to the different electronic characters of the associated excited states, as

unraveled by theory. Moreover, it can be noticed that the RR spectra in resonance with the second absorption bands are strongly modified upon protonation of the imidazole ligand, as it was observed for the spectra in resonance with the first absorption band.

The RR spectra were simulated using the STA for the two pairs of states (S_{11} , S_{17}) for the unprotonated form and (S_7 , S_{12}) for the protonated form. Because these states correspond to IL excitations of the imidazole ligand, their RR spectra display only imidazole vibrations and few vibrations with a mixed terpyridine–imidazole character (Tables 2 and 3).

For RITP (Fig. 5a), the simulated STA RR spectra of state S_{11} and S_{17} show several similarities, arising from the fact that both states involve an IL transition to the π_{im}^* (183) orbital. The agreement with experiment allows the assignment of the most intense RR bands. For example, the two experimental bands at 1357 and 1386 cm^{-1} are assigned to the vibrations 173 and 175, respectively, whereas the bands at 1493 and 1506 cm^{-1} are assigned to the modes 200 and 202, respectively. Additionally, it can be mentioned that the signal of mode 110 could not be detected in experiment due to overwhelming solvent signal. Moreover, it can be noticed that the relative RR intensities obtained for state S_{11} are in better agreement with experiment as those obtained for the state S_{17} . This is clearly visible for the bands in the 1500 – 1650 cm^{-1} frequency range and confirms the assignment deduced by inspection of the absorption spectra *i.e.* the experimental band at 425 nm is assigned to the IL state S_{11} .

Similar conclusions can be drawn in the case of the protonated form. Indeed, the simulated STA RR spectra of the states S_7 and S_{12} show mostly similar RR active vibrations, which arise from the rather comparable orbital character of these states. However, even if less straightforward in this case, it appears that the experimental spectrum is better reproduced by the RR spectrum of state S_7 . This is suggested by the better match of the relative intensities in the 1550 – 1650 cm^{-1} wavenumber range, when comparing experimental and calculated spectra, and the overall intensity pattern in the 1100 – 1350 cm^{-1} region. Similarly to RITP, this indicates that the experimental absorption band at 386 nm can be assigned to state S_7 . This is also in agreement with its larger oscillator strength with respect to state S_{12} . Furthermore, a contribution of state S_7 to the first absorption band can be excluded, because the RR vibrational signatures of state S_7 in the 1500 – 1650 cm^{-1} wavenumber range are noticeably different from the experimental spectrum recorded at 568 nm . Therefore, such investigation shows that, in cases where rather large deviations are obtained for the calculated excitation energies, the determination of RR spectra can help in the assignment of excited states in absorption spectra.

5. Conclusions

The absorption and RR properties of a novel (terpyridine)-Ru(*4H*-imidazole) complex were investigated theoretically and experimentally with the aim of estimating the effects of protonation on its photophysical properties. The complex presents two absorption maxima in the visible region, which are assigned by the calculations to MLCT and IL states,

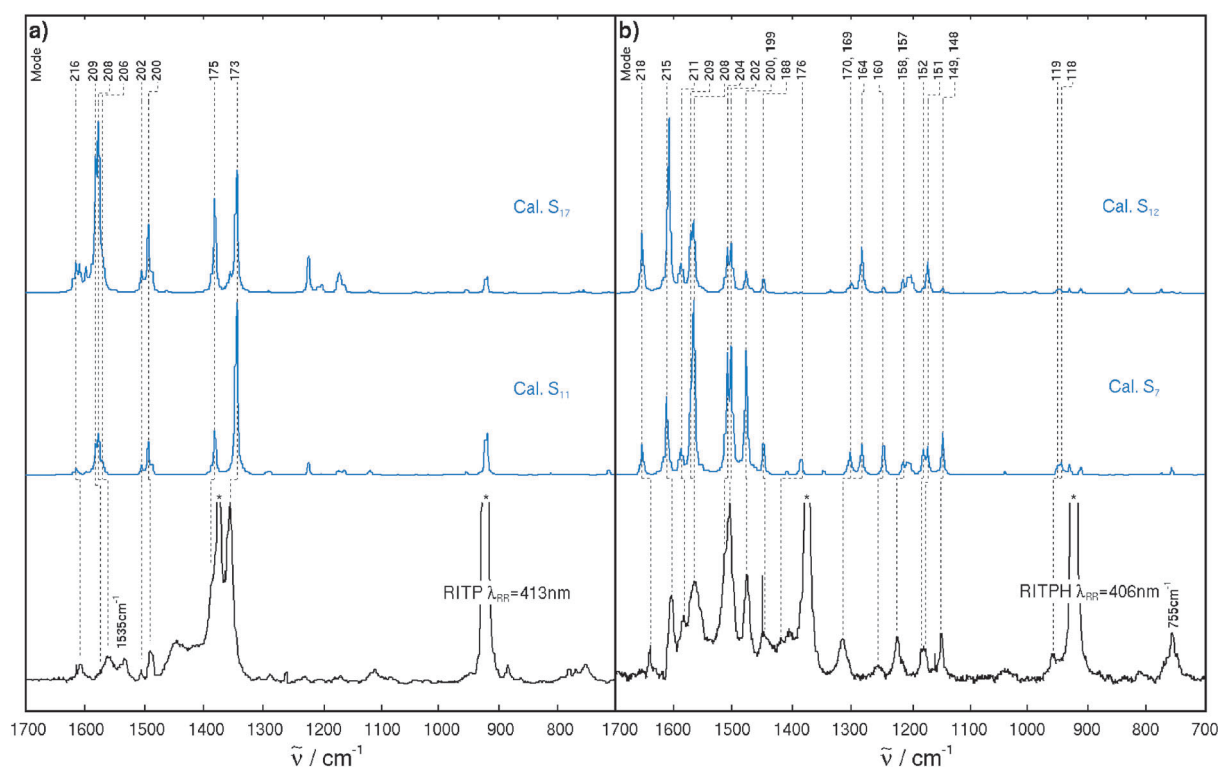


Fig. 5 Experimental and theoretical RR spectra of RITP (STA, state S_{11} and S_{17}) and RITPH (STA, state S_7 and S_{12}) in resonance with the second absorption band. The solvent bands are indicated by asterisks. A Lorentzian function with a FWHM of 5 cm^{-1} is employed to broaden the calculated transitions.

respectively. The investigation of the molecular orbitals and RR spectra in resonance with the MLCT state has shown that the effects of protonation favor a CT photoexcitation to the imidazole sphere. Therefore, it appears that the coordinative linkage, between the Ru-terpyridine unit and the 4*H*-imidazole moiety, leads to a favorable combination of both chromophore properties, while retaining the important CT characteristics. Such results are important in view of employing this compound for applications such as black absorbers in DSSCs, or in general to understand the molecular mechanism underlying the color-change induced by external stimuli such as pH variations.

From a theoretical point of view, it is remarkable that TDDFT can reproduce the RR spectra obtained in resonance with both the MLCT and IL bands, and consequently can accurately describe the effects of protonation on the RR intensities as well as provide an assignment of the main vibrational bands. This shows that the shapes of the excited state potential energy surfaces near the FC region, *i.e.*, the excited state gradients are correctly described by the calculations. Furthermore, for this transition metal complex the good agreement between experimental and theoretical RR spectra is probably related to the fact that a single electronic excited state is in resonance with the excitation wavelength. Indeed, for complexes where several excited states overlap in a single absorption band, previous studies^{46,47} have shown that the simulation of RR intensities requires a proper description of interference effects, which are usually more challenging to estimate. Furthermore, the comparison of simulated RR spectra with experiment has confirmed the assignment of the second absorption band to the IL states S_{11} and S_7 for the

unprotonated and protonated forms, respectively. It is also concluded that the underestimation of the S_7 excitation energy (-0.49 eV) by TDDFT is associated to its more pronounced CT character in comparison to state S_{11} . However, it is interesting to note that this disagreement on the excitation energy does not appear to correlate with the accuracy on the RR spectrum. Therefore, since TDDFT calculations are largely employed for investigating the photophysical properties of transition metal complexes, this study shows the utility of RR simulations in obtaining more detailed information about the character of the excited states as well as a better estimation about the accuracy of the employed computational method.

Acknowledgements

This research was supported financially by the Thüringer Ministerium für Bildung, Wissenschaft und Kultur (PhotoMIC). Further financial support is gratefully acknowledged from the Carl-Zeiss Stiftung (JG), the Studienstiftung des deutschen Volkes (MW), and the Fonds der chemischen Industrie (BD). All the calculations have been performed at the Universitätsrechenzentrum of the Friedrich-Schiller University of Jena and at the HP computers of the Theoretical Chemistry group in Jena.

References

- 1 R. Siebert, A. Winter, B. Dietzek, U. S. Schubert and J. Popp, *Macromol. Rapid Commun.*, 2010, **31**, 883–888.
- 2 R. Siebert, A. Winter, U. S. Schubert, B. Dietzek and J. Popp, *Phys. Chem. Chem. Phys.*, 2011, **13**, 1606–1617.

- 3 P. Coppo, M. Duati, V. N. Kozhevnikov, J. W. Hofstraat and L. De Cola, *Angew. Chem., Int. Ed.*, 2005, **44**, 1806–1810.
- 4 J. C. Chambron, J. P. Sauvage, E. Amouyal and P. Koffi, *Nouv. J. Chim.*, 1985, **9**, 527.
- 5 R. M. Hartshorn and J. K. Barton, *J. Am. Chem. Soc.*, 1992, **114**, 5919–5925.
- 6 Y. Jenkins, A. E. Friedman, N. J. Turro and J. K. Barton, *Biochemistry*, 1992, **31**, 10809–10816.
- 7 I. Haq, P. Lincoln, D. Suh, B. Norden, B. Z. Chowdhry and J. B. Chaires, *J. Am. Chem. Soc.*, 1995, **117**, 4788–4796.
- 8 R. B. Nair, B. M. Cullum and C. J. Murphy, *Inorg. Chem.*, 1997, **36**, 962–965.
- 9 M. Schwalbe, M. Karnahl, S. Tschierlei, U. Uhlemann, M. Schmitt, B. Dietzek, J. Popp, R. Groake, J. G. Vos and S. Rau, *Dalton Trans.*, 2010, **39**, 2768–2771.
- 10 S. Rau, B. Schäfer, D. Gleich, E. Anders, M. Rudolph, M. Friedrich, H. Görls, W. Henry and J. G. Vos, *Angew. Chem., Int. Ed.*, 2006, **45**, 6215–6218.
- 11 S. Tschierlei, M. Karnahl, M. Presselt, B. Dietzek, J. Guthmuller, L. González, M. Schmitt, S. Rau and J. Popp, *Angew. Chem., Int. Ed.*, 2010, **49**, 3981–3984.
- 12 S. Tschierlei, M. Presselt, C. Kuhnt, A. Yartsev, T. Pascher, V. Sundström, M. Karnahl, M. Schwalbe, B. Schäfer, S. Rau, M. Schmitt, B. Dietzek and J. Popp, *Chem.–Eur. J.*, 2009, **15**, 7678–7688.
- 13 M. Elvington, J. Brown, S. M. Arachchige and K. J. Brewer, *J. Am. Chem. Soc.*, 2007, **129**, 10644–10645.
- 14 P. Lei, M. Hedlund, R. Lomoth, H. Rensmo, O. Johansson and L. Hammarström, *J. Am. Chem. Soc.*, 2008, **130**, 26–27.
- 15 B. O'Regan and M. Grätzel, *Nature*, 1991, **353**, 737–740.
- 16 M. Grätzel, *Pure Appl. Chem.*, 2001, **73**, 459–467.
- 17 M. Grätzel, *Inorg. Chem.*, 2005, **44**, 6841–6851.
- 18 G. Benkő, J. Kallioinen, J. E. I. Korppi-Tommola, A. P. Yartsev and V. Sundström, *J. Am. Chem. Soc.*, 2002, **124**, 489–493.
- 19 G. Benkő, J. Kallioinen, P. Myllyperkiö, F. Trif, J. E. I. Korppi-Tommola, A. P. Yartsev and V. Sundström, *J. Phys. Chem. B*, 2004, **108**, 2862–2867.
- 20 J. Kallioinen, G. Benkő, P. Myllyperkiö, L. Khriachtchev, B. Skårman, R. Wallenberg, M. Tuomikoski, J. Korppi-Tommola, V. Sundström and A. P. Yartsev, *J. Phys. Chem. B*, 2004, **108**, 6365–6373.
- 21 C. Kuhnt, M. Karnahl, S. Tschierlei, K. Griebenow, M. Schmitt, B. Schäfer, S. Kriek, H. Görls, S. Rau, B. Dietzek and J. Popp, *Phys. Chem. Chem. Phys.*, 2010, **12**, 1357–1368.
- 22 P. Shen, Y. Liu, X. Huang, B. Zhao, N. Xiang, J. Fei, L. Liu, X. Wang, H. Huang and S. Tan, *Dyes Pigm.*, 2009, **83**, 187–197.
- 23 S. S. Pandey, T. Inoue, N. Fujikawa, Y. Yamaguchi and S. Hayase, *J. Photochem. Photobiol., A*, 2010, **214**, 269–275.
- 24 Y. Xie, P. Joshi, M. Ropp, D. Galipeau, L. Zhang, H. Fong, Y. You and Q. Qiao, *J. Porphyrins Phthalocyanines*, 2009, **13**, 903–909.
- 25 C.-P. Hsieh, H.-P. Lu, C.-L. Chiu, C.-W. Lee, S.-H. Chuang, C.-L. Mai, W.-N. Yen, S.-J. Hsu, E. W.-G. Diau and C.-Y. Yeh, *J. Mater. Chem.*, 2010, **20**, 1127–1134.
- 26 K. Hara, H. Horiuchi, R. Katoh, L. P. Singh, H. Sugihara, K. Sayama, S. Murata, M. Tachiya and H. Arakawa, *J. Phys. Chem. B*, 2002, **106**, 374–379.
- 27 H. Shang, Y. Luo, X. Guo, X. Huang, X. Zhan, K. Jiang and Q. Meng, *Dyes Pigm.*, 2010, **87**, 249–256.
- 28 K. Kilsa, E. I. Mayo, N. S. Lewis, J. R. Winkler and H. B. Gray, *Abstr. Pap. Am. Chem. Soc.*, 2003, **225**, U167–U168.
- 29 H. Park, E. Bae, J.-J. Lee, J. Park and W. Choi, *J. Phys. Chem. B*, 2006, **110**, 8740–8749.
- 30 B. Önfelt, P. Lincoln, B. Nordén, J. S. Baskin and A. H. Zewail, *Proc. Natl. Acad. Sci. U. S. A.*, 2000, **97**, 5708–5713.
- 31 K. Hara, T. Nishikawa, M. Kurashige, H. Kawauchi, T. Kashima, K. Sayama, K. Aika and H. Arakawa, *Sol. Energy Mater. Sol. Cells*, 2005, **85**, 21–30.
- 32 M. K. Nazeeruddin, R. Humphry-Baker, P. Liska and M. Grätzel, *J. Phys. Chem. B*, 2003, **107**, 8981–8987.
- 33 Z.-S. Wang, T. Yamaguchi, H. Sugihara and H. Arakawa, *Langmuir*, 2005, **21**, 4272–4276.
- 34 M. K. Nazeeruddin, P. Péchy, T. Renouard, S. M. Zakeeruddin, R. Humphry-Baker, P. Comte, P. Liska, L. Cevey, E. Costa, V. Shklover, L. Spiccia, G. B. Deacon, C. A. Bignozzi and M. Grätzel, *J. Am. Chem. Soc.*, 2001, **123**, 1613–1624.
- 35 F. Odobel and H. Zabri, *Inorg. Chem.*, 2005, **44**, 5600–5611.
- 36 J. Blumhoff, R. Beckert, S. Rau, S. Losse, M. Matschke, W. Günther and H. Görls, *Eur. J. Inorg. Chem.*, 2009, 2162–2169.
- 37 S. Rau, T. Büttner, C. Temme, M. Ruben, H. Görls, D. Walther, M. Duati, S. Fanni and J. G. Vos, *Inorg. Chem.*, 2000, **39**, 1621–1624.
- 38 A. Vleck Jr. and S. Zális, *Coord. Chem. Rev.*, 2007, **251**, 258–287.
- 39 D. Escudero, M. Assmann, A. Pospiech, W. Weigand and L. González, *Phys. Chem. Chem. Phys.*, 2009, **11**, 4593–4600.
- 40 M.-F. Charlot and A. Aukaaloo, *J. Phys. Chem. A*, 2007, **111**, 11661–11672.
- 41 F. D. Angelis, L. Belpassi and S. Fantacci, *THEOCHEM*, 2009, **914**, 74–86.
- 42 M. Atsumi, L. González and C. Daniel, *J. Photochem. Photobiol., A*, 2007, **190**, 310–320.
- 43 M. K. Nazeeruddin, F. De Angelis, S. Fantacci, A. Selloni, G. Viscardi, P. Liska, S. Ito, B. Takeru and M. Grätzel, *J. Am. Chem. Soc.*, 2005, **127**, 16835–16847.
- 44 F. De Angelis, S. Fantacci, E. Mosconi, M. K. Nazeeruddin and M. Grätzel, *J. Phys. Chem. C*, 2011, **115**, 8825–8831.
- 45 C. Herrmann, J. Neugebauer, M. Presselt, U. Uhlemann, M. Schmitt, S. Rau, J. Popp and M. Reiher, *J. Phys. Chem. B*, 2007, **111**, 6078–6087.
- 46 J. Guthmuller, B. Champagne, C. Moucheron and A. Kirsch-De Mesmaeker, *J. Phys. Chem. B*, 2010, **114**, 511–520.
- 47 J. Guthmuller and L. González, *Phys. Chem. Chem. Phys.*, 2010, **12**, 14812–14821.
- 48 M. J. Frisch, G. W. Trucks, H. B. Schlegel, G. E. Scuseria, M. A. Robb, J. R. Cheeseman, G. Scalmani, V. Barone, B. Mennucci, G. A. Petersson, H. Nakatsuji, M. Caricato, X. Li, H. P. Hratchian, A. F. Izmaylov, J. Bloino, G. Zheng, J. L. Sonnenberg, M. Hada, M. Ehara, K. Toyota, R. Fukuda, J. Hasegawa, M. Ishida, T. Nakajima, Y. Honda, O. Kitao, H. Nakai, T. Vreven, J. A. Montgomery Jr, J. E. Peralta, F. Ogliaro, M. Bearpark, J. J. Heyd, E. Brothers, K. N. Kudin, V. N. Staroverov, R. Kobayashi, J. Normand, K. Raghavachari, A. Rendell, J. C. Burant, S. S. Iyengar, J. Tomasi, M. Cossi, N. Rega, J. M. Millam, M. Klene, J. E. Knox, J. B. Cross, V. Bakken, C. Adamo, J. Jaramillo, R. Gomperts, R. E. Stratmann, O. Yazyev, A. J. Austin, R. Cammi, C. Pomelli, J. W. Ochterski, R. L. Martin, K. Morokuma, V. G. Zakrzewski, G. A. Voth, P. Salvador, J. J. Dannenberg, S. Dapprich, A. D. Daniels, Ö. Farkas, J. B. Foresman, J. V. Ortiz, J. Cioslowski and D. J. Fox, *GAUSSIAN 09 (Revision A.02)*, Gaussian, Inc., Wallingford CT, 2009.
- 49 A. D. Becke, *J. Chem. Phys.*, 1993, **98**, 5648.
- 50 C. Lee, W. Yang and R. G. Parr, *Phys. Rev. B: Condens. Matter*, 1988, **37**, 785.
- 51 D. Andrae, U. Häußermann, M. Dolg, H. Stoll and H. Preuß, *Theor. Chim. Acta*, 1990, **77**, 123–141.
- 52 P. C. Hariharan and J. A. Pople, *Theor. Chim. Acta*, 1973, **28**, 213–222.
- 53 J. P. Merrick, D. Moran and L. Radom, *J. Phys. Chem. A*, 2007, **111**, 11683–11700.
- 54 J. Tomasi, B. Mennucci and R. Cammi, *Chem. Rev.*, 2005, **105**, 2999–3094.
- 55 E. J. Heller, R. Sundberg and D. Tannor, *J. Phys. Chem.*, 1982, **86**, 1822–1833.
- 56 J. Guthmuller and B. Champagne, *J. Chem. Phys.*, 2007, **127**, 164507.
- 57 A. G. Walstrom, M. Pink, X. Yang and K. G. Caulton, *Dalton Trans.*, 2009, 6001–6006.
- 58 J. Atzrodt, R. Beckert, W. Günther and H. Görls, *Eur. J. Org. Chem.*, 2000, 1661–1668.
- 59 S. Tschierlei, B. Dietzek, M. Karnahl, S. Rau, F. M. MacDonnell, M. Schmitt and J. Popp, *J. Raman Spectrosc.*, 2008, **39**, 557–559.
- 60 A. Dreuw and M. Head-Gordon, *Chem. Rev.*, 2005, **105**, 4009–4037.
- 61 R. J. Magyar and S. Tretiak, *J. Chem. Theor. Comput.*, 2007, **3**, 976–987.
- 62 C. Adamo and V. Barone, *J. Chem. Phys.*, 1999, **110**, 6158.
- 63 T. Yanai, D. P. Tew and N. C. Handy, *Chem. Phys. Lett.*, 2004, **393**, 51–57.
- 64 J. Guthmuller, *J. Chem. Theor. Comput.*, 2011, **7**, 1082–1089.

4.5 Influence of Multiple Protonation on the Initial Excitation in a Black Dye

Reproduced with permission from Kupfer, S. *J. Phys. Chem. C* **116**, 19968-19977 (2011).

Copyright 2011 American Chemical Society.

<http://pubs.acs.org/doi/abs/10.1021/jp2100717>

Influence of Multiple Protonation on the Initial Excitation in a Black Dye

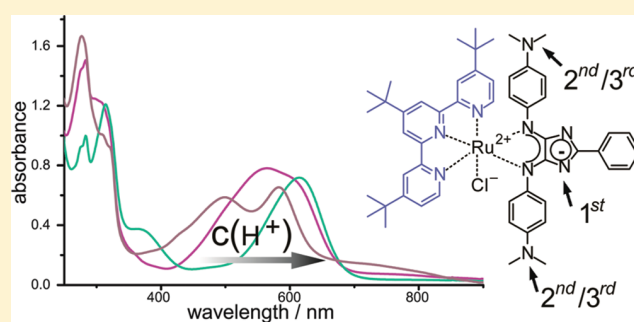
Maria Wächtler,^{†,‡} Stephan Kupfer,[†] Julien Guthmüller,^{†,§} Jürgen Popp,^{†,‡} Leticia González,^{*,†,⊥} and Benjamin Dietzek^{*,†,‡}

[†]Institute of Physical Chemistry and Abbe Center of Photonics, Friedrich-Schiller University Jena, Helmholtzweg 4, 07743, Jena, Germany

[‡]Institute of Photonic Technology Jena e.V., Albert-Einstein-Strasse 9, 07745, Jena, Germany

S Supporting Information

ABSTRACT: Solvent pH influences electronic and optical properties of photoactive systems by protonation/deprotonation of basic/acidic positions. In this study a joint experimental and theoretical approach is presented to analyze the acid/base properties of a new 4*H*-imidazole ruthenium(II) complex (**Ru**). The imidazole ligand is substituted by two dimethylamino groups and hence offers four positions for protonation. To identify the species present in certain acid concentration ranges calculated absorption and resonance Raman (RR) spectra are compared to experimental results. It is shown that three different protonated species can be prepared separately from each other by varying the acid concentration in solution and the character of the substituent can be switched from electron donating to electron withdrawing by protonation, which plays an important role in the further analysis of pH-dependent photoinduced processes in these systems.



I. INTRODUCTION

Ruthenium(II) polypyridine complexes are among the most studied compounds in coordination chemistry.^{1–6} They show a unique combination of chemical stability, strong visible absorption, and redox and catalytic activities. By incorporation of Ru centers in supramolecular assemblies, devices capable of vectorial electron and energy transfer can be designed. The interest in such assemblies is twofold: (i) They play an important role in investigating the nature of electron- and energy-transfer processes^{6–13} and (ii) they are valuable candidates for a wide variety of light-harvesting applications as, e.g., in photocatalysis^{14–22} and as sensitizers in dye-sensitized solar cells (DSSCs).^{23–27} Furthermore, Ru(II) polypyridine complexes can be employed as sensors^{28–32} and in molecular wires.^{33–35} In these applications the environmental conditions have to be monitored closely because the pH value of the solvent may influence the electronic and optical properties of the complexes by protonation/deprotonation of basic/acidic positions in the ligand sphere. This dependence can be exploited for pH sensing or switching, as environmental properties have a strong impact on the functionality by influencing, e.g., electron and energy transfer rates and redox potentials.^{32,36–52} For example, in Ru complexes containing imidazole ligands the pH-dependent properties were studied: in imidazo[4,5-*f*][1,10]phenanthroline coordinating complexes, the protonation state of the imidazole ring has been shown to modify the luminescence behavior, and solvent pH

modulates the electron transfer in imidazo[4,5-*f*][1,10]phenanthroline-bridged supramolecular assemblies and across an electrode interface.^{36,41,48,51–55} Another group of complexes with pH-dependent properties coordinates benzimidazole ligands:^{32,38–40,46,47,49} in binuclear benzimidazole-bridged complexes metal–metal interactions can be switched on and off by varying the protonation state of the ligand.

In this study, the impact of solvent acidity on the absorption properties and the character of the initial electronic excitation in the Ru(II) polypyridine dye chloro- η^3 -4,4',4''-tri-*tert*-butyl-2,2':6',2''-terpyridine- η^2 -2-phenyl-4,5-(*p*-dimethylaminophenyl-imino)-imidazolate-ruthenium(II) (**Ru**) (Figure 1) containing a new imidazole-type ligand is investigated. This complex is derived from a recently introduced 4*H*-imidazole coordinating ruthenium complex⁵⁶ by exchanging the methyl groups of the terminal tolyl rings by dimethylamino groups. Compared to the methyl-substituted analogue, **Ru** exhibits an exceptional broad absorption spectrum covering the entire visible range and reaching even into the near-infrared (NIR). This makes Ru related structures containing—additional—suitable coupling groups promising candidates for sensitizers in DSSCs.^{57–59} In comparison to the methyl-substituted 4*H*-imidazole complex, where only protonation of the imidazole ring is possible, further positions for

Received: October 20, 2011

Published: November 15, 2011

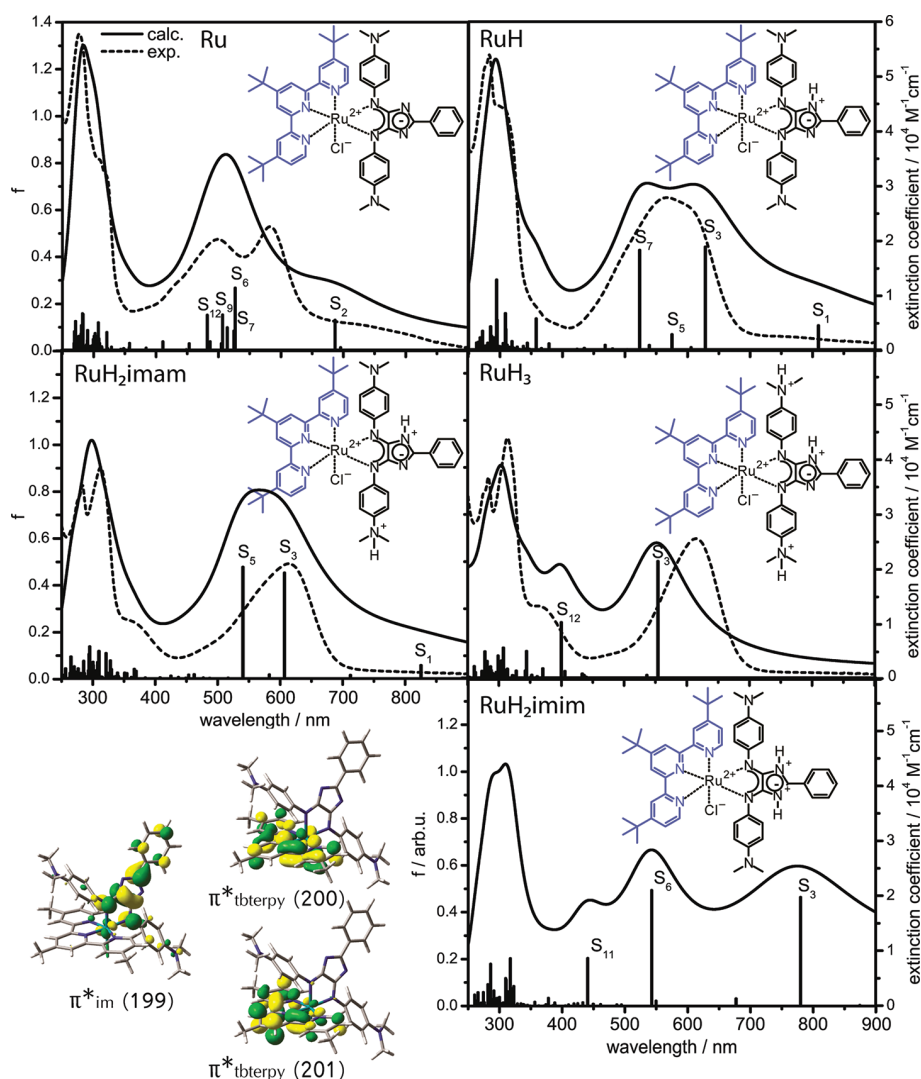


Figure 1. Calculated (solid line) and experimental (dashed line) absorption spectra of different protonated forms of **Ru**. The calculated oscillator strengths are represented by black sticks. A Lorentzian function with a fwhm of 4000 cm^{-1} is employed to broaden the calculated intensities. The experimental spectra of **Ru**, **RuH**, and **RuH₃** were measured in solutions of certain acid concentrations; the experimental spectrum of **RuH₂imam** is the result of the evolving factor analysis (EFA) of the titration data presented in Figure 2. Below the absorption spectra the accepting π^* orbitals involved in the MLCT excitation of **Ru** are displayed.

protonation provided by the dimethylamino groups are available in **Ru**, and a more complex protonation behavior is expected. By protonation involving the dimethylamino groups, it is possible to change the character of the substituent from electron donating to electron withdrawing, which might be used as switch to control photoinduced processes.

To investigate the influence of solvent pH and to assign the species responsible for the properties observed in the UV/vis absorption and resonance Raman (RR) spectra, a combination of theoretical and experimental methods is applied in this study. Due to the large size of the system under consideration, time-dependent density functional theory (TDDFT) is used to calculate the molecular properties of unprotonated and selected protonated species of **Ru**. Previous DFT/TDDFT calculations on Ru(II) complexes have established the accuracy of this computational approach to describe absorption spectra^{51,60–79} and RR spectra.^{56,80–82} Recently, we investigated the effects of protonation on the electronic structure of a related Ru(II) complex,⁵⁶ for

which the RR spectra were simulated within the short-time approximation.⁸³ It was shown that calculations are capable of capturing the effects of protonation on both the absorption and RR spectra. However, in the present study the vibronic theory of RR scattering⁸⁴ is employed due to the more complex absorption spectra of the investigated compounds, which display several overlapping excited states. This methodology takes account of the dependence of the RR spectra on the excitation wavelength and includes interference effects between the different excited states in resonance with the excitation light. This last effect was studied theoretically in recent investigations^{81,82,85,86} and is important for the systems considered in this work.

II. THEORY AND COMPUTATIONAL DETAILS

In order to reduce the computational cost of the simulations without affecting the spectroscopic properties of the complexes, the three *tert*-butyl groups of **Ru** were approximated in the calculations

by methyl groups. The structural and electronic data for the different protonated species of **Ru** were obtained from quantum chemistry calculations performed with the GAUSSIAN 09 program.⁸⁷ The geometry, vibrational frequencies, and normal coordinates of the ground state were calculated by means of density functional theory (DFT) with the XC functional B3LYP.^{88,89} The 28-electron relativistic core potential MWB⁹⁰ was used with its basis set for the ruthenium atom, that is, 4s, 4p, 4d, and 5s electrons are treated explicitly, whereas the first three inner shells are described by the core pseudopotential. The 6-31G(d) double- ζ basis set⁹¹ was employed for the ligands. To correct for the lack of anharmonicity and the approximate treatment of electron correlation⁹² the harmonic frequencies were scaled by the factor 0.97. The vertical excitation energies, oscillator strengths, and analytical Cartesian energy derivatives of the excited states were obtained from TDDFT calculations within the adiabatic approximation with the same XC functional, pseudopotential, and basis set. It was shown by several groups that B3LYP provides a balanced description of the absorption features of such complexes.^{56,62,63,93,94} Absorption spectra were simulated by determining the excitation energies and oscillator strengths of the 80 lowest singlet excited states. The effects of the interaction with a solvent (acetonitrile, $\epsilon = 35.688$, $n = 1.344$) on the geometry, frequencies, excitation energies, and excited-state gradients were taken into account by integral equation formalism of the polarizable continuum model.⁹⁵ The nonequilibrium procedure of solvation was used for the calculation of the excitation energies and of the excited-state gradients, which is well-adapted for processes where only the fast reorganization of the electronic distribution of the solvent is important.

Assuming a conventional 90° scattering arrangement, the Raman differential cross section for a fundamental transition $0 \rightarrow 1_l$ is given by^{84,96,97}

$$\frac{d\sigma_{0 \rightarrow 1_l}}{d\Omega} = \frac{\omega_L \omega_S^3}{16\pi^2 \epsilon_0^2 c^4} \frac{1}{45} (45a^2 + 5\delta^2 + 7\gamma^2) \quad (1)$$

where ω_L is the frequency of the incident light, ω_S is the frequency of the scattered light, and a^2 , δ^2 , and γ^2 are the three invariants for randomly oriented molecules, which depend on the Raman polarizability tensor $(\alpha_{\alpha\beta})_{g_0 \rightarrow g_1}$.

The RR spectra were calculated within the independent mode displaced harmonic oscillator model (IMDHOM), which assumes that the electronic ground and excited state potential energy surfaces are harmonic and that they only differ by their equilibrium geometry (i.e., they share the same set of vibrational frequencies and normal coordinates). Within this approach and assuming only Condon-type scattering (A term contribution⁸⁴), the Raman polarizability tensor can be calculated from^{82,98}

$$(\alpha_{\alpha\beta})_{g_0 \rightarrow g_1} = \frac{1}{\hbar} \sum_e (\mu_{ge})_\alpha (\mu_{ge})_\beta \frac{\Delta_{e,l}}{\sqrt{2}} \{ \Phi_e(\omega_L) - \Phi_e(\omega_L - \omega_l) \} \quad (2)$$

where $(\mu_{ge})_\alpha$ is a component of the electronic transition dipole moment at the ground state equilibrium geometry, $\Delta_{e,l}$ is the dimensionless displacement of the e th excited state potential minimum with respect to the ground state for the l th normal coordinate, and ω_l is the vibrational frequency of the l th normal mode. Equation 2 allows us to take into account the contribution of several electronic excited states and to describe possible interference effects between them. Generally, the function $\Phi_e(\omega_L)$

includes a summation over Franck–Condon (FC) factors.^{82,98} However, in the present study the contribution of FC factors has been neglected and the function $\Phi_e(\omega_L)$ is approximated by

$$\Phi_e(\omega_L) = \frac{1}{\omega_{e,g} - \omega_L - i\Gamma} \quad (3)$$

where $\omega_{e,g}$ is the vertical excitation energy from the electronic ground state g to the excited state e and Γ is a damping factor describing a homogeneous broadening. A value of Γ equal to 2000 cm^{-1} was assumed in the simulations to reproduce the experimental broadening. An excitation wavelength of 568 nm was employed to calculate the RR spectra, for which the calculated vertical excitation energies $\omega_{e,g}$ were corrected so that experimental and theoretical absorption maxima coincide. The use of eq 3 is appropriate for the investigated complexes because the RR measurements are performed at an excitation wavelength in resonance with absorption bands displaying a large broadening and nonresolved vibronic structure.

The dimensionless displacement $\Delta_{e,l}$ of the excited state e is defined in the IMDHOM by the partial derivative of the excited-state potential energy E^e along the normal mode Q_l evaluated at the ground state equilibrium geometry

$$\Delta_{e,l} = - \frac{1}{\sqrt{\hbar} \omega_l^{3/2}} \left(\frac{\partial E^e}{\partial Q_l} \right)_0 \quad (4)$$

These derivatives were obtained from the analytical derivatives of the excited-state electronic energy (E^e) along the Cartesian coordinates.

III. EXPERIMENTAL METHODS

Ru was synthesized according to a procedure as described in Kupfer et al.⁵⁶

The measurements of UV/vis spectra were carried out at room temperature in air-equilibrated acetonitrile in a quartz cell with 1 cm path length. The spectra were recorded with a Jasco V-670 spectrophotometer. The titration was performed on a solution (3 mL) of the metal complex by adding small aliquots (2.5 μL) of a 0.01 M trifluoroacetic acid solution in acetonitrile (first protonation step). After no further changes in the absorption spectra were observed aliquots (1 μL) of pure trifluoroacetic acid were added. The corresponding acid constants were determined by analyzing the changes in the absorption spectra using the ReactLabEQUILIBRIA global analysis program with a model based on eq 5. In the calculations a $\text{p}K_a$ value of 12.65 for trifluoroacetic acid⁹⁹ in acetonitrile was employed.

The resonance Raman spectra were recorded in a conventional 90° scattering arrangement. Excitation light at 568 nm was delivered by a krypton-ion laser (model Coherent Innova 301C). A rotating cell was utilized to prevent the heating of the sample. The scattered light was focused onto the entrance slit of an Acton SpectraPro 2758i spectrometer, and the dispersed light was detected by a liquid-nitrogen-cooled CCD camera (Princeton Instruments). The sample concentration was optimized to obtain the maximum signal-to-noise ratio and was in the range of 10^{-4} M. The acid concentration of the solution was adjusted in a way that only one species of **Ru** was dominating the spectra. No changes in the absorption spectra could be detected after the exposure to the laser light caused by sample degradation. RR Spectra were background corrected and normalized to a solvent band (919 cm^{-1}).

IV. RESULTS AND DISCUSSION

IV.A. Calculated Absorption Spectra. The 4*H*-imidazole ligand offers four positions for protonation, i.e., at the imidazole nitrogen atoms and both dimethylamino groups. Absorption spectra were calculated for the unprotonated form **Ru** and for selected protonated species (solid lines and stick plots in Figure 1). It was concluded that the first protonation most likely occurs at one of the imidazole nitrogen atoms forming the singly protonated species **RuH**. This is due to the stronger basicity of the imidazole nitrogens (4*H*-imidazole coordinated to ruthenium $pK_a \approx 7.4$ in water/acetonitrile mixture 1/1)¹⁰⁰ compared to the dimethylamino groups (*N,N*-dimethylaniline in water $pK_a \approx 5$).¹⁰¹ For the second protonation step protonation in two different positions was regarded: spectra of a species protonated at both imidazole nitrogen atoms (**RuH₂imim**) and a species with protonation at one imidazole nitrogen atom and one dimethylamino group (**RuH₂imam**) were calculated. **RuH₃** is a triple-protonated form with protonation of one imidazole nitrogen atom and both dimethylamino groups. A complete protonation of all four positions was not regarded as no experimental indications were present for such a process as will be described below. With ongoing protonation the calculations predict a 40 nm red-shift of the absorption maximum in the visible spectral range (corresponding to a bathochromic shift of 1408 cm^{-1}). Not only the main band but also the shoulder in the red part of the spectrum is red-shifted upon stepwise protonation. In **RuH₂imim** the redmost absorption feature in the UV/vis spectrum is centered at 780 nm and is strongly enhanced, whereas for all other species a decrease of the intensity of the red shoulder is predicted.

A closer analysis of the underlying electronic states involved in the absorption process allows us to dissect the structural elements responsible for light absorption and to observe the influence of ligand protonation on the electronic properties of the excited states. The properties of the main excited states present in the visible range are detailed in Table 1. The lowest unoccupied molecular orbitals involved in the excitations of **Ru** are depicted partly in Figure 1 (for complete sets of molecular orbitals for all species see the Supporting Information). For **Ru**, the strong visible absorption band is caused by a superposition of six excited states of metal-to-ligand charge-transfer (MLCT) character. State S_6 is described by CT from the ruthenium center to the 4*H*-imidazole ligand. At shorter wavelengths the terpyridine ligand is stronger involved in the configuration of the states S_7 , S_8 , S_9 , and S_{12} . State S_2 , responsible for the absorption in the red shoulder, is a MLCT state with electron transfer from the ruthenium center to the 4*H*-imidazole ligand. Protonation at the imidazole ring nitrogen atom, i.e., formation of **RuH**, reduces the number of states dominating the absorption. The main contributions in the visible absorption spectrum of **RuH** are delivered by the states S_3 , S_5 , and S_7 . All three states are of MLCT character with CT from the metal center to the imidazole ligand. No contributions of the terpyridine ligand to the visible absorption of **RuH** are found. S_1 describes the red shoulder, which shows reduced oscillator strength and is red-shifted by 122 nm (2063 cm^{-1}) compared to S_2 of **Ru**. In the case of a second protonation at the imidazole ring (**RuH₂imim**) the intensity of the long-wavelength absorption feature is strongly enhanced resulting in a very broad spectrum covering the whole visible range. However, when considering the second protonation to take place at an amino group (**RuH₂imam**) a further decrease of the oscillator strength of the redmost absorption band is predicted. In both double-protonated species

Table 1. Calculated Vertical Excitation Energies (E^c), Oscillator Strengths (f), and Singly Excited Configurations of the Main Excited States and Experimental Absorption Maxima in the Visible Range^a

state	transition	weight (%)	E^c/eV	λ/nm	f	$\lambda_{\text{exp}}/\text{nm}$
Ru						
S_2	$d_{\text{Ru}}(198) \rightarrow \pi^*_{\text{im}}(199)$	86	1.81	687	0.1309	710
S_6	$d_{\text{Ru}}(196) \rightarrow \pi^*_{\text{im}}(199)$	53	2.35	527	0.2682	583
	$d_{\text{Ru}}(197) \rightarrow \pi^*_{\text{im}}(199)$	13				
S_7	$d_{\text{Ru}}(194) \rightarrow \pi^*_{\text{tberpy}}(200)$	11	2.36	525	0.0848	
	$d_{\text{Ru}}(196) \rightarrow \pi^*_{\text{tberpy}}(200)$	46				
S_8	$d_{\text{Ru}}(195) \rightarrow \pi^*_{\text{tberpy}}(200)$	43	2.41	514	0.0991	
	$d_{\text{Ru}}(196) \rightarrow \pi^*_{\text{tberpy}}(200)$	10				
	$d_{\text{Ru}}(197) \rightarrow \pi^*_{\text{tberpy}}(200)$	14				
S_9	$d_{\text{Ru}}(194) \rightarrow \pi^*_{\text{im}}(199)$	15	2.45	507	0.1533	
	$d_{\text{Ru}}(195) \rightarrow \pi^*_{\text{im}}(199)$	29				
	$d_{\text{Ru}}(195) \rightarrow \pi^*_{\text{tberpy}}(201)$	13				
S_{12}	$d_{\text{Ru}}(196) \rightarrow \pi^*_{\text{tberpy}}(201)$	22	2.57	482	0.1527	499
	$d_{\text{Ru}}(195) \rightarrow \pi^*_{\text{im}}(199)$	10				
	$d_{\text{Ru}}(195) \rightarrow \pi^*_{\text{tberpy}}(201)$	43				
	$d_{\text{Ru}}(197) \rightarrow \pi^*_{\text{im}}(199)$	21				
RuH						
S_1	$d_{\text{Ru}}(196) \rightarrow \pi^*_{\text{im}}(199)$	34	1.53	809	0.1074	760
	$d_{\text{Ru}}(198) \rightarrow \pi^*_{\text{im}}(199)$	64				
S_3	$d_{\text{Ru}}(196) \rightarrow \pi^*_{\text{im}}(199)$	57	1.97	629	0.4415	608
	$d_{\text{Ru}}(198) \rightarrow \pi^*_{\text{im}}(199)$	34				
S_5	$d_{\text{Ru}}(194) \rightarrow \pi^*_{\text{im}}(199)$	29	2.16	575	0.0691	
	$d_{\text{Ru}}(195) \rightarrow \pi^*_{\text{im}}(199)$	17				
	$d_{\text{Ru}}(197) \rightarrow \pi^*_{\text{im}}(199)$	43				
S_7	$d_{\text{Ru}}(194) \rightarrow \pi^*_{\text{im}}(199)$	48	2.37	523	0.4279	567
	$d_{\text{Ru}}(195) \rightarrow \pi^*_{\text{im}}(199)$	22				
	$d_{\text{Ru}}(197) \rightarrow \pi^*_{\text{im}}(199)$	10				
RuH₂imim						
S_3	$d_{\text{Ru}}(196) \rightarrow \pi^*_{\text{im}}(199)$	38	1.59	780	0.4640	
	$\pi_{\text{im}}(197) \rightarrow \pi^*_{\text{im}}(199)$	10				
	$\pi_{\text{im}}(198) \rightarrow \pi^*_{\text{im}}(199)$	49				
S_6	$d_{\text{Ru}}(194) \rightarrow \pi^*_{\text{im}}(199)$	85	2.28	543	0.4936	
	S_{11} $\pi_{\text{im}}(198) \rightarrow \pi^*_{\text{im}}(202)$	93				
RuH₂imam						
S_1	$d_{\text{Ru}}(197) \rightarrow \pi^*_{\text{im}}(199)$	41	1.50	826	0.0555	
	$\pi_{\text{im}}(198) \rightarrow \pi^*_{\text{im}}(199)$	54				
S_3	$d_{\text{Ru}}(195) \rightarrow \pi^*_{\text{im}}(199)$	20	2.04	607	0.4500	615
	$d_{\text{Ru}}(196) \rightarrow \pi^*_{\text{im}}(199)$	8				
	$d_{\text{Ru}}(197) \rightarrow \pi^*_{\text{im}}(199)$	30				
S_5	$\pi_{\text{im}}(198) \rightarrow \pi^*_{\text{im}}(199)$	39	2.29	540	0.4744	
	$d_{\text{Ru}}(195) \rightarrow \pi^*_{\text{im}}(199)$	61				
	$d_{\text{Ru}}(196) \rightarrow \pi^*_{\text{im}}(199)$	15				
	$d_{\text{Ru}}(197) \rightarrow \pi^*_{\text{im}}(199)$	11				
RuH₃						
S_3	$d_{\text{Ru}}(196) \rightarrow \pi^*_{\text{im}}(199)$	86	2.24	554	0.5010	615
S_{12}	$\pi_{\text{im}}(195) \rightarrow \pi^*_{\text{im}}(199)$	77	3.10	400	0.2416	368

^a The principal orbitals are depicted partially in Figure 1 and in Table S1 in the Supporting Information.

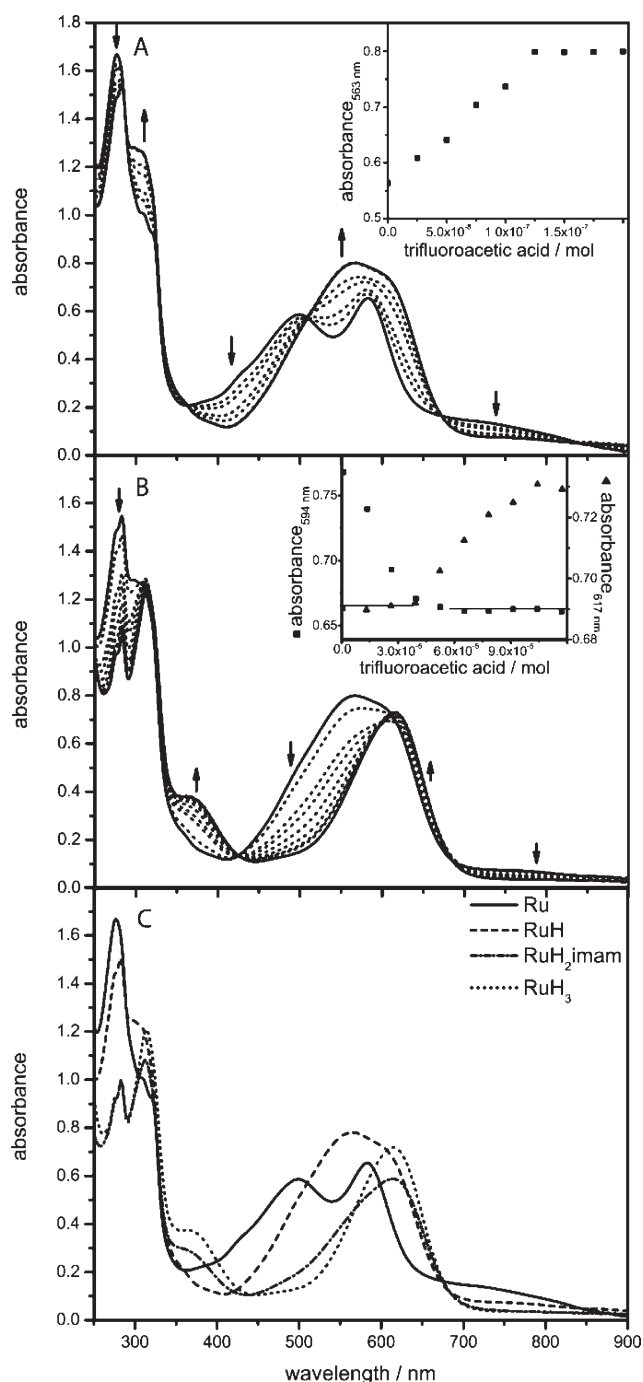


Figure 2. Absorption spectral changes observed for a 2.88×10^{-5} mol L^{-1} solution of **Ru** in acetonitrile upon (A) addition of aliquots of 0.01 M TFA/acetonitrile; the insets show the titration curves obtained by monitoring the absorbance at 563 nm (λ_{max} of the monoprotonated form) as a function of added acid; (B) addition of aliquots of pure TFA; the inset shows the absorbance changes at 594 nm ■ (isosbestic point of the third protonation step) and 617 nm ▲ (isosbestic point second protonation step); (C) spectra obtained by EFA (evolving factor analysis).

the character of the excited states is a mixture of MLCT and IL (intraligand) excitations involving only the 4*H*-imidazole ligand. The spectrum of **RuH₃** shows a narrowing of the absorption band

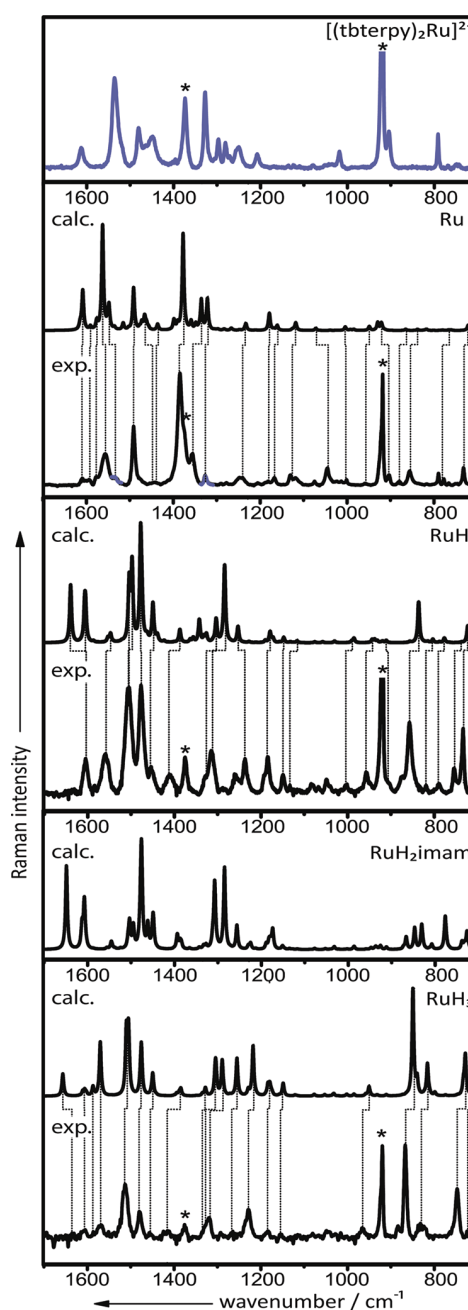


Figure 3. Calculated and experimental resonance Raman spectra of **Ru** and its protonated forms in resonance with the absorption band in the visible range ($\lambda_{ex} = 568$ nm). The experimental resonance Raman spectrum of the homoleptic reference complex $[(tbterpy)_2Ru]^{2+}$ ($\lambda_{ex} = 476$ nm) is given for the assignment of the terpyridine vibrations (blue). The solvent bands are indicated by asterisks. A Lorentzian function with a fwhm of 5 cm^{-1} is employed to broaden the calculated intensities.

in comparison to the spectra of both double-protonated forms and only contributions of two excited states are found: S_3 responsible for the absorption around 554 nm reveals **Ru** \rightarrow 4*H*-imidazole MLCT character and S_{12} (absorption at 400 nm) shows IL character involving only the 4*H*-imidazole ligand.

IV.B. Experimental Absorption Spectra. To validate the predictive strength of the calculated absorption spectra a careful acid concentration dependent experimental study of the absorption

spectra was performed (Figure 2). Upon addition of aliquots of a diluted solution of trifluoroacetic acid (TFA) in acetonitrile to a solution of **Ru** a red-shift of the absorption maximum is observed as predicted by the calculations. Furthermore, the observed double-peak structure of the absorption in the visible range vanishes. The existence of five isosbestic points (841, 673, 509, 364, 286 nm) during the addition of diluted acid shows that only two absorbing species are present and only one protonation step is observed. After addition of 3.5 equivalents of TFA no further changes upon addition of diluted TFA were detectable, and for further protonation aliquots of pure TFA were added. This results in an additional red-shift and narrowing of the absorption band. These findings are in agreement with the calculation results. Two sets of isosbestic points are present (first 694, 617, 423, 306, 241 nm; final steps 655, 594, 427, 318 nm; see the inset in Figure 2B and Figure S1 in the Supporting Information) indicating the presence of two protonation steps with very close pK_a values. In particular, no rise of the NIR absorption feature, characteristic for the **RuH₂imim** species (see Figure 1), was observed, indicating that double imidazole protonation does not occur. This is in agreement with observations made with the methyl-substituted imidazole complex where only one protonation step was observed under similar conditions.⁵⁶

From these observations, we postulate the following model for the stepwise protonation of **Ru**: In the first step **Ru** is protonated at the imidazole ring forming **RuH**. In the second step upon addition of higher concentrated acid both dimethylamino groups are protonated, and finally **RuH₃** is present in solution. However, no **RuH₂imam** can be detected in its pure form. This doubly protonated species can only be found in a mixture with **RuH** and **RuH₃** as the pK_a values of both amino groups differ by less than 2 pK_a units.

IV.C. RR Spectra. To provide further support for the existence of two protonation stages in the second titration step and to verify the model proposed above, RR spectroscopy was applied, exploiting the fact that the different protonated species should deliver characteristic distinguishable spectra. RR spectra with excitation at 568 nm were recorded of the starting solution of the titration, after the first titration step (addition of 3.5 equivalents TFA), and at the end of the titration (addition of 1500 equivalents of TFA) and compared to calculated RR spectra of the different protonated species. The simulated RR spectra were obtained by considering the contributions of all main electronic excited states presented in section IV.A (Table 1). As can be seen from Figure 3, the calculations yield good agreement with the experimental results. Furthermore, an unambiguous assignment of the experimental spectra to specific protonated species is possible. The assignment of individual vibrational modes to particular molecular moieties/ligands was confirmed by a comparison of the spectra of **Ru** and its protonated species with the RR spectrum of the homoleptic [(tbterpy)₂Ru]²⁺ complex. The spectra of the latter system recorded at 476 nm served as reference to assign the vibrational modes coupled to the MLCT transition from the ruthenium center to the terpyridine ligand (see Table S2 in the Supporting Information).

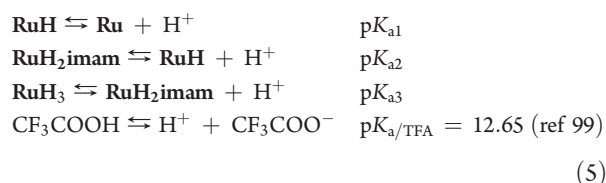
The RR spectrum of the unprotonated species, **Ru**, is dominated by signals of ring-breathing vibrations localized on the 4*H*-imidazole ligand. The modes between 1300 and 1600 cm^{-1} display the highest intensities. The calculated wavenumbers in this spectral range, i.e., 1336, 1379, 1492, 1564 cm^{-1} , are in good agreement with the experiment (1357, 1386, 1492, 1558 cm^{-1}).

The presence of some other bands with low intensities, which are assigned to vibrations localized on the terpyridine ligand (calculation, 1323, 1536 cm^{-1} ; experiment, 1328, 1535 cm^{-1}), is attributed to the fact that MLCT to the terpyridine partly contributes to the electronic transition in the investigated spectral range.

Upon protonation a strong change in the RR spectrum is found. Compared to the spectrum of unprotonated **Ru** a different intensity pattern is observed and the signals with the strongest intensities are detected at higher wavenumbers (experiment, 1476, 1504 cm^{-1} ; calculation, 1477, 1498, 1504 cm^{-1}). Additional signals appear below 900 cm^{-1} . This characteristic change in the RR spectrum upon protonation is clearly reproduced in the calculations. The experimental spectrum after the first titration step resembles the calculated spectrum of the monoprotonated form **RuH** in agreement with the model proposed above. In analogy, a similar development of the RR spectrum with protonation at the ring nitrogen position was observed for the methyl-substituted 4*H*-imidazole complex.⁵⁶ The assignment of the vibrational bands to distinct molecular substructures reveals a reduced participation of the terpyridine ligand in the absorption process as already observed in the character of the excited states involved. Most vibrations are imidazole centered or involve both ligands (calculated 1477, 733 cm^{-1}).

Only marginal changes in the band positions are observed upon further protonation, but the intensity pattern of the spectra change characteristically both in experiment and calculation. The signals which display small shifts (for details see Figures S3 and S4 in the Supporting Information) are modes involving the substituent bearing rings (ring-breathing), and protonation of the substituent influences their exact position (calculated signal positions, 722/728, 836/849, 1498/1505, and 1504/1510 cm^{-1} in **RuH/RuH₃**). The spectrum recorded upon maximum addition of TFA can be assigned to **RuH₃**. Together with the unambiguous assignment of the first titration product to **RuH** by its RR spectrum this fact delivers proof that in the second step of the titration experiment two protonation stages are observed.

IV.D. Discussion. On the basis of these observations the following model describing the acid/base equilibria during titration could be established:



To quantify the observed changes in the absorption spectra the number of species involved in the observed absorption changes and their corresponding absorption spectra were calculated by means of singular value decomposition (SVD) and evolving factor analysis (EFA) using the ReactLabEQUILIBRIA software (Figure 2). The characteristic features reproduced by the SVD analysis are the following: (i) the absorption spectrum of **Ru** shows a double-peak structured broad absorption (582 nm, 22 600 $M^{-1} cm^{-1}$ and 499 nm, 20 400 $M^{-1} cm^{-1}$) covering almost the whole visible range; (ii) the first protonation step shifts the center of the absorption band to longer wavelengths and the extinction coefficient increases (569 nm, 27 900 $M^{-1} cm^{-1}$), the red shoulder (720 nm in **Ru**) loses intensity and is red-shifted to 760 nm; (iii) further protonation finally shifts the absorption maximum to 615 nm (**RuH₃**, 25 800 $M^{-1} cm^{-1}$) and the width of

absorption band is reduced, the red shoulder disappears, while a new absorption band at 386 nm appears in the spectrum of the diprotonated form and is present in the spectrum of RuH_3 , as well. The observed differences between the experimental absorption spectra and the absorption spectra calculated by TDDFT are caused by errors in the energetic positions of the excited states contributing to the absorption in the visible range in the TDDFT calculations. In general, a discrepancy between the energy scale of calculated and experimental spectra is observed, and most excitation energies are overestimated by 0.25 eV at most, which is within the typical accuracy of TDDFT calculations for MLCT excitations in transition metal complexes.^{56,64,82}

By global analysis the $\text{p}K_{\text{a}}$ values were determined to be $\text{p}K_{\text{a}1} = 13.8 \pm 0.4$, $\text{p}K_{\text{a}2} = 10.6 \pm 0.4$, $\text{p}K_{\text{a}3} = 9.7 \pm 0.4$. Taking into account the differences of $\text{p}K_{\text{a}}$ values in water and acetonitrile,¹⁰² the $\text{p}K_{\text{a}}$ value of the imidazole nitrogen atom was estimated to be 14. A similar estimation and literature values for *N,N*-dimethylaniline in acetonitrile (11.43)¹⁰² deliver a $\text{p}K_{\text{a}}$ value of 11 for the dimethylamino groups, which is in perfect agreement with the experimental results. The fact that $\text{p}K_{\text{a}2}$ and $\text{p}K_{\text{a}3}$ describing consecutive protonation steps of the two equal dimethylamino groups are slightly different indicates that protonation of the first dimethylamino group affects the basicity of the second one, an effect which may be mediated by the conjugated system and/or electrostatic effects related to the change in the overall charge of the complex brought about by protonation.

V. CONCLUSION

A joint theoretical–experimental study of the protonation-dependent optical properties of a new 4*H*-imidazole coordinating Ru(II) complex was described. The combination of experimental and theoretical data delivers a valuable tool for the identification of species present in particular acid concentration ranges. In the system under investigation four species were identified to participate in the observed acid/base equilibria. Three of the identified species, i.e., the unprotonated form **Ru**, the monoprotated form **RuH**, and the triple-protonated form **RuH₃**, can be prepared separately from each other by adjusting the acid concentration in solution. **RuH** and **RuH₃** differ in the protonation stage of the dimethylamino group and by varying solution pH the character of this substituent can be switched from electron donating to electron withdrawing. The influence of the character of this substituent on the photophysical properties will be subject of upcoming work.

■ ASSOCIATED CONTENT

S **Supporting Information.** Tabulated transitions calculated absorption spectra, pictures of the molecular orbitals contributing to the configuration of the states involved in the absorption, tabulated assignment Raman signals, experimental UV/vis spectra illustrating isosbestic points, figure signal shifts in experimental and calculated resonance Raman signals with protonation. This material is available free of charge via the Internet at <http://pubs.acs.org>.

■ AUTHOR INFORMATION

Corresponding Author

*E-mail: benjamin.dietzek@uni-jena.de (B.D.); leticia.gonzalez@uni-jena.de (L.G.). Phone: +49 (0)3641 206-332 (B.D.); +49 (0)3641 9-48360 (L.G.). Fax: +49 (0)3641 206-399 (B.D.); +49 (0)3641 9-48302 (L.G.).

Present Addresses

[§]Faculty of Applied Physics and Mathematics, Gdansk University of Technology, Narutowicza 11/12, 80233, Gdansk, Poland.

[†]Institute of Theoretical Chemistry, University of Vienna, Währinger St. 17, 1090 Vienna, Austria.

■ ACKNOWLEDGMENT

This research was supported financially by the Thüringer Ministerium für Bildung, Wissenschaft und Kultur (PhotoMIC, Grant No. B 514-09049). Further financial support is gratefully acknowledged from the Carl-Zeiss Stiftung (J.G.), the Studienstiftung des deutschen Volkes (M.W.), and the Fonds der Chemischen Industrie (B.D., J.P.). All calculations were performed at the Universitätsrechenzentrum of the Friedrich-Schiller University of Jena and at the HP computers of the Theoretical Chemistry group.

■ REFERENCES

- (1) Huynh, M. H. V.; Dattelbaum, D. M.; Meyer, T. J. *Coord. Chem. Rev.* **2005**, *249*, 457.
- (2) Hammarström, L.; Johansson, O. *Coord. Chem. Rev.* **2010**, *254*, 2546.
- (3) Zeitler, K. *Angew. Chem., Int. Ed.* **2009**, *48*, 9585.
- (4) Dixon, I. M.; Lebon, E.; Sutra, P.; Igau, A. *Chem. Soc. Rev.* **2009**, *38*, 1621.
- (5) Gao, F.; Chao, H.; Ji, L.-N. *Chem. Biodiversity* **2008**, *5*, 1962.
- (6) Campagna, S.; Puntoriero, F.; Nastasi, F.; Bergamini, G.; Balzani, V. *Photochemistry and Photophysics of Coordination Compounds I*; Springer: Berlin, Germany, 2007; Vol. 280.
- (7) Falkenström, M.; Johansson, O.; Hammarström, L. *Inorg. Chim. Acta* **2007**, *360*, 741.
- (8) Benniston, A. C.; Harriman, A. *Chem. Soc. Rev.* **2006**, *35*, 169.
- (9) Wenger, O. S. *Inorg. Chim. Acta* **2011**, *374*, 3.
- (10) Balzani, V.; Bergamini, G.; Ceroni, P. In *Advances in Inorganic Chemistry*; van Eldik, R., Stochel, G., Eds.; Elsevier, 2011; Vol. 63, p 105.
- (11) Fletcher, S. J. *Solid State Electrochem.* **2010**, *14*, 705.
- (12) Meylemans, H. A.; Lei, C. F.; Damrauer, N. H. *Inorg. Chem.* **2008**, *47*, 4060.
- (13) Meylemans, H. A.; Damrauer, N. H. *Inorg. Chem.* **2009**, *48*, 11161.
- (14) Akita, M.; Inagaki, A. *Coord. Chem. Rev.* **2010**, *254*, 1220.
- (15) Sakai, K.; Kobayashi, M.; Masaoka, S. *Molecules* **2010**, *15*, 4908.
- (16) Alstrum-Acevedo, J. H.; Brennaman, M. K.; Meyer, T. J. *Inorg. Chem.* **2005**, *44*, 6802.
- (17) Rau, S.; Schäfer, B.; Gleich, D.; Anders, E.; Rudolph, M.; Friedrich, M.; Görls, H.; Henry, W.; Vos, J. G. *Angew. Chem., Int. Ed.* **2006**, *45*, 6215.
- (18) Tschierlei, S.; Karnahl, M.; Presselt, M.; Dietzek, B.; Guthmüller, J.; Gonzalez, L.; Schmitt, M.; Rau, S.; Popp, J. *Angew. Chem., Int. Ed.* **2010**, *49*, 3981.
- (19) Tschierlei, S.; Presselt, M.; Kuhnt, C.; Yartsev, A.; Pascher, T.; Sundström, V.; Karnahl, M.; Schwalbe, M.; Schäfer, B.; Rau, S.; Schmitt, M.; Dietzek, B.; Popp, J. *Chem.—Eur. J.* **2009**, *15*, 7678.
- (20) Lei, P.; Hedlund, M.; Lomoth, R.; Rensmo, H.; Johansson, O.; Hammarström, L. *J. Am. Chem. Soc.* **2008**, *130*, 26.
- (21) Andreiadis, E. S.; Chavarot-Kerlidou, M.; Fontecave, M.; Artero, V. *Photochem. Photobiol.* **2011**, *87*, 946.
- (22) Concepcion, J. J.; Jurss, J. W.; Brennaman, M. K.; Hoertz, P. G.; Patrocínio, A. O. T.; Iha, N. Y. M.; Templeton, J. L.; Meyer, T. J. *Acc. Chem. Res.* **2009**, *42*, 1954.
- (23) Oregon, B.; Grätzel, M. *Nature* **1991**, *353*, 737.
- (24) Grätzel, M. *Nature* **2001**, *414*, 338.
- (25) Robertson, N. *Angew. Chem., Int. Ed.* **2006**, *45*, 2338.
- (26) Polo, A. S.; Itokazu, M. K.; Iha, N. Y. M. *Coord. Chem. Rev.* **2004**, *248*, 1343.
- (27) Grätzel, M. *Acc. Chem. Res.* **2009**, *42*, 1788.

- (28) Friedman, A. E.; Chambron, J. C.; Sauvage, J. P.; Turro, N. J.; Barton, J. K. *J. Am. Chem. Soc.* **1990**, *112*, 4960.
- (29) Rice, C. R.; Guerrero, A.; Bell, Z. R.; Paul, R. L.; Motson, G. R.; Jeffery, J. C.; Ward, M. D. *New J. Chem.* **2001**, *25*, 185.
- (30) Anzenbacher, P.; Tyson, D. S.; Jursikova, K.; Castellano, F. N. *J. Am. Chem. Soc.* **2002**, *124*, 6232.
- (31) Wei, H.; Wang, E. *Luminescence* **2011**, *26*, 77.
- (32) Saha, D.; Das, S.; Bhaumik, C.; Dutta, S.; Baitalik, S. *Inorg. Chem.* **2010**, *49*, 2334.
- (33) Launay, J.-P.; Coudret, C. *Electron Transfer in Chemistry*; Wiley-VCH: Weinheim, Germany, 2001.
- (34) Schlicke, B.; De Cola, L.; Belsler, P.; Balzani, V. *Coord. Chem. Rev.* **2000**, *208*, 267.
- (35) Belsler, P. *Chimia* **2010**, *64*, 356.
- (36) Keyes, T. E.; Pellegrin, Y.; Forster, R. J. *Inorg. Chim. Acta* **2009**, *362*, 1715.
- (37) Constable, E. C.; Housecroft, C. E.; Thompson, A. C.; Passaniti, P.; Silvi, S.; Maestri, M.; Credi, A. *Inorg. Chim. Acta* **2007**, *360*, 1102.
- (38) Baitalik, S.; Dutta, S.; Biswas, P.; Florke, U.; Bothe, E.; Nag, K. *Eur. J. Inorg. Chem.* **2010**, 570.
- (39) Haga, M.; Ano, T.; Kano, K.; Yamabe, S. *Inorg. Chem.* **1991**, *30*, 3843.
- (40) Haga, M.; Takasugi, T.; Tomie, A.; Ishizuya, M.; Yamada, T.; Hossain, M. D.; Inoue, M. *Dalton Trans.* **2003**, 2069.
- (41) Chao, H.; Ye, B. H.; Zhang, Q. L.; Ji, L. N. *Inorg. Chem. Commun.* **1999**, *2*, 338.
- (42) Zhang, H. G.; Tao, X. T.; Chen, K. S.; Yuan, C. X.; Yan, S. N.; Jiang, M. H. *Chin. Chem. Lett.* **2011**, *22*, 647.
- (43) de Tacconi, N. R.; Lezna, R. O.; Konduri, R.; Ongeri, F.; Rajeshwar, K.; MacDonnell, F. M. *Chem.—Eur. J.* **2005**, *11*, 4327.
- (44) de Tacconi, N. R.; Lezna, R. O.; Chitakunye, R.; MacDonnell, F. M. *Inorg. Chem.* **2008**, *47*, 8847.
- (45) Joo, F.; Kovacs, J.; Benyei, A. C.; Katho, A. *Angew. Chem., Int. Ed.* **1998**, *37*, 969.
- (46) Carina, R. F.; Verzegnassi, L.; Bernardinelli, G.; Williams, A. F. *Chem. Commun.* **1998**, 2681.
- (47) Kobayashi, K.; Ishikubo, M.; Kanaizuka, K.; Kosuge, K.; Masaoka, S.; Sakai, K.; Nozaki, K.; Haga, M. *Chem.—Eur. J.* **2011**, *17*, 6954.
- (48) Li, Z. S.; Yang, H. X.; Zhang, A. G.; Luo, H.; Wang, K. Z. *Inorg. Chim. Acta* **2011**, *370*, 132.
- (49) Rau, S.; Buttner, T.; Temme, C.; Ruben, M.; Gors, H.; Walther, D.; Duati, M.; Fanni, S.; Vos, J. G. *Inorg. Chem.* **2000**, *39*, 1621.
- (50) McGarvey, J. J.; Browne, W. R.; Henry, W.; Passaniti, P.; Gandolfi, M. T.; Ballardini, R.; O'Connor, C. M.; Brady, C.; Coates, C. G.; Vos, J. G. *Photochem. Photobiol. Sci.* **2007**, *6*, 386.
- (51) Fan, S. H.; Zhang, A. G.; Ju, C. C.; Gao, L. H.; Wang, K. Z. *Inorg. Chem.* **2010**, *49*, 3752.
- (52) Gao, F.; Chen, X.; Zhou, F.; Weng, L. P.; Guo, L. T.; Chen, M.; Chao, H.; Ji, L. N. *Inorg. Chim. Acta* **2009**, *362*, 4960.
- (53) Quaranta, A.; Lachaud, F.; Herrero, C.; Guillot, R.; Charlot, M. F.; Leibl, W.; Aukauloo, A. *Chem.—Eur. J.* **2007**, *13*, 8201.
- (54) Pellegrin, Y.; Forster, R. J.; Keyes, T. E. *Inorg. Chim. Acta* **2008**, *361*, 2683.
- (55) Forster, R. J.; Pellegrin, Y.; Keyes, T. E. *Electrochem. Commun.* **2007**, *9*, 1899.
- (56) Kupfer, S.; Guthmuller, J.; Wächter, M.; Losse, S.; Rau, S.; Dietzek, B.; Popp, J.; Gonzalez, L. *Phys. Chem. Chem. Phys.* **2011**, *13*, 15580.
- (57) Robson, K. C. D.; Koivisto, B. D.; Gordon, T. J.; Baumgartner, T.; Berlinguette, C. P. *Inorg. Chem.* **2010**, *49*, 5335.
- (58) Robson, K. C. D.; Koivisto, B. D.; Yella, A.; Spornova, B.; Nazeeruddin, M. K.; Baumgartner, T.; Grätzel, M.; Berlinguette, C. P. *Inorg. Chem.* **2011**, *50*, 5494.
- (59) Chou, C. C.; Wu, K. L.; Chi, Y.; Hu, W. P.; Yu, S. J.; Lee, G. H.; Lin, C. L.; Chou, P. T. *Angew. Chem., Int. Ed.* **2011**, *50*, 2054.
- (60) De Angelis, F.; Lobello, M. G.; Fantacci, S.; Credi, A. *Eur. J. Inorg. Chem.* **2011**, 1605.
- (61) Jakubikova, E.; Chen, W. Z.; Dattelbaum, D. M.; Rein, F. N.; Rocha, R. C.; Martin, R. L.; Batista, E. R. *Inorg. Chem.* **2009**, *48*, 10720.
- (62) Badaeva, E.; Albert, V. V.; Kilina, S.; Kopusov, A.; Sykora, M.; Tretiak, S. *Phys. Chem. Chem. Phys.* **2010**, *12*, 8902.
- (63) Constable, E. C.; Devereux, M.; Dunphy, E. L.; Housecroft, C. E.; Rudd, J. A.; Zampese, J. A. *Dalton Trans.* **2011**, *40*, 5505.
- (64) Vlcek, A.; Zalis, S. *Coord. Chem. Rev.* **2007**, *251*, 258.
- (65) Charlot, M. F.; Aukauloo, A. *J. Phys. Chem. A* **2007**, *111*, 11661.
- (66) Atsumi, M.; Gonzalez, L.; Daniel, C. J. *Photochem. Photobiol., A* **2007**, *190*, 310.
- (67) Nazeeruddin, M. K.; De Angelis, F.; Fantacci, S.; Selloni, A.; Viscardi, G.; Liska, P.; Ito, S.; Bessho, T.; Grätzel, M. *J. Am. Chem. Soc.* **2005**, *127*, 16835.
- (68) De Angelis, F.; Fantacci, S.; Mosconi, E.; Nazeeruddin, M. K.; Grätzel, M. *J. Phys. Chem. C* **2011**, *115*, 8825.
- (69) De Angelis, F.; Fantacci, S.; Gebauer, R. *J. Phys. Chem. Lett.* **2011**, *2*, 813.
- (70) Li, M.-X.; Zhang, H.-X.; Zhou, X.; Pan, Q.-J.; Fu, H.-G.; Sun, C.-C. *Eur. J. Inorg. Chem.* **2007**, 2171.
- (71) Li, M. X.; Zhou, X.; Xia, B. H.; Zhang, H. X.; Pan, Q. J.; Liu, T.; Fu, H. G.; Sun, C. C. *Inorg. Chem.* **2008**, *47*, 2312.
- (72) Gao, X. Q.; Pan, Q. J.; Li, L.; Guo, Y. R.; Zhang, H. X.; Fu, H. G. *Chem. Phys. Lett.* **2011**, *506*, 146.
- (73) Wilson, G. J.; Will, G. D. *Inorg. Chim. Acta* **2010**, *363*, 1627.
- (74) Wadman, S. H.; Kroon, J. M.; Bakker, K.; Havenith, R. W. A.; van Klink, G. P. M.; van Koten, G. *Organometallics* **2010**, *29*, 1569.
- (75) Zhang, X.; Zhang, J. J.; Xia, Y. Y. *J. Photochem. Photobiol., A* **2007**, *185*, 283.
- (76) Barolo, C.; Nazeeruddin, M. K.; Fantacci, S.; Di Censo, D.; Comte, P.; Liska, P.; Viscardi, G.; Quagliotto, P.; De Angelis, F.; Ito, S.; Grätzel, M. *Inorg. Chem.* **2006**, *45*, 4642.
- (77) De Angelis, F.; Fantacci, S.; Selloni, A.; Grätzel, M.; Nazeeruddin, M. K. *Nano Lett.* **2007**, *7*, 3189.
- (78) De Angelis, F.; Fantacci, S.; Selloni, A.; Nazeeruddin, M. K.; Grätzel, M. *J. Am. Chem. Soc.* **2007**, *129*, 14156.
- (79) Al-Noaimi, M.; El-Khateeb, M.; Haddad, S. F.; Sunjuk, M.; Crutchley, R. J. *Polyhedron* **2008**, *27*, 3239.
- (80) Herrmann, C.; Neugebauer, J.; Presselt, M.; Uhlemann, U.; Schmitt, M.; Rau, S.; Popp, J.; Reiher, M. *J. Phys. Chem. B* **2007**, *111*, 6078.
- (81) Guthmuller, J.; Champagne, B.; Moucheron, C.; Kirsch-De Mesmaeker, A. *J. Phys. Chem. B* **2010**, *114*, 511.
- (82) Guthmuller, J.; Gonzalez, L. *Phys. Chem. Chem. Phys.* **2010**, *12*, 14812.
- (83) Heller, E. J.; Sundberg, R. L.; Tannor, D. J. *J. Phys. Chem.* **1982**, *86*, 1822.
- (84) Albrecht, A. C. *J. Chem. Phys.* **1961**, *34*, 1476.
- (85) Silverstein, D. W.; Jensen, L. J. *Chem. Theory Comput.* **2010**, *6*, 2845.
- (86) Lubner, S.; Neugebauer, J.; Reiher, M. *J. Chem. Phys.* **2010**, *132*.
- (87) Frisch, M. J.; Trucks, G. W.; Schlegel, H. B.; Scuseria, G. E.; Robb, M. A.; Cheeseman, J. R.; Scalmani, G.; Barone, V.; Mennucci, B.; Petersson, G. A.; Nakatsuji, H.; Caricato, M.; Li, X.; Hratchian, H. P.; Izmaylov, A. F.; Bloino, J.; Zheng, G.; Sonnenberg, J. L.; Hada, M.; Ehara, M.; Toyota, K.; Fukuda, R.; Hasegawa, J.; Ishida, M.; Nakajima, T.; Honda, Y.; Kitao, O.; Nakai, H.; Vreven, T.; Montgomery, J. A., Jr.; Peralta, J. E.; Ogliaro, F.; Bearpark, M.; Heyd, J. J.; Brothers, E.; Kudin, K. N.; Staroverov, V. N.; Kobayashi, R.; Normand, J.; Raghavachari, K.; Rendell, A.; Burant, J. C.; Iyengar, S. S.; Tomasi, J.; Cossi, M.; Rega, N.; Millam, J. M.; Klene, M.; Knox, J. E.; Cross, J. B.; Bakken, V.; Adamo, C.; Jaramillo, J.; Gomperts, R.; Stratmann, R. E.; Yazyev, O.; Austin, A. J.; Cammi, R.; Pomelli, C.; Ochterski, J. W.; Martin, R. L.; Morokuma, K.; Zakrzewski, V. G.; Voth, G. A.; Salvador, P.; Dannenberg, J. J.; Dapprich, S.; Daniels, A. D.; Farkas, Ö.; Foresman, J. B.; Ortiz, J. V.; Cioslowski, J.; Fox, D. J. *Gaussian 09*, revision A.02; Gaussian Inc.: Wallingford, CT, 2009.
- (88) Becke, A. D. *J. Chem. Phys.* **1993**, *98*, 5648.
- (89) Lee, C. T.; Yang, W. T.; Parr, R. G. *Phys. Rev. B* **1988**, *37*, 785.
- (90) Andrae, D.; Haussermann, U.; Dolg, M.; Stoll, H.; Preuss, H. *Theor. Chim. Acta* **1990**, *77*, 123.

- (91) Harihara, P.; Pople, J. A. *Theor. Chim. Acta* **1973**, *28*, 213.
- (92) Merrick, J. P.; Moran, D.; Radom, L. *J. Phys. Chem. A* **2007**, *111*, 11683.
- (93) Cramer, C. J.; Truhlar, D. G. *Phys. Chem. Chem. Phys.* **2009**, *11*, 10757.
- (94) Gorelsky, S. I.; da Silva, S. C.; Lever, A. B. P.; Franco, D. W. *Inorg. Chim. Acta* **2000**, *300*, 698.
- (95) Tomasi, J.; Mennucci, B.; Cammi, R. *Chem. Rev.* **2005**, *105*, 2999.
- (96) Long, D. A. *The Raman Effect: An Unified Treatment of the Theory of Raman scattering by Molecules*; John Wiley & sons Ltd.: Chichester, U.K., 2002.
- (97) Kelley, A. M. *J. Phys. Chem. A* **2008**, *112*, 11975.
- (98) Peticolas, W. L.; Rush, T. J. *Comput. Chem.* **1995**, *16*, 1261.
- (99) Izutsu, K. *Acid–Base Dissoziation Constants in Dipolar Aprotic Solvents*; Blackwell: Oxford, U.K., 1990.
- (100) Losse, S. Redoxaktive Metallorganische Farbstoffkomplexe zur Verwendung in Photovoltaik und Photokatalyse. Dissertation, Friedrich-Schiller-Universität, 2010.
- (101) Perrin, D. D. *Dissociation Constants of Organic Bases in Aquous Solution*; Butterworths (IUPAC): London, 1965.
- (102) Kaljurand, I.; Kutt, A.; Soovali, L.; Rodima, T.; Maemets, V.; Leito, I.; Koppel, I. A. *J. Org. Chem.* **2005**, *70*, 1019.

4.6 A Novel Ru(II) Polypyridine Black Dye Investigated by Resonance Raman Spectroscopy and TDDFT Calculations

Reproduced with permission from Wächtler, M. *J. Phys. Chem. C* **115**, 24004-24012 (2012).
Copyright 2012 American Chemical Society.

<http://pubs.acs.org/doi/abs/10.1021/jp3067958>

A Novel Ru(II) Polypyridine Black Dye Investigated by Resonance Raman Spectroscopy and TDDFT Calculations

Stephan Kupfer,^{†,∇} Maria Wächtler,^{†,‡,§,∇} Julien Guthmuller,^{||} Jürgen Popp,^{†,‡,§,⊥}
Benjamin Dietzek,^{*,†,‡,§,⊥} and Leticia González^{*,#}

[†]Institute for Physical Chemistry, Friedrich Schiller University Jena, Helmholtzweg 4, 07743 Jena, Germany

[‡]Abbe Center of Photonics, Friedrich Schiller University Jena, Helmholtzweg 4, 07743 Jena, Germany

[§]Institute of Photonic Technology (IPHT) Jena, Albert-Einstein-Str. 9, 07745 Jena, Germany

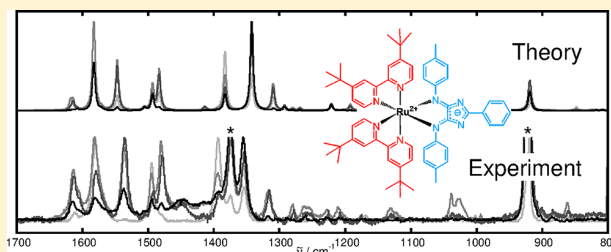
^{||}Faculty of Applied Physics and Mathematics, Gdansk University of Technology, Narutowicza 11/12, 80233 Gdansk, Poland

[⊥]Jena Center for Soft Matter (JCSM), Humboldtstr. 10, 07743 Jena, Germany

[#]Institute of Theoretical Chemistry, University of Vienna, Währinger Str. 17, 1090 Vienna, Austria

Supporting Information

ABSTRACT: The optical properties of a new (bipyridine)₂Ru(4*H*-imidazole) complex presenting a remarkable broad absorption in the visible range are investigated. The strong overlap of the absorption with the solar radiation spectrum renders the studied complex promising as a black absorber and hence as a starting structure for applications in the field of dye-sensitized solar cells. The correlations between structural and electronic features for the unprotonated and protonated forms are studied by means of UV–vis absorption and resonance Raman (RR) spectroscopy modeled with the help of time-dependent density functional theory (TDDFT) calculations. The absorption spectra show two bands in the visible region, which TDDFT assigns to a metal-to-ligand charge-transfer (MLCT) state and to a superposition of three excited states with MLCT and intraligand charge-transfer character, respectively. Additionally, the analysis of the molecular orbitals and RR spectra in resonance with the first MLCT band shows that the effects of protonation favor a charge-transfer photoexcitation to the 4*H*-imidazole ligand. The RR spectra simulated for several excitation wavelengths covering the visible region are in excellent agreement with experimental data. In particular, it is noteworthy that the calculations are able to reproduce the wavelength dependence of the RR spectra provided that corrected excitation energies are employed. Interference effects between the electronic states contributing to the RR scattering are small for the investigated complex.



1. INTRODUCTION

Ruthenium(II) polypyridine complexes have gained an enormous interest in a wide range of chemical and photophysical applications. These transition-metal complexes exhibit a strong stability on light, heat, and electricity as well as a substantial visible absorption combined with redox and catalytic activities. These properties open a manifold of applications, for example, in the field of DNA-sensors,^{1–6} semiconductors,^{7,8} light-emitting diodes^{9–11} and as a sensitizer for dye-sensitized solar cells (DSSCs).^{12–15}

A predominant focus is set on their potential to construct efficient and economically priced sensitizers for DSSCs. To this aim, many investigations have been performed in order to maximize the overlap of the absorption bands of Ru complexes with the solar spectrum in the visible region. Typically, the absorption band of ruthenium(II) polypyridine complexes, such as in Ru(II)-bipyridine dyes, is located below 550 nm. This overlap can be enlarged mainly via two different strategies: (i) Several attempts have been made to increase the absorbance in the NIR range¹⁶ by increasing the π system of the polypyridine

ligands with additional dyes.¹⁷ However, such systems show merely a weak coupling between the chromophores. Recently, we investigated systems with a 4*H*-imidazole ligand,¹⁸ which allowed us to shift the visible absorption maximum to approximately 600 nm.^{19–21} (ii) Another attempt is to broaden the absorbance in the visible region. Hence, several bright absorption bands in the visible region of the solar radiation spectrum are crucial in order to pursue this objective.

The targeted design of optimal dyes can only be achieved with the help of theoretical modeling. A great number of theoretical investigations have been carried out in order to study the absorption spectrum of ruthenium complexes; see a few examples in refs 22–32. Because of the computational demand of such calculations, mostly time-dependent density functional theory (TDDFT)³³ is employed to study the excited states of Ru(II) complexes.³⁴ Such calculations usually give a satisfactory

Received: July 9, 2012

Revised: August 9, 2012

Published: August 22, 2012

reproduction of the observed absorption bands, provided that the interaction with the solvent is taken into account. Typically, hybrid exchange-correlation (XC) functionals are applied because they are capable of estimating the band shape and the energetic position of the different types of excitations, for example, metal-to-ligand charge-transfer (MLCT) states and local intraligand (IL) states, with reasonably small deviation. The computation of RR spectra is less extended in the literature³⁵ due to its intrinsic difficulties and computational demands. Nevertheless, the investigation of the RR intensity pattern both experimentally and theoretically is extremely useful to unravel structural and photophysical characteristics.

In the present paper, we investigate a Ru(II) 4*H*-imidazole chromophore system (bis-4,4'-di-*tert*-butyl-2,2'-bipyridin-2-phenyl-4,5-(*p*-tolylimino)-imidazol-ruthenium(II)-hexafluorophosphate; see Figure 1a,b) in its unprotonated (RIBP) and

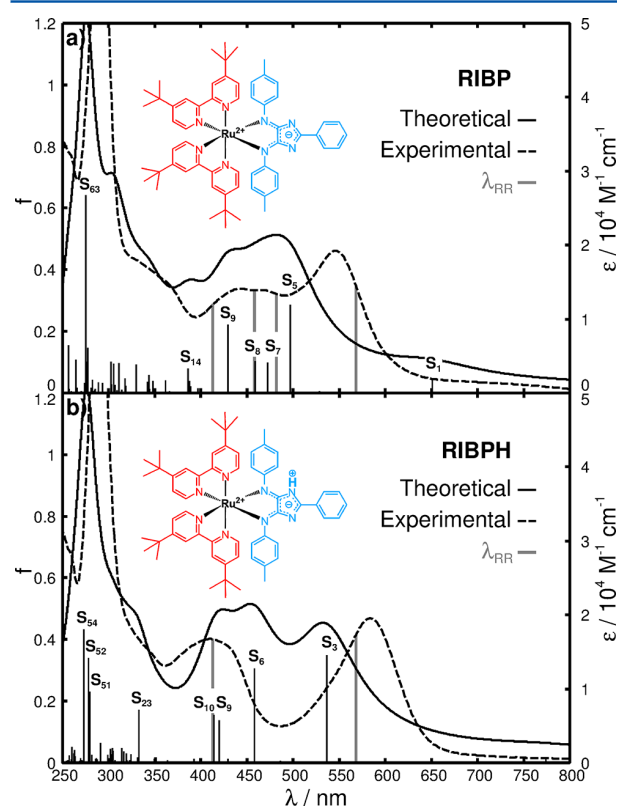


Figure 1. Experimental (dashed line) and theoretical (black line) absorption spectra of the RIBP and RIBPH species in acetonitrile. The calculated oscillator strengths are represented by black sticks. A Lorentzian function with a full width at half-maximum (fwhm) of 3000 cm^{-1} is employed to broaden the transitions in the simulated spectrum. The four vertical lines indicate the wavelengths at which the RR measurements are performed for the unprotonated (568, 482, 458, and 413 nm) and the protonated species (568 and 413 nm).

protonated (RIBPH) forms. The investigated complex resembles one of our recently studied systems^{20,21} containing a terpyridine ligand instead of a bipyridine ligand sphere in conjunction with the 4*H*-imidazole chromophore. As in the previous study, the contributions of the individual structural elements to the unusually broad and pH-responsive absorption spectrum are unraveled theoretically and experimentally. Particular emphasis is put on the correlation between electronic and structural

properties. Moreover, measured RR spectra are modeled by means of TDDFT. In Kupfer et al.,²⁰ the RR intensity pattern was calculated for each individual state due to the predominant intensity of that particular electronic excited state. In Wächtler et al.,²¹ resonance with several electronic excited states was investigated for a multiple protonation for only one particular excitation wavelength. In the present study, RR spectra are investigated for several excitation wavelengths in the visible region and they are modeled including the contributions of all excited states in resonance. The magnitude of the interference effects between the electronic states is also analyzed because such effects can enhance or de-enhance the intensity of Raman bands. Despite the challenge posed by the present calculations, the RR spectra are in excellent agreement with the experimental results.

2. THEORY AND COMPUTATIONAL DETAILS

To reduce the computational cost of the simulations without affecting the spectroscopic properties of the complexes, the four *tert*-butyl groups of the compounds (Figure 1a,b) were approximated in the calculations by methyl groups. The structural and electronic data of the unprotonated (RIBP) and protonated (RIBPH) complexes were obtained from quantum chemistry calculations performed with the Gaussian 09 program.³⁶ The geometry, vibrational frequencies, and normal coordinates of the ground state were calculated by means of DFT with the XC functional B3LYP.^{37,38} The 28-electron relativistic effective core potential MWB³⁹ was used with its basis set for the ruthenium atom; that is, 4s, 4p, 4d, and 5s electrons are treated explicitly, whereas the three first inner shells are described by the core pseudopotential. The 6-31G(d) double- ζ basis set⁴⁰ was employed for the ligands. To correct for the lack of anharmonicity and the approximate treatment of electron correlation, the harmonic frequencies were scaled by the factor⁴¹ 0.97. The vertical excitation energies, oscillator strengths, and analytical Cartesian energy derivatives of the excited states were obtained from TDDFT calculations within the adiabatic approximation with the same XC functional, pseudopotential, and basis set. It was shown in several papers that B3LYP can provide a reasonable balanced description of the absorption features of such complexes.^{20,21,23,42} In particular, in ref 20, different functionals, including B3LYP, PBE0,⁴³ and CAM-B3LYP,⁴⁴ which contain different amounts of exact exchange, were tested in a similar Ru complex and it was found that B3LYP provides the lowest average deviation for different excited states.

The absorption spectra were simulated by determining the excitation energies and oscillator strengths of the 80 lowest singlet excited states. The effects of the interaction with a solvent (acetonitrile, $\epsilon = 35.688$, $n = 1.344$) on the geometry, frequencies, excitation energies, and excited-state gradients were taken into account by the integral equation formalism of the polarizable continuum model.⁴⁵ The nonequilibrium procedure of solvation was used for the calculation of the excitation energies and of the excited-state gradients. Such a procedure is well adapted for processes where only the fast reorganization of the electronic distribution of the solvent is important.

Assuming a conventional 90° scattering geometry, the Raman differential cross section for a fundamental transition $0 \rightarrow 1_i$ is given by^{46–48}

$$\frac{d\sigma_{0 \rightarrow 1_i}}{d\Omega} = \frac{\omega_L \omega_S^3}{16\pi^2 \epsilon_0^2 c^4} \frac{1}{45} (45a^2 + 5\delta^2 + 7\gamma^2) \quad (1)$$

Table 1. Calculated Vertical Excitation Energies (E^e), Oscillator Strengths (f), and Main Singly Excited Configurations of the Main Excited States and Experimental Absorption Maxima^a

state	transition	weight (%)	E^e (eV)	λ (nm)	f	λ_{exp} (nm)
RIBP						
S ₁	$d_{xz}(198) \rightarrow \pi_{\text{im}}^*(199)$ (MLCT)	95	1.91	651	0.046	700
S ₅	$d_{yz}(197) \rightarrow \pi_{\text{im}}^*(199)$ (MLCT)	82	2.50	497	0.287	546
	$d_{yz}(197) \rightarrow \pi_{\text{bpy}}^*(200)$ (MLCT)	15				
S ₇	$d_{yz}(197) \rightarrow \pi_{\text{bpy}}^*(200)$ (MLCT)	59	2.63	472	0.098	467
	$d_{xy}(196) \rightarrow \pi_{\text{bpy}}^*(201)$ (MLCT)	30				
S ₈	$d_{xy}(196) \rightarrow \pi_{\text{bpy}}^*(200)$ (MLCT)	72	2.70	459	0.104	467
	$d_{yz}(197) \rightarrow \pi_{\text{bpy}}^*(201)$ (MLCT)	22				
S ₉	$\pi_{\text{im}}(195) \rightarrow \pi_{\text{im}}^*(199)$ (ILCT)	93	2.89	429	0.223	443
S ₁₄	$\pi_{\text{im}}(194) \rightarrow \pi_{\text{im}}^*(199)$ (ILCT)	56	3.21	386	0.079	370
	$\pi_{\text{im}}(195) \rightarrow \pi_{\text{bpy}}^*(201)$ (LLCT)	31				
S ₆₃	$\pi_{\text{bpy}}(188) \rightarrow \pi_{\text{bpy}}^*(201)$ (IL)	44	4.51	275	0.641	293
	$\pi_{\text{bpy}}(187) \rightarrow \pi_{\text{bpy}}^*(200)$ (IL)	23				
	$\pi_{\text{im}}(195) \rightarrow \pi_{\text{bpy}}^*(205)$ (LLCT)	17				
RIBPH						
S ₁	$d_{xz}(198) \rightarrow \pi_{\text{im}}^*(199)$ (MLCT)	94	1.60	774	0.017	
S ₃	$d_{xy}(196) \rightarrow \pi_{\text{im}}^*(199)$ (MLCT)	52	2.31	536	0.348	584
	$d_{yz}(197) \rightarrow \pi_{\text{im}}^*(199)$ (MLCT)	40				
S ₆	$\pi_{\text{im}}(195) \rightarrow \pi_{\text{im}}^*(199)$ (ILCT)	93	2.71	458	0.305	430
S ₉	$\pi_{\text{im}}(194) \rightarrow \pi_{\text{im}}^*(199)$ (ILCT)	94	2.95	420	0.137	410
S ₁₀	$d_{yz}(197) \rightarrow \pi_{\text{bpy}}^*(201)$ (MLCT)	28	2.99	414	0.156	410
	$d_{xy}(196) \rightarrow \pi_{\text{bpy}}^*(200)$ (MLCT)	24				
	$d_{yz}(197) \rightarrow \pi_{\text{bpy}}^*(200)$ (MLCT)	21				
	$d_{xy}(196) \rightarrow \pi_{\text{bpy}}^*(201)$ (MLCT)	21				
S ₂₃	$\pi_{\text{im}}(188) \rightarrow \pi_{\text{im}}^*(199)$ (ILCT)	85	3.73	332	0.173	340
S ₅₁	$\pi_{\text{im}}(195) \rightarrow \pi_{\text{bpy}}^*(202)$ (LLCT)	43	4.44	279	0.231	289
	$\pi_{\text{bpy}}(192) \rightarrow \pi_{\text{bpy}}^*(201)$ (IL)	15				
	$\pi_{\text{bpy}}(191) \rightarrow \pi_{\text{bpy}}^*(200)$ (IL)	8				
S ₅₂	$\pi_{\text{bpy}}(191) \rightarrow \pi_{\text{bpy}}^*(201)$ (IL)	38	4.46	278	0.340	289
	$\pi_{\text{bpy}}(192) \rightarrow \pi_{\text{bpy}}^*(200)$ (IL)	17				
S ₅₄	$\pi_{\text{im}}(195) \rightarrow \pi_{\text{bpy}}^*(202)$ (LLCT)	45	4.54	273	0.433	289
	$\pi_{\text{bpy}}(192) \rightarrow \pi_{\text{bpy}}^*(201)$ (IL)	21				
	$\pi_{\text{bpy}}(191) \rightarrow \pi_{\text{bpy}}^*(200)$ (IL)	17				

^aThe corresponding orbitals are depicted in Figure 3.

where ω_L is the frequency of the incident light, ω_S is the frequency of the scattered light, and a^2 , δ^2 , and γ^2 are the three invariants for randomly oriented molecules, which depend on the Raman polarizability tensor ($\alpha_{\alpha\beta}$) _{$g0 \rightarrow g1$} .

The RR spectra were calculated assuming that the electronic ground- and excited-state potential energy surfaces are harmonic and that they only differ by their equilibrium geometry (i.e., assuming the independent mode displaced harmonic oscillator model). Within this approach and taking into account only Condon-type scattering, the Raman polarizability tensor can be calculated from^{35,49,50}

$$(\alpha_{\alpha\beta})_{g0 \rightarrow g1} = \frac{1}{\hbar} \sum_e (\mu_{ge})_{\alpha} (\mu_{ge})_{\beta} \frac{\Delta_{e,l}}{\sqrt{2}} \{ \Phi_e(\omega_L) - \Phi_e(\omega_L - \omega_l) \} \quad (2)$$

where $(\mu_{ge})_{\alpha}$ is a component of the electronic transition dipole moment at the ground-state equilibrium geometry, $\Delta_{e,l}$ is the dimensionless displacement of the e th excited-state potential minimum with respect to the ground state for the l th normal coordinate, and ω_l is the vibrational frequency of the l th normal mode. The function $\Phi_e(\omega_L)$ can be approximated by³⁵

$$\Phi_e(\omega_L) = \frac{1}{\omega_{e,g} - \omega_L - i\Gamma} \quad (3)$$

where $\omega_{e,g}$ is the vertical excitation energy from the electronic ground state g to the excited state e and Γ is a damping factor describing a homogeneous broadening. A Γ of 1500 cm^{-1} reproduces the experimental broadening. The use of eq 3 is appropriate for the investigated complexes because the RR measurements are performed on absorption bands displaying a large broadening and nonresolved vibronic structure.

The dimensionless displacement $\Delta_{e,l}$ of the excited state e were obtained from the derivatives of the excited-state potential energy E^e along the normal mode Q_l evaluated at the ground-state equilibrium geometry according to the relation^{35,50}

$$\Delta_{e,l} = -\frac{1}{\sqrt{\hbar} \omega_l^{3/2}} \left(\frac{\partial E^e}{\partial Q_l} \right)_0 \quad (4)$$

The use of eq 2 allows us to account for contributions of several electronic excited states and to describe possible constructive/destructive interference effects between them. To quantify the importance of interference effects, the total differential RR cross section—including all interfering states—is compared to the

noninterfering differential RR cross section, which was calculated as a sum of contributions from each state alone:

$$\left(\frac{d\sigma_{0 \rightarrow I_i}}{d\Omega}\right)_{\text{noninterfering}} = \sum_e \left(\frac{d\sigma_{0 \rightarrow I_i}}{d\Omega}\right)_e \quad (5)$$

3. EXPERIMENTAL DETAILS

The electronic absorption spectra in air-equilibrated acetonitrile were measured with a Jasco V-670 spectrophotometer. The protonated form, RIBPH, was generated by adding an excess of trifluoroacetic acid (TFA). The RR spectra were recorded in a conventional 90° scattering arrangement. Excitation light was delivered by either a krypton ion laser (model Coherent Innova 301C) or an argon ion laser (model Spectra-Physics 2010). A rotating cell was utilized to prevent heating of the samples. No changes in the absorption spectra could be detected after the exposure to the laser light. The scattered light was focused onto the entrance slit of an Acton SpectraPro 2758i spectrometer, and the dispersed light was detected by a liquid-nitrogen-cooled CCD camera (Princeton Instruments). The sample concentration was optimized to obtain the maximum signal-to-noise ratio and was in the range of 10⁻⁴ M.

4. RESULTS AND DISCUSSION

4.1. Excited States and Absorption Spectra. The experimental absorption spectra of the unprotonated and the protonated species are depicted in Figure 1a,b, respectively. The absorption spectrum of the unprotonated form in the visible range exhibits a maximum at 546 nm ($\epsilon = 19\,200\text{ M}^{-1}\text{ cm}^{-1}$) and a double peak at 467 ($\epsilon = 13\,950\text{ M}^{-1}\text{ cm}^{-1}$) and 443 nm ($\epsilon = 14\,100\text{ M}^{-1}\text{ cm}^{-1}$). Furthermore, a weak shoulder at about 700 nm is found, which vanishes upon protonation. In addition, protonation induces the absorption maximum at 546 nm to shift bathochromically to 548 nm ($\epsilon = 19\,500\text{ M}^{-1}\text{ cm}^{-1}$), whereas the double band structure (467 and 443 nm) shifts hypsochromically and displays in RIBPH a maximum at 410 nm ($\epsilon = 16\,750\text{ M}^{-1}\text{ cm}^{-1}$) along with a shoulder at 430 nm ($\epsilon = 15\,700\text{ M}^{-1}\text{ cm}^{-1}$). The UV region of both RIBP and RIBPH is mainly featured by an intense band and a shoulder at longer wavelengths. In the unprotonated form, the intense band is found at 293 nm ($\epsilon = 66\,800\text{ M}^{-1}\text{ cm}^{-1}$) and is hypsochromically shifted upon protonation to 289 nm ($\epsilon = 72\,500\text{ M}^{-1}\text{ cm}^{-1}$), while the shoulder is localized at 370 nm ($\epsilon = 14\,050\text{ M}^{-1}\text{ cm}^{-1}$) in RIBP and at 340 nm ($\epsilon = 15\,650\text{ M}^{-1}\text{ cm}^{-1}$) in RIBPH.

The nature of the excited states underlying the absorption features is revealed by quantum chemical calculations at the TDDFT level of theory. The simulated absorption spectra are also depicted in Figure 1, and the photophysical properties of the main contributing states are reported in Table 1. The molecular orbitals involved in the low-lying and high-lying excitations are displayed in Figure 2; remaining orbitals can be found in Figure S1 of the Supporting Information.

The first absorption band at 546 nm of RIBP is assigned to an MLCT state (S_5), mainly characterized by a CT to the 4*H*-imidazole ligand along with a small amount of CT to the bipyridine ligands (see Table 1 and Figure 2). The theoretical excitation energy (TD-B3LYP) shows an overestimation of 0.23 eV with respect to the experimental value. This deviation is within the typical accuracy of TDDFT calculations for MLCT excitations in transition-metal complexes.^{23,51} Furthermore, the small experimental shoulder at about 1.77 eV (700 nm) was identified as a weakly absorbing MLCT excitation (S_1) involving

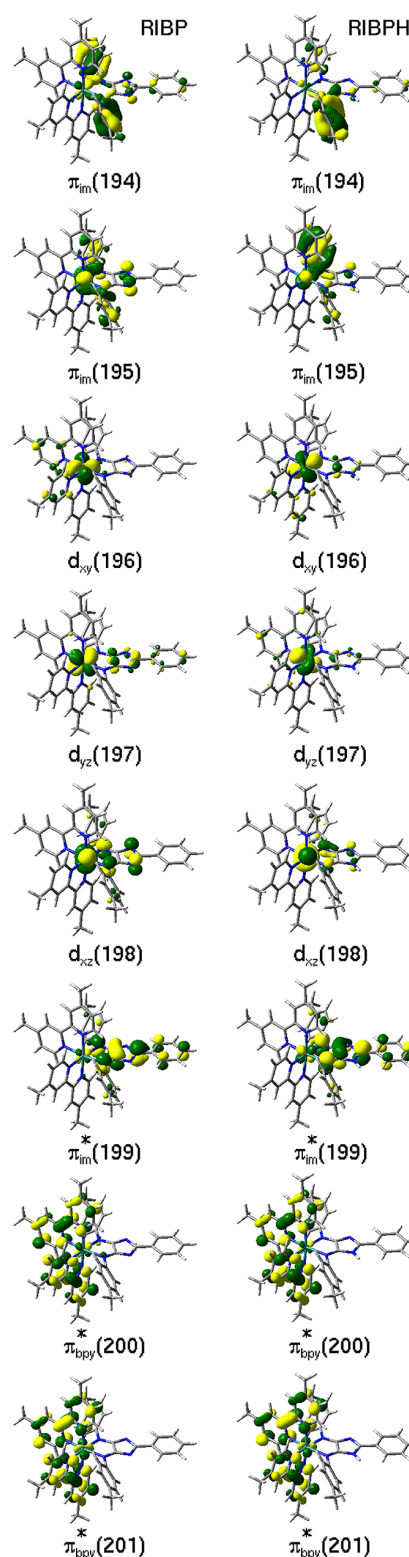


Figure 2. Molecular orbitals involved in the main configurations of the low-lying electronic states responsible for the absorption and RR properties of the unprotonated (RIBP) and protonated (RIBPH) complexes.

a CT to the 4*H*-imidazole ligand with an excitation energy of 1.91 eV (651 nm). The calculations unraveled that three excited states

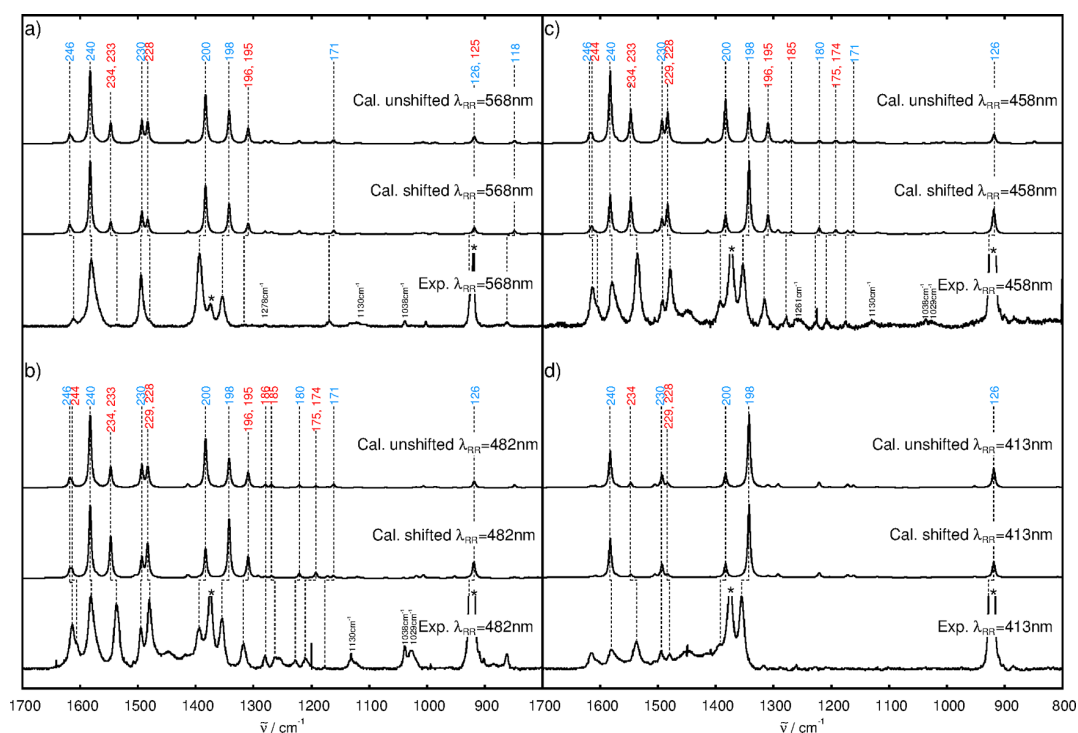


Figure 3. Experimental RR spectra and theoretical RR spectra for RIBP using unshifted and shifted excitation energies in resonance with the states S_5 , S_7 , S_8 , and S_9 at the wavelengths of 568, 482, 458, and 413 nm. The experimental solvent bands are indicated by asterisks. The modes associated with vibrations located on the bipyridine and imidazole ligands are given in red and blue color, respectively. A Lorentzian function with an fwhm of 5 cm^{-1} is employed to broaden the calculated transitions.

(S_7 , S_8 , and S_9) are responsible for the double band structure at 467 and 443 nm. Both the states S_7 and S_8 are composed of MLCT transitions to the bipyridine ligands, while the state S_9 involves mostly an intraligand CT (ILCT) transition located on the 4*H*-imidazole ligand. According to their energetic positions and oscillator strengths, the two MLCT states (S_7 and S_8) were assigned to the band at 467 nm, whereas the ILCT state (S_9) can be assigned to the band at 443 nm. The intense absorption band in the UV region is constructed from excitations of different natures (IL, ILCT, ligand–ligand CT (LLCT), metal-centered (MC), and MLCT). However, the calculations show that a significant fraction of the intensity originates from the IL state S_{63} , which mainly refers to a local excitation within the π system of the bipyridine ligands. The shoulder at 3.35 eV (370 nm) can be associated with the state S_{14} , having both ILCT and LLCT character (see Table 1), as well as to several overlapping higher-energy states.

Protonation of the 4*H*-imidazole ligand induces substantial changes in the properties of the excited states (see Figure 1b). One prominent change in the experimental spectra is the bathochromic shift of the first MLCT absorption band by -0.15 eV. Gratefully, this shift is reasonably reproduced by TDDFT with a value of -0.19 eV. Also interesting is the fact that the associated MLCT state S_3 in RIBPH now shows exclusively transitions to the 4*H*-imidazole ligand, whereas the state S_5 of RIBP features also a fraction of transitions into the π system of the bipyridine ligands. Furthermore, upon protonation, the excitation to the MLCT state S_1 has decreased oscillator strength and excitation energy, which explains the disappearance of the weak shoulder at about 700 nm in the experimental spectrum of RIBPH. The next experimental absorption band at 410 nm with its shoulder at 430 nm is ascribed to a superposition of two ILCT

states (S_6 and S_9) of the 4*H*-imidazole ligand and of one MLCT excitation (S_{10}) to the bipyridine ligands. These states show a somewhat different orbital character than the states (S_7 , S_8 , and S_9) of RIBP (see Table 1). The positions of the states S_9 (420 nm) and S_{10} (414 nm) are in good agreement with the experimental maximum (410 nm), whereas the ILCT state S_6 presents an overestimated wavelength (458 nm) compared with the experimental value of 430 nm. Experimentally, the double-band structure of RIBP is hypsochromically shifted by 0.23 eV upon protonation. The calculations show blue shifts of 0.29 and 0.36 eV between the MLCT state S_{10} (RIBPH) and the MLCT states S_8 and S_7 (RIBP), respectively. These values are in qualitative agreement with experiment. Shifts of -0.18 and 0.06 eV are found between the ILCT state S_9 (RIBP) and the intense ILCT state S_6 and ILCT state S_9 (RIBPH), respectively. This quantitative disagreement concerning the energetic shift of the most intense ILCT state upon protonation was also found in a related complex.²⁰ To see whether this result can be improved with a range-separated functional, the UV–vis spectra of RIBP and RIBPH have been recalculated using the CAM-B3LYP functional. Unfortunately, the disagreement is enhanced in that case (see Figures S2 and S3 and Table S4, Supporting Information), as found in ref 20.

The UV region of the experimental absorption spectra of RIBPH presents one maximum at 289 nm (4.29 eV) and a shoulder at 340 nm (3.65 eV). The calculated UV band results from several excitations of different natures, while mainly three excited states (S_{51} , S_{52} , and S_{54}) contribute at 279, 278, and 273 nm. These states involve transitions of IL character in the bipyridine ligands as well as LLCT transitions from the 4*H*-imidazole ligand to the bipyridine ligands. Finally, the ILCT state

Table 2. Assignment of the Vibrational Frequencies (cm^{-1}) and Calculated Relative RR Intensities (I_{rel}) Using Shifted Excitation Energies of the Unprotonated Complex (RIBP)^a

mode type	freq (calcd) (cm^{-1})	freq (exptl) (cm^{-1})	I_{rel} (568 nm)	I_{rel} (482 nm)	I_{rel} (458 nm)	I_{rel} (413 nm)
im (118)	848	861	0.04	0.02	0.01	0.01
bpy (125)	918	under solvent	0.06	0.04	0.03	0.01
im (126)	919	under solvent	0.03	0.20	0.32	0.21
im (132)	952		<0.01	0.03	0.02	0.01
im (139)	986		0.02	0.01	0.01	<0.01
bpy (148)	1006	1030	<0.01	0.02	0.02	<0.01
im (151)	1018	1038	0.01	0.03	0.01	<0.01
im, bpy (167)	1121	1131	0.01	0.02	0.02	0.01
im (171)	1162	1170	0.05	0.03	0.04	0.03
im (172)	1172		0.01	0.03	0.04	0.03
bpy (174)	1191	1210	<0.01	0.02	0.02	<0.01
bpy (175)	1193	1210	0.01	0.05	0.04	<0.01
im (180)	1221	1227	0.04	0.06	0.08	0.06
bpy (185)	1269	1261	0.03	0.03	0.02	<0.01
bpy (186)	1280	1281	0.03	0.02	0.03	<0.01
im (189)	1292		<0.01	0.03	0.05	0.04
bpy (195)	1310	1317	0.13	0.28	0.24	0.02
bpy (196)	1310	1317	0.01	0.02	0.02	<0.01
im (198)	1342	1354	0.41	0.81	1.00	1.00
im (200)	1383	1393	0.66	0.41	0.27	0.19
bpy (212)	1414		0.03	0.04	0.04	<0.01
bpy (228)	1483	1482	0.18	0.39	0.35	0.03
bpy (229)	1484	1482	<0.01	0.08	0.06	0.01
im (230)	1493	1493	0.31	0.28	0.18	0.18
im (232)	1505		0.01	0.03	0.04	0.04
bpy (233)	1547	1537	0.01	0.04	0.03	<0.01
bpy (234)	1547	1537	0.15	0.53	0.47	0.04
im (238)	1571		0.02	0.02	0.02	0.02
im (240)	1583	1580	1.00	1.00	0.54	0.54
im (242)	1608		<0.01	0.01	0.02	0.02
bpy (244)	1615	1614	0.03	0.10	0.09	0.01
im (246)	1618	1612/1613	0.12	0.10	0.02	<0.01

^aThe theoretical frequencies were scaled by a factor of 0.97.

S_{23} (332 nm) of the 4*H*-imidazole ligand is associated with the shoulder at 340 nm.

4.2. Resonance Raman Spectra. **4.2.1. RR Spectra for RIBP.** The RR spectra for the unprotonated complex were recorded for a set of four excitation wavelengths in the visible range, namely, at 568, 482, 458, and 413 nm. The simulated RR spectra were obtained by considering contributions from the primary excited states in the corresponding energy range (S_5 , S_7 , S_8 , and S_9). The RR spectra were first calculated using the resonant TDDFT excitation energies, as summarized in Table 1. Noticeably, the deviations of the TDDFT predictions with respect to the experimental excitation energies (see section 4.1) lead to inaccuracies in the simulated RR intensities. Hence, the RR spectra were also calculated employing excitation energies that are shifted so as to better reproduce the experimental intensity pattern in the absorption spectrum. Accordingly, the state S_5 was shifted by -2100 cm^{-1} and the states S_7 , S_8 , and S_9 were shifted by -600 cm^{-1} ; the resulting absorption spectrum is depicted in Figure S5 (Supporting Information). After this shift, the resulting theoretical RR spectra, depicted in Figure 3, show a good agreement with the experimental data. In particular, the main intensity patterns as well as the overall wavelength dependence of the RR intensities are very well reproduced by the calculations. Consequently, the simulations allow for an unambiguous assignment of the most intense experimental

bands to vibrational modes centered at either the 4*H*-imidazole or the bipyridine ligands (Figure 1 and Table 2). This assignment was furthermore confirmed experimentally using the RR spectrum of the homolytic tris(bis(*tert*-butyl))bipyridine-ruthenium(II) complex [*tbbpy*₃Ru]²⁺ (see Figure S6 in the Supporting Information) recorded at 458 nm. This spectrum served as a reference system and allowed for the appropriate assignment of the bipyridine vibrational modes.

Both the shifted and the unshifted calculated RR spectra of RIBP at 568 nm excitation (see Figure 3a) are in good agreement with the experimental result because, at this wavelength, the S_5 state is predominant. Therefore, the effect of shifting the excitation energies is rather small on the RR intensities at 568 nm. For the same reason, the interference effects with higher excited states (S_7 , S_8 , and S_9) were found to be negligible at this wavelength (see the Supporting Information). The simulations show that the RR spectrum is dominated by intense vibrational modes localized at the 4*H*-imidazole ligand. Indeed, the vibrational modes 198, 200, 230, and 240 (Table 2) with 4*H*-imidazole character exhibit the strongest RR intensities. The related calculated wavenumbers of 1342, 1383, 1493, and 1582 cm^{-1} are in excellent agreement with the experimental values of 1354, 1393, 1493, and 1580 cm^{-1} , respectively. Moreover, modes (195, 228, and 234) with lower RR intensities are assigned to the bipyridine ligands with wavenumbers of 1310, 1483, and 1547

cm^{-1} corresponding to the experimental values of 1317, 1482, and 1537 cm^{-1} . Additionally, a band corresponding to a superposition of a bipyridine mode (125) and a 4*H*-imidazole mode (126) was found at about 918 cm^{-1} , which is covered in the experimental spectrum by a solvent band. Despite the similarity of both shifted and unshifted spectra, it can be noticed that the spectrum obtained with the shifted excitation energies shows slightly decreased relative intensities of the bipyridine modes (195, 228, and 234) with respect to the spectrum calculated with the unshifted excitation energies, in better agreement with the experiment.

Upon decreasing the excitation wavelength to 482 nm, the experimental RR spectrum presents significant modifications (see Figure 3b). This behavior cannot be fully described theoretically when using unshifted excitation energies because, in this case, the influence of the state S_5 is substantially overestimated and, consequently, the simulated spectrum at 482 nm is very similar to the spectrum at 568 nm. The overestimation of the S_5 is particularly noticeable in the mode 200, whereas the influence of the S_7 , S_8 , and S_9 is underestimated, as can be seen for the modes 198, 228, 229, and 234. Shifting the excited-state energies leads to RR signals in somewhat better agreement with the experimental data recorded with 482 nm excitation. Indeed, besides the intense 4*H*-imidazole modes 198, 200, 230, and 240 (Table 2), the calculated spectrum features also a more pronounced bipyridine character. These enhancements of the bipyridine modes 195, 228, 229, 234, and 244 are induced by the contributions of the states S_7 and S_8 . Furthermore, the increase of the relative intensity of the 4*H*-imidazole mode 198 is related to the contribution of the state S_9 , while the decrease of the 4*H*-imidazole mode 200 is connected to a diminished contribution of state S_5 . Interestingly, it can be seen in Figure 4 that the change in

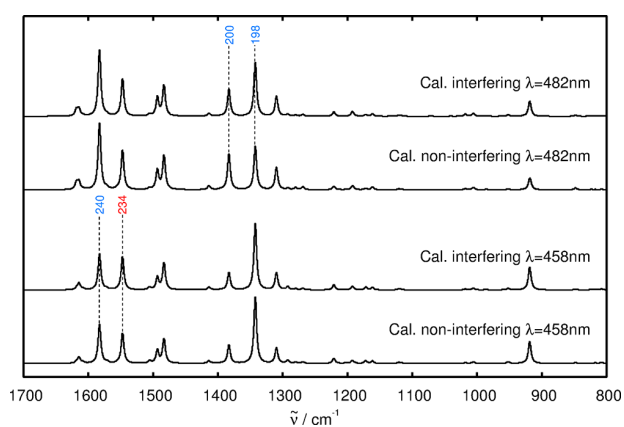


Figure 4. Calculated RR spectra for RIBP at excitation wavelengths of 482 and 458 nm including (interfering) and excluding (noninterfering) interference effects between the states S_5 , S_7 , S_8 , and S_9 .

relative intensities between these two modes originates also noticeably from an interference effect between the states S_5 , S_7 , and S_9 , while such an effect remains almost negligible for the other modes.

The simulated RR spectrum at 458 nm using unshifted excitation energies (Figure 3c) is still dominated by RR signals of the state S_5 , whereas the RR spectrum obtained with the shifted excitation energies is much closer to the experimental spectrum. The intensity pattern resembles the spectrum at 482 nm. However, the relative intensities of the modes 200 and 240

coming from the interaction with the S_5 are further decreased, while the intensity of the mode 198 increases significantly due to the contribution of state S_9 . These changes are in good agreement with the experimental observations and show that the wavelength dependency of the RR intensities is adequately described by the simulations. Figure 4 shows that the decrease of the relative intensity of mode 240 is also partially associated with an interference effect between the states S_5 , S_7 , and S_9 , while the intensities of the other modes remain almost unchanged.

The RR spectrum at 413 nm (Figure 3d) is dominated by RR signals from the state S_9 for both unshifted and shifted excitation energies. For this reason, interference effects are marginal at this excitation wavelength (see Figure S7 of the Supporting Information). The calculated spectrum is in agreement with the experimental results, and the main changes going from an excitation wavelength of 458 to 413 nm are reproduced by the simulations. In particular, this concerns the decrease of the relative intensities for the bipyridine modes 195, 228, 229, and 234, due to the reduced contributions of the states S_7 and S_8 .

In general, the mean absolute deviation between the calculated and the experimental vibrational wavenumbers is 5 cm^{-1} , which is in line with the errors obtained in previous theoretical investigations on RR intensities for transition-metal complexes.^{20,21,50,52}

4.2.2. RR Spectra for RIBPH. The RR signals of the protonated complex have been investigated for two excitation wavelengths, that is, 568 and 413 nm. Therefore, the contributions from the states S_3 , S_6 , S_9 , and S_{10} are required to be taken into account in the calculations. Similar to the unprotonated form, two shifts were applied to correct the TDDFT excitation energies, namely, the state S_3 was shifted by -1500 cm^{-1} , while a shift of 1000 cm^{-1} was used for the states S_6 , S_9 , and S_{10} . The resulting absorption spectrum is depicted in Figure S1 of the Supporting Information.

The RR spectra of the protonated complex (Figure 5 and Table 3) show important differences in comparison to the spectra of the unprotonated form. In particular, the vibrational modes centered at the 4*H*-imidazole ligand present large variations that emphasize the strong effect of protonation within the 4*H*-imidazole ligand sphere. The experimental changes occurring upon protonation are correctly reproduced by the simulations.

At an excitation wavelength of 568 nm, the calculated RR spectrum is dominated by the contribution of state S_3 for both unshifted and shifted excitation energies. Thus, interference effects are negligible (see Figure S8 of the Supporting Information). The RR spectrum of RIBPH at 568 nm is dominated by intense vibrations centered at the 4*H*-imidazole ligand, for example, modes 119, 189, 227, 232, 234, 241, 242, and 250, and unlike RIBP, RIBPH shows several intense bands in the region between 1100 and 1350 cm^{-1} and a different intensity pattern in the $1350\text{--}1650 \text{ cm}^{-1}$ region. Moreover, the vibrational modes of the bipyridine ligands (e.g., mode 229) show only a marginal fraction of intensity for RIBPH compared to RIBP. This difference can be understood from the fact that the state S_3 (RIBPH) involves only MLCT transitions to the π^*_{im} (199) orbital (see Table 1), whereas the state S_5 in the protonated form features both an MLCT transition to the π^*_{im} (199) orbital and an MLCT transition to the π^*_{bpy} (200) orbital (see Table 1). A similar behavior was observed for a related complex²⁰ and confirms that protonation favors a CT excitation to the 4*H*-imidazole ligand and that a control of the pH of the medium is an important factor in designing optimal sensitizers.

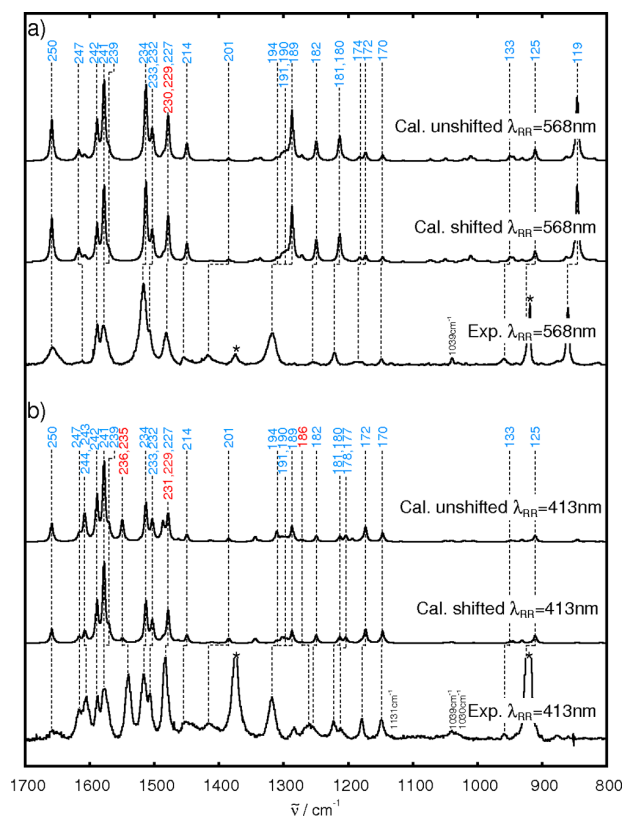


Figure 5. Experimental RR spectra and theoretical RR spectra for RIBPH using unshifted and shifted excitation energies in resonance with the states S_3 , S_6 , S_9 , and S_{10} at the wavelengths of 568 and 413 nm. The experimental solvent bands are indicated by asterisks. The modes associated with vibrations located on the bipyridine and imidazole ligands are given in red and blue color, respectively. A Lorentzian function with an fwhm of 5 cm^{-1} is employed to broaden the calculated transitions.

Excitation at 413 nm leads to modifications of the RR spectrum that are partially captured by the simulations. In this case, the application of shifts on the excitation energies of the contributing states does not improve the agreement with the experiment but leads mainly to a reduction of the intensity of the bipyridine modes 231, 235, and 236, but also of the 4*H*-imidazole modes 243, 244, and 247. These effects are caused by the increasing influence of the state S_6 upon application of the shift of 1000 cm^{-1} . Additionally, the RR intensities of the bipyridine modes, associated with the contribution of state S_{10} , are underestimated in both spectra using unshifted or shifted excitation energies. These deviations with experimental results can be ascribed to errors in relative energies and intensities between the ILCT and MLCT states overlapping in the band centered at 410 nm. In particular, it indicates that the oscillator strength of the ILCT state S_6 is overestimated in comparison with the oscillator strength of the MLCT state S_{10} . Finally, it can be mentioned that interference effects are negligible at this excitation wavelength (see the Supporting Information) and that the mean absolute deviation of the vibrational wavenumbers for the protonated form (6 cm^{-1}) is found comparable to the one (5 cm^{-1}) obtained for the unprotonated complex.

Table 3. Assignment of the Vibrational Frequencies (cm^{-1}) and Calculated Relative RR Intensities (I_{rel}) Using Shifted Excitation Energies of the Protonated Complex (RIBPH)^a

mode type	freq (calcd) (cm^{-1})	freq (exptl) (cm^{-1})	I_{rel} (568 nm)	I_{rel} (413 nm)
im (109)	819		0.02	<0.01
im (119)	846	860	0.98	0.01
im (120)	862		0.05	<0.01
im (125)	911	under solvent	0.14	0.10
im (129)	931		0.03	0.03
im (131)	945		0.04	0.02
im (133)	949	958	0.06	0.02
im (147)	1005		0.02	<0.01
bpy (150)	1011	1030	0.08	<0.01
bpy, im (152)	1020		0.02	<0.01
im (154)	1040		<0.01	0.02
im (160)	1050		0.04	0.01
bpy (162)	1073		0.03	<0.01
im (170)	1147	1149	0.07	0.16
im (172)	1173	1179	0.08	0.17
im (173)	1178	1179	<0.01	0.02
im (174)	1182	1179	0.05	0.01
im (177)	1203	1210	0.01	0.03
im (178)	1204	1210	<0.01	0.04
im, bpy (180)	1212	1222	0.05	0.02
im, bpy (181)	1213	1222	0.31	0.06
im (182)	1249	1255	0.27	0.10
bpy (186)	1272	1261	0.07	0.01
im (189)	1287	1317	0.69	0.15
im (190)	1295	1317	0.07	0.04
im, bpy (191)	1299	1317	0.05	0.03
im, bpy (194)	1303	1317	0.06	0.05
im (199)	1336		0.04	<0.01
im (200)	1344		0.03	0.06
im (201)	1385	1417	0.03	0.06
im (214)	1450	1455	0.23	0.10
im (227)	1479	1482	0.57	0.40
bpy (229)	1486	1482	0.03	0.02
bpy (230)	1486	1482	0.02	<0.01
bpy (231)	1487	1482	<0.01	0.03
im (232)	1503	1507	0.31	0.25
im (233)	1504	1507	0.06	0.02
im (234)	1513	1517	1.00	0.53
bpy (235)	1549	1537	<0.01	0.02
bpy (236)	1550	1537	<0.01	0.03
im (239)	1570	1578	0.08	0.14
im (241)	1578	1578	0.95	1.00
im (242)	1589	1588	0.44	0.50
im (243)	1606	1606	0.02	0.06
im (244)	1608	1606	0.05	0.10
im (247)	1617	1612	0.16	0.06
bpy (249)	1621	1614	0.02	<0.01
im (250)	1659	1658	0.57	0.18

^aThe theoretical frequencies were scaled by a factor of 0.97.

5. CONCLUSIONS

The optical properties, namely, the absorption and RR spectra, of the novel (bipyridine)₂Ru(4*H*-imidazole) complex have been investigated in a joint experimental and theoretical study. Regardless of the protonation state, the absorption spectra feature two absorption bands covering a large part of the visible region, making this Ru complex an attractive black dye. TDDFT

calculations assign the first band to a single MLCT state, whereas the second band having a double peak structure is composed of a superposition of three excited states with MLCT and ILCT characters. Therefore, the new ruthenium(II) complex joins high absorbance, due to a variety of bright transitions involving the bipyridine and 4*H*-imidazole ligands, and an extension of the absorption toward the NIR by virtue of the 4*H*-imidazole ligand. Protonation significantly affects the photophysical properties of the contributing electronic states and leads to a red shift of the lower absorption band and to a blue shift of the second absorption band. These effects are reasonably reproduced by the TDDFT calculations in the case of the MLCT states, whereas the theoretical shifts of the ILCT states are inaccurate due to an unbalanced description of the CT characters of these states with the employed functional. The analysis of the molecular orbitals and RR spectra in resonance with the first MLCT band has shown that the effects of protonation favor a CT photoexcitation to the 4*H*-imidazole ligand. This property is interesting in view of applications of this compound as a black absorber in DSSCs. For real-life applications, the charge can be transferred via a carboxylic acid anchoring group at the phenyl moiety to the electron acceptor surface.

The photophysical properties of both RIBP and RIBPH species were analyzed by RR spectroscopy with excitation wavelengths covering the visible region. The RR intensities were calculated by including the contribution of the four main excited states and considering unshifted and shifted vertical excitation energies. The obtained theoretical RR spectra are in excellent agreement with the experimental data. In particular, the use of shifted excitation energies to compensate for TDDFT deviations is mandatory to reproduce the wavelength dependence of the RR spectra for RIBP. Thus, these results show that a main source of errors in the calculated RR intensities arises from the limited accuracy of the TDDFT excitation energies. However, these energies can be corrected if experimental data are available. Finally, an analysis of the interference effects between the electronic states shows that, with the exception of a few modes of RIBP, these effects are almost negligible for the investigated complex at the considered excitation wavelengths.

In general, this study demonstrates that accurate RR spectra can be obtained with TDDFT for transition-metal complexes even for complicated cases in which several states of different characters contribute to the RR intensities.

■ ASSOCIATED CONTENT

■ Supporting Information

Molecular orbitals of higher excited states, shifted B3LYP absorption spectra, RR spectrum of the homolytic $[rbpy_3Ru]^{2+}$ complex, and calculated RR spectra for RIBP (568, 482, 458, and 413 nm) and RIBPH including and excluding interference effects. This material is available free of charge via the Internet at <http://pubs.acs.org>.

■ AUTHOR INFORMATION

Corresponding Author

*E-mail: benjamin.dietzek@ipht-jena.de (B.D.), leticia.gonzalez@univie.ac.at (L.G.).

Author Contributions

[‡]Both authors contributed equally to this article.

Notes

The authors declare no competing financial interest.

■ ACKNOWLEDGMENTS

This research was supported financially by the Thüringer Ministerium für Bildung, Wissenschaft und Kultur (PhotoMic, Grant No. B 514-09049). Further financial support is gratefully acknowledged from the Carl-Zeiss Stiftung (J.G.), the Studienstiftung des deutschen Volkes (M.W.), and the Fonds der chemischen Industrie (B.D.). Daniel Escudero is acknowledged for preliminary calculations on the UV-vis absorption of the system. All the calculations have been performed at the Universitätsrechenzentrum of the Friedrich-Schiller University of Jena and at the HP computers of the Theoretical Chemistry group in Jena.

■ REFERENCES

- (1) Chambron, J. C.; Sauvage, J. P.; Amouyal, E.; Koffi, P. *Nouv. J. Chim.* **1985**, *9*, 527–529.
- (2) Harthorn, R. M.; Barton, J. K. *J. Am. Chem. Soc.* **1992**, *114*, 5919–5925.
- (3) Jenkins, Y.; Friedman, A. E.; Turro, N. J.; Barton, J. K. *Biochemistry* **1992**, *31*, 10809–10816.
- (4) Haq, I.; Lincoln, P.; Suh, D. C.; Norden, B.; Chowdhry, B. Z.; Chaires, J. B. *J. Am. Chem. Soc.* **1995**, *117*, 4788–4796.
- (5) Nair, R. B.; Cullum, B. M.; Murphy, C. J. *Inorg. Chem.* **1997**, *36*, 962–965.
- (6) Schwalbe, M.; Karnahl, M.; Tschierlei, S.; Uhlemann, U.; Schmitt, M.; Dietzek, B.; Popp, J.; Groake, R.; Vos, J. G.; Rau, S. *Dalton Trans.* **2010**, *39*, 2768–2771.
- (7) Aiga, F.; Tada, T. *J. Mol. Struct.* **2003**, *658*, 25–32.
- (8) Pellegrin, Y.; Pleux, L. L.; Blart, E.; Renaud, A.; Chavillon, B.; Szuwarski, N.; Boujtita, M.; Cario, L.; Jobic, S.; Jacquemin, D.; et al. *J. Photochem. Photobiol., A* **2011**, *219*, 235–242.
- (9) Siebert, R.; Winter, A.; Schubert, U. S.; Dietzek, B.; Popp, J. *Phys. Chem. Chem. Phys.* **2011**, *13*, 1606–1617.
- (10) Siebert, R.; Hunger, C.; Guthmüller, J.; Schlütter, F.; Winter, A.; Schubert, U. S.; González, L.; Dietzek, B.; Popp, J. *J. Phys. Chem. C* **2011**, *115*, 12677–12688.
- (11) Coppo, P.; Duati, M.; Kozhevnikov, V.; Hofstraat, J.; De Cola, L. *Angew. Chem., Int. Ed.* **2005**, *44*, 1806–1810.
- (12) O'Regan, B.; Grätzel, M. *Nature* **1991**, *353*, 737–740.
- (13) Grätzel, M. *Pure Appl. Chem.* **2001**, *73*, 459–467.
- (14) Grätzel, M. *Inorg. Chem.* **2005**, *44*, 6841–6851.
- (15) Grätzel, M. *Acc. Chem. Res.* **2009**, *42*, 1788–1798.
- (16) Nazeeruddin, M.; Pechy, P.; Renouard, T.; Zakeeruddin, S.; Humphry-Baker, R.; Comte, P.; Liska, P.; Cevey, L.; Costa, E.; Shklover, V.; et al. *J. Am. Chem. Soc.* **2001**, *123*, 1613–1624.
- (17) Odobel, F.; Zabri, H. *Inorg. Chem.* **2005**, *44*, 5600–5611.
- (18) Blumhoff, J.; Beckert, R.; Rau, S.; Losse, S.; Matschke, M.; Günther, W.; Görls, H. *Eur. J. Inorg. Chem.* **2009**, 2162–2169.
- (19) Rau, S.; Buttner, T.; Temme, C.; Ruben, M.; Görls, H.; Walther, D.; Duati, M.; Fanni, S.; Vos, J. *Inorg. Chem.* **2000**, *39*, 1621–1624.
- (20) Kupfer, S.; Guthmüller, J.; Wächtler, M.; Losse, S.; Rau, S.; Dietzek, B.; Popp, J.; González, L. *Phys. Chem. Chem. Phys.* **2011**, *13*, 15580–15588.
- (21) Wächtler, M.; Kupfer, S.; Guthmüller, J.; Popp, J.; González, L.; Dietzek, B. *J. Phys. Chem. C* **2011**, *115*, 24004–24012.
- (22) Vlcek, A., Jr.; Zalis, S. *Coord. Chem. Rev.* **2007**, *251*, 258–287.
- (23) Escudero, D.; González, L. *J. Chem. Theory Comput.* **2012**, *8*, 203–213.
- (24) Charlot, M.-F.; Aukauloo, A. *J. Phys. Chem. A* **2007**, *111*, 11661–11672.
- (25) Atsumi, M.; González, L.; Daniel, C. *J. Photochem. Photobiol., A* **2007**, *190*, 310–320.
- (26) Nazeeruddin, M.; De Angelis, F.; Fantacci, S.; Selloni, A.; Viscardi, G.; Liska, P.; Ito, S.; Bessho, T.; Grätzel, M. *J. Am. Chem. Soc.* **2005**, *127*, 16835–16847.
- (27) De Angelis, F.; Fantacci, S.; Mosconi, E.; Nazeeruddin, M. K.; Graetzel, M. *J. Phys. Chem. C* **2011**, *115*, 8825–8831.

- (28) Tschierlei, S.; Karnahl, M.; Presselt, M.; Dietzek, B.; Guthmuller, J.; González, L.; Schmitt, M.; Rau, S.; Popp, J. *Angew. Chem., Int. Ed.* **2010**, *49*, 3981–3984.
- (29) Fantacci, S.; De Angelis, F. D.; Sgamellotti, A.; Re, N. *Chem. Phys. Lett.* **2004**, *396*, 43–48.
- (30) Barolo, C.; Nazeeruddin, M. K.; Fantacci, S.; Di Censo, D.; Comte, P.; Liska, P.; Viscardi, G.; Quagliotto, P.; De Angelis, F.; Ito, S.; et al. *Inorg. Chem.* **2006**, *45*, 4642–4653.
- (31) Lobello, M. G.; Fantacci, S.; Credi, A.; De Angelis, F. *Eur. J. Inorg. Chem.* **2011**, *2011*, 1605–1613.
- (32) Abbotto, A.; Sauvage, F.; Barolo, C.; De Angelis, F.; Fantacci, S.; Grätzel, M.; Manfredi, N.; Marinzi, C.; Nazeeruddin, M. K. *Dalton Trans.* **2011**, *40*, 234–242.
- (33) Runge, E.; Gross, E. K. U. *Phys. Rev. Lett.* **1984**, *52*, 997–1000.
- (34) González, L.; Escudero, D.; Serrano-Andrés, L. *ChemPhysChem* **2012**, *13*, 28–51.
- (35) Wächtler, M.; Guthmuller, J.; González, L.; Dietzek, B. *Coord. Chem. Rev.* **2012**, *256*, 1479–1508.
- (36) Frisch, M. J.; Trucks, G. W.; Schlegel, H. B.; Scuseria, G. E.; Robb, M. A.; Cheeseman, J. R.; Scalmani, G.; Barone, V.; Mennucci, B.; Petersson, G. A.; et al. *Gaussian 09*, revision A.1; Gaussian, Inc.: Wallingford, CT, 2009.
- (37) Becke, A. D. *J. Chem. Phys.* **1993**, *98*, 5648–5652.
- (38) Lee, C.; Yang, W.; Parr, R. G. *Phys. Rev. B* **1988**, *37*, 785–789.
- (39) Andrae, D.; Häussermann, U.; Dolg, M.; Stoll, H.; Preuss, H. *Theor. Chim. Acta* **1990**, *77*, 123–141.
- (40) Hariharan, P. C.; Pople, J. A. *Theor. Chim. Acta* **1973**, *28*, 213–222.
- (41) Merrick, J. P.; Moran, D.; Radom, L. *J. Phys. Chem.* **2007**, *111*, 11683–11700.
- (42) Amor, N. B.; Zálaiš, S.; Daniel, C. *Int. J. Quantum Chem.* **2006**, *106*, 2458–2469.
- (43) Adamo, C.; Barone, V. *J. Chem. Phys.* **1999**, *110*, 6158–6170.
- (44) Yanai, T.; Tew, D.; Handy, N. *Chem. Phys. Lett.* **2004**, *393*, 51–57.
- (45) Tomasi, J.; Mennucci, B.; Cammi, R. *Chem. Rev.* **2005**, *105*, 2999–3093.
- (46) Albrecht, A. C. *J. Chem. Phys.* **1961**, *34*, 1476–1484.
- (47) Long, D. A. *The Raman Effect: A Unified Treatment of the Theory of Raman Scattering by Molecules*; John Wiley & Sons Ltd: New York, 2002.
- (48) Kelley, A. M. *J. Phys. Chem. A* **2008**, *112*, 11975–11991.
- (49) Peticolas, W. L.; Rush, T., III *J. Comput. Chem.* **1995**, *16*, 1261–1270.
- (50) Guthmuller, J.; González, L. *Phys. Chem. Chem. Phys.* **2010**, *12*, 14812–14821.
- (51) Jacquemin, D.; Mennucci, B.; Adamo, C. *Phys. Chem. Chem. Phys.* **2011**, *13*, 16987–16998.
- (52) Guthmuller, J.; Champagne, B.; Moucheron, C.; Kirsch-De Mesmaeker, A. *J. Phys. Chem. B* **2010**, *114*, S11–S20.

4.7 Structural control of photoinduced dynamics in 4*H*-imidazole-Ruthenium dyes

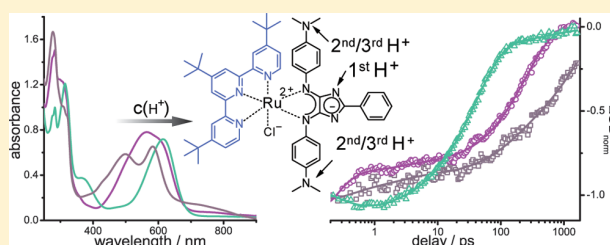
Reproduced with permission from J. Phys. Chem. C, in press. Unpublished work copyright 2012 American Chemical Society.

<http://pubs.acs.org/doi/abs/10.1021/jp309148u>

Structural Control of Photoinduced Dynamics in 4*H*-Imidazole-Ruthenium DyesMaria Wächtler,^{†,‡,∇} Stephan Kupfer,^{†,∇} Julien Guthmuller,[§] Sven Rau,^{||} Leticia González,^{*,⊥} and Benjamin Dietzek^{*,†,‡,‡,#}[†]Institute of Physical Chemistry and Abbe Center of Photonics, Friedrich-Schiller University Jena, Helmholtzweg 4, 07743, Jena, Germany[‡]Institute of Photonic Technology Jena (IPHT) e.V., Albert-Einstein-Strasse 9, 07745, Jena, Germany[§]Faculty of Applied Physics and Mathematics, Gdansk University of Technology, Narutowicza 11/12, 80233, Gdansk, Poland^{||}Institute of Inorganic Chemistry I, University of Ulm, Albert-Einstein-Allee 11, 89081, Ulm, Germany[⊥]Institute of Theoretical Chemistry, University of Vienna, Währinger Strasse 17, 1090 Vienna, Austria[#]Jena Center for Soft Matter (JCSM), Humboldtstrasse 10, 07743, Jena, Germany

Supporting Information

ABSTRACT: The photoinduced dynamics of a series of terpyridine 4*H*-imidazole-ruthenium complexes, which constitute a new family of panchromatic dyes, is investigated. The dynamics involves two excited states localized within the 4*H*-imidazole sphere. Upon MLCT excitation, an excited state is populated, which is localized on the central part of the 4*H*-imidazole ligand caused by its nonplanar conformation. The population of the second excited state is connected to a planarization of the 4*H*-imidazole ligand as revealed by viscosity-dependent measurements, and the excess electronic charge on the ligand is shifted to the terminal rings. The impact on the photoinduced dynamics of the electronic character of the substituent at the terminal rings and the protonation state of the 4*H*-imidazole ligand is studied. Significant changes in the lifetime of the excitation and alterations of the decay mechanism are observed depending on the interplay of the electronic character of the substituent and ligand protonation. In a NMe₂ substituted complex, the character of the substituent is changed from electron donating to electron withdrawing upon stepwise protonation, resulting in pH switchable decay mechanism.



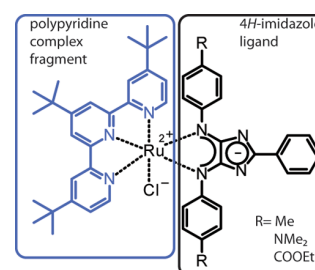
1. INTRODUCTION

Ruthenium polypyridine dyes are in the center of interest delivering valuable insight into photoinduced processes in transition metal coordination compounds.^{1–6} The systems show an extraordinary combination of high stability in several redox stages and often long lifetimes of the photoexcited states, which brings such dyes in the focus of research for the design of optoelectronic devices, for example LEDs,^{7–9} chemical sensors, for example for DNA,^{10–15} or artificial light-harvesting systems, for example for photocatalytic assemblies^{16–26} and dye-sensitized solar cells.^{27–35} To yield high efficient artificial light-collecting systems, the absorption properties of the applied dyes have to be optimized to high extinction coefficients and maximum overlap with the solar radiation spectrum. Consequently, the absorption properties in the red and NIR spectral range need to be improved.^{36–39}

Several routes have been followed to design ruthenium polypyridine dyes with high extinction coefficients in a broad spectral range by combining organic chromophores with Ru-polypyridine chromophores. For example, inspired by natural light-harvesting antenna systems,^{40–42} chromophores were attached in the periphery of the polypyridine ligands capable

of transferring the excitation energy to the ruthenium center.^{39,43–49} In designing the structures investigated here in the present study (Scheme 1), another approach is followed. Here, an organic chromophore, a 4*H*-imidazole,^{50,51} is directly

Scheme 1. Structures of the Investigated Ruthenium Complexes



Received: June 27, 2012

Revised: November 12, 2012

coordinated to a ruthenium-polypyridine fragment (Figure 1). The direct coordination of the organic chromophore to the

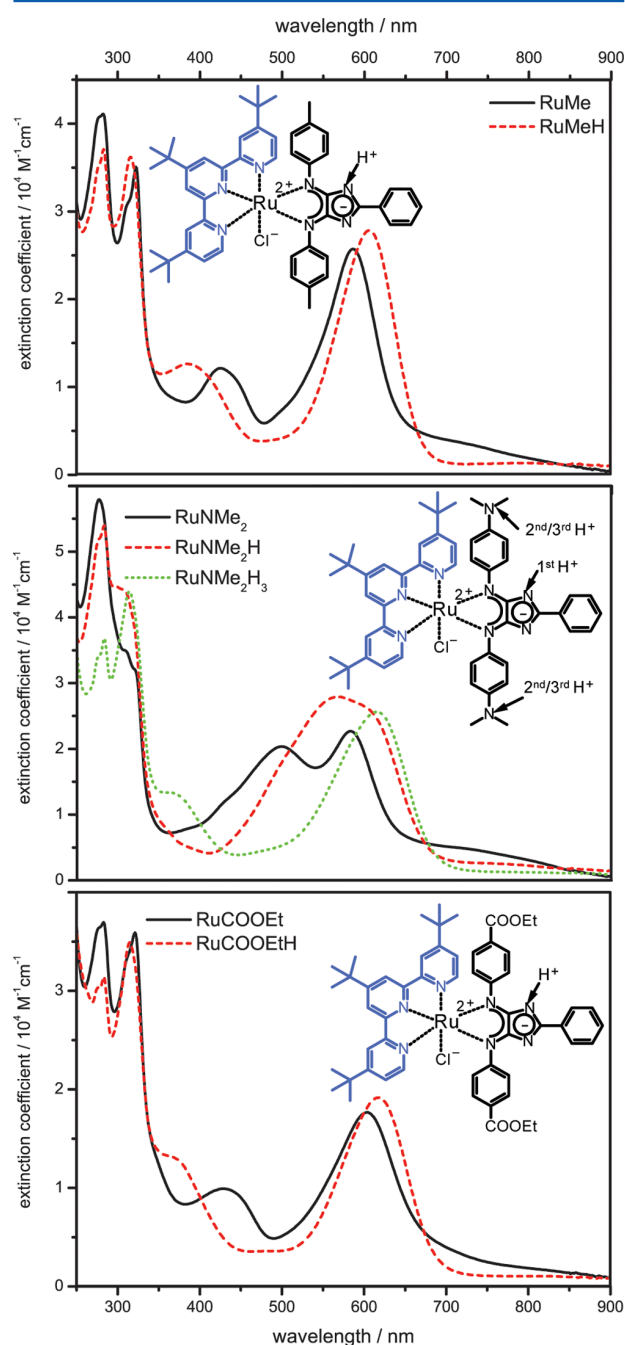


Figure 1. Structures and absorption spectra of the 4*H*-imidazole complexes studied in their unprotonated and protonated forms in ACN. Protonation was assured by addition of TFA.

photoelectroactive Ru center results in substances exhibiting the photoelectrochemical properties of the ruthenium-polypyridine metal center combined with strong and broad absorption in the visible range. Additionally, by providing positions for protonation, the 4*H*-imidazole ligand introduces the possibility to tune the properties of the dye by external pH stimuli.^{52–54}

In preliminary studies, the character of the transitions responsible for the UV/vis absorption in 4*H*-imidazole

terpyridine dyes and the wavelength-dependent localization of the initial excited state in the coordination sphere were investigated. To do so, resonance Raman spectroscopy combined with TDDFT calculations was employed.^{52–55} It was shown that in the complexes under investigation, the broad visible absorption feature (Figure 1) is caused by metal-to-ligand charge transfer (MLCT) transitions mainly of Ru→4*H*-imidazole character with only minor contributions from the terpyridine sphere in the unprotonated form and pure Ru→4*H*-imidazole character in the protonated complexes. The calculations show a strong localization of this initial excited state within the 4*H*-imidazole ligand sphere and a nonplanar conformation of the coordinated 4*H*-imidazole, inhibiting the formation of a completely conjugated system involving the whole ligand sphere (Figure 2).

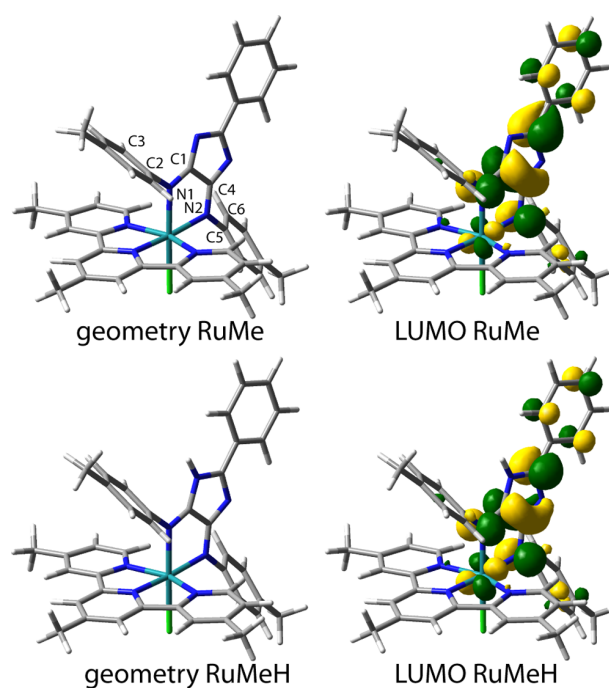


Figure 2. Calculated ground-state geometries and lowest unoccupied molecular orbitals (LUMO) of **RuMe** and **RuMeH**.⁵² The dihedral angles describing the nonplanar conformation of the coordinated ligand have the values $\delta_1(\text{C1N1C2C3}) = 66^\circ$ and $\delta_2(\text{C4N2C5C6}) = 48^\circ$ for the unprotonated form and $\delta_1(\text{C1N1C2C3}) = 61^\circ$ and $\delta_2(\text{C4N2C5C6}) = 46^\circ$ for the protonated form. Values for the dihedral angles of the unprotonated and protonated forms of **RuMe₂** and **RuCOOEt** are given in the Supporting Information.

Typically, for ruthenium-polypyridine systems, excitation in the ¹MLCT transition is followed by ultrafast inter system crossing (ISC) leading to a population of the ³MLCT manifold with a quantum yield close to unity.^{56–58} Upon vibrational relaxation (VR), a thermally relaxed ³MLCT state is populated within a few picoseconds.^{57,59,60} From this state, the systems can decay back to the ground state via emission, nonradiative decay, or thermal activation to higher lying excited states, for example, triplet metal centered (³MC) states.^{6,61} Furthermore, for complexes coordinating extensive ligands, as the 4*H*-imidazole ligand, additional low lying excited states localized on certain ligand subunits, for example, ligand centered states (LC) or “dark” MLCT states, can be involved in the

photoinduced processes.^{62–65} Additionally, a subsequent delocalization of the excited state accompanied by strong conformational changes within the ligand is possible.^{8,66–68} If the initially excited state is strongly localized on only a fraction of the 4*H*-imidazole ligand framework, such delocalization processes will contribute significantly to the observed excited-state dynamics.

In this respect, the present study investigates the photo-induced dynamics after excitation in the MLCT absorption by time-resolved transient absorption spectroscopy in a series of 4*H*-imidazole-ruthenium complexes: chloro- η^3 -4,4',4''-tert-butyl-2,2':6',2''-terpyridine- η^2 -phenyl-4,5-*p*-tolylimino-imidazolate-ruthenium(II) (**RuMe**), chloro- η^3 -4,4',4''-tert-butyl-2,2':6',2''-terpyridine- η^2 -phenyl-4,5-(*p*-dimethylaminophenyl-imino)-imidazolate-ruthenium(II) (**RuNMe₂**), and chloro- η^3 -4,4',4''-tert-butyl-2,2':6',2''-terpyridine- η^2 -phenyl-4,5-(*p*-ethylcarboxyphenyl-imino)-imidazolate-ruthenium(II) (**RuCOOEt**) (Scheme 1). Special emphasis will be laid on the influence of the electronic character of substituents at the terminal rings of the 4*H*-imidazole ligand and the effects of ligand protonation on the excited-state behavior.

The interest in these effects originates from the possibility to energetically tune excited states involved in the photoinduced dynamics by selective substitution with electron-withdrawing or electron-donating substituents.^{20,69–74} In dependence on the position and the character of the substituent as well as the localization of the respective excited states, the lifetimes and spectral characteristics of individual excited states can be controlled. Similar effects can be induced by protonation at certain positions within the ligand sphere.^{75–77} By both ligand substitution and protonation, not only time scales can be affected but the decay mechanisms itself may be altered.^{76–78} Such effects can be used to control excited-state processes and to switch off unwanted decay pathways, but also to gain insight into the localization and character of the states involved in the dynamics. Knowledge of the localization of excited states within large ligand systems is especially interesting for the directed design of supramolecular functional structures capable of vectorial electron transfer by coupling dyes with electron-accepting units, for example, further metal centers^{17–19,21} or semiconductors.^{27,28,33,35}

In this first ever study of the photoinduced dynamics of this novel class of Ru complexes, the methyl-substituted parental complex chloro- η^3 -4,4',4''-tert-butyl-2,2':6',2''-terpyridine- η^2 -phenyl-4,5-*p*-tolylimino-imidazolate-ruthenium(II) **RuMe** (Figure 1) is investigated in solvents of differing viscosity to identify processes connected to large structural changes following excitation. In a second step, the methyl substituent is exchanged by substituents of stronger electron-donating character yielding **RuNMe₂** or electron-withdrawing character yielding **RuCOOEt**. The results give an indication of the different spatial localizations of the excited states contributing to the excited state processes, which is confirmed by the impact of ligand protonation on the decay mechanism as detailed in the last part of the study.

2. EXPERIMENTAL AND THEORETICAL METHODS

RuMe, **RuCOOEt**, and **RuNMe₂** were synthesized according to the procedure reported in Kupfer et al.⁵²

For spectroscopic measurements, the samples were dissolved in aerated acetonitrile (ACN). For investigations of the viscosity dependence of the excited-state properties, the dipolar aprotic solvents γ -butyrolactone (GBL) and 1,3-dimethyl-

trahydropyrimidin-2(1*H*)-one (DMPU) were chosen because of their higher viscosity but similar polarity as compared to ACN.

UV/vis absorption spectra were recorded at room temperature in a quartz cell with 1 cm path length with a Jasco V-670 spectrophotometer. Titration experiments were performed on a solution (3 mL) of the complex by adding small aliquots (1 μ L) of a 0.01 M trifluoroacetic acid solution in acetonitrile. The corresponding pK_a values were determined by analyzing the changes in the absorption spectra using the ReactLabEQUILIBRIA global analysis program. In the calculations, a pK_a value of 12.65 for trifluoroacetic acid in acetonitrile⁷⁹ was employed.

The time-resolved measurements were performed in a cell with 1 mm path length, and the solution was kept static. Sample integrity was ensured by recording absorption spectra prior to and post each measurement. The setup for transient absorption spectroscopy has been described previously.²⁰ The pump pulses to excite the sample were centered in the visible absorption maximum of the respective complex under investigation and delivered by a TOPAS-C. A supercontinuum probe pulse generated in a sapphire plate served as a broad-band probe. The pump-pulse energy was 1.4 μ J, while typical probe intensities fall into the range of hundred nJ. The polarizations of pump and probe were oriented at the magic angle. Probe and reference intensities were detected on a double stripe diode array and converted into differential absorption (DA) signals using a commercially available detection system (Pascher Instruments AB). The time resolution of the experiment was evaluated by the width of the coherent artifact,⁸⁰ allowing an estimation of the cross correlation value between pump and probe to be in the order of 80 fs. The DA signals recorded as a function of the delay time and the probe wavelength were chirp corrected and subsequently subjected to a global fitting routine using a sum of exponential functions for data analysis.⁸¹ To avoid prominent contributions from coherent artifacts,^{80,82} the pulse overlap region (± 150 fs around time zero) was excluded in the data fitting procedure. The wavelength-dependent pre-exponential factors correspond to the decay associated spectra (DAS) connected with the kinetic components.

The structural and electronic data of the investigated structures were obtained from quantum chemistry calculations.^{52,53} To reduce the computational costs of the simulations without affecting the spectroscopic properties of the complex, the three tert-butyl groups of the terpyridine ligand were approximated in the calculations by methyl groups. The calculations were performed using the Gaussian 09 program.⁸³ The geometry, vibrational frequencies, and normal coordinates were calculated by means of DFT with the XC-functional B3LYP.^{84,85} The 28-electron relativistic effective core potential MWB⁸⁶ was used with its basis set for the ruthenium atom; 4s, 4p, 4d, and 5s were treated explicitly, while the three inner shells are described with the core pseudopotential. The 6-31G(d) double- ζ basis set⁸⁷ was employed for the ligands. The effects of the interaction with a solvent (acetonitrile) were taken into account by the integral equation formalism of the polarizable continuum model.⁸⁸ The calculations of the absorption and resonance Raman spectra were performed following the protocol introduced elsewhere.⁵² Furthermore, the deactivation pathway after photoexcitation was investigated. Starting from the Franck–Condon (FC) region, geometry optimizations at the TDDFT level of theory have been carried out for the low-lying excited singlet and triplet states probably involved in the excited-state decay. In each equilibrium

structure, TDDFT calculations including 40 singlet and 40 triplet excited states were performed to map the energies of the electronic states of interest. For further details, see the Supporting Information.

3. RESULTS AND DISCUSSION

3.1. Ground-State Absorption Spectra. The UV/vis absorption spectra deliver a first indication for the influence of the electronic character of the ligand substituent at the terminal rings and the protonation state of the 4*H*-imidazole ligand on the excited states (see Figure 1) of the complexes. The spectral features in the absorption spectra can be assigned to the following types of transitions:^{52,53} The spectral features between 250 and 350 nm result from the superposition of $\pi\pi^*$ intraligand (IL) transitions within the terpyridine and 4*H*-imidazole ligand sphere, $n\pi^*$ transitions involving the lone pairs of the chloro-ligand or the imidazole nitrogen, and interligand charge-transfer transitions. The absorption features between 350 and 450 nm can be assigned to $\pi\pi^*$ IL transitions involving 4*H*-imidazole centered orbitals. Overlapping with the latter at wavelengths longer than 400 nm are MLCT transitions. The MLCT character was confirmed by resonance Raman measurements and TDDFT calculations^{52,53} (for **RuCOOEt**, see the Supporting Information). These investigations^{52,53} further revealed that the MLCT transition responsible for the strong absorption maximum in the visible in the unprotonated forms is mainly due to MLCT to an accepting orbital localized on the 4*H*-imidazole ligand. Additionally, minor contributions from accepting orbitals of the terpyridine ligand were identified. Protonation decreases the terpyridine contributions to the transition leaving pure Ru→4*H*-imidazole MLCT transitions responsible for the strong absorption feature in the visible range. The shoulder in the red part of the absorption spectrum present in both the protonated and, much weaker and red-shifted, the unprotonated forms is caused by a pure Ru→4*H*-imidazole MLCT transition.

Comparing the absorption properties of the different substituted forms (see Figure 1), it can be noticed that for the unprotonated forms the visible absorption maximum shifts upon variation of the substituent. The values for the absorption maxima and extinction coefficients for this transition are given in Table 1. For the complex with the electron-withdrawing

Table 1. Absorption Maxima, Extinction Coefficients, and pK_a Values in ACN

	$\lambda_{\text{max}}/\text{nm}$	$\epsilon(\lambda_{\text{max}})/\text{M}^{-1} \text{cm}^{-1}$	pK_a
RuMe	585 ^a	25 700 ^a	
RuMeH	605 ^a	28 100 ^a	13.6
RuNMe₂	583/499 ^b	22 600/20 400 ^b	
RuNMe₂H	608(sh)/567 ^b	26 000/27 900 ^b	13.8 ^b
RuNMe₂H₃	615 ^b	25 800 ^b	10.6/9.7 ^b
RuCOOEt	600	17 600	
RuCOOEtH	615	19 100	13.3

^aReference 52. ^bReference 53.

substituent **RuCOOEt**, the absorption maximum is red-shifted by 15 nm (427 cm^{-1}) as compared to **RuMe**. The blueshift observed for the electron-donating substituted **RuNMe₂** is less pronounced (4 nm/117 cm^{-1}). This may be explained by mainly electrostatic influences on the electronic properties of the excited state contributing to this electronic transition. In the calculated ground-state geometry (see Figure 2), the sub-

stituted terminal rings are rotated out of the plane formed by the 4*H*-imidazole.^{52,53} No completely conjugated system involving the central part of the 4*H*-imidazole ligand and the terminal rings bearing the substituents can be established. This indicates that inductive and no mesomeric effects play a dominating role. Both the methyl and the NMe₂ substituted terminal rings appear nearly equally electron rich, while **RuCOOEt** differs in this respect from the other two complexes and shows a red-shifted MLCT transition. This is due to a lower relative energy of the accepting orbital with respect to the Ru centered donating orbitals.

Similar effects as caused by electron-withdrawing substitution are expected upon protonation of the 4*H*-imidazole ligand sphere. The introduction of a positive charge in the 4*H*-imidazole ligand enhances its accepting character, stabilizes the excess charge on the ligand in the MLCT state, and hence causes a red-shifted absorption maximum of the MLCT transition as compared to the unprotonated form. For **RuMe** and **RuCOOEt**, only one position at the imidazole ring is available for protonation upon addition of trifluoroacetic acid to a solution of the respective dye in ACN. Attempts to protonate the second imidazole nitrogen atom by adding much larger amounts of trifluoroacetic acid to the solution led to decomposition of the complex observable by a bleaching of the solution within minutes. For **RuNMe₂**, the situation is different; the dimethylamino groups offer additional positions for protonation.⁵³ It was concluded that the first protonation occurs at the imidazole ring, followed by protonation of the two dimethylamino groups with nearly the same pK_a (Table 1). The protonation of the dimethylamino groups changes the character of the substituent from electron donating to electron withdrawing, which induces a further redshift of the absorption band. In general, a redshift of the absorption band by ca. 10 nm (269 cm^{-1}) is observed in the electron-withdrawing substituted complexes **RuCOOEtH** and **RuNMe₂H₃**, as compared to the electron-donating substituted **RuMeH** and **RuNMe₂H**.

In analogy to **RuNMe₂**, the pK_a values in ACN were determined for **RuMe** and **RuCOOEt** (for details, see the Supporting Information). For the protonation step of the imidazole nitrogen position, the determined pK_a values follow the trend predicted by the electron-donating and electron-withdrawing properties of the substituent at the terminal rings: **RuCOOEt** < **RuMe** < **RuNMe₂**.

To summarize, the influence of the terminal-ligand substituents on the singlet MLCT excited states is indicated by the spectral shifts of the visible absorption maximum observed in both protonated and unprotonated 4*H*-imidazole complexes in dependence on the electron-donating or -withdrawing character of the substituent. An additional shift of the absorption band is induced by ligand protonation. Similar effects can be expected to occur in the triplet manifold influencing the relative energetic positions of triplet states and hence the time-scale of the observed photoinduced processes and ultimately altering the excited-state decay mechanism.^{20,69,75} In the following, these effects will be addressed by investigating the excited-state processes in these systems by transient absorption spectroscopy in dependence on substitution and protonation.

3.2. Excited-State Dynamics – RuMe. The discussion of the photoinduced dynamics of the new 4*H*-imidazole-ruthenium dyes starts with the results for the methyl-substituted complex **RuMe**. Figure 3 presents transient absorption data for **RuMe** in ACN.

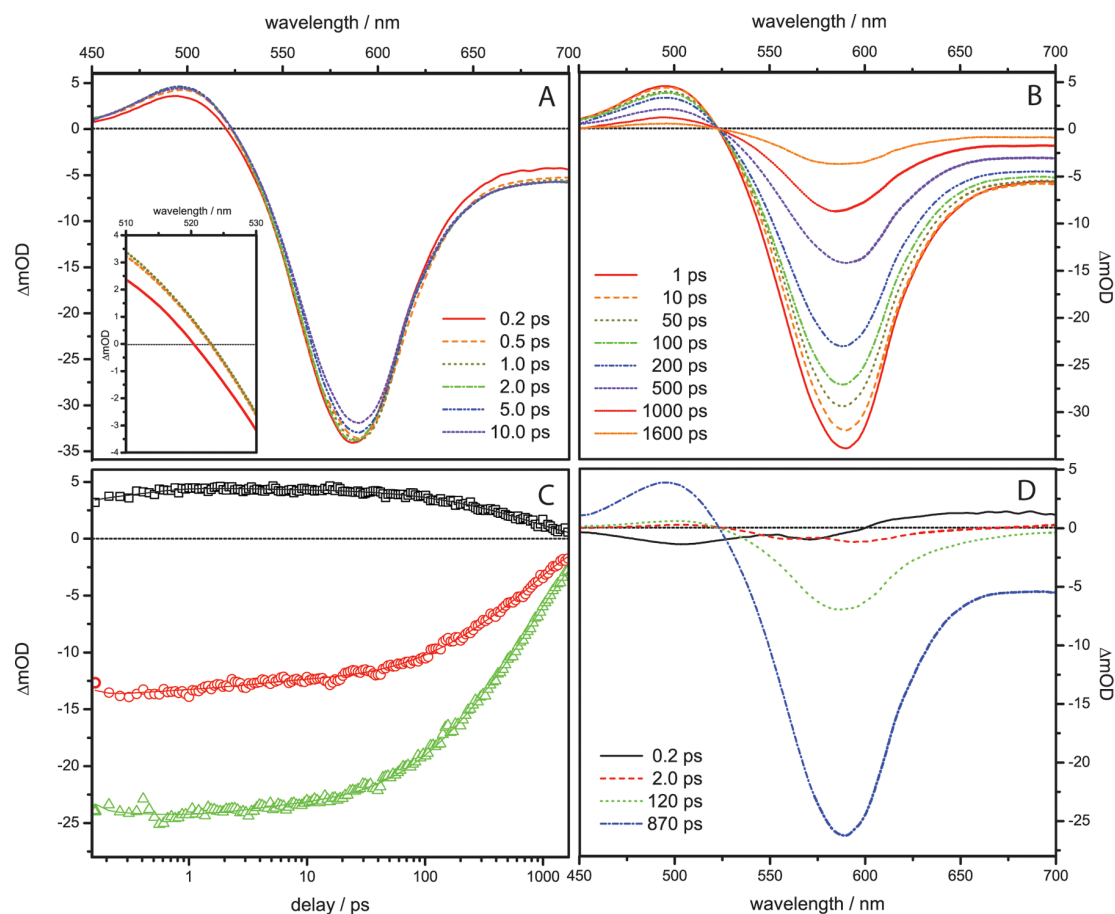


Figure 3. (A and B) Transient absorption spectra of **RuMe** in ACN at different delay times. The inset shows a magnification of the spectral region around the zero crossing. (C) Kinetic traces and fits at certain probe wavelengths (black/ \square 490 nm, red/ \circ 550 nm, green/ \triangle 610 nm). (D) DAS of **RuMe** and values of the corresponding time constants τ_1 (black/—), τ_2 (red/---), τ_3 (green/-.-.), and τ_4 (blue/-.-.-) resulting from a global fit.

Upon excitation in the absorption maximum at 585 nm, the TA spectra show a characteristic form dominated by excited-state absorption (ESA) between 450 and 525 nm and ground-state bleach (GSB) between 525 and 700 nm (see the Supporting Information). Different types of transitions are found to contribute to the ESA spectra of polypyridine-metal complexes. Generally, TA spectra in the visible range show contributions of IL transitions of the reduced ligand and ligand-to-metal charge-transfer (LMCT) transitions to the formally oxidized metal center.^{57,89–92} For a series of ruthenium complexes, a broad and featureless ESA at wavelengths longer than 550 nm assigned to LMCT transitions was observed, which is not present in the data of the 4*H*-imidazole complexes.^{8,21,56,57,69,93} This is due to the strong GSB contributions in this long wavelength range in the investigated systems (see Figure 1 and Supporting Information Figure S9), and ESA contributions may be hidden underneath the stronger GSB feature. The ESA feature between 450 and 525 nm may be connected to IL transitions of the reduced 4*H*-imidazole ligand. Upon reduction of the free ligand, an analogue redshift of the absorption band with respect to the unreduced form is observed.⁹⁴ To perform a reliable assignment, open-shell TD-DFT calculations of the ESA spectra are necessary,⁸⁹ which have not been performed yet.

The temporal evolution of the TA spectra shows an increase of the positive signal up to 1 ps after excitation, and the zero crossing around 525 nm is shifted to higher wavelengths by 4 nm (147 cm^{-1}) on this time scale. Additionally, the negative signal at wavelengths longer than 600 nm is rising. This effect is caused by a superposition of ESA and GSB in the investigated spectral region. The ESA part of the signal longer than 625 nm is decaying, causing the increase in the negative signal, while the ESA part of the signal at shorter wavelengths is increasing. To summarize, the time scale up to 1 ps is dominated by a blueshift of the ESA. On a longer time scale, an overall decay of the signal is observed. The differential absorption signal nearly completely decays back to the ground state within the time window investigated (1.8 ns).

A global fit was applied to quantitatively analyze the TA data. The best fit was achieved by applying a sum of four exponentials. Exemplarily chosen differential absorption kinetics, fits, and the decay associated spectra (DAS) can be found in Figure 3C and D, respectively. As it is known that the lowest MLCT excited states in **RuMe** are mainly localized on the 4*H*-imidazole ligand and the accepting LUMO contributing to the MLCT is localized only over the central part of the 4*H*-imidazole determined by the conformation of the coordinated ligand (Figure 2),⁵² the excited-state processes leading to a decay of the transient absorption signal are anticipated to take

place within the 4*H*-imidazole ligand sphere, and the observed dynamics can be explained as follows.

After excitation in the absorption maximum at 585 nm, a ¹MLCT excited state basically localized on the 4*H*-imidazole ligand is populated. The observed ultrafast process ($\tau_1 = 0.2$ ps) represents the observed blueshift in the ESA within the first picosecond after excitation and can be correlated with the interconversion between the ¹MLCT state and the ³MLCT manifold. This spectral shift correlates well with the observations reported in the literature for ISC in ruthenium-polypyridine complexes.^{56,95} ISC is followed by relaxation (localization of the excitation in the lowest MLCT excited state on the 4*H*-imidazole ligand and VR) within the triplet manifold leading to a thermally relaxed ³MLCT excited state within a few picoseconds ($\tau_2 = 2$ ps), accompanied by a slight broadening in the GSB line width. Starting from this relaxed excited 4*H*-imidazole ³MLCT state, a second excited state, which is localized within the 4*H*-imidazole sphere, is populated ($\tau_3 = 120$ ps), and a new ESA feature centered at 590 nm superimposed on the GSB signal appears (see Supporting Information Figure S9), causing the decay in the negative signal. This new ESA signature indicates severe changes within the electronic structure of the 4*H*-imidazole ligand, which are attributed to the formation of a stronger conjugated system by planarization of the 4*H*-imidazole. Hence, by planarization of the terminal rings, an additional low lying excited state gets available for relaxation. Finally, from this planarized excited state, the system decays radiationless to the ground state ($\tau_4 = 870$ ps).

Time constants connected to rotational motions, that is, planarization, are expected to display strong solvent viscosity dependence due to the interaction with the solvent during molecular motion.^{96–100} Therefore, transient absorption experiments were performed in solvents with varying viscosity while keeping their polarity approximately constant (Table 2). An

Table 2. Dynamic Viscosity η and Dielectric Constant ϵ of the Applied Solvents, and Viscosity-Dependent Time Constants τ of RuMe

	η /mPa·s	ϵ	τ_1 /ps	τ_2 /ps	τ_3 /ps	τ_4 /ps
ACN	0.37	37.5	0.2	2	120	870
GBL	1.72	39.0	0.2	2	280	880
DMPU	2.93	36.1	0.2	3	360	1000

inspection of the respective kinetic traces in Figure 4 shows that upon increasing the solvent viscosity the excited-state decay is decelerated. This is particularly visible in the range between 10 and 500 ps, indicating a decelerated population of the secondary excited state. The viscosity dependence of τ_3 strongly indicates a process connected to a significant structural rearrangement, which we associate with a planarization of the ligand, connected to a rotation around the C2N1 and/or C5N2 bond (Figure 2) connecting the terminal rings to the central part of the 4*H*-imidazole ligand. The time constant τ_4 of the slowest process is influenced by solvent properties, too, as this process leads back from the planarized excited state to the ground state and hence is also coupled to a large amplitude motion. The weak deceleration in GBL as compared to ACN might be caused by the slight differences in solvent polarity.

To complete the understanding of the conformational relaxation behavior, geometry optimizations starting from the FC region have been carried out for electronic states probably

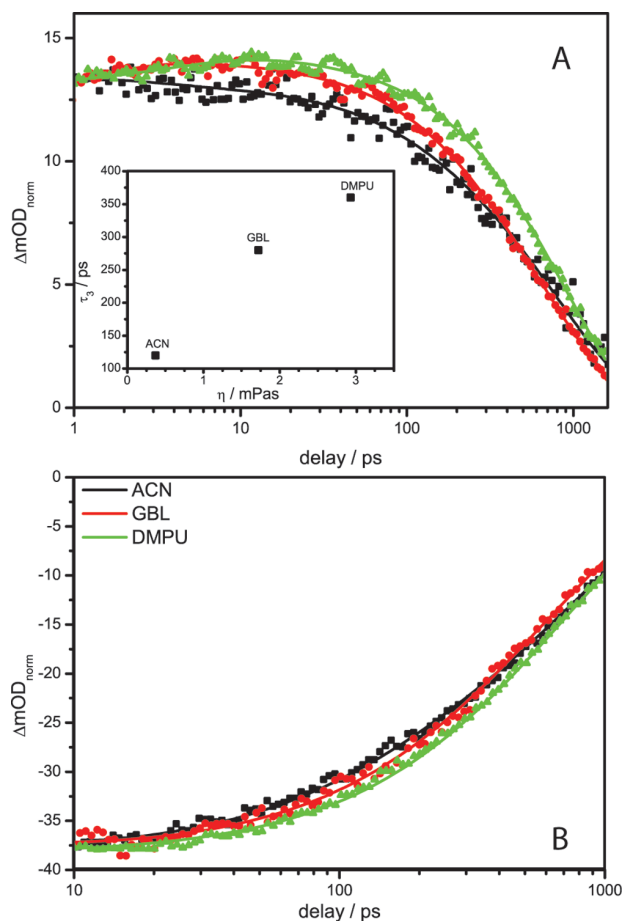


Figure 4. Kinetic traces of RuMe in ACN/■, GBL/●, and DMPU/▲ exemplarily at probe of a wavelength region with (A) dominating excited-state absorption signal (ACN 490 nm, GBL and DMPU 500 nm) and (B) ground-state bleach (ACN 630 nm, BL and DMPU 640 nm), respectively. Absorption spectra and global fits can be found in the Supporting Information.

involved in the relaxation process, the singlet ground state (S_0), the bright low-lying excited state (S_6)⁵² populated upon excitation, the triplet ground state in the FC structure (T_{twist}), and a planarizing triplet state (T_{plan}) (for details, see the Supporting Information). Figure 5 shows the resulting energetic positions of these excited states in each of the four equilibrium structures (FC, ¹MLCT, ³MLCT, and ³MLCT_{plan}).

Following photoexcitation to S_6 (2.41 eV), ultrafast internal conversion (IC), ISC, and VR lead to a population of the nonplanar ³MLCT state (T_{twist} , 1.05 eV). As compared to the geometry at the FC point, this thermally relaxed state, which is localized on the central part of the 4*H*-imidazole ligand, shows only slightly decreased dihedral angles of the terminal rings. The configuration of this excited state can be described as a transfer of an electron from a metal centered molecular orbital to a $\pi^*(4H\text{-imidazole})$ accepting orbital with distribution similar to that of the LUMO at the FC geometry shown in Figure 2 (see the Supporting Information). In agreement with the results from the experiments, the calculations indicate the presence of a secondary triplet state (T_{plan} , 1.07 eV) available for relaxation. The energy of this state, which is much higher than the energy of T_{twist} at the FC geometry, is strongly decreased upon planarization. The similarity of the energies of

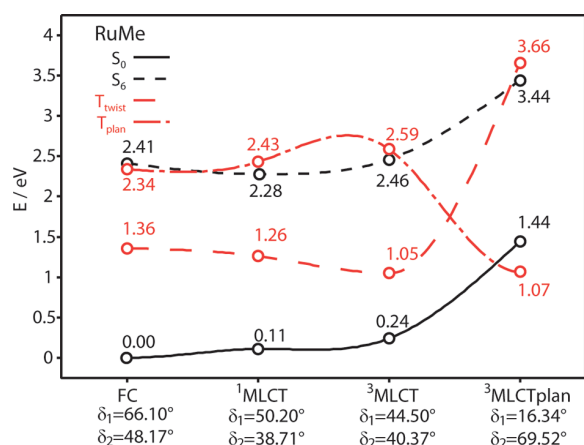


Figure 5. Schematic representation of the relative energies of the singlet ground state S_0 , the singlet excited state populated upon excitation S_1 , the nonplanarized triplet state T_{twist} , and the planarized triplet state T_{plan} for the equilibrium geometries (FC, ¹MLCT, ³MLCT, and ³MLCT_{plan}) of each of the four electronic states for RuMe. Dihedral angles (defined in Figure 2) are given below the graph.

T_{twist} and T_{plan} suggests a thermal equilibrium between those states, which both might decay to the ground state. Further it should be kept in mind that the exact energy values can only be estimations, because of the inherent error of the method for CT states of 0.4 eV.^{101,102} In the optimized geometry of T_{plan} (³MLCT_{plan}), one of the dihedral angles is reduced from 66° to 16°. At the FC point and the ¹MLCT and ³MLCT geometries, T_{plan} is strongly localized on one of the terminal rings. Its configuration is described as the transfer of an electron from a metal localized orbital to an accepting orbital with $\pi^*(4H\text{-imidazole}) \pm \sigma^*(\text{RuN}(4H\text{-imidazole}))$ character mainly localized on one of the terminal rings of the 4H-imidazole (see the Supporting Information). In its minimum geometry, the character of T_{plan} changes significantly as the accepting orbital is now an $\pi^*(\text{terpyridine}) \pm \sigma^*(\text{RuN}(4H\text{-imidazole}))$ orbital. Caused by the partial σ -antibonding character of the accepting orbital, the RuN bond anti to the chloro ligand is significantly lengthened (2.11 Å in the FC geometry, 2.74 Å in the ³MLCT_{plan} geometry). From this state, an efficient radiationless return to the ground state is possible.

With these results, it is shown that several excited states contribute to the excited-state dynamics. The transition between these states is mediated by a rotational motion

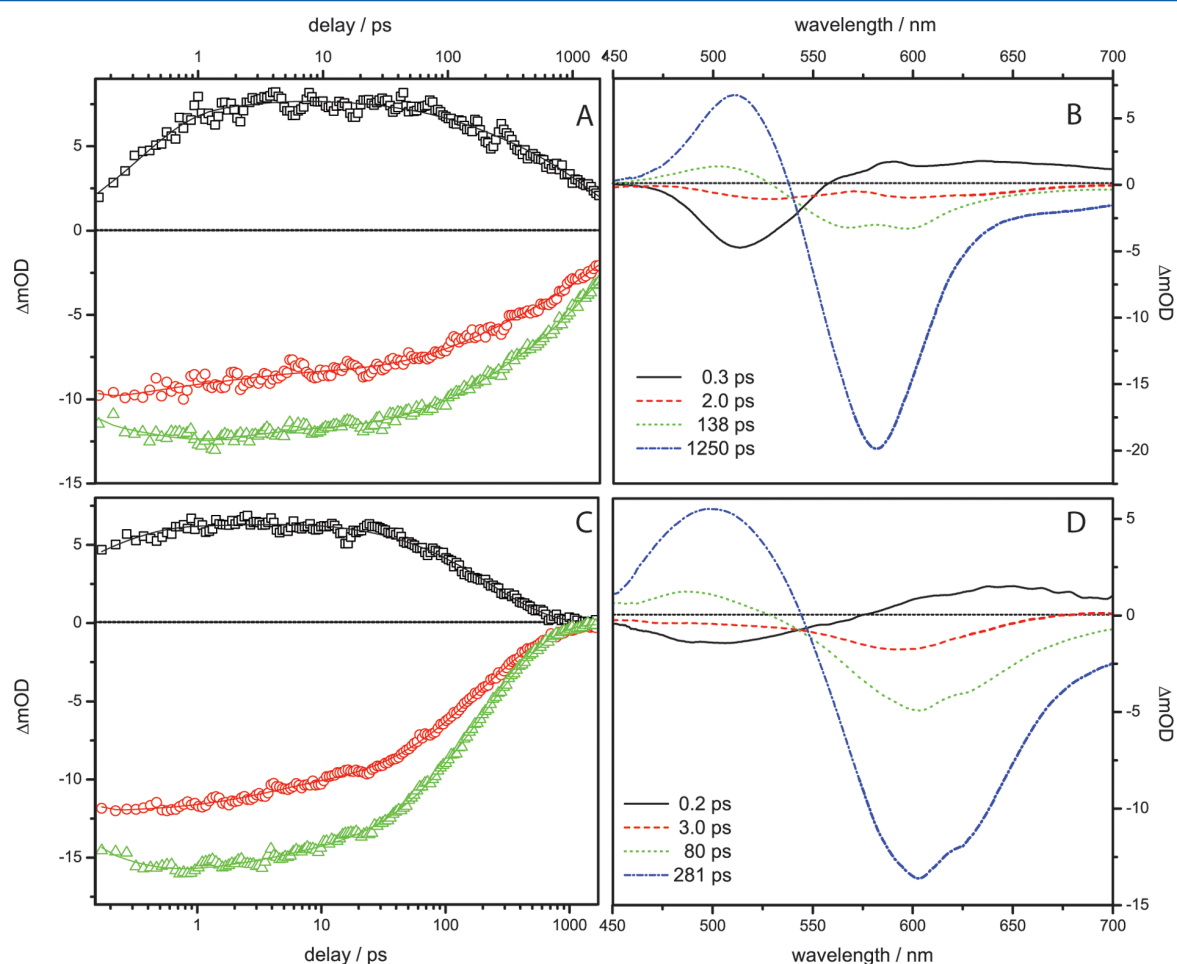


Figure 6. Kinetics, DAS spectra, and values of the corresponding time constants τ_1 (black/—), τ_2 (red/---), τ_3 (green/-.-), and τ_4 (blue/-.-.-) for RuNMe₂ (A, B) and RuCOOEt (C, D) in ACN after excitation in the respective MLCT absorptions maximum in the visible. The kinetic for RuNMe₂ is depicted at 510 nm (black/□), 550 nm (red/O), and 510 nm (green/△) and for RuCOOEt at 500 nm (black/□), 570 nm (red/O), and 530 nm (green/△).

leading to an at least partial planarization of the coordinated ligand, shifting the excess charge on the 4*H*-imidazole ligand from the central part formed by the imidazole and the directly connected phenyl ring to the terminal tolyl groups within several tens of picosecond. This shift might be a major hindrance for the applicability of these systems in electron transfer dyads as it can compete with electron transfer processes to accepting units. To enhance the applicability of these 4*H*-imidazole dyes, it would be beneficial to trap the excitation in the nonplanarized excited state. Therefore, the impact of ligand substitution and protonation on the excited state processes is studied.

3.3. Excited-State Dynamics – Substitution Dependence. In section 3.1, the impact of the electronic character of the substituent in the 4*H*-imidazole ligand on the absorption properties and the pK_a values for protonation of the imidazole nitrogen in the 4*H*-imidazole ligand was discussed. As shown in the previous section, the photoinduced dynamics involves several excited states within the 4*H*-imidazole sphere with differing local charge distributions. The closer spatial vicinity of the secondary planarized excited state and the substituent bearing rings and the possibility of conjugative interactions with the substituents cause the relative energetic position of this state to be more sensitive to changes in the electronic properties of the substituent. Thus, changes in the population dynamics of this state can be anticipated.

In Figure 6 are presented the transient absorption kinetics and the DAS for the electron-donating substituted complex **RuNMe₂** (panels A, B) and the electron-withdrawing substituted complex **RuCOOEt** (panels C, D). It is distinctly visible that, as compared to **RuMe**, the decay of the excited state is slower in **RuNMe₂** and much faster in **RuCOOEt**. Generally, the shape of the TA spectra is very similar to **RuMe**. Below 540 nm, both **RuNMe₂** and **RuCOOEt** show dominating ESA, and at wavelengths longer than 540 nm GSB dominates the TA spectra, probably superimposed on ESA caused by LMCT transitions (see Supporting Information Figure S9). Especially **RuNMe₂** shows a very strong ESA band peaking at approximately 505 nm, completely extinguishing the strong GSB contribution by the second absorption maximum of **RuNMe₂** in the ground state.

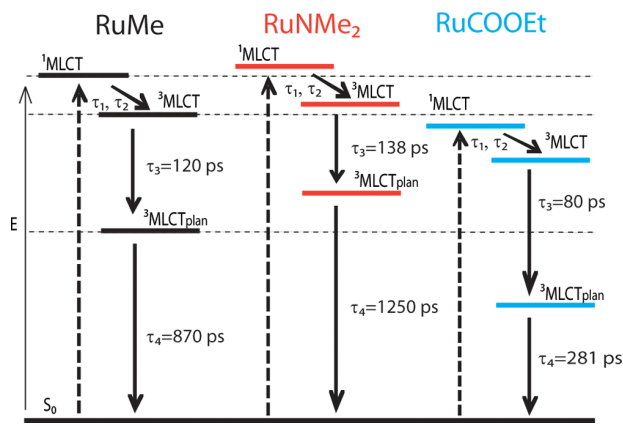
The global fit delivers, in agreement with the results for **RuMe**, four time constants describing the photoinduced dynamics. The DAS spectra closely resemble the DAS spectra of **RuMe**. Shifts, for example, in the position of the zero crossing of the ultrafast component (τ_1) reflect the changes in the electronic structure of the ¹MLCT and ³MLCT. The position of the ESA band, which is built up upon population of the planarized state, follows the shift in the ground-state absorption features: for **RuNMe₂** the center is slightly blue-shifted (584 nm), and for **RuCOOEt** it is shifted bathochromically (600 nm). In agreement with the discussion above, the observed processes are assigned to ultrafast subpicosecond ISC (τ_1) as well as excited-state localization and VR leading to the thermally relaxed triplet excited state on the central part of the 4*H*-imidazole ligand (τ_2). The third process (τ_3) is assigned to the population of the secondary planarized excited state, and the fourth and slowest process describes the repopulation of the ground state from the planarized excited state (τ_4). The values of τ_1 and τ_2 are similar to the values for **RuMe**, and hence these processes are not significantly affected by ligand substitution. The strongest difference describing the slower/faster decay in the substituted species is observed for τ_4 . For **RuNMe₂**, this

process is much slower (1250 ps) than in **RuMe** (870 ps), while in **RuCOOEt** this process is accelerated (281 ps). This behavior is in agreement with predictions by the energy gap law:^{103–106} Already from the absorption spectra a smaller energy gap and hence a faster decay are expected for **RuCOOEt**, in which the excited state is inductively stabilized by the ethylcarboxylate substituent. Consequently, for **RuNMe₂**, a slightly slower decay caused by a higher energy gap is observed. Furthermore, the higher conjugative interaction and hence the strong mesomeric influence of the substituents on the secondary excited state, which causes a strong additional decrease/increase of the energy gap, need to be considered. These mesomeric effects operate in the same direction as the inductive effects, enhancing the predicted effects significantly.

The stronger conjugative interactions in the planarized excited state are not only influencing the energy gap between the secondary planarized excited state and the ground state of the system, but the gap between the nonplanarized state and the planarized state is altered also. For **RuCOOEt** a stronger stabilization of the planarized excited state occurs, which explains the acceleration of τ_3 , by an enhancement of the driving force for this process (for further details, see the Supporting Information). For **RuNMe₂**, on the other hand, this process is slower because in this case the planarized excited state is destabilized by the mesomeric effect of the NMe₂ substituent enhancing the electron density in the terminal rings.

The relative energetic positions of the relevant excited states and the observable processes occurring after light absorption in the unprotonated Ru-4*H*-imidazole complexes are summarized in Scheme 2. The impact of the character of the ligand

Scheme 2. Schematic Representation of the Relative Energetic Position of the Excited States Involved in the Excited-State Processes in the Investigated 4*H*-Imidazole-Ruthenium Dyes



substituent at the terminal ring position is confirming the description of the spatial location of the first excited state only on the central 4*H*-imidazole part, while the second state is much stronger localized toward the terminal rings and hence is much more prone to stabilization/destabilization by the terminal substituents. This result is important for the design of dyes, which are suited for incorporation in electron transfer dyads. A preferable position for introduction of a suited coupling group (e.g., a carboxyl group) would be the phenyl ring directly connected to the imidazole. This should provide close electronic contact with the nonplanarized excited state,

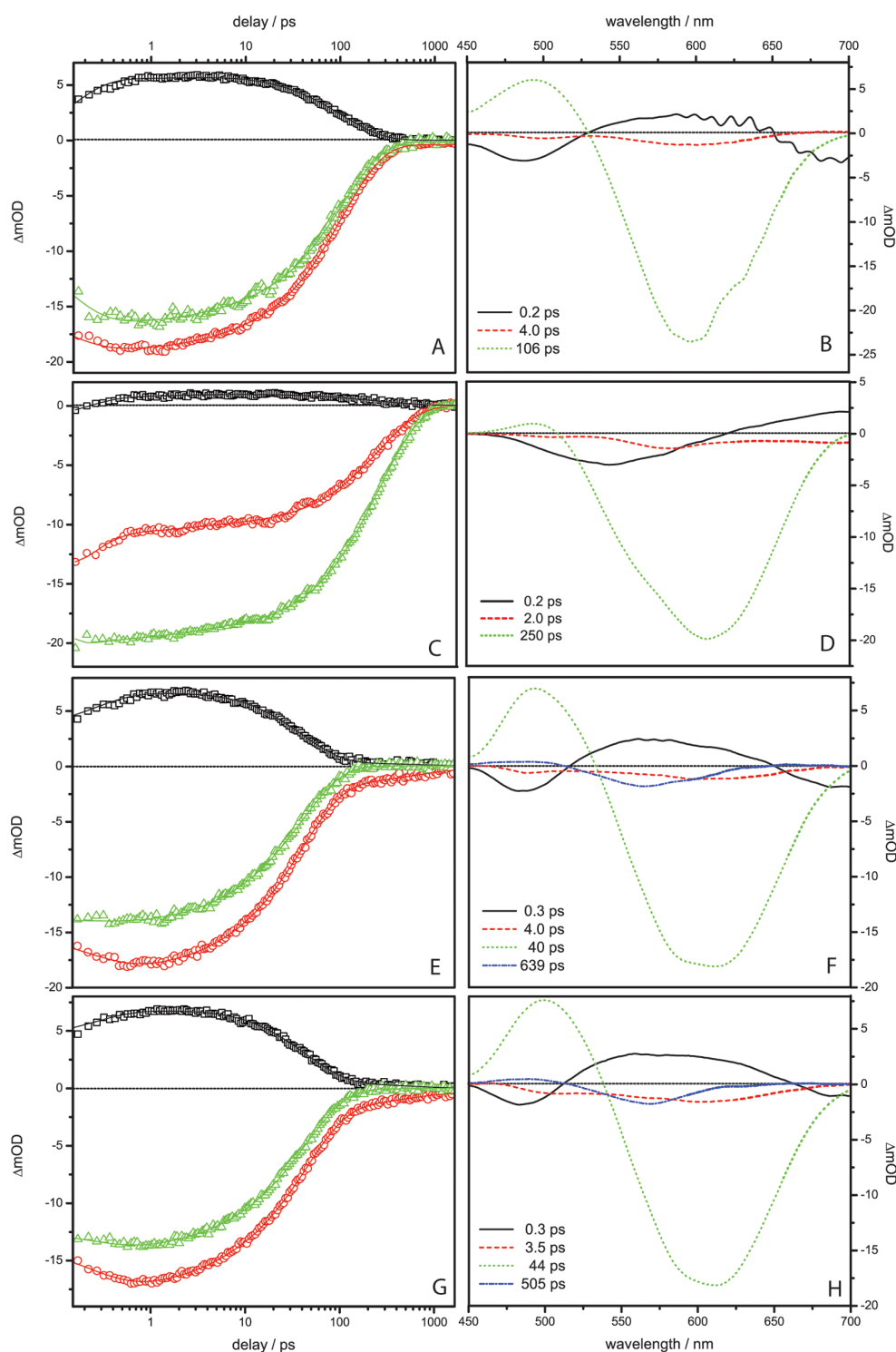


Figure 7. Kinetic, DAS spectra, and values of the corresponding time constants τ_1 (black/—), τ_2 (red/---), τ_3 (green/---), and τ_4 (blue/---) for the protonated complexes with electron-donating substituents **RuMeH** (A, B) and **RuNMe₂H** (C, D) and with electron-withdrawing substituents **RuNMe₂H₃** (E, F) and **RuCOOEtH** (G, H). The kinetic for **RuMeH** is depicted at 490 nm (black/□), 570 nm (red/O), and 630 nm (green/△), for **RuNMe₂H** at 495 nm (black/□), 550 nm (red/O), and 610 nm (green/△), and for **RuNMe₂H₃** and **RuCOOEtH** at 490 nm (black/□), 580 nm (red/O), and 640 nm (green/△).

enabling efficient electron transfer to, for example, TiO₂ originating from this excited state. Another effect of the introduction of this electron-withdrawing group could be the stabilization of the nonplanarized state with respect to the

planarized state, ideally closing the relaxation pathway via the planarized state.

3.4. Excited-State Dynamics – Influence of Protonation. In the previous section, it was shown that the spatial

localization of the excited states within the ligand sphere impacts the effect of the substituents on the relative energetic positions of the respective excited states. Another possibility to influence the energetic position of the MLCT excited states is protonation of the ligand. This is already indicated by the redshift in the absorption spectrum upon protonation (Figure 1). In this respect, the interplay between protonation and the character of the substituent is especially interesting for this series of complexes. By protonation, a stronger stabilizing impact is expected on the energetic position of the nonplanarized excited state, while the choice of the terminal substituent tunes the position of the secondary planarized state.

The transient absorption data for all protonated species investigated (i.e., **RuMeH**, **RuNMe₂H**, **RuNMe₂H₃**, and **RuCOOEtH**) are presented in Figure 7. The kinetic traces show that the signal in all species decays much faster in the protonated forms than in the unprotonated complexes. In all cases, the ground state is completely recovered within 1.8 ns. The shape of the TA spectra shows features analogous to those of the unprotonated forms (see Supporting Information Figure S10). Corresponding to the bathochromic shift of the absorption maximum in the ground-state spectra upon protonation, the GSB maximum is shifted in all protonated forms. Below 550 nm, ESA dominates the spectra of all investigated protonated forms. In **RuNMe₂H**, this positive signal is very weak because of the strong and broad ground-state absorption resulting in strong GSB contributions, which is not present in the spectra of the other protonated species (see Figure 1). For **RuNMe₂H₃** and **RuCOOEtH**, a strong decrease in the overall TA signal and a shift of the zero crossing position on the same time scale are observed, while the zero crossing position in the TA spectra of **RuMeH** and **RuNMe₂H** stays constant as a function of delay.

The global fit reveals systematic differences in the behavior of the electron-donating substituted forms **RuMeH** and **RuNMe₂H** and the electron-withdrawing substituted forms **RuNMe₂H₃** and **RuCOOEtH**. A strong similarity between **RuNMe₂H₃** and **RuCOOEtH** is already observed in the absorption spectra, which are nearly identical, and indeed these two complexes also show exceptional similar photoinduced dynamics. The data for the electron donating substituted forms **RuMeH** and **RuNMe₂H** were best described by a fit with three exponentials representing three processes, while for the forms with electron withdrawing substituent **RuNMe₂H₃** and **RuCOOEtH** four processes are observed.

τ_1 and τ_2 are describing ultrafast ISC and VR within the triplet MLCT manifold populating the thermally relaxed ³MLCT state, localized at the central part of the 4*H*-imidazole. The characteristic time scales of these processes and their spectral characteristics are not changed significantly by protonation, shifts in the zero crossing position of the DAS for the ISC process are observed (**RuMe** 525 nm, **RuCOOEtH** and **RuNMe₂H₃** 510 nm, and **RuNMe₂H** 620 nm), and for **RuMe**, **RuCOOEtH**, and **RuNMe₂H₃**, an additional zero crossing is observable at 650 nm (Figure 7).

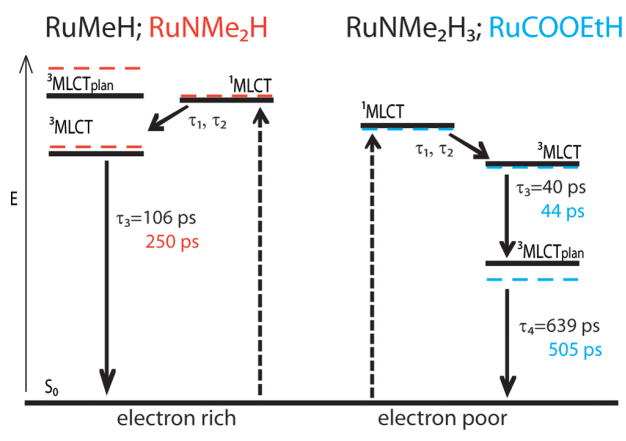
In the electron-donating substituted protonated forms **RuMeH** and **RuNMe₂H**, only one additional process could be identified describing the radiationless decay back to the ground state directly from the thermally relaxed nonplanarized state. The observed time constant τ_3 for this process is for **RuNMe₂H** ($\tau_3 = 250$ ps) larger than for **RuMe** ($\tau_3 = 106$ ps). This can be explained by inductive destabilization of the nonplanarized MLCT excited state by the enhanced electron

density in the ligand caused by the stronger electron-donating properties of the NMe₂ substituent, which increases the energy gap in **RuNMe₂** as compared to **RuMe**. The direct decay from the nonplanarized excited state is due to the stronger stabilization of the nonplanarized excited state by protonation. This can be explained by the stronger localization of this state on the central part of the ligand where, upon protonation, the positive charge resides, which stabilizes the excess electronic density in the nonplanarized state. This changes the energetic ordering of the excited states, and the planarized state is no longer available for relaxation. The results of TDDFT optimizations confirm this result (see the Supporting Information).

When the protonated ligand is substituted with an electron-withdrawing group, four processes, as in the unprotonated forms, are observed. The stabilizing effect of the electron-withdrawing substituent on the planarized state is restoring the energetic ordering of the nonplanarized and planarized triplet state as found in the unprotonated species. The strong (weak) spectral contribution of the third (fourth) process can be explained with the buildup of an excited-state absorption band upon planarization nearly completely diminishing the GSB contribution (see Supporting Information Figure S10). Additionally, it is possible that the planarized and nonplanarized states in these systems are close in energy and that a part of the excited species directly returns to the ground state from the nonplanarized state and the planarized state is only partly populated. This matter cannot fully be resolved by this study but will be subject to further investigations. τ_3 describes the population of a planarized state and possibly in parallel the partial repopulation of the ground state, and τ_4 is associated with the radiationless repopulation of the ground state from the planarized state. For **RuNMe₂H₃**, the decay of the planarized state to the ground state ($\tau_4 = 639$ ps) is faster as compared to the unprotonated form **RuNMe₂** ($\tau_4 = 1250$ ps). This can be understood as a result of both stabilizing influences of protonation and electron-withdrawing substitution lowering the energy gap. In contrary, for the protonated form of **RuCOOEt**, ground-state recovery is significantly slowed (**RuCOOEt** $\tau_4 = 281$ ps, **RuCOOEtH** $\tau_4 = 505$ ps), which is in contrast to the expected decreased energy gap. A possible explanation for this behavior is that in the deprotonated species, higher lying ³MC (metal-centered) states contribute to the excited-state decay and offer a very fast radiationless deactivation path.⁶ In the protonated species, this decay channel is less available due to the higher energy gap between the ³MLCT states and the ³MC states.^{2,61,106–109}

The relative positions of the excited states and the observed processes are schematically summarized in Scheme 3. In the investigated structures, protonation occurs in closer spatial vicinity to the first excited state and is expected to stabilize this state with respect to the planarized state, while, as already detailed below, ligand substitution at the terminal rings has a stronger impact on the second planarized excited state. Hence, the right choice of ligand substituent and protonation state offers the possibility to trap the system in the first nonplanarized excited state. An especially interesting case in this respect is **RuNMe₂**, as the character of the substituent can be changed from electron donating (NMe₂) to electron withdrawing (NMe₂H⁺) by adjusting the pH of the solution. Hence, the electronic situation in **RuNMe₂** can be switched between three states just by controlling the solvent pH.

Scheme 3. Schematic Representation of Relative Energetic Positions of the Excited States Involved in the Excited-State Processes in the Investigated Protonated 4*H*-Imidazole-Ruthenium Dyes



4. CONCLUSION

The photoinduced processes in a series of 4*H*-imidazole-ruthenium dyes were investigated in dependence on the electronic character of the ligand substituents and the protonation state. The results of the time-resolved measurements yielded distinct structure–dynamics relations in the investigated systems.

The data reveal that the excited states after excitation in the MLCT transition of the 4*H*-imidazole-ruthenium dyes are quite short-lived, and the ground state is nearly completely repopulated within at most 3 ns in the deprotonated forms and 1 ns in the protonated forms. The processes leading to a decay of the excitation involve two excited states localized in the 4*H*-imidazole sphere. The conversion between these states occurs within ~100 ps (depending on solvent viscosity) and is coupled to a strong structural rearrangement in the 4*H*-imidazole ligand. This structural rearrangement leads to a planarization of the coordinated ligand. Connected to this planarization is a shift of the excess electronic charge within the 4*H*-imidazole ligand. This shift of the excited state could be severe competition for electron transfer processes to acceptor units attached in close vicinity of the nonplanarized excited state. To improve the functionality of the dyes, it is necessary to find ways to block the population of the second planarized excited state within the 4*H*-imidazole ligand sphere. In this respect, the interplay between ligand substitution and protonation becomes of importance.

In the planarized excited state, the electronic communication between the substituents at the terminal rings and the rest of the ligand system is enhanced by establishing a completely conjugated system. Hence, the influence of the electronic character of the substituent is much stronger than for the nonplanarized state only located at the central imidazole and phenyl ring. This results in a slower population of the planarized state and the ground state in the case of electron-donating substitution. In complexes with electron-withdrawing substituents, the interconversion between these states and the decay to the ground state is accelerated.

In contrary, protonation of the imidazole nitrogen atom occurs in the vicinity of the nonplanarized MLCT state, causing a stronger stabilization of the excess electronic charge in this state. Together with the effects of the substituents, this results

in the case of electron-donating substitution in an inversion of the electronic ordering of the excited states. As a consequence, the planarized state is not available for relaxation, and the system directly decays back to the ground state. The stabilizing effects of electron-withdrawing substituents on the terminal rings restore the energetic ordering present in the deprotonated form, and in those species the planarized state is populated again during the excited-state decay. This results in a pH switchable decay mechanism for **RuNMe₂**, as by protonation of the NMe₂ substituent the character is changed from electron donating to electron withdrawing.

Finally, it can be concluded that by appropriate choice of the substituents and the protonation state, localization of the excitation can be controlled and trapped in the nonplanarized excited state. Such effects need to be kept in mind for the design of dyes with suitable coupling groups in the ligand sphere, for example, to attach the dye on a TiO₂ surface. Their influence depending on their electronic character and position in the 4*H*-imidazole ligand on the excited state processes and the relative energetic positions of the excited states might severely influence the functionality of the dye as sensitizer, by enabling or blocking unwanted quenching processes. This will be the subject of further investigations.

■ ASSOCIATED CONTENT

Supporting Information

Resonance Raman spectra and TDDFT calculations of absorption and resonance Raman spectra for **RuCOOEt**, dihedral angles for the terminal groups, figures of the minimum geometries of the optimized excited states, schematic representation of the relative energies of the contributing excited states for **RuMe** and **RuMeH**, configurations of the contributing excited states at the minimum geometries, figures of the molecular orbitals involved in the configurations of the excited states, spectrophotometric titration curves for p*K*_a determination of **RuMe** and **RuCOOEt**, absorption spectra of **RuMe** in different solvents, DAS spectra for **RuMe** in different solvents and comparison of TA spectra and ground-state absorption spectra for all species, and approximation of the pure ESA spectra. This material is available free of charge via the Internet at <http://pubs.acs.org>.

■ AUTHOR INFORMATION

Corresponding Author

*Tel.: +43 1 4277 52750 (L.G.); +49 (0)3641 206-332 (B.D.). Fax: +43 1 4277 9527 (L.G.); +49 (0)3641 206-399 (B.D.). E-mail: leticia.gonzalez@univie.ac.at (L.G.); benjamin.dietzek@ipht-jena.de (B.D.).

Author Contributions

[∇]These authors contributed equally.

Notes

The authors declare no competing financial interest.

■ ACKNOWLEDGMENTS

This research was supported financially by the Thüringer Ministerium für Bildung, Wissenschaft und Kultur (PhotoMIC, grant no. B 514-09049). Further financial support is gratefully acknowledged from the Studienstiftung des deutschen Volkes (M.W.), the Carl-Zeiss-Foundation (J.G.), and the Fonds der Chemischen Industrie (B.D.).

■ ABBREVIATIONS

ACN, acetonitrile; GBL, γ -butyrolactone; DMPU, 1,3-dimethyltetrahydropyrimidin-2(1H)-one; IL, intraligand; LC, ligand centered; MLCT, metal-to-ligand charge-transfer; MC, metal-centered; DAS, decay associated spectra; TA, transient absorption; ESA, excited-state absorption; GSB, ground-state bleach; ISC, intersystem crossing; VR, vibrational relaxation; IC, internal conversion; TDDFT, time-dependent density functional theory

■ REFERENCES

- (1) Huynh, M. H. V.; Dattelbaum, D. M.; Meyer, T. J. *Coord. Chem. Rev.* **2005**, *249*, 457–483.
- (2) Hammarström, L.; Johansson, O. *Coord. Chem. Rev.* **2010**, *254*, 2546–2559.
- (3) Zeitler, K. *Angew. Chem., Int. Ed.* **2009**, *48*, 9785–9789.
- (4) Dixon, I. M.; Lebon, E.; Sutra, P.; Igau, A. *Chem. Soc. Rev.* **2009**, *38*, 1621–1634.
- (5) Gao, F.; Chao, H.; Ji, L.-N. *Chem. Biodiversity* **2008**, *5*, 1962–1979.
- (6) Campagna, S.; Puntoriero, F.; Nastasi, F.; Bergamini, G.; Balzani, V. *Photochemistry and Photophysics of Coordination Compounds I*; Springer: Berlin, 2007; Vol. 280.
- (7) Siebert, R.; Winter, A.; Dietzek, B.; Schubert, U. S.; Popp, J. *Macromol. Rapid Commun.* **2010**, *31*, 883–888.
- (8) Siebert, R.; Winter, A.; Schubert, U. S.; Dietzek, B.; Popp, J. *Phys. Chem. Chem. Phys.* **2011**, *13*, 1606–1617.
- (9) Coppo, P.; Duati, M.; Kozhevnikov, V. N.; Hofstraat, J. W.; De Cola, L. *Angew. Chem., Int. Ed.* **2005**, *44*, 1806–1810.
- (10) Chambron, J. C.; Sauvage, J. P.; Amouyal, E.; Koffi, P. *New J. Chem.* **1985**, *9*, 527–529.
- (11) Hartshorn, R. M.; Barton, J. K. *J. Am. Chem. Soc.* **1992**, *114*, 5919–5925.
- (12) Jenkins, Y.; Friedman, A. E.; Turro, N. J.; Barton, J. K. *Biochemistry* **1992**, *31*, 10809–10816.
- (13) Haq, I.; Lincoln, P.; Suh, D. C.; Norden, B.; Chowdhry, B. Z.; Chaires, J. B. *J. Am. Chem. Soc.* **1995**, *117*, 4788–4796.
- (14) Nair, R. B.; Cullum, B. M.; Murphy, C. J. *Inorg. Chem.* **1997**, *36*, 962–965.
- (15) Friedman, A. E.; Chambron, J. C.; Sauvage, J. P.; Turro, N. J.; Barton, J. K. *J. Am. Chem. Soc.* **1990**, *112*, 4960–4962.
- (16) Andreiadis, E. S.; Chavarot-Kerlidou, M.; Fontecave, M.; Artero, V. *Photochem. Photobiol.* **2011**, *87*, 946–964.
- (17) Sakai, K.; Kobayashi, M.; Masaoka, S. *Molecules* **2010**, *15*, 4908–4923.
- (18) Rau, S.; Schäfer, B.; Gleich, D.; Anders, E.; Rudolph, M.; Friedrich, M.; Görls, H.; Henry, W.; Vos, J. G. *Angew. Chem., Int. Ed.* **2006**, *45*, 6215–6218.
- (19) Tschierlei, S.; Karnahl, M.; Presselt, M.; Dietzek, B.; Guthmüller, J.; Gonzalez, L.; Schmitt, M.; Rau, S.; Popp, J. *Angew. Chem., Int. Ed.* **2010**, *49*, 3981–3984.
- (20) Karnahl, M.; Kuhnt, C.; Ma, F.; Yartsev, A.; Schmitt, M.; Dietzek, B.; Rau, S.; Popp, J. *ChemPhysChem* **2011**, *12*, 2101–2109.
- (21) Tschierlei, S.; Presselt, M.; Kuhnt, C.; Yartsev, A.; Pascher, T.; Sundström, V.; Karnahl, M.; Schwalbe, M.; Schäfer, B.; Rau, S.; et al. *Chem.-Eur. J.* **2009**, *15*, 7678–7688.
- (22) Elvington, M.; Brown, J.; Arachchige, S. M.; Brewer, K. J. *J. Am. Chem. Soc.* **2007**, *129*, 10644–10645.
- (23) Lei, P.; Hedlund, M.; Lomoth, R.; Rensmo, H.; Johansson, O.; Hammarström, L. *J. Am. Chem. Soc.* **2008**, *130*, 26–27.
- (24) Akita, M.; Inagaki, A. *Coord. Chem. Rev.* **2010**, *254*, 1220–1239.
- (25) Alstrum-Acevedo, J. H.; Brennaman, M. K.; Meyer, T. J. *Inorg. Chem.* **2005**, *44*, 6802–6827.
- (26) Concepcion, J. J.; Jurss, J. W.; Brennaman, M. K.; Hoertz, P. G.; Patrocino, A. O. T.; Iha, N. Y. M.; Templeton, J. L.; Meyer, T. J. *Acc. Chem. Res.* **2009**, *42*, 1954–1965.
- (27) Grätzel, M. *Acc. Chem. Res.* **2009**, *42*, 1788–1798.
- (28) Polo, A. S.; Itokazu, M. K.; Iha, N. Y. M. *Coord. Chem. Rev.* **2004**, *248*, 1343–1361.
- (29) Oregan, B.; Grätzel, M. *Nature* **1991**, *353*, 737–740.
- (30) Grätzel, M. *Nature* **2001**, *414*, 338–344.
- (31) Grätzel, M. *Inorg. Chem.* **2005**, *44*, 6841–6851.
- (32) Benkö, G.; Kallioinen, J.; Korppi-Tommola, J. E. I.; Yartsev, A. P.; Sundström, V. *J. Am. Chem. Soc.* **2002**, *124*, 489–493.
- (33) Benkö, G.; Kallioinen, J.; Myllyperkiö, P.; Trif, F.; Korppi-Tommola, J. E. I.; Yartsev, A. P.; Sundström, V. *J. Phys. Chem. B* **2004**, *108*, 2862–2867.
- (34) Kallioinen, J.; Benkö, G.; Myllyperkiö, P.; Khriachtchev, L.; Skarman, B.; Wallenberg, R.; Tuomikoski, M.; Korppi-Tommola, J.; Sundström, V.; Yartsev, A. P. *J. Phys. Chem. B* **2004**, *108*, 6365–6373.
- (35) Robertson, N. *Angew. Chem., Int. Ed.* **2006**, *45*, 2338–2345.
- (36) Robson, K. C. D.; Koivisto, B. D.; Gordon, T. J.; Baumgartner, T.; Berlinguette, C. P. *Inorg. Chem.* **2010**, *49*, 5335–5337.
- (37) Robson, K. C. D.; Koivisto, B. D.; Yella, A.; Sporinova, B.; Nazeeruddin, M. K.; Baumgartner, T.; Grätzel, M.; Berlinguette, C. P. *Inorg. Chem.* **2011**, *50*, 5494–5508.
- (38) Chou, C. C.; Wu, K. L.; Chi, Y.; Hu, W. P.; Yu, S. J.; Lee, G. H.; Lin, C. L.; Chou, P. T. *Angew. Chem., Int. Ed.* **2011**, *50*, 2054–2058.
- (39) Odobel, F.; Zabri, H. *Inorg. Chem.* **2005**, *44*, 5600–5611.
- (40) Mcdermott, G.; Prince, S. M.; Freer, A. A.; Hawthornthwaitelawless, A. M.; Papiz, M. Z.; Cogdell, R. J.; Isaacs, N. W. *Nature* **1995**, *374*, 517–521.
- (41) Pullerits, T.; Sundström, V. *Acc. Chem. Res.* **1996**, *29*, 381–389.
- (42) Sundström, V.; Pullerits, T.; van Grondelle, R. *J. Phys. Chem. B* **1999**, *103*, 2327–2346.
- (43) Amadelli, R.; Argazzi, R.; Bignozzi, C. A.; Scandola, F. *J. Am. Chem. Soc.* **1990**, *112*, 7099–7103.
- (44) Bignozzi, C. A.; Argazzi, R.; Indelli, M. T.; Scandola, F. *Sol. Energy Mater. Sol. Cells* **1994**, *32*, 229–244.
- (45) Nogueira, A. F.; Furtado, L. F. O.; Formiga, A. L. B.; Nakamura, M.; Araki, K.; Toma, H. E. *Inorg. Chem.* **2004**, *43*, 396–398.
- (46) Peter, K.; Wietasch, H.; Peng, B.; Thelakkat, M. *Appl. Phys. A: Mater. Sci. Process.* **2004**, *79*, 65–71.
- (47) Warman, J.; Buchet, F.; Pellegrin, Y.; Blart, E.; Odobel, F. *Org. Lett.* **2011**, *13*, 3944–3947.
- (48) Fox, M. A.; Whitesell, J. K.; Magde, D.; Zhu, L. Y. *Molecules* **2009**, *14*, 3851–3867.
- (49) Nogueira, A. F.; Formiga, A. L. B.; Winnischofer, H.; Nakamura, M.; Engelmann, F. M.; Araki, K.; Toma, H. E. *Photochem. Photobiol. Sci.* **2004**, *3*, 56–62.
- (50) Atzrodt, J.; Brandenburg, J.; Käßplinger, C.; Beckert, R.; Gunther, W.; Görls, H.; Fabian, J. *J. Prakt. Chem./Chem. Ztg.* **1997**, *339*, 729–734.
- (51) Blumhoff, J.; Beckert, R.; Rau, S.; Losse, S.; Matschke, M.; Gunther, W.; Görls, H. *Eur. J. Inorg. Chem.* **2009**, 2162–2169.
- (52) Kupfer, S.; Guthmüller, J.; Wächtler, M.; Losse, S.; Rau, S.; Dietzek, B.; Popp, J.; Gonzalez, L. *Phys. Chem. Chem. Phys.* **2011**, *13*, 15580–15588.
- (53) Wächtler, M.; Kupfer, S.; Guthmüller, J.; Popp, J.; Gonzalez, L.; Dietzek, B. *J. Phys. Chem. C* **2011**, *115*, 24004–24012.
- (54) Kupfer, S.; Wächtler, M.; Guthmüller, J.; Popp, J.; Dietzek, B.; Gonzalez, L. *J. Phys. Chem. C* **2012**, *116*, 19968–19977.
- (55) Wächtler, M.; Guthmüller, J.; Gonzalez, L.; Dietzek, B. *Coord. Chem. Rev.* **2012**, *256*, 1479–1508.
- (56) Damrauer, N. H.; Cerullo, G.; Yeh, A.; Boussie, T. R.; Shank, C. V.; McCusker, J. K. *Science* **1997**, *275*, 54–57.
- (57) Damrauer, N. H.; McCusker, J. K. *J. Phys. Chem. A* **1999**, *103*, 8440–8446.
- (58) Bhasikuttan, A. C.; Suzuki, M.; Nakashima, S.; Okada, T. *J. Am. Chem. Soc.* **2002**, *124*, 8398–8405.
- (59) Browne, W. R.; Henry, W.; Coates, C. G.; Brady, C.; Ronayne, K. L.; Matousek, P.; Towrie, M.; Botchway, S. W.; Parker, A. W.; Vos, J. G.; et al. *J. Phys. Chem. A* **2008**, *112*, 4537–4544.
- (60) Dietzek, B.; Kiefer, W.; Blumhoff, J.; Böttcher, L.; Rau, S.; Walther, D.; Uhlemann, U.; Schmitt, M.; Popp, J. *Chem.-Eur. J.* **2006**, *12*, 5105–5115.

- (61) Juris, A.; Balzani, V.; Barigelletti, F.; Campagna, S.; Belser, P.; Vonzelewsky, A. *Coord. Chem. Rev.* **1988**, *84*, 85–277.
- (62) Gordon, K. C.; Horvath, R. *Inorg. Chim. Acta* **2011**, *374*, 10–18.
- (63) Loeb, B.; Lopez, R.; Leiva, A. M.; Zuloaga, F.; Norambuena, E.; Omberg, K. M.; Schoonover, J. R.; Striplin, D.; Devenney, M.; Meyer, T. J. *Inorg. Chem.* **1999**, *38*, 2924–2930.
- (64) McKinley, A. W.; Lincoln, P.; Tuite, E. M. *Coord. Chem. Rev.* **2011**, *255*, 2676–2692.
- (65) Wang, X. Y.; Del Guerso, A.; Schmehl, R. H. *J. Photochem. Photobiol., C* **2004**, *5*, 55–77.
- (66) Damrauer, N. H.; Bousie, T. R.; Devenney, M.; McCusker, J. K. *J. Am. Chem. Soc.* **1997**, *119*, 8253–8268.
- (67) Vlcek, A.; Busby, M. *Coord. Chem. Rev.* **2006**, *250*, 1755–1762.
- (68) Laine, P. P.; Campagna, S.; Loiseau, F. *Coord. Chem. Rev.* **2008**, *252*, 2552–2571.
- (69) Kuhnt, C.; Karnahl, M.; Tschierlei, S.; Griebenow, K.; Schmitt, M.; Schäfer, B.; Kriech, S.; Gols, H.; Rau, S.; Dietzek, B.; et al. *Phys. Chem. Chem. Phys.* **2010**, *12*, 1357–1368.
- (70) Ji, S. M.; Wu, W. H.; Wu, W. T.; Song, P.; Han, K. L.; Wang, Z. G.; Liu, S. S.; Guo, H. M.; Zhao, J. Z. *J. Mater. Chem.* **2010**, *20*, 1953–1963.
- (71) Waterland, M. R.; Gordon, K. C.; McGarvey, J. J.; Jayaweera, P. M. *J. Chem. Soc., Dalton Trans.* **1998**, 609–616.
- (72) Schoonover, J. R.; Bates, W. D.; Meyer, T. J. *Inorg. Chem.* **1995**, *34*, 6421–6422.
- (73) Walsh, P. J.; Gordon, K. C.; Lundin, N. J.; Blackman, A. G. *J. Phys. Chem. A* **2005**, *109*, 5933–5942.
- (74) Medlycott, E. A.; Hanan, G. S.; Loiseau, F.; Campagna, S. *Chem.-Eur. J.* **2007**, *13*, 2837–2846.
- (75) Brütigam, M.; Wächtler, M.; Rau, S.; Popp, J.; Dietzek, B. *J. Phys. Chem. C* **2012**, *116*, 1274–1281.
- (76) McGarvey, J. J.; Browne, W. R.; Henry, W.; Passaniti, P.; Gandolfi, M. T.; Ballardini, R.; O'Connor, C. M.; Brady, C.; Coates, C. G.; Vos, J. G. *Photochem. Photobiol. Sci.* **2007**, *6*, 386–396.
- (77) McGarvey, J. J.; Coates, C. G.; Keyes, T. E.; Hughes, H. P.; Jayaweera, P. M.; Vos, J. G. *J. Phys. Chem. A* **1998**, *102*, 5013–5018.
- (78) Rau, S.; Schwalbe, M.; Karnahl, M.; Tschierlei, S.; Uhlemann, U.; Schmitt, M.; Dietzek, B.; Popp, J.; Groake, R.; Vos, J. G. *J. Chem. Soc., Dalton Trans.* **2010**, *39*, 2768–2771.
- (79) Izutsu, K. *Acid-Base Dissoziation Constants in Dipolar Aprotic Solvents*; Blackwell: Oxford, 1990.
- (80) Kovalenko, S. A.; Dobryakov, A. L.; Ruthmann, J.; Ernsting, N. P. *Phys. Rev. A: At., Mol., Opt. Phys.* **1999**, *59*, 2369–2384.
- (81) Dietzek, B.; Tschierlei, S.; Hermann, G.; Yartsev, A.; Pascher, T.; Sundström, V.; Schmitt, M.; Popp, J. *ChemPhysChem* **2009**, *10*, 144–150.
- (82) Dietzek, B.; Pascher, T.; Sundström, V.; Yartsev, A. *Laser Phys. Lett.* **2007**, *4*, 38–43.
- (83) Frisch, M. J.; Trucks, G. W.; Schlegel, H. B.; Scuseria, G. E.; Robb, M. A.; Cheeseman, J. R.; Scalmani, G.; Barone, V.; Mennucci, B.; Petersson, G. A.; Nakatsuji, H.; et al. *Gaussian 09*, revision A.02; Gaussian, Inc.: Pittsburgh, PA, 2009.
- (84) Becke, A. D. *J. Chem. Phys.* **1993**, *98*, 5648–5652.
- (85) Lee, C. T.; Yang, W. T.; Parr, R. G. *Phys. Rev. B: Condens. Matter Mater. Phys.* **1988**, *37*, 785–789.
- (86) Andrae, D.; Hausermann, U.; Dolg, M.; Stoll, H.; Preuss, H. *Theor. Chim. Acta* **1990**, *77*, 123–141.
- (87) Harihara, P.; Pople, J. A. *Theor. Chim. Acta* **1973**, *28*, 213–222.
- (88) Tomasi, J.; Mennucci, B.; Cammi, R. *Chem. Rev.* **2005**, *105*, 2999–3093.
- (89) Zalis, S.; Consani, C.; El Nahhas, A.; Cannizzo, A.; Chergui, M.; Hartl, F.; Vlcek, A. *Inorg. Chim. Acta* **2011**, *374*, 578–585.
- (90) El Nahhas, A.; Cannizzo, A.; van Mourik, F.; Blanco-Rodriguez, A. M.; Zalis, S.; Vlcek, A.; Chergui, M. *J. Phys. Chem. A* **2010**, *114*, 6361–6369.
- (91) El Nahhas, A.; Consani, C.; Blanco-Rodriguez, A. M.; Lancaster, K. M.; Braem, O.; Cannizzo, A.; Towrie, M.; Clark, I. P.; Zalis, S.; Chergui, M.; et al. *Inorg. Chem.* **2011**, *50*, 2932–2943.
- (92) Charlot, M. F.; Pellegrin, Y.; Quaranta, A.; Leibl, W.; Aukauloo, A. *Chem.-Eur. J.* **2006**, *12*, 796–812.
- (93) Meylemans, H. A.; Lei, C. F.; Damrauer, N. H. *Inorg. Chem.* **2008**, *47*, 4060–4076.
- (94) Gebauer, T. *Neuartige zweistufige Redoxsysteme basierend auf 4H-Imidazolen*; Friedrich-Schiller University Jena, 2005.
- (95) Yeh, A. T.; Shank, C. V.; McCusker, J. K. *Science* **2000**, *289*, 935–938.
- (96) Bagchi, B. *Int. Rev. Phys. Chem.* **1987**, *6*, 1–33.
- (97) Siebert, R.; Winter, A.; Schubert, U. S.; Dietzek, B.; Popp, J. *J. Phys. Chem. C* **2010**, *114*, 6841–6848.
- (98) Liu, K. L.; Lee, S. J.; Chen, I. C.; Hsu, C. P.; Yeh, M. Y.; Luh, T. Y. *J. Phys. Chem. A* **2009**, *113*, 1218–1224.
- (99) Nagasawa, Y.; Ando, Y.; Okada, T. *Chem. Phys. Lett.* **1999**, *312*, 161–168.
- (100) Singh, C.; Modak, B.; Mondal, J. A.; Palit, D. K. *J. Phys. Chem. A* **2011**, *115*, 8183–8196.
- (101) Gonzalez, L.; Escudero, D.; Serrano-Andres, L. *ChemPhysChem* **2012**, *13*, 28–51.
- (102) Parac, M.; Grimme, S. *J. Phys. Chem. A* **2002**, *106*, 6844–6850.
- (103) Caspar, J. V.; Meyer, T. J. *J. Phys. Chem.* **1983**, *87*, 952–957.
- (104) Caspar, J. V.; Kober, E. M.; Sullivan, B. P.; Meyer, T. J. *J. Am. Chem. Soc.* **1982**, *104*, 630–632.
- (105) Barqawi, K. R.; Murtaza, Z.; Meyer, T. J. *J. Phys. Chem.* **1991**, *95*, 47–50.
- (106) Schulze, B.; Escudero, D.; Friebe, C.; Siebert, R.; Gols, H.; Sinn, S.; Thomas, M.; Mai, S.; Popp, J.; Dietzek, B.; et al. *Chem.-Eur. J.* **2012**, *18*, 4010–4025.
- (107) Sauvage, J. P.; Collin, J. P.; Chambron, J. C.; Guillerez, S.; Coudret, C.; Balzani, V.; Barigelletti, F.; Decola, L.; Flamigni, L. *Chem. Rev.* **1994**, *94*, 993–1019.
- (108) Medlycott, E. A.; Hanan, G. S. *Coord. Chem. Rev.* **2006**, *250*, 1763–1782.
- (109) Medlycott, E. A.; Hanan, G. S. *Chem. Soc. Rev.* **2005**, *34*, 133–142.

Supporting Information

Structural control of photoinduced dynamics in 4*H*-imidazole-Ruthenium dyes

Maria Wächtler^{†,‡,#}, Stephan Kupfer^{†,#}, Julien Guthmüller[§], Sven Rau[§], Leticia González^{§,**,††}, Benjamin Dietzek^{†,‡,††,*}

[†] *Institute of Physical Chemistry and Abbe Center of Photonics, Friedrich-Schiller University Jena, Helmholtzweg 4, 07743, Jena, Germany*

[‡] *Institute of Photonic Technology Jena (IPHT) e.V., Albert-Einstein-Str. 9, 07745, Jena, Germany*

[§] *Faculty of Applied Physics and Mathematics, Gdansk University of Technology, Narutowicza 11/12, 80233, Gdansk, Poland*

[§] *Institute of Inorganic Chemistry I, University of Ulm, Albert-Einstein-Allee 11, 89081, Ulm, Germany*

& Institute of Theoretical Chemistry, University of Vienna, Währinger Str. 17, 1090 Vienna, Austria

^{††} *Jena Center for Soft Matter (JCSM), Humboldtstr. 10, 07743, Jena, Germany*

Corresponding author:

*with respect to the experimental part:

Benjamin.dietzek@ipht-jena.de

Telefon +49 (0)3641 206-332

Telefax +49 (0)3641 206-399

**with respect to the computational part:

leticia.gonzalez@univie.ac.at

Author Contributions:

These authors contributed equally: experiments (M.W.) and calculations (S.K.).

Computational details:

In order to allow for a reduction of the computational cost of the simulations without affecting the spectroscopic properties of the complexes, the three *tert*-butyl groups were approximated in the calculations by methyl groups. The structural and electronic data were obtained from quantum chemistry calculations performed with the GAUSSIAN 09 program¹. The geometry, vibrational frequencies, and normal coordinates of the ground state were calculated by means of density functional theory (DFT) with the exchange-correlation (XC) functional B3LYP^{2,3}. The 28-electron relativistic effective core potential MWB⁴ was used with its basis set for the ruthenium atom, that is, 4s, 4p, 4d and 5s electrons are treated explicitly, whereas the three first inner shells are described by the core pseudopotential. The 6-31G(d) double- ζ basis set⁵ was employed for the ligands. To correct for the lack of anharmonicity and the approximate treatment of electron correlation, the harmonic frequencies were scaled by the factor 0.97.⁶ The vertical excitation energies, oscillator strengths and analytical Cartesian energy derivatives of the excited states were obtained from time dependant DFT (TDDFT) calculations within the adiabatic approximation with the same XC functional, pseudopotential and basis set. The absorption spectra were simulated by determining the excitation energies and oscillator strengths of the 80 lowest singlet excited states. The effects of the interaction with a solvent (acetonitrile, $\epsilon=35.688$, $n=1.344$) on the geometry, frequencies, excitation energies and excited state gradients were taken into account by the integral equation formalism of the polarizable continuum model⁷. The nonequilibrium procedure of solvation was used for the calculation of the excitation energies and of the excited state gradients, which is well adapted for processes where only the fast reorganization of the electronic distribution of the solvent is important.

The relative RR intensities of **RuCOOEt** and **RuCOOEtH** were obtained within the short-time approximation⁸ (STA). In the STA, the RR intensity for a fundamental transition $0 \rightarrow 1$, is calculated from

the partial derivative of the excited state electronic energy (E^e) along the l th normal coordinate (Q_l) evaluated at the ground state equilibrium geometry,

$$I_{0 \rightarrow l} \propto \frac{1}{\omega_l} \left(\frac{\partial E^e}{\partial Q_l} \right)_0^2 \quad (1)$$

where ω_l is the frequency of the l th normal mode. These gradients were obtained from the analytical derivatives of the excited state electronic energy (E^e) along the non-mass-weighted Cartesian coordinates according to the relation

$$\left(\frac{\partial E^e}{\partial Q} \right)_0 = L^T M^{-\frac{1}{2}} \left(\frac{\partial E^e}{\partial x} \right)_0 \quad (2)$$

where M is the matrix containing the atomic masses, L is the orthogonal matrix obtained from the solution of the ground state normal mode eigenvalue problem, and $(\partial E^e / \partial Q)_0$ and $(\partial E^e / \partial x)_0$ are column vectors containing the derivatives along the normal coordinates and Cartesian coordinates, respectively.

The use of the STA is appropriate for the complexes investigated here. Indeed, the RR measurements are performed for excitation wavelengths in resonance with absorption bands displaying a large broadening and no resolved vibronic structure, each of them being associated with a single electronic excited state. These facts indicate that no significant interference effects should occur between different excited states and that the relative RR intensities should show a weak dependence with respect to the excitation wavelength.

Furthermore, the deactivation pathway after photoexcitation was investigated for **RuMe** and **RuMeH**. Starting from the Franck-Condon (FC) region geometry optimizations at the TDDFT level of theory have

been carried out for the low-lying excited singlet state (**RuMe** S_6 and **RuMeH** S_4) and planarized triplet state (T_{plan}). In addition the triplet ground state in FC structure has been optimized at the DFT level of theory leading to the geometry ${}^3\text{MLCT}$. In each of the four equilibrium structures (FC, ${}^1\text{MLCT}$, ${}^3\text{MLCT}$ and ${}^3\text{MLCTplan}$) TDDFT calculations including 40 singlet and 40 triplet excited states were performed to map the energies of the four electronic states of interest namely the singlet ground state (S_0), the low-lying excited singlet state (S_6 / S_4), the triplet ground state in the FC structure (T_{twist}) and the planarized triplet state (T_{plan}). All calculations have been performed at the same level of theory as stated above. The resulting energy values of the excited states should not be treated as real values because of the inherent error of the method, which was estimated to be 0.4-0.5.^{9,10} These calculations have only exploratory character.

Literatur

- (1) Frisch, M. J. T., G. W.; Schlegel, H. B.; Scuseria, G. E.; Robb, M. A.; Cheeseman, J. R.; Scalmani, G.; Barone, V.; Mennucci, B.; Petersson, G. A.; Nakatsuji, H.; Caricato, M.; Li, X.; Hratchian, H. P.; Izmaylov, A. F.; Bloino, J.; Zheng, G.; Sonnenberg, J. L.; Hada, M.; Ehara, M.; Toyota, K.; Fukuda, R.; Hasegawa, J.; Ishida, M.; Nakajima, T.; Honda, Y.; Kitao, O.; Nakai, H.; Vreven, T.; Montgomery, Jr., J. A.; Peralta, J. E.; Ogliaro, F.; Bearpark, M.; Heyd, J. J.; Brothers, E.; Kudin, K. N.; Staroverov, V. N.; Kobayashi, R.; Normand, J.; Raghavachari, K.; Rendell, A.; Burant, J. C.; Iyengar, S. S.; Tomasi, J.; Cossi, M.; Rega, N.; Millam, J. M.; Klene, M.; Knox, J. E.; Cross, J. B.; Bakken, V.; Adamo, C.; Jaramillo, J.; Gomperts, R.; Stratmann, R. E.; Yazyev, O.; Austin, A. J.; Cammi, R.; Pomelli, C.; Ochterski, J. W.; Martin, R. L.; Morokuma, K.; Zakrzewski, V. G.; Voth, G. A.; Salvador, P.; Dannenberg, J. J.; Dapprich, S.; Daniels, A. D.; Farkas, Ö.; Foresman, J. B.; Ortiz, J. V.; Cioslowski, J.; Fox, D. J. *Gaussian 09, Revision A.02*; Gaussian Inc.: Wallingford, CT, 2009.
- (2) Becke, A. D. *Journal of Chemical Physics* **1993**, *98*, 5648.
- (3) Lee, C. T.; Yang, W. T.; Parr, R. G. *Physical Review B* **1988**, *37*, 785.
- (4) Andrae, D.; Haussermann, U.; Dolg, M.; Stoll, H.; Preuss, H. *Theoretica Chimica Acta* **1990**, *77*, 123.
- (5) Harihara, P.; Pople, J. A. *Theoretica Chimica Acta* **1973**, *28*, 213.
- (6) Merrick, J. P.; Moran, D.; Radom, L. *Journal of Physical Chemistry A* **2007**, *111*, 11683.
- (7) Tomasi, J.; Mennucci, B.; Cammi, R. *Chemical Reviews* **2005**, *105*, 2999.
- (8) Heller, E. J.; Sundberg, R. L.; Tannor, D. *Journal of Physical Chemistry* **1982**, *86*, 1822.
- (9) Gonzalez, L.; Escudero, D.; Serrano-Andres, L. *ChemPhysChem* **2012**, *13*, 28.
- (10) Parac, M.; Grimme, S. *Journal of Physical Chemistry A* **2002**, *106*, 6844.

Computational results – absorption spectra:

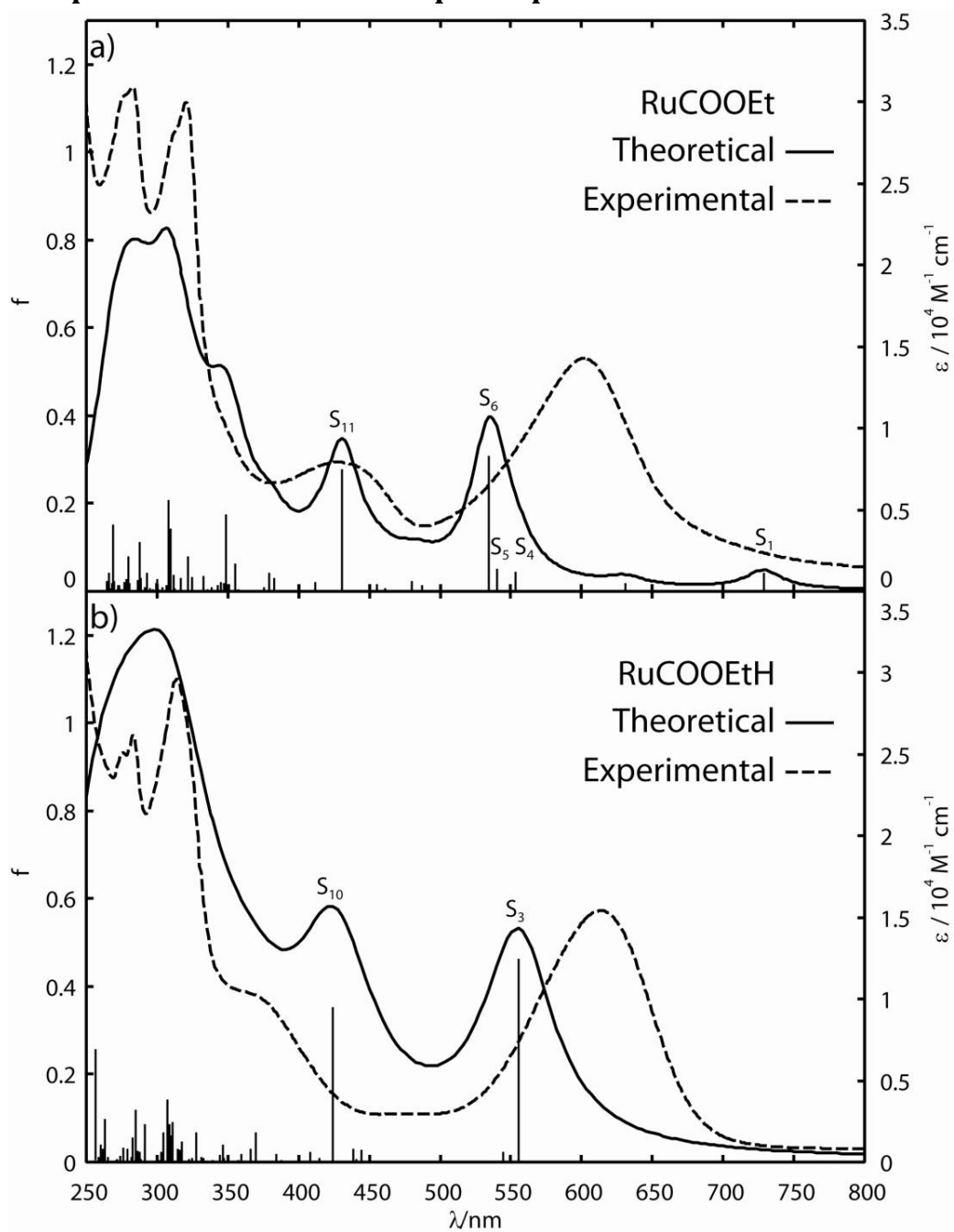


Figure S1: Calculated and experimental absorption spectra of **RuCOOEt** (top) and **RuCOOEtH** (bottom). The calculated oscillator strengths are represented by black sticks. A Lorentzian Function with a fwhm 20 nm is employed to broaden the calculated intensities. The experimental spectra were measured in ACN. The protonated form was prepared by adding trifluoroacetic acid to the solution of the dye in ACN.

Table S1: Calculated vertical excitation energies (E), oscillator strengths (f) and single-excited configurations of the main excited states and experimental absorption maxima in the visible range.

	State	Transition	Weight (%)	E/eV	λ /nm	F	λ_{exp} /nm
RuCOOEt	1	$dxz(212) \rightarrow \pi^*im(213)$	96	1.70	729	0.0413	
	4	$dxz(212) \rightarrow \pi^*terpy(215)$	82	2.24	553	0.0440	
	5	$dxy(210) \rightarrow \pi^*terpy(214)$	14	2.30	540	0.0525	
		$dyz(211) \rightarrow \pi^*terpy(214)$	96				
	6	$dxy(210) \rightarrow \pi^*im(213)$	15	2.32	534	0.3096	600
		$dxy(210) \rightarrow \pi^*terpy(214)$	31				
		$dyz(211) \rightarrow \pi^*im(213)$	48				
	11	$\pi im(209) \rightarrow \pi^*im(213)$	94	2.88	431	0.2784	429
RuCOOEtH	1	$dxy(210) \rightarrow \pi^*im(213)$	17	1.40	885	0.0099	
		$dxz(212) \rightarrow \pi^*im(213)$	96				
	3	$dxy(210) \rightarrow \pi^*im(213)$	84	2.23	556	0.4623	615
	10	$\pi im(209) \rightarrow \pi^*im(213)$	94	2.92	424	0.3530	370

Table S2: Molecular orbitals involved in the main configurations of the states responsible for the absorption and RR properties of RuCOOEt and RuCOOEtH

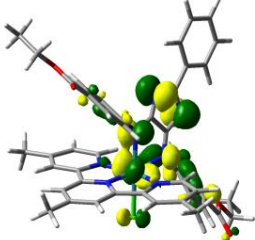
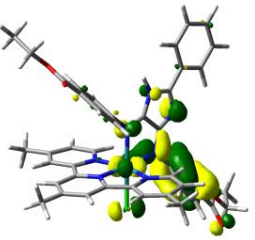
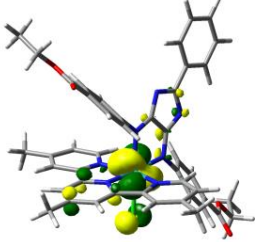
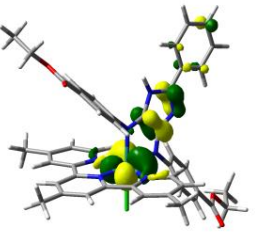
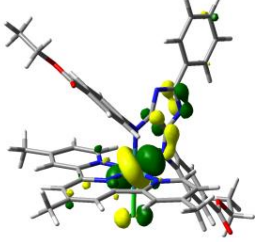
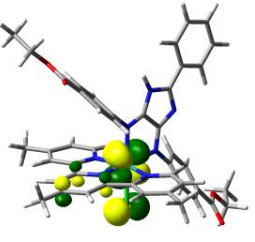
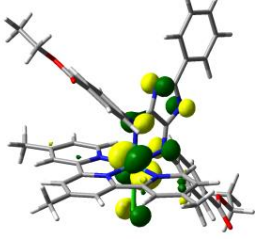
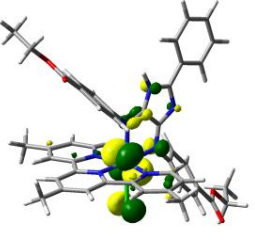
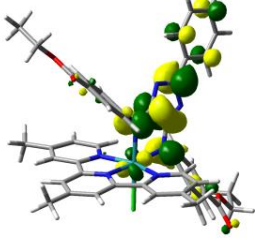
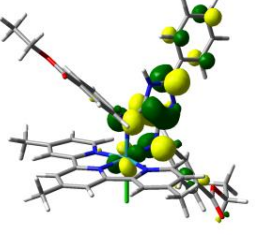
RuCOOEt	RuCOOEtH
 <p>209</p>	 <p>209</p>
 <p>210</p>	 <p>210</p>
 <p>211</p>	 <p>211</p>
 <p>212</p>	 <p>212</p>
 <p>213</p>	 <p>213</p>



Table S3: calculated dihedral angles for the investigated complexes in their unprotonated and protonated forms in the ground state geometry

	δ_1	δ_2
RuMe	66°	48°
RuMeH	61°	46°
RuNMe₂	54°	42°
RuNMe₂H	52°	37°
RuNMe₂H₃	69°	48°
RuCOOEt	61°	46°
RuCOOEtH	65°	46°

Computational results - resonance Raman spectra:

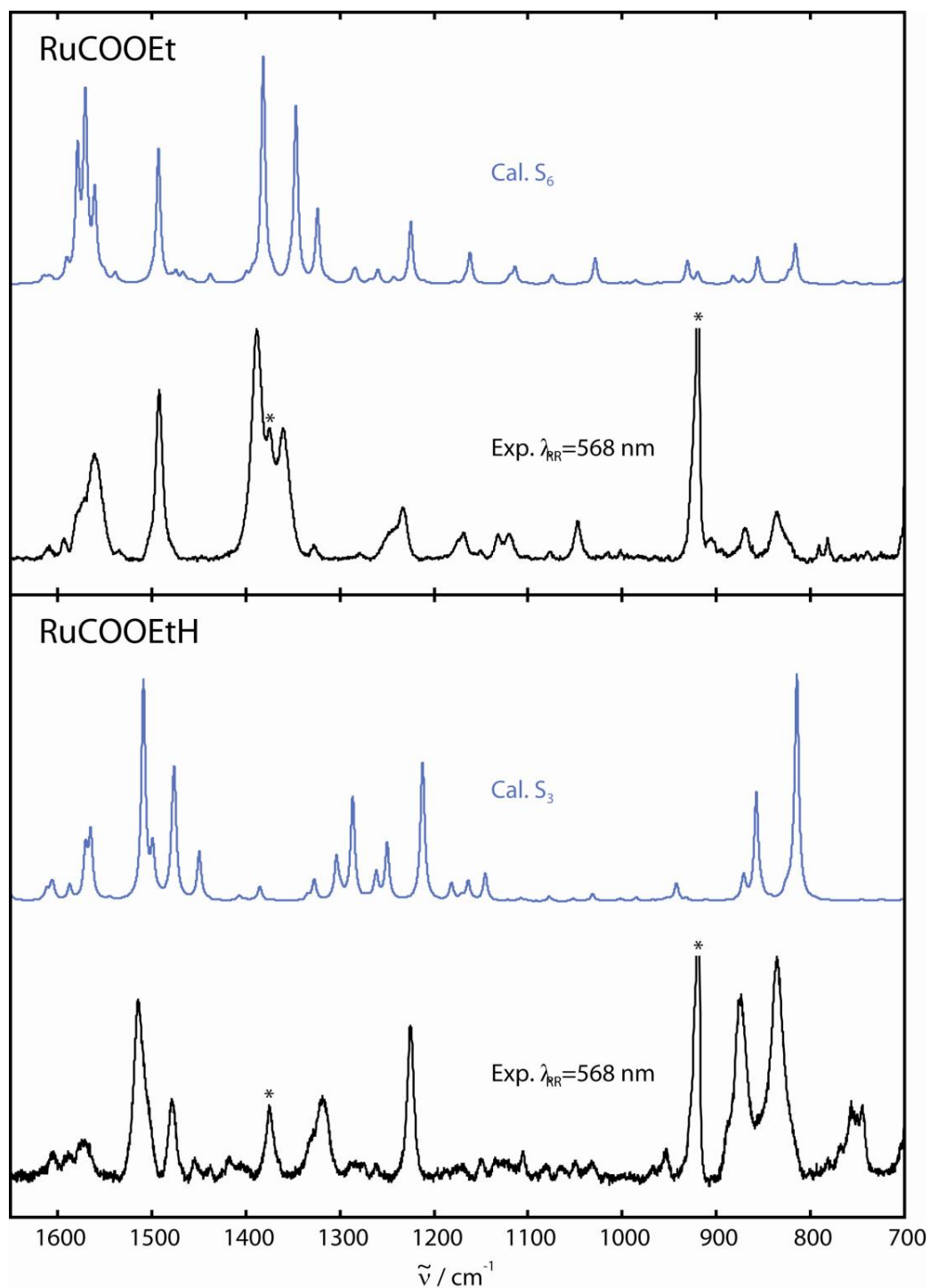


Figure S2: Experimental and calculated resonance Raman spectra of **RuCOOEt** (STA, state S_6) and **RuCOOEtH** (STA, state S_3) in ACN with excitation in the MLCT transition. Solvent bands are marked with an asterisk.

Table S4: Assignment of the vibrational frequencies and relative RR intensities (I_{calc}) in the STA for the MLCT excited state S_6 of RuCOOEt. The theoretical frequencies were scaled by a factor of 0.97

Mode type	Freq. (Calc) / cm^{-1}	I_{calc}	Freq. (Exp.) / cm^{-1}
Im	752.2	0.01	
Tpy	765.7	0.02	
Im	815.9	0.17	835
Im	856.1	0.12	869
Im	872.2	0.01	
im, tpy	882.2	0.04	
Im	919.8	0.05	LM
Tpy	930.7	0.1	
Im	985.9	0.02	
im, tpy	1028.7	0.12	1047
Tpy	1074.6	0.04	1077
Im	1113.8	0.07	1119
Im	1119.3	0.03	1131
Im	1161.6	0.13	1150
Tpy	1178.1	0.01	1168
Im	1224.6	0.28	1232
Im	1242.7	0.03	1232
Im	1259.1	0.03	1248
Im	1259.9	0.03	1248
Tpy	1283.1	0.05	1279
Tpy	1323.7	0.32	1327
Im	1346.7	0.78	1359
im, tpy	1381.5	1.00	1387
Tpy	1437.7	0.04	

Tpy	1466.8	0.04	
Tpy	1474.2	0.05	
Im	1492.9	0.39	1491
Tpy	1538.6	0.04	1531
Im	1560.4	0.37	1559
Im	1570.5	0.79	1572
Im	1578.7	0.56	1578
Im	1590.3	0.08	1592
Tpy	1609.4	0.02	1611
im, tpy	1614.2	0.02	1611

Table S5: Assignment of the vibrational frequencies and relative RR intensities (I_{calc}) in the STA for the MLCT excited state S_3 of RuCOOEtH. The theoretical frequencies were scaled by a factor of 0.97

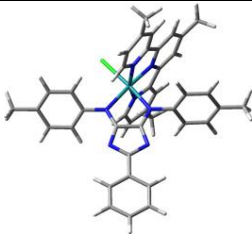
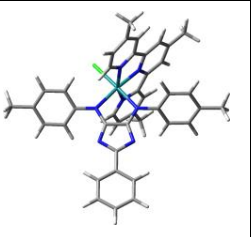
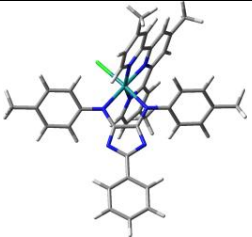
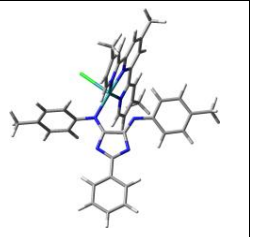
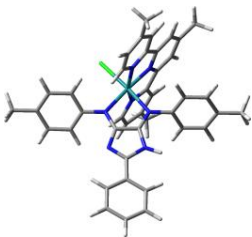
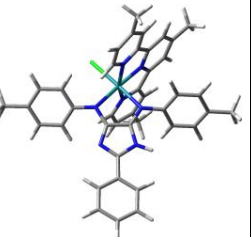
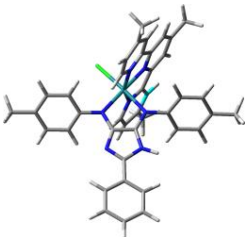
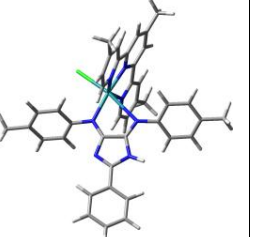
Mode type	Freq. (Calc) / cm^{-1}	I_{calc}	Freq. (Exp.) / cm^{-1}
Tpy	724.2	0.01	
im, tpy	745.5	0.01	
Im	814.4	1.00	834
Im	857.7	0.48	874
Im	871.1	0.11	890
Im	910.9	0.01	
Tpy	931.81	0.01	
Im	942.3	0.08	954
Im	985.2	0.02	967
Im	1002.6	0.01	
Tpy	1031.4	0.03	1029
Im	1052.9	0.01	1050/1068

Тpy	1077.3	0.02	1079
Im	1107.6	0.01	1106
im, tpy	1145.4	0.10	1148
Im	1165.1	0.09	1170
Im	1169.6	0.02	1170
Im	1212.5	0.29	1225
im, tpy	1213.0	0.34	1225
Im	1250.2	0.26	1261
Im	1261.0	0.10	1275
Im	1262.9	0.03	
Im	1287.0	0.39	1317
Тpy	1287.4	0.09	1317
Im	1303.9	0.18	1317
Тpy	1327.3	0.1	1317
Im	1334.1	0.02	1329
Im	1372.9	0.01	LM
Im	1386.1	0.07	LM
Im	1407.4	0.03	
Im	1449.6	0.22	1452
Im	1475.6	0.47	1477
im, tpy	1477.5	0.19	1477
Im	1498.5	0.19	1501
Im	1508.9	0.98	1512
Тpy	1544.3	0.01	
Im	1564.6	0.29	1572

Im	1569.9	0.20	1572
Im	1587.0	0.07	1586
Im	1604.6	0.04	1605
Im	1606.1	0.06	1605
Tpy	1611.6	0.04	1605
Im	1655.7	0.23	1639

Computational results – excited state optimizations:

Table S6: Optimized geometries FC, ¹MLCT, ³MLCT and ³MLCT_{plan} of RuMe and RuMeH

	FC	¹ MLCT (S ₆ / S ₄)	³ MLCT	³ MLCT _{plan}
RuMe	 $\delta_1=66.10^\circ$ $\delta_2=48.17^\circ$ $d_{\text{Ru-N anti}}=2.11\text{\AA}$	 $\delta_1=50.20^\circ$ $\delta_2=38.71^\circ$ $d_{\text{Ru-N anti}}=2.14\text{\AA}$	 $\delta_1=44.50^\circ$ $\delta_2=40.37^\circ$ $d_{\text{Ru-N anti}}=2.07\text{\AA}$	 $\delta_1=16.34^\circ$ $\delta_2=69.52^\circ$ $d_{\text{Ru-N anti}}=2.74\text{\AA}$
RuMeH	 $\delta_1=60.73^\circ$ $\delta_2=46.09^\circ$ $d_{\text{Ru-N anti}}=2.11\text{\AA}$	 $\delta_1=49.46^\circ$ $\delta_2=30.20^\circ$ $d_{\text{Ru-N anti}}=2.18\text{\AA}$	 $\delta_1=49.94^\circ$ $\delta_2=44.83^\circ$ $d_{\text{Ru-N anti}}=2.10\text{\AA}$	 $\delta_1=38.91^\circ$ $\delta_2=59.28^\circ$ $d_{\text{Ru-N anti}}=2.82\text{\AA}$

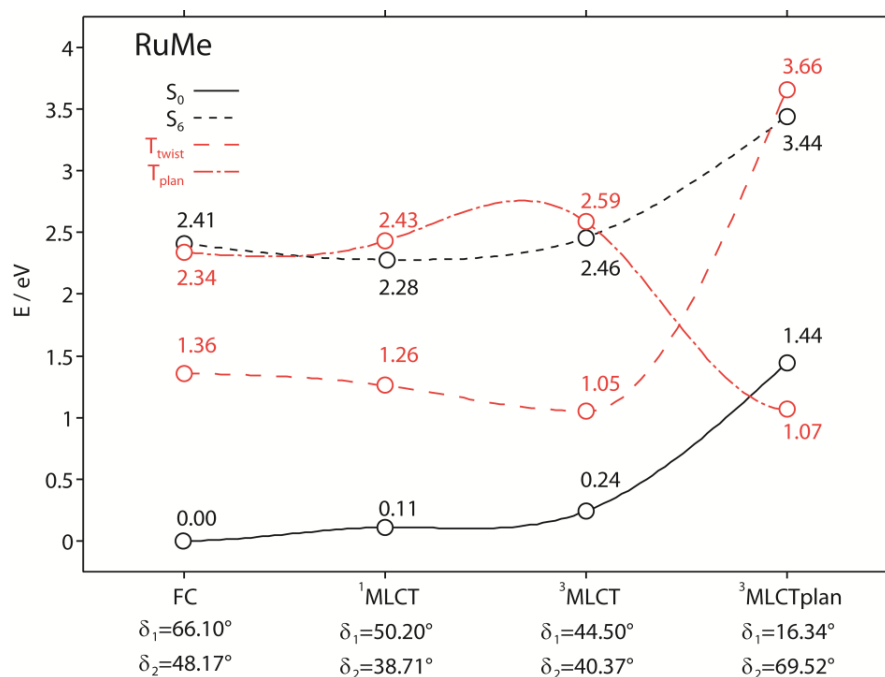


Figure S3. Schematic representation of relative energies of the singlet states S_0 and S_6 and the triplet states T_{twist} and T_{plan} for the equilibrium geometries of each of the four electronic states investigated for **RuMe**.

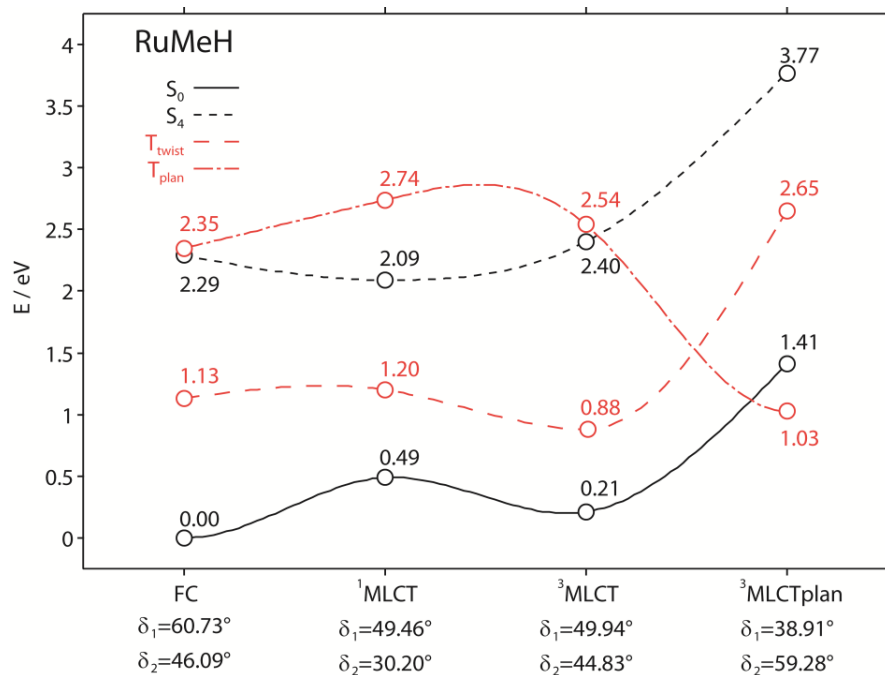


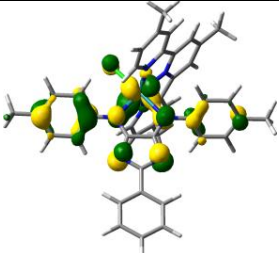
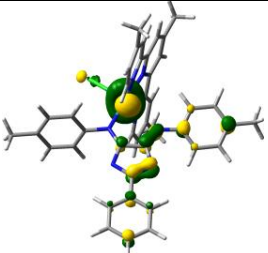
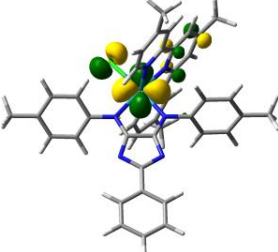
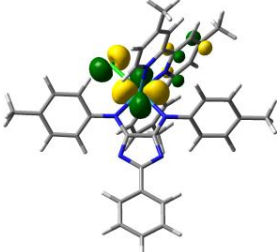
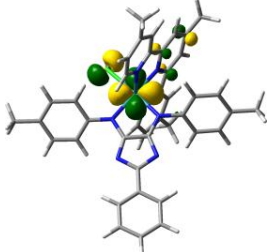
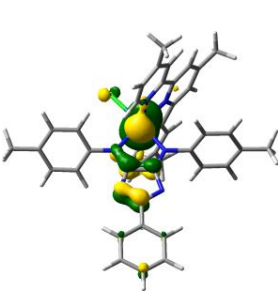
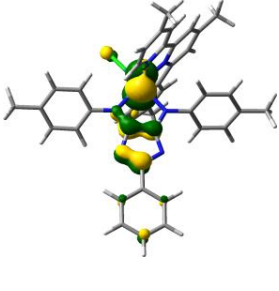
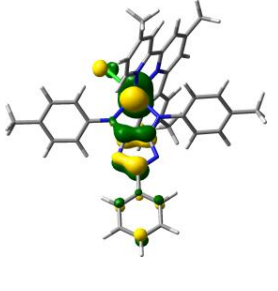
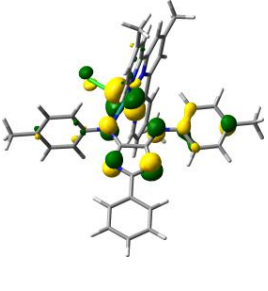
Figure S4. Schematic representation of relative energies of the singlet states S_0 and S_4 and the triplet states T_{twist} and T_{plan} for the equilibrium geometries of each of the four electronic states investigated for **RuMeH**.

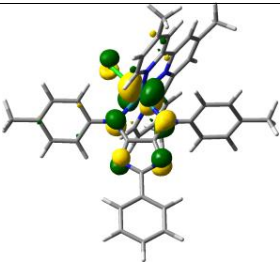
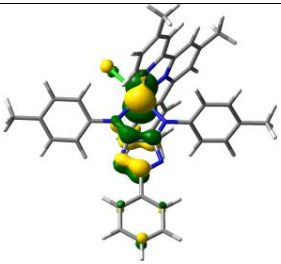
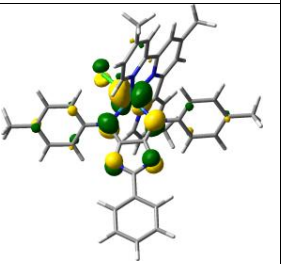
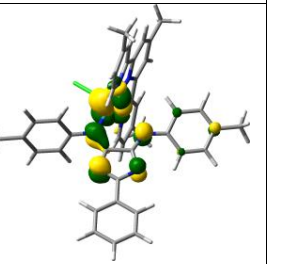
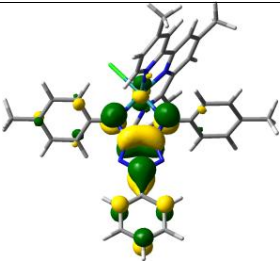
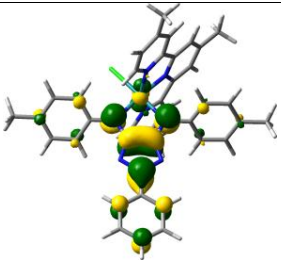
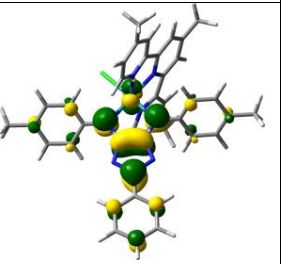
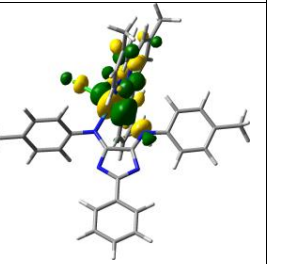
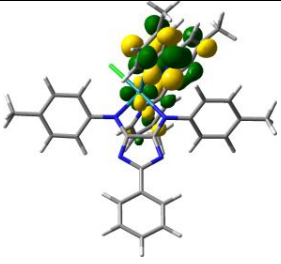
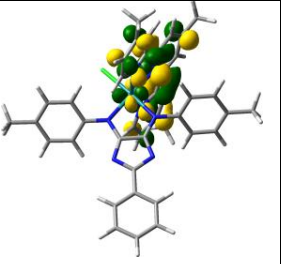
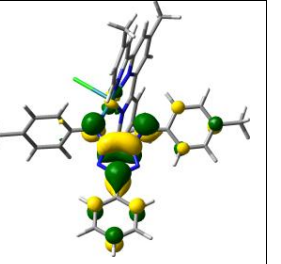
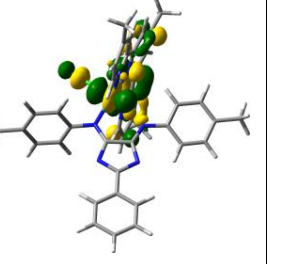
Table S7: Calculated vertical excitation energies (E), oscillator strengths (f) and singly-excited configurations of the main excited states in each of the appropriate minimum structures (FC, ¹MLCT, ³MLCT and ³MLCTplan) contributing to the relaxation pathway in RuMe

State	Transition	Weight (%)	E/eV	F
FC				
S ₆	d _{xy} (181)→π* _{im} (183)	54	2.41	0.4011
	d _{yz} (180)→π* _{terpy} (184)	32		
T _{twist}	d _{xz} (182)→π* _{im} (183)	90	1.36	0.0000
T _{plan}	d _{xz} (182)→σ* _{RuIm} +π* _{im} (188)	55	2.34	0.0000
	d _{xz} (182)→σ* _{RuIm} -π* _{im} (196)	13		
¹MLCT				
S ₆	d _{xy} (181)→π* _{im} (183)	83	2.17	0.3617
	d _{yz} (180)→π* _{terpy} (184)	13		
T _{twist}	d _{xz} (182)→π* _{im} (183)	90	1.15	0.0000
T _{plan}	d _{xz} (182)→σ* _{RuIm} -π* _{im} (189)	30	2.32	0.0000
	d _{xz} (182)→σ* _{RuIm} +π* _{im} (188)	18		
	π _{im} (179)→π* _{im} (183)	14		
	d _{xz} (182)→d _{x²-y²} +π* _{im} (195)	9		
³MLCT				
S ₅	d _{xy} (181)→π* _{im} (183)	69	2.22	0.3792
	d _{yz} (180)→π* _{terpy} (184)	16		
	d _{yz} (180)→π* _{terpy} (184)	8		
T _{twist}	d _{xz} (182)→π* _{im} (183)	98	0.81	0.0000
T _{plan}	d _{xz} (182)→σ* _{RuIm} -π* _{im} (189)	38	2.35	0.0000
	d _{xz} (182)→d _{x²-y²} +π* _{im} (195)	12		
³MLCTplan				
S ₅	d _{xy} (182)→π* _{im} (184)	91	2.00	0.1058

T_{twist}	$d_{xz}(181) \rightarrow \pi^*_{im}(184)$	45	2.16	0.0000
	$d_{yz}(179) \rightarrow \pi^*_{im}(184)$	19		
T_{plan}	$d_{xz}(182) \rightarrow \sigma^*_{RuIm} + \pi^*_{terpy}(183)$	49	-0.37	0.0000
	$d_{xz}(182) \rightarrow \sigma^*_{RuIm} - \pi^*_{terpy}(185)$	21		
	$d_{xz}(181) \rightarrow \sigma^*_{RuIm} + \pi^*_{terpy}(183)$	19		
	$d_{xz}(181) \rightarrow \sigma^*_{RuIm} - \pi^*_{terpy}(185)$	9		

Table S8: Molecular orbitals of RuMe involved in the configurations of the main excited states in each of the appropriate minimum structures (FC, $^1\text{MLCT}$, $^3\text{MLCT}$ and $^3\text{MLCTplan}$).

FC	$^1\text{MLCT}$	$^3\text{MLCT}$	$^3\text{MLCTplan}$
	 179		 179
 180	 180	 180	
 181	 181	 181	 181

181			
			
182	182	182	182
			
183	183	183	183
			
	184	184	184
			
			185

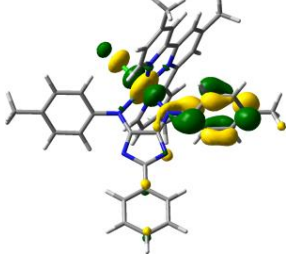
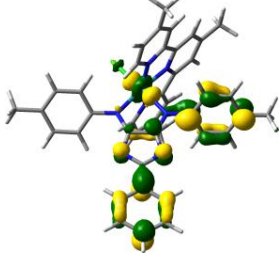
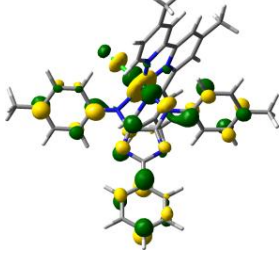
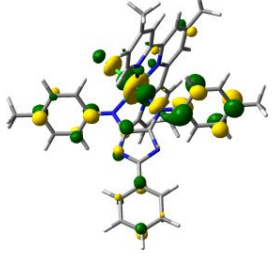
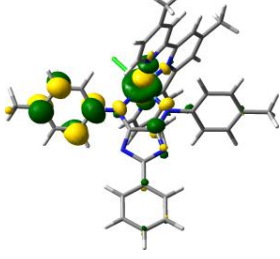
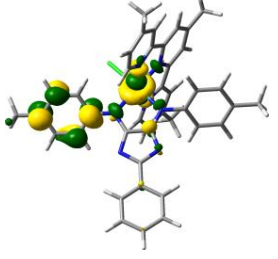
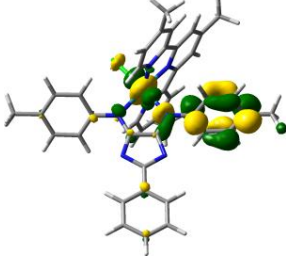
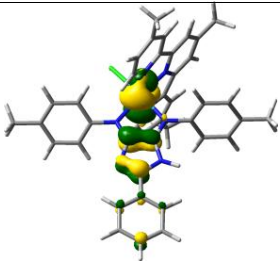
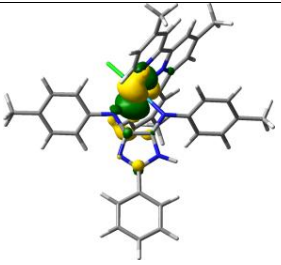
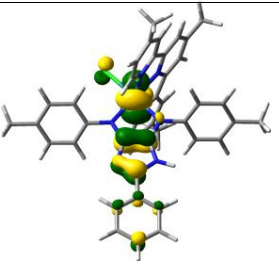
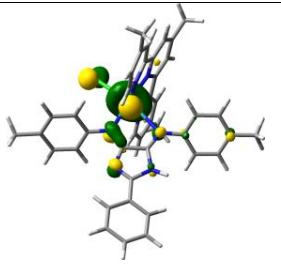
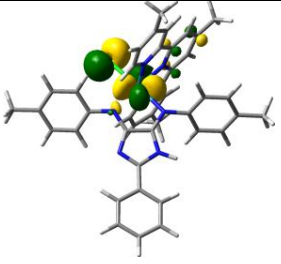
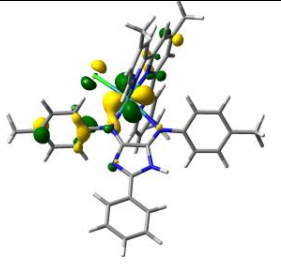
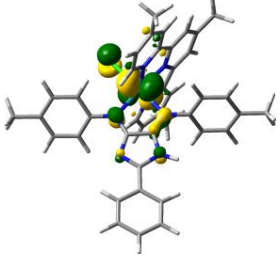
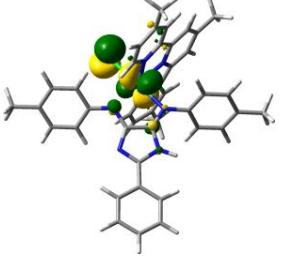
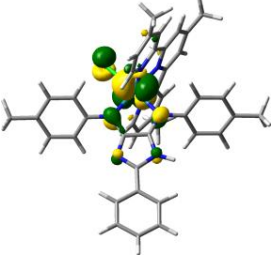
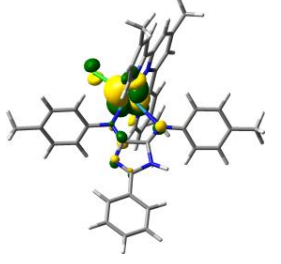
 <p>188</p>	 <p>188</p>		
	 <p>189</p>	 <p>189</p>	
	 <p>195</p>	 <p>195</p>	
 <p>196</p>			

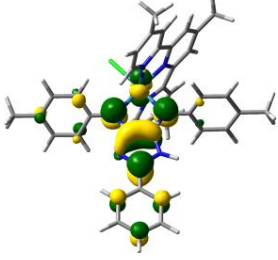
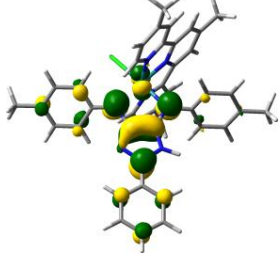
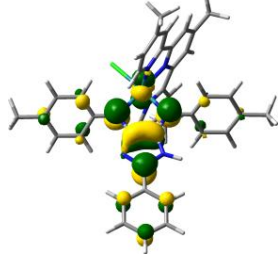
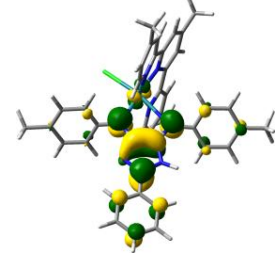
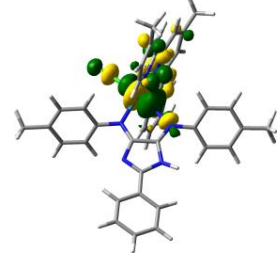
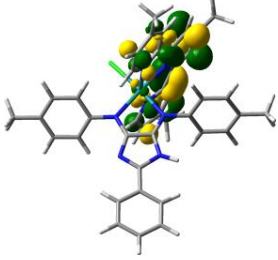
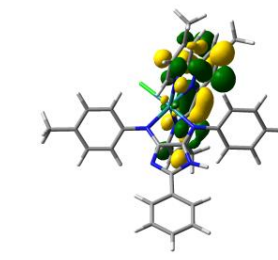
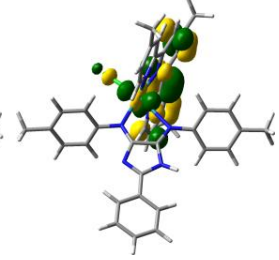
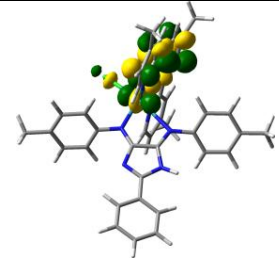
Table S9: Calculated vertical excitation energies (E), oscillator strengths (f) and singly-excited configurations of the main excited states in each of the appropriate minimum structures (FC, ¹MLCT, ³MLCT and ³MLCTplan) contributing to the relaxation pathway in RuMeH

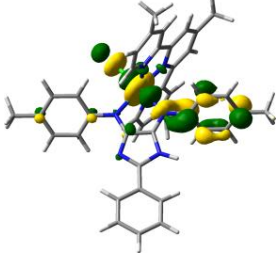
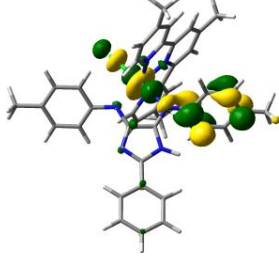
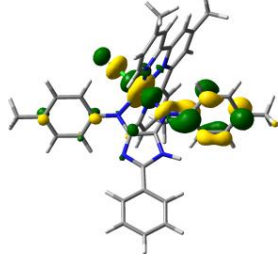
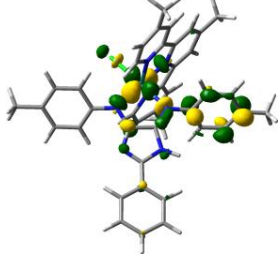
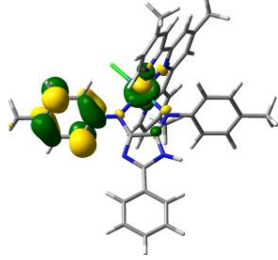
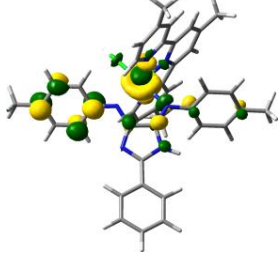
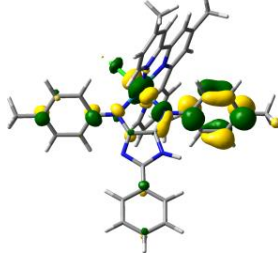
State	Transition	Weight (%)	E/eV	F
FC				
S ₄	d _{xy} (180)→π* _{im} (183)	82	2.29	0.4674
T _{twist}	d _{xz} (182)→π* _{im} (183)	94	1.13	0.0000
T _{plan}	d _{xz} (182)→σ* _{RuIm} +π* _{terpy} (189)	44	2.35	0.0000
	d _{xz} (182)→π* _{terpy} (185)	32		
¹MLCT				
S ₃	d _{xy} (180)→π* _{im} (183)	72	1.60	0.1408
	d _{xz} (182)→π* _{im} (183)	13		
	d _{yz} (181)→π* _{im} (183)	9		
T _{twist}	d _{xz} (182)→π* _{im} (183)	90	0.71	0.0000
T _{plan}	d _{xz} (182)→σ* _{RuIm} +π* _{terpy} (189)	54	2.25	0.0000
	d _{xz} (182)→d _{x²-y²} +π* _{im} (194)	14		
	d _{xz} (182)→d _{x²-y²} +π* _{im} (195)	11		
³MLCT				
S ₄	d _{xy} (180)→π* _{im} (183)	80	2.19	0.4504
	d _{xz} (182)→π* _{terpy} (185)	8		
T _{twist}	d _{xz} (182)→π* _{im} (183)	96	0.68	0.0000
T _{plan}	d _{xz} (182)→σ* _{RuIm} +π* _{terpy} (189)	54	2.33	0.0000
	d _{xz} (182)→σ* _{RuIm} -π* _{terpy} (196)	13		
	d _{xz} (182)→d _{x²-y²} +π* _{im} (194)	10		
³MLCTplan				
S ₅	d _{xy} (180)→π* _{im} (183)	68	2.36	0.2083
	d _{yz} (181)→π* _{im} (183)	11		

T_{twist}	$d_{xz}(182) \rightarrow \pi_{\text{im}}^*(183)$	88	1.24	0.0000
T_{plan}	$d_{xz}(182) \rightarrow \sigma_{\text{RuIm}}^* + \pi_{\text{terpy}}^*(184)$	71	-0.37	0.0000
	$d_{xz}(182) \rightarrow \pi_{\text{terpy}}^*(186)$	11		
	$d_{xz}(182) \rightarrow \pi_{\text{terpy}}^*(185)$	9		

Table S10: Molecular orbitals of RuMeH involved in the configurations of the main excited states in each of the appropriate minimum structures (FC, $^1\text{MLCT}$, $^3\text{MLCT}$ and $^3\text{MLCTplan}$)

FC	$^1\text{MLCT}$	$^3\text{MLCT}$	$^3\text{MLCTplan}$
 180	 180	 180	 180
	 181		 181
 182	 182	 182	 182

 <p>183</p>	 <p>183</p>	 <p>183</p>	 <p>183</p>
			 <p>184</p>
 <p>185</p>		 <p>185</p>	 <p>185</p>
			 <p>186</p>

 <p>189</p>	 <p>189</p>	 <p>189</p>	
	 <p>194</p>	 <p>194</p>	
	 <p>195</p>		
		 <p>196</p>	

The decay pathways after photoexcitation were investigated exemplarily for **RuMe** and its protonated form **RuMeH** using DFT and TDDFT methods. The figures S3 and S4 show the resulting energetic profiles of the four most important states involved in the relaxation mechanism.

In the unprotonated complex **RuMe** an excitation into S_6 (2.41 eV) occurs (Table S7). From this state ISC into the triplet manifold occurs and the system relaxes to the triplet (T_{twist}) equilibrium geometry ($^3\text{MLCT}$). This process is connected with a minor torsion of the tolyl groups as can be seen in the changes of 22 and 8° in the dihedral angles δ_1 and δ_2 . Furthermore, the Ru-4*H*-imidazole RuN bond lengths are slightly contracted from 2.11 Å in the FC region to 2.07 Å. The most important structural parameters of the optimized geometries are summarized in Table S6. The twisted triplet state is dominated by a partial occupation of the d_{xz} and an antibonding π^* -orbital distributed over the 4*H*-imidazole, further insight is provided in Table S7. The T_{twist} stabilizes by 0.31 eV compared to the FC region to 1.05 eV. The main transition in the T_{plan} is characterized by the partial occupation of the d_{xy} and one antibonding σ^* -orbital between the Ru and 4*H*-imidazole ligand. Hence, the respective bond is stretched to 2.74 Å (see Table S6) in the $^3\text{MLCT}_{\text{plan}}$ equilibrium geometry. This structural change is illustrated by Table S6 and accompanied by a pronounced torsion of the corresponding tolyl moiety (from 66.10° in the FC structure to 16.34° in $^3\text{MLCT}_{\text{plan}}$) leading to an almost planar conformation. Due to the localization of the σ^* -orbital on only one Ru-4*H*-imidazole bond the planarization takes place only in one tolyl moiety. In the $^3\text{MLCT}_{\text{plan}}$ structure the electronic ground state is of triplet multiplicity since T_{plan} is by 0.37 eV more stable than S_0 .

Detailed information concerning the relevant excited states of **RuMeH** is provided in Table S9, while the structural data is given in Table S6. In the case of **RuMeH** the excited singlet state (S_4) is lowered compared to **RuMe** by protonation of 4*H*-imidazole. However, T_{plan} is not affected. In the optimized geometry $^3\text{MLCT}_{\text{plan}}$ T_{plan} is stabilized by 1.32 eV to a relative energy of 1.03 eV. The main character of this triplet state is given by a partial occupation of the d_{xy} and σ^* -orbital joining the Ru and the 4*H*-imidazole ligand. The opening of the respective bond is with a bond length of 2.82 Å (2.11 Å in FC geometry) slightly enhanced compared to **RuMe**. Nevertheless, the torsion of the tolyl moieties is with 38.91° (δ_1) and 59.27° (δ_2) much less pronounced. On the other hand T_{twist} is of d_{xz} - π^* character and is clearly stabilized by protonation (1.05 eV **RuMe**, 0.88 eV **RuMeH** in the $^3\text{MLCT}$ geometry). This stabilization is accompanied by marginal torsion of the tolyl groups ($\delta_1=49.94$ and $\delta_2=44.83$), while the bond length of the Ru 4*H*-imidazole is with 2.10 Å very close to the value of 2.11 Å in the FC equilibrium structure. The comparison of the relative energetic positions of T_{twist} and T_{plan} in their respective equilibrium geometries allows a prediction of the decay pathways in dependence on the protonation state of the 4*H*-imidazole ligand. In the unprotonated form **RuMe** the planar (1.07 eV) and the twisted triplet state (1.05 eV) relaxes to approximately the same energy level and population of the planarized state during relaxation is possible, associated with considerable changes in the geometry. This leads to a strong coupling between the vibrational modes of T_{plan} and S_0 offering an effective radiationless decay path. Hence the population of the singlet ground state is high likely to evolve from T_{plan} . On the other hand for the protonated **RuMeH** system due to the stabilization of the T_{twist} by protonation compared to T_{plan} this state is by 0.15 eV lower than the planar triplet state, hence the repopulation of the singlet ground state is more likely to occur from the T_{twist} minimum.

pKa determination RuMe and RuCOOEt

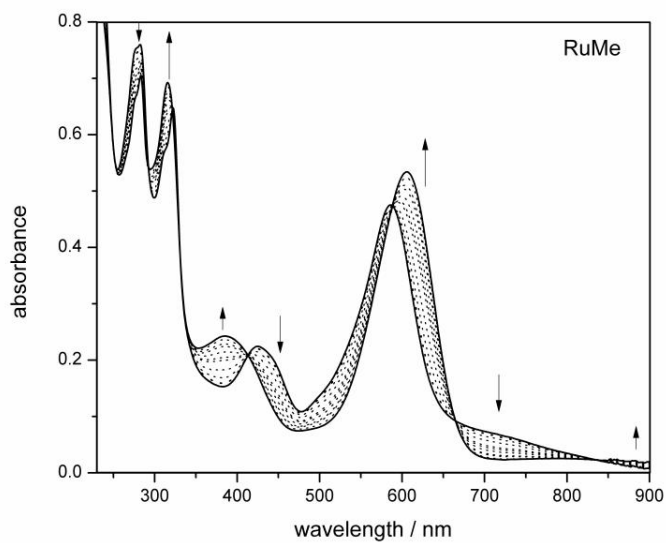


Figure S5: Absorption spectral changes observed for a $1.8 \cdot 10^{-4}$ M solution of **RuMe** in acetonitrile upon addition of aliquots of 0.01 M TFA/acetonitrile.

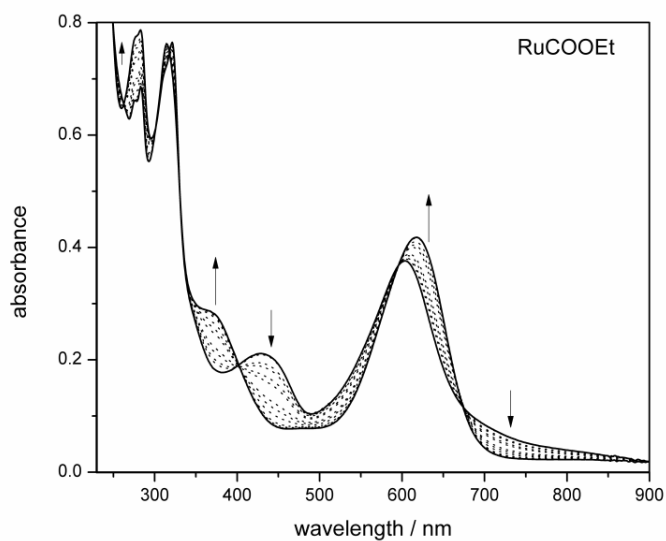


Figure S6: Absorption spectral changes observed for a $2.1 \cdot 10^{-4}$ M solution of **RuCOOEt** in acetonitrile upon addition of aliquots of 0.01 M TFA/acetonitrile.

Solvent viscosity dependent measurements

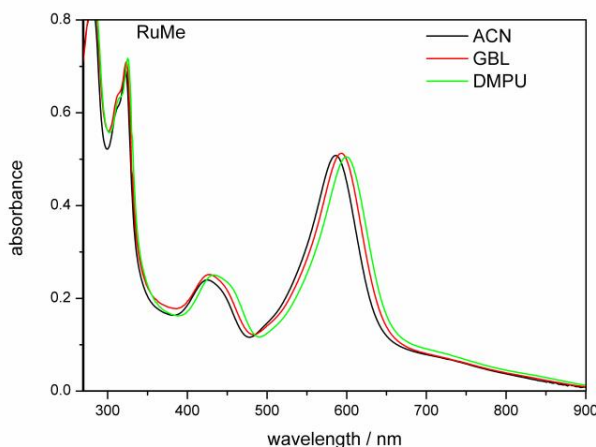


Figure S7: Absorption spectra of **RuMe** in solvents of differing viscosity.

In the applied series of solvents ACN/GBL/DMPU the MLCT band position in the absorption spectrum of **RuMe** is shifted bathochromically (585/594/600 nm). The dipole moment of **RuMe** was determined to increase upon excitation. Hence, in the presence of only dipolar interactions between solvent and solute a bathochromic shift of MLCT bands with increasing solvent polarity expressed in the value of the dielectric constant of the solvent, is expected.^{1,2} Unfortunately solvent polarity does not follow this row (37.5/39/36.1). Hence, in the absorption spectrum of **RuMe** the MLCT band position is not correlated only with solvent polarity. Another effect is reported to determine the solvatochromism of complexes with ligands containing lone pairs, e.g. Cl⁻, CN⁻, NCS⁻,³⁻⁵ which is the interaction of the externally directed lone pair with the (protic) solvent. The strength of this interaction can be correlated with the Gutmann Acceptor Number (AN) of the solvent. For such interaction it is reported to result in a blue shift of the MLCT band with increasing AN, because the π -Donor/Acceptor capability of the respective ligand is decreased/increased. Both effects result in an increase in the ligand field strength of the ligand, which lowers the relative energetic position of the d-Donor orbitals involved in the MLCT transition. In the used polar aprotic solvents AN is relatively small (ACN 19, GBL 17.3, DMPU 14). The observed blueshift with increasing AN is in agreement with a dominating impact of solute solvent interactions involving the lone pairs of the chloro ligand on the position of the absorption band.

1. M. D. Ward, *Coordination Chemistry Reviews*, 2006, 250, 3128-3141.
2. S. Fantacci, F. De Angelis and A. Selloni, *Journal of the American Chemical Society*, 2003, 125, 4381-4387.
3. N. R. M. Simpson, M. D. Ward, A. F. Morales and F. Barigelletti, *J Chem Soc Dalton*, 2002, 2449-2454.
4. C. J. Timpson, C. A. Bignozzi, B. P. Sullivan, E. M. Kober and T. J. Meyer, *Journal of Physical Chemistry*, 1996, 100, 2915-2925.
5. M. T. Indelli, C. A. Bignozzi, F. Scandola and J. P. Collin, *Inorganic Chemistry*, 1998, 37, 6084-6089.

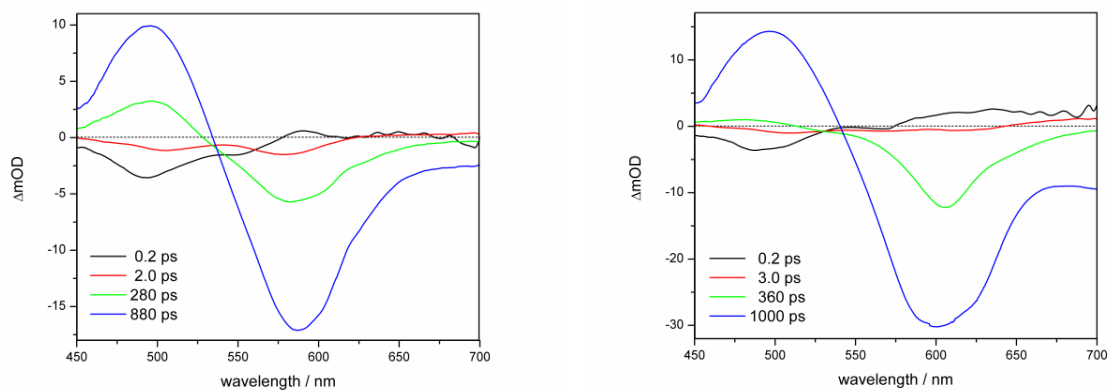


Figure S8: DAS spectra of RuMe in GBL (left) and DMPU (right) and time constants of the respective processes.

Dependence of electron and energy transfer processes on the driving force

The application of both a quantum mechanical approach (Fermi's Golden Law) to electron or energy transfer processes and radiationless decay and a classical description of electron transfer based on Marcus-Hush Theory indicates the presence of two kinetic regimes for electron transfer processes, which need to be distinguished: (1) The "normal" region: the reorganization energy is larger than the driving force. In this case an acceleration of the process with increasing driving force is observed. (2) The "inverted" region: the reorganization energy is smaller than the driving force. Here the known "energy gap law" behavior for radiationless decay is observed.

In the investigated systems we observe both regimes. For the conversion from ${}^3\text{MLCT}$ to ${}^3\text{MLCT}_{\text{plan}}$ the driving force is smaller than the reorganization energy and the normal region behavior is observed. As **RuNMe₂** has the smallest energy gap between these two states it shows the slowest population rate of ${}^3\text{MLCT}_{\text{plan}}$. The decay to the ground state is a process with high driving force, which is larger than the reorganization energy. Hence here a deceleration of the decay with increasing energy gap is observed.

1. Ceroni, P.; Balzani, V.; Photoinduced Energy and Electron Transfer Processes, The Exploration of Supramolecular Systems and Nanostructures by Photochemical Techniques; Springer Netherlands; Ceroni, P. (Ed.), (78) 2012, 21

Extraction of excited-state absorption contributions in the transient spectra

To determine the ESA contribution in the TA spectra a subtraction of the inverted absorption spectrum, reflecting the GSB contribution, from the TA spectra was performed. To determine the early time ESA corresponding to the non-planarized excited state, the TA spectrum recorded at 5 ps after excitation was selected. At this time, according to the kinetic model, most of the excited molecules are in the relaxed non-planarized state, and only a minor fraction of molecules populates the planarized state at this time. To obtain the ESA of the planarized state TA spectra at later times were chosen, where no population of the non-planarized state is left (**RuMe** and **RuNMe₂** at times later than 500 ps, **RuCOOEt** at 400 ps, and **RuCOOEtH** and **RuNMe₂H₃** at 200 ps). The scaling for the subtracted GSB feature at early times was chosen to give a reasonably shaped spectrum without negative values. It should be regarded that this approach may lead to a severe underestimation of the ESA. To get an appropriate scaled GSB at later times partial repopulation of the ground state was considered. By applying the kinetic model the fraction of photoexcited complexes left in the excited state was determined (at a respective time) and the ratio between early time excited-state species and later time excited-state species was used to scale the GSB contribution for subtraction.

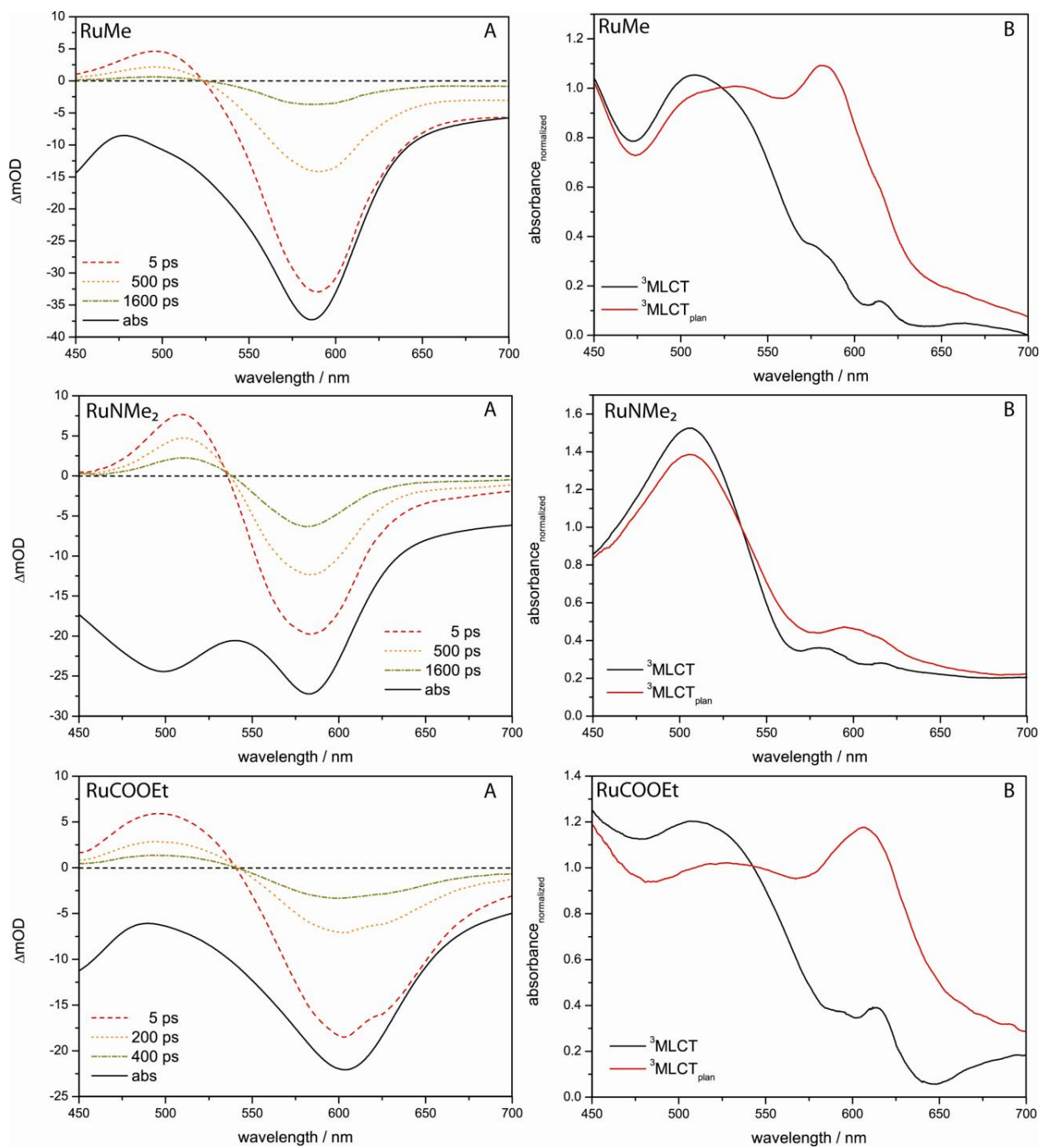


Figure S9: (A) Selected transient absorption spectra of **RuMe**, **RuNMe₂** and **RuCOOEt** and the inverted shape of the respective ground state absorption spectrum. (B) ESA spectra resulting from subtraction of the inverted absorption spectrum from the TA spectra at certain delay times, as described in the text above.

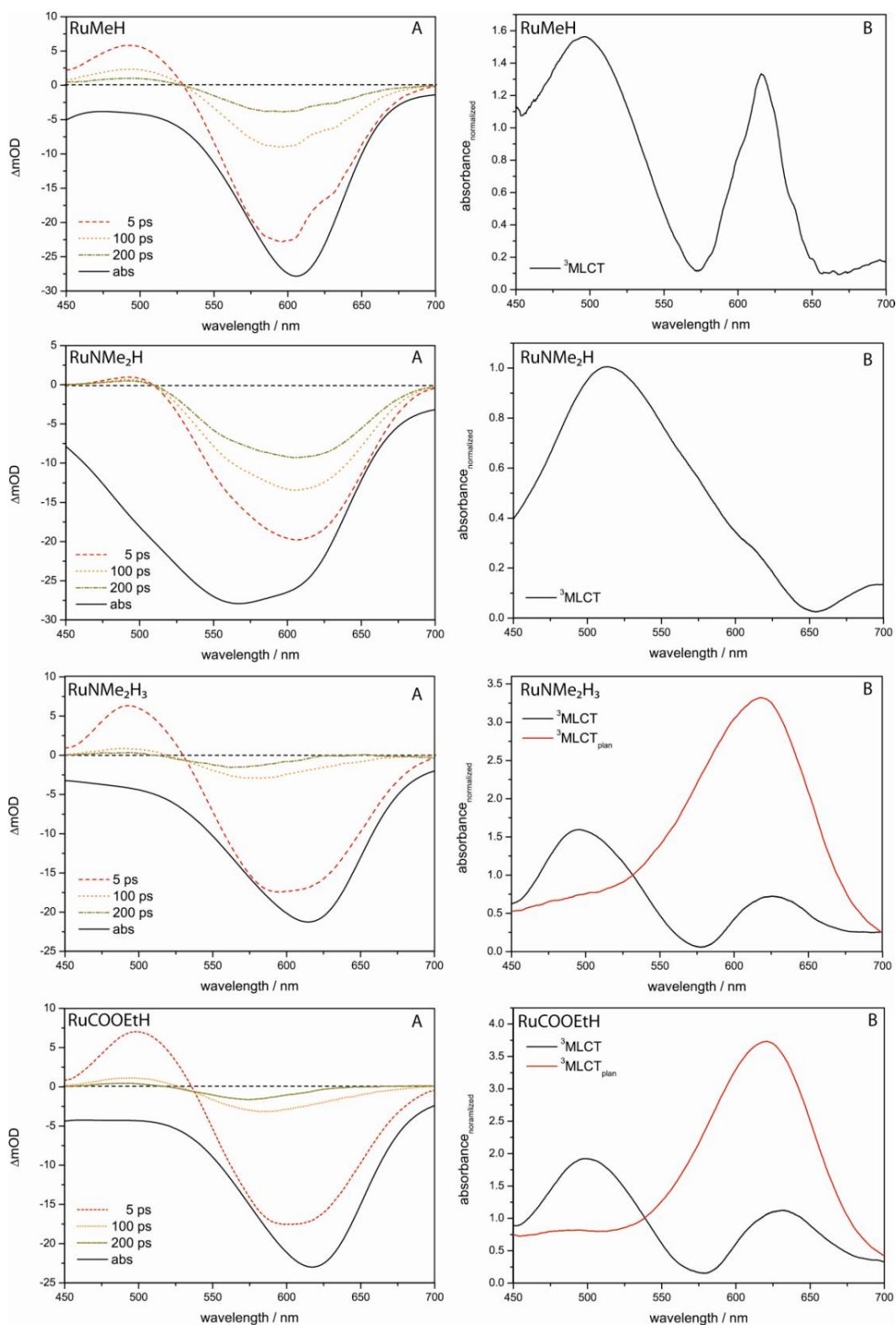


Figure S10: (A) Selected transient absorption spectra of **RuMeH**, **RuNMe₂H**, **RuCOOEtH** and **RuNMe₂H₃** and the inverted shape of the respective ground state absorption spectrum. (B) ESA spectra resulting from subtraction of the inverted absorption spectrum from the TA spectra at certain delay times, as described in the text above.

Chapter 5

Summary and Outlook

Sunlight is an attractive regenerative energy source. Therefore, the design of light-harvesting antennas, collecting large fractions of the solar radiation spectrum, and effective photosensitizers is crucial in the field of solar energy conversion, either via artificial photosynthesis or solar cells, or more precisely DSSCs. A manifold of requirements are put on such antennas and sensitizers: a strong stability on light, heat, and electricity, a pronounced overlap of its absorption bands with the solar radiation spectrum, and a directional and effective ET from the donor to the acceptor groups.

The goal of the present thesis is to characterize novel light-harvesting dyes with potential for DSSCs and artificial photosynthesis. A theoretical study, aiming at determining correlations between structure and photophysical properties with respect to protonation effects, substitution, and solvation, have been carried out. To obtain such information, electronic excited states have been investigated. In contrast to the ground state, these are difficult to calculate, especially if CT states are involved. Incidentally, CT states are essential to accomplish charge separation in any light-harvesting device.

In this thesis, we applied state-of-the-art multiconfigurational and TDDFT methods in order to calculate excited state properties. Multiconfigurational methods are capable to estimate excitation energies with good accuracy for excited states of different character (locally excited and CT states). However, methods like CASPT2/CASSCF are typically highly demanding from a computational point of view. In addition, a substantial knowledge coupled with chemical intuition of the molecular system is required. Therefore, these methods are restricted to small molecular systems. The RASPT2/RASSCF methodology lowers the computational cost by restricting the number of excited configurations. This high flexibility is at the same time the biggest drawback since there is no scheme to select key configurations on a systematic basis. Given the scarce experience in using these methods, in this thesis also special attention was put to find general strategies to calculate excited state energies and gradients using RASPT2/RASSCF. The alternative ansatz, TDDFT, requires a considerably lower computa-

tional effort compared to multiconfigurational methods. Problematic within TDDFT (or rather DFT) is the lack of a straight path to increase the accuracy of the simulation. A large variety of functionals is available that can provide excellent but also poor estimations of excited states depending on their character. These methods are applied here to give a comprehensive picture of the photophysical and photochemical properties of light-harvesting dyes based on organic dyes as well as on transition metal complexes. Particularly, throughout this thesis the following molecular systems have been studied:

- i) organic donor- π -acceptor dyes with applications in DSSCs and as ligands for ruthenium(II) based black absorbers,
- ii) novel ruthenium(II) polypyridine light-harvesting dyes, attractive for DSSCs and as photosensitizer in artificial photosynthesis,
- iii) ET processes at a titanium dioxide-dye interface, such processes are the basis for charge separation in DSSCs.

In the following, a brief resume concerning these three topics is provided.

i) The application of pure organic dyes in DSSCs has the advantage over classical silicon based solar cells that expensive and toxic transition metals are avoided in their production. For this reason, a series of novel 4-methoxy-thiazole based donor- π -acceptor dyes have been investigated by TDDFT and RASPT2/RASSCF methods. The theoretical analysis allowed predictions of photophysical properties, e.g. the positions of absorption and emission bands as well as RR intensities, and gave insight into the underlying electronic states. Substantial knowledge could be obtained with respect to the influence of donor and linker groups on excitation states properties, e.g. excitation energies and CT character. The latter was also found to be in close relation to the measured electron injection efficiency of these dyes on a TiO_2 semiconductor.

Such donor- π -acceptor dyes are not limited to direct applications in DSSCs. They can be also used as ligands for transition metal complexes, in order to enhance their absorption towards the NIR. The photophysical properties and the relaxation pathways upon photoexcitation of two of these 4-methoxy-thiazole ligands have been studied dependent on the solvent polarity. Furthermore, a mechanistic investigation of the ICT state has been carried out.

The theoretical analysis of these donor- π -acceptor dyes gave a rationalization of changes in their optical properties upon functionalization. The gained knowledge is of vital importance for the design of new light-harvesting antennas in the field of DSSCs.

ii) A promising alternative for organic light-harvesting antennas in DSSCs are black absorbers based on transition metal complexes. Here, especially ruthenium(II) polypyridine complexes have been widely studied because their outstanding combination of broad absorption in the

UV/vis region, their redox and catalytic activities, and their remarkable stability on light, heat and electricity. Various modifications in the polypyridine ligand sphere have been made in order to tune their optical properties. Herein, a novel class of ruthenium(II) polypyridine complexes with 4*H*-imidazole ligands have been studied. The introduction of the 4*H*-imidazole into the coordination sphere enabled a substantial extension of the absorption towards the NIR. The applied TDDFT simulations unraveled the contribution of the polypyridine and 4*H*-imidazole ligands to the absorption spectrum, while detailed insight into the nature of the excited states in the FC region was provided by means of RR spectroscopy. The simulation of RR intensities was found to be very beneficial to study the effects of substitution (in the 4*H*-imidazole as well as in the polypyridine ligand sphere). Thus, through the RR analysis we could evaluate the impact of substitution effects on the excited state properties, identify unknown protonation states, and evaluate the directionality of CT. Hence, it was shown that not only modifications of the ligands but also pH-control can be utilized not only to tune excitation energies but also to directionalize the CT excitations on the (4*H*-imidazole) bridging-ligand. Both strategies are highly valuable for designing optimal sensitizers in the field of DSSCs and artificial photosynthesis. Furthermore, protonation is of significant importance for the deactivation pathways upon photoexcitation, leading to the population of different relaxation channels.

In general, the protonated forms feature an increased directional CT capability to the 4*H*-imidazole bridging-ligand combined with a substantially bathochromical shift in the excitation energies. Hence, these species are of potential interest as photosensitizers in artificial photosynthesis devices, as e.g. devised in the frame of the PhotoMic project, but also as dyes in DSSCs. The next step, with respect of applications in DSSCs, is to study these ruthenium(II) complexes on a titanium dioxide surface, in order to provide information concerning ET processes that may compete with unwanted internal deactivation pathways.

iii) Introducing a carboxylic acid group on these ruthenium(II) complexes bearing a 4*H*-imidazole ligand enables its anchoring to a TiO₂ surface and hence make them suitable for DSSCs. Unexpectedly, such anchoring groups were found to significantly influence the excited states properties. pH-dependent optical properties have been rationalized by simulating RR spectra. Only one protonated species showed an almost quantitative and directional CT to the 4*H*-imidazole bridging-ligand. This charge separation is necessary to allow a subsequent ET to the electron acceptor unit, for instance, a titanium dioxide semiconductor (as in DSSCs) or a catalytic center for hydrogen production (as in artificial photosynthesis, e.g. in the frame of PhotoMic). In this thesis, the focus was set to study ET between a photoexcited ruthenium(II) complex and a TiO₂ cluster (rutile), aiming at describing ET rates and, hence, electron injection efficiencies in DSSCs. ET rates are accessible combining QM/MM with MD based on semi-classical Marcus theory. Such simulations are computational very demanding and have,

up to our knowledge, never been attempted before in the field solar energy conversion. The time-evolution of the two reaction states, the charge separated state (located at the dye) and the acceptor state (located at the semiconductor), are here investigated by means of MD coupled with DFT simulations, while the solvent bath is described at the MM level of theory. Due to the high demand of the QM/MM simulations and the size of the considered molecular system, the MD did not yet deliver stable equilibria for these two states. Future research will focus on the construction of the Marcus parabola. This will be achieved using subsequent QM/MM coupled MD simulations in the two, once found, equilibria. The obtained reorganization energy and reaction free energy will be applied to estimate a rate for IET in the dye-rutile model system.

In summary, this thesis provided fundamental understanding into novel light-harvesting dyes by means of a theoretical analysis. The dependency of photophysical properties on pH, solvation, anchoring, and substitution has been successfully rationalized via, absorption, emission, as well as RR spectroscopy. Especially the simulation of RR intensities was found to be highly valuable; in this context, the state-of-the-art RASSCF method was applied for the first time to simulate such intensities. The obtained results and expertise on ET processes are expected to contribute to a deeper understanding of further families of donor- π -acceptor and ruthenium(II) based dyes with potential in the field of solar energy conversion.

Kapitel 6

Zusammenfassung

Um eine Weltbevölkerung von derzeit 7 Milliarden Menschen ökonomisch und ökologisch gerecht mit Energie zu versorgen, ist der Wandel weg von klassischen fossilen Energieträgern hin zu nachhaltigen erneuerbaren Energiequellen unabdingbar. Neben der Windenergie scheint hierfür vor allem die Nutzung des Sonnenlichtes ein vielversprechender Ansatz zu sein. Nach dem Vorbild der Erfolgsgeschichte „Photosynthese“, welche seit 3,5 Milliarden Jahren unseren Planeten mit Sauerstoff und energiereichen organischen Substanzen versorgt, wurden diverse Strategien entwickelt, um Solarenergie auch für den Menschen nutzbar zu machen. Bereits in der Antike nutzte man Spiegel und Linsen um Wasser mittels Sonnenenergie zu erwärmen; so wird z. B. das olympische Feuer seit jeher mit Hilfe von Hohlspiegeln (Skaphia) entzündet. Moderne Verfahren, um die Energie der Sonne zu nutzen, lassen sich in zwei Gruppen einteilen:

- i) Einerseits ist hier die Photovoltaik zu nennen, bei der Sonnenlicht in elektrische Energie umgewandelt wird. Hierfür werden heutzutage vor allem siliciumbasierte Solarzellen verwendet, die allerdings für ihre Herstellung hochreines und daher teures Silicium benötigen. Eine kostengünstige und umweltfreundliche Alternative zu solchen Solarzellen stellt die Grätzel-Zelle dar. Diese elektrochemische Solarzelle verwendet mit (organischen) Farbstoffmolekülen beschichtete Titandioxidhalbleiter an der (Photo-)Anode und meist eine Platinkathode.
- ii) Verfahren, die energiereiche Verbindungen, wie beispielsweise molekularen Wasserstoff, mit Hilfe von Licht erzeugen, werden andererseits unter dem Begriff künstliche Photosynthese zusammengefasst.

Unabhängig ob künstliche Photosynthese oder Solarzelle, der erste Schritt beider Ansätze – die Absorption von Sonnenlicht – ist von entscheidender Bedeutung für die Effektivität des gesamten Prozesses. Um die volle Bandbreite des Sonnenlichts (von UV bis NIR) nutzen zu können, müssen Farbstoffe mit intensiven Absorptionsbanden in diesem Spektralbereich benutzt

werden. Gleichzeitig werden aber auch hohe Anforderungen an die Photo-, Thermo- und Elektrostabilität dieser Farbstoffe gestellt. Diese Anforderungen werden z. B. von Ruthenium(II)-Polypyridin-Lichtsammelkomplexen erfüllt; diese weisen eine außergewöhnliche Kombination aus chemischer und physikalischer Stabilität, gekoppelt mit katalytischer Aktivität auf. Diesen Vorteilen steht jedoch ein Mangel an intensiven Absorptionsbanden im sichtbaren Spektralbereich gegenüber. Eine andere vielversprechende Klasse von schwarzen Strahlern, d. h. Substanzen, welche die einfallende Strahlung nahezu vollständig absorbieren, sind organische Farbstoffe aus der Gruppe der Donor- π -Akzeptor-Systeme. Die photophysikalischen Eigenschaften dieser Farbstoffe können bei der Synthese in der Regel leicht angepasst werden. Zudem besitzen sie stark absorbierende Banden im sichtbaren Wellenlängenbereich und bei ihrer Herstellung kann auf teure Übergangsmetallkomplexe weitgehend verzichtet werden. Allerdings weisen derartige Systeme zumeist eine geringere Photostabilität – verglichen mit übergangsmetallbasierten Lichtsammelkomplexen – auf.

Ziel dieser Arbeit ist die Charakterisierung neuer Lichtsammleinheiten für die künstliche Photosynthese bzw. Grätzel-Zellen. In diesem Zusammenhang wurden Einflüsse wie Funktionalisierung, Protonierung und Lösungsmittelleffekte auf die photophysikalischen Eigenschaften der Lichtsammleinheiten mittels quantenchemischer Rechnungen untersucht. Auf diese Weise können Korrelationen von Struktur und Eigenschaften aufgeklärt und systematisiert werden, was für die weitere Entwicklung von effektiven Lichtsammleinheiten von entscheidender Bedeutung ist. Um diese Korrelationen zu untersuchen, sind akkurate quantenchemische Methoden, die sowohl den elektronischen Grundzustand als auch die angeregten Zustände hinreichend genau zu beschreiben vermögen, unerlässlich. Letzteres ist auch heutzutage noch immer nicht trivial. Besonders schwierig ist es, angeregte Zustände unterschiedlichen Charakters, z. B. lokale oder Ladungstransferzustände, mit gleicher Genauigkeit zu untersuchen.

Für diese Beschreibung geeignete Methoden sind unter anderem Multikonfigurationsmethoden, wie beispielsweise CASPT2 (Störungstheorie zweiter Ordnung basierend auf einer *complete active space self-consistent-field* Wellenfunktion). Solche Methoden ermöglichen eine genaue Untersuchung verschiedener angeregter Zustände aufgrund der Vielzahl der elektronischen Konfigurationen, die sich aus dem *active space* ergeben. Ein Nachteil dieser Methoden ist, neben der Konstruktion eines geeigneten *active space*, vor allem, dass sie enorm große Computerressourcen benötigen, daher ist ihre Anwendung auf relativ kleine molekulare Systeme beschränkt. Um den Rechenaufwand zu reduzieren und so auch einen Einsatz für größere chemische Systeme zu ermöglichen, wurde die RASPT2 Methode (Störungstheorie zweiter Ordnung basierend auf einer *restricted active space self-consistent-field* Wellenfunktion) entwickelt. Hier wird die Anzahl der elektronischen Konfigurationen im *active space* über das Anregungsniveau gesteuert. Diese neu gewonnene Flexibilität ist allerdings gleichzeitig das

größte Manko dieser Methode, da es kein Muster zur Auswahl von wichtigen Konfigurationen gibt, also Erfahrung des Anwenders gekoppelt mit chemischer Intuition notwendig sind.

Eine kostengünstige Alternative zu aufwändigen Multikonfigurationsmethoden stellt die Dichtefunktionaltheorie (DFT), bzw. für angeregte Zustände ihre zeitabhängige Version (TDDFT), dar, welche gerade für mittlere und große molekulare Systeme von Interesse ist. Jedoch mangelt es der DFT an einem klaren Ansatz, die Genauigkeit dieser Methode zu steigern. So steht dem Anwender eine Vielzahl an Funktionalen zur Verfügung, wobei je nach Funktional sehr gute bis mangelhafte Ergebnisse (in Abhängigkeit vom elektronischen Charakter) erzielt werden können.

In dieser Arbeit wurden sowohl Multikonfigurationsmethoden, namentlich RASPT2, als auch DFT- und TDDFT-Methoden zur Aufklärung der photophysikalischen und photochemischen Eigenschaften von Lichtsammelkomplexen (Übergangsmetallkomplexe) und von organischen Farbstoffen, welche Bausteine von Lichtsammleinheiten sind, eingesetzt. Im Einzelnen wurden dabei drei Hauptgruppen von molekularen Systemen untersucht:

- i) organische Lichtsammleinheiten basierend auf Donor- π -Akzeptor-Systemen, im Hinblick auf Anwendungen als Farbstoffe für Grätzel-Zellen und als Liganden für ruthenium(II)-basierte schwarze Strahler,
- ii) neuartige Ruthenium(II)-Polypyridin-Lichtsammelkomplexe, die sowohl für Grätzel-Zellen als auch als Photosensibilisatoren für die künstliche Photosynthese von Interesse sind,
- iii) Elektronentransferprozesse an der Schnittstelle Farbstoff-Titandioxidhalbleiter: Solche Prozesse sind Grundlage der Ladungstrennung in Grätzel-Zellen.

Im Folgenden wird auf diese drei Aspekte näher eingegangen.

i) Grätzel-Zellen haben gegenüber klassischen siliciumbasierten Solarzellen den Vorteil, dass bei ihrer Produktion auf teure und toxische Schwermetalle, wie Cadmium, Arsen und Tellur, weitgehend verzichtet werden kann. In dieser Arbeit wurde eine Reihe von Donor- π -Akzeptor-Farbstoffen mit dem 4-Methoxy-1,3-Thiazol-Chromophor mittels TDDFT und RASPT2/RAS-SCF untersucht. Photophysikalische Eigenschaften, wie die Lage von Absorptions- und Emissionsbanden, aber auch von Resonanz-Raman (RR) Streuintensitäten, konnten aufgrund quantenchemischer Rechnungen ermittelt werden. Auf diese Weise konnten Erkenntnisse über die zugrundeliegenden elektronischen Zustände gewonnen und Einflüsse diverser Donor- und Linkergruppen auf die Anregungsenergie und den (Ladungstransfer-)Charakter der angeregten Zustände ermittelt werden. Die bestimmten Ladungstransfercharaktere der Farbstoffe stehen in engem Zusammenhang mit der Bildung ladungstrennter Zustände und folglich mit den gemessenen Injektionsraten des Farbstoffelektrons in das Leitungsband des TiO_2 -Halbleiters.

Ebenso konnten anhand eines Donor- π -Akzeptor-Farbstoffes wichtige Erkenntnisse über das

Leistungsvermögen der neuen RASPT2/RASSCF-Methodik gewonnen werden. Neben den Anregungsenergien wurde auch die Genauigkeit der RASSCF-Gradienten erstmals mittels berechneter RR-Intensitäten ermittelt. Dies ist insbesondere in solchen Situationen von Interesse, in denen TDDFT-Methoden keine zufriedenstellenden Ergebnisse liefern können.

Donor- π -Akzeptor-Systeme können auch als Liganden für Übergangsmetallkomplexe eingesetzt werden, um deren Absorption im sichtbaren Spektralbereich zu verstärken. Diese Komplexe können dann wiederum als Lichtsammleinheiten für Solarzellen verwendet werden. Für zwei dieser Liganden wurden die photophysikalischen Eigenschaften, z. B. Absorption und Emission, in Abhängigkeit von der Lösungsmittelpolarität untersucht. Des Weiteren wurde der intramolekulare Ladungstransferzustand genau analysiert. Dadurch gelangen Einblicke in die Relaxationspfade nach der Photoanregung. Dies ist besonders für die Beurteilung der Lebensdauer angeregter Zustände in Lichtsammleinheiten von Bedeutung.

Die theoretische Analyse der photophysikalischen Eigenschaften, insbesondere in Abhängigkeit von verschiedenen Donor- und Linkergruppen, ist ein wesentlicher Beitrag für die Entwicklung neuer Lichtsammelsysteme auf dem Gebiet der Grätzel-Zellen.

ii) Neben organischen Farbstoffen sind ebenso Übergangsmetallkomplexe, in erster Linie Ruthenium(II)-Polypyridin-Komplexe, von großem Interesse als Lichtsammleinheiten für Solarzellen. Um die Absorption dieser Komplexe im sichtbaren Spektralbereich, besonders in Richtung des NIRs, zu steigern, werden meist Chromophore in der Peripherie der Polypyridin-Ligandensphäre eingeführt. Allerdings ist in diesen Fällen nur eine schwache Kopplung der verschiedenen Fragmente untereinander vorhanden. Als Ausweg kann ein Teil der Polypyridin-sphäre durch Liganden ausgetauscht werden, die selbst eine starke Absorption im gewünschten Bereich zeigen. Ein Beispiel für derartige Systeme stellt die neue Klasse von Ruthenium(II)-Polypyridin-Komplexen mit 4-*H*-Imidazol-Liganden dar. Die in dieser Arbeit durchgeführten TDDFT-Rechnungen ermöglichten die Zuordnung der Beiträge der Polypyridin- und der 4-*H*-Imidazol-Liganden zum jeweiligen Absorptionsspektrum, sowie einen detaillierten Einblick in die Natur der angeregten Zustände mittels RR-Spektroskopie. Substitutionseffekte, bedingt durch verschiedene elektronenziehende und elektronenschiebende Gruppen am 4-*H*-Imidazol, als auch Variationen der Polypyridinliganden (Bipyridin und Terpyridin), konnten erfolgreich mit Hilfe der berechneten RR-Intensitäten untersucht und systematisiert werden. Auf Grundlage der RR-Spektroskopie konnten neben Substitutionseffekten auf angeregte Zustände, auch unbekannte Protonierungsstufen identifiziert und die Richtung von Ladungstransferzuständen bestimmt werden. Somit erwies sich die Berechnung von RR-Spektren als äußerst gewinnbringend für die Charakterisierung derartiger schwarzer Strahler. Es wurde ebenfalls gezeigt, dass die Absorptionseigenschaften der Komplexe nicht nur durch gezielte Funktionalisierung abgestimmt werden können, sondern dass diese auch vom pH-Wert abhängen. Durch Variation des

pH-Wertes kann neben den Anregungsenergien auch die Richtung der Ladungstransferzustände verändert werden. Neben der Photophysik ist auch die Photochemie dieser Rutheniumkomplexe stark von der Protonierungsstufe abhängig. TDDFT-Berechnungen legten unterschiedliche Relaxationswege nach der Photoanregung nahe. Beide Strategien, Funktionalisierung und pH-Kontrolle, sind von großem Interesse für die Entwicklung neuer, effektiver Lichtsammelkomplexe auf dem Gebiet der Solartechnik.

Unabhängig ob elektronenziehende oder elektronenschiebende Substituenten betrachtet werden, weist die protonierte Spezies eine bathochrome Verschiebung der Anregungsenergie und eine verstärkte Ausrichtung des Ladungstransferzustandes in Richtung des 4-*H*-Imidazol-Brückenliganden auf. Beides ist für Anwendungen im Hinblick auf künstliche Photosynthese, so z. B. im Rahmen des PhotoMic-Projektes, und Grätzel-Zellen erwünscht. Ein nächster Schritt im Hinblick auf eine Anwendung dieser schwarzen Strahler in Grätzel-Zellen könnte die Simulation von Elektronentransferprozessen an der Schnittstelle zwischen Farbstoff und Titandioxidoberfläche sein. Auf diese Weise können Informationen über Elektronentransferraten bzw. über unerwünschte interne Deaktivierungsmechanismen des Lichtsammelkomplexes ermittelt werden.

iii) Unabdingbar um (obige) Ruthenium(II)-Lichtsammelkomplexe in Grätzel-Zellen zu verwenden ist die Einführung einer Ankergruppe, die eine kovalente Bindung zum Titandioxid-halbleiter herstellt. Die hier verwendete Carboxylsäureankergruppe hat unerwarteterweise einen erheblichen Einfluss auf die optischen Eigenschaften der jeweiligen Protonierungsstufen; dies wurde mittels RR-Spektroskopie charakterisiert. Lediglich eine der drei untersuchten Protonierungsstufen weist einen zum 4-*H*-Imidazol-Brückenliganden gerichteten Ladungstransferzustand auf. Ein solcher Zustand ist jedoch von essentieller Bedeutung, um eine Ladungstrennung zwischen dem Farbstoff (Elektronendonator) und dem Titandioxid (Elektronenakzeptor) zu ermöglichen.

In dieser Arbeit wurde ein Modell eines Ruthenium(II)-Komplex-Titandioxid-Clusters erstellt, um Aussagen über Elektronentransfer- bzw. Injektionsraten in Grätzel-Zellen treffen zu können. Die Berechnung derartiger Elektronentransferraten ist sehr kompliziert, es ist im Rahmen der semiklassischen Marcus-Theorie mit einer Kombination aus quantenmechanischen und molekularmechanischen (QM/MM) Rechnungen und molekular-dynamischen (MD) Simulationen möglich. Solche kombinierten Simulationen sind aufgrund des enormen Rechenaufwandes sehr anspruchsvoll und wurden unseres Wissens noch nicht für derartige Farbstoff-Titandioxid-Aggregate durchgeführt. Die zeitliche Entwicklung des Donor- (vor dem Elektronentransfer) und Akzeptorzustandes (nach dem Elektronentransfer) wird mittels MD-Simulationen verfolgt. In jedem Zeitschritt wird der Rutheniumkomplex bzw. das TiO_2 -Cluster mit DFT und das umgebende Lösungsmittel mit MM beschrieben. Fluktuationen des Lösungsmittels bringen die

beiden Reaktionszustände in eine Anordnung, in welcher ein Elektronentransfer zwischen ihnen erfolgen kann. Aufgrund des hohen Rechenaufwandes dieser Simulationen wurden leider noch keine Gleichgewichtsgeometrien der beiden Reaktionszustände gefunden. Daher wird sich die zukünftige Arbeit darauf konzentrieren, die Potenzialkurven beider Zustände um deren Gleichgewichtslagen zu ermitteln und somit die Reorganisationsenergie, die freie Enthalpie und die Elektronentransferrate im untersuchten Farbstoff-Titandioxid-Modellsystem zu bestimmen.

Die vorliegende Arbeit erzielte Erkenntnisse bezüglich einer Reihe von Lichtsammelsystemen mittels theoretischer Methoden. Die photophysikalischen und photochemischen Eigenschaften derartiger Systeme wurden in Abhängigkeit des pH-Wertes, des Lösungsmittels, der Funktionalisierung und der Ankergruppe bestimmt. Dafür wurden unter anderem Absorptions-, Emissions- und RR-Spektren berechnet, wobei sich besonders die Berechnung von RR-Intensitäten als äußerst gewinnbringend für die Charakterisierung angeregter Zustände erwies. Hierfür wurden auch erstmals RR-Intensitäten auf Grundlage der RASSCF-Methode berechnet. Das erworbene Wissen und die Erkenntnisse um Elektronentransferprozesse ermöglichen ein tieferes Verständnis der untersuchten Lichtsammelsysteme auf dem Gebiet der Solarenergie.

Anhang A

Appendix

Equilibrium Geometries

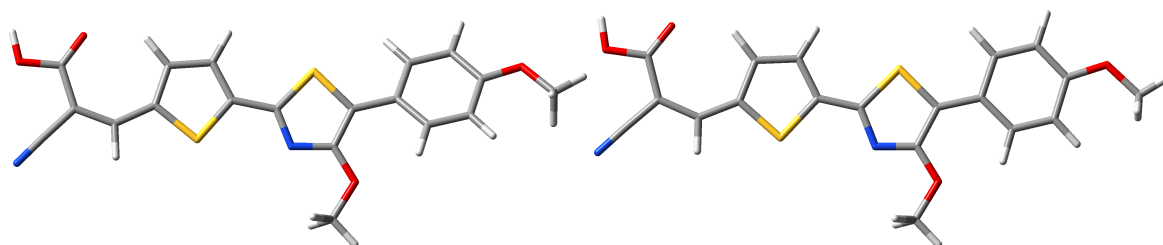


Abbildung A.1: Optimized equilibrium geometries of the electronic ground and first excited singlet states of dye **A** in tetrahydrofurane at the CAM-B3LYP/6-31G(d,p) level of theory.

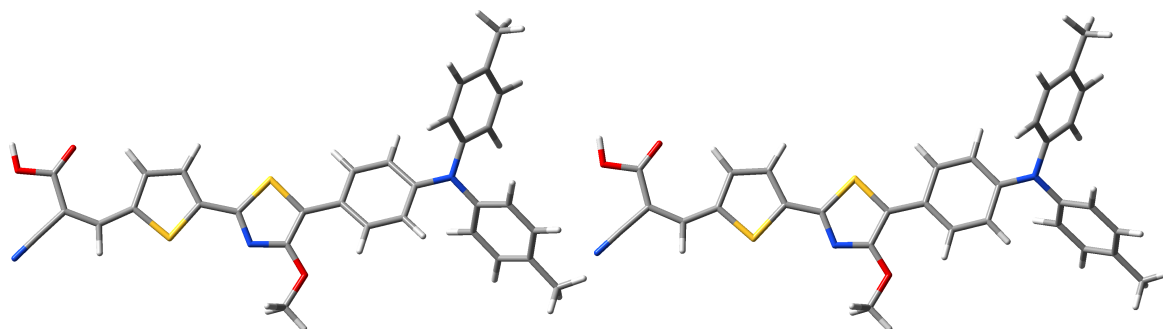


Abbildung A.2: Optimized equilibrium geometries of the electronic ground and first excited singlet states of dye **B** in tetrahydrofurane at the CAM-B3LYP/6-31G(d,p) level of theory.

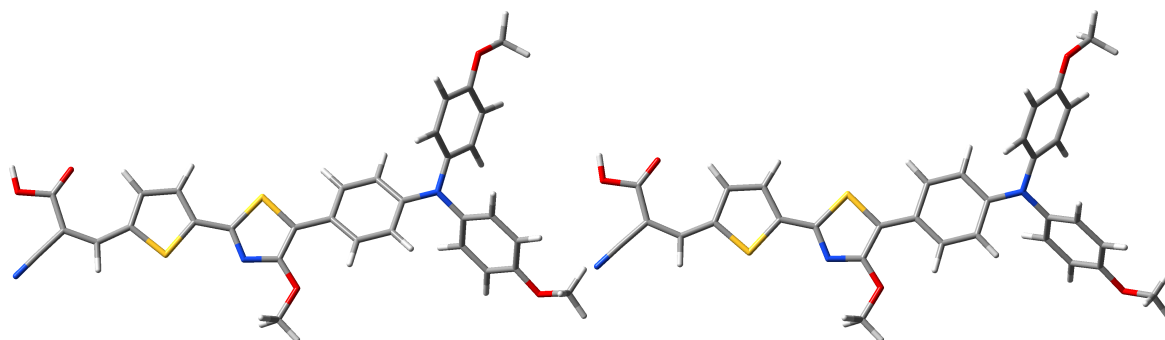


Abbildung A.3: Optimized equilibrium geometries of the electronic ground and first excited singlet states of dye **C** in tetrahydrofurane at the CAM-B3LYP/6-31G(d,p) level of theory.

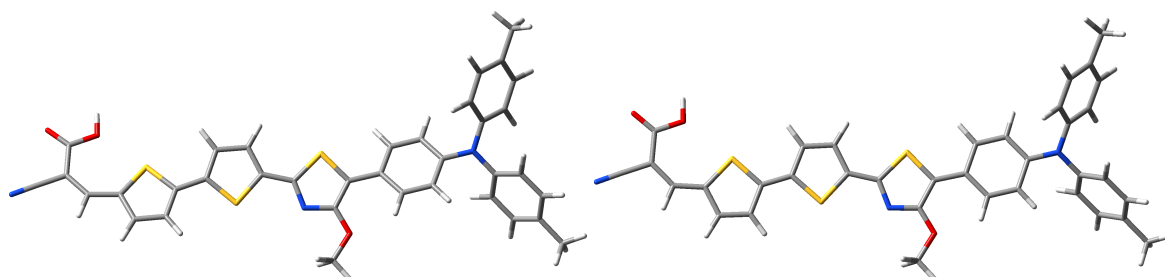


Abbildung A.4: Optimized equilibrium geometries of the electronic ground and first excited singlet states of dye **D** in tetrahydrofurane at the CAM-B3LYP/6-31G(d,p) level of theory.

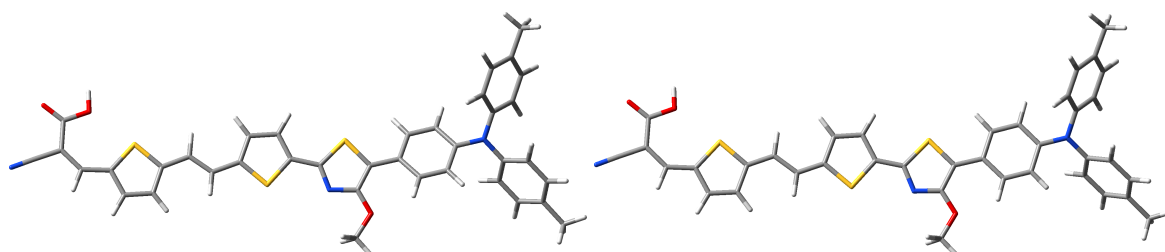


Abbildung A.5: Optimized equilibrium geometries of the electronic ground and first excited singlet states of dye **E** in tetrahydrofurane at the CAM-B3LYP/6-31G(d,p) level of theory.

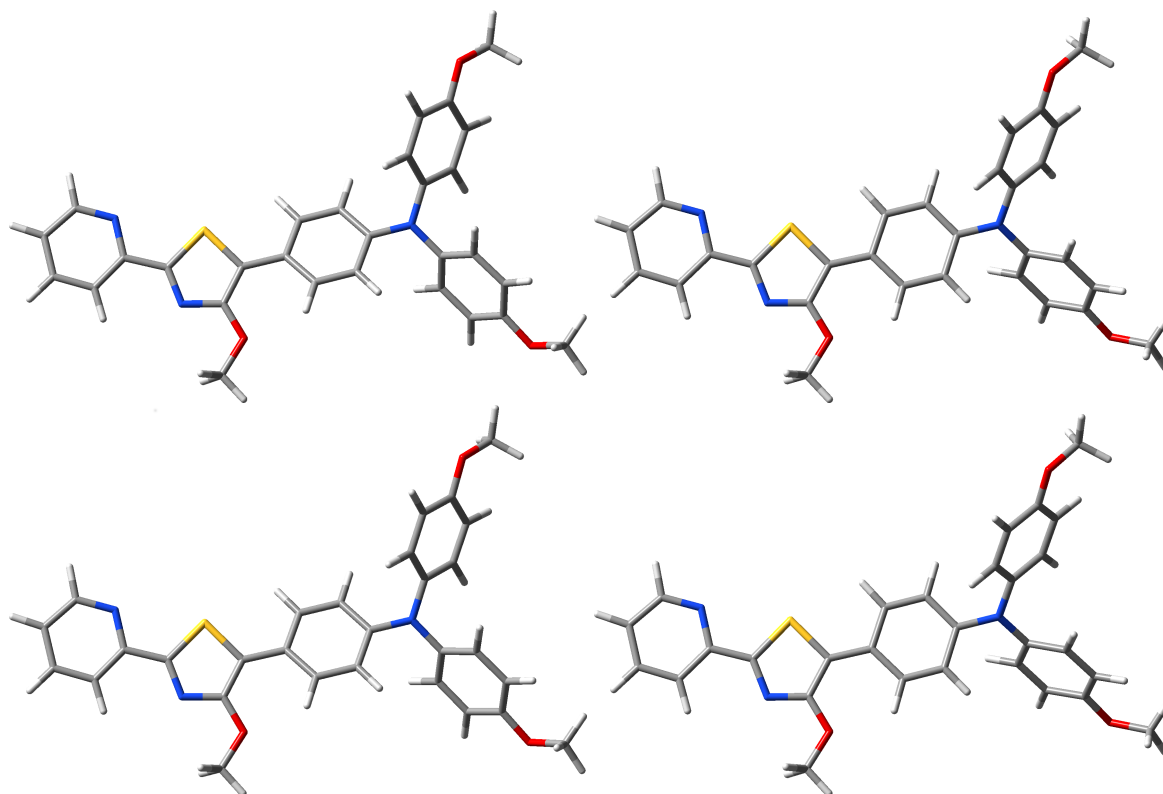


Abbildung A.6: Optimized equilibrium geometries of the electronic ground and first excited singlet states of dye F in MeOH (up) and heptane (down) at the CAM-B3LYP/6-31G(d,p) level of theory.

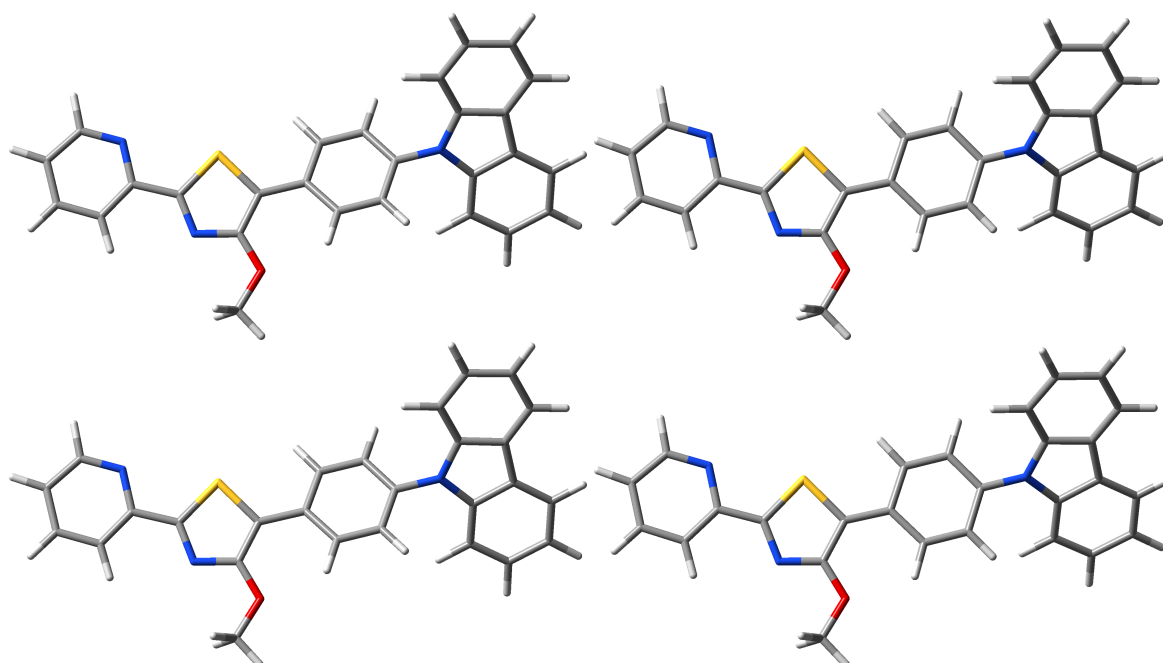


Abbildung A.7: Optimized equilibrium geometries of the electronic ground and first excited singlet states of dye G in MeOH (up) and heptane (down) at the CAM-B3LYP/6-31G(d,p) level of theory.

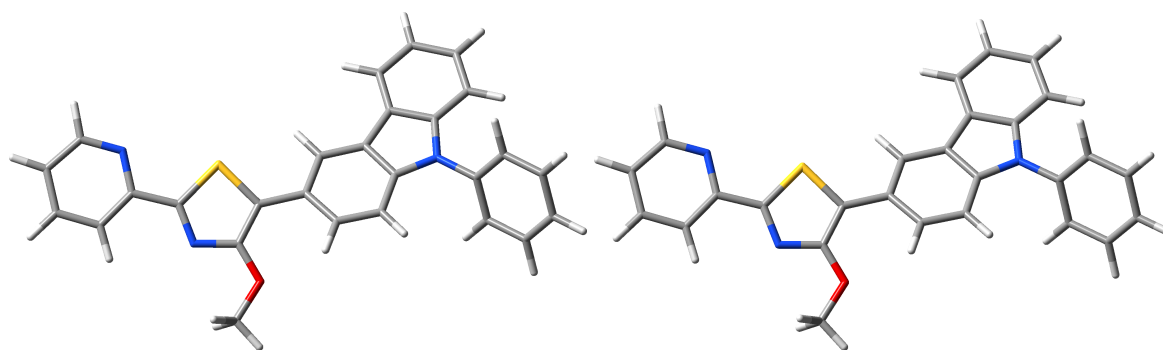


Abbildung A.8: Optimized equilibrium geometries of the electronic ground states of dye **H** in MeOH (left) and heptane (right) at the CAM-B3LYP/6-31G(d,p) level of theory.

Literaturverzeichnis

- [1] Ono, T.-A., Noguchi, T., Inoue, Y., Kusunoki, M., Matsushita, T., and Oyanagi, H. Science **258**, 1335–1337 (1992).
- [2] Yachandra, V. K., Sauer, K., and Klein, M. P. Chem. Rev. **96**, 2927–2950 (1996).
- [3] Messinger, J., Robblee, J. H., Yu, W. O., Yachandra, K. S. V. K., and M. P. Klein, M. J. Am. Chem. Soc. **119**, 11349–11350 (1997).
- [4] Iuzzolino, L., Dittmer, J., Dörner, W., Meyer-Klaucke, W., and Dau, H. Biochemistry **37**, 17112–17119 (1998).
- [5] Messinger, J., Robblee, J. H., Bergmann, U., Iuzzolino, L., Dörner, W., Meyer-Klaucke, W., Sole, V. A., Fernandez, C., Glatzel, H., Visser, R. M., Cinco, R. M., McFarlane, K. L., Bellacchio, E., Pizarro, S. A., Cramer, S. P., Sauer, K., Klein, M. P., and Yachandra, V. K. J. Am. Chem. Soc. **123**, 7804–7820 (2001).
- [6] Ferreira, K. N., Iverson, T. M., Maghlaoui, K., Barber, J., and Iwata, S. Science **303**, 1831–1838 (2004).
- [7] Kulik, V., Epel, B., Lubitz, W., and Messinger, J. J. Am. Chem. Soc. **127**, 2392–2393 (2005).
- [8] Yano, J., Kern, J., Sauer, K., Latimer, M. J., Pushkar, Y., Biesiadka, J., Loll, B., Saenger, W., Messinger, J., Zouni, A., and Yachandra, V. K. Science **314**, 821–825 (2006).
- [9] Siegbahn, P. E. M. and Blomberg, M. R. A. Dalton Trans. , 5832–5840 (2009).
- [10] Umena, Y., Kawakami, K., Shen, J.-R., and Kamiya, N. Nature **473**, 55–60 (2010).
- [11] Proserpio, D. M., Hoffmann, R., and Dismukes, G. C. J. Am. Chem. Soc. **114**, 4374–4382 (1992).
- [12] Mitani, M., Wakamatsu, Y., Katsurada, T., and Yoshioka, Y. J. Phys. Chem. A **110**, 13895–13914 (2006).

- [13] Siegbahn, P. E. M. Chemistry **14**, 8290–8302 (2008).
- [14] Pantazis, D. A., Orio, M., ad S. Zein, T. P., Lubitz, W., Messinger, J., and Neese, F. Phys. Chem. Chem. Phys. **11**, 6788–6798 (2009).
- [15] Siegbahn, P. E. M. Acc. Chem. Res. **42**, 1871–1880 (2009).
- [16] Ames, W., Pantazis, D. A., Krewald, V., Cox, N., Messinger, J., Lubitz, W., and F., F. N. J. Am. Chem. Soc. **133**, 19743–19757 (2011).
- [17] Galstyan, A., Robertazzi, A., and Knapp, E. W. J. Am. Chem. Soc. **134**, 7442–7449 (2012).
- [18] Yamaguchi, K., Yamanaka, S., Isobe, H., Saito, T., Kanda, K., Umena, Y., Kawakami, K., and N. Kamiya, J.-R. S., Okumura, M., Nakamura, H., Shoji, M., and Yoshioka, Y. Int. J. Quantum Chem (2012).
- [19] Kok, B., Forbush, B., and McGloin, M. Photochem. Photobiol. **11**, 457–475 (1970).
- [20] Penner-Hahn, J. E., Fronko, R. M., Pecoraro, V. L., Yocum, C. F., Betts, S. D., and Bowlby, N. R. J. Am. Chem. Soc. **103**, 5529–5537 (1981).
- [21] Loll, B., Kern, J., Saenger, W., Zouni, A., and Biesiadka, J. Nature **438**, 1040–1044 (2005).
- [22] Pushkar, Y., Yano, J., Sauer, K., Boussac, A., and Yachandra, V. K. PNAS **105**, 1879–1884 (2008).
- [23] Dau, H. and Haumann, M. Coord. Chem. Rev. **252**, 273–295 (2008).
- [24] Petrie, S., Gatt, P., Stranger, R., and Pace, R. J. Phys. Chem. Chem. Phys. **14**, 4651–4657 (2012).
- [25] Nakamura, Y., Aratani, N., and Osuka, A. Chem. Soc. Rev. **36**, 831–845 (2007).
- [26] Aratani, N., Kim, D., and Osuka, A. Acc Chem Res. **21**, 1922–1934 (2009).
- [27] Harvey, P. D., Filatov, M. A., and Guillard, R. J. Porphyrins Phthalocyanines **15**, 1150–1171 (2011).
- [28] Nakano, A., Yamazaki, T., Nishimura, Y., Yamazaki, I., and Osuka, A. Acc Chem Res. **6**, 3254–3271 (2000).
- [29] Jiang, D.-L. and Aida, T. J. Am. Chem. Soc. **120**, 10895–10901 (1998).

- [30] Jang, W.-D., Lee, C.-H., Choi, M.-S., and Osada, M. J. Porphyrins Phthalocyanines **13**, 788–793 (2009).
- [31] Uetomo, A., Kozaki, M., Suzuki, S., Yamanaka, K., Ito, O., , and Okada, K. J. Am. Chem. Soc. **133**, 13276–13279 (2011).
- [32] D’Souza, F., Smith, P. M., Zandler, M. E., McCarty, A. L., Itou, M., Araki, Y., and Ito, O. J. Am. Chem. Soc. **126**, 7898–7907 (2004).
- [33] Sutton, L. R., Pirner, M. S. K. S., Hirsch, A., Guldi, D. M., and Gisselbrencht, J.-P. Chemistry **126**, 10370–10381 (2004).
- [34] El-Khouly, M. E., Wijesinghe, C. A., Nesterov, V. N., Zandler, M. E., Fukuzumi, S., and F., F. D. Chemistry **18**, 13844–13853 (2012).
- [35] Menzel, R., Täucher, E., Weiß, D., Beckert, R., and Görls, H. Z. Anorg. Allg. Chem. **636**, 1380–1385 (2010).
- [36] Menzel, R., Breul, A., Pietsch, C., Schäfer, J., Friebe, C., Täuscher, E., Weiß, D., Dietzek, B., Popp, J., Beckert, R., and Schubert, U. S. Macromol. Chem. Phys. **212**, 840–848 (2011).
- [37] Tschierlei, S., Karnahl, M., Presselt, M., Dietzek, B., Guthmuller, J., González, L., Schmitt, M., Rau, S., and Popp, J. Angew. Chem. Int. Ed. **49**, 3981–3984 (2010).
- [38] Förster, T. Ann. Phys. **6**, 55–75 (1948).
- [39] Stryer, L. Ann. Rev. Biochem. **47**, 819–846 (1978).
- [40] O’Regan, B. and Grätzel, M. Nature **353**, 737–740 (1991).
- [41] Aleksic, J., Zielke, P., and Szymczyk, J. A. Ann. N.Y. Acad. Sci. **972**, 158–163 (2002).
- [42] Englman, R. and Jortner, J. Molec. Phys. **18**, 145–164 (1970).
- [43] Odobel, F. and Zabri, H. Inorg. Chem. **44**, 5600–5611 (2005).
- [44] Hagfeldt, A., Boschloo, G., Sun, L., Kloo, L., and Pettersson, H. Chem. Rev. **110**, 6595–6663 (2010).
- [45] Hagberg, D. P., Marinado, T., Karlsson, K. M., Nonomura, K., Qin, P., Boschloo, G., Brinck, T., Hagfeldt, A., and Sun, L. J. Org. Chem. **72**, 9550–9556 (2007).
- [46] Giardi, M. T., Cona, A., and Geiken, B. Bioelectrochem Bioenerg. **38**, 67–75 (1995).

- [47] Rich, P. Biochem. Soc. Trans. **31**, 1095–1105 (2003).
- [48] Peskin, U., Abu-Hilu, M., and Speiser, S. Opt. Mater. **24**, 23–29 (2003).
- [49] Correia, H. M. and Ramos, M. M. Mat. Sci. Eng. C-Biomim. **25**, 682–686 (2005).
- [50] Martsinovich, N. and Troisi, A. Energy Environ. Sci. **4**, 4473–4495 (2011).
- [51] Kelley, S. O. and Barton, J. K. Science **232**, 375–381 (1999).
- [52] Berlin, Y. A., Kurnikov, I. V., Beratan, D., Ratner, M. A., and Burin, A. L. Top Curr. Chem. **237**, 1–36 (2004).
- [53] Brunschwig, B. S., Creutz, C., Macartney, D. H., Sham, T.-K., and Sutin, N. Faraday Discuss. Chem. Soc. **74**, 113–127 (1982).
- [54] Sutin, N. Theory of Electron Transfer Reactions. Wiley-VCH, New York, (1986).
- [55] Moser, C. C., Keske, J. M., Warncke, K., Farid, R. S., and Dutton, P. L. Nature **355**, 796–802 (1992).
- [56] Gray, H. B. and Winkler, J. R. Q. Rev. Biophys. **36**, 341–372 (2003).
- [57] Marcus, R. A. J. Chem. Phys. **24**, 966–978 (1956).
- [58] and R. A. Marcus, P. S. J. Am. Chem. Soc. **103**, 741–747 (1981).
- [59] and R. A. Marcus, P. S. J. Am. Chem. Soc. **103**, 748–752 (1981).
- [60] Song, X. and Marcus, R. A. J. Chem. Phys. **99**, 7768–7773 (1993).
- [61] Arifin, K., Majlan, E. H., Daud, W. R. W., and Kassim, M. B. Int. J. Hydrogen Energy **37**, 3066–3087 (2012).
- [62] Born, M. and Oppenheimer, R. Ann.Phys. **84**, 457–484 (1927).
- [63] Slater, J. C. Phys. Rev. **34**, 1293–1322 (1929).
- [64] Hartree, D. R. Proc. Cambridge Phil. Sc. **24**, 111–132 (1928).
- [65] Roothaan, C. C. J. Rev. Mod. Phys. **23**, 69–89 (1951).
- [66] Hall, G. G. Proc. R. Soc. London A **205**, 541–552 (1951).
- [67] Roos, B. O. Wiley-VCH, Chicester, (1987).
- [68] Malmqvist, P.-Å., Rendell, A., and Roos, B. O. J. Phys. Chem. **94**, 5477–5482 (1990).

- [69] Olsen, J., Roos, B. O., Jørgensen, P., and Jensen, H. J. A. J. Chem. Phys. **89**, 2185–2192 (1988).
- [70] Baron Rayleigh, J. W. S. The Theory of Sound, volume 1. MacMillian and Co., (1877).
- [71] Schrödinger, E. Ann. Phys. **80**, 437–490 (1926).
- [72] Andersson, K., Malmqvist, P.-Å., Roos, B. O., Sadlej, A. J., and Wolinski, K. J. Phys. Chem. **94**, 5483–5488 (1990).
- [73] Andersson, K., Malmqvist, P.-Å., and Roos, B. O. J. Chem. Phys. **96**, 1218–1226 (1992).
- [74] Manni, G. L., Aquilante, F., and Gagliardi, L. J. Chem. Phys. **134**, 0341141–0341145 (2011).
- [75] Malmqvist, P.-Å., Pierloot, K., Shahi, A. R. M., Cramer, C. J., and Gagliardi, L. J. Chem. Phys. **128**, 20410901–20410910 (2008).
- [76] Finley, J., Malmqvist, P.-A., Roos, B. O., and Serrano-Andrés, L. Chem. Phys. Lett. **288-306**, 299 (1998).
- [77] Andersson, K. and Roos, B. . Chem. Phys. Lett. **245**, 215–223 (1995).
- [78] Hohenberg, P. and Kohn, W. Phys. Rev. **136**, 864–871 (1964).
- [79] Kohn, W. and Sham, L. J. Phys. Rev. **140**, 1133–1138 (1965).
- [80] Koch, W. and Holthausen, M. C. A Chemist's Guide to Density Functional Theory. Wiley-VCH, Weinheim, 2nd edition, (2001).
- [81] Levine, I. N. Quantum Chemistry. Prentice Hall, 5th edition, (2000).
- [82] Becke, A. D. J. Chem. Phys. **98**, 5648–5652 (1993).
- [83] Lee, C., Yang, W., and Parr, R. G. Phys. Rev. B **37**, 785–789 (1988).
- [84] Becke, A. D. Phys. Rev. A **38**, 3098–3100 (1988).
- [85] Vosko, S. H., Wilk, L., and Nusair, M. Cad. J. Phys. **58**, 1200–1211 (1980).
- [86] Stephens, P. J., Jalkanen, K. J., Delvin, F. J., and Chabalowski, C. F. J. Phys. Chem. **97**, 6107–6110 (1993).
- [87] Bauernschmitt, R. and Ahlrichs, R. Chem. Phys. Lett. **256**, 454–464 (1996).
- [88] Tozer, D. J. and Handy, N. C. J. Chem. Phys. **109**, 10180–10189 (1998).

- [89] Tozer, D. J., Amos, R. D., Handy, N. C., Roos, B. O., and Serrano-Andrés, L. Mol. Phys. **97**, 859–868 (1999).
- [90] Dreuw, A., Weisman, J. L., and Head-Gordon, M. J. Chem. Phys. **119**, 2943–2946 (2003).
- [91] Dreuw, A. and Head-Gordon, M. J. Am. Chem. Soc. **126**, 4007–4016 (2004).
- [92] Bernasconi, L., Sprik, M., and Hutter, J. J. Chem. Phys. **119**, 12417–12431 (2003).
- [93] Magyar, R. J. and Tretiak, S. J. Chem. Theory Comput. **3**, 976–987 (2007).
- [94] Adamo, C. and Barone, V. J. Chem. Phys. **110**, 6158–6170 (1999).
- [95] Zhao, Y. and Truhlar, D. G. Theor. Chem. Acc. **120**, 215–241 (2008).
- [96] Martínez-Fernández, L., González, L., and Corral, I. Comput. and Theoret. Chem. **975**, 13–19 (2011).
- [97] Guthmuller, J. and Champagne, B. J. Chem. Phys. **127**, 16450701–16450711 (2007).
- [98] Yanai, T., Tew, D. P., and Handy, N. C. Chem. Phys. Lett. **393**, 51–57 (2004).
- [99] Runge, E. and Gross, E. K. U. Phys. Rev. Lett. **52**, 997 (1984).
- [100] Yabana, K. and Bertsch, G. F. Phys. Rev. B **54**, 4484–4487 (1996).
- [101] González, L., Escudero, D., and Serrano-Andrés, L. Chem. Phys. Chem. **13**, 28–51 (2012).
- [102] Warshel, A. and Levitt, M. J. Mol. Biol. **103** (1976).
- [103] Tomasi, J., Mennucci, B., and Cammi, R. Chem. Rev. **105**, 2999–3093 (2005).
- [104] Newton, I. Philosophiae Naturalis Principia Mathematica. (1687).
- [105] Heisenberg, W. Z. Phys. **43**, 172–198 (1927).
- [106] Wigner, E. Phys. Rev. **40**, 749–759 (1932).
- [107] Raman, C. V. The molecular scattering of light. University of Calcutta, (1922).
- [108] Smekal, A. Naturwiss. **11**, 873–875 (1923).
- [109] Landsberg, G. and Mandelstam, L. Naturwiss. **16**, 557–558 (1928).
- [110] Albrecht, A. C. J. Chem. Phys. **34**, 1476–1484 (1961).

- [111] Long, D. A. The Raman Effect A Unified Treatment of the Theory of Raman Scattering by Molecules. John Wiley & Sons Ltd, Chichester, (2002).
- [112] Kramers, H. A. and W. Heisenberg, W. Z. Phys. **31**, 681–708 (1925).
- [113] Dirac, P. A. M. Proc. R. Soc. London Series A **114**, 243–265 (1927).
- [114] Franck, J. Trans Faraday Soc. **21**, 536–542 (1926).
- [115] Condon, E. U. Phys. Rev. **28**, 1182–1201 (1926).
- [116] Condon, E. U. Phys. Rev. **32**, 858–872 (1928).
- [117] Hizhnyak, V. and Tehver, I. Phys. Status Solidi **21**, 755–768 (1967).
- [118] Tonks, D. L. and Page, J. B. Chem. Phys. Lett. **66**, 449–453 (1979).
- [119] Blazej, D. C. and Peticolas, W. L. J. Chem. Phys. **72**, 3134–3142 (1980).
- [120] Page, J. B. and Tonks, D. L. J. Chem. Phys. **75**, 5694–5708 (1981).
- [121] Peticolas, W. L. and Rush, T. J. Comput. Chem. **16**, 1261–1270 (1995).
- [122] Heller, E. J., Sundberg, R. L., and Tannor, D. J. Phys. Chem. **86**, 1822–1833 (1982).
- [123] Marcus, R. A. J. Chem. Phys. **43**, 679–701 (1965).
- [124] Warshel, A. J. Phys. Chem **86**, 2218–2224 (1982).
- [125] Tateyama, Y., Blumberger, J., Sprik, M., and Tavernelli, I. J. Chem. Phys. **122**, 23450501–23450517 (2005).
- [126] Blumberger, J. Phys. Chem. Chem. Phys. **10**, 5651–5667 (2008).
- [127] Zwanzig, R. W. J. Chem. Phys. **22**, 1420–1426 (1954).
- [128] Tachiya, M. J. Phys. Chem. **93**, 7050–7052 (1989).
- [129] Blumberger, J. and Sprik, M. Theo. Chem. Acc. **115**, 113–126 (2006).
- [130] Marcus, R. A. and Sutin, N. Biochim. Biophys. Acta **811**, 265–322 (1985).
- [131] Page, C. C., Moser, C. C., Chen, X. X., and Dutton, P. L. Nature **402**, 47–52 (1999).
- [132] Hu, L., Farrokhnia, M., Heimdal, J., Shleev, S., Rulisek, L., and Ryde, U. J. Phys. Chem. B **115**, 13111–13126 (2011).

- [133] Sigfridsson, E., Olsson, M. H. M., and Ryde, U. *Inorg. Chem.* **40**, 2509–2519 (2001).
- [134] Ryde, U. and Olsson, M. H. M. *Int. J. Quantum Chem.* **81**, 335–347 (2001).
- [135] Zhang, Y. K. and Yang, W. T. *J. Chem. Phys.* **109**, 2604–2608 (1998).
- [136] Marder, S. R., Perry, J. W., Bourhill, G., Gorman, C. B., Tiemann, B. G., and Mansour, K. *Science* **261**, 186–189 (1993).
- [137] Mennucci, B., Cappelli, C., Guido, C. A., Cammi, R., and Tomasi, J. *J Phys. Chem. A* **113**, 3009–3020 (2009).
- [138] Kupfer, S., Guthmuller, J., Wächtler, M., Losse, S., Rau, S., Dietzek, B., Popp, J., and González, L. *Phys. Chem. Chem. Phys.* **13**, 15580–15588 (2011).
- [139] Wächtler, M., Kupfer, S., Guthmuller, J., Popp, J., González, L., and Dietzek, B. *J. Phys. Chem. C* **115**, 24004–24012 (2011).
- [140] Kupfer, S., Wächtler, M., Guthmuller, J., Popp, J., Dietzek, B., and González, L. *J. Phys. Chem. C* **116**, 19968–19977 (2012).
- [141] Andrae, D., Häußermann, U., Dolg, M., Stoll, H., and Preuß, H. *Theor. Chim. Acta* **77**, 123–141 (1990).
- [142] Wächtler, M., Kupfer, S., Guthmuller, J., González, L., and Dietzek, B. *J. Phys. Chem. C* (2012).
- [143] Wyckoff, R. W. G. *Crystal structures*. John Wiley & Sons Ltd, (1963).
- [144] Bates, S. P., Kresse, G., and Gillan, M. J. *Surf. Sci.* **409**, 336–349 (1998).
- [145] Ojamäe, L., Aulin, C., Pedersen, H., and Käll, P.-O. *J. Colloid Interface Sci.* **296**, 71–78 (2006).
- [146] Martsinovich, N., Jones, D. R., and Troisi, A. *J Phys. Chem. C* **114**, 22659–22670 (2010).
- [147] M. Dolg, U. Wedig, H. S. H. P. *J. Chem. Phys.* **86**, 866–872 (1987).
- [148] Lippert, G., Hutter, J., and Parrinello, M. *Mol. Phys.* **92**, 477–487 (1997).
- [149] Lippert, G., Hutter, J., and Parrinello, M. *Theo. Chem Acc.* **103**, 124–140 (1999).
- [150] Laino, T., Mohamed, F., Laio, A., and Parrinello, M. *J. Chem. Theory Comput.* **1**, 1176–1184 (2005).

- [151] Laino, T., Mohamed, F., Laio, A., and Parrinello, M. J. Chem. Theory Comput. **2**, 1370–1378 (2006).
- [152] Perdew, J. P., Burke, K., and Ernzerhof, M. Phys. Rev. Lett. **77**, 3865–3868 (1996).
- [153] Zhang, Y. K. and Yang, W. T. Phys. Rev. Lett. **80**, 890–890 (1998).

Acknowledgements

Here, I want to take the opportunity to thank all people that contributed to this thesis. First of all, I want to thank my parents, **Gabriele** and **Thomas**, for supporting me for the last 27 years. I am very thankful to you, not only for providing me a carefree childhood, but also for arousing my interest in science. Further, I want to show my gratitude to my grandparents, and especially to my grandmother **Traudel** but also to **Helga** and **Gerhard**. I would like to thank my friends, fellow Aikidōka, and Sensei for making my life in Jena more valuable. Last but not least, I want to use the opportunity to thank, you, **Theresa** for enriching my life; at this point I want to show my gratitude to you for enduring my moods, in particular in the last months.

This thesis was prepared in the working group of Prof. Dr. **Leticia González** at the Friedrich-Schiller-Universität Jena. I am very grateful to you, not only for supervising me and giving me the chance to do my PhD in your group but also for the many things I learned from you since I started my “theoretical” OC-V Forschungspraktikum in 2008.

Of fundamental importance for this thesis is Dr. **Julien Guthmuller**, he introduced me to resonance Raman spectroscopy and always had a good advise for me at hand not only in scientific questions. Without his knowledge, helpfulness, and friendship the last years would have been much more troublesome and I am deeply indebted to him.

Special thanks goes to my colleagues, friends and fellow PhD students **Mariana Aßmann**, **Daniel Kinzel**, **Federico Latorre**, and **Martin Richter**. You helped me in countless scientific as well as non-scientific issues and made the time in the office more pleasant, especially in the last months in Vienna. No less Dr. **Daniel Escudero Masa**, Dr. **Marta Łabuda**, Dr. **Verónica Leyva**, Dr. **Guillermo Pérez-Hernández**, **Hartmut Preuß** and **Martin Thomas** are acknowledged for creating a nice working atmosphere in Jena. The same applies to Dr. **Dirk Deubel**, Dr. **Philipp Marquetand**, Dr. **Felix Plasser**, **Leon Freitag**, **Sebastian Mai**, and **Rana Obaid** at the University of Vienna.

Furthermore, I would like to thank Dr. **Dirk Bender**, Dr. **Markus Oppel** and **Michaela Jirowec** for support concerning technical issues. In addition, **Dirk** is acknowledged for many hours of conversations, his friendship, and help in all kinds of life situations. He always had significant influence on me and shaped me to a certain amount for the last seven years.

At this point, I also want to show my gratitude to my experimental partners Prof. Dr. **Benjamin Dietzek** and Prof. Dr. **Rainer Beckert**. Here, **Maria Wächtler** and **Johann Schäfer** are acknowledged for providing me with experimental data such as resonance Raman and absorption spectra and the nice working atmosphere. **Roberto Menzel** is deeply thanked for the nice and fruitful cooperation and of course for the many thiazole systems he synthesized.

Finally, I would like to thank the “Kultusministerium des Freistaats Thüringen” for financial support.

Selbstständigkeitserklärung

Hiermit erkläre ich, dass ich diese Arbeit selbstständig und ohne Zuhilfenahme weiterer als der angegebenen Hilfsmittel angefertigt habe. Alle verwendeten Textausschnitte, Zitate oder Inhalte anderer Verfasser wurden ausdrücklich als solche gekennzeichnet.

Stephan Kupfer

Curriculum vitae

Personal data

Name	Stephan Kupfer
Birth	18 th May 1985, 07381 Pößneck
Citizenship	Federal Republic of Germany
Nationality	Germany
personal status	unmarried
Working address	Friedrich-Schiller-University Jena Institute of Physical Chemistry Helmholtzweg 4, 07743 Jena
E-mail	stephan.kupfer@uni-jena.de

Scientific experience

2010–2012	Doctoral studies in the group of Prof. Dr. Leticia González at the Institute of Physical Chemistry, Friedrich-Schiller-University Jena, Germany
-----------	-------------------------------------------------------------------------------------------------------------------------------------------------

Degrees and education

December 2009	Diploma in Chemistry Thesis: “Quantum Simulations for Light Induced <i>cis/trans</i> Moleculare Switches”
2004–2009	Studies of Chemistry, Friedrich-Schiller-University Jena, Germany
June 2003	Abitur
1995–2003	Staatliches Gymnasium “Am Weißen Turm”, Pößneck
1993–1995	Staatliche Grundschule 4, Pößneck
1991–1993	Staatliche Grundschule 3, Pößneck

Military service

2003-2004	Panzerpionierkompanie 300, Hardheimer Straße 1, 97000 Kulsheim
-----------	----------------------------------------------------------------

Attended conferences

July 2012	24 th IUPAC Symposium on Photochemistry, Coimbra, Portugal
June 2011	Quantum Bioinorganic Chemistry 3, Český Krumlov, Czech Republic
April 2011	Faraday Discussion 150: Frontiers in Spectroscopy, Basel, Switzerland
July 2010	23 th IUPAC Symposium on Photochemistry, Ferrara, Italy

Oral Presentations

22 th October 2012	“From charge transfer to electron transfer or from black absorbers to dye sensitized solar cells”, invited by Prof. Dr. Leticia González, Institute for Theoretical Chemistry, University of Vienna, Austria
15 th March 2012	“Light-harvesting antenna systems: Charge-Transfer traced by TDDFT and RASPT2 methods”, invited by Prof. Jozef Sienkiewicz, Department of Theoretical Physics and Quantum Informatics, Gdańsk University of Technology, Poland
27 th June 2011	“TDDFT and RASSCF calculations on antenna systems based on Ruthenium complexes and organic chromophores”, Quantum Bioinorganic Chemistry 3, Český Krumlov, Czech Republic

Poster Presentations

July 2012	“TDDFT and RASPT2 calculations on light harvesting antennas based on organic chromophores”, Stephan Kupfer, Julien Guthmuller, Leticia González, 24 th IUPAC Symposium on Photochemistry, Coimbra, Portugal
July 2011	“Excited-state Dynamics in Environmentally Responsive Ruthenium(II)-Polypyridine Dyes”, Maria Wächtler, Stephan Kupfer, Benjamin Dietzek, Sven Rau, Rainer Beckert, Julien Guthmuller, Leticia González, Jürgen Popp, 19 th International Symposium on the Photophysics and Photochemistry of Coordination Compounds, Strasbourg, France
April 2011	“Photonic Micelles-Protonation Effectson Ruthenium Complexes with Imidazole Bridging Ligands”, Stephan Kupfer, Julien Guthmuller, Maria Wächtler, Benjamin Dietzek, Jürgen Popp, Leticia González, Faraday Discussion 150: Frontiers in Spectroscopy, Basel, Switzerland
July 2010	“Photonic Micelles-Ruthenium Complexes with Imidazole Bridging Ligands”, Stephan Kupfer, Julien Guthmuller, Maria Wächtler, Benjamin Dietzek, Jürgen Popp, Leticia González, 23 th IUPAC Symposium on Photochemistry, Ferrara, Italy

June 2011 “Excited-state Dynamics in 4*H*-imidazole-Ruthenium(II) Dyes”, Maria Wächtler, Stephan Kupfer, Benjamin Dietzek, Sven Rau, Rainer Beckert, Julien Guthmuller, Leticia González, Jürgen Popp, 110th Bunsentagung, Berlin, Germany

Complementary training in foreign laboratories

April–September 2012 Working in the group of Prof. Dr. Leticia González at the Institute for Theoretical Chemistry, University of Vienna, Austria

March 2012 One week staying in the group of Prof. Jozef Sienkiewicz at the Department of Theoretical Physics and Quantum Informatics, Gdańsk University of Technology, Poland

Teaching experience

2012 Supervision of a bachelor-thesis (Michael Siegmann)

2011 Supervision of two organic chemistry research practica (Forschungspraktikum OC-V; Sebastian Mai and Martin Thomas)

2011 Supervision of one physical chemistry research practica (Forschungspraktikum PC-V; Joachim Kübel)

2010-2011 Quantum Chemistry practica (Vertiefungsfach; 7th and 8th semester)

2010 Quantum Chemistry practica (Wahlpflichtfach; 6th)

Language skills

German Mother tongue

English Fluent in writing and speaking

French Basic knowledge

IT skills

Scientific Quantum chemistry suites (Gaussian 09, Molcas, Turbomole), CP2K, molecular and scientific visualization software, \LaTeX

General Office suites, Windows and UNIX/Linux based OSs

List of Publications

1. Kupfer, S., Guthmuller, J., Wächtler, M., Losse, S., Rau, S., Dietzek, B., Popp, J., and González, L.
Protonation effects on the resonance Raman properties of a novel (terpyridine)Ru(imidazole) complex: An experimental and theoretical case study
Phys. Chem. Chem. Phys. **13**, 15580-15588 (2011)
2. Wächtler, M., Kupfer, S., Guthmuller, J., Popp, J., González, L., and Dietzek, B.
Influence of multiple protonation on the initial excitation in a black dye
J. Phys. Chem. C **115**, 24004-24012 (2011)
3. Menzel, R., Ogermann, D., Kupfer, S., D. Weiß, Görls, H., Kleinermanns, K., González, L., and Beckert, R.
4-Methoxy-1,3-thiazole based donor-acceptor dyes: Characterization, X-ray structure, DFT calculations and test as sensitizers for DSSC
Dyes Pigm. **94**, 512-524 (2012)
4. Menzel, R., Kupfer, S., Mede, R., Weiß, D., Görls, H., González, L., and Beckert, R.
Arylamine-modified thiazoles as donor-acceptor dyes: Quantum chemical evaluation of the charge transfer process and test as ligands in Ruthenium(II) complexes
Eur. J. Org. Chem. **27**, 5231-5247 (2012)
5. Kupfer, S., Wächtler, M., Guthmuller, J., Popp, J., Dietzek, B. and L. González
A novel Ru(II) polypyridine black dye investigated by resonance Raman spectroscopy and TDDFT calculations
J. Phys. Chem. C **116**, 19968-19977 (2012)
6. Kupfer, S., Pérez-Hernández, G., and González, L.
Singlet oxygen generation versus O–O homolysis in phenyl substituted anthracene-endoperoxides investigated by RASPT2, CASPT2, CC2 and TD-DFT methods
Theor. Chem. Acc. **131**, 1295-1308 (2012)

7. Wächtler, M., Kupfer, S., Guthmuller, J., Rau, S., González, L., and Dietzek, B.
Structural control of photoinduced dynamics in 4*H*-imidazole-Ruthenium dyes
J. Phys. Chem. C, (in press), (2012)
8. Kupfer, S., Guthmuller, J., and González, L.
An Assessment of RASSCF and TDDFT Energies and Gradients on an Organic Donor-Acceptor Dye assisted by Resonance Raman Spectroscopy
J. Chem. Theo. Comput., (accepted), (2012)
9. Menzel, R., Kupfer, S., Mede, R., Weiß, D., Görls, H., González, L., and Beckert, R.
Synthesis, properties and quantum chemical evaluation of solvatochromic pyridinium-phenyl-thiazol-4-olate betaine dyes
Tetrahedron Lett., (submitted), (2012)

Contributions to the appended publications

1. Kupfer, S., Guthmuller, J., Wächtler, M., Losse, S., Rau, S., Dietzek, B., Popp, J., and González
**Protonation effects on the resonance Raman properties of a novel (terpyridine)Ru(imi-
dazole) complex: An experimental and theoretical case study**
Phys. Chem. Chem. Phys. **13**, 15580-15588 (2011)

My contribution to this article was the accomplishment of all quantum chemical calculations, their analysis, the simulation of absorption and resonance Raman spectra, and the writing of the manuscript. Julien Guthmuller and Maria Wächtler have been involved in the assignment of simulated and experimental resonance Raman bands. Maria Wächtler performed furthermore all UV/vis absorption and resonance Raman measurements. The complexes were synthesized by Sebastian Loose. Sven Rau, Benjamin Dietzek and Jürgen Popp supervised the synthesis and spectroscopical experiments, respectively. Leticia González and Julien Guthmuller supervised the theoretical work, and polished the manuscript.

2. Wächtler, M., Kupfer, S., Guthmuller, J., Popp, J., González, L., and Dietzek, B.
Influence of multiple protonation on the initial excitation in a black dye
J. Phys. Chem. C **115**, 24004-24012 (2011)

All quantum chemical calculations, the analysis of the theoretical results, the simulation of absorption and resonance Raman spectra, and the writing of the computational details have been performed by myself. Julien Guthmuller assisted with his expertise to the analysis of the theoretical results. The spectroscopy was performed by Maria Wächtler as well as the main writing of the manuscript, except for the computational part. Leticia González supervised the quantum chemical calculations. Jürgen Popp and Benjamin Dietzek supervised the experimental work.

3. Menzel, R. Ogermann, D., Kupfer, S., D. Weiß, Görls, H., Kleinermanns, K., González, L., and Beckert, R.
4-Methoxy-1,3-thiazole based donor-acceptor dyes: Characterization, X-ray structure, DFT calculations and test as sensitizers for DSSC
Dyes Pigm. **94**, 512-524 (2012)

I contributed to this publication with the accomplishment of all quantum chemical calculations, their analysis, and the writing of the "Computational methods" as well as the

"Computational results". The synthesis and experimental characterization was performed by Roberto Menzel, while the X-ray structure was measured by Helmar Görls. Daniel Ogermann prepared the dye sensitized solar cells and measured their performance, this was supervised by Karl Kleinermanns. The theoretical work was guided by Leticia González, while the synthesis was supervised by Dieter Weiß and Rainer Beckert.

4. Menzel, R., Kupfer, S., Mede, R., Weiß, D., Görls, H., González, L., and Beckert, R.
Arylamine-modified thiazoles as donor-acceptor dyes: Quantum chemical evaluation of the charge transfer process and test as ligands in Ruthenium(II) complexes
Eur. J. Org. Chem. **27**, 5231-5247 (2012)

All theoretical calculations have been performed by myself, including the simulation of absorption and emission spectra. The rationalization of planar or twisted intra-molecular charge transfer processes, based on the quantum chemical simulations, was also done by myself. I contributed the section "Quantum Chemical Calculations on A1 and D1". The synthesis and spectroscopy was done by Roberto Menzel and Ralf Mede, while the X-ray spectroscopy was performed by Helmar Görls. Roberto Menzel also wrote the remaining sections of the manuscript. Dieter Weiß and Rainer Beckert, and Leticia González supervised the experimental and theoretical work, respectively.

5. Kupfer, S., Wächtler, M., Guthmuller, J., Popp, J., Dietzek, B. and L. González
A novel Ru(II) polypyridine black dye investigated by resonance Raman spectroscopy and TDDFT calculations
J. Phys. Chem. C **116**, 19968-19977 (2012)

The performed quantum chemical calculations, the simulation of absorption and resonance Raman spectra, the analysis of the corresponding results, the assignment of theoretical of experimental bands (absorption and resonance Raman) and the writing of the article have been done by myself, while Julien Guthmuller contributed with his expertise. The experimental absorption and resonance Raman measurements have been carried out by Maria Wächtler, she also contributed the section "Experimental details". The experimental and theoretical work was supervised by Benjamin Dietzek and Leticia González, respectively.

6. Wächtler, M., Kupfer, S., Guthmuller, J., Rau, S., González, L., and Dietzek, B.
Structural control of photoinduced dynamics in 4H-imidazole-Ruthenium dyes
J. Phys. Chem. C, (submitted), (2012)

The calculation of the relaxation pathways upon photoexcitation as well as the simulation

of absorption and resonance Raman spectra of the complexes RuCOOEt and RuHCOOEt have been performed and rationalized by myself. Furthermore, I wrote the computational details and the discussion of theoretical results concerning the relaxation pathways. Julien Guthmuller contributed with his expertise to the calculation of resonance Raman intensities. All experimental measurements and writing of the manuscript, except for the aforementioned sections, were done by Maria Wächtler and supervised by Benjamin Dietzek. Leticia González supervised the theoretical part of this article.

7. Kupfer, S., Guthmuller, J., and González, L.

An Assessment of RASSCF and TDDFT Energies and Gradients on an Organic Donor-Acceptor Dye assisted by Resonance Raman Spectroscopy

J. Chem. Theo. Comput., (submitted), (2012)

I carried out all calculations, simulations of absorption and resonance Raman spectra, the analysis of the obtained results and the writing of the manuscript. Julien Guthmuller contributed with his expertise concerning the analysis of the TDDFT and calculation of resonance Raman intensities. Leticia González supervised this work and contributed to the writing of the publication.

Prof. Dr. Leticia González

